Analysis of low-mass and high-mass systems after the common-envelope phase

Analyse von Sternsystemen niedriger und hoher Masse nach der Common-Envelope Phase

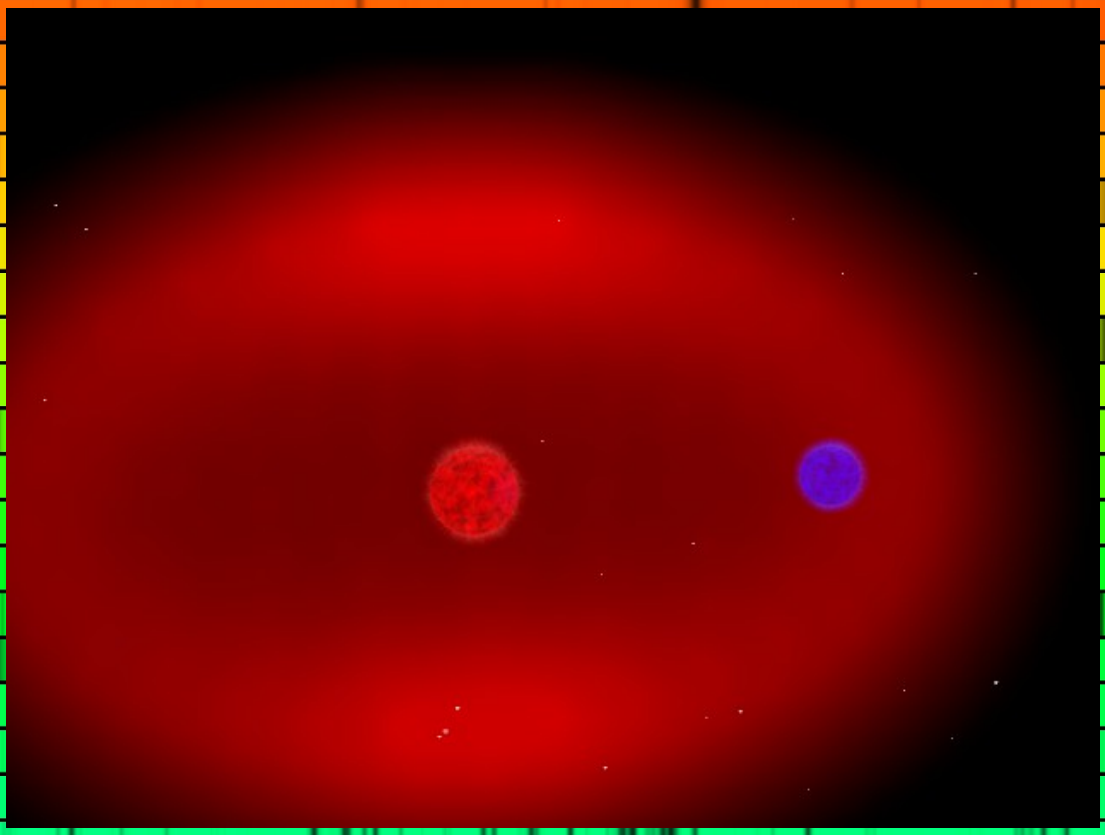

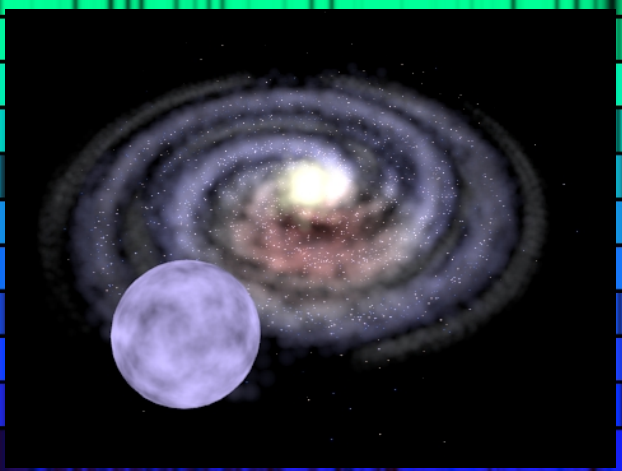

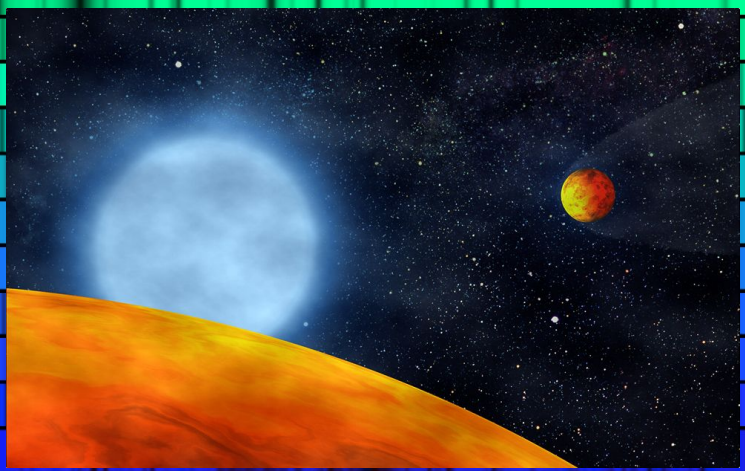

Analysis of low-mass and high-mass systems after the common-envelope phase

Analyse von Sternsystemen niedriger und hoher Masse nach der Common-Envelope Phase

Der Naturwissenschaftlichen Fakultät
der Friedrich-Alexander-Universität Erlangen-Nürnberg
zur Erlangung des Doktorgrades Dr. rer. nat.
vorgelegt von

Veronika Katharina Schaffenroth

aus
Sulzbach-Rosenberg

Als Dissertation genehmigt
von der Naturwissenschaftlichen Fakultät
der Friedrich-Alexander-Universität Erlangen-Nürnberg

Tag der mündlichen Prüfung: 17.07.2015

Vorsitzender des Promotionsorgans: Prof. Dr. Jörn Wilms
Gutachter: Prof. Dr. Ulrich Heber und Prof. Dr. Norbert Przybilla
Gutachter: Prof. Dr. Rolf-Peter Kudritzki

Cover page: Illustrations of the common-envelope phase of two stars and the ejection of a runaway star out of the galaxy by Andreas Irrgang, and an illustration of planets orbiting a hot subdwarf star by Stephane Charpinet.
Background: Solar spectrum, credit: N. A. Sharp, NOAO/NSO/Kitt Peak FTS/AURA/NSF

Zusammenfassung

Als enge Doppelsterne bezeichnet man zwei gravitativ gebundene Sterne mit so geringem Abstand, dass sie in ihrer Lebenszeit mindestens einmal wechselwirken. Dies geschieht meistens durch Massentransfer in der Roten Riesen Phase. Wenn beide Sterne ähnliche Masse besitzen, beginnt ein stabiler Massentransfer über den Lagrange Punkt zwischen beiden Sternen auf den Begleiterstern, sobald der massereichere Stern sich zur Roten Riesen Phase hin entwickelt und dabei ausdehnt. Wenn der Massenunterschied in einem engen Doppelstern $M_1/M_2 > 1.5$ überschreitet, kann der Begleiter jedoch nicht die gesamte transferierte Masse aufnehmen und es bildet sich eine gemeinsame Hülle (Common Envelope) um beide Sterne. Dieses kurze Stadium wird "Common-Envelope Phase" genannt. Aufgrund von Reibung mit der Hülle schrumpft der Abstand beider Sterne und die dabei frei werdende Orbitalenergie kann benutzt werden, um die Hülle abzustoßen. Dabei entsteht ein sehr enges post Common-Envelope Doppelsternsystem (PCEB). Diese Phase ist äußerst wichtig für das Verständnis der Doppelsternentwicklung und dient der Erklärung einiger Phänomene von kosmologischer Bedeutung wie zum Beispiel die Supernovae vom Typ Ia. Trotz ihrer großen Bedeutung ist unser Verständnis dafür leider noch sehr begrenzt. Die Beobachtung von Doppelsternsystemen, in denen der Abstand beider Sterne im Bereich von einem Sonnenradius ist – viel kleiner als die typische Ausdehnung eines Roten Riesen – zeigt, dass diese Phase existieren muss. Jedoch sind die physikalischen Prozesse noch nicht verstanden. Im Moment wird diese Phase in der Modellierung nur parameterisiert. Die Modellparameter für die Effizienz von Energie- und Drehimpulstransport sind jedoch noch immer unbekannt.

Diese Arbeit beschäftigt sich mit der Analyse von Systemen mit geringer Masse nach der Common-Envelope Phase sowie einem einzigartigen, massereichen Stern, einem sogenannten Hyper-Runaway Stern, der ebenfalls durch eine Common-Envelope Ejektionsphase (CEE) gegangen sein muss. Die Systeme mit niedriger Masse, die hier untersucht wurden, bestehen aus einem heißen Subdwarf Primärstern mit einem Hauptreihenstern niedriger Masse oder einem braunen Zwerg als Begleiter. Heiße Subdwarfs vom Spektraltyp B (sdBs) sind Sterne, die sich in der Phase des Kern-Helium-Brennens befinden, jedoch fast ihre gesamte Wasserstoffhülle auf dem Roten Riesenast verloren haben. Da 50% der sdBs in engen Doppelsternen gefunden wurden, kann man ihre Entstehung am besten durch Doppelsternentwicklung erklären. Besonders enge Doppelsterne mit Perioden von Stunden, in denen das Massenverhältnis beider Komponten 5:1 beträgt, müssen eine CEE Phase durchlaufen haben. Ein anderer Erklärungsvorschlag ist, dass nicht nur massearme Hauptreihensterne sondern auch Planeten oder braune Zwerge für die Entstehung des sdB verantwortlich sein könnten, wenn sie vom Stern auf dem Roten Riesenast "verschluckt" werden. Deshalb sind enge sdB Doppelsterne ideal, um den Einfluss von Planeten auf die Sternentwicklung zu untersuchen. Bedeckende Doppelsternsysteme bestehend aus sdB Sternen und massearmen, kühlen Begleitern (HW Virginis Systeme) sind besonders wichtig und interessant, da man in diesen die Inklination des Systems und damit auch die Massen und den Abstand beider Begleiter bestimmen kann. Diese Information ist essentiell, um die Common-Envelope Phase zu verstehen.

Der erste Teil dieser Arbeit beschäftigt sich mit der Analyse und der Suche nach HW Virginis Systemen. Doppelsterne bestehend aus heißen sdB Sternen (mit Effektivtemperatur $T_{\rm eff} \sim 30\,000\,{\rm K}$) mit massearmen, kühlen Begleitern ($T_{\rm eff} \sim 3\,000\,{\rm K}$) zeigen charakteristische Lichtkurven, die sich durch den Reflexionseffekt auszeichnen. Dieser resultiert aus der großen Temper-

aturdifferenz, die bewirkt, dass der kühle Begleiter auf der dem heißen Primärstern zugewandten Seite aufgeheizt wird. Je mehr von der aufgeheizten Seite des Begleiters sichtbar ist, desto größer ist seine Helligkeit, ähnlich wie bei den verschiedenen Mondphasen. Da eine Lichtkurve die Variation der Gesamthelligkeit darstellt, bewirkt die wechselnde Helligkeit des Begleiters eine sinusförmige Variation in der Lichtkurve. Aufgrund ihrer unverwechselbaren Lichtkurve wurden viele der HW Virginis Systeme in photometrischen Durchmusterungen gefunden, die Lichtkurven von einer großen Anzahl von Sternen beobachten. Mehrere interessante enge, bedeckende Doppelsterne, die auf diese Art entdeckt wurden, wurden in dieser Arbeit durch eine kombinierte spektroskopische und photometrische Analyse untersucht. Dies erhöht die Anzahl der untersuchten HW Virginis Systeme um 40% auf 17. Dies bietet genug Statistik, um Schlüsse über die Massen- und Periodenverteilung der bedeckenden sdB PCEB Systeme zu ziehen und diese mit PCEB Systemen mit weißen Zwergen und kühlen, massearmen Begleitern, zu denen sich sdBs entwickeln werden, zu vergleichen. Unsere photometrische Untersuchung von spektroskopisch selektierten sdB Doppelsternen im MUCHFUSS (Massive Unseen Companion to Hot Faint Underluminous Stars from SDSS) Projekt mit Hilfe des Sloan Digital Sky Surveys (SDSS) erlaubte uns außerdem zum ersten Mal, den Anteil an Reflexionseffekt-Doppelsternen und substellareren Begleitern um sdB Sterne zu bestimmen. Deren Analyse zeigte, dass mehr als 3% der sdB Doppelsterne Braune Zwerg Begleiter besitzen. Dies zeigt, dass substellare Begleiter sehr wohl die Sternentwicklung beeinflussen können. Diese Doktorarbeit ist die Grundlage für das EREBOS (Eclipsing Reflection Effect Binaries from the OGLE Survey) Projekt, das wir gerade begonnen haben. Dieses Projekt hat zum Ziel 36 im OGLE (Optical Gravitational Lensing Experiment) Survey neu entdeckte HW Virginis Systeme zu untersuchen und damit das Sample zu verdreifachen, um die Rolle von Planeten auf die Sternentwicklung besser zu untersuchen und die Common-Envelope Phase besser zu verstehen.

Der zweite Teil dieser Doktorarbeit beschäftigt sich mit einem einzigartigen Runaway Stern. Als Runaway Sterne werden (massereiche) Sterne bezeichnet, die ihre Entstehungsregion mit hoher Geschwindigkeit verlassen (haben). Bei den im Galaktischen Halo in geringer Zahl auftretenden massereichen Sternen muss es sich um Runaway Sterne handeln, da dort aufgrund der geringen Dichte des interstellaren Mediums keine Sternentstehung stattfindet. Diese Sterne müssen in der Scheibe entstanden sein und binnen kurzer Zeit ausgeworfen worden sein. Um Runaway Sterne mit sehr hohen Geschwindigkeiten zu erklären, wurde das Standard-Auswurfszenario in einem Doppelstern von Przybilla et al. (2008) auf enge PCEB Systeme erweitert. Dabei entwickelt sich der deutlich massereichere Primärstern schnell, was zu einer gemeinsamen Hülle aufgrund des instabilen Massentransfers führt. Nach der Common-Envelope Phase bleibt ein enges Doppelsternsystem zurück. Sobald der Primärstern in einer Kernkollapssupernova explodiert, kann sich der Begleiter mit nahezu der Orbitalgeschwindigkeit entfernen. Dabei kann die Atmosphäre des Begleiters Supernova-Auswurfmaterial akkretieren. Das bedeutet, dass solche Sterne sehr geeignet sind, um die Nukleosynthese während einer Kernkollapssupernova zu untersuchen.

HD 271791 ist der einzig bekannte Runaway Stern dessen galaktische Ruhesystem-geschwindigkeit ($750 \pm 150 \mathrm{km\,s^{-1}}$) die Fluchtgeschwindigkeit der Galaxis übersteigt. Er wird daher als Hyper-Runaway Stern bezeichnet. Die bisherigen Studien zu diesem Stern durch Przybilla et al. (2008) haben eine Anreicherung der $\alpha-$Prozess Elemente gezeigt. Dies weist auf die Akkretion von Supernova Auswurfmaterial hin. Da im normalen Supernova Szenario solch hohe Geschwindigkeiten nicht erreicht werden, wird ein sehr massereicher, jedoch kompakter Primärstern benötigt, höchstwahrscheinlich ein Wolf-Rayet-Stern, der entstehen sollte, wenn in der Common-Envelope Phase die Hülle abgestoßen wird. Die theoretische Untersuchung dieses Systems durch Gvaramadze (2009) hat jedoch bezweifelt, dass es möglich ist durch eine Supernova den Runaway zu solchen Geschwindigkeiten zu beschleunigen.

Die vorherige Untersuchung von HD 271791 wurde nur an optischen Spektren durchgeführt, in denen nur wenige Elemente sichtbar sind. Weitere chemische Elemente können nur anhand von Ultraviolettspektren untersucht werden. Dazu wurden Beobachtungen mit dem Hubble

Space Teleskop durchgeführt. Das Ziel ist es die Nukleosynthese in einer Kernkollapssupernova näher zu untersuchen, indem die Modelle für die Spektrumsyntheserechnungen für das UV erweitert werden, um in diesem Wellenlängenbereich Elementhäufigkeiten zu bestimmen. In diesem Bereich ist ein Großteil der Linien der schwereren Elemente sichtbar. Vor allem sind dort auch Linien der Elemente zu sehen, die nur durch schnellen Neutroneneinfang (r-Prozess) produziert werden können. Dieser sollte in Kernkollapssupernovae stattfinden, da dort die notwendigen hohen Neutronenflüsse auftreten. Die Spektrumsynthese wurde an vier hellen B Sternen mit verschiedenen Temperaturen von 17500-33000 K getestet, basierend auf Sternparametern, die im Optischen bestimmt wurden. Anschließend wurde HD 271791 mit einem Spektrum mit besserer Qualität im Optischen erneut untersucht, um genauere Sternparameter und Elementhäufigkeiten zu bestimmen. Es wurden auch einige Simulationen durchgeführt, um zu bestimmen, welche Geschwindigkeiten unser Objekt im Supernova Szenario erreichen kann, was Rückschlüsse auf das post Common-Envelope System zulässt. Basierend auf den stellaren Parametern, die im Optischen bestimmt wurden, konnten Elementhäufigkeiten für Elemente bis zur Eisengruppe bestimmt werden. Diese Arbeit bietet nun die Grundlage für die Bestimmung von Elementhäufigkeiten von B Sternen im UV. Es ist jetzt möglich Elementhäufigkeiten auch für die Eisengruppe und Elemente darüber hinaus zu bestimmen. Damit sollte die genauere Untersuchung der Nukleosynthese in einer Kernkollapssupernova, insbesondere der r-Prozess Elemente, in naher Zukunft möglich sein.

Abstract

Close binaries are two gravitationally bound stars, which orbit each other with a sufficiently small separation so that they interact with each other at least once in their lifetime. This happens mostly by mass transfer in the red giant phase. If both stars have similar masses, a stable mass transfer via the Lagrange points between them will be initiated as soon as the more massive star evolves towards the red giant branch and is expanding. In close binaries with sufficient mass difference ($M_1/M_2 > 1.5$) the companion cannot accrete all mass transfered and a common envelope around both stars is formed. Because of friction in the envelope the separation of both stars shrinks and the free orbital energy can be used to eject the envelope. The outcome is a very close binary, a post common-envelope binary system (PCEB). This phase is highly important for the understanding of binary evolution and as well as for the explanation of for example supernovae of type Ia, which are of cosmological significance. Despite this fact, our understanding of this immensely important phase is quite limited. The observation of binaries with separations of the order of a solar radius – much smaller than the typical radius of a red giant of hundreds of solar radii – shows that the common-envelop phase has to exist, but the physical processes are only qualitatively understood. The description of this phase is only parametrized in binary stellar evolution models at the moment. The model parameters for the efficiency of the transport of the energy and angular momentum, however, are still unknown.
This thesis covers the analysis of low-mass systems as well as the analysis of a unique, massive star, a so-called hyper-runaway star, which has to have undergone a common-envelope ejection phase. The low-mass systems investigated here are very close binaries consisting of a hot subdwarf primary star and a low-mass main-sequence or brown dwarf companion. Hot subdwarf stars of spectral type B (sdB) are core-helium burning stars on the extreme horizontal branch, which lost almost their entire hydrogen envelope on the tip of the red giant branch. As about 50% of the sdBs are found in close binary systems, the best explanation for their formation is binary evolution. In particular close sdB binaries with periods of hours and with a mass ratio of 5:1 can only be explained by a previous common-envelope phase. It was also suggested that not only low-mass stars but also planets or brown dwarfs could be responsible for the mass loss, when they are engulfed in the envelope of the star. Therefore, close sdB binaries with low-mass companions are ideal to study the influence of planets on stellar evolution. Of those, eclipsing (HW Virginis systems) are in particular important, as the inclination can be determined and, hence, the masses and separation can be derived, which are essential for the understanding of the common-envelope phase.
The topic of the first part of this thesis is the analysis and the search for common-envelope systems. Binaries consisting of hot subdwarf stars (with effective temperature $T_{\rm eff} = 30\,000\,\mathrm{K}$) with low-mass, cool companions ($T_{\rm eff} = 3\,000\,\mathrm{K}$) have characteristic lightcurves showing the reflection effect. This effect results from the large temperature difference between the two objects. Consequently, the cool companion is heated up on one side by the close hot primary star. The more of the heated side of the companion is visible, the higher is its luminosity similar to the different moon phases. As a lightcurve represents the time evolution of the combined luminosity of both components, the varying flux of the companion causes a sinusoidal variation in the lightcurve. Many of the HW Virginis systems have been found in photometric surveys, which observe lightcurves of a large number of stars, due to the easily recognizable lightcurve. Several eclipsing sdB binaries, which have been found in this way, were investigated in this

thesis by a combined photometric and spectroscopic analysis. This increased the number of analyzed HW Virginis systems by 40 % to 17 providing a sufficiently large sample to draw first conclusions about their mass and period distribution and a comparison to PCEBs with white dwarf primaries, which are the successors of the sdB binaries. Our photometric investigation of spectroscopically selected sdB binaries from the Sloan Digital Sky Survey allowed us to determine the fraction of reflection effect binaries and substellar objects around sdB stars for the first time. The analysis showed that more than 3% of the sdB binaries have substellar companions. This shows that substellar companions can indeed influence stellar evolution. This work is the basis for the EREBOS (Eclipsing Binaries from the OGLE Survey) that we just started. This project aims at studying 36 HW Virginis systems recently discovered by the OGLE (Optical Gravitational Lensing Experiment) survey in order to further investigate the role of planets on stellar evolution and develop a better understanding of the common-envelope phase.
The topic of the second part of this thesis is a unique runaway star. Runaway stars are (massive) stars that are currently leaving or already have left their birth-place with high velocity. The massive stars found in low numbers in the halo have to be runaway stars, as no star formation occurs there because of the low density of the interstellar medium. Those stars have to be formed in the Galactic disk and be ejected shortly afterwards. Przybilla et al. (2008) developed one ejection scenario: a supernova in a close PCEB system. The much more massive primary is evolving very fast and a common envelope around both stars is formed due to unstable mass transfer. The result is a massive binary in a very short orbit. When the more massive star explodes in a core-collapse supernova, the companion may be released nearly at its orbital velocity. The atmosphere of the runaway star can be polluted with the supernova ejecta in this process. Therefore, such kind of stars are ideally suited to study nucleosynthesis in a core collapse supernova.
HD 271791 is the only known runaway star, whose galactic restframe velocity ($740 \pm 150\,\mathrm{km\,s^{-1}}$) exceeds the escape velocity of the Galaxy. Hence, it is called a hyper-runaway star. A prior investigation of this star by Przybilla et al. (2008) has shown an enhancement of the $\alpha-$process elements. This indicates the capture of supernova ejecta. As such high space velocities are not reached by the runaway stars in classical binary supernova ejection scenarios, a very massive but compact primary, probably of Wolf-Rayet type, is required, which is expected to be formed by ejecting the envelope in a common-envelope phase. A later theoretical investigation by Gvaramadze (2009) of this system put the acceleration scenario in question, finding it unlikely to accelerate a star with this properties to such high velocities.
The first quantitative analysis of the star was based on optical spectra, which allowed abundances of only a small number of elements to be determined. More chemical elements can only be investigated with the help of ultraviolet spectra. Therefore, Hubble Space Telescope observations were obtained. The goal of this project is to further investigate nucleosynthesis in a core-collapse supernova. Hence, the spectrum synthesis computations were extended to the UV to facilitate abundance determinations in this spectral region, where many chemical species produce a dense forest of spectral lines. In particular, also the lines of elements that can only be produced by rapid neutron capture (r process) are visible there. They are suggested to be synthesized in core-collapse supernovae, as high neutron fluxes are available there. Hence, it could provide evidence for the r process taking place in core-collapse supernovae, if the r-process elements were found to be enhanced. The spectrum synthesis was tested by the abundance determination of four bright B stars with different temperatures from $17500 - 33000$ K based on the stellar parameters determined from the analysis of the optical spectra. Afterwards, we re-investigated HD 271791 based on higher quality optical spectra to determine the stellar parameters and abundances with higher accuracy. We also performed some simulations to re-investigate the velocities a star, which has the properties of HD 271791, can reach in the supernova scenario. Based on the parameters from the optical analysis, our spectrum synthesis was used to derive abundances of HD 271791 for elements until the iron group in a second step.

In summary, this work establishes the basis for comprehensive abundance determinations of B stars in the UV in the future, comprising iron-group elements and many heavier chemical species. This will ultimately facilitate to investigate nucleosynthesis in a core-collapse supernova in great detail by this novel approach.

Contents

1. Introduction

The main goal of astrophysics is to develop a comprehensive understanding of the universe and our place in it. We are living in the Milky Way, which is one of the uncountable number of galaxies that are populating the universe. Each galaxy is composed of billions of stars that are gravitationally bound. In order to understand the evolution of galaxies, it is essential to know how stars evolve, as they are the main drivers of galactic evolution. In particular massive stars are highly important sources of heavy elements, the so-called metals, which they release by the action of stellar winds and, at the end of their lifetime, in supernovae. This enriches the interstellar medium out of which new stars are formed. However, most stars are not born single. The multiplicity fraction is depending strongly on the mass, as shown in Fig. 1.1. In particular stars with higher masses are almost all born in binaries (Sana et al. 2012). Hence, stellar evolution cannot be understood without investigating binary evolution.

Two different types of binaries exist. The wide binaries do only interact gravitationally. They do not influence the evolution of their companion and can therefore be treated as two single stars. On the other hand, also close binaries exist, which are defined as binaries which are interacting with each other at some point in their lifetime, in particular during the giant phase. This interaction takes place mostly via mass transfer, which is influencing the evolution of both donor and gainer star in a decisive way.

Very close binaries with large differences in their masses are experiencing a so-called common-envelope phase. Common-envelope ejection (CEE) is the name of a short phase in the life of a close binary star during which both companions orbit inside a single, shared envelope. Common-envelope evolution is believed to be a vital process for the understanding of very close binary stars, which have separation smaller than the radius of a red giant star. Such binaries are essential for the explanation of some highly important phenomena, such as Type Ia supernovae or double neutron stars, which are the most important cosmological standard candles and primary targets for the direct detection of gravitational wave emission, respectively.

Binary systems with separations smaller than the radius of the red giant, which can only be explained by CEE, are found in large numbers. Yet, the theoretical understanding of this very important phase is still limited. The current knowledge is summarized by Ivanova et al. (2013). Hydrodynamic simulations of the common-envelope phase still struggle to explain the removal of the envelope (see Fig. 1.2 for an example), however the observed post common-envelope systems discovered prove that this phenomenon occurs. The understanding is that, when the more massive star consumes its hydrogen in the core and evolves to a red giant, an unstable mass transfer is initiated in binaries with large mass difference. The consequence is a common-envelope around both stars. Friction in the envelope leads to shrinking of the orbit. The released orbital energy is somehow transferred to the envelope and leads to its ejection. Another viable outcome could be the merger of both stars. However, the physical processes are still not yet fully understood.

In the absence of a complete physical explanation, this phase is treated in a simplified way using free parameters, which are tuned to match the observations, or values are assumed to facilitate predictions. It is assumed that the binding energy E_{bind} is equal to the difference in

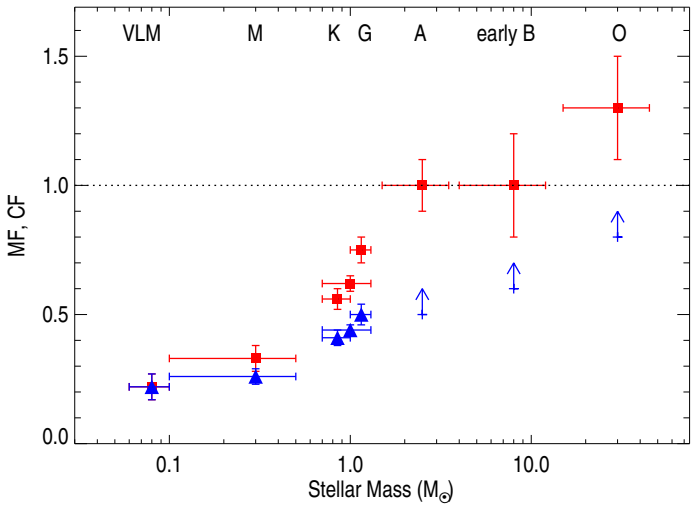

Figure 1.1.: Dependency of the companion frequency (CF = average number of companions per observing target; red squares) and of the multiplicity frequency (MF; blue triangles) as a function of primary mass for main-sequence stars and very low-mass (VLM) objects in the field. The horizontal error bars represent the approximate mass range for each population. For B and O stars, only companions down to $q \approx 0.1$ are included and only lower limits for the multiple system fraction (adopted from Duchêne & Kraus 2013).

the orbital energy $\Delta E_{\rm orbb}$:

$$E_{\rm bind} = G\frac{m_1 m_{1,\rm env}}{\lambda R_1} = \Delta E_{\rm orbb} = \alpha_{\rm CE}\left(-\frac{G m_1 m_2}{2a_{\rm i}} + \frac{G m_{1,\rm c} m_2}{2a_{\rm f}}\right) \tag{1.1}$$

where λ is a parameter to allow for differences in the envelope structure, $a_{\rm i}$ and $a_{\rm f}$ is the initial and final binary separation, $G = 6.67384 \cdot 10^{-11}\mathrm{m}^3\,\mathrm{kg}^{-1}\,\mathrm{s}^{-2}$ is the gravitational constant, m_1, $m_{1,\rm c}$ and $m_{1,\rm env}$ are the mass of the primary star and the mass of its core and envelope, R_1 is the radius of the primary star, and m_2 is the mass of the companion. As not all available orbital energy can be used to eject the envelope the common-envelope efficiency α_{CE} is introduced, which gives the fraction of usable orbital energy.

Since, CEE is central for the understanding of many types of different observed binary systems, it is uncomfortable that no physically robust explanation has been found for the process to date. Common-envelope evolution is one of the most important unsolved problems in stellar evolution, and is of critical importance for the understanding of binary evolution.

As this phase is only short lived it is very difficult to discover systems that are currently in this phase. However, the investigation of different post common-envelope binary (PCEB) systems can help to understand this important phase and hopefully solve its mystery. Particular of importance are eclipsing PCEB systems as they allow the determination of the masses and separations of the companions. Most studies undertaken until now with eclipsing PCEBs use the $\alpha_{\rm CE}$-formalism and aim to calibrate the existing parametrization (e.g., Zorotovic et al. 2010). On the other hand, the hydrodynamic simulations make several predictions of the characteristics of the PCEBs, as, e.g, a small eccentricity is expected. These predictions can be tested by observed PCEBs.

In this work we investigate post common-envelope systems originating from low-mass binaries as well as one high-mass star thought to be the remnant of a disrupted PCEB system. The properties and evolution of these systems differ significantly. The low-mass binaries investigated in this thesis are PCEBs consisting of hot subdwarf stars of spectral type B (sdB) and low-mass main sequence or brown dwarf companions.

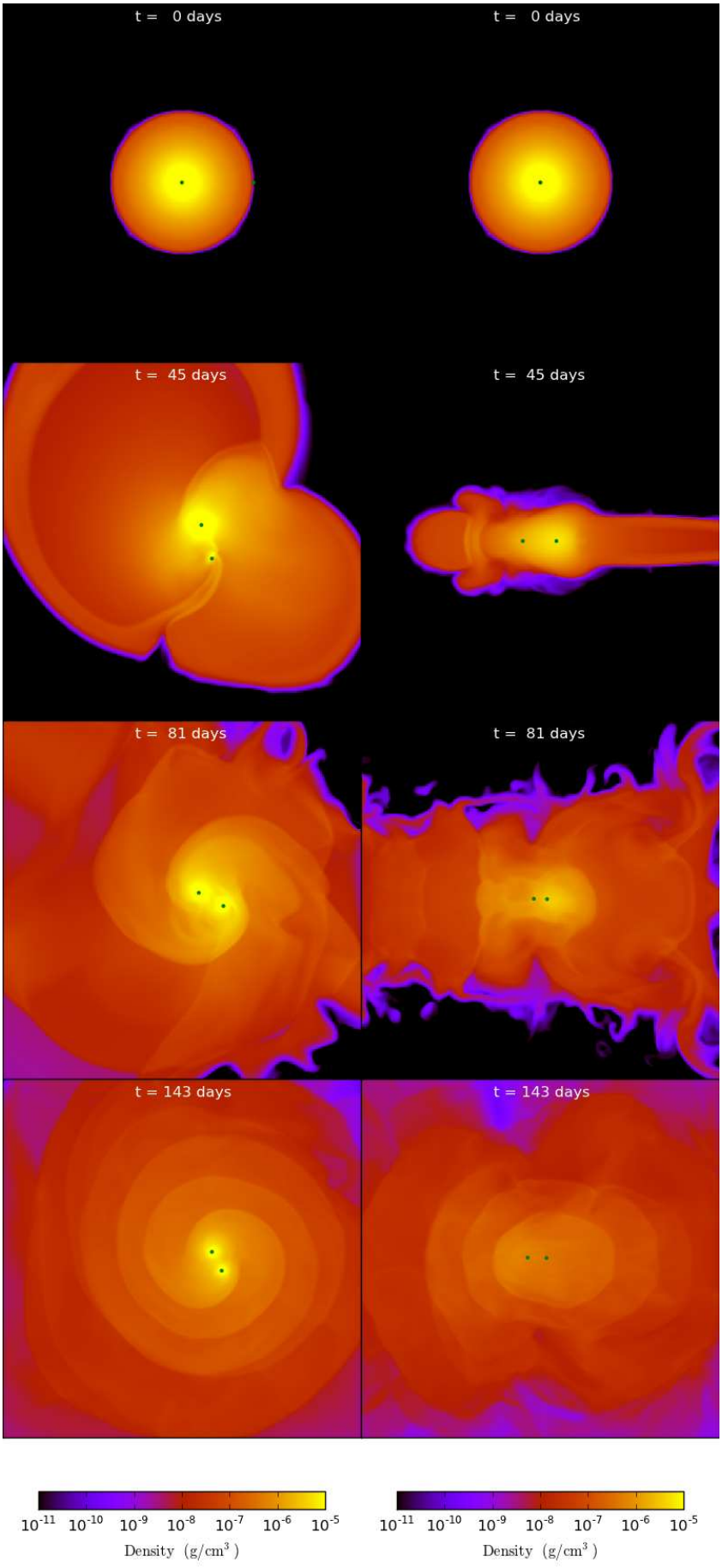

Figure 1.2.: Numerical simulation of a common envelope event with a 0.88 $M_{\odot}$ giant and a 0.6 $M_{\odot}$ main-sequence (MS) star likely leading to the formation of a close binary (Ivanova et al. 2013) in the orbital plane (left panel) and the perpendicular plan (right panel).

This class of systems is called HW Virginis systems after the prototype, when eclipsing. SdB stars are helium-burning cores that lost almost all their hydrogen envelope on the red giant branch (RGB). As about half of this systems are found in close binaries, binary evolution is considered to be the best explanation for the high mass loss on the RGB. In particular the eclipsing sdB binaries with periods of 0.065 to 0.5 d can only be explained by a previous common-envelope phase. This implies that binary evolution and common-envelope evolution is playing a highly important role in the formation of sdB stars. As the radii of both components in these binaries are of similar size ($\sim 0.1 - 0.2\,R_{\odot}$), they are suited very well to investigate the CEE due to the high probability of being eclipsing. These allows to determine the inclination and, hence, the separation of the system and the masses of both components, which is necessary to understand the previous CEE.
Furthermore, this work investigates the massive runaway star HD 271791 in the Galactic halo, which shows unusual properties. Because of its large distance to the Galactic plane HD 271791 was regarded a runaway B star. HD 271791 attracted attention because of its very high radial velocity of 442 $\mathrm{km\,s^{-1}}$ (Kilkenny & Muller 1989). Heber et al. (2008) investigated this star by using high-resolution, high-S/N spectra. They derived that the star is a massive B giant. From the proper motions of the star they get a Galactic rest-frame velocity of $530 - 920\,\mathrm{km\,s^{-1}}$, which implies that this star is unbound to the Galaxy. The birth-place was discovered to be on the outskirts of the Galactic disc with a Galactocentric distance of $\gtrsim 15$ kpc. Przybilla et al. (2008) performed a quantitative analysis of the star to get some hints on the ejection scenario. One theory for its origin is that it was member of a close post common-envelope system. The more massive companion exploded in a supernova, which lead to the ejection of the runaway. The runaway is, moreover, hit by the ejecta of the supernova, which polluted its atmosphere. An accurate determination of the surface composition confirmed the low [Fe/H] expected for a star born in the outer Galactic rim. The detected $\alpha-$enhancement points towards an extreme case of the binary-supernova runaway scenario. Therefore, this star promises to shed light on nucleosynthesis that is expected to take place in a core-collapse supernova. In particular, it may facilitate an empirical verification of the occurrence of the r-process in core-collapse supernovae. As it turned out complicated to derive detailed abundance information from direct observations of core-collapse supernovae, and the observation of nebula spectra provides only abundance data for few elements. At the moment observational constraints on SN nucleosynthesis are only obtained by indirect methods, like the secondary stars in low-mass X-ray binaries or the abundance patterns of metal-poor halo stars. Our approach is adding a new promising method to investigate this. In order to shed further light on the topic, we re-investigate in this thesis this highly interesting star by using higher S/N optical spectra taken with ESO-VLT/UVES, as well as UV spectra taken with HST/STIS and COS to investigate the abundances of the heavier elements.
The first part of this thesis concentrates on the discussion of the (astro)physical background. To understand the formation of an sdB and a runaway star it is necessary to understand the stellar evolution of low-mass as well as high-mass stars. Chapter 2 summarizes the basics of stellar evolution, with a particular focus on nucleosynthetic processes taking place in stars and core-collapse supernovae, information which is highly important for the understanding of the analysis of the runaway star. Chapter 3 and 4 gives some details about the current knowledge of hot subdwarf stars as well as massive runaway stars. Model atmospheres and the calculation of synthetic spectra are discussed in Chapter 5 and the analysis methods employed in this work in Chapter 6. After introducing all the basics, the results of the analysis of the hot subdwarf stars with cool low mass companions is then presented in Chapter 7. As the majority of spectral lines in hot massive stars is located in the UV, spectral synthesis at these wavelengths had to be implemented for the present project, which is discussed in Chapter 8. Tests and first applications to a sample of four bright, sharp-lined stars for a range of effective temperatures are presented in Chapter 9. The runaway star HD 271791 is investigated in Chapter 10, focusing

on an analysis of its optical and UV spectrum and of its kinematics to determine its birthplace in the Galactic disk. Finally an outlook is given in Chapter 11.

2. Stellar evolution and nucleosynthesis

To understand the low-mass sdB PCEB systems and the massive runaway star investigated in this thesis it is necessary to get an idea about the stellar evolution of low-mass as well as high-mass stars. As the stellar evolution differs greatly with mass will introduce stellar evolution in some detail. This will be followed by an introduction to the nucleosynthetic processes, which is essential for the understanding of the analysis of the post-supernova companion. As the stellar evolution in binaries differs from the single star evolution, I will discuss this also shortly at the end of the chapter. This chapter is mostly based on the textbooks of Kippenhahn & Weigert (1994), Iliadis (2007), Clayton (1983), Carroll & Ostlie (2007), and lecture notes by O.R. Pols[1].

2.1. Stellar evolution

2.1.1. Stellar structure

To understand stellar evolution and the calculation of stellar evolution tracks, it is important to first learn about the principle laws used to calculate the stellar structure. For simplicity some assumptions were adopted: no rotation, no magnetic fields, no mass loss, spherical symmetry, no companion. The conditions in the interior of a star are described completely by a set of four differential equations for the mass M, the density ρ, the luminosity L, and the pressure P. These equations representing the fundamental conservation laws:

- **mass conservation**

$$\frac{dM_r}{dr} = 4\pi\rho(r)r^2 \rightarrow M = \int_0^R 4\pi\rho(r)r^2 dr \tag{2.1a}$$

  thereby is M_r the mass within the radius r and R the stellar radius

- **hydrostatic equilibrium**: momentum conservation

$$dF_\mathrm{pres} + dF_\mathrm{grav} = dP(r)dA - G\frac{M_r dm}{r^2} = 0 \longrightarrow \frac{dP(r)}{dr} = -G\frac{M_r\rho(r)}{r^2}, \tag{2.1b}$$

  where dF_pres is the pressure force, which acts on the area dA of an small mass element dm and dF_grav the gravitational force, which acts on this mass element.

- **energy conservation**

$$\frac{dL(r)}{dr} = \epsilon 4\pi\rho(r)r^2,\ \epsilon = \epsilon_n + \epsilon_g - \epsilon_\nu \tag{2.1c}$$

  thereby is ϵ_ν the energy carried away by neutrinos, ϵ_n the energy production due to nuclear fusion and $\epsilon_g = -T\frac{dS}{dt}$ the gravothermal energy. S is the entropy and T the temperature, and this means that energy also can be absorbed and transferred to heat $dQ = TdS$.

[1] `http://www.astro.uni-bonn.de/~nlanger/siu_web/teach_sse.html`

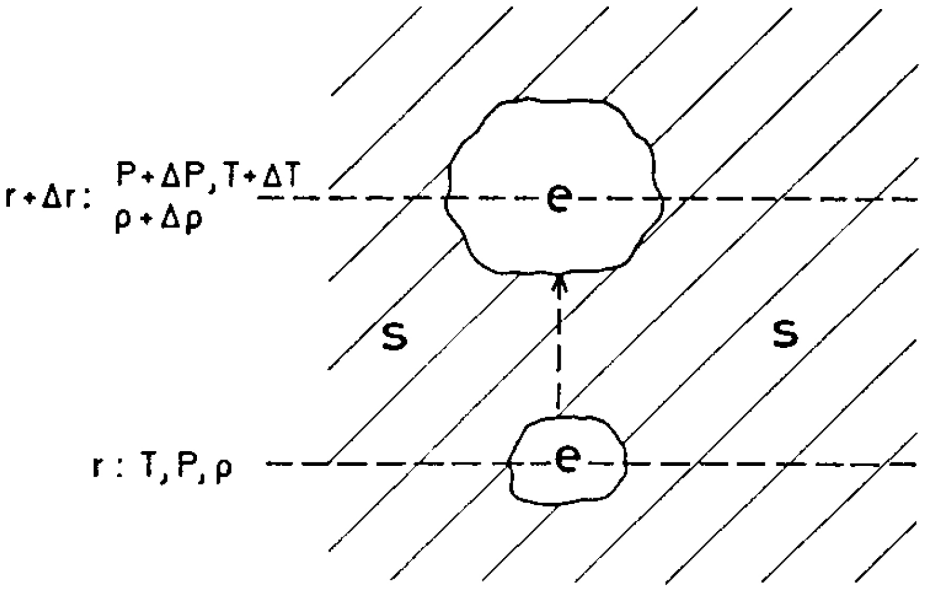

Figure 2.1.: Illustration of the test of stability of the surrounding layer (s) by lifting a test element (e) (Kippenhahn & Weigert 1994)

- **energy transport**

$$\frac{dT(r)}{dr} = -\frac{3}{4ac}\frac{\kappa_\nu}{T^3}\frac{L(r)}{4\pi r^2} \text{ (radiative) or } \frac{dT(r)}{dr} = -\frac{T(r)}{P(r)}\frac{GM_r\rho(r)}{r^2}\nabla \text{ (convective)} \quad (2.1d)$$

thereby is $\nabla = \frac{d\ln T}{d\ln P}$ and κ_ν (the Rosseland opacity) the frequency dependent absorption coefficient, c the speed of light and $a = 7.57 \cdot 10^{-15}\mathrm{erg\,cm^{-3}\,K^{-4}}$ the radiation-density constant. There exists also energy transport by conduction, which plays only a minor role in normal stars, but is important for example in white dwarfs. To discriminate which kind of energy transport is dominant the Schwarzschild criterion is used. If κ or $L(r)$ is large, the temperature gradient becomes large. However, there exists an upper limit for the possible temperature gradient inside stars - if it is exceeded, instability of the gas sets in. Therefore, energy cannot be transported by radiation alone any more. This instability leads to cyclic macroscopic motions of the gas, known as convection. Figure 2.1 illustrates the test used by Schwarzschild to determine the conditions for stability against convection. If the density of the element (e) is smaller than the density of the surrounding layer (s), the test element is able to rise and convection is initiated. Hence, the stability criterion is

$$\left(\frac{\partial\rho}{dr}\right)_e - \left(\frac{\partial\rho}{dr}\right)_s > 0 \rightarrow \nabla_{\mathrm{rad}} < \nabla_{\mathrm{ad}} \approx \nabla \text{ (Schwarzschild criterion)}$$

From the stability criterion together with the equation of state ($pV = nkT$, for an ideal gas) the Schwarzschild criterion can be derived in a more practical way by using temperature gradients. Therefore, convection is possible, if $\nabla_{\mathrm{rad}} > \nabla_{\mathrm{ad}}$, $\nabla_{\mathrm{ad}} = \left(\frac{d\ln T}{d\ln P}\right)_{S=const} = \frac{\gamma}{\gamma-1}$ (γ is the adiabatic coefficient, for an ideal gas: $\gamma = \frac{5}{3}$) means the temperature gradient for an adiabatic expansion (no transfer of energy as heat) and ∇_{rad} can be calculated by $\nabla_{\mathrm{rad}} = \frac{P}{T}\frac{dT}{dr}\frac{dr}{dP} = \frac{3}{16\pi acG}\frac{\kappa_\nu L(r)P}{mT^4}$.

- Additionally there exists a fifth differential equation for the changes of the **chemical composition** with time

$$\frac{\partial X_i}{\partial t} = \frac{m_i}{\rho}\left[\sum_j r_{ji} - \sum_k r_{ik}\right], \qquad i = 1...I \quad (2.1e)$$

thereby is X_i the mass fraction of the element i and r_{ij} the reaction rate for a transformation from element i in j. Each element i is produced by the reaction $j \rightarrow i$ and destroyed by the reaction $i \rightarrow j$.

These five differential equations can only be solved by assuming boundary conditions. Those are typically the central conditions:

$$m(0) = 0,\ L(0) = 0$$

and the surface conditions:

$$m(R) \rightarrow M,\ L(R) \rightarrow L$$

The effective temperature T_{eff}, which is defined by the Stefan-Boltzmann law:

$$L = 4\pi R^2 \sigma {T_{\text{eff}}}^4 \tag{2.2}$$

with $\sigma = 5.670373 \cdot 10^{-8}\,\text{W}\,\text{m}^{-2}\,\text{K}^{-4}$ the Stefan-Boltzmann constant, is equal to the temperature at the photosphere $T_{r=R}$. Also $\epsilon(r), \rho(r), \kappa, \gamma, T(r), S, P(\rho, T)$ have to be known to calculate the stellar structure. Based on the stellar structure it is possible to derive the stellar evolution, which is a time sequence of stellar structure calculations for modified chemical composition.

2.1.2. Star formation

Stars form out of interstellar matter. A cloud of compressible gas can become gravitational unstable and collapse. To describe the condition when a gas cloud becomes unstable, the Jeans criterion is used. If gravity overcomes the gas pressure, the gas cloud becomes unstable. Only a small perturbation is required to initiate the gas cloud collapse. For the description of stars the Virial theorem ($E_{\text{kin}} + 2E_{\text{grav}} = 0$; E_{kin} is the kinetic energy and E_{grav} is the gravitational energy), known from statistical physics for a system in hydrostatic equilibrium, is also highly important. Using it we can derive the minimum mass needed to destabilize a gas cloud, called Jeans mass M_{J}. For the spherical case we derive $M_{\text{J}} > \left(\frac{3}{4\pi\rho}\right)^{1/2} \cdot \left(\frac{5kT}{G\mu}\right)^{5/2}$. The time-scale τ for such a collapse is $\tau \approx (G\rho)^{-1/2}$, the free-fall time. For typical values we get a Jeans mass of about $M_{\text{J}} = 10^5 M_{\odot}$, much larger than the stellar masses. The cloud fragments during the collapse into smaller clumps, which form the protostars. When the gas cloud is contracting, the temperature and the pressure in the core is increasing. Therefore, the collapse stops first in the core, where a state close to hydrostatic equilibrium is reached. However, surrounding mass is still accreted until the temperature and pressure is high enough to fuse hydrogen in the core. The radiation pressure resulting from the fusion processes prevents then the newly formed star from accreting additional mass. After some relaxation time a stable state is reached. The star has reached the main sequence. Massive stars can, in contrast to low-mass stars, only be formed in clusters or associations resulting from the collapse of giant molecular clouds.

2.1.3. Main sequence

In the main-sequence phase the energy losses from a star's surface are compensated by the energy production of hydrogen burning. These reactions release nuclear binding energy by converting hydrogen into helium. The evolution timescales differ by orders of magnitude with the stellar mass. As hydrogen is by far the most abundant element, the time spend on the main sequence is most of the lifetime of the star. It depends on the amount of nuclear fuel and the energy consumption (it can be approximated by $\tau \propto M/L$). This assumption is confirmed by stellar evolutionary tracks, which show that stars at the lower end of the main sequence (MS) with low masses and low luminosities live for billions of years while massive, early-type stars with high luminosities end their life after a few hundred million years or less.

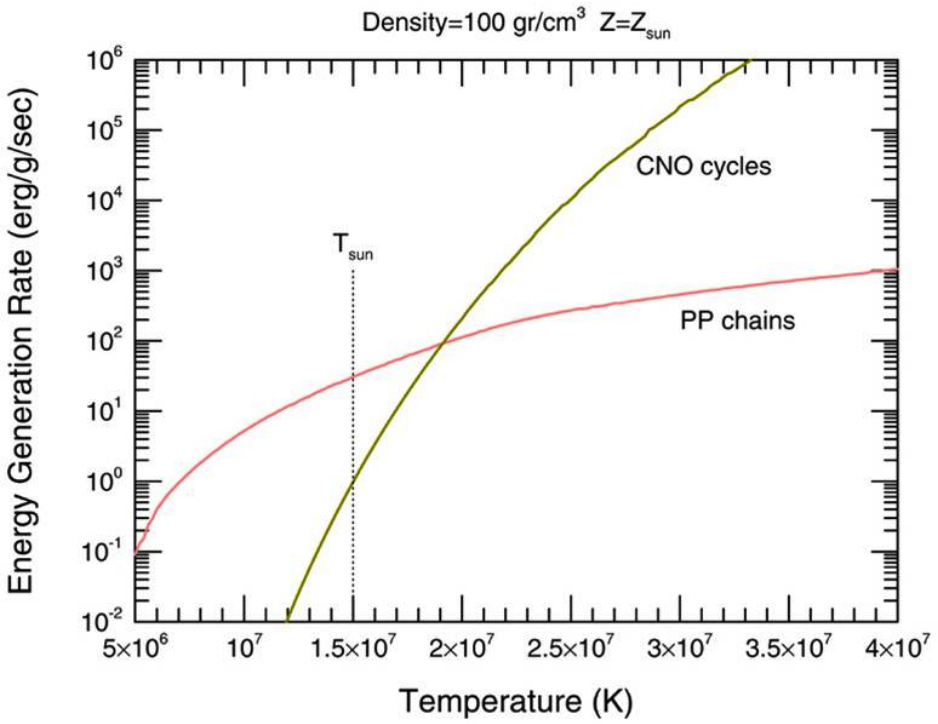

Figure 2.2.: Comparison of the energy rate of the CNO1 cycle and the pp1 chain at different temperatures (`http://www.nscl.msu.edu/~kontos/cnocycle.html`)

Hydrogen burning

Two different processes can occur during hydrogen-burning. For low-mass stars the pp-chains are the dominant reactions due to the lower core temperatures (see Fig. 2.2). The first two reactions are the same for each chain: $\mathrm{p(p,e^+\nu)d}$ (d=^{2}H) and $\mathrm{d(p,\gamma)^3He}$. The three pp-chains are displayed in Fig. 2.3. In the pp1 chain we get ^{4}He from $^3\mathrm{He}(^3\mathrm{He},2p)^4\mathrm{He}$. If the temperature is high enough and the abundance of ^{3}He is high enough, also the pp2 and pp3 chain become possible, as the reaction $^3\mathrm{He}(\alpha,\gamma)^7\mathrm{Be}$ becomes dominant. As low-mass stars $0.35 \lesssim M \lesssim 1M_\odot$ have radiative cores, no mixing takes place and the hydrogen burning stops as soon as the hydrogen concentration in the core gets too low. Even lower mass stars are fully convective and will contract directly into white dwarfs after the hydrogen is exhausted.

For more massive stars the CNO cycles are the dominant reactions to produce helium. However, that is only possible, if also heavier nuclides like C, N and O exist in the star, i.e. in all except the very first ones. C, N and O function only as catalysts for the transformation of hydrogen to helium. However, the cycles will change the abundances of the individual heavy nuclei. The reactions of the CNO cycles are displayed in Fig. 2.4. The dominant cycle is the CNO1 cycle. The bottle-neck in this cycle is the $^{14}\mathrm{N}(p,\gamma)^{15}\mathrm{O}$ reaction, as this is the slowest process for temperatures below $T < 0.1$ GK. The net effect of the CNO1 cycle is, therefore, the conversion of carbon and nitrogen seed nuclei to ^{14}N, which becomes by far the most abundant heavy nucleus when steady state is reached. Depending on the temperature also a small amount of ^{15}N can capture a proton and we get the CNO2 cycle instead. Further branching points to get the CNO2 and CNO3 cycle are ^{17}O and ^{18}O. These two cycles are only significant in massive stars. As the CNO cycle is very temperature sensitive, the helium production is concentrated to a very small area in the core. Therefore, we get a steep temperature gradient and energy transport by radiation is impossible. Hence, we have a convective core that mixes material inside the core so rapidly that the core is chemically homogeneous all the time.

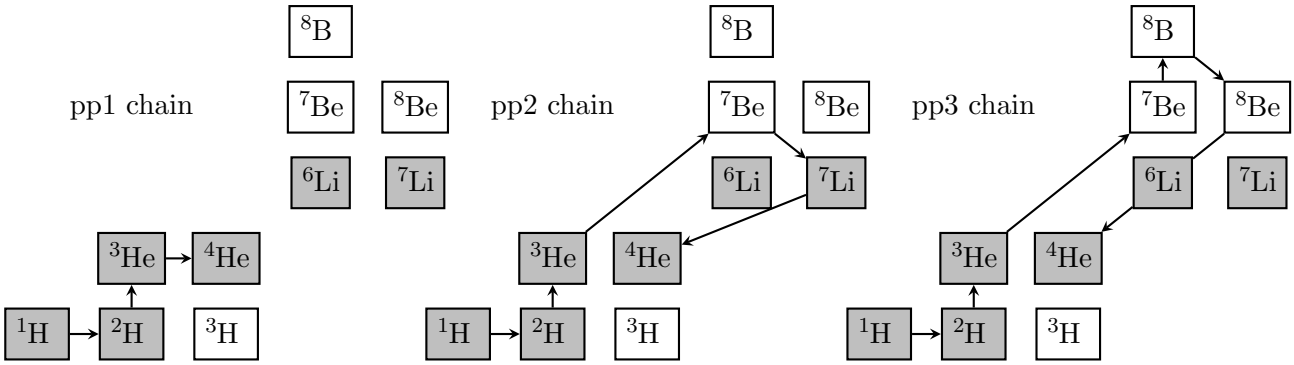

Figure 2.3.: Representation of the three pp chains in the nuclide chart (stable nuclides are shown as shaded squares).

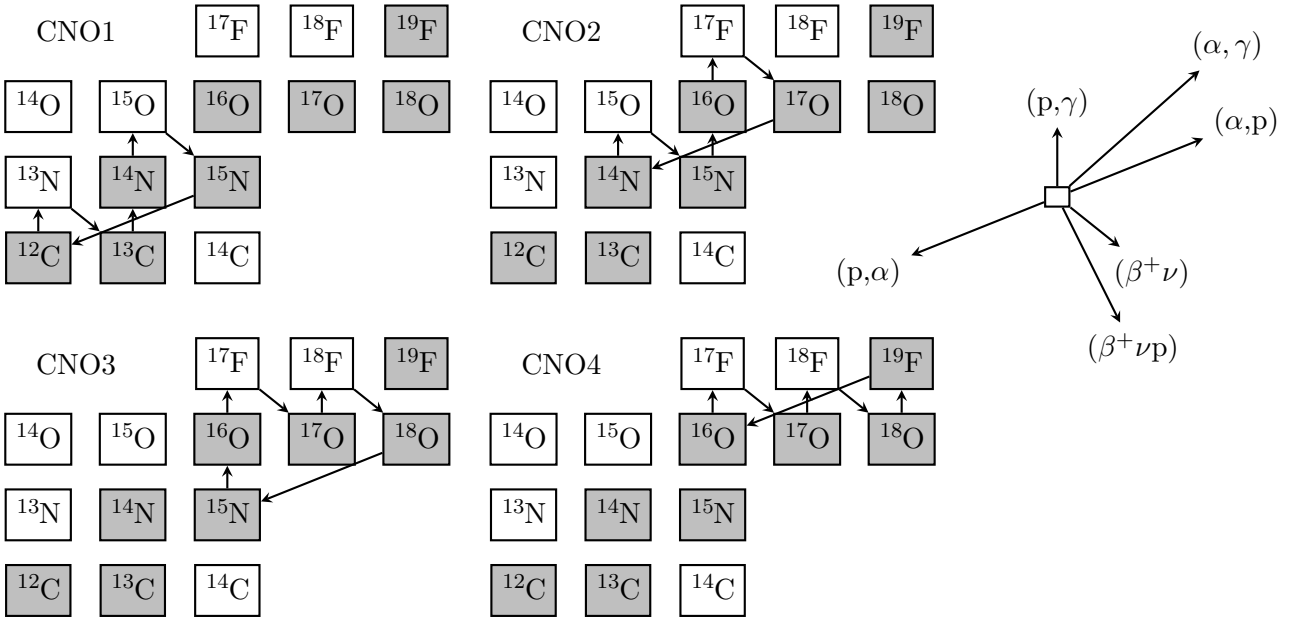

Figure 2.4.: Representation of the four CNO cycles

In Fig. 2.2 the energy production in the pp chains is compared to the energy production in the CNO cycles. At a temperature of about 20 MK the CNO cycles become dominant. Therefore, they are the main process for hydrogen burning in massive stars. The CNO cycles play only a very minor role for the Sun.
For both processes, the pp-chains and the CNO cycles, we get an effective reaction of:

$$4\,^{1}\mathrm{H} \rightarrow {}^{4}\mathrm{He} + 2e^{+} + 2\nu \tag{2.3}$$

After the hydrogen fuel in the core is exhausted the nuclear fusion stops. Therefore, the core begins to contracts, as no force counteracts gravity any more. The star evolves off the main sequence.

2.1.4. Evolution after the main sequence

The post main-sequence evolution depends on the stellar mass. Figure 2.5 shows the evolution of low-mass and intermediate-mass stars. For a 1 $M_{\odot}$ mass star, the core begins to contract, while a thick hydrogen-burning shell continues to consume available fuel. As the core contracts, its temperature increases. Therefore, the shell-burning produces more energy than the core-burning on the main sequence. This causes the luminosity to increase, the envelope to slightly

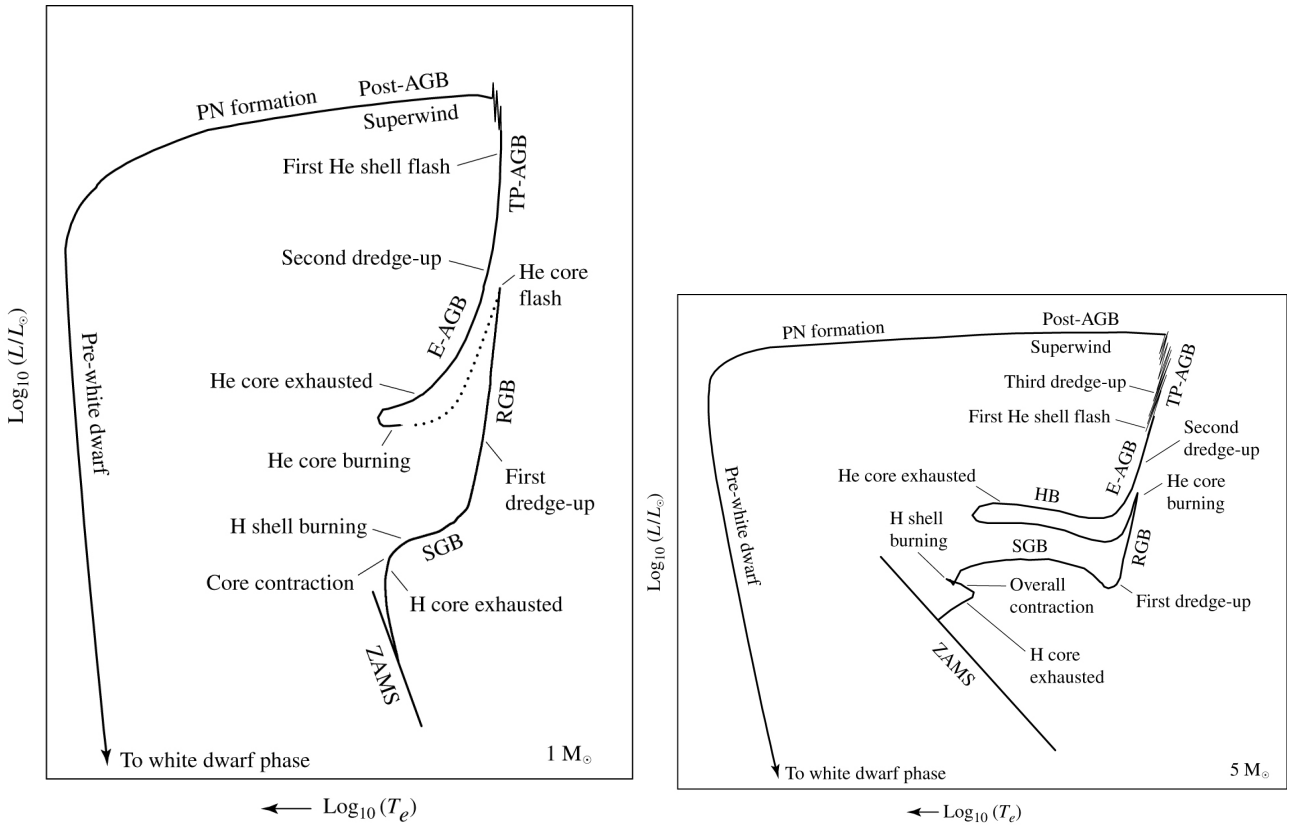

Figure 2.5.: Schematic diagram of the a 1 $M_\odot$ mass (left) and a 5 $M_\odot$ mass (right) star in the Hertzsprung-Russell diagram. (Carroll & Ostlie 2007)

expand and the effective temperature to decrease.
For a intermediate-mass star the evolution is different. The entire star contracts, which increases the temperature and decreases the radius. Eventually the temperature outside the helium core increases sufficiently to cause a thick shell of hydrogen to burn. This leads to a slight expansion of the envelope and, hence, to a decrease in temperature and luminosity.
Afterwards for low- and intermediate mass stars the core is growing, as the shell continues to convert hydrogen to helium. The gravitational energy released causes the envelope of the star to expand and, therefore, the effective temperature decreases. This phase is called the **sub-giant branch** (SGB). With the expansion of the stellar envelope and the decrease in effective temperature a convection zone near the surface develops, which expands deep into the interior of the star. Due to the highly efficient energy transport of convection the star begins to climb the **red giant branch** (RGB). During the climb on the RGB the convection zone also reaches into regions, which have been chemically altered due to the hydrogen burning. The CNO-cycled material becomes mixed with the pristine material above it. This is called the **first dredge-up** phase. The abundances on the surface are altered by this phase, which means it can be observed directly in the stellar spectra. Hence, predictions of stellar evolution theory can be tested in this phase.
When the conditions in the core are sufficient, the tip on the red giant branch is reached and helium core-burning sets in for stars with masses of more then 0.5 $M_\odot$. This results in an abrupt decrease in luminosity.

Helium burning

At this point the evolution of stars $< 1.8 M_\odot$ differs from the evolution of stars with higher masses. The core of lower-mass stars collapses until it becomes electron-degenerate. The helium-

burning sets in almost explosively in the so-called **helium flash** on the tip of the RGB. A large amount of energy is released in a few seconds, which is absorbed by the overlaying layers, causing some mass loss.
Both low-mass and intermediate-mass stars are located on the **horizontal branch** (HB) during the helium core-burning phase. It is called horizontal branch (HB), as the luminosity of all stars on the HB is very similar. For low-mass stars the observed effective temperature differs, depending on how much envelope is left. Stars that lost much of the envelope on the RGB are found on the blue horizontal branch (BHB) or even on the extreme horizontal branch (EHB), as the burning helium core is closer to the surface. A more detailed discussion of the EHB is given in Chapter 3. Contrary to low-mass stars, which jump to the HB after the helium-flash, intermediate-mass stars evolve in a loop on the HB.
Helium-burning takes place via the triple α process:

$$^4\mathrm{He} + {}^4\mathrm{He} \rightleftharpoons {}^8\mathrm{Be} \qquad (T_{1/2} = 6.7 \cdot 10^{-17}\mathrm{s}) \tag{2.4}$$

$$^8\mathrm{Be} + {}^4\mathrm{He} \rightarrow {}^{12}\mathrm{C}^* \tag{2.5}$$

$$^{12}\mathrm{C}^* \rightarrow {}^{12}\mathrm{C} + \gamma \tag{2.6}$$

In the first step of the triple α process an unstable beryllium nucleus ($T_{1/2} = 6.7 \cdot 10^{-17}$s) is produced by the fusion of two α-particles. The nucleus will disintegrate into two helium nuclei, if another α particle is not added immediately. Further α-captures lead to additional reactions during helium burning:

$^{12}\mathrm{C}(\alpha,\gamma)^{16}\mathrm{O}$
$^{16}\mathrm{O}(\alpha,\gamma)^{20}\mathrm{Ne}$ $\qquad$ $^{20}\mathrm{Ne}(\alpha,\gamma)^{24}\mathrm{Mg}$ only at high temperatures

Moreover, secondary reactions may occur, which produce free neutrons that play an important role in nucleosynthesis (more details later):

$^{14}\mathrm{N}(\alpha,\gamma)^{18}\mathrm{F}(\beta^+\nu)^{18}\mathrm{O}(\alpha,\gamma)^{22}\mathrm{Ne}$ $\qquad$ $^{22}\mathrm{Ne}(\alpha,\mathrm{n})^{25}\mathrm{Mg}$

The ash left behind by helium burning consists mainly of ^{12}C and ^{16}O. Therefore, the stellar core after helium-burning consists mainly of these two nuclides. During their passage along the horizontal branch, many intermediate-mass stars develop instabilities in their outer envelopes leading to long-period pulsations. These stars are called Cepheids. They provide another test of stellar structure theory with the help of asteroseismology, as the pulsations depend sensitively on the internal structure of the star. When the molecular weight of the core has increased to the point that the core contracts again, the most blue-ward point is reached. Shortly afterwards the helium in the core is exhausted and the further evolution is very similar to the evolution after the exhaustion of hydrogen in the core. We get helium and hydrogen shell-burning. This phase is called **asymptotic giant branch** (AGB). The envelope becomes convective again, resulting in the **second dredge-up**, which increases the helium and nitrogen content of the envelope. At the upper part of the AGB helium shell-burning begins to turn on and off quasi periodically because the hydrogen-burning shell is dumping ashes onto the helium burning shell. They are called **thermal pulses**. During this flashes a convective zone is established between the helium-burning shell and the hydrogen-burning shell. For stars with masses $> 2M_\odot$ the convection zone reaches deep into the interior of the star resulting in the **third dredge-up**. For stars with masses smaller than about 8 $M_\odot$ on the ZAMS the carbon-oxygen core will never reach a mass and temperature sufficient for further nuclear burning and is, hence, contracting. In the latest stage of evolution on the AGB, a **super-wind** (maybe due to shell flashes or envelope pulsations) develops with $\dot{M} \sim 10^{-4} M_\odot \mathrm{yr}^{-1}$. This high mass loss makes sure that the stellar core does not experience catastrophic core-collapse. The maximum value of 1.4 $M_\odot$ for a completely degenerate core is known as the **Chandrasekhar limit**. As the cloud (due to

the mass loss) around the star expands, it becomes optically thin, exposing the central star. The star is leaving the AGB and its effective temperature increases. The star is called a **post-AGB star** in this phase. A final phase of mass loss is following, in which the envelope is ejected. With only a thin layer of material left, the hydrogen- and helium-burning shells will extinguish. Therefore, no energy production in the star is left, and the luminosity of the star will drop significantly. The hot central object, will cool to become a **white dwarf** (WD), which is essentially the old red giant's degenerate core (CO or NeOMg depending on the progenitor mass). Due to the pressure of the degenerate electron-gas the core collapse is stopped and the core is reaching hydrostatic equilibrium. The expanding shell around the white dwarf progenitor is called **planetary nebula** (PN). The gas is excited or ionized by the ultraviolet light emitted by the hot central star. Typical temperatures of the PN are around 10^4 K. Only few of the PNs are spherical symmetric. Explanations for the different observed geometries encompass binarity or magnetic fields.

2.1.5. Evolution of massive stars

The evolution of more massive stars differs significantly. Figure 2.6 shows the evolutionary tracks for massive stars. For stars with masses larger than 15 $M_\odot$ mass loss through stellar winds becomes important throughout the entire life-time. That are rapid mass outflows driven by the strong radiation that erode the outer layers of the star. This changes the evolution significantly. The normal evolution of a not too massive star ($M \lesssim 15 M_\odot$) after the main sequence is to become first a red super-giant (RSG, cool, luminous star). Afterwards they become blue super-giants (BSG, hot luminous star) in a blue loop before they explode in a supernova (more details later). More massive stars evolve first to a BSG before they become a RSG. Depending on the mass they explode in a supernova afterwards or become a Wolf-Rayet star before. The most massive stars avoid the RSG stage and evolve into WR stars after a brief BSG phase. Due to the strong winds more massive stars become Wolf-Rayet (WR) stars after the RSG phase. WR stars are hot, very luminous stars with bright emission lines in their spectra. The emission indicates very strong, optically thick stellar winds, with high mass-loss rates. The winds are driven by radiation pressure. Depending on their spectra WR stars are grouped into different classes, which represent an evolutionary sequence of exposure of deeper and deeper layers, as a massive star is peeled off to a larger and larger extent by mass loss:

- **WNL stars** have hydrogen present on their surfaces (with $X_\mathrm{H} < 0.4$) and increased He and N abundances, consistent with equilibrium values from the CNO-cycle
- **WNE** stars are similar to WNL stars in terms of their He and N abundances, but they lack hydrogen ($X_\mathrm{H} = 0$)
- **WC** stars have no hydrogen, little or no N, and increased He, C and O abundances (consistent with partial He-burning)
- **WO** stars are similar to WC stars with strongly increased O abundances (as expected for nearly complete He burning)

Very massive stars become Luminous Blue Variables (LBV). This a very unstable stars with high luminosities showing outbursts accompanied by enormous mass loss. The most famous example in our galaxy is η Carinae.

In summary the evolution of massive stars depends very strong on the mass:

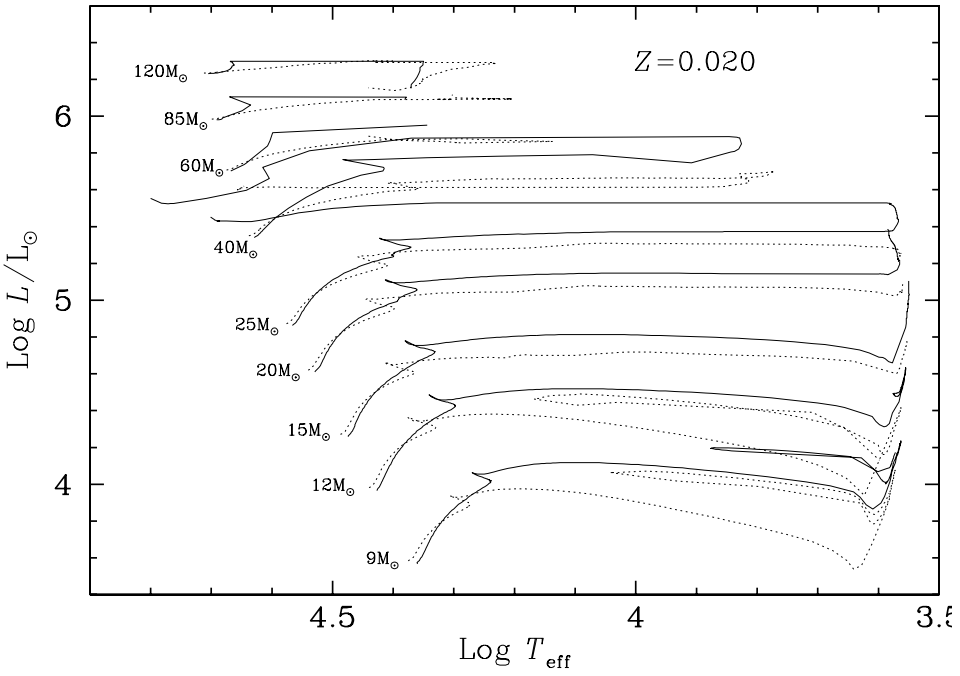

Figure 2.6.: Evolutionary tracks for non-rotating (dotted lines) and rotating (continuous lines) models for massive stars of different masses (Meynet & Maeder 2003)

$M \lesssim 15M_\odot$	MS(OB) → RSG → (BSG in blue loop? → RSG) → SNII mass loss relatively unimportant $\lesssim$ few $M_\odot$during entire evolution
$15M_\odot \lesssim M \lesssim 25M_\odot$	MS(O) → BSG → RSG → SNII mass loss is strong during the RSG phase, but not strong enough to remove the whole H-rich envelope
$25M_\odot \lesssim M \lesssim 40M_\odot$	MS(O) → BSG→ RSG → WNL → WNE → WC → SN Ib the H-rich envelope is removed during the RSG stage, turning the star into a WR star
$40M_\odot \lesssim M \lesssim 85M_\odot$	MS(O) → Of → WNL → WNE → WC → SN Ib/c Of stars are O supergiants with pronounced emission lines
$M \gtrsim 85M_\odot$	MS(O) → Of → LBV → WNL → WNE → WC → SN Ib/c an LBV phase blows off the envelope before the RSG can be reached

After helium-burning, as soon as the conditions in the core are sufficient, massive stars also start further burning-stages, before they explode in a supernova.

Carbon burning

Stars with masses larger than 8 $M_\odot$ can ignite carbon-burning in their core when $T_c > 5 \cdot 10^8$ K and $\rho_c > 3 \cdot 10^9 \mathrm{kg\,m^{-3}}$. During carbon-burning basically two different reactions take place, both fusing two ^{12}C nuclei:

$^{12}\mathrm{C}(^{12}\mathrm{C},\mathrm{p})^{23}\mathrm{Na}$	($\sim 50\%$)
$^{12}\mathrm{C}(^{12}\mathrm{C},\alpha)^{20}\mathrm{Ne}$	($\sim 50\%$)
$[(^{12}\mathrm{C}(^{12}\mathrm{C},\mathrm{n})^{23}\mathrm{Mg}]$	

Moreover, several side reactions exist:

$$^{23}\mathrm{Na(p,\alpha)^{20}Ne},\ ^{20}\mathrm{Ne}(\alpha,\gamma)^{24}\mathrm{Mg},\ ^{12}\mathrm{C(p,\gamma)^{13}N}(\beta^{+}\nu)^{13}\mathrm{C}(\alpha,\mathrm{n})^{16}\mathrm{O},\ ...$$

Carbon burning leaves ^{16}O, ^{20}Ne, ^{23}Na, and ^{24}Mg as ashes behind. Therefore, the result of carbon-burning is in principle an O-Ne-Mg core. The timescale for this phase is in the order of 500 years.

Neon burning

As next burning phase, we would expect oxygen-burning via the fusion of two ^{16}O nuclei, as this is the element with the lowest mass in the core. However, before this occurs in stars with masses larger than $\sim 10 M_{\odot}$ that reach temperatures $T_{\mathrm{c}} > 10^9$ K, photo-disintegration reactions become important for ^{20}Ne, which are liberating α-particles:

$$^{20}\mathrm{Ne}(\gamma,\alpha)^{16}\mathrm{O}$$
$$^{20}\mathrm{Ne}(\alpha,\gamma)^{24}\mathrm{Mg}(\alpha,\gamma)^{28}\mathrm{Si}$$
$$^{23}\mathrm{Na}(\alpha,\mathrm{p})^{26}\mathrm{Mg}(\alpha,\mathrm{n})^{29}\mathrm{Si}$$

Those α particles can then be captured and produce ^{24}Mg and ^{28}Si. The effective reaction is, therefore, $^{20}\mathrm{Ne} + {}^{20}\mathrm{Ne} \rightarrow {}^{16}\mathrm{O} + {}^{24}\mathrm{Mg} + 4586\,\mathrm{keV}$. Neon-burning leaves mainly ^{16}O, ^{24}Mg, and ^{28}Si in the core. This phase lasts only for about the order of a year.

Oxygen burning

After neon burning terminates, the core of the star consists mainly of oxygen, magnesium and silicon. $^{16}\mathrm{O}{+}{}^{16}\mathrm{O}$ fusion is now the most likely process to occur, as it has the lowest Coulomb barrier (that is the energy barrier due to electrostatic repulsion that two nuclei need to overcome so they get close enough to undergo a nuclear reaction). Stars with masses larger than 10 $M_{\odot}$ reach temperatures higher than $2 \cdot 10^9$ K in the core, sufficient for oxygen burning.

$^{16}\mathrm{O}(^{16}\mathrm{O},\mathrm{p})^{31}\mathrm{P}$	$\sim 40\%$
$^{16}\mathrm{O}(^{16}\mathrm{O},2\mathrm{p})^{30}\mathrm{Si}$	
$^{16}\mathrm{O}(^{16}\mathrm{O},\alpha)^{28}\mathrm{Si}$	$\sim 60\%$
$[^{16}\mathrm{O}(^{16}\mathrm{O},2\alpha)^{24}\mathrm{Mg}]$	$\mathrm{Q} < 0$
$[^{16}\mathrm{O}(^{16}\mathrm{O},\mathrm{d})^{30}\mathrm{P}]$	$\mathrm{Q} < 0$
$^{16}\mathrm{O}(^{16}\mathrm{O},\mathrm{n})^{31}\mathrm{S}$	

During oxygen burning also many side reactions take place capturing the free protons and α particles:

$$^{31}\mathrm{P(p,\gamma)^{32}S},\ ^{31}\mathrm{P}(\mathrm{p},\alpha)^{28}\mathrm{Si},\ ^{31}\mathrm{S}(\gamma,\mathrm{p})^{30}\mathrm{P}(\gamma,\mathrm{p})^{29}\mathrm{Si}(\alpha,\mathrm{n})^{32}\mathrm{S},\ ...$$

After oxygen-burning the core is composed mainly of ^{28}Si and ^{32}S.

Silicon burning

The final burning phase in stars with masses of 11 $M_{\odot}$ or more is silicon-burning, which occurs, if the core temperature reaches $T_{\mathrm{c}} > 3{\cdot}10^9$ K. The fusion reaction of two silicon or two sulfur atoms are too unlikely to occur because of the large Coulomb barrier. Instead, the nucleosynthesis

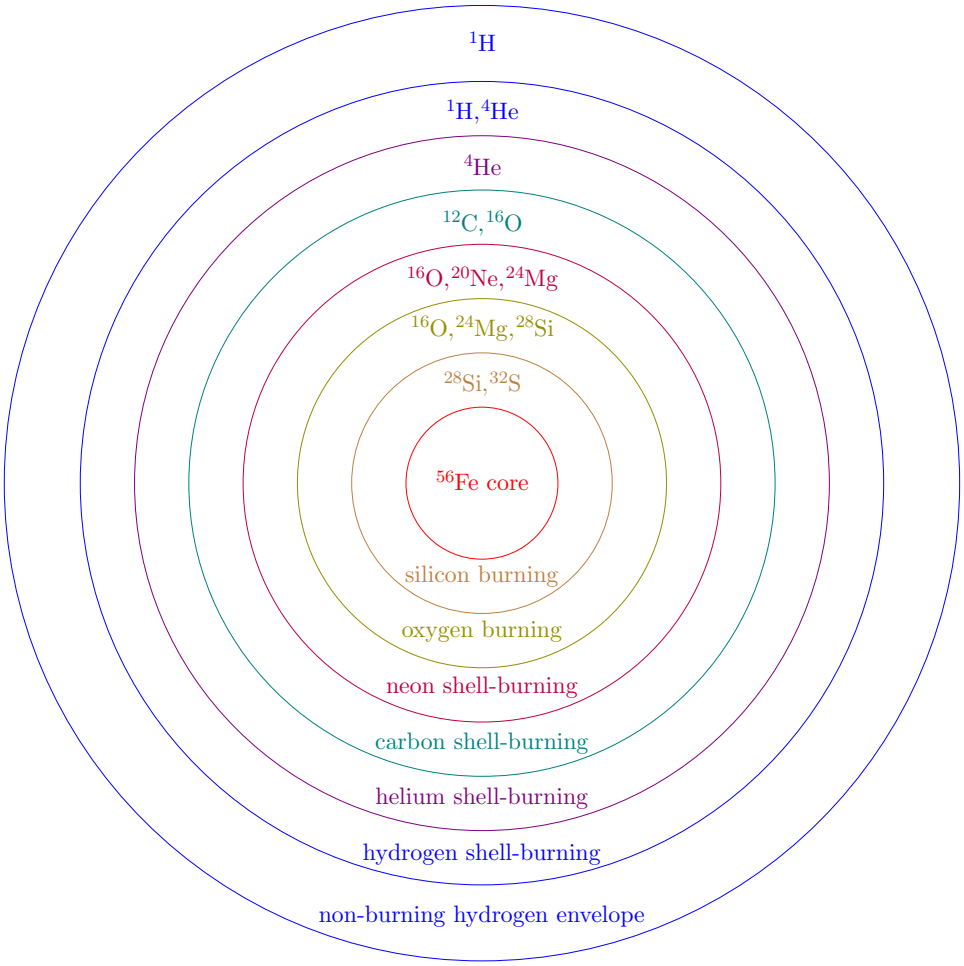

Figure 2.7.: Onion-like shell structure of massive stars at the end of their evolution. Each shell represents a nuclear burning stage that was originally located at the center of the star. After depletion of the central fuel, the burning continued as shell-burning in the adjacent, heated layers and gradually moved outwards. The drawing is not to scale.

proceeds via the photo-disintegration of lighter particles and the capture of liberated light particles (protons, neutrons, α particles) similar to neon burning:

$$^{28}\mathrm{Si}(\gamma,\mathrm{p})^{27}\mathrm{Al}$$
$$^{28}\mathrm{Si}(\gamma,\alpha)^{24}\mathrm{Mg}(\gamma,\alpha)^{20}\mathrm{Ne}(\gamma,\alpha)^{16}\mathrm{O}(\gamma,\alpha)^{12}\mathrm{C}(\gamma,\alpha)2\alpha$$
$$^{28}\mathrm{Si}(\alpha,\gamma)^{32}\mathrm{S}(\alpha,\gamma)^{36}\mathrm{Ar}(\alpha,\gamma)^{40}\mathrm{Ca}(\alpha,\gamma)^{44}\mathrm{Ti}(\alpha,\gamma)\ldots\,^{56}\mathrm{Fe}$$

The entire process of silicon-burning lasts about one day. As all these reactions are in equilibrium, the abundances can be described by the *nuclear statistical equilibrium (NSE)*. Therefore, ^{56}Fe is the most abundant nuclide, because it has the highest binding energy per nucleus. Figure 2.7 shows schematically the inner structure of a massive star after silicon-burning. The different burning stages result in an onion-like structure, with shells containing the ashes of each burning phase.

Fate of massive stars

After the silicon-burning phase the core consists mainly of ^{56}Fe. From the iron core it is not possible to extract more energy by nuclear fusion. Due to the high temperature and density the electrons are relativistic. Therefore, the core is dynamically unstable and core-collapse sets in.

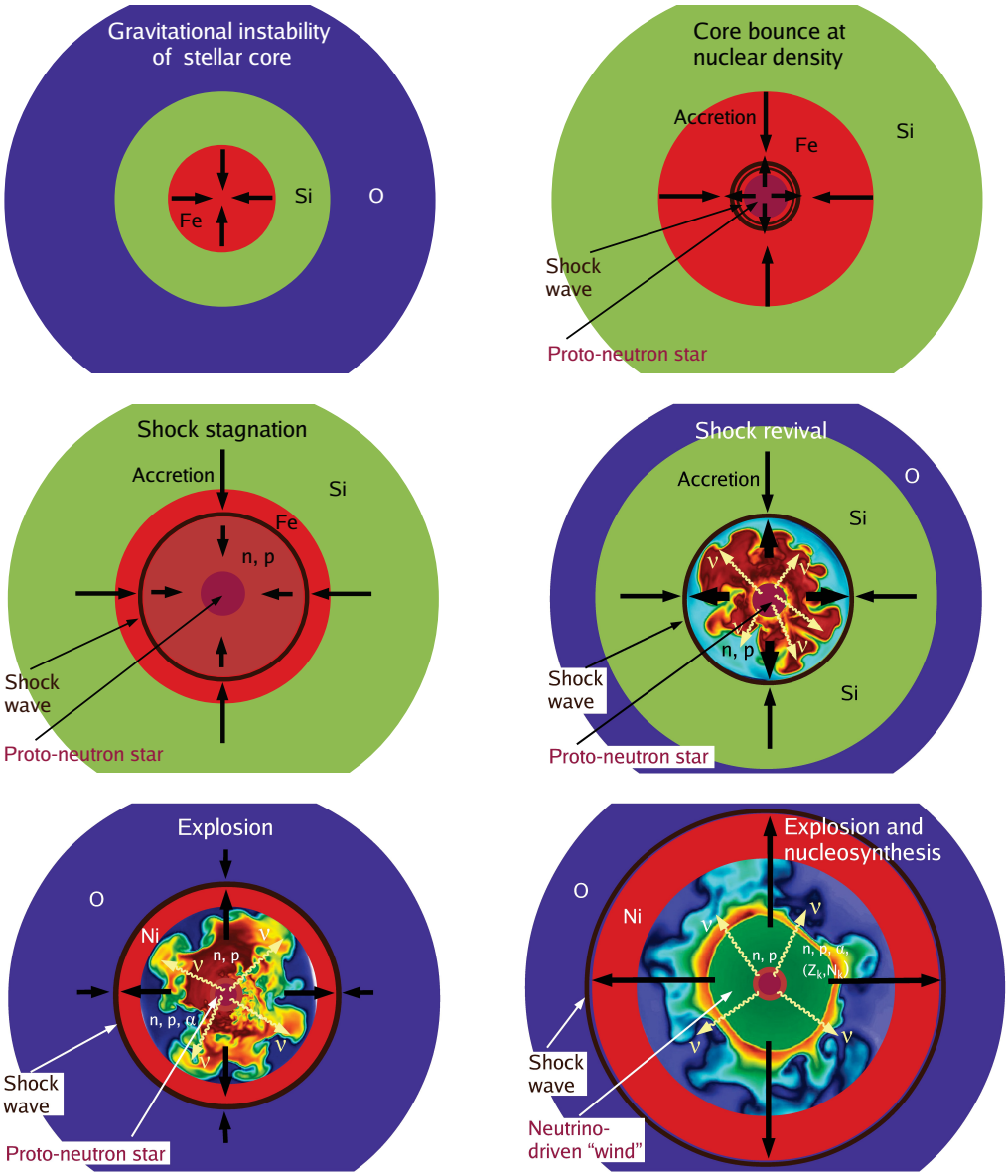

Figure 2.8.: Schematic representation of the evolution stages from the onset of stellar core collapse (*top left*) to the development of a supernova explosion on a scale of several 1000 kilometres. The displayed intermediate stages show the moment of core bounce and shock formation (*top right*), shock stagnation and onset of quasi-stationary accretion (*middle left*), beginning of the re-expansion of the shock wave ("shock revival",*middle right*), and acceleration of the explosion (*bottom left*). (adopted from Janka et al. 2012).

Fore less massive stars the relativistic electrons are degenerate. Then electron-capture by heavy nuclei reduce the pressure and starts the collapse. When the core reaches a temperature of 10^{10} K the energy of the photons becomes large enough to break up heavier nuclei (photo-disintegration):

$$^{56}\mathrm{Fe} + \gamma \rightleftarrows 13\alpha + 4n \qquad\qquad \alpha + \gamma \rightleftarrows 2p^{+} + 2n$$

At the extreme conditions the free electrons are now captured by the protons:

$$p^{+} + e^{-} \rightarrow n + \nu_{\mathrm{e}}$$

As most electrons have been captured, the electron pressure, that acted against gravity, vanishes. Hence, the core collapses rapidly, almost in a free fall, similar to the collapse of a molecular

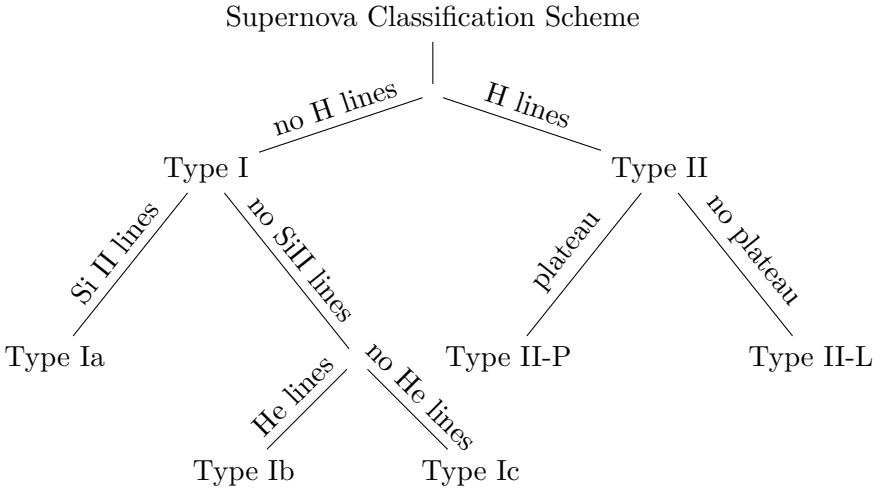

Figure 2.9.: The classification of supernovae based on their spectra at maximum light and the existence or absence of a plateau in the Type II lightcurve.

cloud into a protostar. The collapse is extreme rapid of the order of 10 msec. When the density exceeds the nuclear density, the matter cannot be compressed any more, because of Pauli's exclusion principle for fermions, and the collapse stops abruptly. This leads to a rebounce of the inner core, sending away pressure waves into the outer, in-falling material. When the velocity of the pressure-waves reaches sound speed, a shock-wave is formed. Much of the shock energy is drained by further photo-disintegration. Nevertheless, the shock continues to propagate outward in mass and radius. When the accretion rate has decayed sufficiently, the shock stagnates. During the transformation of protons to neutrons by electron-capture a large amount of neutrinos is released. As the matter during the collapse becomes very dense, even neutrinos cannot escape without interaction. With $\rho \sim 10^{12}\mathrm{g\,cm^{-3}}$ the neutrinos cannot escape in the free-fall time. They are trapped and build a neutrinosphere. In their way to the neutrinosphere they deposit their energy by absorption-, emission- and scattering-processes. Hence, cooling of the core sets in. Since the degeneracy is partially lifted, the production of $\bar{\nu}_\mathrm{e}$ by positron-capture of protons becomes possible. How the shock is revived stays still an open question. The most promising mechanism is the re-acceleration of the shock due to neutrinos because they can transport energy from the hot proto-neutron star to the shock. This leads then to an explosion, where the outer layers with the produced elements is ejected, the **supernova**. The proto-neutron star then cools by emitting neutrinos. The energy deposited by this neutrinos powers a baryonic outflow that expands at supersonic velocities and is known as the **neutrino-driven wind** (Arcones & Thielemann 2013). This neutrino-driven wind is a promising site for nucleosynthesis processes. This will be discussed in the next Section. Figure 2.8 shows a schematic view of the different stages of the supernova explosion adopted by Janka et al. (2012).

The supernovae are classified into different types on the basis of their spectra and lightcurves. This classification scheme is showed in Fig. 2.9. The absence of hydrogen lines in the Type I supernovae suggests that the hydrogen envelope has been stripped off. Progenitors of Type Ic supernovae also lost their helium envelope. Type Ia supernovae differ from the rest, as this represents the explosion of a white dwarf reaching the Chandrasekhar limit. As the mass exploding is always similar, they can be used as standard candles (Nobel Prize 2011). The other types are all core-collapse supernovae with different progenitors. Type Ib and c are found in spiral galaxies with massive progenitors that might be more massive than Type II supernova progenitors (Turatto 2003).

The outcome of the supernova explosion depends on the core mass. For stars with initial masses

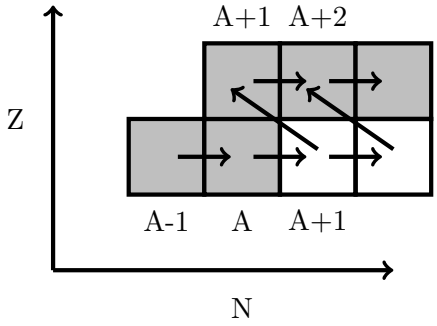

Figure 2.10.: Sketch of a neutron-capture path in the nuclide chart with branching point due to similar times needed for $\beta-$decay and neutron-capture.

above 25
Msun the neutron degeneracy is not enough to stop the collapse. The final collapse will be complete, producing a **black hole**. In all other cases the remnant will be a **neutron star**. The maximum mass of a neutron star is given by the **Tolman-Oppenheimer-Volkoff limit**. As the equation of state for neutron stars is not known very well, at the moment this limit can only be given in a range from 2-3 $M_{\odot}$.

2.2. Nucleosynthesis beyond the iron peak

For elements beyond the iron group it is not possible to be formed by charged particle reactions because of the too small cross-sections (σ). However, the cross-sections for neutron capture are quite large, as there is no Coulomb barrier. Neutron capture leads to:

$$(Z, A) + n \rightarrow (Z, A + 1) + \gamma$$

Neutrons can be captured as long as the resulting nuclide is stable. This series can only cut off by a β-decay:

$$(Z, A + 1) \rightarrow (Z + 1, A + 1) + \mathrm{e}^{-} + \bar{\nu}_{\mathrm{e}}$$

Figure 2.10 shows the path of such an neutron-capture in a nuclide chart. Depending on the neutron flux we get two different neutron capture processes.

- τ (n-capture)$\gg \tau(\beta) \rightarrow$ s-process
- τ (n-capture)$\ll \tau(\beta) \rightarrow$ r-process

s stands for 'slow' and r for 'rapid'. The s-process always stays near the valley of stable nuclei, whereas in the r-process neutrons are captured until the nuclide is not stable any more.

2.2.1. Slow neutron capture process

During helium shell-burning, taking place in stars on the AGB, some free neutrons are produced via the reaction: ^{13}C(α,n)^{16}O, and ^{22}Ne(α, n)^{25}Mg. Those neutrons are available for neutron-capture reactions. As we have only low neutron fluxes on the AGB, the time required for β-decay is shorter than the time for a neutron-capture. Therefore, we get the s-process. The most massive stable nucleus is ^{209}Bi, which is, hence, the termination point of the s-process.

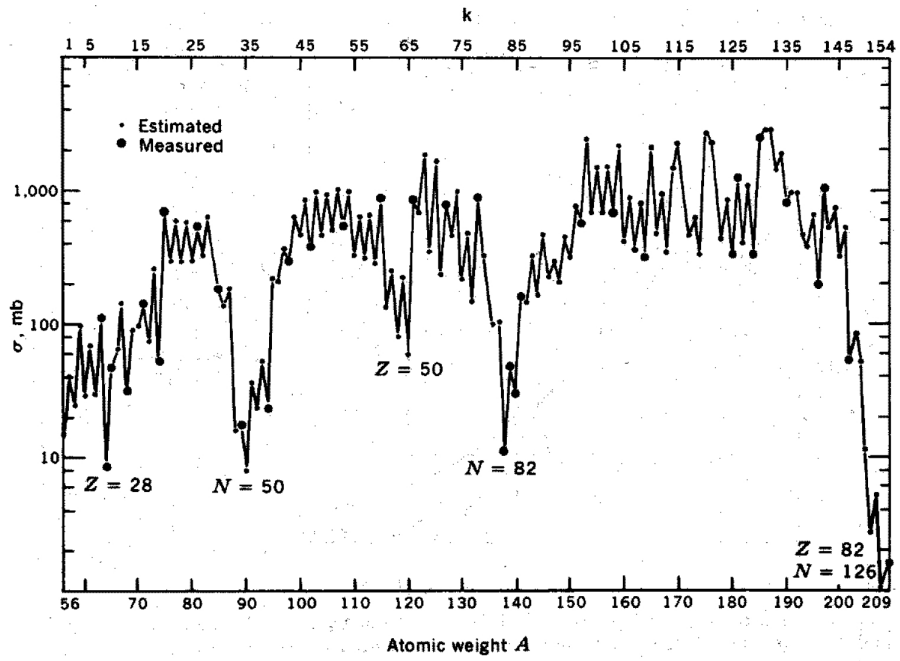

Figure 2.11.: Measured and estimated neutron-capture cross-sections of nuclei on the s-process path. The neutron energy is near 25 keV (Clayton 1983)

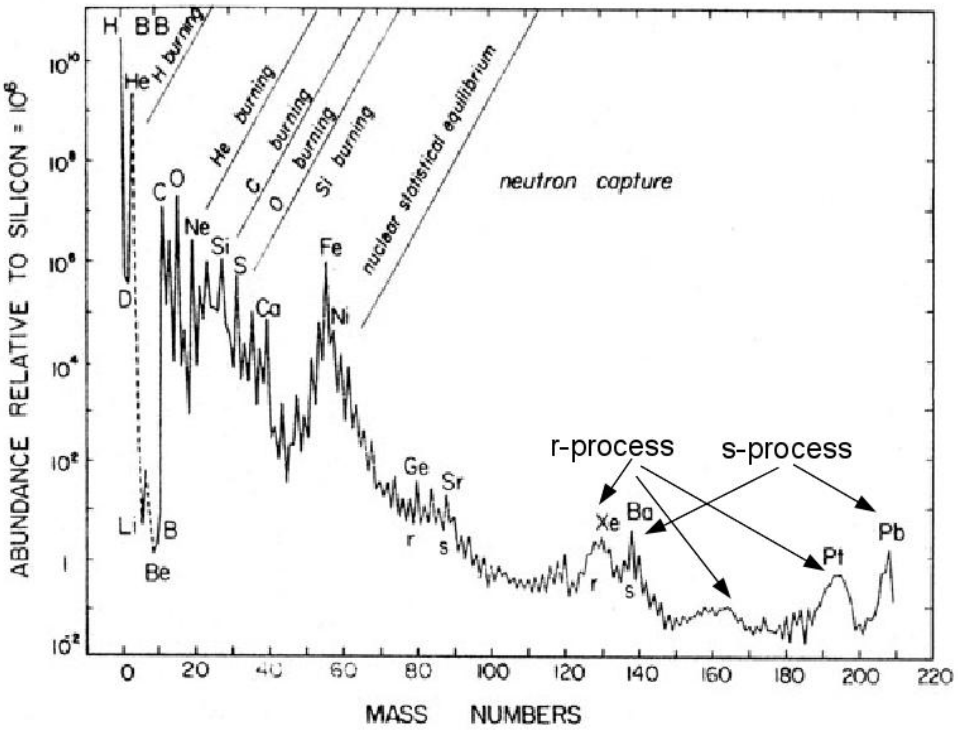

Figure 2.12.: Solar abundances showing several humps due to the s- and r-process, and the nucleosynthesis in the different burning stages (adopted from Pagel 2009).

As there do not exist any s-process elements in the beginning, seed nuclei are necessary to build the heavy elements. The solar abundances shows a peak for ^{56}Fe, which is therefore a perfect seed nucleus. The abundances of the s-process elements depend mostly on the cross-section for neutron-capture. Due to the fact that there is no Coulomb barrier, the cross-section depends in principle only on the velocity of the neutrons: $\sigma \sim \frac{1}{v}$. Therefore, the changing abundances

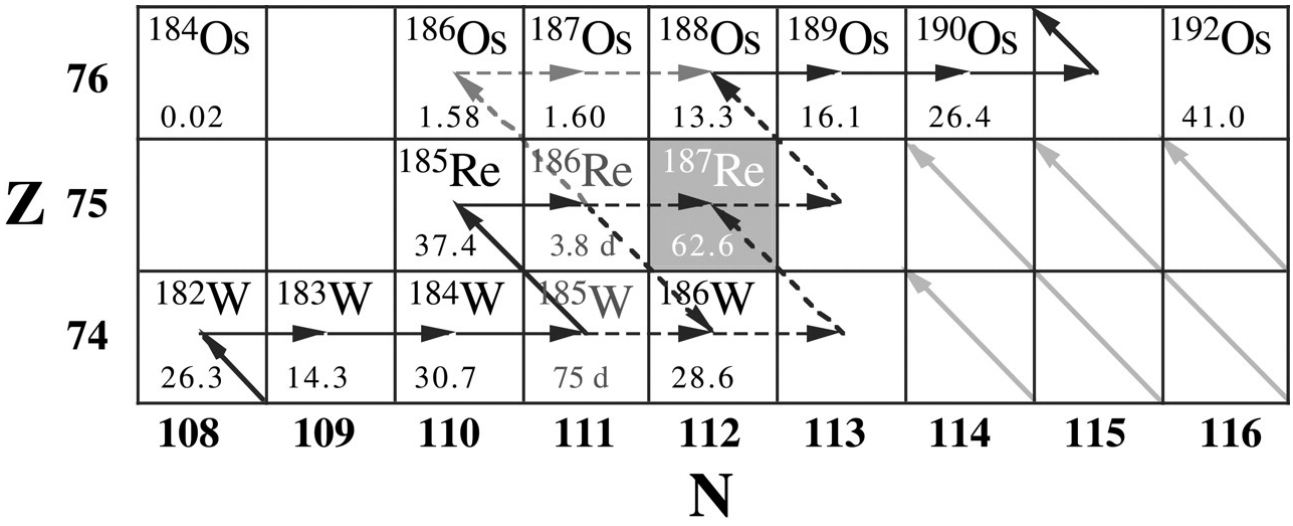

Figure 2.13.: Example for the s-process path from tungsten to osmium (Brandon et al. 2005)

can be calculated by:

$$\frac{dN_s(A)}{dt} = -N_\mathrm{n} N_s(A)\langle\sigma v\rangle_A + N_\mathrm{n} N_s(A-1)\langle\sigma v\rangle_{A-1}, \quad \langle\sigma v\rangle_A = \langle\sigma\rangle_A v_\mathrm{T}, \quad v_\mathrm{T} = \sqrt{\frac{2kT}{\mu}} \tag{2.7}$$

thereby is $N_s(A)$ and $N_\mathrm{n}(t)$ the number densities of nucleus A and of free neutrons. v_T is the thermal velocity, which is almost independent of the target mass. This equation shows that the abundances of the s-process elements should correlate directly with the cross-section for neutron-capture. The measured cross-sections for a neutron energy of 25 keV are shown in Fig. 2.11. The cross-sections show a strong odd-even effect because the average density of resonant states in the compound nucleus is less in even nuclei. Even more obvious is the strong influence of closed nuclear shells, or magic numbers (50, 82, 126). Those small capture cross-sections for the magic numbers represent bottlenecks for a continuous abundance flow. Therefore, higher abundances of elements with this magic numbers are expected and found (see Fig. 2.12). Highly important are also the so-called branching points, where the time for β-decay is equal to the time for neutron-capture. This influences the abundances of the s-process elements. Figure 2.13 shows an example for an s-process path with multiple branching points.
The abundances of the s-process elements found in the solar system cannot be explained by only one s-process model (**main s-process** component). The main process is believed to originate from thermally pulsing, low-mass AGB stars. In this scenario protons are mixed from the H-rich envelope to an intershell consisting of ^{12}C and ^{4}He after the termination of a thermal pulse. The protons are captured and we get the sequence $^{12}\mathrm{C}(p,\gamma)^{13}\mathrm{N}(\beta^+\nu)^{13}\mathrm{C}(p,\gamma)^{14}\mathrm{N}$. So there form two separated regions in the intershell, a ^{13}C and a ^{14}N pocket. α-capture in the ^{13}C pocket releases neutrons that can be captured by the seed nuclei ($^{13}\mathrm{C}(\alpha,\mathrm{n})^{16}\mathrm{O}$). For mass numbers $A < 90$ the abundances are higher than expected. Therefore, a second component is needed to explain them. This process is called **weak s-process component**. For this component, the neutron flux is lower, but the number of seed particles is higher. It is believed that this component takes place during helium core-burning in massive stars. For stars with masses $< 30 M_\odot$ also an s-process during carbon shell-burning is possible via the reaction: $^{22}\mathrm{Ne}(\alpha,\mathrm{n})^{25}\mathrm{Mg}$. Core-carbon burning is not ideal, as the temperatures are too low. For higher mass stars no ^{22}Ne is left after helium-burning. In this stars the temperatures are much higher and the neutron fluxes lower than in low-mass stars on the AGB. A third component the **strong s-process component** has also be postulated to explain the discrepancies for the heavy nuclides. This component is believed to come from low-metallicity stars on the AGB.

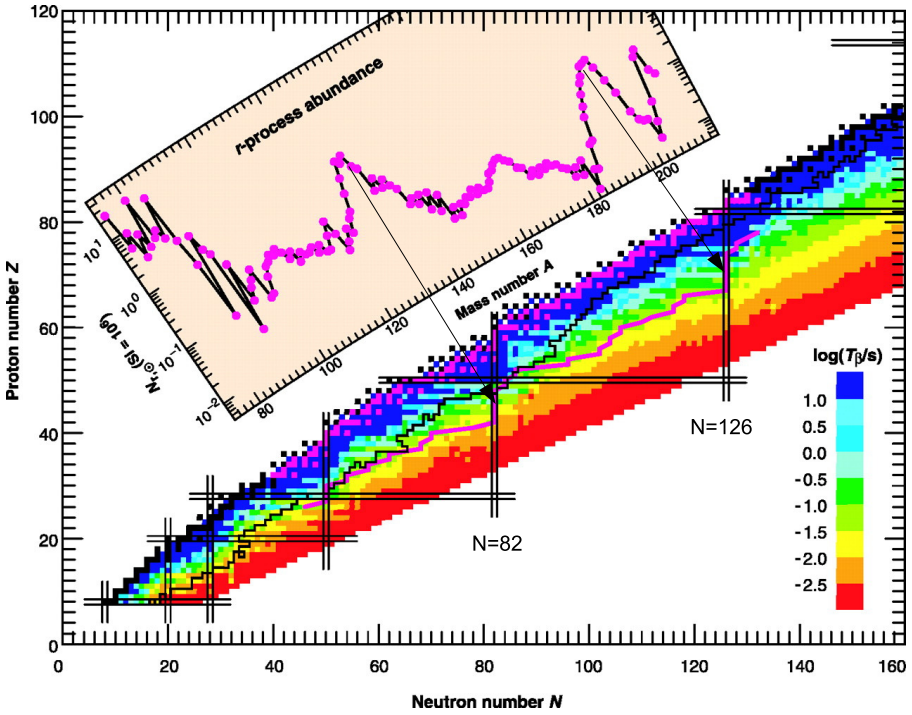

Figure 2.14.: Solar abundances coming from the r-process. The humps correspond to the magic numbers N=82 and N=126 (adopted from Sneden & Cowan 2003).

2.2.2. Rapid neutron capture process

To produce the heaviest nuclides the neutron capture has to be much quicker than in the s-process (τ (n-capture)$\ll \tau(\beta)$). As above stated, this is the case in the r-process. This means that we need much higher temperatures and neutron fluxes. The r-process path is much farther away from the valley of the stable nuclei (see Fig. 2.14).

By subtracting the s-process abundance distribution, calculated by modeling the s-process, from the solar abundances it is possible to determine the r-process abundance distribution. This distribution shows two broader humps at lower mass numbers compared to the s-process. It is remarkable that two so vastly different processes provide abundances of similar magnitude. Figure 2.15 shows the solar system abundances divided into r- and s-process components. It is clear that there exist elements that can be produced by both s- and r-process but also elements that are mostly synthesized in either one of the processes.

It is believed that the humps in the r-process abundance distribution are also due to the neutron magic numbers $N = 82$ and 126. These neutron magic numbers are proton deficient compared to the ones in the s-process. After the termination of the neutron flux all nuclei undergo a sequence of β-decays (A=const) until the most neutron-rich stable isobar is reached. This gives the final abundances. Hence, the r-process abundance maxima are located below the corresponding s-process peaks. Contrary to the s-process abundances are the r-process abundances not related to the neutron-capture cross-sections but reflect the nuclear properties of radioactive progenitors on the neutron-side far away from the stability valley. Due to the high temperature photo-disintegration plays an important role in the r-process. The rates for neutron-capture and reverse photo-disintegration are in thermal equilibrium along an isotopic chain ($dN(Z,A)/dt \approx 0$ for Z =const) for high enough temperatures and neutron fluxes ($T \geq 1\,\mathrm{GK}, \mathrm{N_n} \geq 10^{21}\,\mathrm{cm}^{-3}$). For the calculation of the r-process path and abundances the **waiting point approximation** is taken. It assumes that the even-N isotopes with significant abundances in each isotopic chain represent waiting points for the abundance flow. There, the r-process must continue with β^--decays, which are so slow that they do not effect the thermal equilibrium in the chain (see

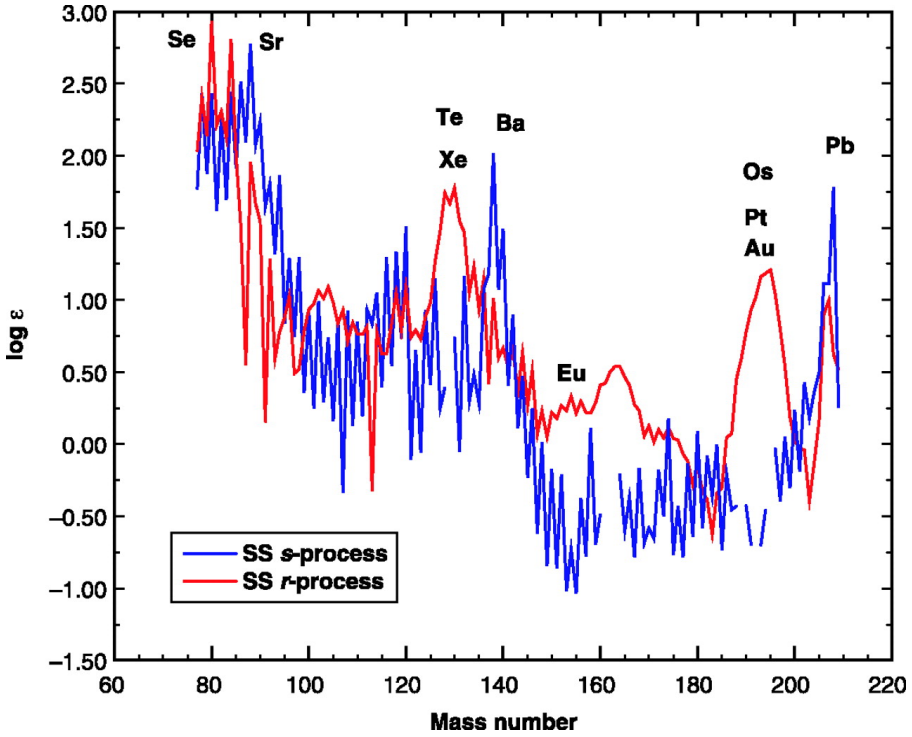

Figure 2.15.: The breakdown of solar system (meteoritic) n-capture isotopic abundances into r- and s-process components (Sneden & Cowan 2003).

Fig. 2.16 for a schematic of the main processes during the r-process). The β^--decays transfer matter from one isotopic chain to the next.

However, if the r-process comes close to one of the neutron magic numbers, it is seen that the reaction energy Q for the (n,γ) reaction becomes very small. Anyhow, for the previous (n,γ) reaction Q becomes maximal. Therefore, nuclides with magic n numbers represent waiting points and we get a subsequent series of β^--decays (see Fig. 2.16c). If the nuclei is sufficiently close to the stable nuclei, this can be overcome. Moreover, the β^--decay half-lives are much longer near the neutron magic nuclei. This means the abundance flow is significantly delayed and these isotopes will build up high abundances, which explains the broader humps.

The observed abundances of the r-process elements give constrains to the conditions that have to be met (high temperatures and high neutron fluxes, time scales of seconds). At the moment there are different sites discussed where the r-process could happen. As high temperatures and short time-scales are required, explosive events are needed. At the moment one of the sites discussed for the r-process is the neutrino-driven wind in the core-collapse supernova of a massive star (see previous chapter). However, it is unclear, if the conditions are sufficient for a successful r-process up to uranium. But it is certain that core-collapse supernovae are fascinating hosts of various nucleosynthesis processes that can produce neutron-rich nuclei. It was also suggested that the neutrino-driven wind could produce lighter heavy elements (e.g. Sr, Zr, Y) by the weak r-process (Arcones & Thielemann 2013). Neutron star mergers are another possible site of the r-process. The enormous density of neutrons ($\sim 10^{33}\,\mathrm{cm}^{-3}$) available in the merger of neutron stars would build up heavy elements. For $A > 210$ the β-decay towards the valley of stability reaches (β-stable) α-particle emitters. The transmutation of these nuclei along α-decay chains lead to the production of very long-lived nuclides (e.g. ^{235,238}U). It would be consistent with r-process elements in the solar system for $A > 130$. This means it could be possible that the light and the heavy r-process elements are produced in different environments.

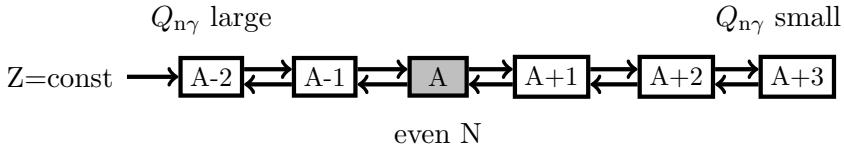

(a) isotopic chain in $(n, \gamma) \leftrightarrow (\gamma.n)$ equilibrium. It is assumed that most of the abundance resides in a single isotope (shaded square, waiting point approximation).

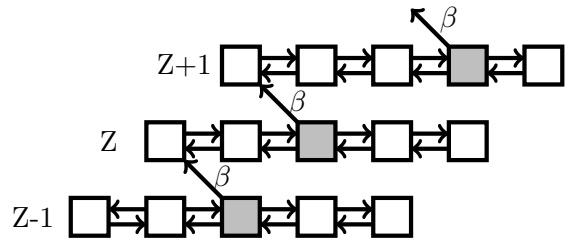

(b) β^- decay of the waiting point nuclei transfers matter from one isotopic chain to the next

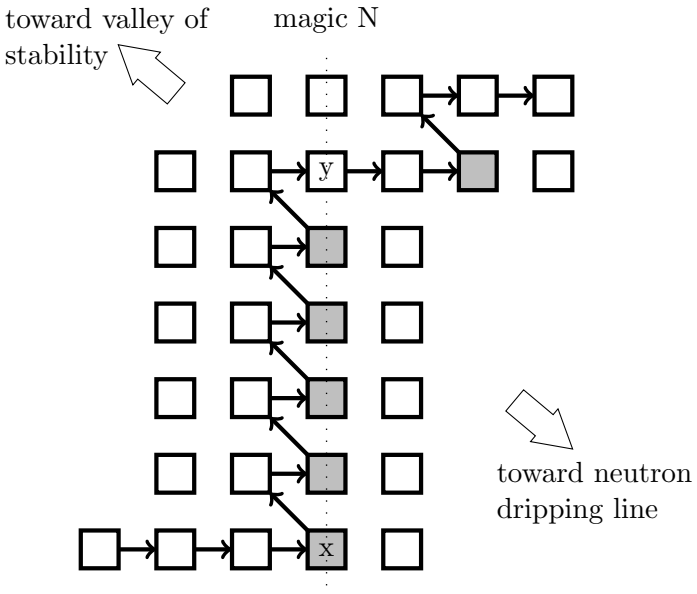

(c) special case when the r-process encounters a neutron magic number

Figure 2.16.: Basic building blocks of the r-process path

2.3. Massive binary evolution

The whole stellar evolution and nucleosynthesis discussed until now is only valid for single stars or stars in very wide binaries that do not interact in their lifetime at all. For close binaries, which are binaries that interact in their lifetime at least at one point, the evolution and also the nucleosynthesis will change because of the mutual influence. In particular mass transfer, and also increasing rotation, or mergers play a very important role. Investigations show that the binarity increases with mass. Massive stars are believed to be all in binaries. Of them 70% are expected to interact at least once (Sana et al. 2012) and therefore this cannot be neglected. Close binary interaction takes place mostly by mass transfer from one companion to the other. This can take place via Roche lobe overflow (see Chapter 3), if both components are sufficiently close together, or by wind accretion. Even if two stars are not close enough together for Roche-lobe overflow to occur, mass may may be possible, if one star has a very strong outward flowing wind. As the secondary moves through the ejected material it can accrete some fraction of that material. Mass transfer changes of course the mass significantly. As described before, the mass, however, has a major impact on the stellar evolution and the nucleosynthesis occurring. It is also possible that mass transfer truncates the time on the giant branches and can therefore prevent the nucleosynthesis on the giant branches from happening. The star can also be stripped off its outer envelope and layers that have been exposed to nuclear burning can become visible leading to strange abundances. As stated before, the stellar winds in massive stars, are strong enough to strip stars to their helium-rich core and form Wolf-Rayet stars. In stars $\lesssim 10 M_\odot$ Roche lobe overflow (see next chapter) can achieve the same result. Common-envelope evolution represents an even more extreme form of mass stripping.

The companion, however, could change his surface abundances by the accretion of already processed material. Moreover, when stars accrete their convective core grows and mixes in new hydrogen-rich fuel, hence the star is effectively younger. This is one explanation for blue stragglers. When stars in binaries accrete matter from a companion, not only can this matter be chemically peculiar but it can carry significant angular momentum. Mixing of the accretor can then follow, with consequences for its surface abundance (Izzard 2013).
Moreover, the existence in a binary system can speed up the rotation. This changes the evolution significantly as is shown in Fig. 2.6. It has a deep influence on the stellar properties. The most important influences are structural effects due to centrifugal force, rotational mixing of chemical elements, anisotropic stellar winds and the enhancements of the mass loss rates, and magnetic fields created by dynamos in rotating stars (Meynet & Maeder 2003).
The change of nucleosynthesis by binarity is still not very well understood and investigated. More details of the evolution of massive single and binary stars can be found in the reviews by Vanbeveren et al. (1998) and Langer (2012), and in the research paper by Wellstein et al. (2001).

3. Hot subdwarf stars

The low-mass PCEBs discussed in this thesis consists of hot subdwarf stars of spectral type B and very low-mass, cool companions. Therefore, it is necessary to understand the formation and properties of the hot subdwarf stars. They will be introduced in this chapter, which is for the most part based on the review on subdwarfs by Heber (2009), complemented by new results published since then. We focus on the binary aspects in particular the HW Virginis systems.

3.1. General properties

In a Hertzsprung-Russell diagram, the most fundamental diagram in stellar astrophysics, the traditional subdwarfs are located to the left below the main sequence of cool population II core hydrogen-burning stars, see Fig. 3.1. The hot subdwarfs have little in common with the traditional subdwarfs. They represent different stages of the late evolution of low-mass stars. They can be classified in different types. B-type Subdwarfs (sdBs) are core-helium burning objects located on the extreme horizontal branch (EHB). On the other hand hot subdwarfs of O-type (sdOs) represent a mixture of post-RGB stars, post-HB stars and post-AGB stars. More about stellar evolution was already explained in Chapter 2. Some stars in the center of planetary nebulae are also called sdO stars. The hot sub-luminous stars were first discovered already in the 1950s by exploiting the photometric survey by Humason & Zwicky (1947). Until the Palomar-Green survey (Green et al. 1986) of the northern Galactic hemisphere the number of known hot subdwarfs stayed relatively small. This survey, however, revealed that hot subdwarfs dominate faint blue objects, even WDs at all apparent magnitudes brighter than B = 18. The Sloan Digital Sky Survey (SDSS) is a new rich source for hot subdwarf stars, in SDSS-Data Release 7 alone 1369 new ones could be found (Geier et al. 2015).
The hot subdwarfs were found to be spectroscopically quite inhomogeneous. Among the sdOs as well as the sdBs helium rich (He-sdBs, He-sdOs) and helium poor objects (sdB, sdOB, sdO) are found. However, most of the sdBs are helium poor, whereas that is not the case for sdO stars. The spectra of sdBs show strong Balmer lines, broader than in B main sequence stars, and weak lines of neutral helium. Stars that have broad Balmer lines, but also weak He I and He II lines are called sdOB stars. SdOs display only He II lines besides the strong Balmer lines. He-sdOs on the other hand show only strong He II and maybe weak He I but no Balmer lines or only weak Balmer lines heavily blended with the Pickering series of He II. Figure 3.2 shows the spectrum of a typical sdB and He-sdO star, respectively. A more detailed classification scheme is given by Moehler et al. (1990) and Drilling et al. (2013).
Hot subdwarfs are highly important for the study of the physical properties of hot star atmospheres. The spectra show a helium deficiency and peculiar metal abundances. Some elements show solar abundances, other are depleted or even enriched. Diffusion was suggested to explain these strange abundances. However, at least in the case of the He-sdOs diffusion alone cannot explain the observed abundance patterns (Hirsch et al. 2008). As the spectra in the UV show many more lines than in the optical, they are more suitable for the investigation of elemental abundances in hot subdwarf stars (see for example O'Toole & Heber 2006).
Besides objects in the field, hot subdwarfs are also found in globular clusters. The horizontal branch morphology of globular clusters was found to vary to a striking degree. The common

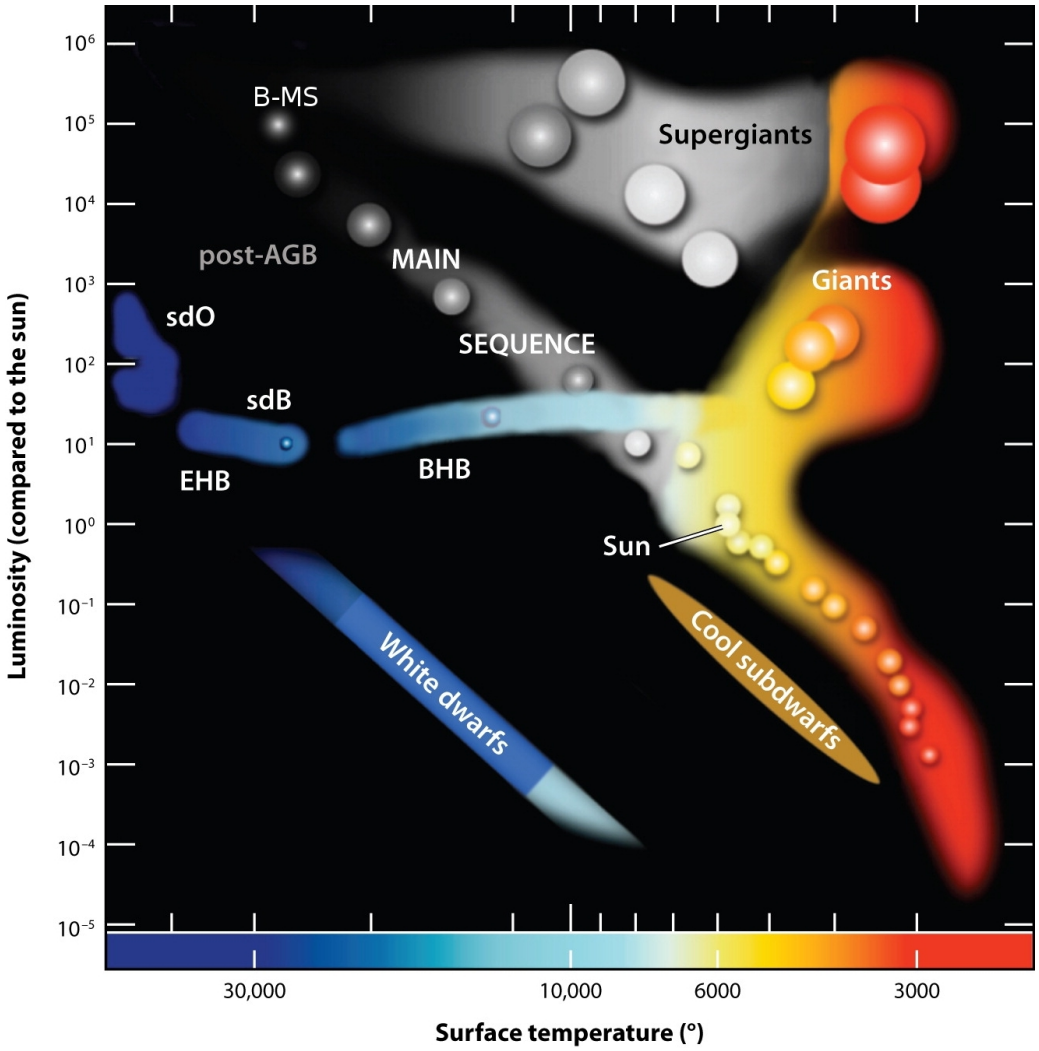

Figure 3.1.: Sketch of a Hertzsprung-Russell diagram highlighting the position of B-main sequence stars, and hot subdwarf (sdB and sdO) stars together with the extreme horizontal branch (EHB) located to the left and below the hot end of the main sequence but above the white dwarf cooling sequence, from Heber (2009).

consensus is that this variation is due to different stellar evolution caused by different primordial metallicities of the clusters (Sandage & Wallerstein 1960). However, this cannot explain the entire phenomenon (Sandage & Wildey 1967). It is conceivable that in globular clusters additional formation scenarios are possible compared to the formation scenarios in the field, because of the dense environment. The scenarios for the formation of field sdB stars will be discussed in the next section.

With the beginning of UV astronomy an excess in the FUV (called UV-upturn) in elliptical galaxies was discovered (see Yi 2008, for a review). This was totally unexpected, as elliptical galaxies were supposed to be composed of old, red stars. Spectral evidence suggested that hot subdwarfs stars are the best candidates to explain this UV excess (Brown et al. 1997). This implies that they must be sufficiently common in early-type galaxies. Brown et al. (2000) could resolve and identify hot subdwarfs in M32, a compact elliptical galaxy with a small UV excess. They constructed a UV color-magnitude diagram showing that most of the UV radiation is coming from EHB stars. Therefore, the understanding of the UV-upturn is closely related to the understanding of the formation of hot subdwarfs, which will be discussed in the next section.

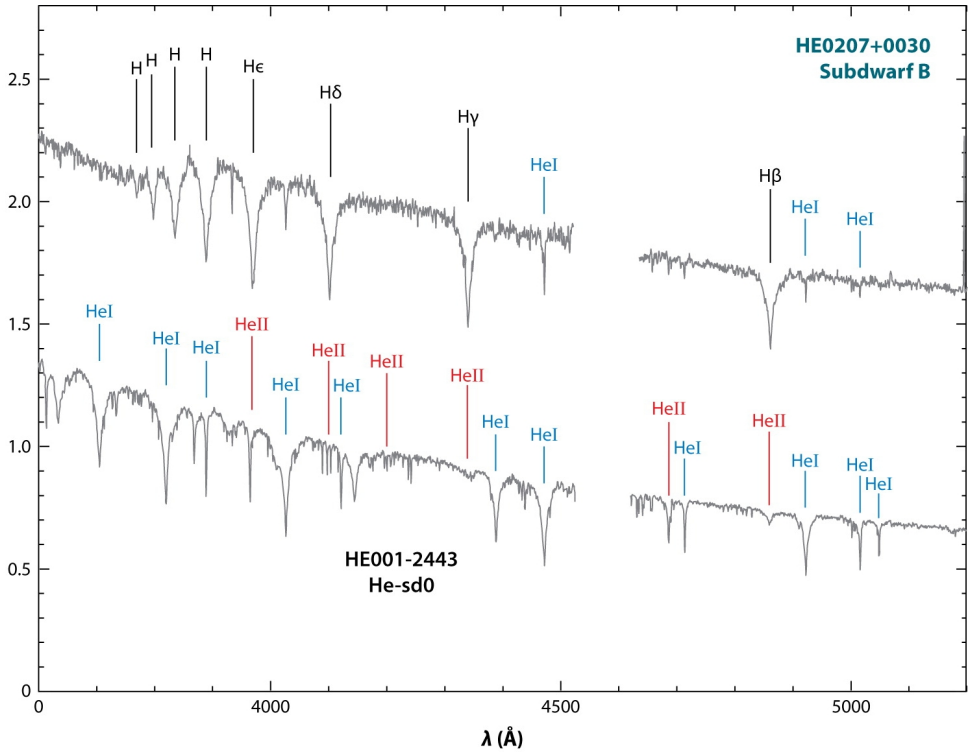

Figure 3.2.: Spectra of typical sdB and He-sdO stars from the ESO Supernova Ia Progenitor Survey. Important lines of hydrogen and helium are indicated, from Heber (2009).

3.2. Formation scenarios

As this work investigates helium-poor stars of spectral type B, the focus will be on sdB and sdOB stars throughout the rest of this chapter. As already mentioned above, sdB stars are core helium-burning stars. The hot burning helium core is surrounded by a only very thin, inert hydrogen envelope. The formation is puzzling, as almost the entire hydrogen envelope has to be lost at the red giant branch. An investigation of the sdB stars showed that about half of the sdBs reside in close binaries with periods of 0.05-30 d (Maxted et al. 2001; Copperwheat et al. 2011). Further details about hot subdwarfs in binaries will be discussed in the next section. This high frequency of sdB stars in close binaries, which is much higher than in other stars, suggests that binary evolution could be an important factor in the formation of these systems. Han et al. (2002, 2003) proposed several different formation channels originating from binary evolution:

- stable Roche lobe overflow (RLOF)
- common-envelope ejection (CEE)
- stable Roche lobe overflow and common-envelope ejection
- double helium white dwarf mergers

Figure 3.3 shows the three different channels resulting in sdB binaries with different types of companions. Depending on the mass ratio and the separation of the system the binary system evolves differently. If the mass ratio of the system is smaller than 1.2-1.5 a stable mass transfer (Roche lobe overflow) to the companion near the tip of the red giant branch. The separation of the system remains almost unchanged in this case. The mass transfer results in a wide sdB binary with periods between 10 and 500 days with F-to-K type main sequence companions or sub-giants. Figure 3.4 shows mass range for the sdB predicted by binary population synthesis

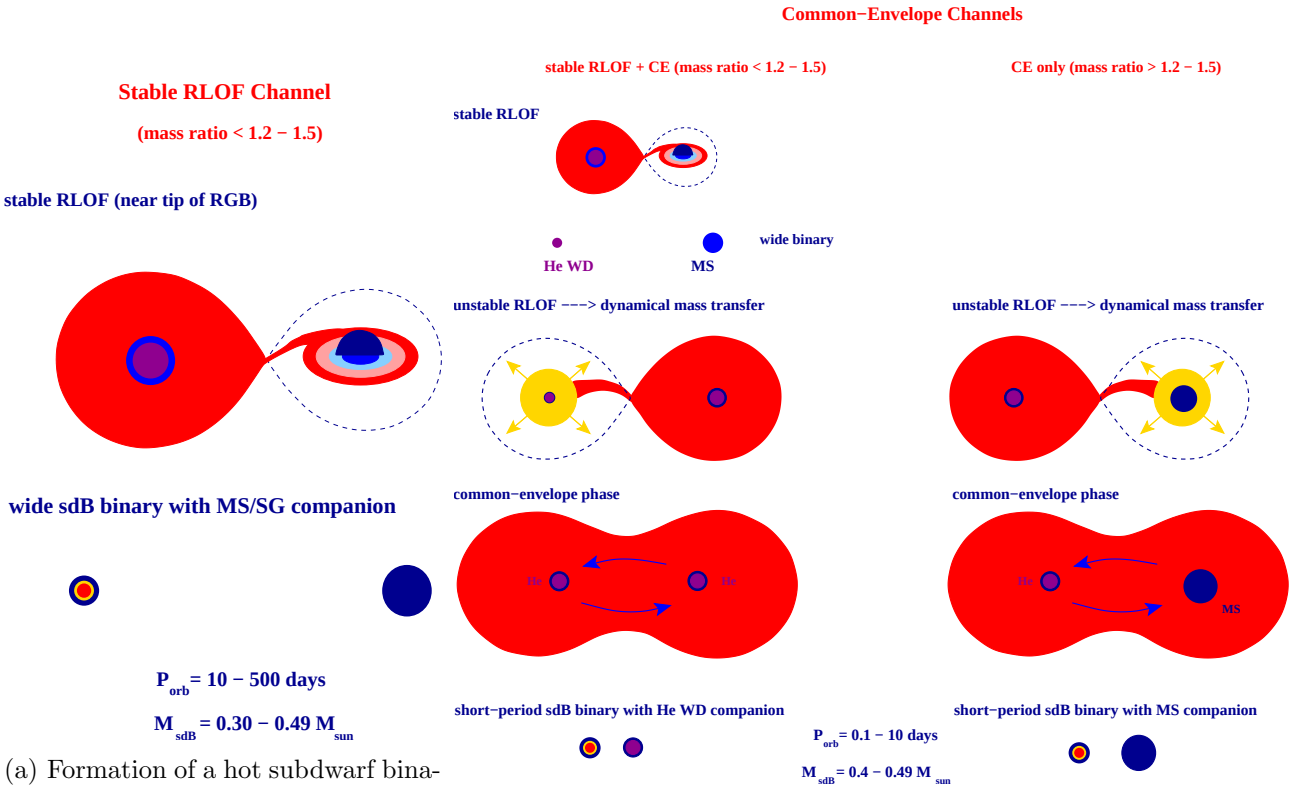

(a) Formation of a hot subdwarf binary by a stable Roche-lobe overflow.

(b) Formation of a hot subdwarf binary by a common-envelope. The result is a sdB in a very short binary system with either white dwarf or low-mass main sequence companion.

Figure 3.3.: Formation of subdwarfs in binary systems by stable or unstable mass transfer (Podsiadlowski 2008)

from the different channels. For the RLOF channel a mass range $M_{\rm sdB} = 0.30 - 0.49\,M_{\odot}$ is expected. If the mass ratio of the system is larger than 1.2-1.5 the mass transfer is not stable any more as the companion cannot accrete all mass transferred and overfills its Roche lobe. Therefore, a common-envelope is formed around both stars. Due to friction the separation of the system shrinks and the orbital energy released is used to eject the envelope. Hence, we obtain a short-period sdB binary with a low-mass main sequence companion. The predicted period of the system is between 0.1 and 10 days. For sdBs formed by a common-envelope ejection a mass distribution is expected that peaks sharply around 0.47 $M_{\odot}$. Moreover, it is possible that after a stable RLOF, the more massive component evolves into a He-WD. As soon as the companion evolves on the red giant branch unstable mass transfer sets in and the system experiences a common-envelope phase. The resulting system has very similar properties to sdB binaries after a common-envelope but the companion is a He-WD companion instead of a low-mass main sequence companion.

However, only half of the sdBs are found in close binaries. But binary evolution can also be used to explain single sdB stars. That is shown in Fig. 3.5. After one or two common-envelope phases a very close binary consisting of two He-WDs is formed. Due to gravitational radiation the separation of the system shrinks. If the separation is small enough, a single sdB can be formed with a wider mass distribution of $M_{\rm sdB} = 0.45 - 0.49\,M_{\odot}$, the maximum is found at $M_{\rm sdB} = 0.47 M_{\odot}$, which is therefore called the canonical mass.

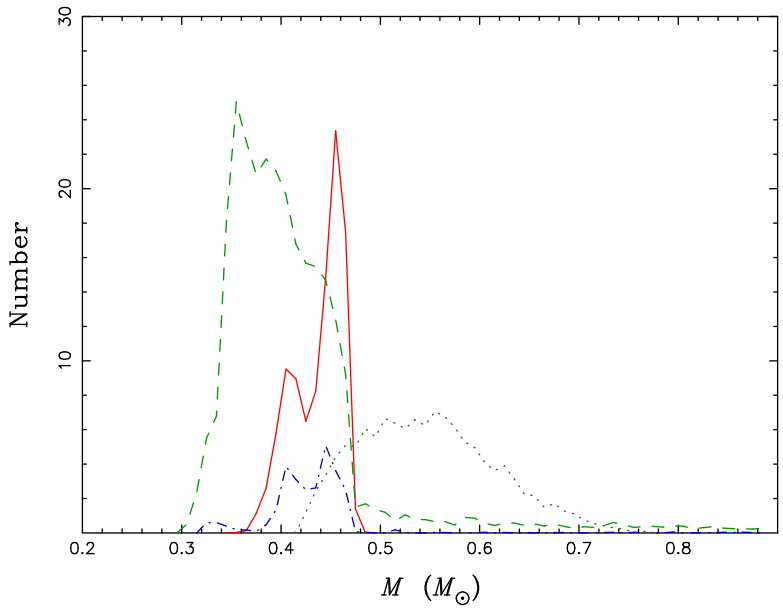

Figure 3.4.: Mass distribution predicted for the different sdB formation scenarios by binary population synthesis (Han et al. 2002, 2003). The solid and the dashed-dotted line gives the mass distribution for the common-envelope channels, the dashed line for the Roche lobe overflow channel, and the dotted line for the merger channel.

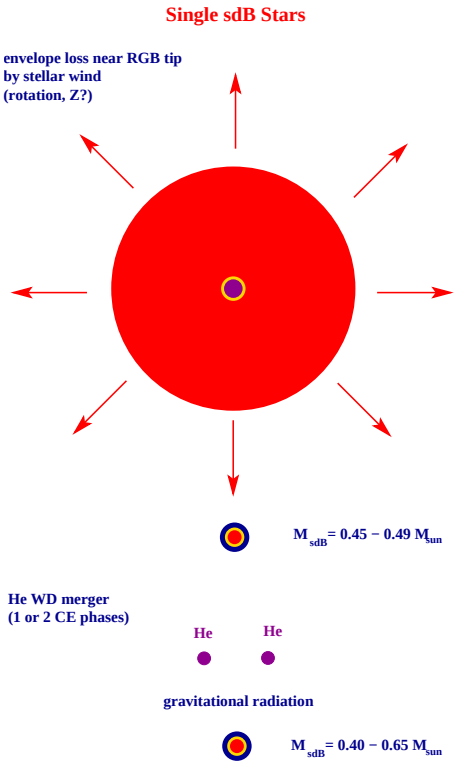

Figure 3.5.: Single star/merger scenario for the formation of single sdBs, from Podsiadlowski (2008).

Another possibility, which I will discuss in detail later, is the merger of a substellar companion with the star during a common-envelope phase. However, in both channels we would expect a single, fast-rotating sdB, because the sdB cannot get rid of the angular momentum. However, rotation velocities of single sdB stars are usually very slow (Geier & Heber 2012), which is in contradiction with the merger scenario.

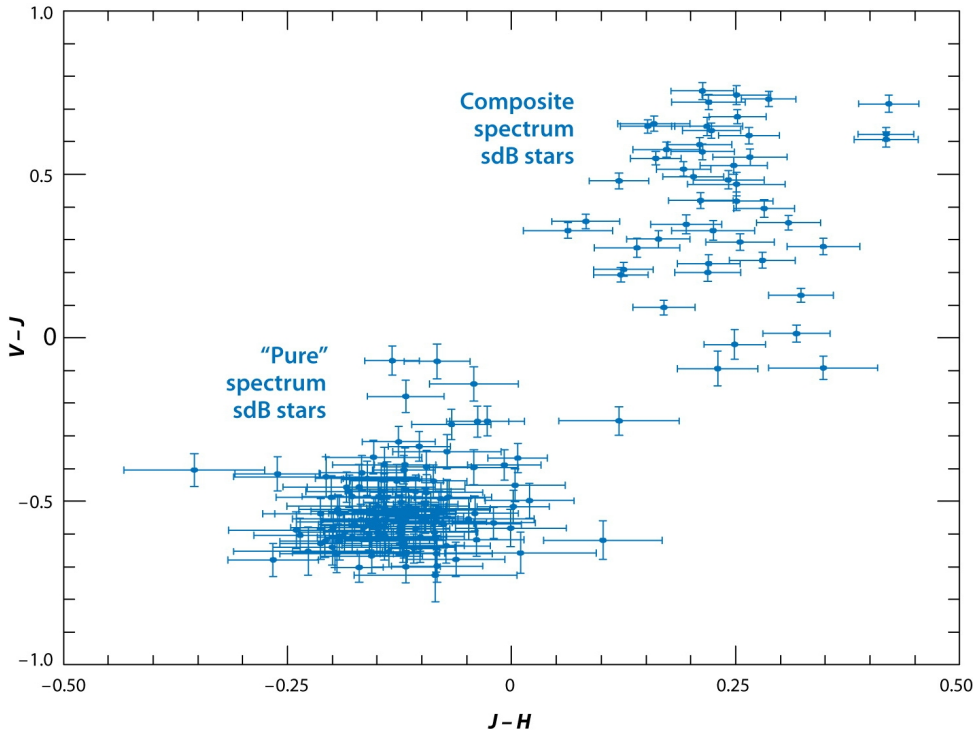

Figure 3.6.: Two-color plot of V – J versus J – H of sdB stars from the sample of Green et al. (2008). The composite-spectrum sdB-stars are in the upper right and the stars with 'pure' sdB spectra at the lower left, from Heber (2009).

3.3. Hot subdwarfs in (eclipsing) binaries

3.3.1. Hot subdwarf binaries with composite spectra

Already the PG survey in the 1980s revealed that a significant fraction (at least 20%, Ferguson et al. 1984) of sdB stars have composite spectra and colors. The 2MASS survey provided infrared colors for many sdB stars. A combination of infrared together with optical photometry is perfect to detect sdBs with cool companion, as the sdB dominates the blue, and the cool companion the infrared. Figure 3.6 shows a color-color diagram. The composite-spectrum sdB-stars are located in the upper right and the stars with 'pure' sdB spectra at the lower left. The latter group includes the 'apparently single' sdBs that show no radial velocity variations above a level of a few kilometers per second over periods of many months, as well as sdB binaries with invisible secondaries. These are either degenerate objects or dwarf M companions too faint to affect the V – J or J – H colors. All known binaries that show 'pure' sdB spectra are post common-envelope systems with periods of a few hours to several days, whereas all of the composite-spectrum binaries at the upper right have much longer periods of many months or more (see for example, Barlow et al. 2012b; Vos et al. 2013).
The gap in the two color diagram corresponds to a companion mass of 0.3 $M_{\odot}$, and is yet unexplained.

3.3.2. Hot subdwarfs in close binaries

As already mentioned before, overwhelming evidence shows that a high percentage of sdBs is located in close binaries. Maxted et al. (2001) found two-thirds of their sdB sample to be such binaries, whereas a lower fraction of 40% was found for the sample containing sdBs from the SPY project (Napiwotzki et al. 2004a). On average the stars in the SPY sample are fainter than those from the Maxted et al. (2001) sample. Hence, the samples may contain a different mix

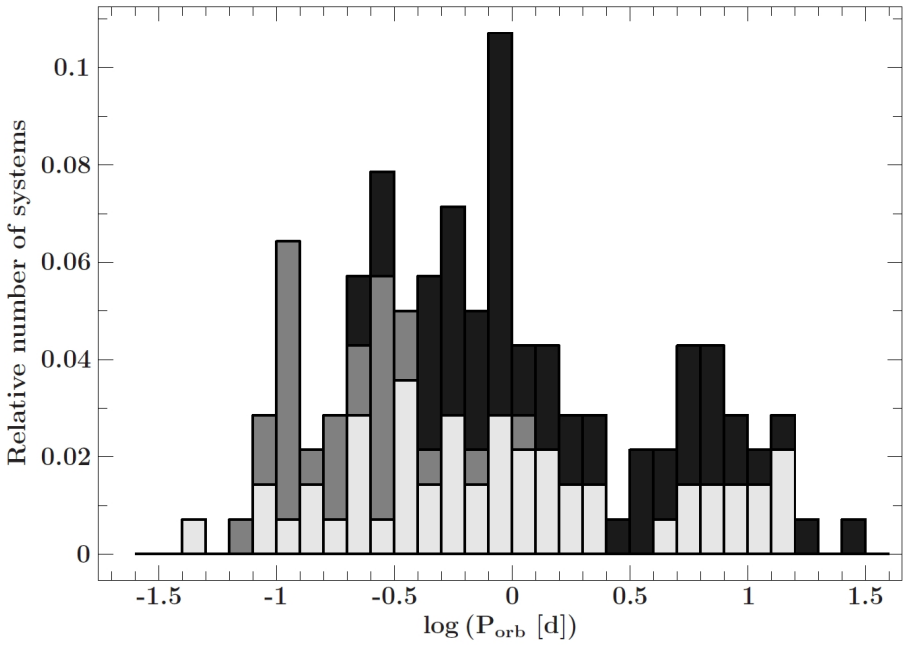

Figure 3.7.: Period distribution of all single-lined sdB binaries with measured mass-functions (Kupfer et al. 2015). Light gray: WD companions, gray: dM companions, dark gray: companion type unknown.

of populations. As the binary fraction may decrease with age (Han 2008), both results need not be inconsistent. Contrary to the sdB stars, He-sdO show almost no signs of binarity. Some have peculiar radial velocity and also lightcurve variations, which cannot be explained until now (Green et al. 2014a). Figure 3.7 displays the distribution of all single-lined sdB binaries with known mass functions (Kupfer et al. 2015). The mass distribution appears to be double-peaked. A strong peak can be found at 0.3 days, with mostly dM companions, and another one around 0.8-0.9 days. The peak found at about 0.1 days is due to a strong selection effect, as it contains all the eclipsing systems, mostly found in photometric surveys by their lightcurve. See next subsection for more details. The gap at ~ 3 days remains unexplained. A lower limit for the mass of the companion can be determined from the mass function, as only the sdB is visible in the spectrum. The different formation scenarios already showed that the companion is either a low-mass main sequence companion or a degenerate companion, for example a white dwarf. The problem is now to distinguish between them, when only a lower mass limit for the companion is known. A cool companion of spectral type M1 − M2 or earlier is detectable from an infrared excess even if the spectra in the optical range are not contaminated with spectral lines from the cool companion. However, if the minimum mass is below $\sim 0.4 M_{\odot}$, it is not possible to determine the nature of the companion from the spectrum alone. With the help of a photometric follow-up, it is possible to discriminate them. The lightcurve of an sdB with a cool companion has a distinctive feature, the so-called reflection effect, which is not visible in sdB+WD systems. The origin of the reflection effect is illustrated in Fig. 3.8a. It is only visible in close binaries with components of very different luminosities but similar radii. Therefore, according to the Stefan-Boltzmann law (eq. 2.2), one star has to be much hotter. Hot subdwarfs with low-mass main sequence companions meet this criteria. In such close binaries the rotation of the companion is synchronized with the orbital period and the sdB star can, hence, heat up the side of the companion facing it to 10 000-20 000 K. With changing period more or less of the illuminated side of the companion is visible. This results in a sinusoidal variation in the lightcurve. An example lightcurve of the reflection effect binary KBS 13 is shown in Fig. 3.8b. The amplitude changes with wavelength and is largest in the I band. This is because the

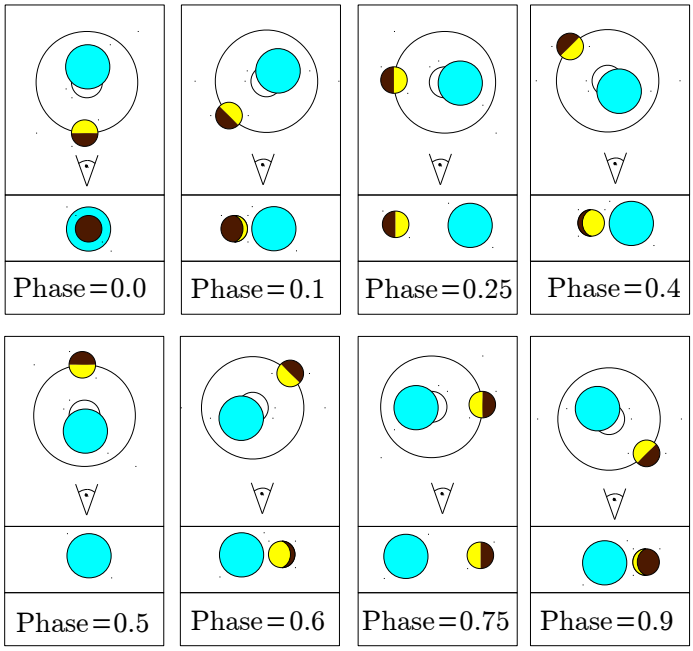

(a) Illustration of the change of the reflection effect at different phases (illustration by S. Müller)

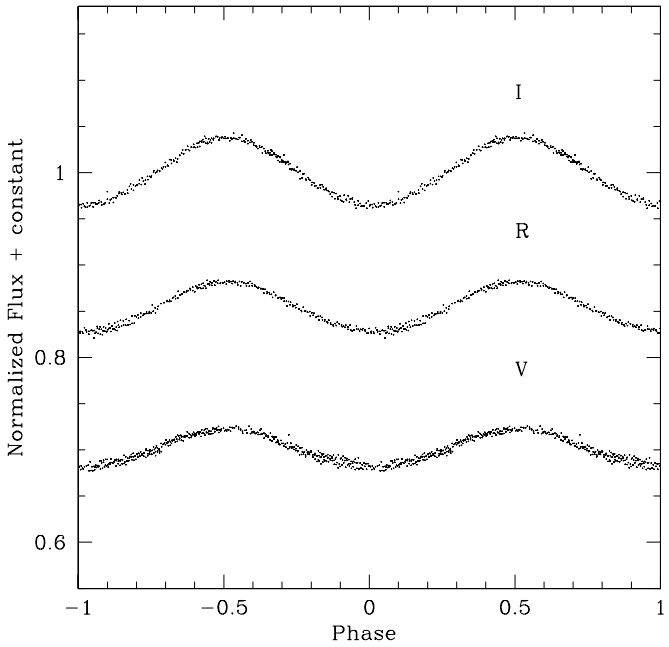

(b) Lightcurve of the reflection effect binary KBS 13 in different bands, from Green et al. (2008)

Figure 3.8.: Appearance and origin of the reflection effect in close sdB+dM binaries

illuminated side of the cool companion has a lower temperature than the sdB, and, hence the maximum more to the red. As the inclination in this sdB+dM binary is too low no eclipses are visible. The reflection effect is also visible at quite low inclinations. The amplitude of the reflection effect depends on the temperature of the sdB and the separation of the system, and therefore also from the period of the system. For a WD companion the irradiated area is so small that the reflection effect is difficult to be detected. Another light variation, however, is induced by tidal forces acting on the sdB star, which leads to an ellipsoidal deformation of the star. If the separation of the system is small enough it is possible to distinguish a low-mass main sequence companion from a compact companion by help of the lightcurve. Further details can be found in Sections 7.8 and 7.5. A summary of the orbital parameters of all known post common-envelope systems (sdB/WD+dM/BD) can be found in Table A1.

3.3.3. Eclipsing sdB binaries - HW Virginis systems

Eclipsing binaries are of particular importance in astrophysics, as they allow the direct determination of stellar radii. Eclipsing sdB stars with low-mass, cool companions are called HW Virginis systems, after the prototype. Until 2010 only 9 such systems and 8 more non-eclipsing systems were known. Table A1 summarizes the data on sdB+dM systems known.

The lightcurve is characteristic (see Fig. 3.9) and, therefore, easy recognizable. It shows a prominent reflection effect and a primary as well as a secondary minimum. The periods are around 0.1 days with AA Dor being an exception with a period of 0.2614 days and an sdOB primary. Due to the large number of photometric surveys, ground-based as well as space-based, the number of known HW Virginis systems almost tripled since 2010. A lot new eclipsing sdB binaries with cool companions have been found with the ASAS, SuperWASP, OGLE and Kepler survey. Developments in the discovery and investigation of HW Vir and reflection effect binaries in the last four years along with the analysis of some of these systems will be given

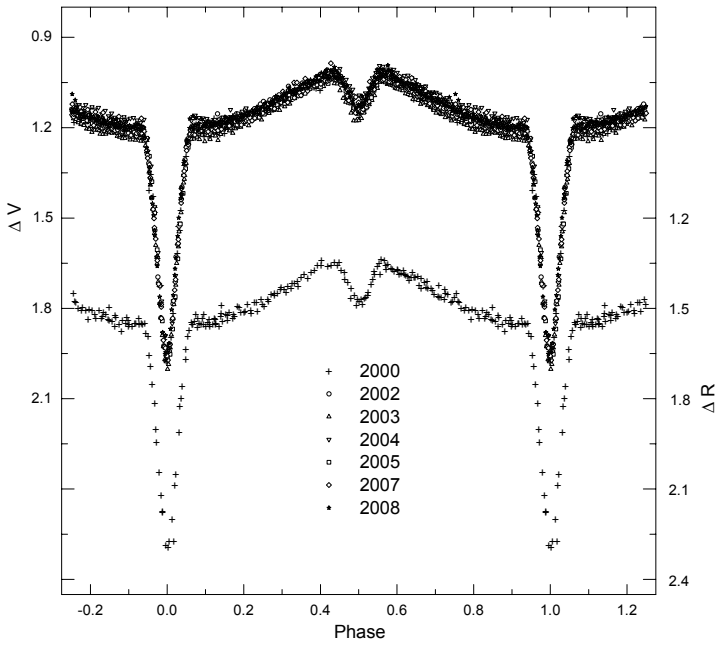

Figure 3.9.: Lightcurve of HW Virginis in two different bands V and R (Lee et al. 2009). This system was the first eclipsing sdB+dM system found by Menzies & Marang (1986) and is one of the best investigated HW Vir systems observed now for over 25 years.

in Chapter 7. The HW Vir systems are usually one-lined spectroscopic binaries, because the companion does not show any absorption lines in the spectrum. However, for the two brightest systems, HW Vir and AA Dor (Vučković et al. 2008, 2014), it was possible to find emission lines. Those originate from the illuminated side of the companion. Hence, a determination of the mass ratio independent from the lightcurve analysis is possible, which is not possible from a photometric analysis alone. This problem will be discussed further in Chapter 7.

3.4. Subdwarfs and substellar companions

Soker (1998) and Nelemans & Tauris (1998) proposed that not only stellar companions but also substellar companions such as planets or brown dwarfs could be responsible for the mass loss that is required on the red giant branch to form an sdB star. As soon as the host star evolves to become a red giant, close substellar companions will be engulfed by a common-envelope. Whether the substellar companions are able to eject the envelope and survive, evaporate or merge with the stellar core is unclear. The calculation of the fate of the companion by Nelemans & Tauris (1998), for the example of a pre-He WD with a core mass of 0.33 $M_{\odot}$, is shown in Fig. 3.10. For an sdB star the calculation would be analogue with a core mass of about half a solar mass. In this example a minimum planetary mass of ~ 21 $M_{\rm J}$ is needed to expel the entire envelope. Less massive planets are seen to be evaporated. However, for $15 < m_{\rm p}/M_{\rm J} < 25$ the planet fills its Roche-lobe and is likely to be disrupted as a result. Planets more massive than ~ 25 $M_{\rm J}$ survive the common-envelope phase but will later spiral in due to gravitational wave radiation. A single sdB results, if the substellar object that helps to eject the envelope , is destroyed afterwards or merges with the core. This could explain at least some of the single sdBs.

Planets around pulsating and close binary sdBs have indeed been discovered (e.g. Silvotti et al. 2007), but these are too far away from their hosts for such interactions and the Soker scenario

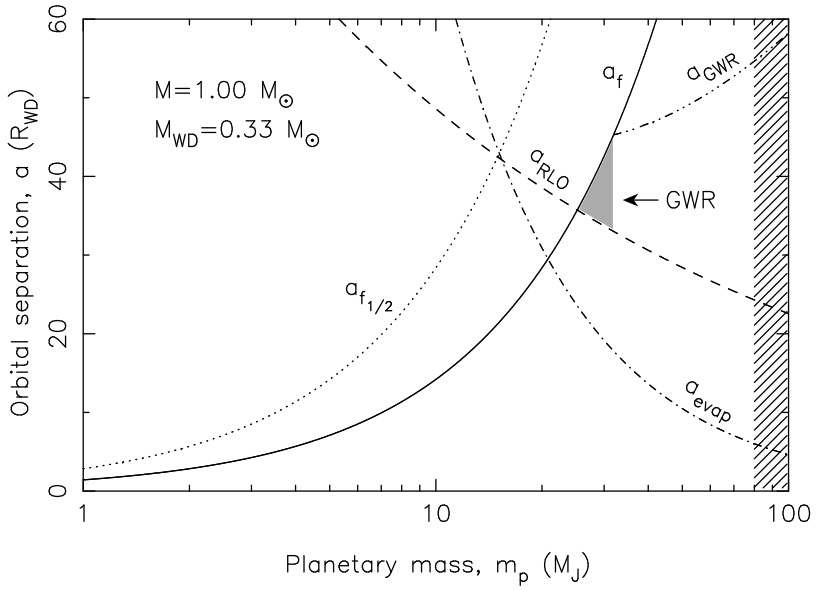

Figure 3.10.: Separations after the spiral-in phase for a 1 $M_\odot$ star with a core of 0.33 $M_\odot$ as a function of planetary mass. The solid line gives the separation for which the liberated orbital energy is equal to the binding energy of the envelope. The dashed line gives the separation below which the planet fills its Roche-lobe and is hence likely to be disrupted. The dash-dotted line gives the separation at which the planet is evaporated. The shaded area indicates a spiral-in timescale of less than 5 Gyr due to gravitational radiation. Above 80 M_J, the companions are heavy enough to ignite hydrogen as stars (Nelemans & Tauris 1998).

remains under debate. Charpinet et al. (2011) discovered Earth-size objects in close orbits around a pulsating sdB observed by the Kepler mission. Those objects may be the remnants of one or more massive planets destroyed during the common-envelope phase. Our discovery of an eclipsing sdB binary with a companion with a mass in the range of $45 - 67\,M_\mathrm{J}$, J0820+0008 (Geier et al. 2011c), shows that substellar companions are indeed able to form an sdB star. This implies that planets may have a yet underestimated influence on stellar evolution.

Moreover, eclipsing binaries offer the perfect method to search for small, low-mass third bodies in the system. They allow to use the eclipse timing method. For this the exact eclipse times are measured. Without any disturbances those should always be exactly after one period. Therefore, we measure the difference between the observed and the calculated eclipse time. This is visualized in an O-C diagram. In this diagram a period change is visible as a parabola. The presence of a third object is seen as a sinusoidal variation in the O-C diagram, because the barycenter "wobbles" due to the third object in the system (more details in Chapter 7.2). This effect is also sensitive to very low-mass objects with larger separations. As the periods of the HW Virginis systems is so short they are the perfect candidates for applications of this method.

Period variations have been found for almost all of the HW Vir systems that have accurate eclipse timings covering more than five years (except for AA Dor and J0820 (see Sect. 7.2), which have companions with masses close to the hydrogen-burning limit). This may be explained by the presence of a third body, which is likely to be one (or two) giant planet(s) in several cases. These discoveries were unexpected, because it is considered to be difficult for giant planets to form around main sequence binaries because of the short lifetime of circumbinary disks. In addition, such planets may not be able to survive common envelope evolution. Instead, it has been suggested that these circumbinary planets are second generation (Zorotovic & Schreiber 2013), which are formed from the instability of a post-CE disk. This has been challenged by

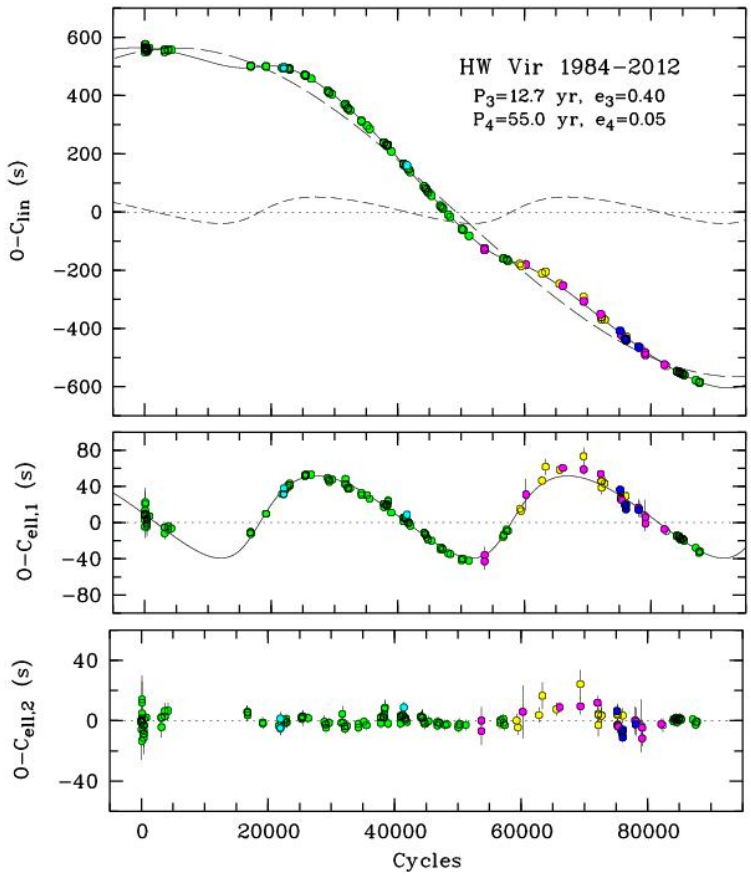

Figure 3.11.: O-C diagram of HW Virginis (Beuermann et al. 2012b) with fit of two Keplerian orbits to the eclipse-time variations

Bear & Soker (2014).
Figure 3.11 shows the O-C diagram of HW Virginis with the fit of two substellar objects. A summary of all claimed substellar objects around eclipsing sdB/WD stars can be found in Table A2.
However, there is also evidence, which argues against the explanation of the O-C variation by third bodies. Recently the third body around V471 Tau was disproved (Hardy et al. 2015). Zorotovic & Schreiber (2013) also proposed an alternative scenario for the period variations due to processes acting in deeply convective secondary stars.

3.5. Pulsating hot subdwarfs and asteroseismology

Besides the eclipsing binaries, another important class of stars are pulsating stars. It is possible to determine the stellar mass, the mass of the envelope, the age and other very important parameters with asteroseismology. Two different classes of pulsators are found among the sdB stars. The sdBV$_r$ stars (V361 Hya stars), discovered by Kilkenny et al. (1997) and independently theoretically predicted by Charpinet et al. (1996), are low-amplitude multi-mode pulsators with typical periods ranging between 80-600 s. Their pulsation amplitudes are generally of the order of a few milimag. The short periods, being of the order of and shorter than the radial fundamental mode for these stars, suggest that the observed modes are low-order, low-degree p-modes (Charpinet et al. 2000). The driving mechanism was identified to be due to an iron opacity bump. The known sdBV$_r$ stars occupy a region in the $T_{\rm eff} - \log g$ plane with effective temperatures between 28 000 K and 36 000 K and surface gravities (log g) between 5.2 and 6.2 (see Fig. 3.13). Only 10% of all stars falling in this region show pulsations. Green et al. (2003)

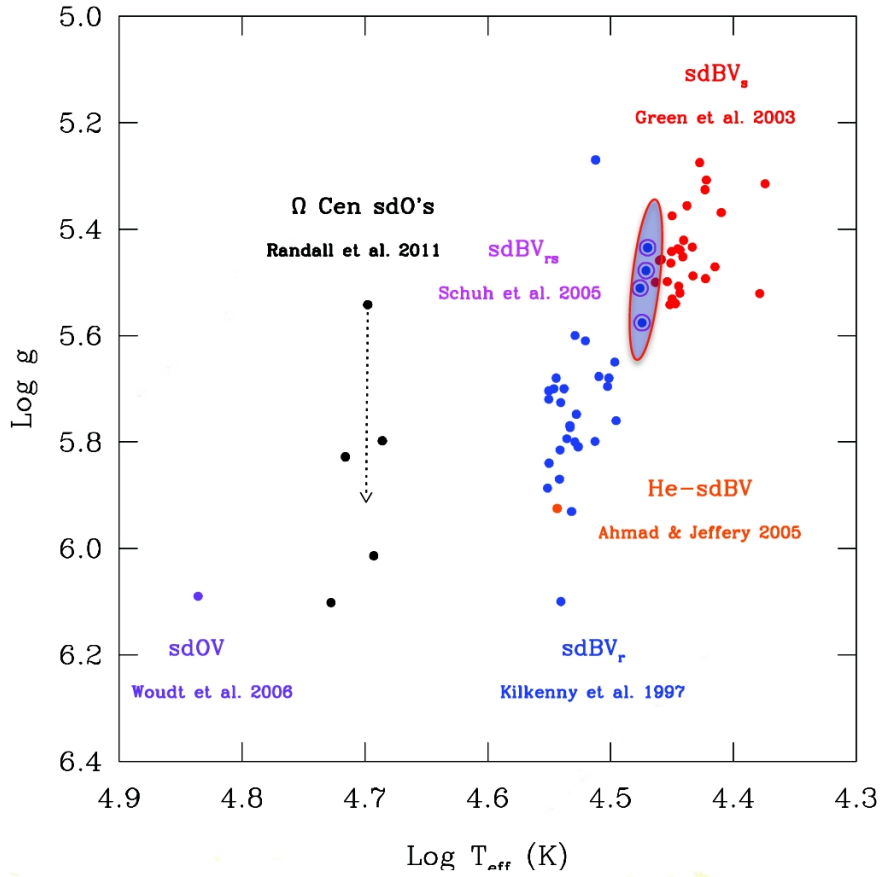

Figure 3.12.: $T_{\rm eff} - \log g$ diagram of the sdB pulsators (`http://www.astro.uni.wroc.pl/IAUS301_Talks/Day4-1430-Randall.pdf`)

discovered a new class of sdB pulsators, the V1039 Her stars, with much longer periods from 45 min to a few hours. This corresponds to mid- and high-order low-degree g-modes, which can propagate in deep regions of the star, down to the convective He-burning core (Van Grootel et al. 2013). In the $T_{\rm eff} - \log g$ plane they occupy the region between effective temperatures of 22 000 to 29 000 K and surface gravities between 5.2 and 5.6. Both kinds of pulsations are driven by the κ-mechanism associated with a local overabundance of iron-peak elements in the driving region. Figure 3.13 shows some example lightcurves of sdBV$_{\rm r}$ and sdBV$_{\rm s}$ pulsators. Figure 3.12 shows a $T_{\rm eff} - \log g$ diagram with all known hot subdwarf pulsators. Besides the already mentioned sdBV$_{\rm r}$ and sdBV$_{\rm s}$ pulsators,there exist also some hybrid pulsators, sdBV$_{\rm rs}$ in the overlap region showing both short and long period pulsations. Moreover, also one sdO and one He-sdB pulsator was found. Another class are the sdO pulsators found in the globular cluster Ω Cen.

As asteroseismology allows the determination of the mass of the pulsating subdwarf, those stars are ideal to determine the mass distribution of the pulsating sdBs and compare them to the theoretical mass distribution for the different formation scenarios to get clues about the formation of sdB stars. This is shown in Fig. 3.14. The observed mass distribution determined from 22 single, pulsating sdB stars shows a strong peak at the 0.47 $M_\odot$. It matches perfectly with the prediction from the common-envelope channel, but is in contradiction to the merger channel, which was regarded to form single sdB stars.

Of utmost importance are the eclipsing binaries containing a pulsating sdB star. The problem with typical HW Vir systems has been that they are single–lined spectroscopic binaries (see e.g. Schaffenroth et al. 2013, 2014c), and as such it is normally not possible to derive a unique mass ratio. HW Vir systems harboring a *pulsating* sdB primary, however, offer additional pos-

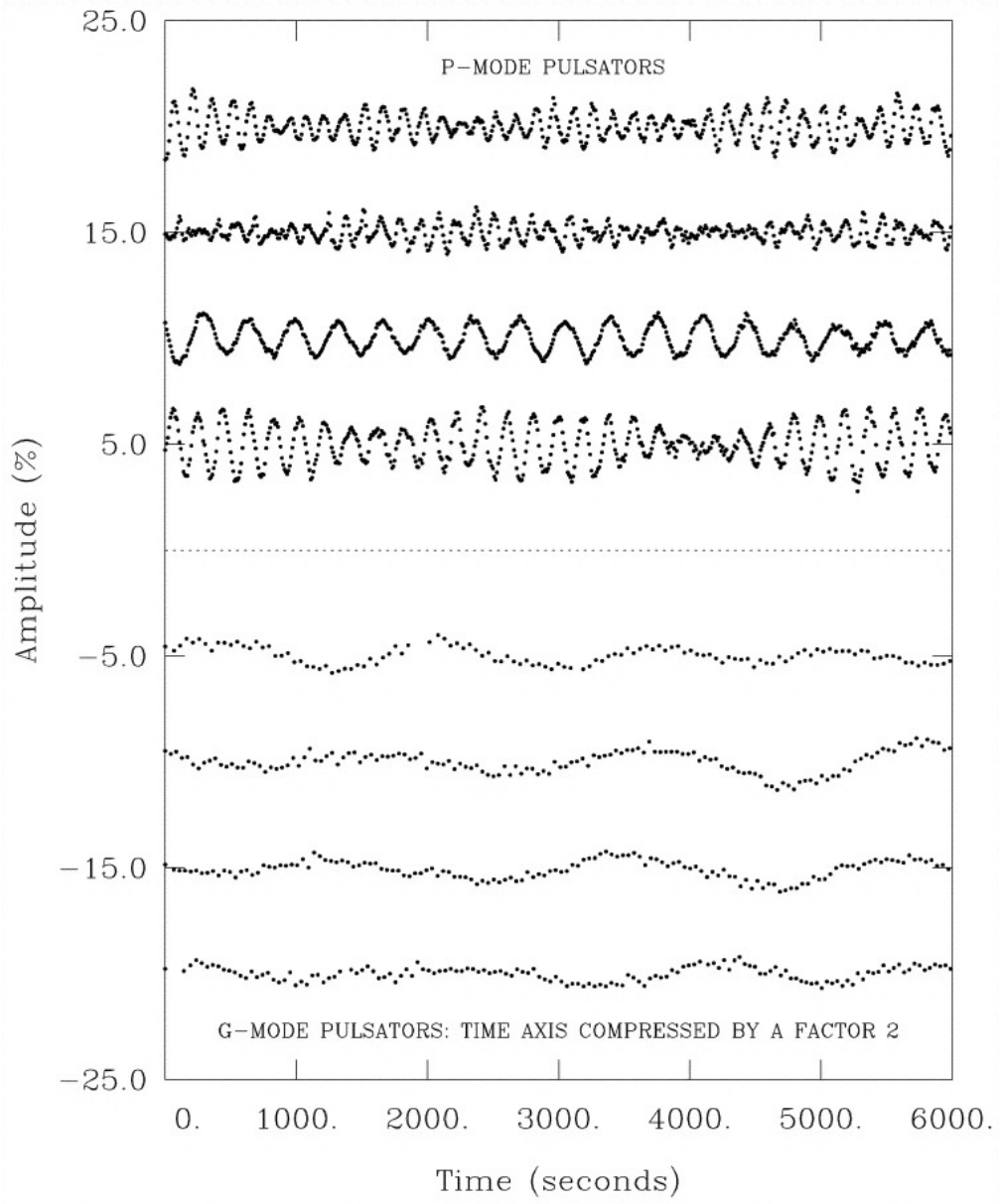

Figure 3.13.: Example for sdBV$_r$ and sdBV$_s$ pulsators (adopted from Fontaine et al. 2003)

sibilities, as the stellar properties can be constrained by the light curve and asteroseismological analyses. Until recently, only two HW Vir systems with pulsating sdBs were known. The first such object – NY Vir – was found to be a pulsating sdB in an eclipsing binary by Kilkenny et al. (1998). It shows more than 20 pulsation modes with amplitudes of several milimag (see Fig. 3.15). An asteroseismic analysis facilitated the stellar parameters of this system to be determined independently from the lightcurve analysis (Van Grootel et al. 2013). Østensen et al. (2010) found another pulsating sdB + dM HW Vir binary (2M1938+4603). Unfortunately, the amplitudes of the pulsations, which were detected by *Kepler* in a 8-d lightcurve, are so small that they cannot be observed by ground-based telescopes. Thus, this star is therefore not an ideal target for asteroseismological modeling.

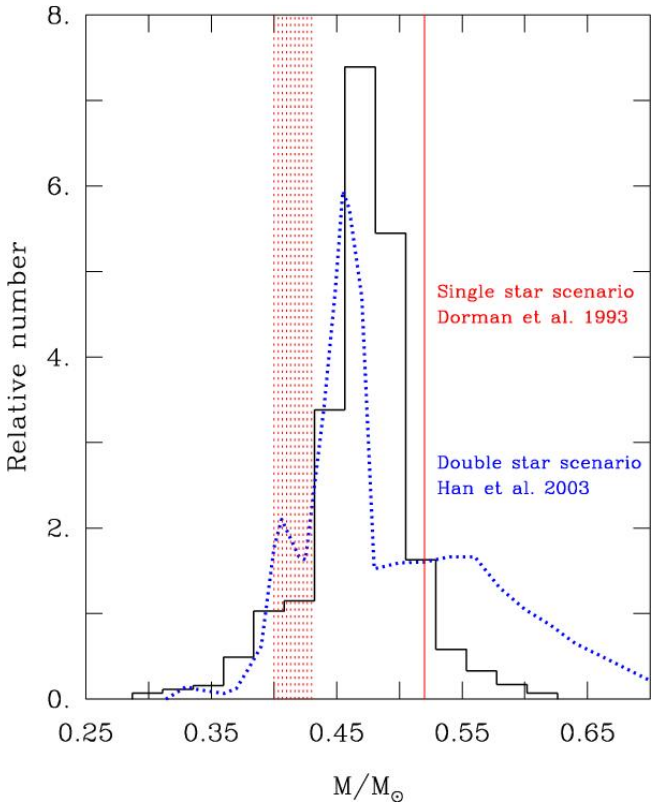

Figure 3.14.: Comparison of the empirical mass distribution of sdB stars (adopted from Fontaine et al. 2012) based on a sample of 22 stars (histogram) with the range of possible masses predicted by single star evolution according to Dorman et al. (1993) and the predicted mass distributions of sdB stars due to binary evolution according to Han et al. (2003).

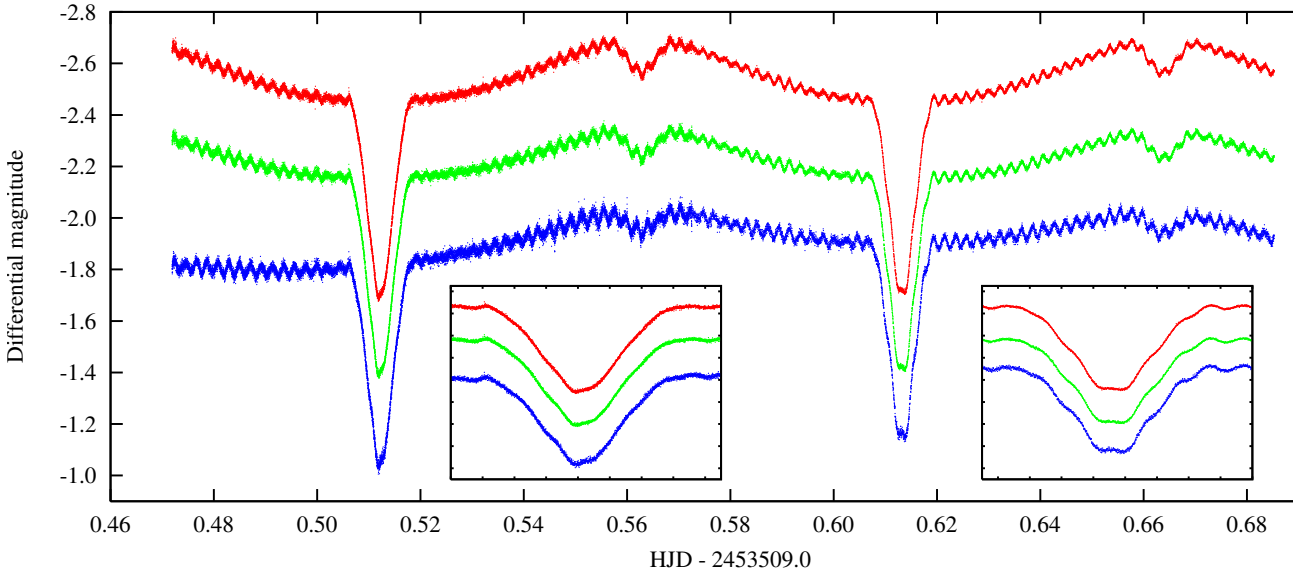

Figure 3.15.: 1. ULTRACAM/VLT r' (upper), g' (middle) and u' (bottom) lightcurves of the eclipsing sdBV star PG 1336-018 (NY Vir). The insets show enlarged sections of the two primary eclipses, where pulsations are clearly visible, from Vučković et al. (2007).

4. Runaway stars

As we investigate a unique runaway star in the second part of this thesis, a short introduction into the different ejection scenarios and their properties will be given here. Some massive, young stars are found in the Galactic halo far away from the star-forming regions in the disk. As the life-time of those massive stars is very short, of the order of millions to a few tens of million years, they are not expected to be found far away from star clusters or associations. Hence, ejection mechanisms have to exist that accelerate these stars to high velocities, sufficient to reach those remote places.
Blaauw (1961) discovered first that there exists a group of early-type stars with high velocities, in contrast to the generally low space velocities for stars of these types. Stars with peculiar space velocities in excess of $40\,\mathrm{km\,s^{-1}}$ and directed away from known clusters or associations were termed runaway stars, as they 'run away' from their birthplaces. About 10-30% of the O stars and 5-10% of the B stars (Stone 1991; Gies & Bolton 1986) have been found to have such large peculiar velocities. The measured velocity dispersion of these stars is $\sigma_\mathrm{v} \sim 30\,\mathrm{km\,s^{-1}}$, much larger than that of "normal" early-type stars ($\sigma_\mathrm{v} \sim 10\,\mathrm{km\,s^{-1}}$). Besides the velocities they are distinguished from the normal early-type stars also because by a low fraction of multiplicity ($\sim 10\%$). The binary fraction of normal early-type stars is $> 50\%$. Moreover, over 50% of the (massive) runaways show large rotational velocities and enhanced surface helium abundances (Blaauw 1993).
Several scenarios for the acceleration of the runaway stars have been proposed. A good summary, on which this chapter is partial based, is given by Hoogerwerf et al. (2001).

4.1. Binary-supernova scenario (BSS)

The first scenario for the acceleration of runaways was proposed by Blaauw (1961). Figure 4.1 shows an illustration of this scenario. A close binary system may originate from a previous common-envelope phase or it may have experienced a Roche lobe overflow. Blaauw (1961) suggested that the runaway star receives its velocity when the primary component of this massive, close binary explodes in a supernova. Because of the huge mass loss the gravitational attraction on the secondary is considerably reduced, and the companion is ejected at about the orbital velocity. The exact velocity (Tauris & Takens 1998) is given by:

$$v_\mathrm{sec} = \sqrt{1 - 2M_\mathrm{co}\frac{M_1 + M_2}{M_1^2}}\, v_\mathrm{orb},\ v_\mathrm{orb} = \sqrt{G\frac{M_1^2}{a(M_1 + M_2)}}$$

where M_1 and M_2 are the pre-SN masses of the primary and secondary and M_co is the mass of the compact object formed by the supernova explosion.
The remnant of the primary after the explosion will be a compact object, either a neutron star or a black hole. Whether the compact object stays bound to the runaway star depends on the previous history of the binary system (eccentricity). Furthermore, it also depends on the kick velocity due to an asymmetry of the supernova explosion (see for example Burrows et al. 1995). In most cases the mass loss is insufficient to break up the binary (Blaauw 1961). Hence, most BSS runaways are expected to remain double, which is inconsistent with the low

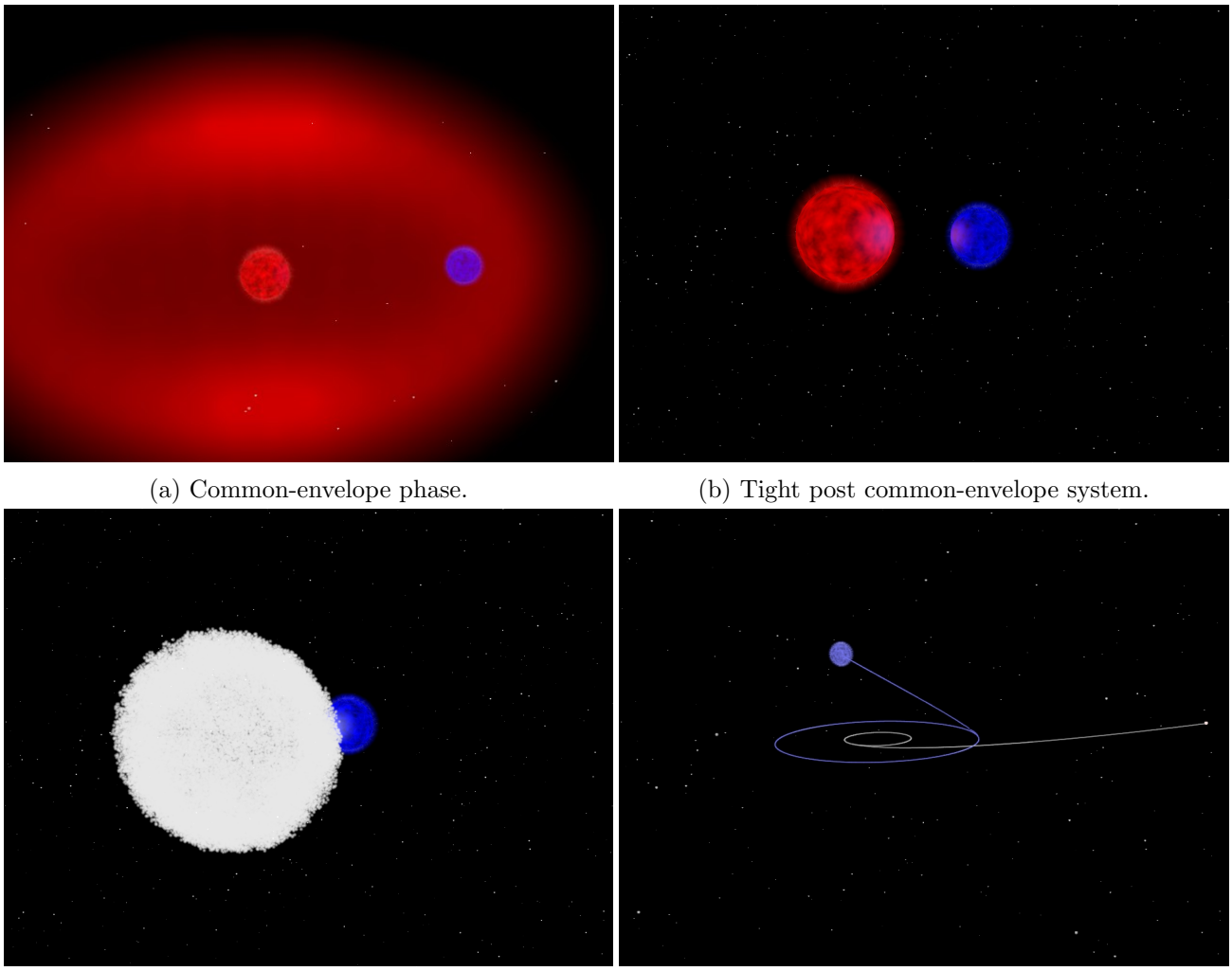

(a) Common-envelope phase.

(b) Tight post common-envelope system.

(c) Supernova explosion.

(d) Release of the runaway star.

Figure 4.1.: Disruption of a post common-envelope binary system in a supernova explosion: After the common-envelope phase a very tight binary system is formed. The primary (red) explodes in a supernova explosion, which reduces its mass significantly. The gravitational pull by the compact remnant is insufficient to keep the system bound, such that the secondary leaves the former binary as a high-velocity runaway star with about its orbital velocity[1].

multiplicity fraction. The high-mass X-ray binaries are examples of such systems. Their typical velocities of $\sim 50\,\mathrm{kms}^{-1}$ (Chevalier & Ilovaisky 1998) are the result of kick velocity acquired by the supernova shell leaving the system.
The search for compact companions to the OB runaway stars stayed unsuccessful (see, e.g. Gies & Bolton 1986). This suggests that the kick velocity must have been large enough to unbind the system. Because of the large velocities found in single BSS runaways the progenitor systems must have been very close binaries so that the orbital velocity is high enough to explain the velocity of the runway. This implies that the progenitor system has to have experienced close binary evolution and, for the highest velocities, a common-envelope phase. This should lead to the following properties that should be observed in BSS runaway stars:

- They are expected to have increased helium abundances and high rotational velocities: when the primary fills its Roche lobe, mass and angular momentum transfer from the binary to the runaway progenitor should enrich the runaway with helium and spin it up

[1]Illustrations by Andreas Irrgang (`http://www.sternwarte.uni-erlangen.de/~irrgang/animations`)

(Blaauw 1993).

- They could become blue stragglers, because the fresh fuel they receive during the mass transfer can rejuvenate them.
- The flight-time should be smaller than the age of the cluster or association, where the runaway originates from. It takes several Myr for the more massive star to evolve and explode in a supernova.
- Because of the low separation of the stars in the pre-supernova binary, high-velocity BSS runaways are expected to accrete some of the material ejected by the companion in the core-collapse supernova. Hence, we expect a pollution of the surface abundances by the elements characteristic for the supernova ejecta. An enhancement of the α-elements, (e.g. Ne, Mg, Si, S Przybilla et al. 2008) and of r-process elements is expected.

4.2. Dynamical interaction scenario (DES)

Another scenario to eject runaway stars was proposed by Poveda et al. (1967). Runaway stars are formed by gravitational interactions between stars in dense, compact clusters. Although runaways can also be produced by the encounter of a single star with a binary system, the most efficient interaction is the encounter of two hard binary systems. Figure 4.2 shows different possible outcomes for such an encounter:

- exchange of partners
- one single runaway and an hierarchical triple system
- formation of a new binary system and double ejection
- four single stars

Detailed simulations showed that these collisions can produce runaways with velocities up to 200 $\mathrm{km\,s^{-1}}$, and even higher velocities in rare cases (Leonard 1991). Such a collision will result in a binary and two single stars in most cases. The resulting binary is thereby the most massive end product and, hence, will unlikely be accelerated to high speeds. This means that a low binary fraction is expected by this scenario (Gies & Bolton 1986). In a three-body encounter typically the least massive star is ejected (Heggie 1975).
DES runaways are expected to have the following properties:

- They are most efficiently produced in a high-density environment, e.g. young open clusters. Therefore, the age of the cluster should be about the same time as the flight-time of the runaway, as clusters are expected to expand over time, which reduces the density.
- They are not expected to show signs of binary evolution (increased He abundance, large rotational velocities). However, some binary-binary encounters could lead to mergers, which could show these characteristics.
- They are expected to be single stars in most cases.

4.3. Hills mechanism

Furthermore, for the explanation of high-velocity stars a third scenario was proposed by Hills (1988). He suggested that a close encounter between a tightly bound binary and a supermassive

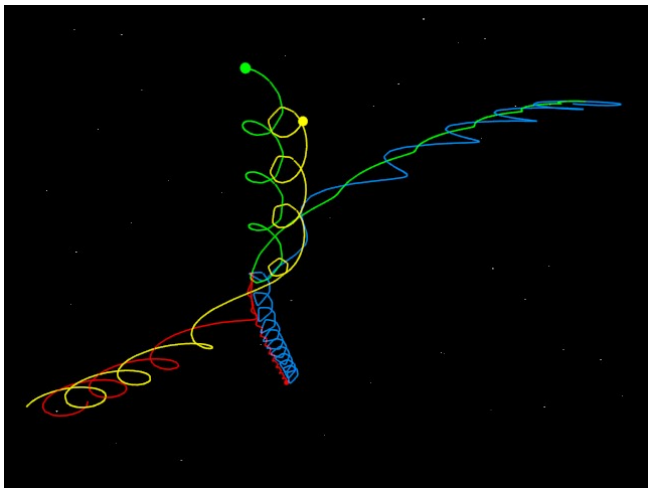

(a) Exchange of partners. No ejection.

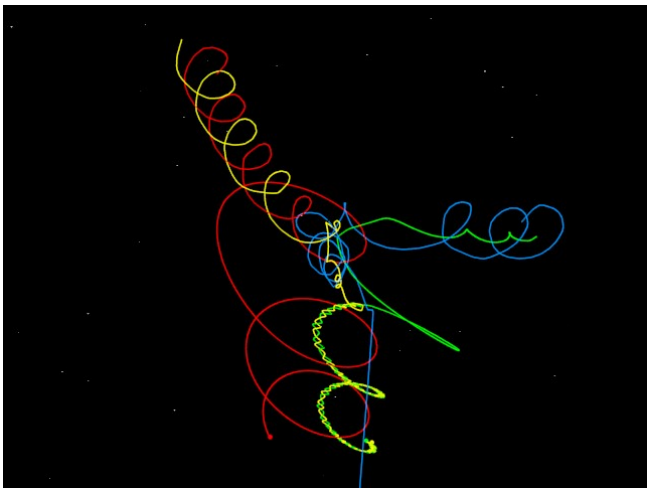

(b) Formation of a stable triplet system. Single ejection.

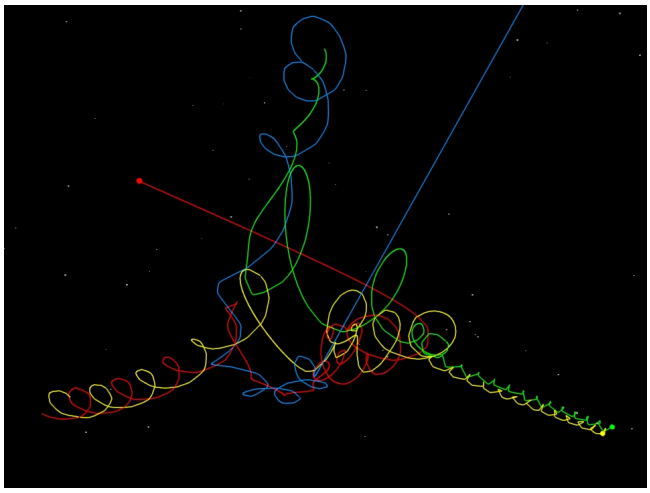

(c) Formation of a new binary system. Double ejection.

Figure 4.2.: Dynamical binary-binary interactions visualized with the help of trails: Two initially separated binary systems – red and yellow, blue and green – interact via a close encounter[1].

black hole (SMBH) , like the one in the center of our galaxy, could cause one binary component to become bound to the black hole and the other to be ejected with a velocity of up to $4000\,\mathrm{km\,s^{-1}}$, much larger than the escape velocity from our galaxy. This scenario is called Hills mechanism or slingshot mechanism. Figure 4.3 shows an illustration of this mechanism. Stars, which are unbound to the galaxy, are called hypervelocity stars (HVS). Until now about 20 HVS are known of late B or early A type (Brown et al. 2014). There are some doubts if all these HVS in fact result from a tidal disruption by the SMBH. Abadi et al. (2009) proposed an alternative origin for the HVSs. They show that the tidal disruption of a dwarf galaxies by the Milky Way may produce stars with about or exceeding the escape velocity. They could be stripped from the dwarf galaxy during the latest pericentric passage.

4.4. Importance of the different formation scenarios?

It has been debated vigorously, which of the formation processes is responsible for runaway stars. The birthplace can be calculated with a kinematics study. If an encounter with the SMBH can be excluded, this scenario can be ruled out easily. The other scenarios, however, are both able to produce stars with peculiar velocities that allow them to run away from their birthplaces. By studying the statistical properties of all runaways and the investigation of single runaway

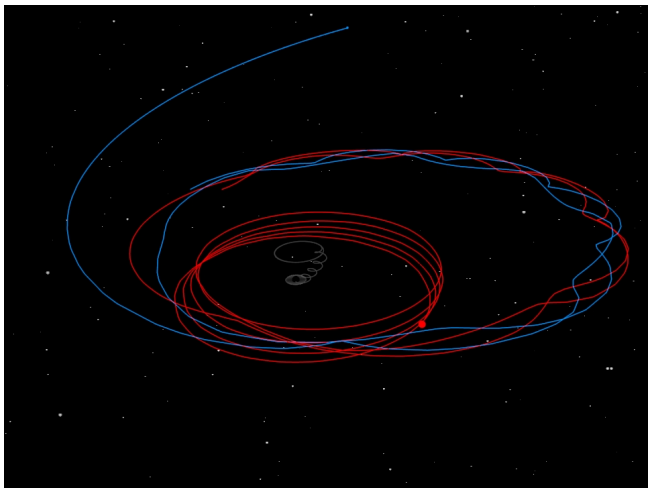

Figure 4.3.: Tidal disruption of an initially bound binary system (red and blue trails) by a massive black hole (gray trail): One component (blue) is accelerated at the expense of the companion's (red) potential energy. Hills (1988) showed that ejection velocities up to a few thousand kilometers per second are possible to be reached via this so-called Hills or slingshot mechanism[1].

stars in detail, it is possible to determine the relative importance of both scenarios.
Hoogerwerf et al. (2001) identified a candidate runaway that may have been ejected scenario in a supernova event, and also may be associated with a young pulsar. This could be a direct observation of both companion of a pre-SN binary system, which produced a runaway star. More recently, Tetzlaff et al. (2014) found another such candidate. Portegies Zwart (2000) studied the characteristics of runaway OB stars from the supernova scenario and stated that the majority of the B runaways but at most 30% of the O runaway stars could be explained by this scenario. However, Stone (1991) claimed that the observed frequencies of O and B runaways and in particular the sharp decrease in the space frequency between O and B runaways agrees with the supernova scenario and is in contrast to the predictions of the dynamical scenario.
However, one major problem of the BSS scenario is that it predicts most massive close binaries not to be disrupted. Until now most of the runaways found are single. Another problem is that the binary is ejected only after the companion exploded. Therefore, the time to reach large distances from the Galactic plane is much shorter than in DES. Furthermore, Fujii & Portegies Zwart (2011) stated that the majority of the galactic OB runaways seem to originate from star clusters that experienced core collapse within the first 1 Myr of their existence. The mass function of the more than 634 identified OB runaways is consistent with their simulations of young core-collapsed star clusters of 6300 $M_{\odot}$.

5. Model Atmosphere Analysis & Spectral Line Formation

The analysis of the spectra is based on the calculation of synthetic spectra by using model atmospheres and solving the radiative transfer. Therefore, model atmospheres, radiative transfer and spectral line formation will be introduced in the following. All our knowledge on stars is derived from the analysis of their radiation. This radiation is emitted in the outermost layers, the stellar atmosphere. To be able to extract information from a stellar spectrum, a physical understanding of the origin and appearance of the spectra is required. The methods to calculate synthetic spectra are provided by the theory of stellar atmospheres, which describes the complex interaction of radiation and matter in the stellar plasma. In this chapter a short overview is given on the basic concepts of radiative transfer, model atmosphere construction and spectral line formation. It is based mostly on the seminal article by Kurucz (1970) and the textbooks by Hubeny & Mihalas (2015) and Gray (2005).

5.1. Model Atmospheres

The atmosphere is the region of the star from where the observed light is emitted. In principle it can be calculated by the stellar structure equations 2.1. However, to simplify the calculation several assumptions are made:

- The atmosphere is stationary. Time-dependent phenomena like pulsations are neglected.
- The flux of energy is constant with depth in the atmosphere, since the energy source of the star lies far below the atmosphere and since no energy comes into the atmosphere from the outside. The flux is given by the Stefan-Boltzmann law $F = \sigma T_{\rm eff}^4$.
- The atmosphere is homogeneous except in the normal direction. This means magnetic fields, spots, granules, etc. are ignored.
- The atmosphere is thin relative to the stellar radius (plane-parallel geometry).
- There is no relative motion of the layers in the normal direction. Therefore, we have hydrostatic equilibrium ($\rho \frac{d^2r}{dt^2} = -\rho g + \frac{dP}{dr}$).
- The atomic abundances are specified and constant throughout the atmosphere.
- The charge is conserved: $\sum_i n_i Z_i - n_e = 0$. Thereby is Z_i the the charge associated with level i (0 for a neutral species, 1 for single-ionized species, ...).

Given these assumptions, we go through an iteration process to find the parameters that describe the model atmosphere. Highly important in this context is the radiative transfer through the atmosphere that will be discussed in the next section.This allows the calculation of the radiation field and flux at each point.

5.1.1. LTE vs. NLTE

Apart from a precise description of the atomic structure (energy levels, statistical weights, transition probabilities) of the different elements, given via the so-called model atoms, the computation of the radiation field requires detailed knowledge of the statistical properties of the plasma: What percentage of atoms of a certain element is found in a specific ionization stage? What is the population number for the different energy levels? What is the number density and the velocity distribution of the particles? To solve this problems different approaches can be used.

Thermodynamic equilibrium (TE)

The description of the material properties is greatly simplified, if TE is fulfilled. In this state, the particle velocity distributions as well as the distributions of atoms over excitation and ionization states can be specified uniquely by the absolute temperature T and the total particle number density N_x, or the electron density n_e. These distributions are determined by the Maxwellian velocity distribution, the Boltzmann excitation formula, and the Saha ionization equation:

- the particles follow the Maxwellian velocity distribution
$$f(v)\mathrm{d}v = (m/2\pi kT)^{3/2} \exp(-mv^2/2kT) 4\pi v^2 \mathrm{d}v \tag{5.1}$$
- the energy-level populations are related by the Boltzmann excitation formula
$$\frac{n(u)}{n(l)} = \frac{g(u)}{g(l)} \mathrm{e}^{-(\mathrm{E_u}-\mathrm{E_l})/\mathrm{kT}} \tag{5.2}$$
- the number densities of different ionization stages are related by the Saha ionization equation
$$\frac{N_I}{N_{I+1}} = n_e \frac{U_I}{U_{I+1}} (h^2/2\pi mk)^{3/2} T^{-3/2} \exp(\chi_I/kT) \tag{5.3}$$
with the partition function $U = \sum g_i \exp(-E_i/kT)$ and the ionization potential of the ion χ_i.
- I_ν is described by the Planck function
$B_\nu = \frac{2\mathrm{h}\nu^3}{\mathrm{c}^2} (\mathrm{e}^{\mathrm{h}\nu/\mathrm{kT}} - 1)^{-1}$
- the photon number density is given by $N_\nu = B_\nu/\mathrm{ch}\nu$

As the stars emit radiation the assumption of TE obviously cannot be applied to stellar atmospheres.

Local thermodynamic equilibrium (LTE)

However, even if TE does not hold globally for the stellar atmosphere, the standard thermodynamic relations can be applied locally. This concept is called local thermodynamic equilibrium (LTE). The equilibrium values of distribution functions are thereby only assigned to particles with mass only. The radiation field is calculated via the transfer equation (next section), and it is not affecting the local material properties.
LTE is a very good approximation as long as there is no interaction of particles and photons from regions with different temperatures. However, if the particle density is so low that the mean free path of photons can exceed the typical distance between two zones of different temperature, or the photon flux is so high that there is always a non-negligible fraction of photons that links zones with different temperatures, this assumption is not valid any more. That means that for hot stars as O or B stars or for stars with low densities as giants and supergiants the population numbers deviate from LTE values.

Non-local thermodynamic equilibrium (Non-LTE)

All deviations from the LTE description are called Non-LTE (or NLTE). Usually, this means that deviations of the population numbers of some energy levels of some atoms/ions from their LTE values are allowed, while the velocity distributions of all particles remain Maxwellian, with the same kinetic temperature, T. That implies that only the Saha-Boltzmann equations have to be replaced by a more sophisticated approach. They are replaced by more general equations, the so-called statistical equilibrium or rate equations:

$$n_i \sum_{j \neq i} (R_{ij} + C_{ij}) = \sum_{j \neq i} n_j \, (R_{ji} + C_{ji}) \tag{5.4}$$

where R_{ij} and C_{ij} are the radiative and collisional rates, respectively, for the transitions from i to level j. The left-hand side of Eqn. 5.4 represents the transitions depopulating the level i, while the right-hand side describes the processes populating this level. Radiative upward rates are described by

$$R_{ij} = 4\pi \int \sigma_{ij} \frac{J_\nu}{h\nu} \, \mathrm{d}\nu \tag{5.5}$$

with σ_{ij} are the atomic cross-sections for bound-bound and bound-free processes, whereas the downward rates are given by

$$R_{ji} = 4\pi \left(\frac{n_i}{n_j} \right)^* \int \frac{\sigma_{ij}}{h\nu} \left(\frac{2h\nu^3}{c^2} + J_\nu \right) \exp(-h\nu/kT) \, \mathrm{d}\nu \tag{5.6}$$

where the asterisk denotes the LTE population numbers. The first term describes spontaneous emission, while the second is due to stimulated emission. The upward-rates for collisional processes are given by

$$C_{ij} = n_e \int \sigma_{ij}(v) f(v) \, \mathrm{d}v \tag{5.7}$$

where $f(v)$ is the velocity distribution of the colliding particles, which are mainly electrons in hot stars. The collisional downward rates can be calculated by $C_{ji} = (n_i/n_j)^* C_{ij}$.
The set of rate equations for all levels of an atom form a linearly dependent system. In order solve the system, one of these equations has to be replaced by another relation, usually the total number conservation equation, $\sum_i n_i = N_{\mathrm{atom}}$, with the summation extending over all levels of all ions of a given species.

Thermodynamic quantities

In LTE no coupling between radiation field and temperature is given. This simplifies the determination of the thermodynamic quantities significantly. Since the atmosphere is only a small layer at the outer rim of the star, hydrostatic equilibrium simplifies to $\frac{dP}{dx} = -g\rho(x)$. P consists of several components ($P = P_{\mathrm{gas}} + P_{\mathrm{rad}} + P_{\mathrm{turb}}$): the gas pressure P_{gas}, the radiation pressure $\frac{dP_{\mathrm{rad}}}{dx} = -\frac{\kappa_\nu}{c} F_\nu$, and the turbulence pressure $P_{\mathrm{turb}} = \frac{1}{2}\rho v_{\mathrm{turb}}^2$, which is caused by random motion of small gas elements with the velocity v_{turb}. For most models P_{turb} is neglected. Therefore, we can derive:

$$\frac{dP_{\mathrm{gas}}}{dx} = -\rho(x)(g - g_{\mathrm{rad}}), \; g_{\mathrm{rad}} = \frac{1}{\rho(x)c} \int_0^\infty \kappa_\nu F_\nu \mathrm{d}\nu \tag{5.8}$$

For main-sequence B stars one can assume $g \gg g_{\rm rad}$. However, the stellar winds of massive O-type or Wolf-Rayet stars are a direct consequence of $g_{\rm rad} > g$, resulting in a break-down of hydrostatic equilibrium and the onset of dynamic outflow of stellar matter into space.
Since we want to derive the pressure at different optical depths τ, we can also rewrite this equation:

$$\frac{dP}{d\tau} = \frac{g}{\kappa} \Rightarrow P(\tau_1) = P(\tau_0) + \frac{g}{\kappa(\tau_0)}(\tau_1 - \tau_0) \tag{5.9}$$

As κ depends on T and P, this equation is iterated until the difference $P^{\rm new} - P^{\rm old}$ is very small.
For the determination of the temperature structure temperature correction schemes are applied. The temperature gradient $T(\tau)$ is modified from a given temperature gradient, e.g. from a gray stratification, such that flux conservation ($\int F_\nu {\rm d}\nu = \sigma T_{\rm eff}^4/\pi$) is fulfilled at each depth point. Due to the weak coupling between radiation field and temperature in NLTE, is the generalization to NLTE not straightforward. However, in this work the model atmosphere is calculated only in LTE.

5.1.2. Line blanketing

The basic parameters determining the continuum energy distribution and the line spectrum of a star are its effective temperature, surface gravity, and chemical composition. To use Planck functions for the spectral energy distribution is inadequate, as the opacity of stellar material has large variations at photo-ionization edges and in spectral lines and depends on the excitation and ionization state. In a stellar atmosphere the temperature increases inwards, which means that layers from which we receive radiation in opaque spectral lines and continua are cooler, end hence emit less energy, than the layers where the material is more transparent. Thus the flux in bands with numerous spectral lines is reduced, which is called **line blocking**. However, the flux integrated over all wavelengths has to be conserved. Therefore, the blocked energy is redistributed to other wavelengths in the spectrum. Moreover, a steeper temperature gradient is required to drive the flux as the spectral lines restrict the bandwidth of the spectrum in which energy transport is efficient. This is called the **backwarming effect**. The collective effects of spectral lines in a star's opacity are referred to as **line blanketing**. For B-type stars iron group elements are the main contributors to the line blanketing. In particular the abundant elements Fe and Ni have numerous lines primarily in the UV. which will be discussed later in detail. For hot stars the larger part of the spectral lines are located in the UV, giving rise to the so-called line forest.
Line blocking and blanketing cannot be solved for individual transitions as the iron group has millions of transitions between hundreds to thousands of energy levels per ion. Therefore, a statistical approach is required to account for the energy redistribution caused by line blocking in the spectra. There exist Two different approaches exist: Opacity Distribution Functions (ODF) or Opacity Sampling (OS). The idea of the ODFs is to form a monotonic function in frequency by re-sampling the detailed line opacity distribution in adequately chosen wavelength bins. The calculations are performed only once and the ODFs are tabulated for discrete frequency intervals and can then be used in further applications. The idea of OS is a simple Monte Carlo-like sampling of the line opacity distribution, offering many advantages in the treatment of line blends and overlaps.
Since the opacities are directly calculated for the current conditions of the atmosphere, OS is very flexible and can also be applied to stars with non-standard elemental compositions. On the other hand, ODFs are calculated once for a certain chemical composition and than tabulated as function of frequency, temperature, and pressure. ODFs are calculated on a very fine frequency grid, which is typically much finer than that of OS. ODFs allow thus quick access to the source

function since one only has to interpolate pre-tabulated values. Yet to analyze stars with a non-standard chemical composition ODFs are not applicable.

5.2. Radiative transfer

5.2.1. Radiative transfer equation

For the calculation of the radiation field the radiative transfer equations have to be solved. In order to derive these equation we will follow a beam of photons of frequency ν, as it passes through the atmosphere. The number density of photons per solid angle and frequency $N_\nu(\omega)$ will change with time because of the presence of absorbing, emitting, and scattering atoms, molecules, electrons, or ions (we will call them atoms in the following). In an absorption process a photon of energy $\mathrm{h}\nu$ is removed from the beam by an atom. It is also possible that an photon is added to the beam in proportion to the number of photons in the beam (negative absorption or stimulated emission). In an emission process a photon of energy $\mathrm{h}\nu$ is added, independent of the existing number of photons in the beam. In a scattering process an atom removes a photon from the beam and re-emits another of slightly different energy in a different direction. Considering all these processes with l denoting the lower and u the upper energy level ($n(l)$ and $n(u)$ are the number densities of atoms in the lower or upper levels) of any transition we derive the change in the photon number density:

$$\begin{aligned}\frac{dN_\nu(\omega)}{dt} = &- N_\nu(\omega) \sum \left[\text{absorption coefficient } \mathrm{a}_\nu(l \to u)\right] n(l) \\ &+ N_\nu(\omega) \sum \left[\text{absorption coefficient } \mathrm{a}_\nu(u \to l)\right] n(u) \\ &- N_\nu(\omega) \sum \left[\text{scattering coefficient } \mathrm{s}_\nu(l \to u)\right] n(l) \\ &+ \sum \left[\text{emission coefficient } \mathrm{e}_\nu(u \to l)\right] n(u) \\ &+ \sum \left[\text{scattering emission coefficient}(u \to l)\right] n(u) \end{aligned} \tag{5.10}$$

As we are interested in the structure of the atmosphere, we convert the coordinates from coordinates moving with the photons to coordinates fixed in the atmosphere:

$$\frac{d}{dt} = \vec{v} \cdot \vec{\nabla} + \frac{\partial}{\partial t} = c\frac{d}{dz} \tag{5.11}$$

because we assume the atmosphere to be stationary. The photon number density can also better be expressed by an intensity ($I_\nu(\omega) = \mathrm{ch}\nu N_\nu(\omega)$, energy per cm^{-2}, sec, ster, and Hz). Furthermore, we assume that the scattering emission is isotropic, which implies that the scattering and scattering emission rates are equal. The absorption coefficients in both directions ($u \to l$ and $l \to u$) are, thus, related by the statistical weights:

$$\frac{\mathrm{a}_\nu(l \to u)}{\mathrm{a}_\nu(u \to l)} = \frac{\mathrm{g}(u)}{\mathrm{g}(l)} \tag{5.12}$$

By assuming TE the emission and the absorption coefficient can be related:

$$\frac{\mathrm{e}_\nu(u \to l)}{\mathrm{a}_\nu(l \to u)} = \frac{\mathrm{g}(l)}{\mathrm{g}(u)} \frac{2\mathrm{h}\nu^3}{\mathrm{c}^2} \tag{5.13}$$

We assume that this equation can also be applied when there is no TE, as it does not depend on the properties of the gas.

To simplify the equation, we also define the mass absorption coefficients or opacities:

$$\kappa_\nu(l \to u) = n(l)\mathrm{a}_\nu(l \to u)\left\{\frac{1-[n(u)/n(l)][g(l)/g(u)]}{\rho}\right\}, \qquad \kappa_\nu = \sum \kappa_\nu(l \to u)$$

$$\sigma_\nu(l \to u) = \frac{n(l)\mathrm{s}_\nu(l \to u)}{\rho}, \qquad \sigma_\nu = \sum \sigma_\nu(l \to u)$$

as well as the optical depth:

$$\mathrm{d}\tau_\nu = -(\underbrace{\kappa_\nu + \sigma_\nu}_{\chi_\nu})\rho \mathrm{d}z$$

To simplify the radiative transfer equation further, we change the variables; The **mean free path** for a photon is given by $1/\chi_\nu$. For the plane-parallel case we can measure distances and optical depth in terms of the normal distance x:

$$z = x/\cos\theta = x/\mu \tag{5.14}$$

By applying all definitions and selecting the **source function** S_ν in the way we get the final form of the **radiative transfer equation**:

$$\boxed{\mu\frac{dI_\nu}{d\tau_\nu} = I_\nu - S_\nu} \tag{5.15}$$

The source function is expressed by:

$$\boxed{S_\nu = \frac{\sum \kappa_\nu(l \to u)S_\nu(u \to l) + \sigma_\nu \int I_\nu(\mathrm{d}\omega/4\pi)}{\chi_\nu} \equiv \frac{\eta_\nu}{\chi_\nu}} = B_\nu\,(\text{in TE})$$

$$S_\nu(u \to l) = \frac{2\mathrm{h}\nu^3}{\mathrm{c}^2}\left[\frac{n(l)}{n(u)}\frac{g(u)}{g(l)} - 1\right]^{-1}$$

η_ν is the amount of energy emitted thermally and inscattered into the beam by the material and χ_ν is the absorption coefficient (5.16)

5.2.2. Properties of the radiation field

The specific intensity can be calculated by

$$I_\nu = \int_{\tau_\nu}^{\infty} S_\nu \mathrm{e}^{-(t-\tau_\nu)/\mu}\frac{\mathrm{d}t}{\mu} \tag{5.17}$$

Several important physical quantities are determined by the radiation field. The radiation field that each atom sees is the integrated intensity $\int I_\nu\,\mathrm{d}\omega$. The radiative energy that passes through the atmosphere per unit area per second, is the flux $\int \mu I_\nu\,\mathrm{d}\omega$. The radiation pressure is given by $(1/c)\int \mu^2 I_\nu\,\mathrm{d}\omega$. To formalize this, we introduce the intensity moments:

mean intensity $$J_\nu = \int I_\nu \frac{\mathrm{d}\omega}{4\pi} = M_0(\tau)$$

Eddington flux $$H_\nu = \int \mu I_\nu \frac{\mathrm{d}\omega}{4\pi} = 4\pi F_\nu = M_1(\tau)$$

related to radiation pressure $(4\pi K_\nu/\mathrm{c})$ $$K_\nu = \int \mu^2 I_\nu \frac{\mathrm{d}\omega}{4\pi} = M_2(\tau)$$

To simplify the notation we introduce the exponential integral: $\mathrm{E_n(x)} = \int_0^1 \mathrm{e}^{-\mathrm{x}/\mu}\mu^{\mathrm{n}-2}\mathrm{d}\mu$. Therefore we get for example for the mean intensity:

$$J_\nu(\tau_\nu) = \frac{1}{2}\int_0^\infty S_\nu(t)E_1(|t-\tau_\nu|)\mathrm{d}t = \Lambda_{\tau_\nu}[S(t)] \tag{5.18}$$

Thereby, $\Lambda_{\tau_\nu}[S(t)]$ is the Λ-operator.

5.2.3. Methods to solve the transfer equation

To solve the transfer equations different methods can be employed. In the program ATLAS (Kurucz 1970) it is solved by dividing the atmosphere into N layers. The first step is the calculation of the optical depth.

Computing the optical depth

For the computation of the optical depth τ we change to mass coordinates: dM=$-\int \rho \mathrm{d}x$. For the numerical calculation we assume that the opacity is known. The most important processes that contribute to the opacity are bound-bound absorption, bound-free absorption, free-free absorption, and scattering from free electrons. 'Bound' or 'free' mean in this context that the electron incorporated in a transition is bound to an atom or not. That means

- bound-bound transition: an electron in an atom makes a transition from one energy level to another. The transition contributes significantly to the opacity only over a small wavelength interval (line opacity).
- bound-free absorption: also called photo-ionization, occurs when the photon has sufficient energy to ionize an atom
- free-bound emission: electron recombines with an ion, emitting one ore more photons in random directions.
- free-free absorption: is a scattering process, an electron absorbs a photon in the vicinity of an atom. This increases the velocity of the electron.
- free-free emission: the reverse process is called bremsstrahlung.
- electron scattering: no absorption but scattering of the photon by a free electron through Thomson scattering or Compton scattering, or scattering by atoms through Rayleigh scattering.

All opacity sources but the bound-bound transitions contribute to the continuum opacity. Hydrogen and helium are the most important opacity sources in hot stars because of their high abundances. It depends on the wavelength though. The contribution of each source varies strongly with the temperature. Electron scattering is only effective at high temperatures, as only there most of the hydrogen is ionized and therefore many free electrons are available. In stars with low temperatures the photon energy is to low to induce bound-free transitions in hydrogen nor is the number of free electrons large enough for scattering to be important- instead the continuous and free-free opacity of the negative hydrogen ion H^- prevails. For intermediate temperatures, none of the four absorption processes substantially drops off, which results in a maximum value for the continuous κ.

For the calculation of the optical depth we divide the atmosphere into N layers each labeled by depth M_j. The optical depth is then easily found by the numerical integration of

$$\tau_{\nu\mathrm{j}} = \int_0^{M_\mathrm{j}} (\kappa_\nu + \sigma_\nu)\,\mathrm{d}M = \sum_{j=1}^{N} (\kappa_\nu + \sigma_\nu)\Delta M_j \tag{5.19}$$

Computing the mean intensity, flux and the source function

To calculate the mean intensity, flux and the source function in ATLAS integration matrices are used. To derive them the integration ranges are divided in N subintervals:

$$M_{\mathrm{n}l} = M_\mathrm{n}(\tau_l) = \frac{1}{2}\sum_{j=1}^{\mathrm{N}} \int_{\tau_j}^{\tau_{j+1}} S(t) E_\mathrm{n}(t-\tau_l)\mathrm{d}t \tag{5.20}$$

S can be approximated by a parabola in the interval (τ_j, τ_{j+1}): $S(t) = \sum_{k=1}^{3} t^{k-1} \sum_{i=1}^{\mathrm{N}} s_i$, where s_i are the parameter of the parabola. By rearranging the sums we get an analytically solvable integral ($\eta_{nljk} = \frac{1}{2}\sum_{j=1}^{\mathrm{N}} \int_{\tau_j}^{\tau_{j+1}} t^{k-1} E_\mathrm{n}(t-\tau_l)\mathrm{d}t$). Combining all together we can express M_{nl} by:

$$M_{nl} = \sum_{j=1}^{\mathrm{N}}\sum_{k=1}^{3}\sum_{i=1}^{\mathrm{N}} \eta_{nlik} s_j = \sum_{j=1}^{\mathrm{N}} \Xi_{nlj} s_j \Rightarrow M_n = \Xi_n S \tag{5.21}$$

Ξ_n is then the desired matrix operator ($\Xi_0 = \Lambda$).
To compute the source function we rewrite equation 5.16 and define $a_\nu = \frac{\kappa_\nu}{\kappa_\nu + \sigma_\nu}$:

$$S_\nu = (1-a_\nu)\bar{S}_\nu + a_\nu J_\nu \Rightarrow (\mathbb{1} - a\Lambda)S = (\mathbb{1} - a)\bar{S} \tag{5.22}$$

This equation is solved by an iteration processes starting with an initial guess (e.g. $S = \bar{S}$). The difference $\Delta = (\mathbb{1} - a\Lambda)S - (\mathbb{1} - a)\bar{S}$ should be reduced in each step ($S^\mathrm{new} = S^\mathrm{old} + \Delta S$, $\Delta S \simeq -\frac{\Delta}{1 - a_i \Lambda_{i1}}$) until it is smaller than the convergence criterion.

Accelerated Lambda Iteration

Hubeny & Mihalas (2015) described several other methods to solve the radiative transfer equation. A very simple method is the Λ Iteration. For further explanation we take a source function $S_\nu = (1-a_\nu)J_\nu + a_\nu B_\nu$, which consists of an LTE thermal emission component (see next section) and a coherent scattering term. The solution for the transfer equation for the mean intensity is then

$$J_\nu(\tau_\nu) = \Lambda_{\tau_\nu}[S_{\tau_\nu}] = \Lambda_{\tau_\nu}[(1-a_\nu)J_\nu] + \Lambda_{\tau_\nu}[a_\nu B_\nu] \tag{5.23}$$

This is an integral equation for $a_\nu < 1$. To solve it, we could represent J_ν, B_ν, a_ν by, e.g. spline approximations, on a discrete grid of optical depths τ_j. Analytically integrating the splines times the exponential integral generates a matrix equation:

$$\sum_{j=1}^{\mathrm{N}} \Lambda_{ij} J_j = b_i \tag{5.24}$$

As the inversion of this matrix is expensive an iteration process called the Lambda Iteration is used to solve this equation. Based on an initial guess $J_\nu^{(0)}$, for which the Planck function B_ν is a

reasonable choice, as it becomes accurate deep in the atmosphere, we compute a new estimate:

$$J_\nu^{(1)} = \Lambda_{\tau_\nu}[(1-a_\nu)J_\nu^{(0)}] + \Lambda_{\tau_\nu}[a_\nu B_\nu] \Rightarrow J_\nu^{(n+1)} = \Lambda_{\tau_\nu}[(1-a_\nu)J_\nu^{(n)}] + \Lambda_{\tau_\nu}[a_\nu B_\nu] \tag{5.25}$$

As on the right hand side now all variables are known, only an integration is required. This is iterated until the convergence criterion is met:

$$|(J_\nu^{(n)} - J_\nu^{(n-1)})/J_\nu^{(n-1)}| < e_n \tag{5.26}$$

We also can solve the source function with this method:

$$S = (1-a)J + aB \rightarrow S^{(n+1)} = (1-a)\Lambda[S^{(n)}] + aB \tag{5.27}$$

However, this method has the problem that, if $a_\nu \ll 1$, the convergence will be very slow or fail at all. That means, if a lot of scattering occurs, as is the case at large optical depth (e.g. in line cores), this method will fail.
The most powerful technique at the moment is the Accelerated Lambda Iteration (ALI). It allows the construction of very realistic and complex theoretical models. The basic idea is to realize that some part of the physical coupling in the radiation transfer problem is more important than others. Cannon (1973) introduced the method of operator splitting into astrophysical radiative transfer. The idea consists of writing

$$\Lambda = \Lambda^* + (\Lambda - \Lambda^*) \tag{5.28}$$

where Λ^* is a 'judiciously chosen' approximate Λ-operator. The action of the exact Λ-operator is thus split into two contributions: the approximate Λ-operator acts on the new iterate of the source function, whereas the difference $(\Lambda - \Lambda^*)$ acts on the old known source function. Then the iterative scheme becomes

$$S^{(n+1)} = (1-a)\Lambda^*[S^{(n+1)}] + (1-a)(\Lambda - \Lambda^*)[S^{(n)}] + aB \tag{5.29}$$

This accelerates the convergence compared to the normal Lambda Iteration by the acceleration operator $[\mathbb{1} - (1-a)\Lambda^*]^{-1}$.
Hubeny & Mihalas (2015) give an overview over the mathematical properties of the ALI method. They state that an optimum Λ^* has to be constructed based solely on mathematical analysis, not using physical considerations. The nearly optimum Λ^* is the diagonal part of the exact Λ matrix. The preferred recipe for the realization of the ALI scheme for numerical radiative transfer was developed in the study of Rybicki & Hummer (1991, 1992). It is this formulation that is implemented in the DETAIL and SURFACE codes, which are used in this work amongst others.

5.3. Spectral line formation

The analysis of spectral lines in a star's spectrum is our most effective tool for determining the conditions in, the composition, and the structure of a stellar atmosphere. The quantitative analysis of spectral lines requires the knowledge of

- the number of atoms that can absorb radiation at each frequency in a line
- the wavelength distribution of the line's opacity, i.e. the absorption profile
- the dependence of the profile on the temperature and density of the plasma

The line strength is basically given by the number of absorbers and the line absorption cross-section, which is given by

$$\sigma_{ij} = \frac{\pi e^2}{mc} f_{ij} \Phi_\nu = B_{ij} \frac{h\nu_{ij}}{4\pi} \Phi_\nu \tag{5.30}$$

where f_{ij} is the oscillator strength (more details later), Φ_ν the absorption profile and ν_{ij} the central wavelength of the line. It is related to the Einstein coefficient B_{ij}, which gives the absorption probability.
A common approach is to measure the integrated line profile, which is expressed in terms of the equivalent width

$$W_\lambda = \int_0^\infty \frac{F_c - F_\lambda}{F_c} \, \mathrm{d}\lambda \tag{5.31}$$

where F_c is the flux of the continuum and F_λ is the flux in the line. However, this result depends on the line profile used and the interpretation on the basis of the equivalent width can be misleading because lines of different shape may have the same W_λ. Therefore, analyses should preferably rely on the modeling of the detailed line profile.
The line profile is depending on the properties of the plasma and the atomic properties of the atom under investigation. There are several mechanisms causing line broadening.

Natural damping

As the different atomic levels have a finite life time after that a radiative decay takes place, the line gets broadened due to the uncertainty principle $\Delta E \Delta t \geq h$. Δt is the characteristic life time for a decaying state and ΔE refers to the resulting energy width of the state. Only ground levels are stable. Typical life times of an excited state is of the order of 10^{-8}s. There exist also meta-stable levels with significantly larger lifetimes that can only be depopulated via 'forbidden' transitions (see Table 8.1). Radiation damping yields a Lorentz profile

$$\Phi_\nu^{\mathrm{rad}} = \frac{\gamma_{\mathrm{rad}}/4\pi^2}{(\nu - \nu_{ij})^2 + (\gamma_{\mathrm{rad}}/4\pi)^2} \tag{5.32}$$

γ_{rad} is the full width at half maximum (FWHM) of the curve. It can be calculated by the sum of the reciprocal mean lifetimes of the upper and lower level for all possible radiative decays of both levels.

$$\gamma_{\mathrm{rad}} = \sum_{n<i} A_{in} + \sum_{m<j} A_{jm} = \frac{1}{\tau_{\mathrm{low}}} + \frac{1}{\tau_{\mathrm{up}}} \tag{5.33}$$

Natural broadening is important primarily for strong lines in low-density media like for example the interstellar medium and occurs even in single atoms. For stellar atmospheres, however, other broadening mechanisms play a bigger role.

Pressure broadening

An atom in a plasma will also experience pressure broadening caused by collisions with other atoms, or charged particles, in the gas. For hot stars collisions with electrons are the most important process. The most important mechanism for collisional broadening is the Stark effect: for lines of hydrogen and hydrogen like ions (e.g., He II) the linear Stark effect and for non-hydrogenic atoms and ions the quadratic Stark effect. For the quadratic Stark widths a approximation formula by Cowley (1971) is given by

$$\gamma_{\mathrm{col}} = 4.335 \cdot 10^{-7} Z^2 (Rc)^2 (E_u^{-2} + E_l^{-2}) \tag{5.34}$$

where Z is the ionic charge ($Z = 1$ for neutrals, 2 for single-ionized species, ...), $R = R_\infty \mu/m$ the Rydberg constant (with the reduced mass μ and $R_\infty = 109737.315\,\mathrm{cm}^{-1}$) and $E_{u/l}$ the ionization energy of the upper/lower level (in s^{-1}). For determining the ionization energy it is very important to know the energy level to which an electron from a specific energy level is ionized, as not always a ionization to the ground level is possible because of the selection rules. In this work this formula is used whenever no accurate line-broadening data is available calculated from the quantum theory of pressure broadening.
Calculations derived by a more sophisticated approach can be found in the Stark-b database (Sahal-Bréchot et al. 2014)[1] and were used in this work whenever available. It is evaluating electron and ion impact broadening of isolated spectral lines of neutral atoms and ions using the semiclassical-perturbation approach developed by Sahal-Brechot (1969a,b, 1974).
With the exception of the linear Stark effect at high densities pressure broadening also results in a Lorentz profile. Therefore, the combined line profile is a Lorentzian with a total width of $\gamma = \gamma_{\mathrm{rad}} + \gamma_{\mathrm{col}}$. It is assumed that both damping processes are completely unrelated. For the linear Stark effect tables have been calculated by Smith et al. (1969). Approximate formulae have been derived by Griem (1974). The most sophisticated theory, the so-called Unified theory is frequently used in modern codes.

Van der Waals broadening

In solar-type stars also the van der Waals interactions have to be taken into account. They describe the collisions of non-hydrogenic atoms with neutral hydrogen atoms. For hot stars only few neutral hydrogen atoms exist and this effect can, hence, be neglected.

Thermal and microturbulent broadening

The lines seen in a stellar spectrum are produced by absorption or emission of all atoms along the line of sight. Each atom has a velocity component v due to its thermal movement. This results in a frequency shift due to the Doppler effect:

$$\frac{\nu - \nu_0}{\nu} = \frac{v}{c} \rightarrow \nu = \frac{\nu_0}{v/c + 1} \overset{v \ll c}{\approx} \left(1 - \frac{v}{c}\right) \nu_0 \tag{5.35}$$

In thermal equilibrium the velocity distribution is given by eq. (5.1), which leads to a velocity dispersion of $\bar{v} = \sqrt{\frac{2kT}{m}}$. The line profile is given by a Gaussian with a Doppler width $\nu_{\mathrm{D}} = \nu_0 \cdot \bar{v}/c$

$$\Phi_\nu^{\mathrm{Doppler}} = \frac{1}{\sqrt{\pi}\Delta\nu_{\mathrm{D}}} \exp(-(\nu - \nu_0)/\Delta\nu_{\mathrm{D}})^2 \tag{5.36}$$

In order to match model spectra to observations not only the thermal Doppler broadening but also an additional non-thermal Doppler broadening component often is required. This is parametrized by the so-called microturbulence ξ. For hot stars, Cantiello et al. (2009) suggested the microturbulence parameter ξ might be a tracer of a sub-surface convection zone driven by opacity peaks associated with iron. They predict that the sub-photospheric convection zone and, hence, the microturbulence becomes more pronounced at higher luminosities. This connection could be demonstrated by the investigation of 63 B-type main sequence stars by Irrgang (2014). For simplicity a Gaussian velocity distribution $p(v) = \frac{1}{\sqrt{\pi}\xi} \exp(-\frac{v^2}{\xi^2})$ is assumed. The total Doppler width is then given by

$$\Delta\nu_{\mathrm{D}} = \frac{\nu_0}{c}\sqrt{\frac{2kT}{m} + \xi^2} \tag{5.37}$$

[1] `http://stark-b.obspm.fr/`

Total line profile

The total line profile, except for hydrogen-like ions, accounting for natural, pressure and Doppler broadening, results from the convolution of a Lorentzian (from natural and pressure broadening) and a Gaussian (from Doppler broadening). This convolved profile is called Voigt profile. The total line profile is, hence, given by

$$\Phi_\nu = \Phi_\nu^{\mathrm{Doppler}} * \Phi_\nu^{\mathrm{Lorentz}} = \frac{\gamma/4\pi^2}{\sqrt{(\pi)}\Delta\nu_\mathrm{D}} \int_{-\infty}^{\infty} \frac{\exp[-((\nu-\nu_0)/\Delta\nu_\mathrm{D})^2]}{(\nu-\nu_0-\Delta\nu_\mathrm{D})^2+(\gamma/4\pi)^2}\,\mathrm{d}(\nu-\nu_0) \equiv \Phi_\nu^{\mathrm{Voigt}} \quad (5.38)$$

Rotational broadening and macroturbulence

All broadening mechanisms mentioned so far are of microscopic nature. To reproduce the observations also two macroscopic mechanisms have to be considered.
The rotational velocity v_rot of stars ranges from a few up to several hundred kilometers per second. In particular massive stars on the main sequence rotate fast. We can only observe the projection of the rotational velocity on the line-of-sight direction. This means that we observe: $v_\mathrm{rot,observ} = v_\mathrm{rot}\sin i$. The projected rotational velocity results in a relative Doppler shift of light coming from different parts of the visible stellar disk. To calculate the rotational broadening, the fluxes emerging from the different parts of the projected disk have to be summed up. An important effect is the so-called limb-darkening, which results from the fact that at the limb the radiation is originating from higher photospheric and therefore cooler layers, which are less bright, than in the center of the stellar disk. The limb-darkening can be approximated by a linear function:

$$I(0,\cos\theta)/I(0,1) = 1 - x(1-\cos\theta) \quad (5.39)$$

where x, the limb darkening coefficient, is a slowly varying function depending on the wavelength, and the surface gravity and effective temperature of the star. It is tabulated for different wavelengths or photometric filters, temperatures, and surface gravities by e.g., Wade & Rucinski (1985) or Claret & Bloemen (2011). An expression for the line profile due to rotational broadening is given by Eqn. 18.14 in Gray (2005).
Turbulent motions on a scale large compared to the mean free path of a photon can also induce an broadening. These turbulent motion of cells in a stellar atmosphere are referred to as macroturbulence. Individual macroturbulence cells induce Doppler shifts corresponding to the velocity of the cell. Therefore, macroturbulence acts in a very similar way as rotation on the line profile. It can be calculated by the symmetric radial-tangential model using a radial-tangential macroturbulence parameter ζ (see pp. 433-437, Gray 2005).
In cold stars this motion is driven by the convection. For hot stars it was suggested by Aerts et al. (2009) that high-order non-radial pulsations could provide an explanation for the macroturbulence.

Instrumental profile

The measuring processes also introduces an additional broadening of the spectral lines depending on the spectral resolving power $R = \Delta\lambda/\lambda$. The instrumental profile can be assumed to be a Gaussian with a FWHM corresponding to $v = c/2\sqrt{\ln 2}R$. In order to fully resolve the line profile, the spectral resolution has to be sufficiently high ($\Delta\lambda_\mathrm{instrument} < \Delta\lambda$). For sufficient high resolution spectra this effect can be neglected as other broadening mechanisms dominate. For spectra with lower resolution the instrumental profile is important to be taken it into account.
The microscopic broadening mechanisms like natural broadening, pressure broadening and Doppler broadening have to be considered in the radiative transfer equation and affect the

distribution as well as the number of emitted photons at a given wavelength. That means that they influence the shape as well as the strength of a spectral line. On the other hand, the macroscopic broadening, like the rotational or the macroturbulent broadening, and the instrumental broadening cause only a redistribution of the photons and have no effect on the equivalent width. That is why these effects can be applied to the calculated synthetic spectra afterwards.

6. Analysis methods

The previous chapters were explaining all theoretical basics required to understand the objects investigated in this thesis. This chapter shall introduce the methods used to analyze the objects.

6.1. Analysis of (eclipsing) binaries

To derive the system parameters and the atmospheric parameters of both components of an eclipsing binary a combined spectroscopic and photometric analysis is required.

6.1.1. Lightcurve analysis

In order to derive parameters from a lightcurve it is essential to have a physical model of the binary system from which a synthetic lightcurve can be calculated. This synthetic lightcurves are then fitted to the observation to derive the parameters of the best-fitting model, which are supposed to agree with the actual parameters of the system.

Roche model

In very close binaries the stars are not spherical any more, as the shape of the stars is distorted by tidal forces. Therefore, a realistic model of the stellar shapes is important. The most common model used is based on the model described by the French mathematician Edouard Albert Roche (1849), the so-called Roche model. It is based on the three-body problem. For simplifications several assumptions are made:

- both stars act gravitationally as point masses (surrounded by essentially massless envelopes): as in stars most of the mass is concentrated in the core, this assumption is very reasonable
- both components move in circular orbits around the common center of mass: due to tidal friction circular orbits normally develop on short time scales
- the rotational axis of both stars are perpendicular to the stellar orbits
- the rotational period matches the orbital period (bound rotation): because of tidal friction this assumption is normally fulfilled (more later)

Due to these assumptions only gravitational and centrifugal forces have to be considered. For the calculation a perpendicular coordinate system is chosen, which is co-rotating with the orbit. The origin of this coordinate system is located at the common center of mass of both stars (see Fig. 6.1). The resulting potential Ψ, considering gravitational and centrifugal forces, can, hence, be written as

$$-\Psi = G\frac{M_1}{r_1} + G\frac{M_2}{r_2} + \frac{\omega^2}{2}\left[\left(x - \frac{M_2 a}{M1 + M2}\right)^2 + y^2\right] \tag{6.1}$$

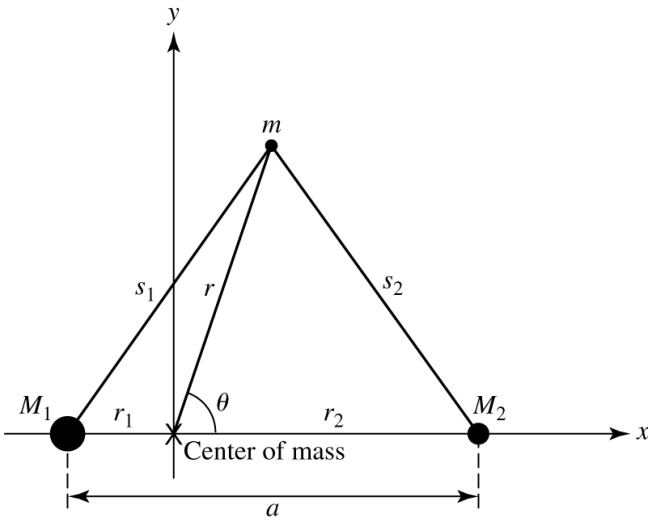

Figure 6.1.: co-rotating coordinate system for the Roche model (Carroll & Ostlie 2007)

thereby is $r_1 = \sqrt{x^2+y^2+z^2}$, $r_2 = \sqrt{(a-x)^2+y^2+z^2}$, a the separation of both stars and the angular velocity $\omega^2 = \frac{G(M_1+M_2)}{a^3}$. The so-called Roche potential is defined as a normalized potential:

$$\Omega := -\frac{1}{GM_1}\Psi = \frac{1}{r_1} + \frac{q}{r_2} + \frac{q+1}{2}(x^2+y^2) - qx + \frac{q^2}{2(1+q)} \tag{6.2}$$

with $q = M_2/M_1$ ($M_1 > M_2$) the mass ratio of both stars. By changing to spherical coordinates ($x = r \cdot \sin\theta\cos\phi$ and $x^2+y^2 = (1-\cos^2\theta)$), and moving the origin of the coordinate system to the center of mass of both stars respectively, we can derive for both stars a Roche potential:

$$\begin{aligned}\Omega_1 &= \frac{1}{r_1} + q\left(\frac{1}{\sqrt{1-2\lambda r_1 + r_1^2}} - \lambda r_1\right) + r_1^2\frac{q+1}{2}(1-\nu^2) \\ \Omega_2 &= \frac{1}{r_2} + q\left(\frac{1}{\sqrt{1-2\lambda r_2 + r_2^2}} - \lambda r_2\right) + r_2^2\frac{q+1}{2}(1-\nu^2) + \frac{1-q}{2}\end{aligned} \tag{6.3}$$

with $r_n = \sqrt{x_n^2+y_n^2+z_n^2}$, $\lambda = \sin\theta\cos\phi$, and $\nu = \cos\theta$.
To describe the stellar surfaces the equipotential surfaces are used, which consist of the points with the same potential Ω. With decreasing Ω the surface increases until a critical Roche potential Ω_{crit} is reached that reaches the Lagrange points $L_{1/2/3}$. This is called the Roche lobe, which is depending on the mass ratio.

Calculation of synthetic lightcurves

For the calculation of the synthetic lightcurves the Wilson-Devinney (WiDe) method is used (Wilson & Devinney 1971). This method uses $12+5n$ (n is the number of lightcurves at different wavelength bands fitted simultaneously) parameters (see Table 6.1). A lightcurve represents the change of the flux with time or phase. In the WD method the monochromatic flux from both stars together at each phase is summed up. Several physical effects are considered in the calculation of the flux:

– **Limb darkening** (cf. Sect. 5.3)

$$D = \frac{I(0,\cos\theta)}{I(0,1)} = 1 - x(1-\cos\theta) \tag{6.4}$$

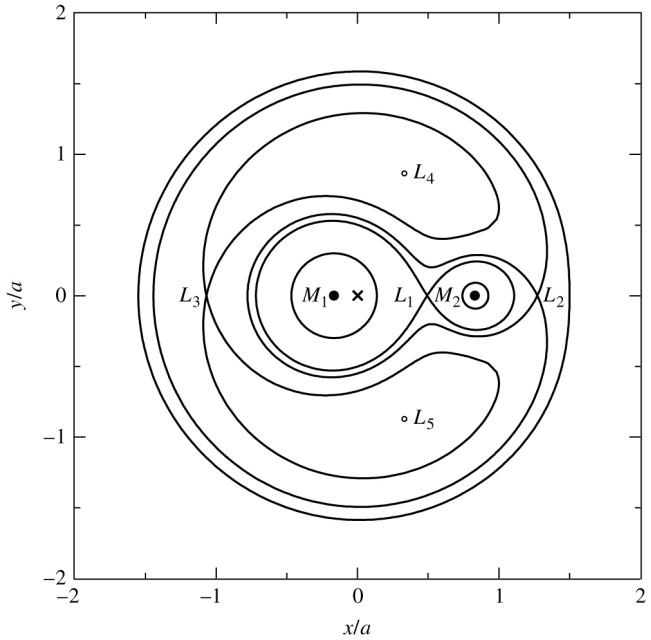

Figure 6.2.: Cross-section of some Roche equipotential surfaces at a mass ratio $q = 0.17$ (Carroll & Ostlie 2007)

Table 6.1.: Parameters used for the lightcurve calculation

i	inclination
q	mass ratio M_2/M_1 with $M_1 > M_2$
Ω_1, Ω_2	surface potentials
T_1, T_2	effective temperatures
A_1, A_2	albedo
g_1, g_2	gravitational darkening coefficients
δ_1, δ_2	radiation pressure coefficients
$L_1(\lambda), L_2(\lambda)$	monochromatic luminosities
$x_1(\lambda), x_2(\lambda)$	limb darkening coefficients
$l_3(\lambda)$	third light

– **Gravity darkening**
As stars are rotating the effective surface gravity is smaller at the equator than at the poles because of centrifugal forces. This leads to a lower flux. The flux change is given by

$$F_l = F_p \left(\frac{g_l}{g_p}\right)^g, \qquad g = \begin{cases} 1.00, & \text{for completely radiative envelopes (von Zeipel 1924)} \\ \approx 0.32, & \text{for completely convective envelopes (Lucy 1967)} \end{cases} \tag{6.5}$$

g_l is thereby the local surface gravity and g_p the surface gravity at the poles. With the help of the Stephan-Boltzmann law ($F_{l/p} \sim T_{l,p}^4$) and the Planck function, the gravitational darkening factor G can be derived

$$G = \frac{I_{\text{local}}}{I_{\text{pole}}} = \frac{e^{\frac{hc}{\lambda T_p}} - 1}{e^{\frac{hc}{\lambda T_l}} - 1} \tag{6.6}$$

– **Reflection effect**
The reflection effect is a very important effect in close binaries consisting of a hot and a cool

star, such as the sdB binaries studied in this thesis. It was already introduced in Sect. 3.3.2. The hot star is illuminating the cool companion resulting in a sinusoidal flux variation, as the visible area of the bright, illuminated side is changing with phase. Physically the illuminated side of the companion is heated up from ~ 3000 K to temperatures of 10000 to 20000 K depending on the separation and temperature of the hot primary. The flux is, therefore, increasing according to the Stephan-Boltzmann law. In the WD model this effect is considered only in a very simplistic way as a reflection of incoming flux. This is calculated with the help of albedos, which indicate the percentage of flux that is reflected. As we calculate only monochromatic fluxes, it is also not physically inconsistent to get albedos > 0, which results from flux redistributions in the heated hemisphere. We can determine the change in temperature caused by the reflection effect with the help of the Stephan-Boltzmann law and from this the change of flux caused by the reflection effect.

$$T_R = T_2 \left(1 + \frac{A_2 F_1}{F_2}\right)^{\frac{1}{4}} \rightarrow R = \frac{I_{\mathrm{ref}}}{I_{\mathrm{noref}}} = \frac{e^{\frac{hc}{\lambda T_2}} - 1}{e^{\frac{hc}{\lambda T_R}} - 1} \tag{6.7}$$

– **Radiation pressure**
For hot, luminous stars the radiation pressure on the companion plays an important role. It can even influence the shape of the star. In the most extreme cases, radiation pressure from the companion also affects the shape of the hot primary. More details for the impact of the radiation pressure on the shape of the star can are described in (Haas 1993).

In order to calculate the lightcurve the shape of the star is first calculated with the help of the Roche model. This shape is then modified accounting for radiation pressure. Afterwards, each star is divided into small surface elements. For each surface element the flux is calculated including the before mentioned effects.

$$l(\Phi) = r^2 \sin\theta \Delta\theta \Delta\Phi \frac{\cos\gamma}{\cos\beta} GDRI \tag{6.8}$$

In each phase the flux of the visible surface elements of both stars is summed up, which results in the change of flux with phase. The WiDe method also includes different modes that are suited for different system configurations. In this work we used only WiDe mode 2, which links the luminosity of the companion to its temperature with the help of the Planck function.

MORO

There exist several implementations of the WiDe model that allow the calculation of synthetic lightcurves and the fitting of these to observational data. In this work MORO (MOdified ROche program) was used. This program was developed at the Dr. Karl Remeis Observatory. A detailed description of MORO can be found in Drechsel et al. (1995) and Lorenz (1988). In MORO the WiDe method has been modified to account for the effect of radiation pressure on the shape of a star to be able to analyze eclipsing binaries consisting of young, massive stars. The fitting of synthetic lightcurves to the observations is performed with a classical χ^2 minimization with the help of the simplex algorithm (Kallrath & Linnell 1987). The simplex algorithm defines a set of m+1 start parameter sets (m the number of parameters), the so-called simplex, around the start parameters that were defined by the user. For each of these parameter sets a synthetic lightcurve is calculated. This synthetic lightcurve is then compared to the observations. From the residuals ($d_\nu = l_\nu^O - l_\nu^C$) the standard deviation σ is calculated.

$$\sigma_{\mathrm{fit}}(x) = \sqrt{\frac{n}{n-m} \frac{1}{\sum_{\nu-1}^{n} w_\nu} \sum_{\nu=1}^{n} w_\nu d\nu^2(x)} \tag{6.9}$$

n is the number of points in the lightcurve and w_ν the weight of each point. The parameter set with the largest standard deviation is discarded and replaced by a new parameter set that is found by fixed operations (reflection, contraction, expansion, shrinkage). This step is repeated until the abort criterion is reached. As always the parameter set with the largest standard deviation is discarded, this algorithm is quite stable and will reach a minimum in any case. This minimum, however, may only be local but not necessarily the global one we look for.
Several of the parameters used in the lightcurve analysis are correlated parameters. This can cause severe problems, if too many and inadequate combinations of parameters are adjusted simultaneously. In particular, there is a strong degeneracy with respect to the mass ratio. Besides the orbital inclination, this parameter has the strongest effect on the light curve, and it is highly correlated with the component radii. Therefore, as many parameters as possible have to be fixed at values from theory, or values determined from the spectroscopic analysis. In particular the mass ratio is not adjusted but kept fixed and a possible mass ratio range has to be determined by spectroscopy. For several different mass ratios in the expected range, a number of fits with different start parameters is performed to ensure that the global minimum is found. The solution with the lowest standard deviation is supposed to be the final and best solution. For the error determination the bootstrapping method was used. For this, random data points from the data set are taken and a new fit is performed. This step is repeated about 500 times. The standard deviation of all adjusted parameters in all solutions gives the statistical errors.

Orbital period determination

The orbital period is the most fundamental parameter in lightcurve analysis. Additional light variations may arise from pulsations.

- **FAMIAS**[1] (Frequency Analysis And Mode Identification For Asteroseismology) For the period determination and correction in continuous lightcurves FAMIAS is an easy to use program. It was developed at the Insituut voor Sterrenkunde, K.U. Leuven by Zima (2008). This program can be used to analyze time-series photometry and spectroscopy. Periodicities are found with the help of a Discrete Fourier transformation. It is also possible to determine the statistical significance of the peaks found in the Fourier periodogram. Moreover, it is possible to pre-whiten the data from periods already determined. This is done by computing a non-linear multi-periodic least-squares fit of a sum of sinusoidals to the data. The fitting formula is

$$Z + \sum_i A_i \sin[2\pi(F_i t + \Phi_i)] \tag{6.10}$$

  where Z is the zero-point, and A_i, F_i and Φ_i are amplitude, frequency and phase (in units of 2π) of the i-th frequency respectively. The least-squares fit is carried out with the Levenberg-Marquardt algorithm. The data can then be pre-whitened with the computed fit.

- **Lomb-Scargle periodogram**
  However, for unevenly sampled or non-continuous lightcurves a Fourier transformation does not work well. For such data, it is preferable to use the Lomb-Scargle method (Press & Rybicki 1989), which estimates a frequency spectrum based on a least squares fit of sinusoid. The periodogram is described by

$$P_x(\omega) = \frac{1}{2}\left(\frac{\left[\sum_j X(t_j)\cos\omega(t_j-\tau)\right]^2}{\sum_j \cos^2\omega(t_j-\tau)} + \frac{\left[\sum_j X(t_j)\sin\omega(t_j-\tau)\right]^2}{\sum_j \sin^2\omega(t_j-\tau)}\right) \tag{6.11}$$

[1] `http://www.ster.kuleuven.be/~zima/famias/`

The time-delay τ is defined as $\tan 2\omega\tau = \frac{\sum_j \sin 2\omega t_j}{\sum_j \cos 2\omega t_j}$ and $X(t_j)$ represent the unevenly spaced data values. This periodogram can be used to identify the periodicities.

6.1.2. Time dependent spectroscopy

From the lightcurve it is only possible to determine relative parameters, as the luminosity ratio, the radii ratio, or the mass ratio. To be able to derive the masses and radii of both components also a spectroscopic analysis is essential. From time-series spectroscopy we can determine in this work only the radial velocity (RV) curve of the primary and the mass function, as all eclipsing binaries under investigation are single-lined. This is due to the huge luminosity difference between both components of the binaries. The semiamplitude of the RV curve K is derived by fitting sine curves to the RV points, which were phased with the period determined from the lightcurve. Due to the short period, a circular orbit is expected, and eccentricity can be neglected. From the semi-amplitude of the RV curve K, together with the period P, the mass ratio q and the inclination i derived by the lightcurve analysis, we can calculate the masses and the separation of the system:

$$M_1 = \frac{PK_1^3}{2\pi G} \frac{(q+1)^2}{(q \cdot \sin i)^3} \tag{6.12}$$

$$M_2 = q \cdot M_1 \tag{6.13}$$

$$a = \frac{P}{2\pi} \frac{K_1}{\sin i} \cdot \left(\frac{1}{q} + 1\right) \rightarrow R_{1/2} = \frac{r_{1/2}}{a} \cdot a \tag{6.14}$$

This also allows the radii of the stars to be derived, as the lightcurve analysis provides $r_{1/2}/a$.

6.1.3. Atmospheric parameters

Moreover, the effective temperature, surface gravity, and helium abundance of the primary star can be determined by a quantitative spectral analysis. The helium abundance is determined by modeling the He line profiles. In hot stars the surface gravity can be determined by fitting the wings of the H lines, which are sensitive to the pressure broadening by the Stark effect. The temperature can be derived by the line depth of the hydrogen lines. The maximum depth can be found in A0 stars. For hotter stars the line depth gets shallower, as more and more of the hydrogen is ionized. As $T_{\rm eff}$ and $\log g$ both are derived by the hydrogen lines, they are both correlated and cannot be disentangled easily. Therefore, the availability of ionization equilibria is very important, which are only sensitive to the temperature. Unfortunately, in the low-resolution spectra of the sdB binaries we have at our disposal there are no equilibria present.

For the spectral analysis we used SPAS (Spectrum Plotting and Analysis Suite), which was developed by Hirsch (2009). This program fits synthetic spectra to the observational data by interpolating in a three-dimensional grid of pre-calculated synthetic spectra. To save computer time, pre-defined wavelength ranges around single lines are fitted. It is possible to fit all lines simultaneously or separately and determine the standard deviation. Moreover, an statistical error determination is possible with the bootstrapping method. SPAS is a re-implementation of FITSB2 by R. Napiwotzki. In contrast to this program SPAS possesses a user-friendly interface and additional functions, like for example it is possible to co-add single spectra, or apply a Doppler shift. A downhill simplex algorithm is employed to find the best possible fit by linear interpolation in the model spectrum grid. It is possible to broaden the model spectra by rotation or macroturbulence. For the determination of the radial velocity a simple combination of Gaussians and Lorentzians are fitted to the spectral lines together with a linear offset.

6.2. Quantitative spectral analysis

6.2.1. Fundamental parameters and abundances

The atmospheres of OB stars are characterized by several atmospheric parameters and the elemental abundance. These parameters can be determined by a quantitative spectral analysis. All parameters are determined by fitting the observed spectrum with a grid of synthetic spectra, which was calculated the same way as described in Chap. 8. We used the method introduced by Irrgang et al. (2014) to analyze high-resolution B star spectra in the optical. In contrast to most other methods this method is fitting the complete spectrum at the same time and therefore using all parameter indicators simultaneously. Previously, we used the method described by Nieva & Przybilla (2010) for a quantitative analysis. This method is based on an iterative process to bring all indicators into agreement. Both methods are compatible and rely on the same indicators. However, the previous method is slower, and the new approach allows the analysis of many stars in a short time.
In the following the spectral features are briefly discussed, from which the atmospheric parameters are primarily constrained. Effects of parameter variations on strategic spectral lines are also displayed in Fig. 6.3.

- **Effective temperatures** $T_{\rm eff}$: As already mentioned it is a key parameter for the description of the atmospheric structure. Since the local temperature is crucial for the excitation of the elements, each spectral line is sensitive to the effective temperature. In particular in the UV it can be observed that the number and depth of the spectral lines is changing rapidly with the temperature (see Appendix C). As long as the population of the lower state of a transition is increasing, the line gets strengthened. If most atoms are ionized, the spectral lines are getting shallower. Therefore, the best indicators for $T_{\rm eff}$ are elements showing spectral lines of different ionization stages simultaneously.

- **Surface gravity** $\log g$: The surface gravity determines the pressure and density structure, which implies that in principle all spectral lines are affected. A larger surface gravity also implies a denser plasma, which increases the probability of electron captures by ions and, hence, decreases the degree of the ionization. Therefore, also lines of different ionization stages can be used to constrain $\log g$. In hot stars the surface gravity is primarily determined by fitting the wings of the Balmer lines, which are highly sensitive to $\log g$ because they are broadened by the linear Stark effect. However, the strength of the Balmer lines is also very sensitive to the temperature. This means the Balmer lines alone are not sufficient to determine both at the same time, in addition the ionization equilibria have to be used. That is why a method fitting the whole spectrum is very useful to limit the errors.

- **Microturbulence** ξ: As described in Sect. 5.3, the microturbulent velocity is a microscopic parameter, which can affect the strength and shape of all spectral lines. Weak lines have a Gaussian shape. An increasing microturbulent velocity produces a wider shallower Gaussian shape, what does not affect the equivalent width. However, stronger lines get saturated (more details later). This implies that increasing ξ, widens the wavelength range covered by the absorption and reduces the saturation, thus increasing th total absorption. This means that in particular saturated lines are ideal to determine the microturbulence.

- **Projected rotational velocity** $v \sin(i)$ and **macroturbulence** ζ: These macroscopic broadening parameters describe the blurring of spectral lines and can be derived from the shape of spectral lines, preferably from those which are intrinsically sharp, as most metal lines.

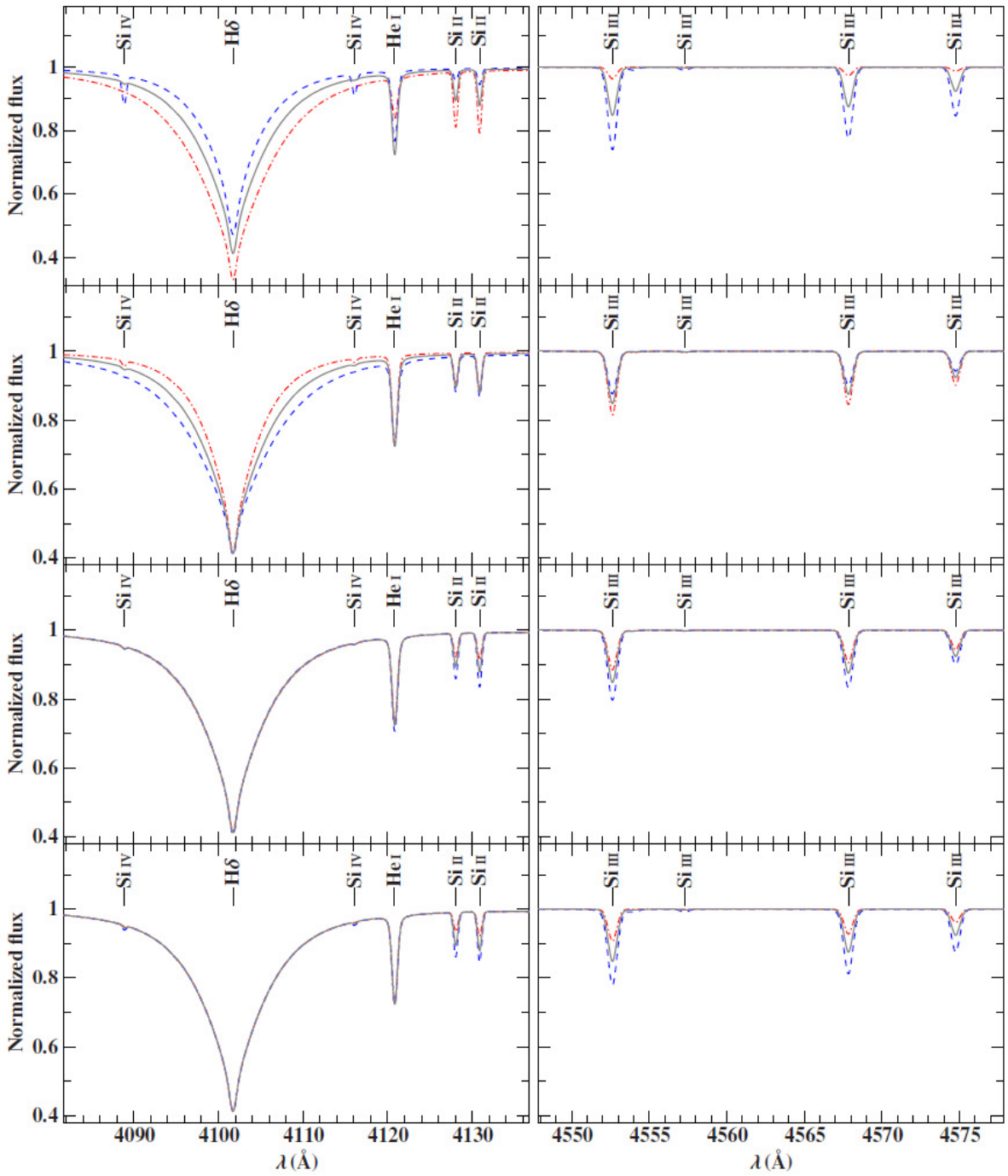

Figure 6.3.: Effects of changes in effective temperature, surface gravity, microturbulence, and silicon abundance on lines of hydrogen, helium, and silicon. The parameter under consideration is increased in the blue dashed model and decreased in the red dashed-dotted model with respect to the gray solid reference model ($T_{\rm eff}$ = 20 000 K, $\log(g)$ = 4.0 dex, ξ = 4 km s^{-1}, $\log(n(\mathrm{He}))$ = −1.15 dex, $\log(n(\mathrm{Si}))$ = −4.5 dex) by $T_{\rm eff}$ = ±5000 K (top row), $\log(g)$ = ±0.4 dex (second row), ξ = ±4 km s^{-1}(third row), and $\log(n(\mathrm{Si}))$ = ±0.6 dex (bottom row). Adopted from Irrgang (2014).

- **Radial velocity** $v_{\rm rad}$: The radial velocity, which is the velocity of the star in the line-of-sight, leads to a shift of the spectrum due to the Doppler effect. The amount of the shift can directly be translated in a Doppler velocity ($\lambda' = \lambda_0(1 - \frac{v}{c})$).

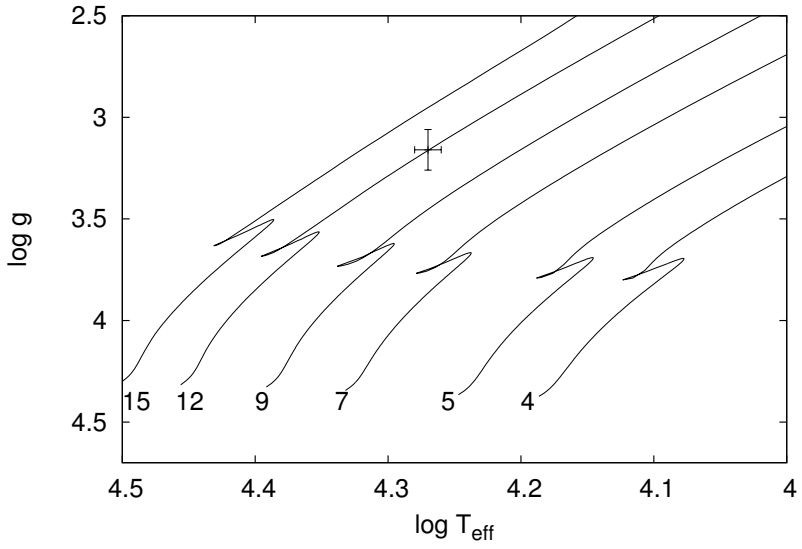

Figure 6.4.: Evolutionary tracks by Georgy et al. (2013) in the $T_{\rm eff} - \log g$ diagram for different initial masses ($M_\odot$) together with the position of HD 271791

- **Elemental abundances:** The abundances of all elements besides H and He are small. The metals, therefore have little impact on the continuum in hot stars. However, the number of metal absorbers has a strong effect on the strength of lines, which are therefore good indicator for elemental abundances. The relation between the strength of spectral and elemental abundances is, however, not linear. It can be described by a curve of growth, which shows three domains of behavior. For weak lines the growth is linear, which are therefore ideal to determine abundances. For stronger lines saturation is observed, which means the lines become more insensitive to abundance changes. Even stronger lines begin to develop damping wings as seen, e.g. in the Balmer lines, which lead again to an increase of the equivalent width. For a detailed discussion see Gray (2005) pp.326-335.

6.2.2. Mass, age and radius of the star

The atmospheric parameters ($T_{\rm eff}$ and $\log g$) can also be used for the determination of the mass, age and radius of the star with the help of stellar evolution models. The evolution of a star in the the $T_{\rm eff}$-$\log g$ diagram (see Fig. 2.6) mostly depends on the initial mass. As can be seen in Fig. 6.4 the tracks run parallel depending on the initial mass of the star crossing the $T_{\rm eff}$-$\log g$-diagram as they evolve. Therefore, the position in the $T_{\rm eff} - \log g$-diagram can be used to derive the fundamental stellar parameter mass $M_{\rm initial}$, M and age τ. The luminosity L can be derived from $L/L_\odot = M/M_\odot \frac{{T_{\rm eff}}^4/{T_{\rm eff}}_\odot^4}{g/g_\odot}$. In the last years it became clear that the rotation of a star is an important parameter for the evolution of a star, which has, hence, to be considered, too. As the inclination of the system is typically unknown, we can only use a statistical approach and use the spherically averaged value $\pi/4$ for the inclination when matching $v \sin(i)$ to the equatorial velocity $v_{\rm rot}$ predicted by the evolutionary tracks. In this work we determined the parameters (M, age, L) from fitting single-star evolutionary tracks that account for stellar rotation by Georgy et al. (2013) to the $T_{\rm eff}$ and $\log g$ determined by the spectral analysis. The radius can be calculated by the from the surface gravity and the determined stellar mass $R = g/GM$. The errors in the parameters have been determined from the error in $T_{\rm eff}$ and $\log g$.

6.2.3. Distances

It is possible to derive the distance to the star, with the help of a synthetic spectrum $F(\lambda)$, which represents the flux coming from the surface of the star. This flux is distributed uniformly in a sphere with the radius equals the distance d. Applying flux conservation we can determine the angular diameter by using the measured flux $f(\lambda)$:

$$4\pi\theta^2 f(\lambda) = 4\pi R^2 F(\lambda) \tag{6.15}$$

If the stellar radius R is known, this can be used to derive the distance $d = 2R/\theta$, assuming small angles.
Instead of using monochromatic fluxes, it is more convenient to use photometric measurements in a suitable filter: The corresponding magnitude mag_x to an arbitrary photometric passband can be derived by

$$\mathrm{mag}_x = -2.5 \log \left(\frac{\int_0^\infty r_x(\lambda) f(\lambda) \lambda \mathrm{d}\lambda}{\int_0^\infty r_x(\lambda) f^{\mathrm{ref}}(\lambda) \lambda \mathrm{d}\lambda} \right) + \mathrm{mag}_x^{\mathrm{ref}} \tag{6.16}$$

using, a suitable reference star, e.g. Vega. Thereby is $r_x(\lambda)$ the system response function.
More details about the distance determination together with an example can be found in Nieva & Przybilla (2014).
However, the existence of interstellar dust and gas leads to an absorption of photons along the line of sight, which is called interstellar extinction. This causes also a reddening and therefore a change in the slope of the spectral energy distribution (SED). This effect has to be accounted for with the help of a reddening factor $10^{-0.4A(\lambda)}$, with $A(\lambda)$ the extinction in magnitude at wavelength λ. Fitzpatrick (1999) gives a relation for $A(\lambda)$ as a function of the color excess $E(B-V)$ and the extinction parameter $R_V = A(V)/E(B-V)) =$ (3.1 for the diffuse interstellar medium, often used for Galactic interstellar extinction), which can be used to account for the extinction $M_{\mathrm{corr}}(X) = M(X) + A(X)E(B-V)$. Therefore, we determine E(B-V) as well as the distance by fitting the measured photometry in several passbands.

6.3. Stellar kinematics

The spectroscopic analysis facilitates the distance d to the star and its radial velocity v_{rad} to be derived. The Hipparcos satellite launched in 1989 and operated until 1993, measured the positions and proper motions in right ascension ($\mu_\alpha \cos(\delta)$) and declination (μ_δ) of more than 180000 bright stars with a precision of about 1 mas (milli arc second). For bright stars also less accurate proper motion measurements are available covering typically much larger time spans. The Gaia spacecraft launched in December 2013, however, is measuring the parallax and proper motion of about 1 billion stars brighter than 20th magnitude at the moment with an accuracy $< 20\mu as$. This may revolutionize the stellar astrophysics, as for all brighter stars distances and proper motions will be available.
With the help of the proper motions and the radial velocity v_{rad} the full six-dimensional kinematics of the object at present time can be derived. The Galactic rest-frame velocity can then be determined by the three-dimensional velocities $\mathbf{v} = (v_x, v_y.v_z) \rightarrow v_{\mathrm{Grf}} = \sqrt{\mathbf{v} \cdot \mathbf{v}}$. By using a model for the gravitational potential of the Galaxy $\Phi(\mathbf{x})$ the star's local escape velocity $v_{\mathrm{esc}}(\mathbf{x}) = \sqrt{-2\Phi(\mathbf{x})}$, from which we can conclude whether the star is still bound to the Galaxy by comparing the escape velocity to the rest-frame velocity. In this work we used the three different models that were described by Irrgang et al. (2013):

- a revised Galactic gravitational potential by Allen & Santillan, Model I in Irrgang et al. (2013)
- potential with a Miyamoto & Nagai bulge and disk component and a Navarro, Frenk, & White dark matter halo, Model III in Irrgang et al. (2013)
- potential with a Miyamoto & Nagai bulge and disk component and a truncated, flat rotation curve halo model

They were determined by fitting different models with certain parameters to the rotation curve of the Milky Way and other constraints. With the help of the potential it is also possible to trace the orbit of the star back in time. The intersection of the star's orbit with the Galactic disk is possibly the birthplace of the star, which can be characterized by the Galactocentric radius $r_d = \sqrt{\mathbf{x}^2 + \mathbf{y}^2}$. Moreover, the flight time τ and the ejection velocity v_{ej} defined as the velocity at disk intersection relative to the rotating Galactic disk can be determined with this method. These parameters can be used to check how realistic the runaway ejection models in this case are and if the evolutionary age of the runaway star enables an ejection scenario at all. Uncertainties in the input parameters are obtained from 100000 Monte Carlo runs for different Milky Way mass models using different initial values for the parameters within the errors for them.

7. Analysis of hot subdwarfs with cool companions

After the introduction into the basic principles and the analysis methods, I will now come to the actual analysis done in my thesis. I worked with two very different groups of post-common envelope systems: low-mass and high-mass systems. In this chapter I will describe the analyses of a special group of low-mass post common-envelope systems, sdB+dM binaries. They were introduced in Chapter 3. I will first discuss the MUCHFUSS project, which amongst other things aims at discovering such systems. Afterwards I present the analysis of some individual sdB+dM binaries. I conclude with a comparison of the known reflection effect binaries with the known eclipsing WD+dM systems.

7.1. The MUCHFUSS project

The project Massive Unseen Companions to Hot Faint Underluminous Stars from SDSS (MUCHFUSS) aims to find hot subdwarf stars with massive compact companions like massive white dwarfs ($> 1.0 M_{\odot}$), neutron stars or stellar mass black holes (see Geier et al. 2011a, 2015). Hot subdwarf stars were selected from the Sloan Digital Sky Survey (SDSS) by colour and visual inspection of the spectra. Hot subdwarf stars with high radial velocity variations were selected as candidates for follow-up spectroscopy to derive the radial velocity curves and the binary mass functions of the systems. The selection criteria turned out to be not only suitable to find massive, compact companions but also binaries with low-mass companions with short periods were discovered. With the help of a photometric follow-up, it is possible to distinguish between low-mass, white dwarf or main-sequence companions.

7.1.1. Target selection

The target selection of the MUCHFUSS project was discussed by Geier et al. (2011a). The selection criteria were applied to the SDSS Data Releases 6 and 7 (Adelman-McCarthy et al. 2008; Abazajian et al. 2009). Hot subdwarf candidates were selected by applying a color cut to SDSS photometry. All point source spectra within the colours $u - g < 0.4$ and $g - r < 0.1$ were selected and downloaded from the SDSS Data Archive Server[1]. Objects fainter than $g = 18.5$ mag have been excluded because of insufficient quality. The SDSS spectra are co-added from at least three individual integrations with typical exposure times of 15 min taken consecutively. We have obtained those individual spectra for all selected stars. Moreover, second epoch medium resolution spectroscopy ($R = 1800 - 4000$) was obtained from SDSS as well as our own observations, using ESO-VLT/FORS1, WHT/ISIS, CAHA-3.5m/TWIN and ESO-NTT/EFOSC2 (see Geier et al. 2011a). The RVs have been measured as described by Geier et al. (2011b). Each single fit has been inspected visually and outliers caused by cosmic rays and other artefacts have been excluded. We selected all objects with RVs discrepant at the formal 1σ-level and found 81 candidates for RV variability in SDSS DR 6 (Geier et al. 2011a) and 196 candidates in SDSS DR 7 (Geier et al. 2015). The highest RV shift over the corresponding

[1] `http://das.sdss.org`

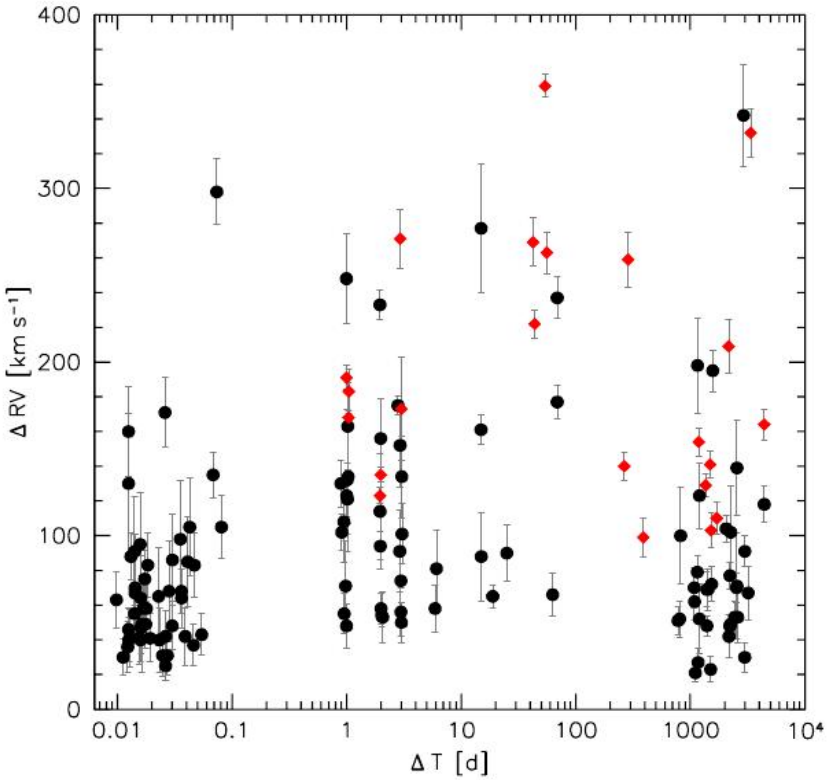

Figure 7.1.: Highest radial velocity shift between individual spectra plotted against time difference between the corresponding observing epochs. The filled red diamonds mark sdO/B binaries with known orbital parameters (Kupfer et al. 2015), while the filled black circles mark the rest of the hydrogen-rich sdB, sdOB and sdO sample of RV variable stars (Geier et al. 2015).

time difference is shown in Fig. 7.1. To determine the true nature of the unseen companion, the period and the RV semi-amplitude has to be measured. Even so the inclination is still undetermined. This means the mass of the companion is not constrained very well. Often it is not possible to distinguish between a low-mass stellar or a white dwarf companion. Only if the minimum mass is more than 0.45 $M_{\odot}$, we can exclude a stellar companion, as it should be visible in the spectrum (Lisker et al. 2005). With the help of a photometric follow-up, we can determine the nature of the companion and the period of the system, if light variations are visible. Even without variations, it can help to select interesting targets. Moreover, we can derive the fraction of reflection effect binaries and close substellar companions around hot subdwarf stars, as the targets are RV selected.

7.1.2. Light variations and their observations with BUSCA

Observations with BUSCA

Based on the target selection of the MUCHFUSS project (Geier et al. 2011a) we selected targets with radial velocity variations on very short time scales (smaller than 0.1 d) for a photometric follow-up. The MUCHFUSS photometric follow-up (more details on the analysis in Sect. 7.8) was done with BUSCA (Bonn University Simultaneous CAmera; see Reif et al. 1999) on the 2.2m-telescope located at the Calar Alto Observatory in Spain. This instrument turned out to be perfect for our purposes, as it is possible to observe in four bands simultaneously.

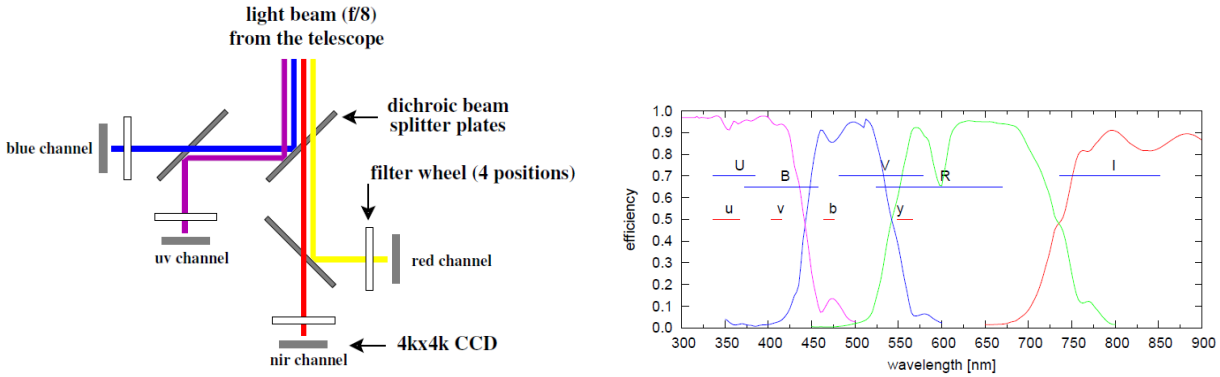

Figure 7.2.: Light path in the BUSCA instrument and transmission curve of the four different channels (U_B, B_B, R_B, I_B).

Table 7.1.: Log of observations with BUSCA

Year/Month/Date	P.I.	Observer
2010/06/11	SG	VS
2010/09/29-2010/10/03	SG	VS & EZ
2011/02/25-2010/03/01	SG	VS
2011/05/30,31;2011/06/03	OC	VS
2011/09/28-2011/10/02	SG	RG
2011/10/17-21	OC	VS
2012/01/13,14	SG	EZ
2012/10/10-14	SG	VS

The observers and P.I.s of the observation are: OC (Oliver Cordes), SG (Stephan Geier), RG (Raoul Gerber), VS (Veronika Schaffenroth), EZ (Eva Ziegerer)

The light is splitted by a beam splitter into four different arms, which can be directly used without a filter (U_B, B_B, R_B, I_B). The transmission curve of the four channels is displayed in Fig. 7.2. To distinguish between different effects causing light variations, lightcurves in several wavelength bands are highly important. We did not use any filters but used the intrinsic transmission curve given by the beam splitters, as that way all visible light is used and no light is wasted.
The data was taken in several runs listed in Table 7.1. For each star a lightcurve between 1.5 and 2.5 h with exposure times from 30 to 180 seconds was taken to check for any light variations. BUSCA allows to observe in windows to decrease the read-out time to about 15-20 seconds compared to a full-frame read-out time of about two minutes. Therefore, we observed our target and four comparison stars in 60 x 60 pixel windows to perform relative photometry to correct for the changing airmass, changing conditions, and clouds.
The reduction was done using the aperture photometry package provided by IRAF. In total we found 6 stars showing light variations out of 59 checked systems (more details in Sect. 7.8.2). This variations are shown in Fig. 7.35.

Lightcurve variations or not?

There are several effects that lead to light variations of hot subdwarf binaries, and if the lightcurve shows periodic variation we can restrict the nature of the companion.
One of the possible effects is the so-called reflection effect. It results from a huge temperature difference of both components and rather similar radii and is for this reason visible, if the companion is a low mass main-sequence star or even a brown dwarf. The companion is heated

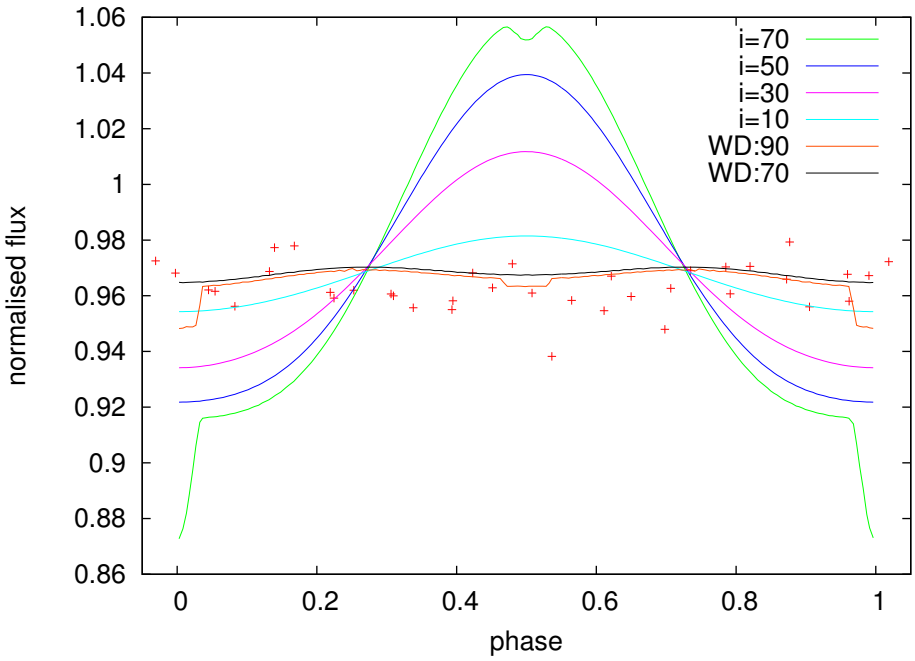

Figure 7.3.: Lightcurve models in R_B of a typical HW Virginis system at different inclinations and of an sdB binary system with a low mass WD with the same period and RV semi-amplitude at 90° and 70 ° together with a typical non-detection lightcurve.

up on one side due to the immense radiation of the sdB. Therefore, the contribution of the companion to the total flux of the system is changing with the phase and is apparent as a sinusoidal variation with a period equal to the orbital period.

Due to the short periods found for these systems, which result from the formation by a common envelope, and the similarity of the radii, sdB+dM systems have a high probability to be eclipsing. Such systems are of high value because they allow to determine the masses and radii of both components by a combined photometric and spectroscopic analysis. Moreover, the separation of the system can be measured. Eclipsing binaries with low-mass stellar companions or substellar companions are called HW Virginis systems after their prototype.

The reflection effect is also visible at rather small inclinations, if the period is small. In Fig. 7.3 one can see how the amplitude of the reflection effect changes with the inclination for the parameters of a typical HW Vir system compared to a typical non-detection lightcurve. Even for an already very unlikely inclination of 10°, we would expect variations of almost 2%, which would be possible to be seen in the lightcurve. The reflection effect is easily recognizable, if a lightcurve in several bands is available, as this effect depends on the wavelength and is usually getting bigger in the redder bands, because the temperature of the heated side is not as hot as the sdB and, hence, the hot side of the companion is brighter in the redder bands. Due to the smaller radius the reflection effect is not visible in sdB+WD systems, as can be seen in Fig. 7.3 for the example of a low-mass WD, which has, therefore, a rather large radius compared to more massive ones.

A different lightcurve variation occurs in short period sdB binary systems with white dwarf companions. The close companion distorts the subdwarf, which is, hence, not spherical any more, but has an ellipsoidal shape. This effect is, therefore, called ellipsoidal deformation and manifests itself in a sinusoidal variation with half the orbital period. The variation gets larger with shorter period of the system and a more massive white dwarf companion. It is easily distinguishable from the reflection effect, even if the period is not known, as the amplitude of the ellipsoidal deformation is wavelength independent.

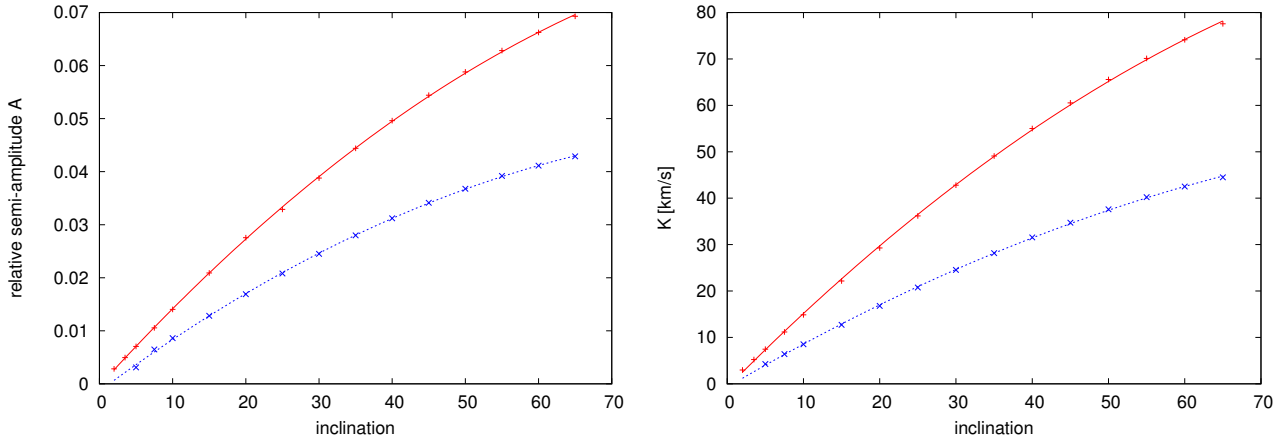

Figure 7.4.: Expected relative semi-amplitude of the reflection effect in $R_{\rm B}$ and expected semi-amplitude of the radial velocity of the hot subdwarf for different inclinations for the R_B band for the parameters of a typical HW Virginis system like the prototype HW Vir (+) and for an sdB+BD system like J1622 (x) with the functions given by Eq. (7.5) and (7.6).

Moreover, recently unperiodical light variations in He-sdO stars were found (Green et al. 2014b). It is not yet clear were this strange variations come from but they are similar to variations found in cataclysmic variables. Moreover, the reason for the observed radial velocity variations in He-sdOs is not understood, as no periodicities can be found. We found also one He-sdO showing such strange light variations (see Fig. 7.35f).
In the following we show at first the analysis of several newly discovered eclipsing sdB PCEB systems with substellar companions, substellar companion candidates or low-mass main sequence companions. Afterwards we summarize the analysis of the photometric follow-up of the MUCHFUSS project. The last section gives some statistics of the period and mass distribution of the hot subdwarfs of spectral type B with cool,low-mass companions and a comparison with systems consisting of white dwarfs and low-mass companions, which are the successors of sdB with low-mass companions.

7.2. Eclipse time variations in J0820

The fist HW Virginis system found in the course of the MUCHFUSS project was J08205+0008 (hereforth abbreviated J0820, Geier et al. 2011c; Schaffenroth 2010). As the spectroscopic follow-up suggested a short period of this system of 0.096 d and a very low minimum mass for the companion, this system was prioritized for a photometric follow-up. The observations with the Flemish 1.2 m Mercator Telescope on La Palma, Canary Islands, showed a deep primary and shallow secondary eclipses superimposed on a strong reflection effect in the lightcurves. The spectroscopic and photometric analysis confirmed the first unambiguously detected substellar object ($M_{\rm comp} = 0.045 - 0.068 M_{\odot}$) around an sdB star. Eclipsing binaries are with such short periods ideal for eclipse timing. This facilitates small third bodies, like for example planets, in the system to be detected. Therefore, we obtained more photometric data with BUSCA and with the 1m-telescope located at the South African Astronomical Observatory using the SAAO STE3 CCD, a 512x512 detector, which has a read out time of only about 5 s in the 2x2 prebinned mode.
The eclipse times of the observations with the SAAO STE3 CCD were measured by the bisected chords method – essentially measuring the mid-points of a number of chords joining eclipse ingress and egress curves and running parallel to the time axis in a magnitude/time plot. These

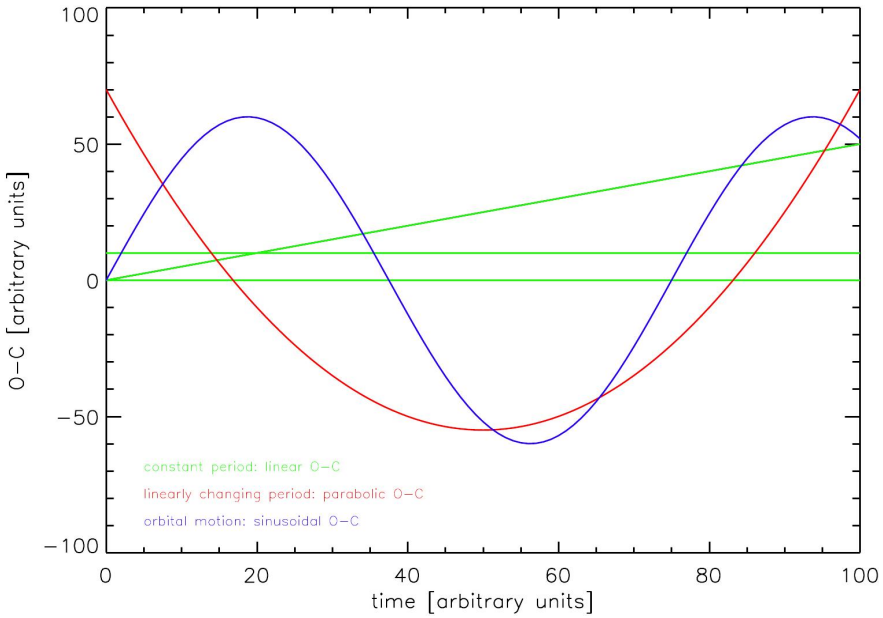

Figure 7.5.: Different cases in an O-C diagram. See text for further explanations (Lutz 2011).

mid-points always lie very close to a line perpendicular to the time axis, indicating eclipse symmetry, and such a fit has been demanded in every case. Further details about the reduction and analysis methods are discussed in (Kilkenny 2011).
For BUSCA the eclipse minima were determined with another method. One observation of an eclipse was extracted and shifted to zero. Afterwards, this reference eclipse was moved across the complete lightcurve in given time steps and the χ^2 in each time step was measured. The respective χ^2 minimum, which corresponds to the eclipse minimum, is then measured by fitting a Gaussian to the χ^2 distribution. In order to compare the eclipse times from different instruments and observation runs the times are converted from UTC to BJD (Eastman et al. 2010, `http://astroutils.astronomy.ohio-state.edu/time/utc2bjd.html`).
Table 7.2 summarizes the measured eclipse times together with the cycle numbers. In order to determine these numbers the period was measured with the help of a Lomb-Scargle periodogram (see Sect. 6.1.1). The eclipse with cycle number 0 was taken as reference point. Therefore, we get an improved ephemeris:

$$\mathrm{BJD} = 2455942.46813(5) + 0.096240737(2) \cdot E \tag{7.1}$$

Starting from there the cycle number is calculated as $E = \frac{T_0 - T}{P}$. From this also an O-C diagram can be derived:

$$\begin{aligned} \text{O-C} &= (T - (T_0 + EP) = T - T_0 - EP \qquad (7.2)\\ &= \Delta t_0 + \Delta P_0 E + \frac{1}{2} P_0 \dot{P} E^2 + \frac{M_P G^{\frac{1}{3}} P_P^{\frac{2}{3}}}{(M_{\mathrm{sdB}} + M_{\mathrm{comp}} + M_P)^{\frac{2}{3}} 4^{\frac{1}{3}} \pi^{\frac{2}{3}}} \cdot \frac{\sin i}{c} \sin(2\pi E / P_P + \Phi) \end{aligned}$$

There are several effects, which can lead to variations in the O-C diagram (see Fig. 7.5). An error in the zero point T_0 will lead to an offset. Any inaccuracies in the period can immediately be detect in the O-C diagram, if a linear slope is visible. The correction to the period can then be calculated by the slope of the straight line. Moreover, changes of the period can be detected, if a parabola is visible in the O-C diagram, An downward open parabola implies a period decrease. Another possible effect is an orbital motion caused by third body in the system. This will cause a sinusoidal change in the O-C diagram.

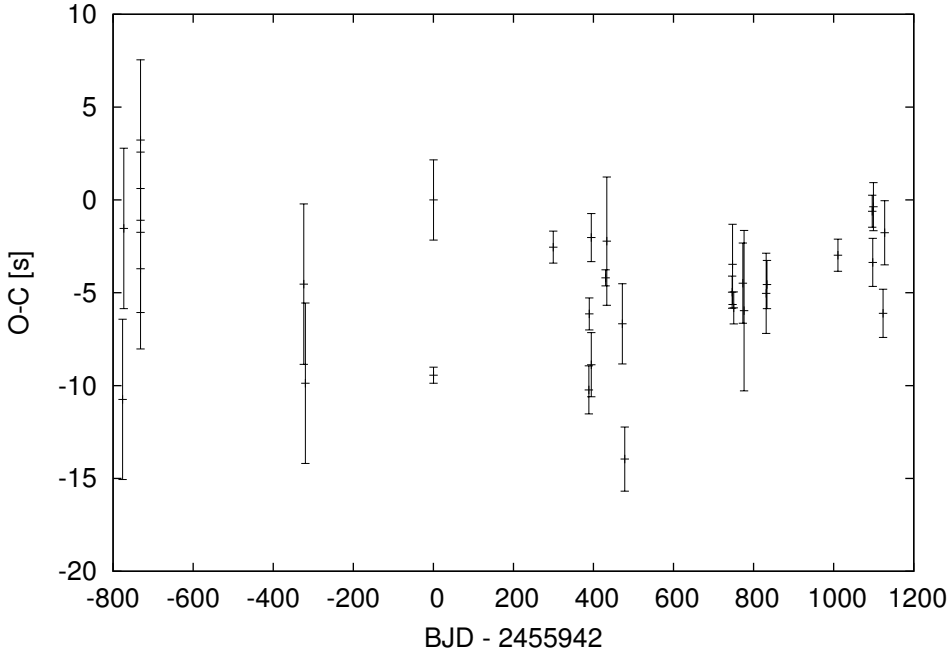

Figure 7.6.: O-C curve of J0820

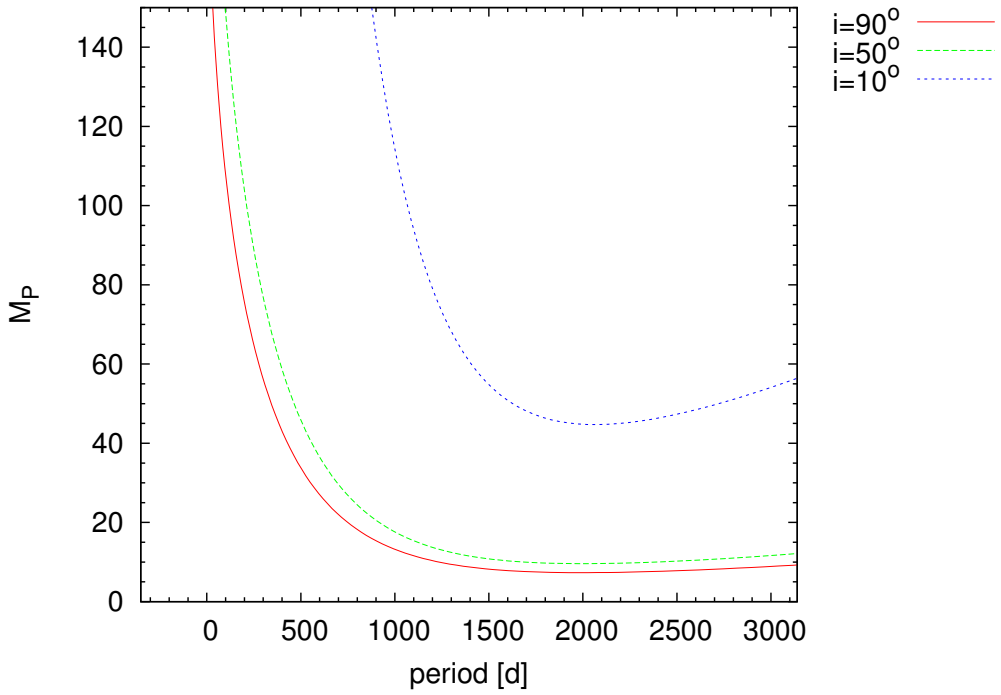

Figure 7.7.: Detection limit of the timing method for different inclinations assuming an 10 s error in our measurements and a time-base of 1610 d.

The amplitude of this sine curve can be calculated from the mass function and depends of the masses of the third body M_P, the masses of both components of the binary $M_{\rm sdB}$, $M_{\rm comp}$, the period of the third body P_P, and inclination i, and the speed of light c. The O-C curve of the sdB+BD system J0820 is given in Fig. 7.6. The baseline of the O-C diagram is 5.3 yr. The period was already adjusted so that no slope is visible, which constrains the period to about 40 μs. No variation in the O-C diagram is recognisable. This means we cannot detect an period

Table 7.2.: Eclipse minima of J0820, the positive numbers were observed with the SAAO STE3 CCD, the negative observation numbers with BUSCA

cycle number E	T [BJD]	error
0000	2455942.46813	0.00005
0001	2455942.56448	0.00001
3108	2456241.58437	0.00002
4032	2456330.51090	0.00003
4042	2456331.47326	0.00002
4093	2456336.38149	0.00003
4094	2456336.47781	0.00004
4466	2456372.27931	0.00001
4497	2456375.26275	0.00008
4902	2456414.24030	0.00005
4964	2456420.20731	0.00004
7751	2456688.43014	0.00002
7761	2456689.39253	0.00005
7792	2456692.37602	0.00002
8030	2456715.28130	0.00005
8061	2456718.26478	0.0001
8632	2456773.21823	0.00005
8653	2456775.23928	0.00003
-8071	2455165.70928	0.00005
-8040	2455168.69268	0.00005
-7606	2455210.46121	0.00005
-7605	2455210.55741	0.0005
-7604	2455210.65364	0.0005
-3367	2455618.42562	0.00005
-3326	2455622.37155	0.00005

change or third body in the system yet. We have an error of about 10 s in the system, from which we can give an upper limit for a third body in the system depending on the period and inclination (see Fig. 7.7).

7.3. J1920 – A new typical HW Virginis system

In the course of the photometric follow-up we discovered a new HW Virginis system J192059+372220 (J1920). The lightcurve is shown in Fig. 7.35c. It shows a prominent reflection effect and grazing eclipses. We also started a spectroscopic follow-up and got 39 medium resolution ($R \sim 4000$) spectra with the TWIN spectrograph on the 3.5m-telescope at Calar Alto and 11 spectra from the ISIS spectrograph at the William Herschel Telescope at the Roque de los Muchachos Observatory on La Palma with the same resolution.

Those spectra were used to determine the radial velocity curve. The RV was measured using SPAS (Hirsch 2009) by fitting Gaussians and Lorentzians to the Balmer and helium lines. Due to the short period a circular orbit was assumed and, therefore, a sine function was fitted to the measured RVs to determine the semi-amplitude $K = 59.8 \pm 2.5\,\mathrm{km\,s^{-1}}$ and the systemic velocity $\gamma = 16.7 \pm 2.0\,\mathrm{km\,s^{-1}}$ and the period $P = 0.168876\,\mathrm{d}$. The results are summarized in Table 7.3.

The spectra were, moreover, used to determine the atmospheric parameters by fitting synthetic spectra, which were calculated using LTE model atmospheres with solar metallicity and metal line blanketing (Heber et al. 2000), to the Balmer and helium lines.

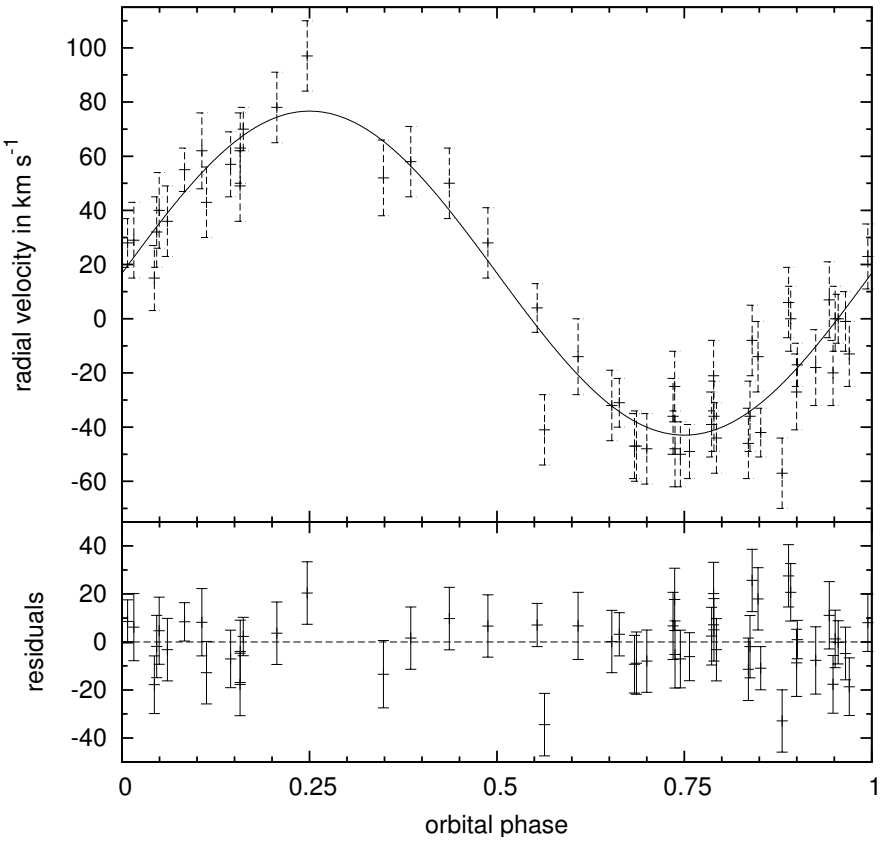

Figure 7.8.: Radial velocity curve of J1920 with the best sine fit. The residuals are shown in the lower panel.

Table 7.3.: Results and parameter of J1920

coord.	ep=2000	19 20 59 +37 22 20		
g'	[mag]	15.58		
K	[$\mathrm{km\,s^{-1}}$]	59.8	±	2.5
γ	[$\mathrm{km\,s^{-1}}$]	16.8	±	2.0
P	[d]	0.168876	±	0.00035
a	[$\mathrm{R_\odot}$]	1.078	±	0.0449
T_{eff}	[K]	27500	±	1000
$\log g$	[cgs]	5.4	±	0.1
$\log y$		-2.5	±	0.25
i	[°]	67		
M_{sdB}	[$M_\odot$]	0.47		
M_{comp}	[$M_\odot$]	0.116	±	0.007

Each spectrum was fitted separately. In other HW Vir systems an apparent change of the atmospheric parameters with the phase was found (Schaffenroth et al. 2013) due to contaminating light from the heated hemisphere of the companion. As the S/N is high enough, we do not see this effect and we, therefore, averaged all single values. The results can be found in Table 7.3. The parameters are with an effective temperature of $T_{\mathrm{eff}} = 27500 \pm 1000\,\mathrm{K}$ and a surface gravity of $\log g = 5.4 \pm 0.1$ typical for an sdB lying on the extreme horizontal branch.
Unfortunately, we do not have enough photometric data to measure the period from the lightcurve. Also the S/N of our data is not high enough for a proper lightcurve analysis. A

preliminary analysis using MORO (MOdified ROche program, see Drechsel et al. 1995), however, showed that the inclination must be about 67°. With the help of this information, we are able to calculate the separation of the system and the mass of the companion, assuming a canonical mass of 0.47 $M_\odot$ for the sdB, from the mass function. Accordingly, the companion has a mass of 0.116 $M_\odot$ and is, therefore, a late M dwarf, like the companions of all but two of known HW Vir systems.

7.4. J1622 – A subdwarf B star with brown dwarf companion[2]

Here, we report on the discovery of the second short period eclipsing hot subdwarf binary with a substellar companion found in the course of the MUCHFUSS project. As mentioned above this object was found in the photometric follow-up. As the RV curve suggested a short period of only 1.65 h, this was our primary target. In this section, we describe the spectroscopic and photometric observations in Sect. 7.4.1 and their analysis in Sect. 7.4.2 (spectroscopy) and 7.4.4 (photometry). Evidence for the brown dwarf nature of the companion is given in Sect. 7.4.4 and the lack of synchronization of the sdB star is discussed in Sect. 7.4.5. Finally, we conclude and present suggestions on how to improve the mass determination.

7.4.1. Observations

Spectroscopy

The SDSS spectra of SDSS J162256.66+473051.1 (J1622 for short, also known as PG1621+476, g'=15.96 mag) showed a radial velocity shift of 100 $\mathrm{km\,s^{-1}}$ within 1.45 h. Therefore, the star was selected as a high priority target for follow-up. The eighteen spectra were taken with the ISIS instrument at the William Herschel Telescope on La Palma, from 24 to 27 August 2009 at medium resolution (R∼4000). Additional 64 spectra with the same resolution were obtained with the TWIN spectrograph at the 3.5 m telescope at the Calar Alto Observatory, Spain, from 25 to 28 May 2012. Moreover, ten higher resolution spectra (R∼8000) were observed with ESI at the Keck Telescope, Hawaii, on 13 July 2013. The TWIN and ISIS data were reduced with the MIDAS package distributed by the European Southern Observatory (ESO). The ESI data was reduced with the pipeline **Makee[3].**

Photometry

When the RV-curve from the ISIS spectra showed a short period of only 0.069 d, a photometric follow-up was started. The object J1622 was observed with the Bonn University Simultaneous Camera (BUSCA) at the 2.2 m telescope at the Calar Alto Observatory. The instrument BUSCA (Reif et al. 1999) can observe in four bands simultaneously. We did not use any filters but we used instead the intrinsic transmission curve given by the beam splitters, which divides the visible light into four bands U_B, B_B, R_B, and I_B (implying no light loss). Four sets of lightcurves, each covering one orbit of J1622, were obtained on 12 June 2010, 29 September 2010, 28 February 2011, and 1 June 2011. They were reduced by using the aperture photometry package of IRAF. As the comparison stars have different spectral types, we observed a long-term trend in the lightcurve with changing air mass due to the different wavelength dependency of atmospheric extinction, which cannot be corrected.

[2]This chapter is based on Schaffenroth et al. (2014c)

[3]`http://www.astro.caltech.edu/~tb/ipac_staff/tab/makee/`

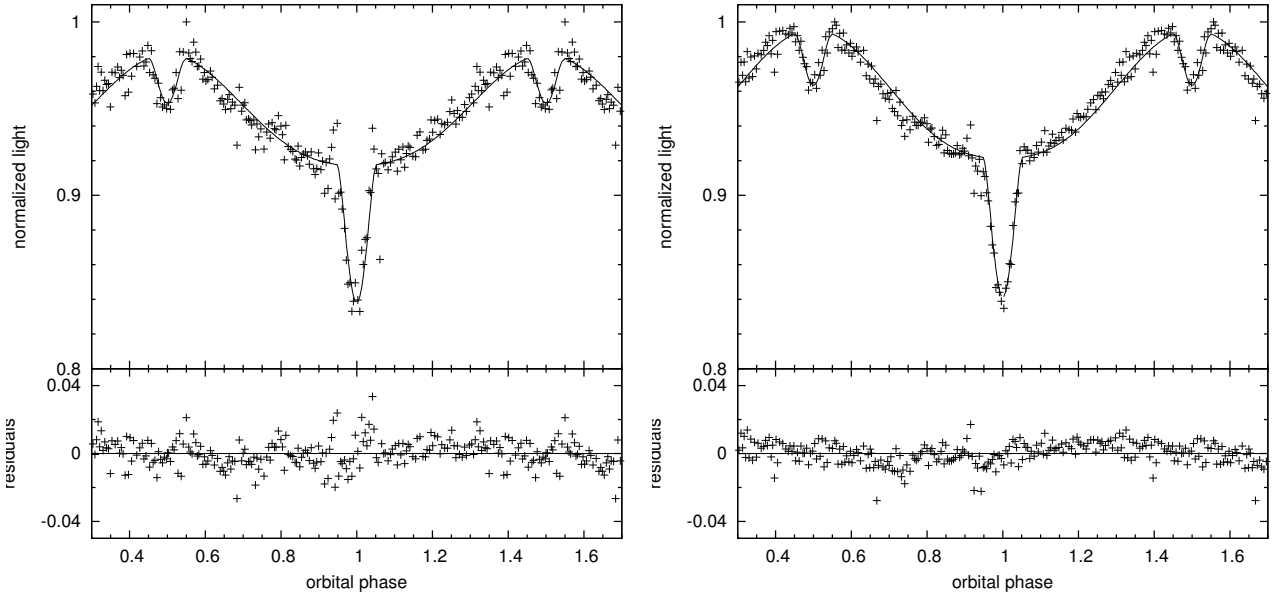

Figure 7.9.: Phased BUSCA lightcurve in B_B and R_B of J1622. The solid line demonstrates the best-fit model. In the bottom panel, the residuals can be seen.

7.4.2. Spectroscopic analysis

Radial velocity curve

The radial velocities were measured by fitting a combination of Gaussians, Lorentzians, and polynomials to the Balmer and helium lines of all spectra, which are given in Table 7.6. Since the phase-shift between primary and secondary eclipses in the phased lightcurve (see Fig. 7.9) is exactly 0.5, we know that the orbit of J1622 is circular. Therefore, sine curves were fitted to the RV data points in fine steps over a range of test periods. For each period, the χ^2 of the best-fit sine curve was determined (see Geier et al. 2011b). All three datasets were fit together. The orbit is well covered. Figure 7.10 shows the phased RV curve with the fit of the best solution. It gives a semi-amplitude of $K = 47.2 \pm 2.0\,\mathrm{km\,s^{-1}}$, a system velocity of $\gamma = -54.7 \pm 1.5\,\mathrm{km\,s^{-1}}$, and a period of 0.0696859 ± 0.00003 d. The period is consistent with the period from the photometry (see Sect. 7.4.3) and is the second shortest ever measured for an sdB binary.

Atmospheric parameters

The atmospheric parameters were determined by fitting synthetic spectra, which were calculated using LTE model atmospheres with solar metallicity and metal line blanketing (Heber et al. 2000), to the Balmer and helium lines using SPAS (Hirsch 2009). of the HW Vir stars and similar non-eclipsing systems, it was found that the atmospheric parameters seemed to vary with the phase (e.g. Schaffenroth et al. 2013), as the contribution of the companion to the spectrum varies with the phase. Therefore, all spectra were fitted separately. Figure 7.11 shows the effective temperature and the surface gravity determined from the TWIN spectra plotted against orbital phase. No change with the orbital phase can be seen. Therefore, we co-added all 64 TWIN spectra and derived the atmospheric parameters ($T_{\mathrm{eff}} = 29000 \pm 600\,\mathrm{K}$, $\log g = 5.65 \pm 0.06$, $\log y = -1.87 \pm 0.05$). In Fig. 7.12 the best fit to the Balmer and helium lines of the co-added spectrum is shown.
In Fig. 7.13, the position of J1622 in the $T_{\mathrm{eff}} - \log g$ diagram is compared to those of the known HW Vir systems and other sdB binaries. It is worthwhile to note that all of the HW Vir systems, but two, which have evolved off the EHB, have very similar atmospheric parameters.

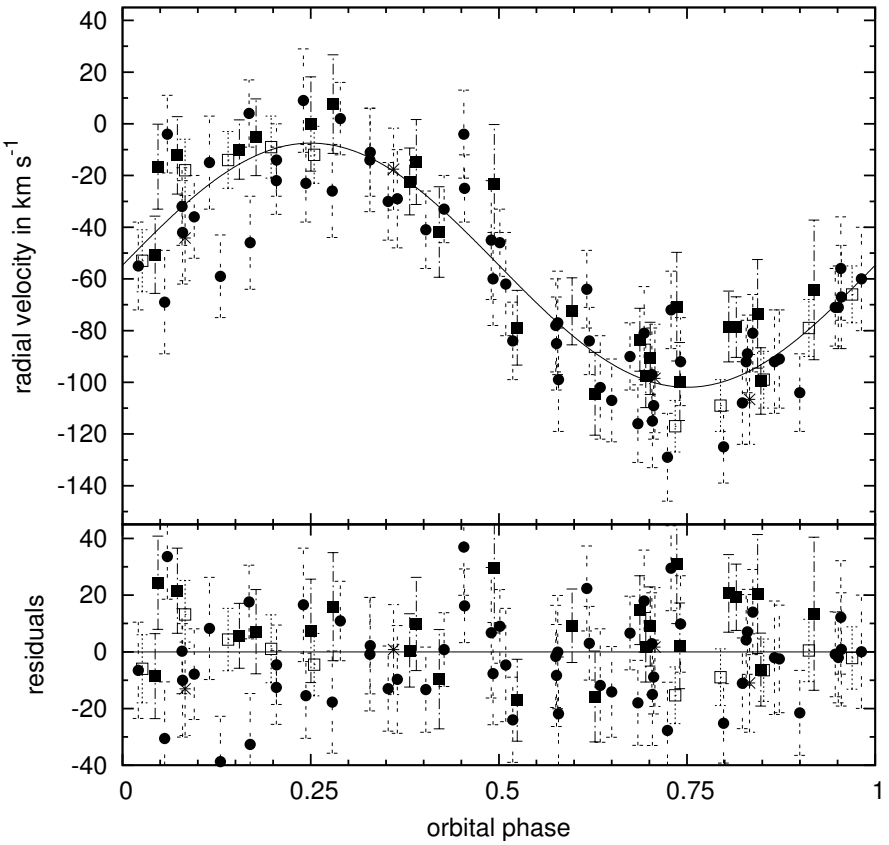

Figure 7.10.: Radial velocity plotted against orbital phase of J1622. The radial velocity was determined from the SDSS, ISIS, TWIN, and ESI spectra. All spectra were fitted together. The stars mark the SDSS spectra, the dots the TWIN spectra, the filled squares the ISIS spectra, and the open squares the ESI spectra. The errors are formal 1-σ uncertainties. The lower panel shows the residuals.

Those systems cluster in a distinct region of the $T_{\rm eff} - \log g$ diagram. Unlike the HW Vir stars, other sdB binaries are distributed more or less uniformly across the extreme horizontal branch (see Fig. 7.13). In this respect, J1622 turns out to be a typical HW Vir system.
Due to their higher resolution, the ESI spectra are suitable to measure the rotational broadening of spectral lines of the sdB. We co-added all 10 spectra and determined the projected rotational velocity of the sdB primary by adding a rotational profile to the fit of the Balmer and helium lines. The other atmospheric parameters were kept fixed to the values determined from the TWIN spectra. The best fit for $v_{\rm rot} \sin i = 71 \pm 7\,{\rm km\,s^{-1}}$ is displayed in Fig. 7.14. Surprisingly, the projected rotational velocity is only about two thirds of the one expected for tidally locked rotation of the hot subdwarf primary. This issue is further discussed in Sect. 7.4.5.

7.4.3. Photometric analysis

The BUSCA lightcurves clearly show a strong reflection effect and grazing eclipses, as can be seen in Fig. 7.9. Unfortunately, the signal-to-noise of the U_B and I_B lightcurves is insufficient, so that only the B_B and R_B lightcurves were used for the analysis. The ephemeris was determined from the BUSCA lightcurves by fitting parabolas to the cores of the primary eclipses. The period was derived with the help of the Lomb-Scargle Algorithm (Press & Rybicki 1989).
The ephemeris of the primary minimum is given by
HJD = 2455359.58306(2) + 0.0697885(53) · E

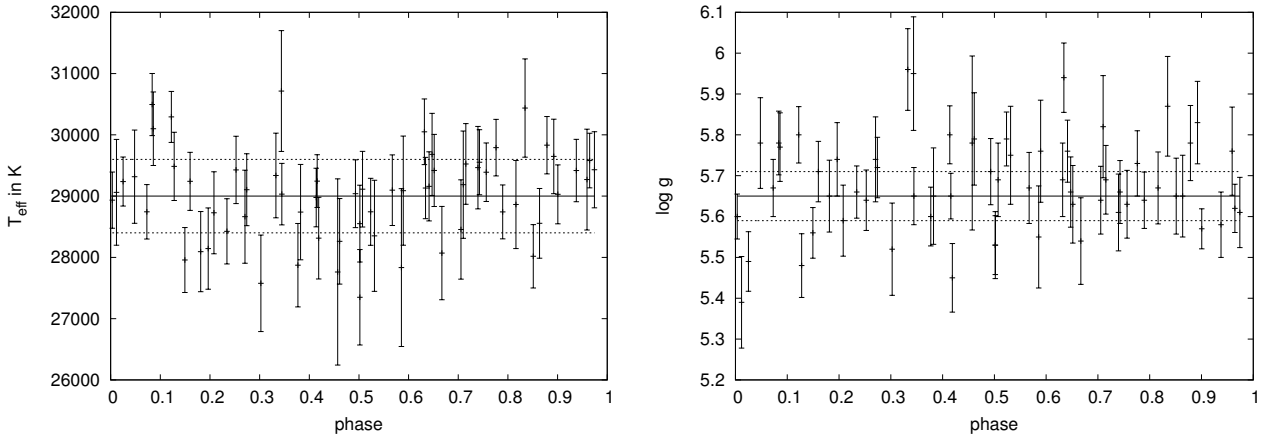

Figure 7.11.: Effective temperature and surface gravity plotted over the phase of J1622. $T_{\rm eff}$ and $\log g$ were determined from the TWIN spectra. The errors are statistical 1-σ errors. The lines represent the parameters from the co-added spectrum with the errors.

(thereby E is the eclipse number, see Drechsel et al. 2001).

The phased lightcurves are shown in Fig. 7.9 . The lightcurve analysis was performed by using MORO (MOdified ROche Program, see Drechsel et al. 1995), which calculates synthetic lightcurves, which were fitted to the observation. This lightcurve solution code is based on the Wilson-Devinney approach (Wilson & Devinney 1971) but uses a modified Roche model that considers the radiative pressure of hot binaries. More details of the analysis method are described by (Schaffenroth et al. 2013) and Chapter 6.

The main problem of the lightcurve analysis is the large number of parameters. To calculate the synthetic lightcurves, 12+5n (n is the number of lightcurves) parameters that are not independent are used. Therefore, strong degeneracies exist, in particular in the mass ratio, which is strongly correlated with the other parameters. The mass ratio is, therefore, fixed, and solutions for different mass ratios are calculated. To resolve this degeneracy, it is, moreover, important to constrain as many parameters as possible from the spectroscopic analysis or theory.

From the spectroscopic analysis, we derived the effective temperature and the surface gravity of the sdB primary. Due to the early spectral type of the primary star, the gravity darkening exponent can be fixed at $g_1 = 1$, as expected for radiative outer envelopes (von Zeipel 1924). For the cool convective companion, g_2 was set to 0.32 (Lucy 1967). The linear limb darkening coefficients were extrapolated from the table of Claret & Bloemen (2011).

To determine the quality of the lightcurve fit, the sum of the deviations from each point to the synthetic curve is calculated, and the solution with the smallest sum is supposed to be the best solution. The difference between the solutions for the different mass ratios is unfortunately small, as expected. Therefore, we cannot determine a unique solution from the lightcurve analysis alone and adopted the solution closest to the canonical mass for the sdB star. The corresponding results of the lightcurve analysis are given in Table 7.4 with errors determined by the bootstrapping method. The lightcurves in the B_B and R_B band are displayed in Fig. 7.9 with the best-fit models for these parameters. The apparent asymmetries of the observed lightcurve can not be modelled, but we are not sure if this effect is real or is due to uncorrected long-term trends in the photometry (see Sect. 7.4.1). The parameters of the system resulting from the adopted solution with the mass function are summarised in Table 7.5. The uncertainties result from error propagation of the errors of K, P, and i.

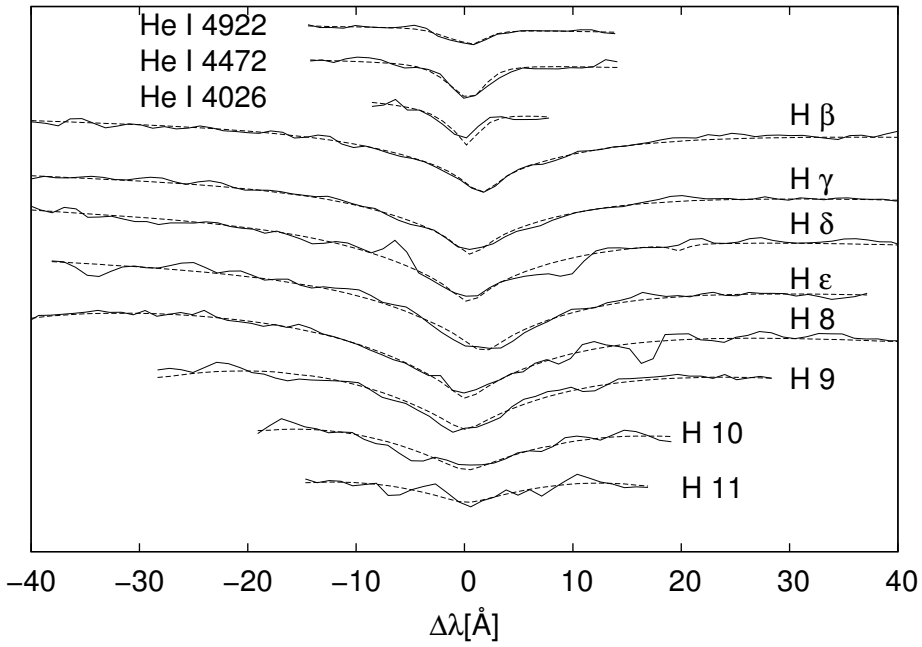

Figure 7.12.: Fit of the Balmer and helium lines in the co-added TWIN spectrum. The solid line shows the measurement, and the dashed line shows the best fitting synthetic spectrum.

7.4.4. The brown dwarf nature of the companion

From the semi-amplitude of the radial velocity curve and the orbital period, we can derive the masses and the radii of both components for each mass ratio. To constrain the solutions further, we first compared the photometric surface gravity, which can be derived from the mass and the radius, to the spectroscopic surface gravity. This is displayed in Fig. 7.15. The spectroscopic surface gravity is consistent with the lightcurve solution for sdB masses from 0.25 to 0.6 $M_{\odot}$. It is, therefore, possible to find a self-consistent solution. This is not at all a matter of course, because gravity derived from photometry was found to be inconsistent with the spectroscopic result in other cases, such as AA Dor (Vučković et al. 2008).

We also compared the radius of the companion to theoretical mass-radius relations for low-mass stars and brown dwarfs with ages of 1, 5, and 10 Gyrs, respectively (Baraffe et al. 2003). As can be seen from Fig. 7.16, the measured mass-radius relation is well matched by theoretical predictions for stars $\gtrsim$ 3 Gyrs for companion masses between 0.055 $M_{\odot}$ and 0.075 $M_{\odot}$. The corresponding mass range for the sdB star is from 0.39 $M_{\odot}$ to 0.63 $M_{\odot}$, which is calculated from the mass ratio.

However, the companion is exposed to intense radiation of a luminous hot star that is only 0.58 $R_{\odot}$ away, which could lead to an underestimate of the radius, if compared to non-irradiated models (Baraffe et al. 2003). Such inflation effects have been found in the case of hot Jupiter exoplanets (e.g. Udalski et al. 2008) but also in the MS+BD binary CoRoT-15b (Bouchy et al. 2011). We can estimate the maximum inflation effect from theoretical mass-radius relations shown in Fig. 7.16. As can be seen from Fig. 7.16, inflation by more than 10% can be excluded because none of the theoretical mass-radius relations otherwise would match the measured one, even if the star was as old as 10 Gyrs (the age of the Galactic disk).

If we assume an inflation of 5-10%, the mass-radius relation for the companion would be in perfect agreement with the light curve solution for a companion with a mass of 0.064 $M_{\odot}$ and a radius of 0.085 $R_{\odot}$, and an age of $\sim$ 5-10 Gyrs. The corresponding mass of the sdB is close to the canonical sdB mass, which we therefore adopt for the sdB throughout the following discussion. As we calculated solutions for discrete q and, hence, discrete masses for the sdB and

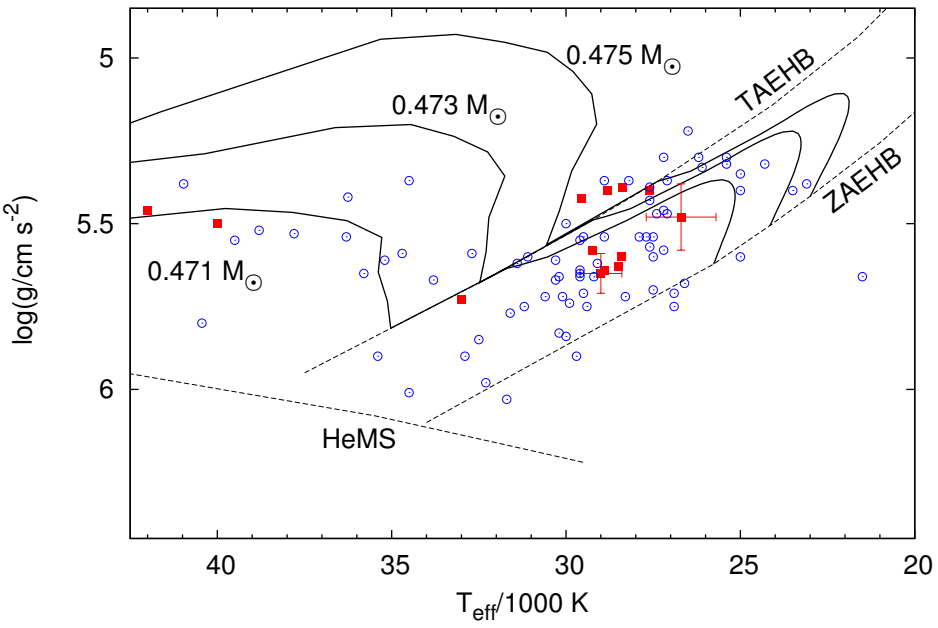

Figure 7.13.: $T_{\rm eff} - \log g$ diagram of the HW Vir systems. The solid lines are evolutionary tracks by Dorman et al. (1993) for an sdB mass of 0.471, 0.473, and 0.475 $M_\odot$. The positions of J1622 and J0820 are indicated with crosses. The other squares mark the position of other HW Vir-like systems (Van Grootel et al. 2013; Drechsel et al. 2001; For et al. 2010; Geier et al. 2011c; Maxted et al. 2002; Klepp & Rauch 2011; Østensen et al. 2008, 2010; Wood & Saffer 1999; Almeida et al. 2012; Barlow et al. 2013). The open dots represent other sdB binaries from the literature.

the companion, we adopted the solution closest to the canonical mass, which is also marked in Fig. 7.16.

7.4.5. Synchronisation

Most HW Vir systems have orbital separations as small as one solar radius. Hence, it is reasonable to expect that the rotation of both components is tidally locked to the orbit. Indeed the rotation rates of HW Vir and other objects of the class with similarly short periods (0.1d) are found to be synchronised. It is worthwhile to note that the system PG 1017−036, a reflection-effect binary with almost the same parameters as J1622 ($P = 0.072\,\mathrm{d}$, $K = 51\,\mathrm{km\,s^{-1}}$, $T_{\rm eff} = 30300\,\mathrm{K}$, $\log g = 5.61$), has a measured $\mathrm{v_{rot}\sin i} = 118\,\mathrm{km\,s^{-1}}$ (Maxted et al. 2002), which is fully consistent with synchronised rotation. However, J1622 ($P = 0.0698\,\mathrm{d}$, $K = 47\,\mathrm{km\,s^{-1}}$, $T_{\rm eff} = 29000\,\mathrm{K}$, $\log g = 5.65$) rotates with $\mathrm{v_{rot}\sin i} = 71\,\mathrm{km\,s^{-1}}$. With an inclination of 72.33°, this results in a rotational velocity of $74\,\mathrm{km\,s^{-1}}$, which is only about two thirds of the rotational velocity expected for a synchronous rotation ($P_{\rm orbit} = P_{\rm rot} = \frac{2\pi R}{v_{\rm rot}}$).
The physical processes leading to synchronisation are not well understood in particular for stars with radiative envelopes, such as sdB stars and rivalling theories (Zahn 1977; Tassoul & Tassoul 1992)0.4 predict very different synchronisation timescales (for details see Geier et al. 2010). The synchronisation timescales increase strongly with orbital separation, hence with the orbital period of the system. Actually the objects J1622 and PG 1017−036 have the shortest periods and the highest probability for tidally locked rotation amongst all known HW Vir systems. Therefore, it is surprising that J1622 apparently is not synchronised, while PG 1017−036 is. Calculations in the case of the less efficient mechanism (Zahn 1977) predict that the synchronisation should be established after 10^5 yr, a time span much shorter than the EHB lifetime

Table 7.4.: Adopted lightcurve solution.

Fixed parameters:		
$q\,(=M_2/M_1)$		0.1325
$T_{\rm eff}(1)$	[K]	29000
g_1^b		1.0
g_2^b		0.32
$x_1(B\_B)^c$		0.25
$x_1(R\_B)^c$		0.20
δ_2^d		0.0
Adjusted parameters:		
i	[°]	72.33 ± 1.11
$T_{\rm eff}(2)$	[K]	2500 ± 900
A_1^a		1.0 ± 0.03
A_2^a		0.9 ± 0.2
Ω_1^f		3.646 ± 0.17
Ω_2^f		2.359 ± 0.054
$\frac{L_1}{L_1+L_2}(B_B)^g$		0.99996 ± 0.00077
$\frac{L_1}{L_1+L_2}(B_R)^g$		0.99984 ± 0.00247
δ_1		0.001 ± 0.003
$x_2(B_B)$		1.0 ± 0.005
$x_2(R_B)$		1.0 ± 0.005
$l_3(B_B)^f$		0.0
$l_3(R_B)^f$		0.045 ± 0.008
Roche radii^h:		
r_1(pole)	[a]	0.284 ± 0.013
r_1(point)	[a]	0.290 ± 0.015
r_1(side)	[a]	0.290 ± 0.014
r_1(back)	[a]	0.290 ± 0.014
r_2(pole)	[a]	0.142 ± 0.009
r_2(point)	[a]	0.150 ± 0.011
r_2(side)	[a]	0.144 ± 0.009
r_2(back)	[a]	0.149 ± 0.011

[a] Bolometric albedo
[b] Gravitational darkening exponent
[c] Linear limb darkening coefficient; taken from Claret & Bloemen (2011)
[d] Radiation pressure parameter, see Drechsel et al. (1995)
[e] Fraction of third light at maximum
[f] Roche potentials
[g] Relative luminosity; L_2 is not independently adjusted, but recomputed from r_2 and $T_{\rm eff}(2)$
[h] Fractional Roche radii in units of separation of mass centres

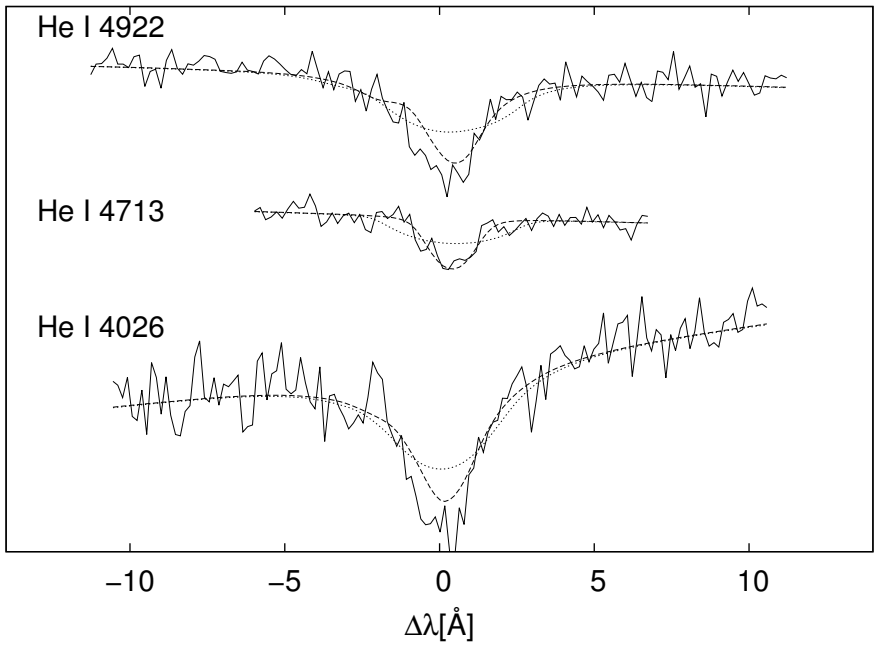

Figure 7.14.: Fit of the helium lines in the co-added ESI spectrum. The solid line shows the measurement and the dashed line shows the best fitting synthetic spectrum. The dotted line shows the line-broadening, if we assume synchronisation.

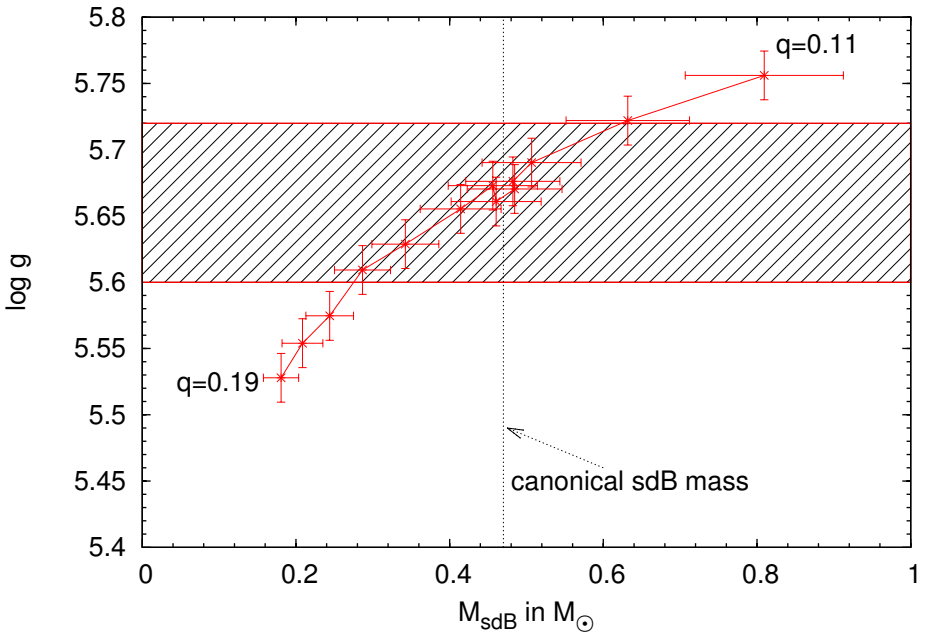

Figure 7.15.: Comparison of the photometric and spectroscopic surface gravity for the solutions with different mass ratio $q = 0.11-0.19$ (marked by the error cross). The spectroscopic surface gravity with uncertainty is given by the shaded area.

of 10^8 yr.

Evidence for a non-synchronous rotation of sdB stars in reflection-effect binaries was presented recently by Pablo et al. (2011, 2012), who measured the rotational splittings of pulsation modes in three reflection-effect sdB binaries observed by the Kepler space mission, which reveals that the subdwarf primaries rotate more slowly than synchronised.

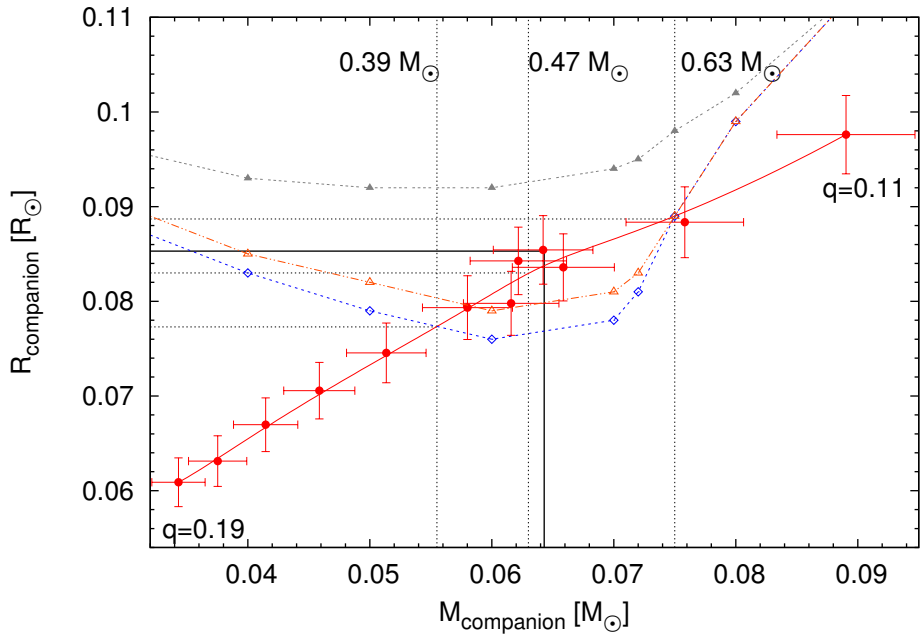

Figure 7.16.: Comparison of theoretical mass-radius relations of brown dwarfs by Baraffe et al. (2003) for an age of 1 Gyr (filled triangles), 5 Gyrs (triangles) and 10 Gyrs (diamond) to results from the lightcure analysis. Each error cross represents a solution from the lightcurve analysis for a different mass ratio ($q = 0.11 - 0.19$). The dashed vertical lines mark different values of the corresponding sdB masses. The solid lines mark the solution closest to the canonical mass for the sdB star of 0.47 $M_\odot$ that was adopted.

Table 7.5.: Parameters of J1622.

SDSS J162256.66+473051.1		
i	°	72.33 ± 1.11
$M_{\rm sdB}$	$[M_\odot]$	0.48 ± 0.03
$M_{\rm comp}$	$[M_\odot]$	0.064 ± 0.004
a	$[R_\odot]$	0.58 ± 0.02
$R_{\rm sdB}$	$[R_\odot]$	0.168 ± 0.007
$R_{\rm comp}$	$[R_\odot]$	0.085 ± 0.004
$\log g$(sdB, phot)		5.67 ± 0.02
$\log g$(sdB, spec)		5.65 ± 0.06

However, those binaries have rather long periods (~ 0.5 d), and predicted synchronisation time scales are much longer than for J1622 and even exceed the EHB life time if the least efficient synchronisation process (see Fig. 19 in Geier et al. 2010) is adopted. Hence, unlike for J1622, the non-synchronisation of those systems is not in contradiction to synchronisation theory.

It is quite unlikely that J1622 is too young for its rotation to be tidally locked to the orbit. Hence, we need to look for an alternative explanation. Tidal forces leading to circularisation and synchronisation may lead to stable configurations, in which the rotational and the orbital periods are in resonance; that is, their ratio is that of integer numbers as observed for Mercury. Comparing the observed rotational period of J1622 to the orbital one, we find that the ratio is 0.607 ± 0.065, hence close to a 2 to 3 resonance. However, J1622 must have undergone a spiral-in phase through the common-envelope phase and it must be investigated, whether such a resonant configuration can persist through that dynamical phase.

7.4.6. Conclusions

We performed a spectroscopic and photometric analysis of the eclipsing hot subdwarf binary J1622, which was found in the course of the MUCHFUSS project. The atmospheric parameters of the primary are typical for an sdB star in a HW Vir system. Mass-radius relations were derived for both components. The mass of the sdB star is constrained from spectroscopy (surface gravity) to 0.28 $M_\odot$ to 0.64 $M_\odot$. The mass of the companion can be constrained by theoretical mass-radius relations to lie between 0.055 $M_\odot$ and 0.075 $M_\odot$, which implies that the sdB mass is between 0.39 $M_\odot$ and 0.63 $M_\odot$.
Assuming small corrections of about 5-10% to the radius due to the inflation of the companion by the strong irradiation from the primary, a companion mass of 0.064 $M_\odot$ appears to be the most plausible choice that results in a mass of the sdB close to the canonical mass of $0.47 M_\odot$. Accordingly, the companion is a substellar object. This is the second time that a brown dwarf is found as a close companion to an sdB star. The object J1622 provides further evidence that substellar objects are able to eject a common envelope and form an sdB star. Finding more of these systems, helps to constrain theoretical models (Soker 1998; Nelemans & Tauris 1998).
An important result of the spectral analysis is that the sdB star is rotating slower than expected, if its rotation was locked to its orbit, as observed for the very similar system PG 1017−036. The non-synchronous rotation of J1622 is in contradiction to the predictions of tidal interaction models unless the sdB star is very young. The ratio of the rotational to the orbital period is close to a resonance of 2 to 3. However, it has to be investigated further, if such a configuration can survive the common envelope phase.
Future investigations should aim at the detection of spectral lines from the secondary to measure its radial velocity, which turns the system into an double-lined spectroscopic binary that would allow to pin down the mass ratio. Emission lines of the companion's irradiated atmosphere have been detected in the sdOB system AA Dor (Vučković et al. 2008) and also for the prototype HW Vir (Vučković et al. 2014) most recently. Since J1622 is quite compact and the irradiation of the companion strong, such emission lines might be detectable in high-resolution spectra of sufficient quality. Accurate photometry is needed to confirm or disprove any asymmetries in its lightcurve, which hints at flows at the surface of the companion.

Table 7.6.: Radial velocities with errors of J1622.

SDSS		
HJD	RV in $km\,s^{-1}$	
2452378.381481	-107	17
2452378.398900	-44	16
2452378.418200	-18	16
2452378.442390	-99	21
WHT		
2455039.90179	-64	27
2455068.90762	-10	11
2455068.92338	-22	13
2455068.94468	-84	12
2455069.85954	-79	12
2455069.92083	-98	12
2455069.93150	-100	13
2455070.85307	-12	1
2455070.86036	-5	15
2455070.86749	8	19
2455070.87733	-42	18
2455070.88454	-79	14
2455070.89174	-104	16
2455071.93491	-73	13
2455071.94215	-91	14
2455071.94942	-78	14
2455071.96599	-51	15
2455071.96626	-17	16
2455071.98042	0	18
2455071.99018	-15	16
2455071.99739	-23	23
2455072.01429	-71	21
2455072.01457	-100	15
2455072.02178	-74	21
TWIN		
2456073.37085	26	20
2456073.33931	-4	13
2456073.38513	-62	20
2456073.39285	-84	13
2456073.40042	-72	15
2456073.40799	-81	15
2456073.41591	-71	16
2456073.42347	-4	15
2456073.43104	4	13
2456073.43950	2	14
2456073.44741	-41	15
2456073.45546	-84	15
2456073.45951	-85	18
2456073.46356	-102	20
2456073.46762	-81	18
2456074.37223	-90	13
2456074.37296	-116	15
2456074.38264	-108	16
2456074.38795	-104	15
2456074.39366	-60	20
2456074.39883	-69	20
2456074.40400	-59	16
2456074.40918	-14	14
2456074.41435	-26	18
2456074.41952	-30	15
2456074.42470	-33	13
2456074.42987	-46	13
2456074.43504	-78	18
2456074.44022	-107	16
2456074.44539	-129	17
2456074.45057	-125	14
2456074.45574	-91	19
2456074.46091	-71	15
2456074.46607	-55	17
2456074.47125	-36	16
2456074.47643	-46	18
2456074.48159	-23	15
2456075.47452	-60	18
2456075.48320	-64	15
2456075.49189	-92	17
2456075.50058	-92	20
2456075.51796	-15	18
2456075.52665	9	20
2456075.53535	-29	19
2456075.54404	-45	23
2456076.53468	-109	13
2456076.54337	-89	15
2456076.55206	-67	20
2456076.56075	-42	20
2456076.56944	-22	13
2456076.57813	-11	17
2456077.35340	-25	13
2456077.36210	-99	20
2456077.37079	-115	18
2456077.37948	-92	16
2456077.52761	-56	20
2456077.53631	-32	15
2456077.55370	-14	
2456077.56240	-4	17
2456077.57110	-77	20
2456077.57980	-97	18
ESI		
2456121.76284	-117	10
2456121.76704	-109	10
2456121.77103	-99	11
2456121.77522	-79	11
2456121.77922	-66	11
2456121.78318	-53	12
2456121.78715	-18	12
2456121.79114	-14	11
2456121.79511	-9	12
2456121.79910	-12	11

7.5. Two candidate brown dwarf companions around core helium burning objects[4]

Here we report the discovery of a reflection effect, but no eclipses, in the light curves of two close sdB binaries. CPD-64°481 and PHL 457 have been reported to be close sdB binaries with small RV shifts by Edelmann et al. (2005). Furthermore, PHL 457 has been identified as long-period pulsator of V 1093 Her type (Blanchette et al. 2008). Those two sdBs are among the best studied close sdB binaries. Detailed analyses showed that both are normal sdB binaries with typical atmospheric parameters (CPD-64°481: $T_{\rm eff} = 27500 \pm 500$ K, $\log g = 5.60 \pm 0.05$ (Geier et al. 2010); PHL 457: $T_{\rm eff} = 26500 \pm 500$ K, $\log g = 5.38 \pm 0.05$, (Geier et al. 2013a)).
Geier et al. (2010) constrained the companion mass of CPD-64°481 to be as high as 0.62 $M_\odot$ by measuring the projected rotational velocity of the sdB and assuming synchronised rotation. This assumption is reasonable, as the theoretical synchronisation timescales with stellar mass companions due to tidal interactions for binaries with periods of about 0.3 d are much smaller or comparable to the lifetime of the sdB on the EHB, depending on the theory (see Geier et al. 2010). The inclination angle was predicted to be as small as 7°. Because no traces of the companion are seen in the spectrum, they concluded that the companion must be a WD, as main-sequence stars would be visible in the optical spectra, if their masses are higher than $\sim 0.45\,M_\odot$ (Lisker et al. 2005). However, the detection of the reflection effect rules out such a compact companion.
Using the same method we constrained the companion mass of PHL 457. Although the companion mass assuming synchronisation ($\sim 0.26\,M_\odot$) would still be consistent with observations, the derived inclination angle of 8° is very small and therefore unlikely.
Moreover, observational evidence, both from asteroseismic studies (Pablo et al. 2011, 2012) and spectroscopic measurements (Schaffenroth et al. 2014c), indicates that synchronisation is not generally established in sdB binaries with low-mass companions (see also the discussion in Geier et al. (2010). Therefore, the rotation of the sdBs in CPD-64°481 and PHL 457 is most likely not synchronised with their orbital motion and the method described in Geier et al. (2010) not applicable.

7.5.1. Time-resolved spectroscopy and orbital parameters

In total, 45 spectra were taken with the FEROS spectrograph ($R \simeq 48000, \lambda = 3800 - 9200$ Å) mounted at the ESO/MPG-2.2m telescope for studies of sdB stars at high resolution (Edelmann et al. 2005; Geier et al. 2010; Classen et al. 2011). The spectra were reduced with the FEROS pipeline available in the `MIDAS` package. The FEROS pipeline, moreover, performs the barycentric correction.
To measure the RVs with high accuracy, we chose a set of sharp, unblended metal lines situated between 3600 Å and 6600 Å. Accurate rest wavelengths were taken from the NIST database. Gaussian and Lorentzian profiles were fitted using the SPAS (Hirsch Hirsch (2009)) and FITSB2 routines (Napiwotzki et al. 2004b, for details see Classen et al. (2011)). To check the wavelength calibration for systematic errors we used telluric features as well as night-sky emission lines. The FEROS instrument turned out to be very stable. Usually corrections of less than 0.5 km s^{-1} had to be applied. The RVs and formal 1σ-errors are given in Table 7.8 and 7.9.
The orbital parameters and associated false-alarm probabilities are determined as described by Geier et al. (2011b). In order to estimate the significance of the orbital solutions and the contributions of systematic effects to the error budget, we normalised the χ^2 of the most probable solution by adding systematic errors $e_{\rm norm}$ in quadrature until the reduced χ^2 reached $\simeq 1.0$. The hypothesis that both orbital periods are correct can be accepted with a high degree of

[4]This chapter is based on Schaffenroth et al. (2014a)

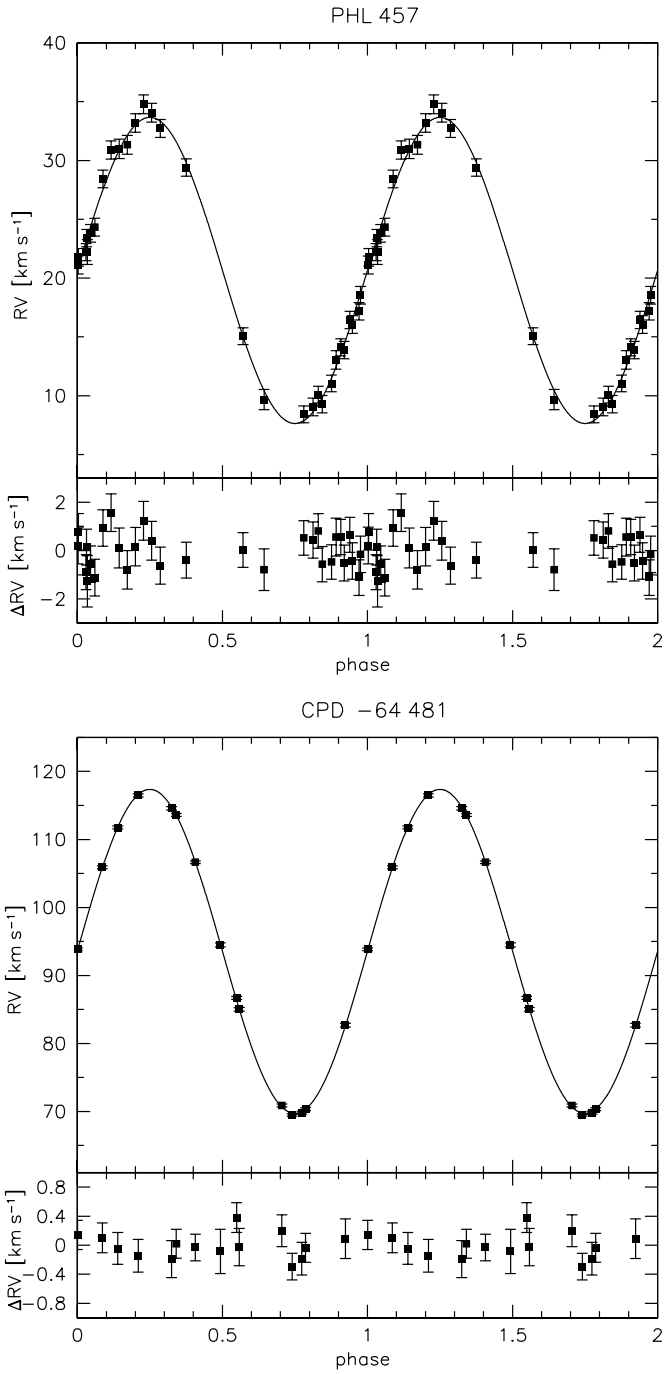

Figure 7.17.: Radial velocity plotted against orbital phase. The RV data were phase folded with the most likely orbital periods. The residuals are plotted below.

confidence. The phased RV curves for the best solutions are of excellent quality (see Fig. 7.17). The derived orbital parameters are given in Table 7.7 and the orbital solution for CPD-64°481 is perfectly consistent with the result presented in Edelmann et al. (2005).

7.5.2. Photometry

Time-resolved differential photometry in BVR-filters for CPD-64°481 and VR filters for PHL 457 was obtained with the SAAO STE4 CCD on the 1.0m telescope at the Sutherland site of the South African Astronomical Observatory (SAAO). Photometric reductions were performed us-

Table 7.7.: Derived orbital solutions, mass functions and minimum companion masses

Object	T_0^a $[-2\,450\,000]$	P[a] [d]	γ^a $[\mathrm{km\,s^{-1}}]$	K[a] $[\mathrm{km\,s^{-1}}]$	e_{norm} $[\mathrm{km\,s^{-1}}]$	$f(M)$ $[M_\odot]$	M_2^b $[M_\odot]$	i^c_{max} °
CPD-64°481	3431.5796 ± 0.0002	$0.27726315 \pm 0.00000008$	93.54 ± 0.06	23.81 ± 0.08	0.16	0.0004	> 0.048	70
PHL 457	5501.5961 ± 0.0009	0.3131 ± 0.0002	20.7 ± 0.2	13.0 ± 0.2	0.7	0.00007	> 0.027	75

[a] The systematic error adopted to normalise the reduced χ^2 (e_{norm}) is given for each case.

[b] The minimum companion masses take into account the highest possible inclination.

[c] $i = 90$ is defined as an edge-on orbit

Table 7.8.: CPD-64°481: All spectra were acquired with the FEROS instrument

mid−HJD $-2\,450\,000$	RV $[\mathrm{km\,s^{-1}}]$
3249.89041	70.87 ± 0.15
3250.89408	114.58 ± 0.20
3251.85033	69.81 ± 0.16
3252.88158	94.51 ± 0.26
3252.89956	85.03 ± 0.20
3253.83281	82.69 ± 0.22
3253.87777	105.90 ± 0.13
3253.91205	116.47 ± 0.16
3425.51834	111.76 ± 0.15
3426.51685	69.48 ± 0.09
3427.53343	106.65 ± 0.09
3428.52983	93.84 ± 0.12
3429.51370	86.71 ± 0.13
3430.56510	113.59 ± 0.12
3431.52045	70.33 ± 0.12

ing an automated version of DOPHOT (Schechter et al. 1993).
The differential light curves have been phased to the orbital periods derived from the RV-curves and binned to achieve higher S/N. The light curves show sinusoidal variations (~ 10 mmag) with orbital phase characteristic for a reflection effect (Fig. 7.18). It originates from the irradiation of a cool companion by the hot subdwarf primary. The projected area of the companion's heated hemisphere changes while it orbits the primary. Compared to other reflection effect binaries the amplitude of the reflection effect in both systems is quite small. The amplitude of the reflection effect depends mostly on the separation of the system, the effective temperature of the subdwarf, and the visible irradiated area of the companion. Seen edge-on, the relative change of this area is the highest. However, for small inclinations the derived mass of the companion becomes higher and because there is a strong correlation between mass and radius on the lower main sequence (see Fig. 7.19), the radius of the companion and the absolute irradiated area becomes larger as well. Due to this degeneracy it is therefore not straight forward to claim that small reflection effects can simply be explained by small inclination angles.
We fitted models calculated with MORO, which is based on the Wilson-Devinney code (MOdified ROche model, Drechsel et al. (1995)), to the light curves as described in (Schaffenroth et al. 2013). As no eclipses are present, the inclination is difficult to determine and we fitted light curve solutions for different fixed inclinations. The mass ratio, which can be calculated from the mass function for different inclinations, was also kept fixed, so that the mass of the sdB

Table 7.9.: PHL 457: All spectra were acquired with the FEROS instrument

mid−HJD −2 450 000	RV [km s^{-1}]
3249.64149	10.1 ± 0.2
3250.64322	22.2 ± 0.2
3251.58746	23.8 ± 0.3
3253.56948	29.4 ± 0.3
5500.52235	15.1 ± 0.2
5500.54504	9.7 ± 0.5
5501.52731	8.4 ± 0.2
5501.53727	9.1 ± 0.3
5501.54722	9.3 ± 0.2
5501.55718	11.0 ± 0.1
5501.56712	14.1 ± 0.2
5501.57705	16.4 ± 0.2
5501.58698	17.2 ± 0.2
5501.59692	21.1 ± 0.3
5501.60685	22.2 ± 0.8
5502.50148	13.0 ± 0.4
5502.51028	13.9 ± 0.2
5502.51908	16.1 ± 0.3
5502.52785	18.5 ± 0.3
5502.53663	21.8 ± 0.3
5502.54542	23.4 ± 0.3
5502.55420	24.3 ± 0.3
5502.56298	28.4 ± 0.3
5502.57175	30.9 ± 0.3
5502.58053	31.0 ± 0.4
5502.58932	31.3 ± 0.4
5502.59811	33.2 ± 0.4
5502.60688	34.8 ± 0.4
5502.61566	34.1 ± 0.4
5502.62502	32.7 ± 0.3

is equal to the canonical sdB mass $M_{\rm sdB} = 0.47\,{\rm M}_\odot$ (see Fontaine et al. 2012, and references therein). Shape and amplitude of the variation mostly depends on the orbital inclination and the mass ratio, but also on the radius ratio of both components and the unknown albedo of the companion. Due to this high number of parameters, that are not independent from each other, we cannot find a unique solution.

Selecting only solutions for which the photometric radius is consistent with the spectroscopic radius derived from the surface gravity, we narrow down the number of solutions. Unfortunately, due to the degeneracy between the binary inclination and the radius of the companion we find equally good solutions for each inclination (see also Østensen et al. 2013). In the case of CPD-64°481, see Fig. 7.19, the derived mass and radius of the companion are in agreement with theoretical relations by Chabrier & Baraffe (1997) for the entire range of inclinations. In the case of PHL 457 the theoretical mass-radius relation is only consistent for an inclination of 50-70°. For lower inclinations the measured radius would be larger than expected by the models. However, due to the many assumptions used in the analysis, it is difficult to estimate the significance of this result, as a smaller mass for the sdB could solve this issue.

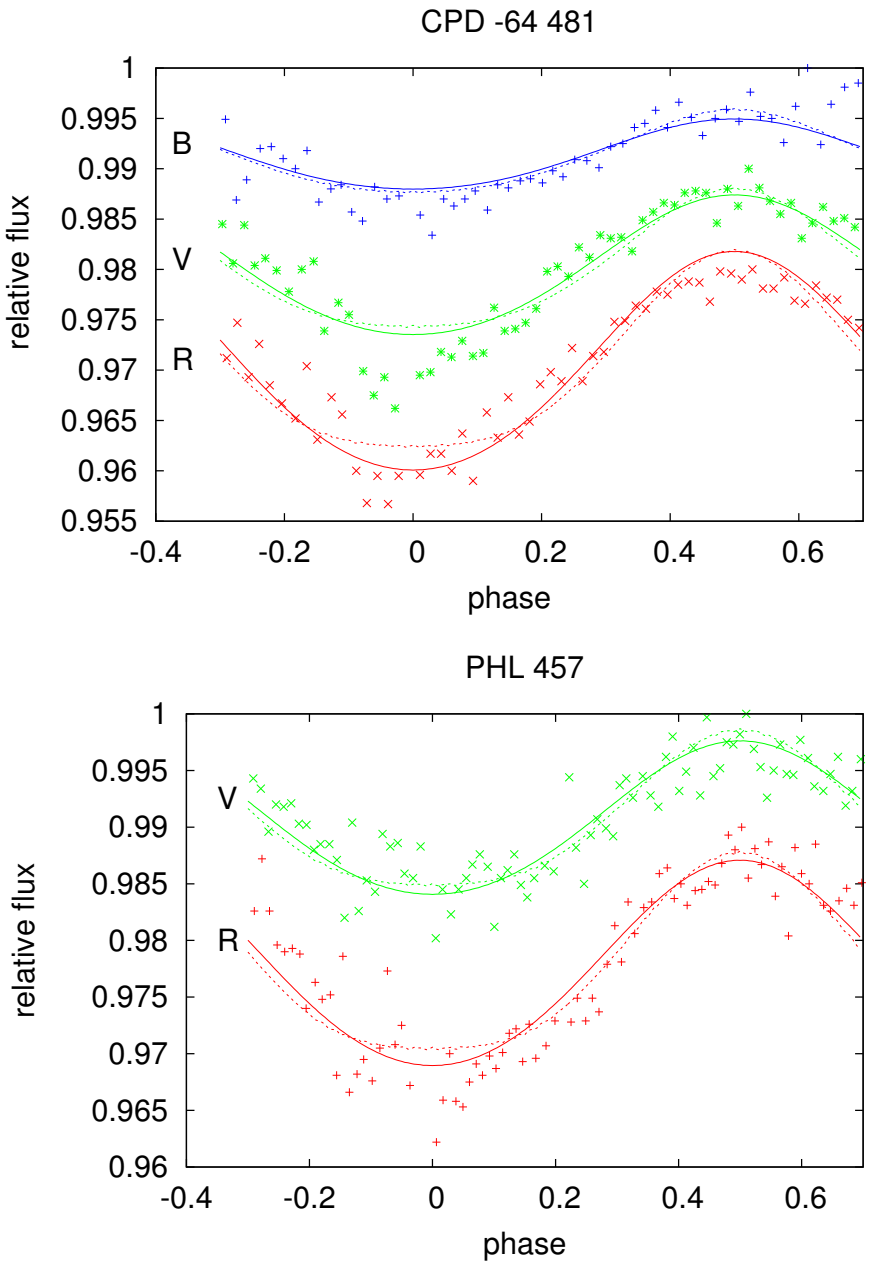

Figure 7.18.: Phased and binned light curves in B-, V- and R-bands in the case of CPD-64°481 (upper panel) and V- and R-bands in the case of PHL 457 (lower panel). Overplotted are two models for an inclination of 10° (solid) and 65° (dashed) for CPD-64°481 and 10° (solid) and 70°(dashed) for PHL 457. The lightcurve models with higher inclinations (dashed) have broader minima and shallower maxima.

In Fig. 7.18 we show model light curves for high and low inclination. Although small differences are present, a much better quality light curve is required to resolve them. The sum of the deviations between the measurements and the models are somewhat, but not significantly, smaller for low inclinations. Therefore, we cannot draw firm conclusions from our photometric data at hand.

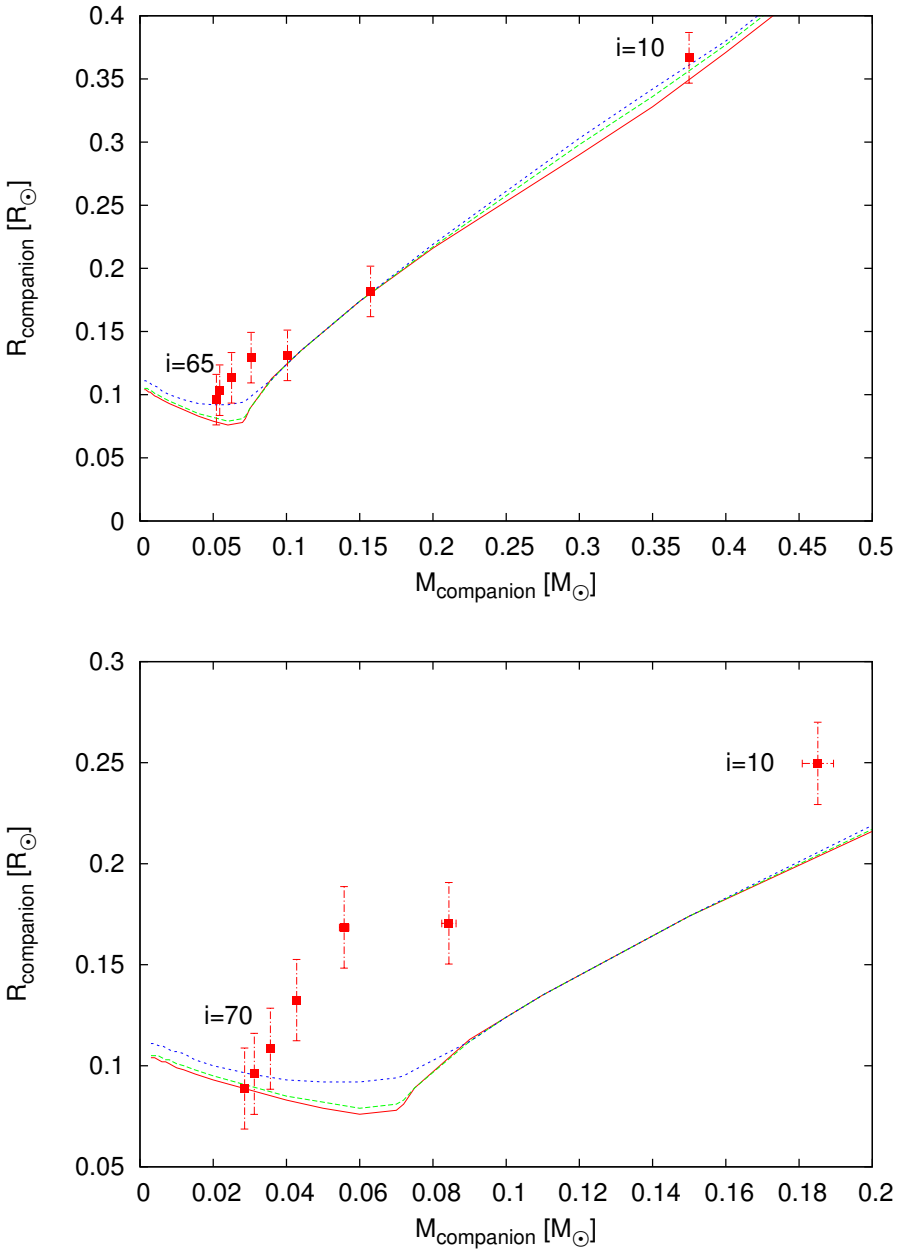

Figure 7.19.: Mass-radius relation of the companion of CPD-64°481 (upper panel) and PHL 457 (lower panel) for different inclinations (filled rectangles), compared to theoretical relations by Chabrier & Baraffe (1997) for an age of the system of 1Gyr (short dashed line), 5 Gyr (long dashed line) and 10 Gyr (solid line). For all shown solutions mass and radius of the sdB are also consistent with the spectroscopic surface gravity measurement of $\log g = 5.60 \pm 0.05$ for CPD-64°481 (Geier et al. 2010) and $\log g = 5.38 \pm 0.05$ (Geier et al. 2013a) for PHL 457.

7.5.3. Brown dwarf nature of the unseen companions

The two binaries are single-lined and their binary mass functions $f_\mathrm{m} = M^3_\mathrm{comp} \sin^3 i/(M_\mathrm{comp} + M_\mathrm{sdB})^2 = PK^3/2\pi G$ can be determined. The RV semi-amplitude and the orbital period can be derived from the RV curve, but the sdB mass M_sdB, the companion mass M_comp and the inclination angle i remain free parameters. Adopting the canonical sdB mass $M_\mathrm{sdB} = 0.47\,\mathrm{M}_\odot$ and the i_max, that can be constrained, because no eclipses are present in the lightcurve, we

derive lower limits for the companion masses (see Table 7.7).
Those minimum masses of $0.048\,M_\odot$ for CPD-64°481 and $0.027\,M_\odot$ for PHL 457 - the smallest minimum companion mass measured in any sdB binary so far - are significantly below the hydrogen-burning limit ($\sim 0.07 - 0.08\,M_\odot$, Chabrier et al. (2000)). As no features of the companion are found in the spectrum, we also derive an upper mass limit of $\sim 0.45\,M_\odot$ (Lisker et al. 2005) .
The initial sample of Edelmann et al. (2005) consisted of known, bright hot subdwarf stars. Because no additional selection criteria were applied, it can be assumed that the inclination angles of the binaries found in this survey are randomly distributed. Due to the projection effect it is much more likely to find binary systems at high rather than low inclinations. The probability, that a binary has an inclination higher than a certain angle, can be calculated as described in Gray (2005), $P_{i>i_0} = 1 - (1 - \cos i_0)$. Since the companion mass scales with the inclination angle, we can derive the probability that the mass of the companion is smaller than the hydrogen-burning limit of $\sim 0.08\,M_\odot$, which separates stars from brown dwarfs.
For CPD-64°481, the inclination angle must be higher than 38°, which translates into a probability of 79%. In the case of PHL 457, an inclination higher than 21° is required and the probability for the companion to be a brown dwarf is as high as 94%. We therefore conclude that the cool companions in those two binary systems are likely brown dwarfs.
The only chance to constrain the inclination better would be very high signal-to-noise lightcurves. Moreover, high resolution, high S/N spectra could help to constrain the mass ratio of the system. They could allow to discover emission lines from the irradiated hemisphere of the companion, as done for the sdOB+dM system AA Dor (Vučković et al. 2008). The strength of the emission lines should be independent of the inclination, depending only on the size of the companion, the separation of the system and the effective temperature of the primary. As the systems are very bright, it might be possible to find these emission lines despite the larger separation and lower effective temperature of our systems.

7.5.4. Discussion

Figure 7.20 gives an overview of the 29 sdB binaries with reflection effect and known orbital parameters (Kupfer et al. 2015). While most companions are late M-dwarfs with masses close to $\sim 0.1\,M_\odot$, there is no sharp drop below the hydrogen-burning limit. The fraction of close substellar companions is substantial. An obvious feature in Fig. 7.20 is the lack of binaries with periods shorter than $\sim 0.2\,\mathrm{d}$ and $K < 50\,\mathrm{km\,s^{-1}}$ corresponding to companion masses of less than $\sim 0.06\,M_\odot$.
This feature could not be due to selection effects. About half of the known reflection effect binaries have been found based on RV-shifts detected in time-resolved spectra. As has been shown in this work, RV-semiamplitudes of a few tens of $\mathrm{km\,s^{-1}}$ are easily measurable. Furthermore, short-period binaries are found and solved easier than long-period systems.
The other half of the sample has been discovered based on variations in their light curves. Shape and amplitude of the light curves depend mostly on the radius of the companion for similar orbital periods and separations. Since the radii of late M-dwarfs, brown dwarfs and also Jupiter-size planets are very similar ($\sim 0.1\,R_\odot$), their light curves are expected to be very similar as well.
The most likely reason for this gap is the merger or evaporation of low-mass companions either before or after the CE-ejection corresponding to a population of single sdB stars. Other recent discoveries are perfectly consistent with this scenario. Charpinet et al. (2011) reported the discovery of two Earth-sized bodies orbiting a single pulsating sdB within a few hours. These might be the remnants of a more massive companion evaporated in the CE-phase (Bear & Soker 2012). Geier et al. (2011b, 2013b)) found two fast rotating single sdBs, which might have formed in a CE-merger. Those discoveries provide further evidence that substellar companions

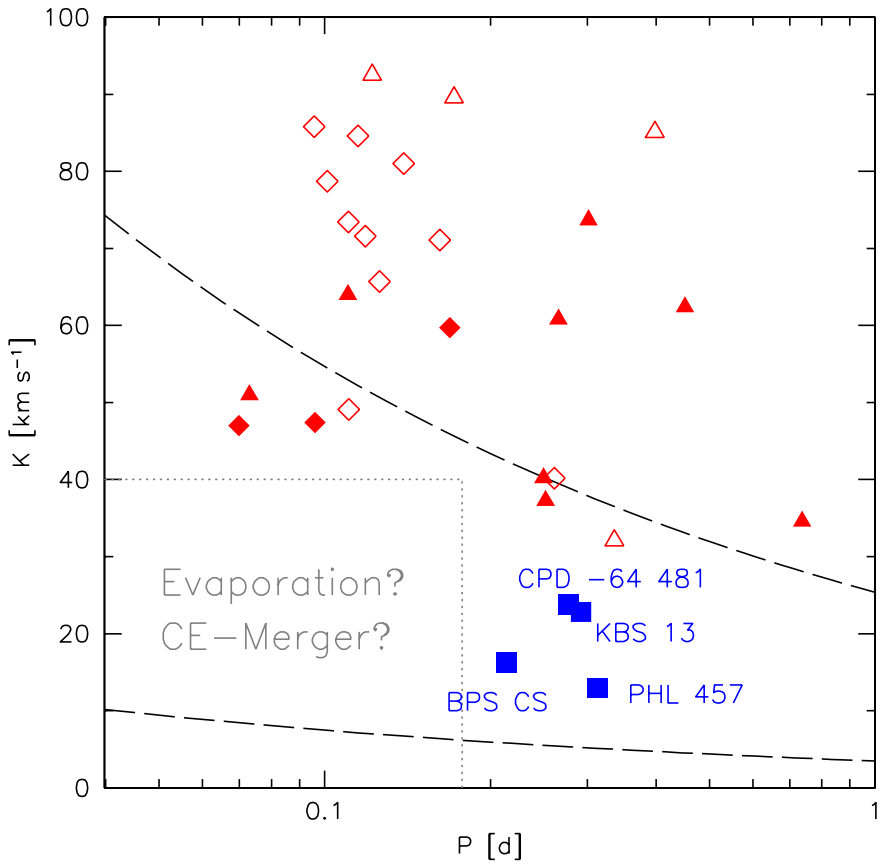

Figure 7.20.: The RV semiamplitudes of all known sdB binaries with reflection effects and spectroscopic solutions plotted against their orbital periods (Kupfer et al. 2015). Diamonds mark eclipsing sdB binaries of HW Vir type where the companion mass is well constrained, triangles systems without eclipses, where only lower limit can be derived for the companion masses. Squares mark CPD-64°481, PHL 457, KBS 13 and BPS CS 22169−0001. Open symbols mark systems that have been discovered based on photometry, filled symbols have been discovered based on spectroscopy. The dashed lines mark the regions to the right where the minimum companion masses derived from the binary mass function (assuming 0.47 $M_\odot$ for the sdBs) exceed 0.01 $M_\odot$ (lower curve) and 0.08 $M_\odot$ (upper curve).

play an important role in the formation of close binary and likely also single sdB stars.

We therefore conclude that the lack of short period systems with small RV variations K $<$ 50 km s^{-1} is real. However, the probability that substellar companions are present in systems with longer periods ($>$ 0.2 d) is quite high. In addition to the two binaries discussed here, two more systems with similar orbital parameters and reflection effects have been found (KBS 13, For et al. (2008); BPS CS 22169−0001, Geier & Heber (2012)). Following the line of arguments outlined above, we calculate the probability for those two systems to host a stellar companion to be 9% for BPS CS 22169−0001 and 20% for KBS 13. Multiplying those numbers for all four binaries, we conclude that the probability that none of them has a substellar companions is less than 0.02%.

7.6. An eclipsing post common-envelope system consisting of a pulsating hot subdwarf B star and a brown dwarf companion[5]

Van Noord et al. (2013) reported the discovery of a promising new HW Virginis system, V2008-1753 (CV=16.8 mag), which was found during an automatic search for variable stars conducted with the 0.4 m Calvin College Robotic Telescope in Rehoboth, New Mexico. Their relatively noisy light curve showed eclipses and a strong reflection effect. Interestingly, this sdB binary has an orbital period of only 1.58 h, the shortest period ever found in an HW Virginis system. Here we present the first thorough analysis of this unique system, along with the discovery of low–amplitude pulsations in the sdB primary. Section 7.6.1 describes the observational data. The analysis is discussed in Sects. 7.6.2 (spectroscopy) and 7.6.3 (photometry). Evidence for the brown dwarf nature of the companion is discussed in Sect. 7.6.4. Finally, we end with conclusions and suggest further opportunities that are offered by this one-of-a-kind system.

7.6.1. Observations

Time–series spectroscopy

We used the Goodman Spectrograph on the 4.1–m SOuthern Astrophysical Research (SOAR) telescope to obtain time–series spectroscopy of V2008-1753 over a full orbital cycle and determine the orbital velocity of its primary sdB component. A 1.35" longslit and a 930 mm^{-1} VPH grating from Syzygy Optics, LLC, were employed to cover the spectral range 3600–5250 Å with an approximate resolution of 3.8 Å (0.84 Å per binned pixel). The position angle was set to 197.8 degrees E of N so that we could place a nearby comparison star on the slit, with the intention of characterizing and removing instrumental flexure effects. In order to maximize our duty cycle, we binned the spectral images by two in both the spatial and dispersion directions and read out only a 2071 x 550 (binned pixels) subsection of the chip. Each exposure had an integration time of 90 s, with 8 s of overhead between successive images, yielding a duty cycle of approximately 92%. Overall, we acquired 70 spectra of V2008-1753 between 23:49:20.87 UT (2013-08-31) and 01:42:07.17 UT (2013-09-01). The airmass decreased from 1.22 to 1.03 over this time period. Upon completion of the time series, we obtained several FeAr comparison lamp spectra and quartz–lamp spectra for wavelength calibration and flat–fielding.
Standard routines in IRAF, primarily *ccdproc*, were used to bias–subtract and flat–field the spectral images. Given the low thermal noise in the spectrograph system, we did not subtract any dark frames, as we wanted to avoid adding noise to the images. We used *apall* to optimally extract one–dimensional spectra and subtract a fit to the sky background for both the target and constant comparison star. Finally, we wavelength–calibrated each spectrum using the master FeAr comparison lamp spectrum taken at the end of the time–series run. The resulting individual spectra of V2008-1753 had a signal–to–noise ratio (S/N) around 15–20 $pixel^{-1}$, while the individual spectra of the comparison star (which looked to be G or K–type), had a S/N twice as high.

Time–series photometry

High–precision photometry was acquired with SOAR/Goodman through i' and g' filters on 15/16 August 2013. Although our primary goal was to model the binary light curve, our secondary goal was to look for stellar pulsations, and thus we used an instrumental setup that had both a high duty cycle and a Nyquist frequency above those of most known sdB pulsation modes. We binned the images 2 x 2 and read out only a small 410 x 540 (binned pixel) subsection of the chip that included both the target and 10 comparisons stars with the same

[5]This chapter is heavily based on Schaffenroth et al. (2015)

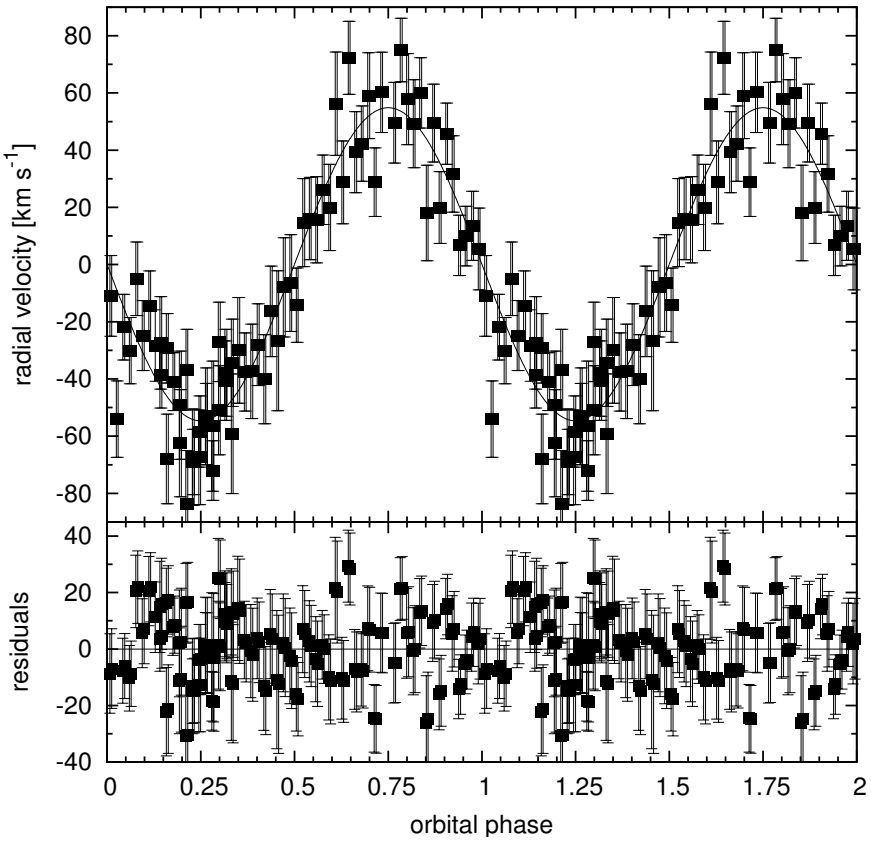

Figure 7.21.: *Top panel:* Radial velocity curve for the sdB primary in V2008-1753, plotted twice for better visualization. The solid line denotes the best–fitting circular orbit to the data. *Bottom panel:* Residuals after subtracting the best–fitting sine wave from the data.

approximate brightness level. We achieved an 87% duty cycle with 25-s exposures for the g' light curve and a 81.4% duty cycle with 14-s exposures for the i' light curve. In both cases, we observed the field for at least one full orbital cycle near an airmass of 1.1. We concluded each night with a set of bias frames and dome flats. Thermal count rates were too low to warrant the acquisition of dark frames.

All object images were bias–subtracted and flat–fielded using IRAF's *ccdproc* package. We extracted light curves with an IDL program we wrote that uses the function APER, which is based on DAOPHOT (Stetson 1987). We produced light curves over a wide range of aperture radii and selected the aperture that maximized the S/N in the light curve. To mitigate the effects of atmospheric extinction and transparency variations, we divided the light curve of V2008-1753 by the average of those of the constant comparison stars, after verifying they were indeed non–variable. Residual extinction effects are often removed in light curves of this duration by fitting and dividing the light curve by the best-fitting parabola. However, given the large-amplitude binary signals present, this process would distort the actual stellar signal, Instead, we fit straight lines through points of the same phase and, informed by these fits, removed the overall 'tilt' in each light curve. While not perfect, this process helps to mollify the effects of residual extinction variations. We then divided each light curve by its mean value and subtracted a value of one from all points to put them in terms of fractional amplitude variations.

7.6.2. Spectroscopic analysis

Radial velocity curve

Radial velocity shifts were determined by measuring the positions of the hydrogen Balmer profiles Hβ through H9; although H10, H11, and several He I lines were also present, they were too noisy to provide reliable positions. We used the MPFIT routine in IDL (Markwardt 2009), which relies on the Levenberg-Marquardt method, to fit simple inverse Gaussians to the line profiles and determine their centroids. The only available guide star near our field was significantly redder than the sdB target, and, consequently, its use led to a gradual shift in the slit alignment over the course of our observations (the Goodman spectrograph had no atmospheric dispersion corrector at the time); this drifting results in a color–dependent velocity shift. Additionally, instrumental flexure as the Nasmyth cage rotates also affected the stars' alignment on the slit, although only slightly. We removed both of these time–dependent wavelength solution effects by tracking the absorption–line features in the constant comparison star. Figure 7.21 presents the resulting radial velocity curve for V2008-1753, plotted twice for better visualization

We again used MPFIT to fit a sine wave to the data and determine the semi–amplitude of the velocity variation; the orbital period and phase were fixed during this process. We derive an orbital velocity of $K = 54.6 \pm 2.4$ km s^{-1} for the sdB primary. Eccentric orbits were also fitted to the radial velocity curve, but as we currently have no reason to prefer them over $e = 0$, we continue the analysis under the assumption that the orbit is circular. Residuals from the best–fitting sine wave are shown in the bottom panel of Figure 7.21 and are consistent with noise. The mean noise level in the Fourier transform of the residual velocity curve is 2 km s^{-1}.

Atmospheric parameters

In preparation for determining the atmospheric parameters of the sdB, we first de–shifted all individual spectra according to our orbital solution above and then co–added them to improve the overall S/N. We fit synthetic spectra, which were calculated using local thermodynamical equilibrium model atmospheres with solar metallicity and metal line blanketing (Heber et al. 2000), to the Balmer and helium lines of the co-added SOAR spectrum using SPAS (SPectral Analysis Software, Hirsch 2009). The best–fitting synthetic spectrum had the following orbital parameters:

$$\begin{aligned} T_{\rm eff} &= 32800 \pm 250 \\ \log g &= 5.83 \pm 0.04 \\ \log y &= -2.27 \pm 0.13 \end{aligned}$$

with 1-σ statistical errors determined by bootstrapping. For some sdB systems with reflection effects, an analysis of spectra with sufficiently high S/N taken at different phases shows that the atmospheric parameters apparently vary with phase (e.g. Schaffenroth et al. 2013, 2014c). These variations can be explained by the companion's contribution to the spectrum (reflection only) varying with orbital phase. Systems with similar parameters show such variations in temperature and surface gravity on the order of $1000 - 1500$ K and 0.1 dex, respectively. To account for the apparent change in the parameters we formally adopt the values determined from the co-added spectrum, which represents a mean value, with a larger error: $T_{\rm eff} = 32800 \pm 750$ K and $\log g = 5.83 \pm 0.05$ for the sdB. Figure 7.22 shows the corresponding fit of the Balmer and helium lines. We excluded Hϵ from the fit, as this line is mostly blended with the Ca II H-line and hence is less well represented by this fit.

The $T_{\rm eff} - \log g$ diagram is displayed in Fig. 7.23 and shows that V2008-1753 lies in the middle of the extreme horizontal branch. Although it was previously suggested that HW Virginis systems

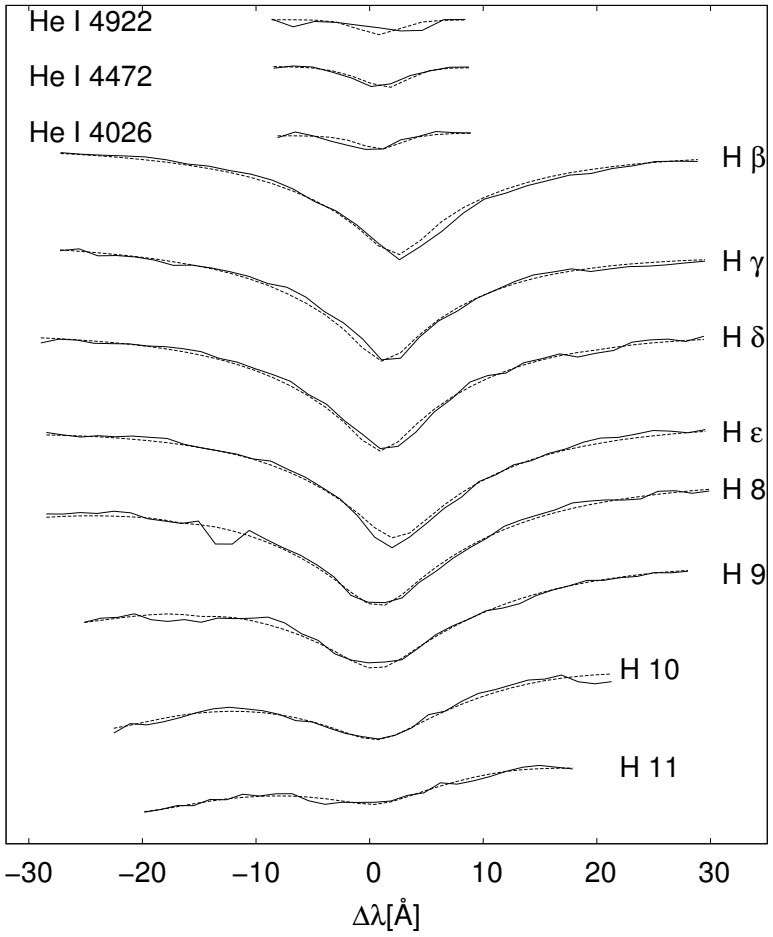

Figure 7.22.: Fit of the Balmer and helium lines in the co-added SOAR spectrum. The solid line shows the measurement, and the dashed line shows the best fitting synthetic spectrum. As the H ϵ seems to be effected by a blend of the Ca line next to it, it was excluded from the fit.

cluster together only in a small part of the $T_{\rm eff} - \log g$ diagram (Schaffenroth et al. 2014c), the position of V2008–1753 seems to go against this hypothesis. However, it is still apparent that most of the known HW Vir systems and reflection effect binaries (both sdB+dM systems with different inclinations) concentrate in a distinct region between a $T_{\rm eff}$ of 26000-30000 K and a $\log g$ of about 5.3 to 5.7, only at the edge of the instability strip. There are five exceptions of binaries with sdOB star primaries and M star companions at higher temperatures, which are possibly just more evolved. Yet, the three HW Vir systems showing short-period p-mode pulsations with amplitudes observable from the ground lie in a different part of the $T_{\rm eff} - \log g$ diagram, nearer to the He-MS, in the central part of the instability strip for sdBV$_{\rm r}$s, as expected. In contrast to that the other sdB binaries with either white dwarf secondaries or companions of unknown type do not show any clustering but are uniformly distributed over the EHB. This could indicate that the sdBs with low-mass main-sequence companions differ from the sdBs with white dwarf companions.

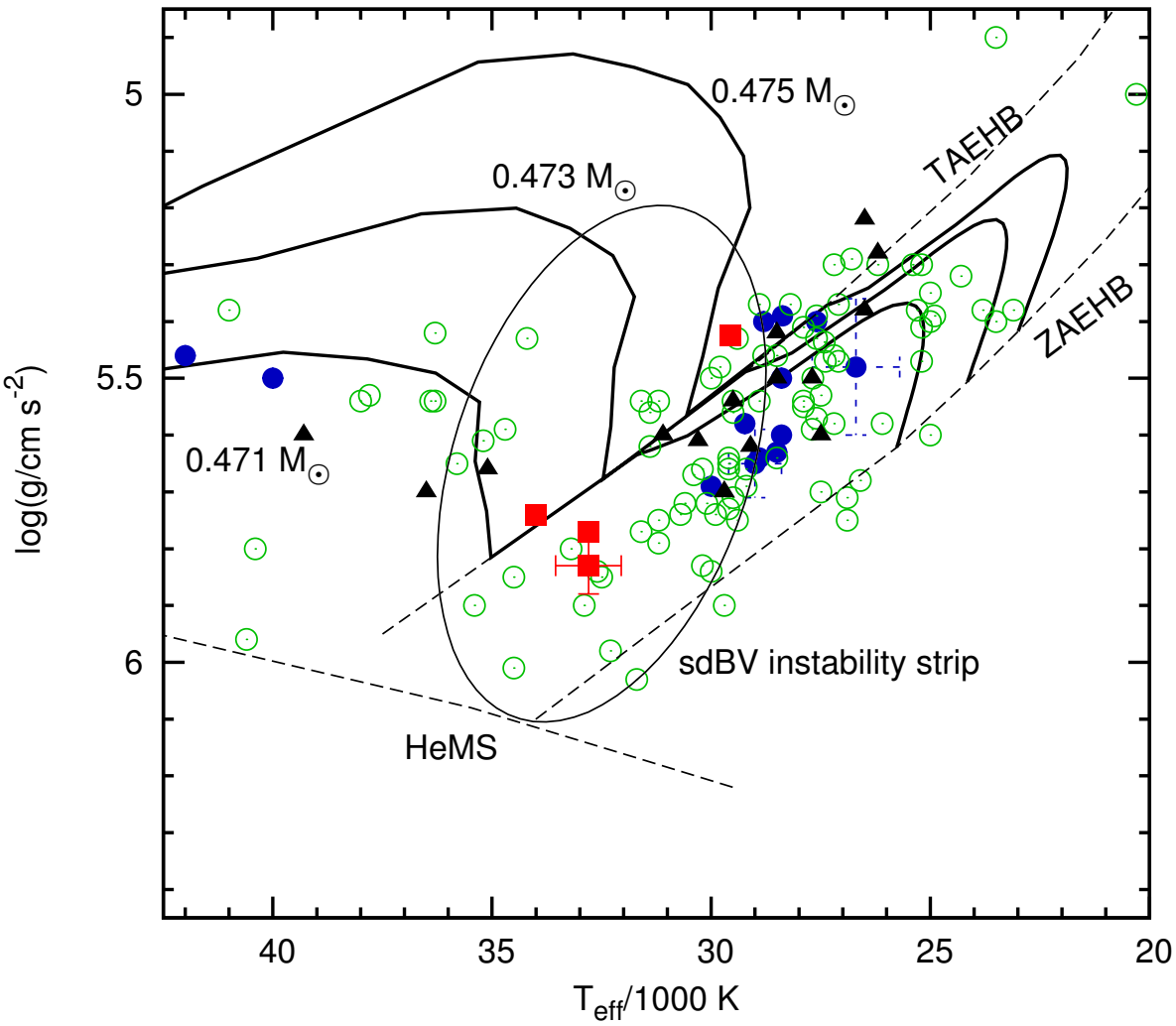

Figure 7.23.: $T_{\rm eff} - \log g$ diagram of the HW Vir systems. The helium main sequence (HeMS) and the EHB band (limited by the zero-age EHB, ZAEHB, and the terminal-age EHB, TAEHB) are superimposed by evolutionary tracks by Dorman et al. (1993) for sdB masses of 0.471, 0.473, and 0.475 $M_\odot$. The positions of the HW Vir systems with pulsating sdBs – V2008-1753 (this work, with error bars), NY Vir (Van Grootel et al. 2013), 2M1938+4603 (Østensen et al. 2010), and PTF1 J072456+125301 (Schindewolf et al. submitted, Kupfer priv. com.) – are marked by red squares. Blue dots mark the positions of other HW Vir-like systems (Drechsel et al. 2001; For et al. 2010; Maxted et al. 2002; Klepp & Rauch 2011; Østensen et al. 2008; Wood & Saffer 1999; Almeida et al. 2012; Barlow et al. 2013; Schaffenroth et al. 2013, 2014b, Schaffenroth et al., in prep, Kupfer, priv. com.). The positions of the two HW Vir systems with BD companions J1622 (Schaffenroth et al. 2014c) and J0820 (Geier et al. 2011c) are indicated by the blue dots with error bars. The black triangles mark sdB+dM systems showing a reflection effect but no eclipses (Kupfer et al. 2015, and references therein). The green, open dots represent other sdB+WD binaries or sdB binaries with unknown companion type (Kupfer et al. 2015). The approximate location of the $\mathrm{sdBV_r}$ instability strip is indicated by an ellipse.

Table 7.10.: Pulsation frequencies and amplitudes

	$f^{a,b}$ [mHz]	amplitude [ppt]	phase^c	S/N
F1	6.565±0.005	3.5± 0.2	0.739±0.019	14.5
F2	5.494±0.008	3.1± 0.2	0.82±0.03	12.6
F3	6.289±0.006	3.1± 0.2	0.74±0.02	12.5
F4	5.638±0.011	2.2± 0.2	0.71±0.05	9.2
F1	6.572±0.006	3.2± 0.3	0.12±0.03	8.7
F2	–	–	–	–
F3	6.295±0.006	2.8± 0.3	0.90±0.04	7.6
F4	5.685±0.008	2.3± 0.3	0.87±0.03	6.2

[a] upper half: frequencies found in g' light curve
lower half: frequencies found in i' light curve
[b] errors as given by FAMIAS, more realistic is an error around 0.1-0.2 mHz
[c] reference time: first point of light curve
(g': $\mathrm{BJD_{TBD}} = 2456519.5846905$)
(i': $\mathrm{BJD_{TBD}} = 2456520.53415896$)

7.6.3. Photometric analysis

Pulsations

Both the g' and i' light curves from the SOAR telescope exhibit pulsations too low in amplitude to have been detected in the data analysed by Van Noord et al. (2013). In order to disentangle the pulsations from the binary effects in the light curve, we used an approach similar to that demonstrated by Vučković et al. (2007). First, we fit the eclipses and reflection effect as described in Section 7.6.3) and subtracted the best-fitting model from the observed light curve. The original g' and i' filter light curves are displayed in Fig. 7.24, along with the same curves after the subtraction of the binary signal. The pulsations are visible by eye in the g' curve but less apparent in the i' data, due to its lower S/N and lower pulsation amplitudes at redder wavelengths. The large–scale trends in both residual light curves are likely due to residual atmospheric extinction and transparency variations.

We calculated the Fourier transformations (FTs) of the light curves using FAMIAS[6] (Zima 2008). The resulting FTs are displayed in Fig. 7.25. We detect at least four independent pulsation modes with periods ranging from 2.5 to 3 min and amplitudes < 4 ppt. The best–fit frequencies, along with their amplitudes and S/N, are listed in Table 7.10. The mode with the second–highest amplitude in the g' light curve (F2) was not clearly detected in the i' light curve, but its apparent absence might be explained by the high noise level in this data set. The elevated power at lower frequencies is likely due to inaccuracies in the binary light curve modeling, along with the atmospheric extinction and transparency corrections. A much longer time base is needed to improve the frequency determination and to be able to use the pulsations for asteroseismology. Consequently, we do not perform a more thorough pulsation analysis than this and limit our result simply to the detection of pulsations alone. To prepare the light curve for binary modeling, we use the results from Table 7.10 to subtract the detected pulsations from the original light curves.

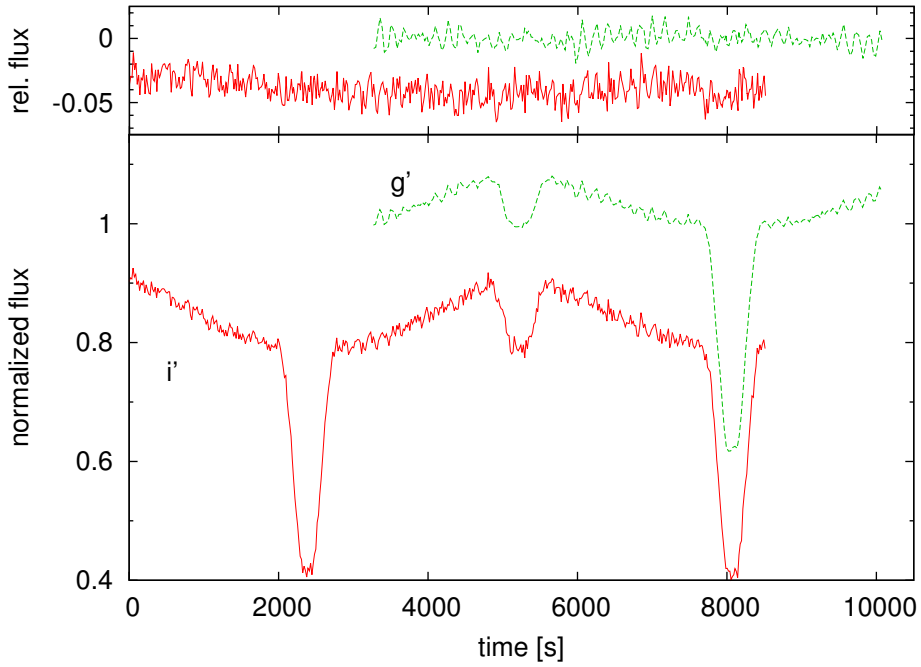

Figure 7.24.: g' (dashed line) and i' (solid line) filter light curves of V2008-1753 taken with SOAR. The two light curves were taken in subsequent orbital cycles. The sub-figure shows the pulsation signal after the subtraction of the binary signal by the best-fitting light curve model.

Binary Light Curve Modeling

The binary light curve exhibits all the typical features of a HW Vir system. Due to the short period and the relatively high temperature of the subdwarf, the reflection effect is rather strong, with an amplitude around 10 %. The secondary eclipse appears to be nearly total, in accordance with the high inclination and the very deep primary eclipse. As our light curves only cover one complete orbital cycle, it is not possible to determine an accurate period from our data alone. For the ephemeris we hence cite the period derived by Van Noord et al. (2013), which was determined from a much larger baseline. We were able to determine precise eclipse timings using our data by fitting parabolas to the minima. They are summarized in Table 7.11. Using these values and the period from Van Noord et al. (2013), the ephemeris of the primary minimum is given by

$$\mathrm{BJD_{TBD}} = 2456519.64027(1) + 0.065817833(83) \cdot \mathrm{E} \tag{7.3}$$

where E is the cycle number. The error in the period quoted by Van Noord et al. (2013) is likely to be an underestimate given the omission of systematics and the poor sampling. We believe an error of 0.0001 to be more appropriate. A comparison of the secondary eclipse compared to the primary eclipse of both light curves separately reveals a slight departure of the secondary mid-eclipse from phase 0.5; such an offset can be caused by both the Rømer delay (extra light travel time due to the binary orbit) and an eccentricity $e > 0$. For small eccentricities, the total shift of the secondary eclipse with respect to phase 0.5 is given in Barlow et al. (2012a):

$$\Delta t_{\mathrm{SE}} \backsimeq \Delta t_{\mathrm{Rømer}} + \Delta t_{\mathrm{ecc}} \backsimeq \frac{PK_{\mathrm{sdB}}}{\pi c}\left(\frac{1}{q} - 1\right) + \frac{2P}{\pi} e \cos\omega$$

From both light curves we measure a shift of 3 ± 1 s between the time of the secondary minimum and phase 0.5. With our system parameters we would expect a theoretical shift of the secondary

[6] http://www.ster.kuleuven.be/~zima/famias

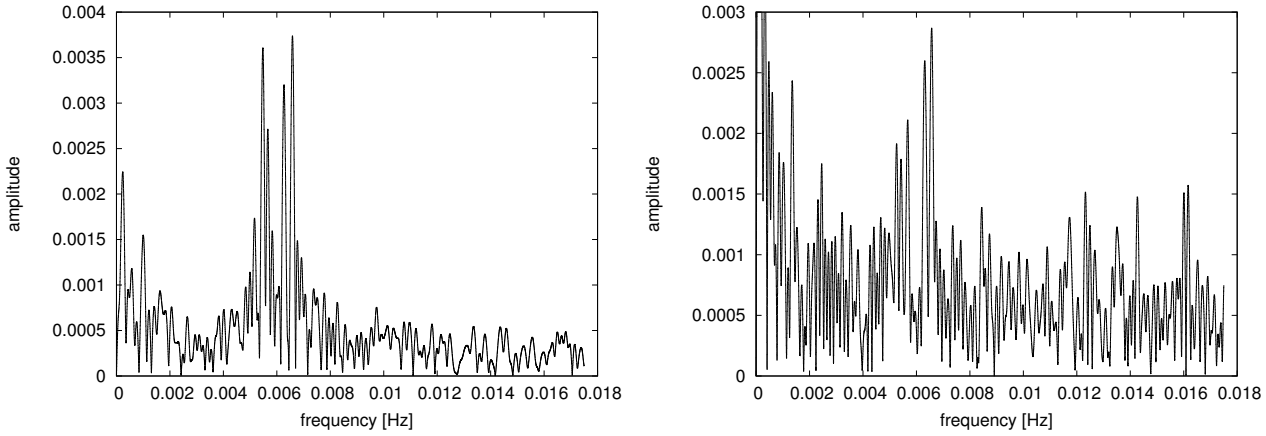

Figure 7.25.: Fourier transform of the pulsation signal shown in the sub-figure of Fig. 7.24. The right and left figures show the FTs of the g' and the i' filter light curves, respectively.

Table 7.11.: Eclipse times

filter	eclipse	BJD_{TBD}[d]
g'	primary	2456519.64027(1)
g'	secondary	2456519.60733(2)
i'	primary	2456520.56176(1)
i'	secondary	2456520.59463(1)
i'	primary	2456520.62757(1)

eclipse with respect to phase 0.5 due to the Rømer delay of 2 s. If we take that into account, we would get a maximal eccentricity of $e \cdot \cos\omega < 0.00055$. Ignoring the Rømer delay results in a maximum eccentricity of $e \cdot \cos\omega < 0.0011$. Because of the large errors in the radial velocity determinations, the eccentricity cannot be constrained by the radial velocity curve to that precision.

A photometric solution to the binary light curve (with pulsations removed; Fig. 7.26) was determined using MORO (MOdified ROche program, see Drechsel et al. 1995). This program calculates synthetic light curves which we fit to the observations using the SIMPLEX algorithm. This light curve solution code is based on the Wilson-Devinney approach (Wilson & Devinney 1971) but uses a modified Roche model that considers the mutual irradiation of hot components in close binary systems. More details of the analysis method are described in Schaffenroth et al. (2013).

To calculate the synthetic light curves, $12 + 5n$ (n is the number of light curves) parameters are used. Such a high number of partially–correlated parameters will inevitably cause severe problems if too many and wrong combinations are adjusted simultaneously. In particular, there is a strong degeneracy with respect to the mass ratio. After the orbital inclination, this parameter has the strongest effect on the light curve, and it is highly correlated with the component radii. Hence we kept the mass ratio fixed at certain values and calculated solutions for these mass ratios, which were subsequently compared and evaluated according to criteria explained below.

Given the large number of parameters present in the code, it is imperative to constrain as many parameters as possible based on independent inputs from spectroscopic analyses or theoretical constraints. From the spectroscopic analysis, we derived the effective temperature and the surface gravity of the sdB primary and fixed these parameters during the fitting. Due to the early spectral type of the primary star, the gravity darkening exponent was fixed at $g_1 = 1$, as expected for radiative outer envelopes (von Zeipel 1924). For the cool convective companion,

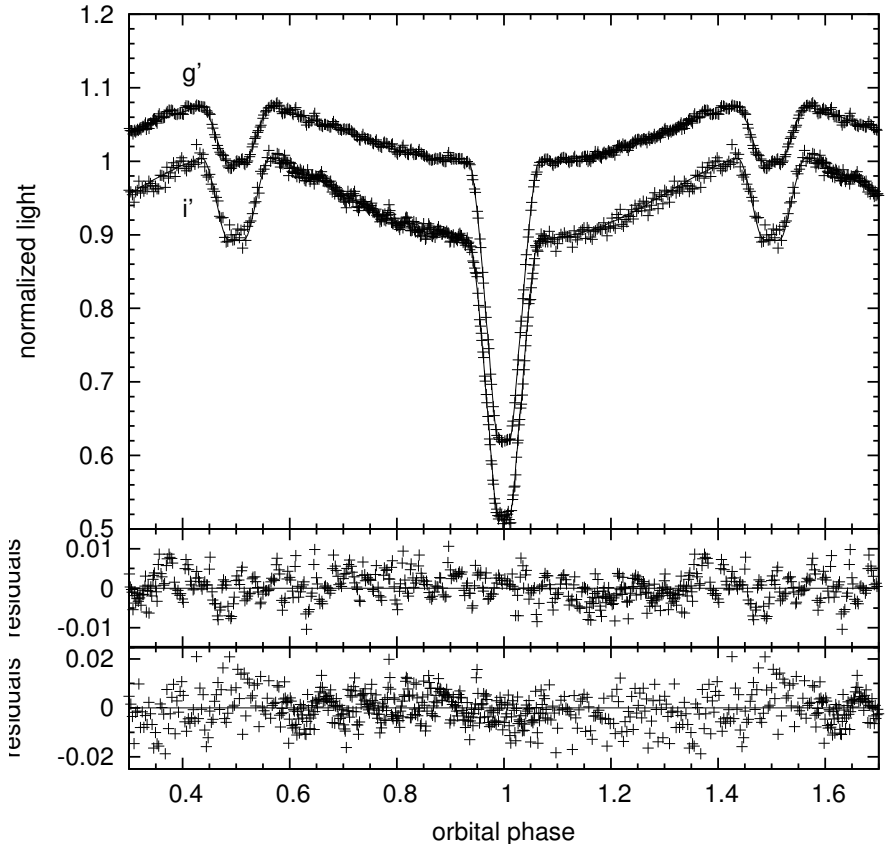

Figure 7.26.: g' and i' light curves after the removal of the pulsation signal as explained in Sect. 7.6.3 together with the best-fitting light curve model. The residuals displayed in the two lower panels still show signs of low-amplitude pulsations.

g_2 was set to 0.32 (Lucy 1967). The linear limb darkening coefficients were extrapolated from the table of Claret & Bloemen (2011).

To determine the quality of the light curve fit, the sum of squared residuals σ of all observational points with respect to the synthetic curve was calculated as a measure of the goodness of the fit. Unfortunately, the σ values of the best light curve fits for the different mass-ratios did not differ significantly. Therefore, we cannot determine a unique solution from the light curve analysis alone. The full set of parameters describing the best–fitting solution for a mass ratio of $q = 0.146$, which corresponds to an sdB with the canonical mass of 0.47 $M_\odot$ are given in Table 7.13, with errors determined by the bootstrapping method. The light curves in the g' and i' bands are displayed in Fig. 7.26 together with the best-fit models for these parameters. The parameters of the system derived from this lightcurve solution together with the semi-amplitude of the RV curve are summarized in Table 7.12. The errors result from propagation of the uncertainties in K and P.

7.6.4. The brown dwarf nature of the companion

From the semi-amplitude of the radial velocity curve, the orbital period, and the inclination, we can derive the masses and radii of both components for each mass ratio. The masses follow

Table 7.12.: Parameters of V2008-1753

V2008-1753		
coordinates	20 08 16.355 -17 53 10.52 (J2000.0)	
cv	[mag]	16.8
i	$^\circ$	86.83 ± 0.45
K	$[\mathrm{km\,s^{-1}}]$	54.6 ± 2.4
P	[h]	1.5796280 ± 0.0000002
M_{sdB}	$[M_\odot]$	0.47 ± 0.03
M_{comp}	$[M_\odot]$	0.069 ± 0.005
a	$[R_\odot]$	0.56 ± 0.02
R_{sdB}	$[R_\odot]$	0.138 ± 0.006
R_{comp}	$[R_\odot]$	0.086 ± 0.004
$\log g(\mathrm{sdB,phot})$		5.83 ± 0.02
$\log g(\mathrm{sdB,spec})$		5.83 ± 0.05
$T_{\mathrm{eff,sdB}}$	[K]	32800 ± 750

from:

$$M_1 = \frac{PK_1^3}{2\pi G} \frac{(q+1)^2}{(q \cdot \sin i)^3}$$
$$M_2 = q \cdot M_1$$

and the fractional radii of the light curve solution together with

$$a = \frac{P}{2\pi} \frac{K_1}{\sin i} \cdot \left(\frac{1}{q} + 1\right)$$

yield the radii. For each mass ratio we get different masses and radii. It was stated already in Sect. 7.6.3 that it is not possible to determine the mass ratio from the light curve analysis alone. However, from the sdB mass and radius determined by the light curve analysis we can calculate a photometric surface gravity and compare that to the surface gravity derived by the spectroscopic analysis. The result is shown in Fig. 7.27. An agreement of spectroscopic and photometric surface gravity values is reached for solutions that result in sdB masses between 0.35 and 0.62 $M_\odot$. It is therefore possible to find a self-consistent solution. This is a fortunate situation, because gravity derived from photometry was found to be inconsistent with the spectroscopic result in other cases, such as AA Dor (Vučković et al. 2008).
To constrain the solutions even more, we can also use theoretical mass-radius relations for the low-mass companions by Baraffe et al. (2003) and compare them to the masses and radii of the companion derived by the light curve solutions for the various mass ratios. This was done in a similar way as in Schaffenroth et al. (2014c). This comparison is displayed in Fig. 7.28. Relations for different ages of 1, 5 and 10 Gyrs were used. The measured mass-radius relation is well matched by theoretical predictions for stars $\gtrsim 3$ Gyrs for companion masses between 0.056 $M_\odot$ and 0.073 $M_\odot$. The corresponding mass range for the sdB star extends from 0.35 $M_\odot$ to 0.53 $M_\odot$.
However, inflation effects have been found in the case of hot Jupiter exoplanets (e.g. Udalski et al. 2008) and also in the MS + BD binary CoRoT-15b (Bouchy et al. 2011). As the companion is exposed to intense radiation of a luminous hot star at a distance of only 0.56 $R_\odot$, this effect

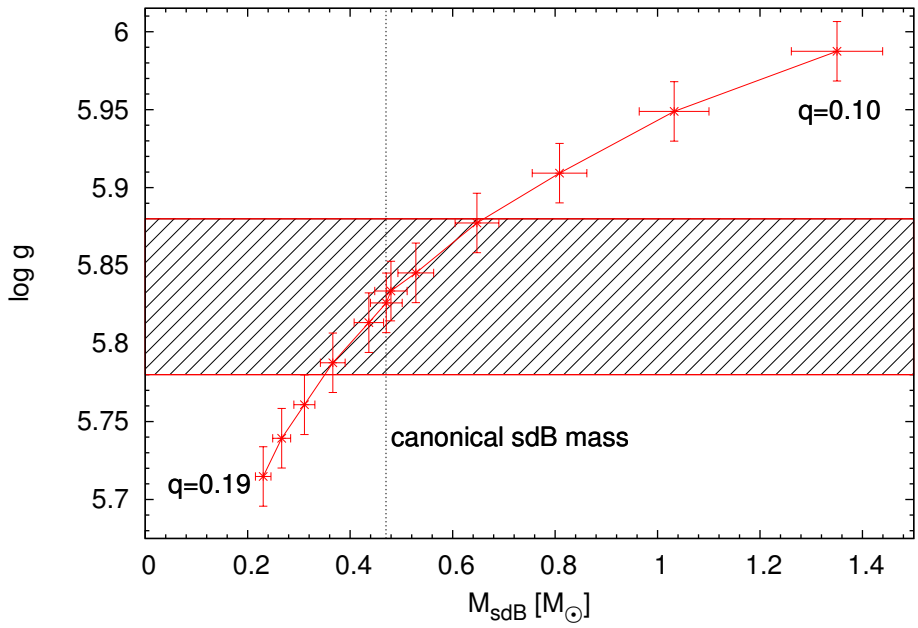

Figure 7.27.: Comparison of the photometric and spectroscopic surface gravity for the solutions with different mass ratio $q = 0.10-0.19$ (marked by the error cross). The spectroscopic surface gravity with uncertainty is given by the shaded area.

cannot be neglected and would result in an underestimation of the radius, if compared to non-irradiated models (Baraffe et al. 2003). The maximum inflation effect can be estimated from the comparison of our solutions to the theoretical mass-radius relations shown in Fig. 7.28. This figure shows that an inflation of more than about 10 % can be excluded, because otherwise none of the theoretical mass-radius relations would match the measured one, even if the star were as old as 10 Gyrs.
The mass-radius relation for the companion would be in perfect agreement with the light curve solution for a companion with a mass of $0.069\,M_\odot$, a radius of $0.086\,R_\odot$, and an age of $\sim$ 5-10 Gyrs, if we assume an inflation of 6-11 %. The corresponding mass of the sdB is $0.47\,M_\odot$, exactly the canonical sdB mass, which we therefore adopt for the sdB throughout the rest of this section. A similar result was found in the analysis of the sdB + BD binary J1622 (Schaffenroth et al. 2014c), which has a comparable period and parameters.
The companion has a mass below the limit for hydrogen-burning and thus appears to be a brown dwarf – the third confirmed around a hot subdwarf star.

7.6.5. Summary and conclusions

We performed an analysis of the spectrum and light curve of V2008-1753 and find that this eclipsing binary consists of a pulsating sdB with a brown dwarf companion. This is the first system of this kind ever found. Similar to J1622, an inflation of the brown dwarf by more than about 10 % can be excluded.
V2008-1753 has the shortest period of all known HW Vir systems and the second shortest period of any sdB binary discovered to date. Due to the small separation distance and high temperature of the sdB, the amplitude of the reflection effect is relatively large (more than 10 %). Consequently, this system might provide the chance to detect and evaluate spectral features of the irradiated companion, similar to AA Doradus and HW Vir (Vučković et al. 2008, 2014). If the companion's spectral features are detected, the radial velocities of both components could be determined. We then could derive an unbiased mass ratio of the system

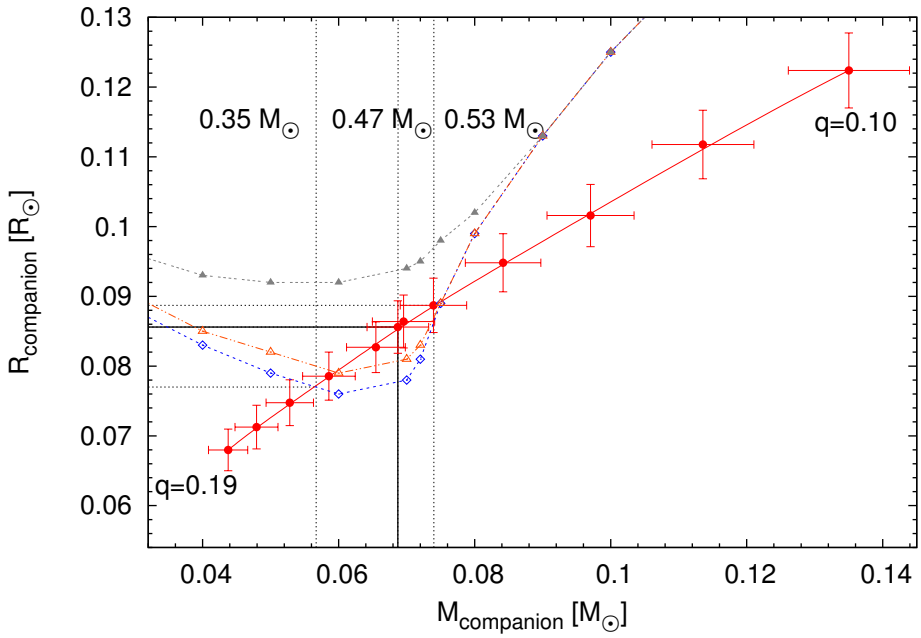

Figure 7.28.: Comparison of theoretical mass-radius relations of brown dwarfs by Baraffe et al. (2003) for an age of 1 Gyr (filled triangles), 5 Gyrs (triangles) and 10 Gyrs (diamond) to results from the lightcure analysis. Each error cross represents a solution from the light curve analysis for a different mass ratio ($q = 0.10 - 0.19$). The dashed vertical lines mark different values of the corresponding sdB masses. The solid line marks the most probable solution with $q = 0.146$, which results in an sdB mass of $0.47\,M_{\odot}$.

and obtain a unique spectroscopic and photometric solution.

Higher quality and resolution spectra should also allow the detection of the Rossiter-McLaughlin (RM) effect (cf. Vučković et al. 2007). This effect is due to the selective blocking of the light of the rotating star during an eclipse. The amplitude is mainly depending on radius ratio, the rotational velocity of the primary star, and the inclination of the system. As our system has a high inclination and a high radius ratio, the expected amplitude is quite high. From the RM effect it is, hence, possible to determine the rotational velocity independent from spectral line modelling. With the help of the rotational velocity we can verify, whether the sdB is synchronized, which should be the case due to synchronization theories, but is currently under debate (Schaffenroth et al. 2014c).

The presence of stellar pulsations in the sdB offers further possibilities to characterize this system. Once the pulsation frequencies are fully resolved and their modes identified with higher–precision data over a longer time base, the mass and other properties of the sdB can be constrained by asteroseismology. These results can be compared to the light curve models. To date, only NY Vir (Van Grootel et al. 2013) has offered this opportunity. However, no signature of the companion could be identified in the spectrum of this system, and the masses from the light curve analysis remain biased.

The combined presence of pulsations and eclipses, furthermore, offers the possibility of eclipse mapping, as done for example for NY Vir (Reed et al. 2005; Reed & Whole Earth Telescope Xcov 21 and 23 Collaborations 2006). Thereby, the eclipses can be used to determine pulsation modes, which are often difficult to uniquely identify. During the eclipse parts of the star are covered. Changing the amount and portion of regions of the star visible affects the pulsation amplitudes. The effect is changing for different pulsation modes, which can be identified in this way.

V2008-1753 has the potential to eventually replace NY Vir as the benchmark system for understanding sdB stars and their binary nature, if emission lines of the companion are detected. It would permit the direct comparison of independent techniques (namely light curve modelling, asteroseismology, spectroscopy, and radial velocity variations) used to derive the stellar parameters. Hence, the reliability of these methods and models could be checked as well as possible systematic errors of the derived parameters could be further investigated. Most notably, the mass determined by asteroseismology could be checked at a high precision level, if the semi-amplitudes of the radial velocity curves could be determined for both components.

Table 7.13.: Adopted light curve solution.

Fixed parameters:		
$q\,(=M_2/M_1)$		0.146
$T_{\rm eff}(1)$	[K]	33000
g_1^b		1.0
g_2^b		0.32
$x_1(g')^c$		0.21
$x_1(i')^c$		0.14
δ_2^d		0.0
Adjusted parameters:		
i	[°]	86.83 ± 0.45
$T_{\rm eff}(2)$	[K]	2960 ± 550
A_1^a		1.0 ± 0.002
A_2^a		1.2 ± 0.05
Ω_1^f		4.10 ± 0.05
Ω_2^f		2.389 ± 0.008
$\frac{L_1}{L_1+L_2}(g')^g$		0.99995 ± 0.00007
$\frac{L_1}{L_1+L_2}(i')^g$		0.99926 ± 0.00068
δ_1		0.026 ± 0.01
$x_2(g')$		0.44 ± 0.06
$x_2(i')$		0.62 ± 0.07
$l_3(g')^f$		0.007 ± 0.001
$l_3(i')^f$		0.0 ± 0.0
Roche radii^h:		
r_1(pole)	[a]	0.246 ± 0.001
r_1(point)	[a]	0.249 ± 0.002
r_1(side)	[a]	0.249 ± 0.002
r_1(back)	[a]	0.249 ± 0.002
r_2(pole)	[a]	0.150 ± 0.001
r_2(point)	[a]	0.154 ± 0.002
r_2(side)	[a]	0.152 ± 0.001
r_2(back)	[a]	0.158 ± 0.001

[a] Bolometric albedo
[b] Gravitational darkening exponent
[c] Linear limb darkening coefficient; taken from Claret & Bloemen (2011)
[d] Radiation pressure parameter, see Drechsel et al. (1995)
[e] Fraction of third light at maximum
[f] Roche potentials
[g] Relative luminosity; L_2 is not independently adjusted, but recomputed from r_2 and $T_{\rm eff}(2)$
[h] Fractional Roche radii in units of separation of mass centres

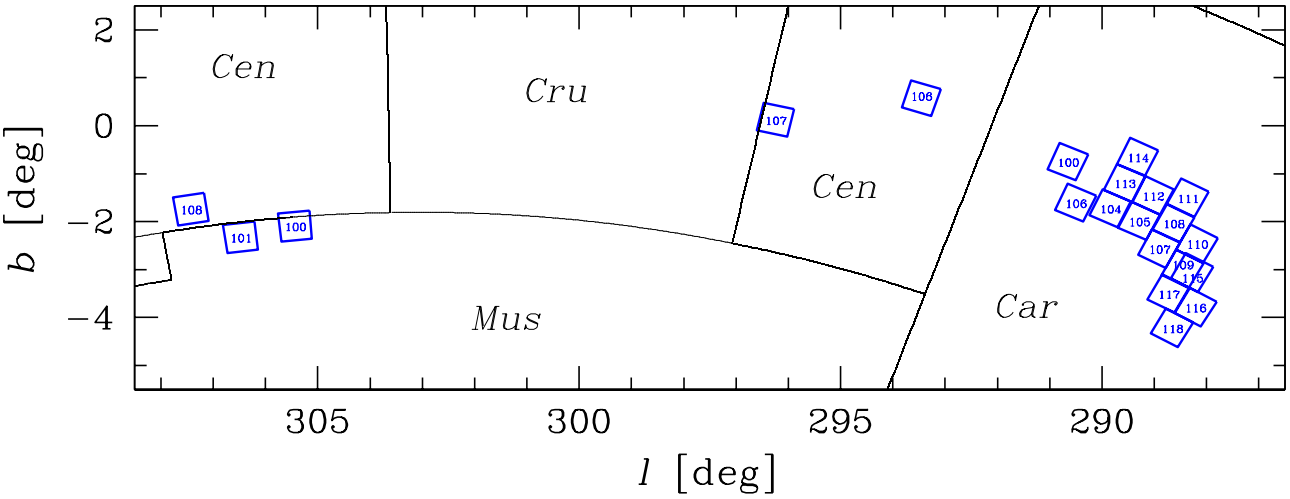

Figure 7.29.: Location of the twenty-one OGLE-III disk fields in the Galactic coordinates. Each field covers 35'x35' in the sky. Two fields, CAR109 and CAR115, overlap with each other in ≈ 67%. The total monitored area is 7.12 deg^2

7.7. OGLE-GD-ECL-08577 – The longest period HW Virginis system

Almost all of the HW Virginis systems but for the systems we found in the course of the MUCHFUSS project, have been found due to the characteristic shape of the lightcurve. Therefore, photometric surveys are suited perfectly to look for such systems. One such survey is the OGLE (Optical Gravitational Lensing Experiment) survey. The OGLE project is a collaboration between the Warsaw University Observatory, Carnegie Observatory, and Princeton University Observatory. Observations were done in the beginning with the 1 meter Swope telescope and were then continued with the 1.3-m Warsaw telescope at the Las Campanas Observatory, operated by the Carnegie Institution of Washington. In the following we will discuss the analysis of OGLE-GD-ECL-08577. which is with a period of about 0.5 d the HW Vir system with the longest period ever discovered. OGLE is a long-term project with the main aim to detect microlensing events toward the Galactic bulge (Udalski et al. 1993; Udalski 2003). However, regular observations of the Milky Way and Magellanic Cloud stars, conducted in some fields for over 21 years, allowed the discovery and exploration the variety of variable objects. As a matter of fact in the OGLE-III Galactic Disk Fields (Fig. 7.29) 10 new HW Vir candidates were found with periods from 0.077 to 0.50 d (Fig. 7.30, Pietrukowicz et al. 2013).

7.7.1. Observations

Photometry

All the data in the observation of the OGLE-III Galactic Disk Fields were collected with the 1.3-m Warsaw telescope at Las Campanas Observatory, Chile. During the OGLE-III project, conducted in years 2001-2009, the telescope was equipped with an eight-chip CCD mosaic camera with 8192 x 8192 pixels and with a scale of 0.26 arcsec/pixel and a field of view of 35' x 35'. Each chip of the mosaic is a SITe ST-002a CCD detector with 2048 x 4096 pixels of 15 μm size. They are cooled and held at the temperature of 95 (Udalski 2003). Twenty-one fields covering the total area of 7.12 deg^2 around the Galactic plane between longitudes +288° and +308° were observed. Their location in the sky is shown in Fig. 7.29. The time coverage as well as the number of data points obtained by the OGLE project varies considerably from field to field. The vast majority of the observations, typically of 1500 to 2700 points per field, were collected through the I-band filter with exposure times of 120 s and 180 s. Additional

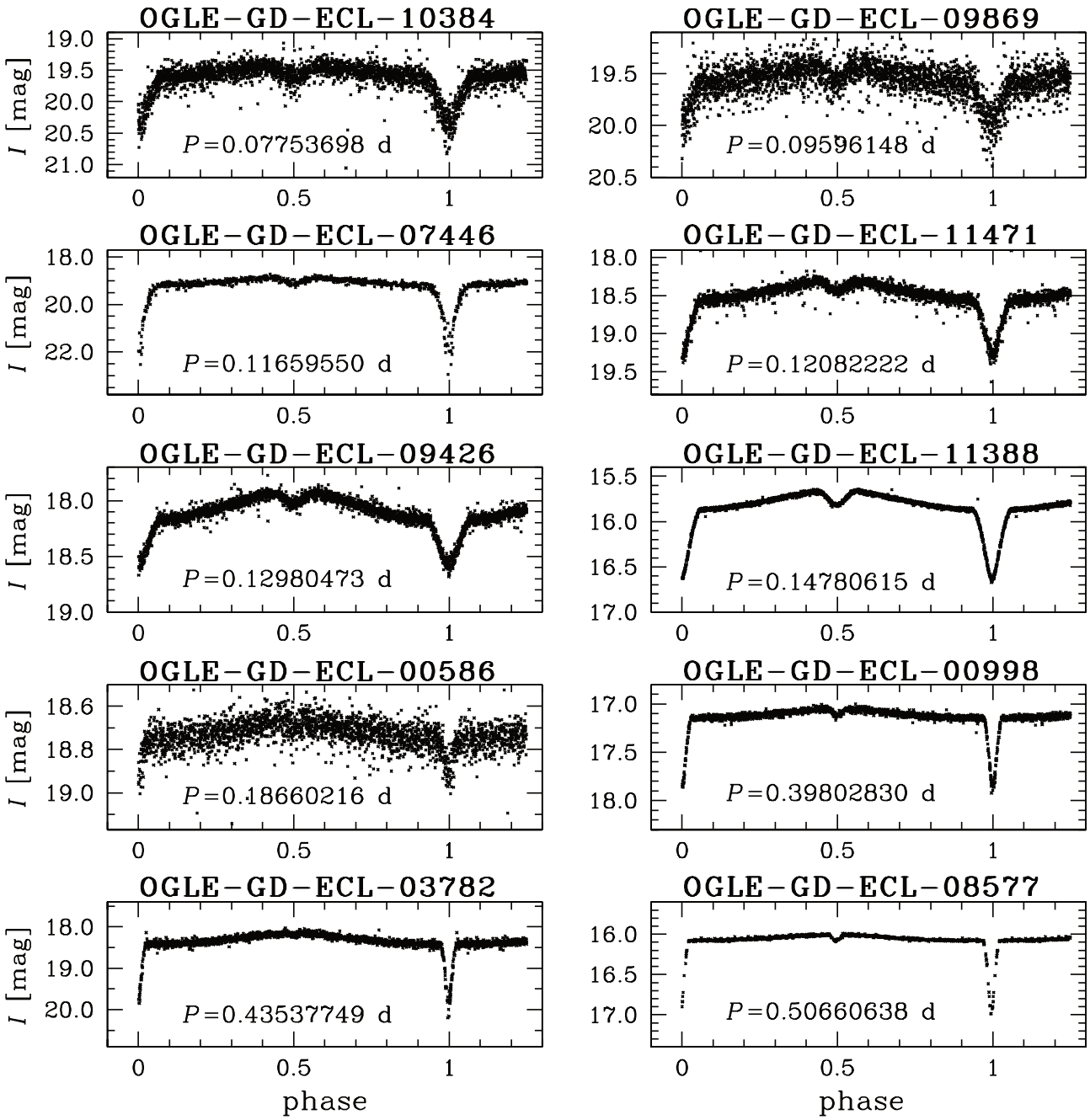

Figure 7.30.: Light curves of ten newly discovered sdB type binaries arranged with the increasing orbital period.

observations, consisting of only 3-8 measurements, were carried out in the V-band filter with an exposure time of 240 s. The time-series photometry was obtained with the standard OGLE data reduction pipeline. The CCD reduction is based on the standard IRAF[7] routines from CCDPROC. Afterwards it is processed by the main OGLE-III photometric data pipeline. The photometry software applies the image subtraction method. In the first step of reductions the shift between the frame and the reference image, which is a co-added image of several best individual images, is calculated. In the next step the difference image of the current frame is searched for objects that brightened or faded. The positions of these detections are cross-correlated with the positions of stars detected in the reference image and two files containing the known variable stars and 'new" variable stars in the current difference image are created. Finally, the photometry of all objects identified earlier in the reference image at the position of their centroids is derived (Udalski 2003).
About 345 500 detections with a signal to noise S/N > 10 were visually checked for any kind of variability. The search resulted in about 13 000 eclipsing binary candidates, $\approx$ 1000 ellipsoidal-like candidates, $\approx$ 1000 pulsating star candidates, and $\approx$ 15000 miscellaneous variables (mostly stars with spots) (Pietrukowicz et al. 2013). The periods were then determined by the TATRY code (Schwarzenberg-Czerny 1996) and false detections were removed from the list of eclipsing binary candidates. The final OGLE-III catalog[8] of eclipsing binaries in the Galactic disk, contains tables with basic parameters and time-series I- and V -band photometry (Pietrukowicz et al. 2013), We downloaded the photometry from ftp server, converted the magnitudes to relative flux, and phased the lightcurve with the given ephemeris for OGLE-GD-ECL-08577.

$$\mathrm{HJD} = 242735.23316 + 0.50660638(4231) \cdot E \tag{7.4}$$

Spectroscopy

The HW Virginis system with the largest period known so far is AA Dor with a period of 0.2614 d. As the period of OGLE-GD-ECL-08577 with 0.5066 d is almost doubling the period of AA Dor, and it is relatively bright ($I = 16$ mag) we obtained time-series spectroscopy for this HW Vir candidate. Several spectra were taken with the ESO-NTT/EFOSC2 spectrograph from the 1-4 Feb 2014. We obtained 10 spectra with the Grism 19 covering a wavelength range from $4450 - 5110$ Åat a resolution $R \approx 2200$, which are suitable for the measurement of RVs only. Moreover we took two spectra with Grism 7 with a wavelength range of $3500 - 5200$ AA and a resolution of ≈ 6 Å, from which it is possible to derive also atmospheric parameters. All spectra were corrected with an average bias frame constructed from several individual bias frames as well as an average flat field constructed from several flat field lamps. Reduction was done with the MIDAS[9] package. For the wavelength calibration several HeAr lamps were taken during the night and the lamp frame closest to the observation was used.

7.7.2. Analysis

Spectroscopic analysis

Radial velocity curve The radial velocities (RVs) were measured by fitting a set of mathematical functions matching the individual line shapes to the hydrogen Balmer lines as well as helium lines using SPAS (Hirsch 2009) to the 12 EFOSC2 spectra. Polynomials were used to match the continua and a combination of Lorentzian and Gaussian functions to match cores and wings of

[7] IRAF is distributed by National Optical Observatories, which is operated by the Association of Universities for Research in Astronomy, Inc., under cooperative agreement with National Science Foundation.
[8] `ftp://ftp.astrouw.edu.pl/ogle/ogle3/OIII-CVS/gd/ecl/`
[9] The ESO-MIDAS system provides general tools for data reduction with emphasis on astronomical applications including imaging and special reduction packages for ESO instrumentation at La Silla and the VLT at Paranal

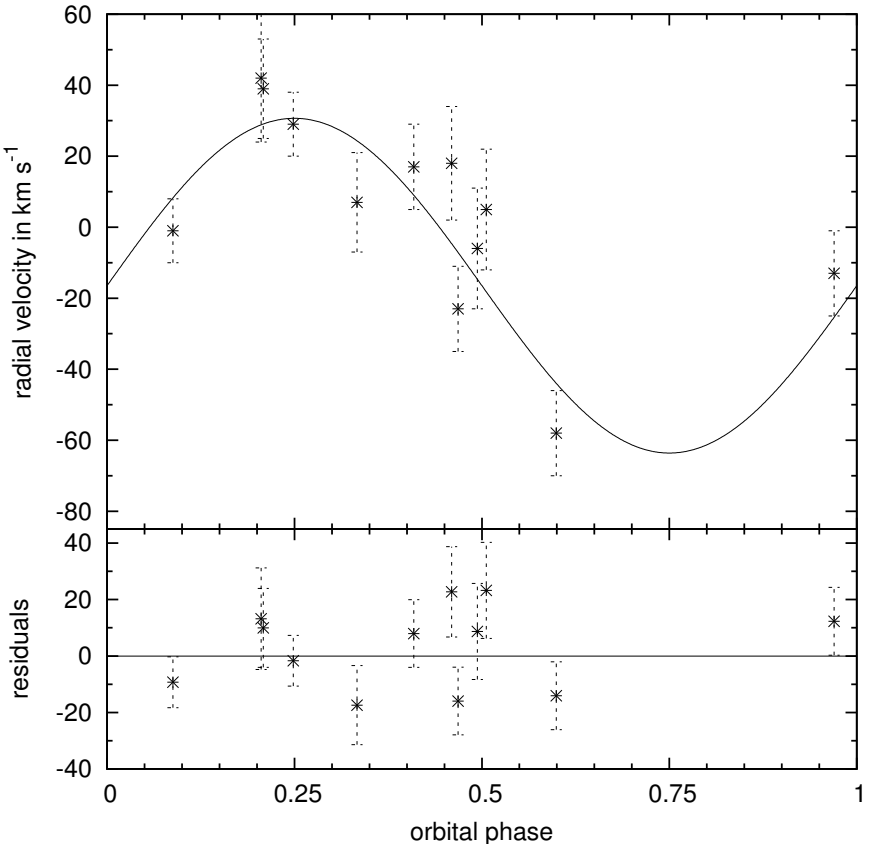

Figure 7.31.: RV curve of OGLE-GD-ECL-08577

the lines. The single measurements can be found in Table 7.14. As the secondary minimum of the lightcurve is exactly at phase 0.5 we can exclude eccentricity. Therefore, the RV measurements were fitted with a sine curve ($v_{\rm rad}(\phi) = K \sin(2\pi\phi/P) + \gamma$) with the period determined by the lightcurve.

$$K = 47 \pm 7.5\,\mathrm{km\,s^{-1}}$$
$$\gamma = -16 \pm 5\mathrm{km\,s^{-1}}$$

The RV curve with a fit with these parameters is shown in Fig. 7.31.

Atmospheric parameters The two ESO-NTT/EFOSC2 spectra with larger wavelength coverage were used to determine the atmospheric parameters of the hot subdwarf primary. We shifted them with their radial velocity and coadded both. For the determination of the parameters the hydrogen and helium lines were fitted with synthetic model spectra calculated with metal line-blanketed LTE model atmospheres (Heber et al. 2000).

$$T_{\rm eff} = 28400 \pm 1000\,\mathrm{K}$$
$$\log g = 5.43 \pm 0.15$$
$$\log y = -2.00$$

As the S/N of the combined spectrum is low in the higher Balmer lines (S/N= 15), we obtained large statistical errors. Hence, we do not have to consider the apparent change of parameters seen in some HW Vir systems (Schaffenroth et al. 2013) caused by the changing continuum due to the reflection effect. Figure 7.32 shows the fit of the hydrogen and helium lines with the derived parameters.

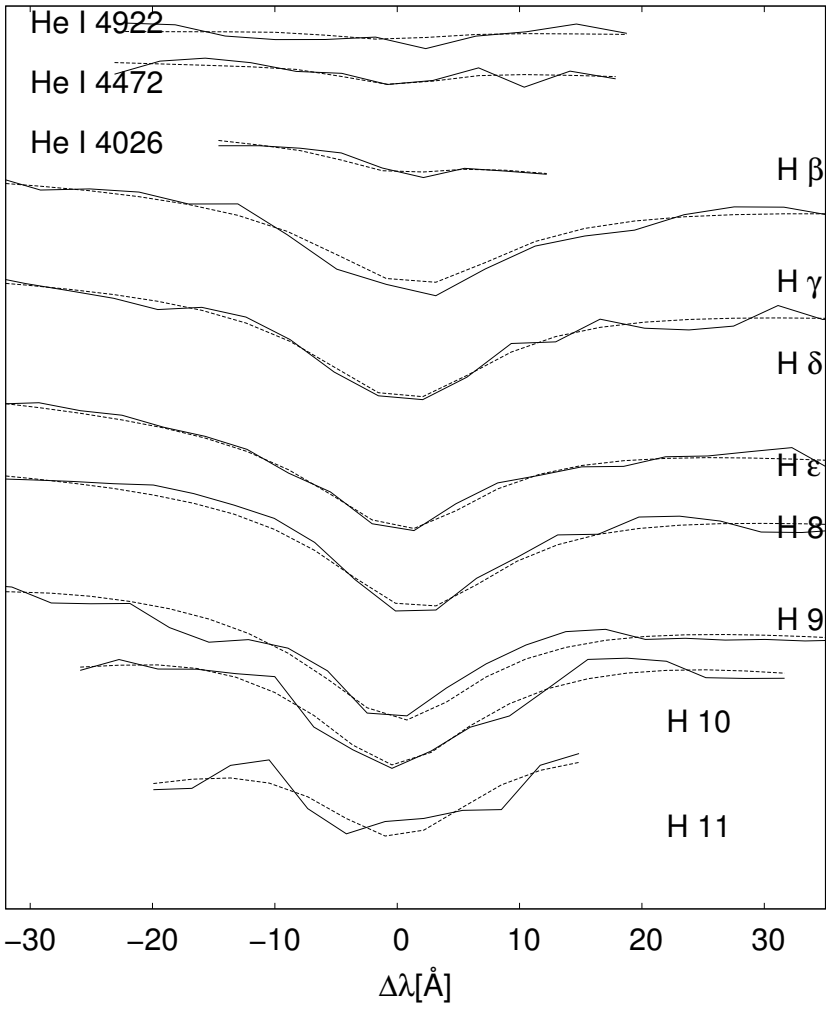

Figure 7.32.: Fit of the Balmer and helium lines in the co-added EFOSC spectrum. The solid line shows the measurement, and the dashed line shows the best fitting synthetic spectrum.

Lightcurve analysis

The lightcurve of OGLE-GD-ECL-08577 shows the typical shape for an HW Vir system (Fig. 7.33). We performed a lightcurve analysis using MORO the same way as already shown in Schaffenroth et al. (2013) and Sect. 7.4, 7.5 and 7.6. We calculated only two solutions for two different q. One solution with the q corresponding to a mass for the sdB near the canonical mass and one solution corresponding to the highest possible mass for the companion. Companions with masses larger than $\gtrsim 0.45 M_\odot$ are expected to be visible in the spectrum and can, hence, be excluded.

Unfortunately, we can find a lightcurve fit of similar quality for both mass ratios, as often the case in a lightcurve analysis. However, deviating from the lightcurve analyses of all other HW Virginis system, it was not possible to fit the amplitude of the reflection effect with the normally used parameter range. The amplitude of the reflection effect depends on the teimperature differenece and the separation of both components. A fit of the amplitude was only possible with a very high albedo of between 6-7. This is highly non-physical. This problem has to be investigated further.

Table 7.16 shows the parameter of the lightcurve solution with $q = 0.267$ and $q = 0.14$. Together with the results from the spectroscopic analysis we can determine the parameters of the system. They are listed in Table 7.15. As a additional check, we can compare the radius of the sdB

Table 7.14.: RVs of OGLE-GD-ECL-08577: The observations were taken with the EFOSC instrument

mid−BJD −2 450 000	RV [km s^{-1}]
56690.1794435	29 ± 9
56690.3571400	-58 ± 12
56691.3039611	-23 ± 12
56692.1841074	42 ± 18
56692.2873668	17 ± 12
56691.3169969	-6 ± 17
56693.0779898	-13 ± 12
56693.1377761	-1 ± 9
56693.1988405	39 ± 14
56693.2621304	7 ± 14
56693.3261146	18 ± 16
56693.3494806	5 ± 17

Table 7.15.: Parameters of OGLE-GD-ECL-08577

OGLE-GD-ECL-08577			
coordinates	11:56:30.82 -62:14:35.3 (J2000.0)		
cv	[mag]	16.0	
K	[km s^{-1}]	47.14 ± 7.5	
P	[h]	0.50660638	
$q\,(= M_2/M_1)$		0.267	0.14
i	$^\circ$	89.54	89.52
$M_{\rm sdB}$	$[M_\odot]$	0.46 ± 0.11	2.60 ± 0.62
$M_{\rm comp}$	$[M_\odot]$	0.12 ± 0.03	0.36 ± 0.09
a	$[R_\odot]$	2.24 ± 0.36	3.84 ± 0.61
$R_{\rm sdB}$	$[R_\odot]$	0.22 ± 0.03	0.37 ± 0.06
$R_{\rm comp}$	$[R_\odot]$	0.16 ± 0.02	0.27 ± 0.04
$\log g(\mathrm{sdB}, \mathrm{phot})$		5.43 ± 0.07	5.71 ± 0.07
$\log g(\mathrm{sdB}, \mathrm{spec})$		5.43 ± 0.15	
$T_{\rm eff,sdB}$	[K]	28400 ± 1000	

from the spectroscopic analysis with the one from the lightcurve analysis. From the photometric radius together with the mass a photometric $\log g$ can be calculated. For this solution also the radius of the companion is consistent with theoretical predictions (see 7.19). This shows that only the solution with a mass near the canonical mass gives a consistent solution. A solution with a high mass for the sdB and the companion, which is also excluded from theory, can, hence, also be excluded by our analysis.

To sum up we cannot determine a unique solution for OGLE-GD-ECL-08577. However, only a solution with a mass near the canonical mass for the sdB gives a consistent solution. This means the companion is a late M dwarf with a quite low mass around 0.12 $M_\odot$. This was unexpected as the period is much larger, we expected a larger companion mass. However, this was also not observed for the HW Vir system with the second largest period AA Dor. Moreover, the reflection effect is much stronger, as expected for this long period. Until now we have no explanation for this. This is the only HW Vir system, for which no lightcurve solution with reasonable parameters, especially albedo, is possible. We will obtain another lightcurve of this system in the V and R band, which will hopefully help to solve this system. Moreover, there are

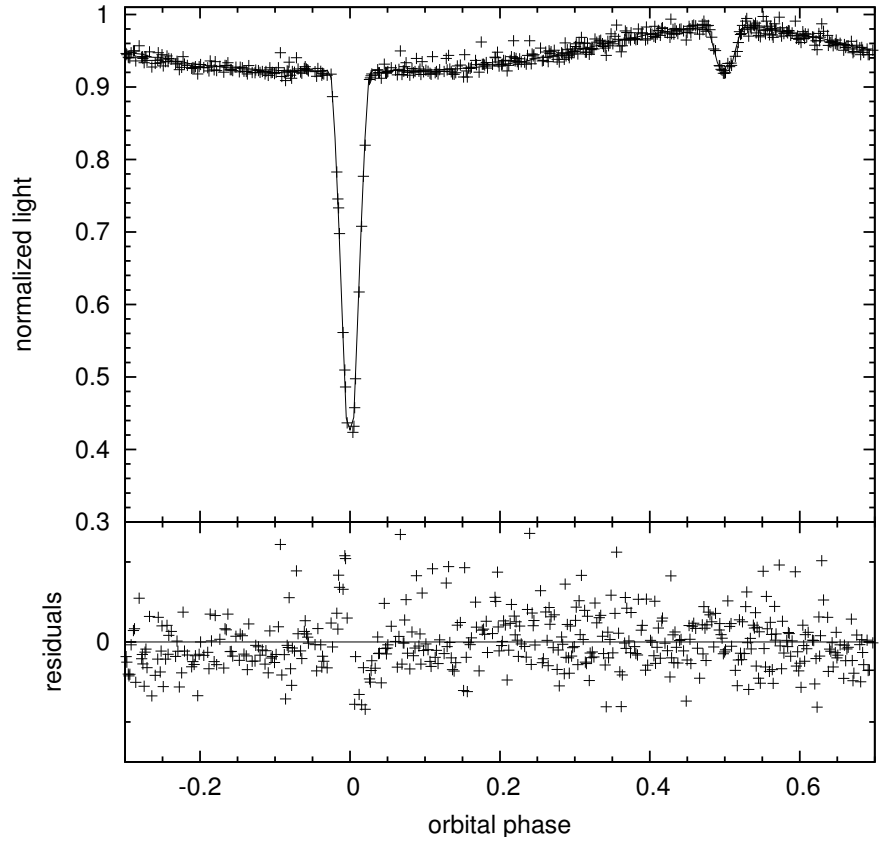

Figure 7.33.: Lightcurve of OGLE-GD-ECL-08577 in the I band.

two other fainter long period OGLE HW Virginis candidates, where we will obtain photometric and spectroscopic follow-up, which will hopefully also help to shed light on the reflection effect in longer period sdB+dM binaries.

Table 7.16.: Light curve solutions for different q.

Fixed parameters:			
$q\,(=M_2/M_1)$		0.267	0.14
$T_{\rm eff}(1)$	[K]	33000	
g_1^b		1.0	
g_2^b		0.32	
$x_1(g')^c$		0.21	
$x_1(i')^c$		0.14	
δ_2^d		0.0	
Adjusted parameters:			
i	[°]	89.54	89.52
$T_{\rm eff}(2)$	[K]	0.247	0.278
A_1^a		1.00	1.00
A_2^a		7.21	6.88
Ω_1^f		9.64	10.42
Ω_2^f		5.16	3.42
$\frac{L_1}{L_1+L_2}(g')^g$		0.9996639	0.9992417
δ_1		0.09059	0.00039
x_2		0.954	1.00
$l_3(g')^f$		0	0
Roche radii^h:			
r_1(pole)	[a]	0.09698	0.09720
r_1(point)	[a]	0.09708	0.09727
r_1(side)	[a]	0.09704	0.09725
r_1(back)	[a]	0.09707	0.09727
r_2(pole)	[a]	0.07038	0.07034
r_2(point)	[a]	0.06882	0.07070
r_2(side)	[a]	0.07045	0.07044
r_2(back)	[a]	0.07058	0.07069

[a] Bolometric albedo
[b] Gravitational darkening exponent
[c] Linear limb darkening coefficient; taken from Claret & Bloemen (2011)
[d] Radiation pressure parameter, see Drechsel et al. (1995)
[e] Fraction of third light at maximum
[f] Roche potentials
[g] Relative luminosity; L_2 is not independently adjusted, but recomputed from r_2 and $T_{\rm eff}(2)$
[h] Fractional Roche radii in units of separation of mass centres

7.8. The fraction of substellar and low-mass stellar companions in hot subdwarf binaries: Photometric follow-up of the MUCHFUSS project

After the analysis of single HW Virginis systems, we come now to the statistical results of the photometric follow-up of the MUCHFUSS projects. The selection of the targets due to radial velocity shifts in the continuous spectra in SDSS and not by the lightcurve, as usual the case, allowed us to determine the percentage of reflection effect binaries and substellar companions to sdB binaries. Therefore, we calculated expected amplitude of the light variations and the RV curve. As stated before, if we have a typical system with an M dwarf or brown dwarf as companion, light variations are visible, even for low inclinations. Figure 7.4 shows the expected semi-amplitude of the light variations in $R_{\rm B}$ and the expected semi-amplitude of the radial velocity at different inclinations. We determined the relative semi-amplitude by calculating synthetic lightcurves for the parameters of the prototype HW Virginis and the sdB+BD system J1622 for different inclinations with MORO. Using the mass ratio and the separation of these systems we could, moreover, calculate the expected semi-amplitude of the radial velocity for different inclinations (see Fig. 7.4). We also fitted a parabola through the determined points in order to be able to get the relative semi-amplitude of the lightcurve variation A and the semi-amplitude of the radial velocity K at any inclination.

for HW Vir:

$$K = -0.00691662\,i^2 + 1.66477\,i - 0.80223 \tag{7.5a}$$

$$A = -6.79716 \cdot 10^{-6}\,i^2 + 0.00151838\,i - 0.000361173 \tag{7.5b}$$

for J1622:

$$K = -0.00416351\,i^2 * 0.970709\,i - 0.73049 \tag{7.6a}$$

$$A = -5.25819 \cdot 10^{-6}\,i^2 + 0.00102431\,i - 0.00137412 \tag{7.6b}$$

where i the inclination in degree is. It is clearly visible that K and A is higher in the case of HW Vir despite its longer period due to the greater mass and radius of its companion.

Because of changing conditions the quality of the observed lightcurves is not always the same. To estimate the possible amplitude of a hidden sinusoidal signal in the non-detection lightcurves we normalised the lightcurve to one and calculated the standard deviation in the $R_{\rm B}$. One difficulty in this context was that for some of the lightcurves a linear trend was found with changing airmass. This is due to the fact that the target is much bluer than the comparison stars and the atmospheric extinction is wavelength depended. This effect leads to an overestimation of the standard deviation and, hence, the measurement is even more conservative. As the maximum possible inclination, we defined the inclination at which A is equal to the measured standard deviation for the two example cases of HW Vir and J1622 (Eq. (7.5a) and (7.6a)). For the derived inclination we get the expected K from Eq. (7.5b) and (7.5b). If the radial velocity shift measured from the SDSS spectra is larger than the expected one, we can exclude systems with parameters similar to HW Vir or J1622. The period distribution of the known sdB+dM or BD systems (see Jeffery & Ramsay 2014) shows that most sdB+dM systems have periods similar to the prototype for an eclipsing sdB+dM system HW Vir. This is, therefore, a system typical for an sdB with low-mass main-sequence companion. Until now no He-sdO+dM systems have been found. Therefore, we cannot draw conclusions about the possible companion of the observed He-sdOs. However, one of the He-sdOs shows light variations, which are probably due to ellipsoidal deformation of the sdB (Fig. 7.34). This points toward a compact, massive companion, as for example a massive WD companion. Not for all observed systems radial velocity shifts have been

measured, as not all observed systems are from the MUCHFUSS project, but some are also back-up targets, for which we choose known bright hot subdwarf stars. We cannot draw any conclusions on these stars, but we also show them for completion.
The results for all observed lightcurves, except for the ones found in Fig 7.35(a),(b),(c),(d), are displayed in Tables 7.17, 7.18 and 7.19.

Table 7.17.: Back-up targets

target	primary	survey	σ^a	$\Delta T^b_{\rm lc}$ h
J074508+381106	sdB	Galex	0.008300	0.43
J071011+403621	sdB	Galex	0.017000	1.42
J073646+220115	sdB	SDSS	0.027600	1.72
J234528+393505	He sdO	SDSS	0.007150	1.67
J074811+435239	sdB	SDSS	0.005160	1.90
HE2208	sdB	SPY	0.005640	1.26
PG0026	sdB	SPY	0.005000	2.61
J030749+411401	sdB	SDSS	0.016680	1.74
J015026-094227	sdB	SDSS	0.006957	2.21

[a] standard deviation of the normalised lightcurve in $R_{\rm B}$
[b] length of the observed lightcurve

Table 7.18.: He sdO/sdOB and sdO from the MUCHFUSS project

target	primary	σ^a	$\Delta T^b_{\rm lc}$ h
J141549+111213	He-sdO	0.055700	1.05
J030607+382335	sdO	0.006400	1.74
J232757+483755	He-sdO	0.007650	1.53
J221920+394603	sdO	0.006280	0.92
J090957+622927	sdO	0.024000	2.03
103549+092551	He-sdO	0.007710	2.38
J161015+045051	He-sdO	0.012000	1.70
J112414+402637	He-sdO	0.013500	2.78
J163416+22114	He-sdOB	0.004340	2.14
J012739+404357	sdO	0.010000	0.00

[a] standard deviation of the normalised lightcurve in $R_{\rm B}$
[b] length of the observed lightcurve

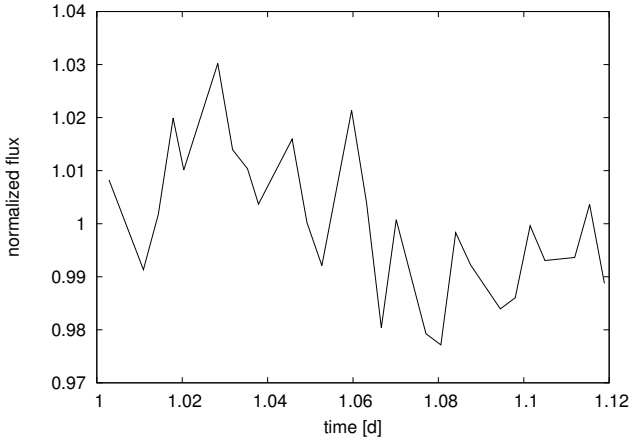

Figure 7.34.: Lightcurve of the He-sdO J1124 showing sinusoidal light variations

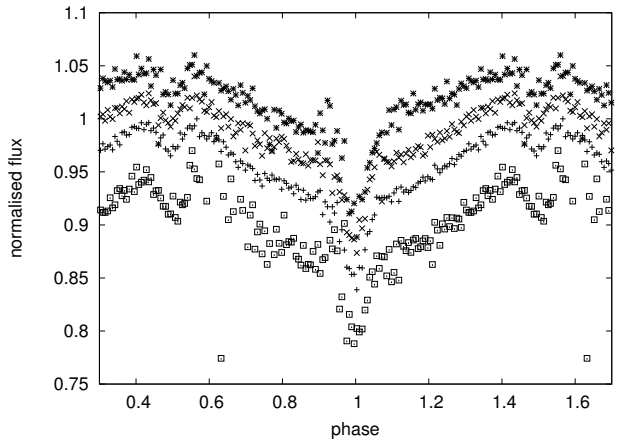

(a) sdB+BD system J1622

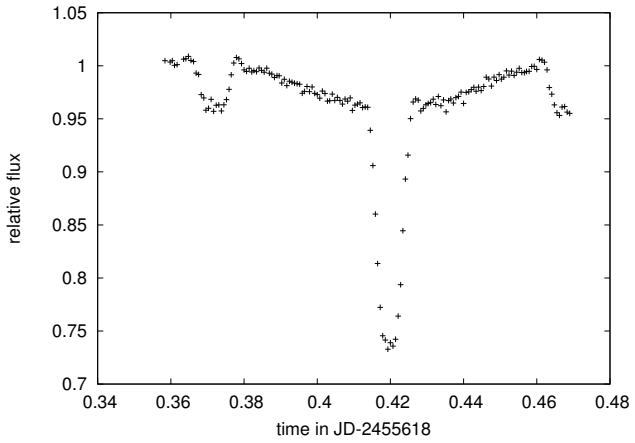

(b) sdB+BD system J0820 in U_B

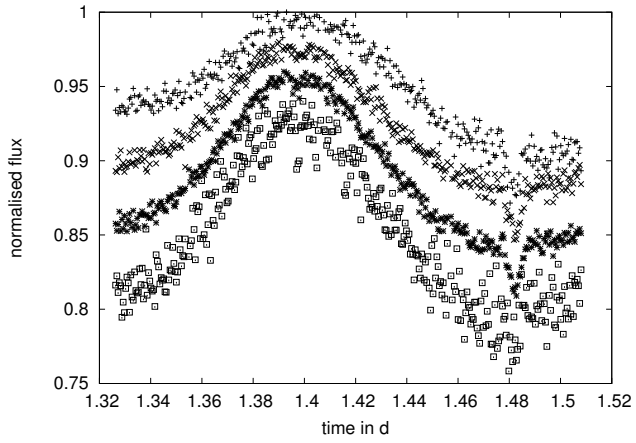

(c) sdB+dM system J1920

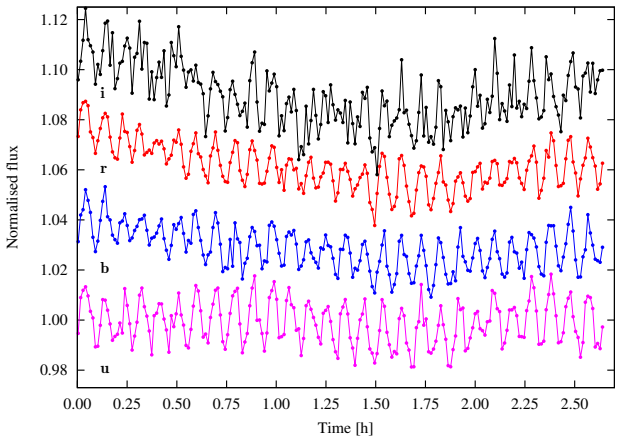

(d) pulsating sdB+dM system J0120

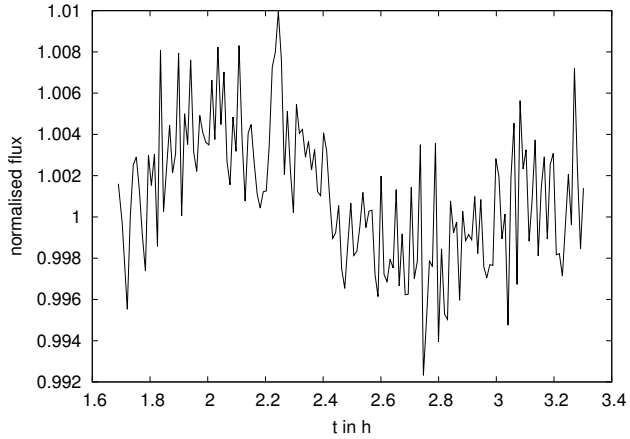

(e) sdB+WD system J0507 in B_B

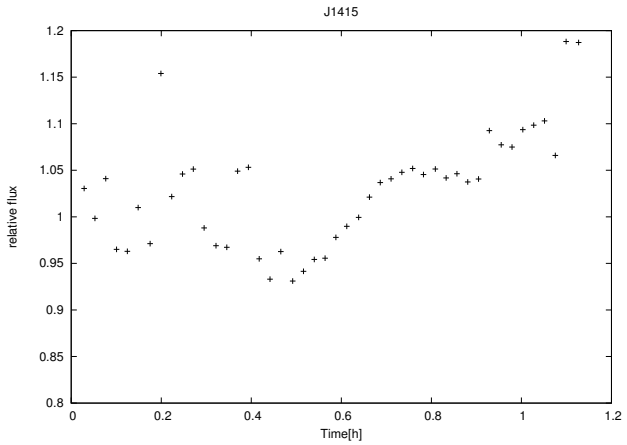

(f) He-sdO J1415 in V_B

Figure 7.35.: example lightcurves of systems with light variations found in the course of the MUCHFUSS project. a,b,c are three newly found HW Virginis systems (Schaffenroth et al. 2014c; Geier et al. 2011c; Schaffenroth et al. 2014b), d is a sdB+dM system with a pulsating sdB and the system is also showing the reflection effect (Østensen et al. 2013), e is probably a sdB+WD system showing ellipsoidal deformation, f is a He-sdO showing random light variations

Table 7.19.: Results of the analysis of the observed lightcurves in the MUCHFUSS follow-up

target	primary	σ^a	$\Delta T^b_{\rm lc}$ h	$i^c_{\rm J1622,max}$ °	$2K^d_{\rm J1622,max}$ kms^{-1}	$i^c_{\rm HWVir,max}$ °	$2K^d_{\rm HWVir,max}$ kms^{-1}	$\Delta v^e_{\rm rad,max}$ kms^{-1}			$\Delta T^f_{\rm vrad,max}$ d	system excluded^g
J171629+575121	sdOB	0.027500	1.41	34.19	55.18	19.99	59.43	67.0	±	15.5	3195.9096	-
J215053+131650	sdB	0.006300	2.23	7.80	13.18	4.32	12.53	24.0	±	13.5	0.0154	J1622 & HW Vir
J185129+182358	sdB	0.008000	1.40	9.63	16.46	5.50	16.27	105.0	±	18.0	0.0808	J1622 & HW Vir
J002323-002953	sdB	0.004000	1.90	5.40	8.77	2.76	7.48	168.0	±	4.0	1.0413	J1622 & HW Vir
J050735+034815	sdB+WD	0.003100	1.61	4.47	7.05	2.15	5.50	??	±	??	??	J1622 & HW Vir
J073701+225637	sdB	0.008000	2.19	9.63	16.46	5.50	16.27	53.0	±	14.5	2.0639	J1622 & HW Vir
J074551+170600	sdOB	0.005300	3.07	6.75	11.26	3.64	10.33	65.0	±	12.0	9.9390	J1622 & HW Vir
J093059+025032	sdB	0.003520	2.04	4.90	7.85	2.44	6.42	91.0	±	9.0	2986.7695	J1622 & HW Vir
J095238+625818	sdB	0.003670	1.54	5.05	8.14	2.54	6.75	154.0	±	8.0	1183.7390	J1622 & HW Vir
J112242+613758	sdB	0.002870	1.50	4.24	6.61	2.00	5.00	83.0	±	18.5	0.0469	J1622 & HW Vir
J115358+353929	sdOB	0.016000	2.18	18.77	32.05	11.19	33.92	79.0	±	9.5	1151.6544	J1622 & HW Vir
J134632+281722	sdB	0.005570	3.47	7.03	11.78	3.83	10.93	191.0	±	7.0	0.9988	J1622 & HW Vir
J065044+383133	sdOB	0.010600	2.33	12.49	21.49	7.31	22.00	88.0	±	13.5	0.0131	J1622 & HW Vir
J224518+220746	sdB	0.005730	1.93	7.20	12.09	3.93	11.28	70.0	±	11.5	1080.8857	J1622 & HW Vir
J072245+305233	sdB	0.007510	1.50	9.10	15.51	5.16	15.19	123.0	±	12.0	1.0019	J1622 & HW Vir
J220810+115913	sdB	0.005786	2.12	7.26	12.19	3.97	12.49	42.0	±	12.5	2172.7020	J1622 & HW Vir
J191908+371423	sdB	0.010600	2.00	12.49	21.49	7.31	22.00	237.0	±	12.0	68.8608	J1622 & HW Vir
J083006+475150	sdB	0.006300	2.14	7.80	13.18	4.32	12.53	164.0	±	9.0	4405.6747	J1622 & HW Vir
J052544+630726	sdOB	0.009200	1.82	10.94	18.78	6.33	18.91	42.0	±	15.0	0.0264	J1622 & HW Vir
J233406+462249	sdB	0.008145	1.69	9.78	16.74	5.59	16.59	31.0	±	12.0	0.0248	J1622 & HW Vir
J092520+470330	sdB	0.008070	1.87	9.70	16.59	5.54	16.43	40.0	±	12.5	0.0126	J1622 &HW Vir
J032138+053840	sdB	0.002600	1.52	3.96	6.10	1.82	4.40	110.0	±	9.0	1699.1435	J1622 & HW Vir
J153411+543345	sdOB	0.013870	1.17	16.23	27.86	9.64	29.21	83.0	±	18.5	0.0184	J1622 & HW Vir
J130439+312904	sdOB	0.007300	2.12	8.87	15.11	5.01	14.73	49.0	±	27.5	0.0163	J1622 & HW Vir
J204613-045418	sdB	0.005470	0.67	6.93	11.59	3.76	10.71	259.0	±	16.0	286.2265	J1622 & HW Vir
J011857-002546	sdOB	0.004390	1.98	5.80	9.52	3.02	8.33	140.0	±	8.0	265.2187	J1622 & HW Vir
J074534+372718	sdB	0.007450	2.55	9.03	15.40	5.12	15.06	64.0	±	17.0	0.0363	J1622 & HW Vir
J133639+111948	sdB	0.009500	1.97	11.27	19.36	6.54	19.58	48.0	±	14.0	0.0301	J1622 & HW Vir
J121150+143716	sdB	0.008500	2.02	10.17	17.42	5.84	17.37	?	±	?	?	J1622 & HW Vir
J113304+290221	sdB/DA	0.013600	2.84	15.92	27.33	9.45	28.62	95.0	±	30.0	0.0158	J1622 & HW Vir
J075937+541022	sdB	0.013600	2.34	15.92	27.33	9.45	28.62	40.0	±	18.5	0.0233	-
J115716+612410	sdB	0.005190	2.17	6.63	11.05	3.57	10.09	102.0	±	27.0	2250.6902	J1622 & HW Vir
J130439+312906	sdOB	0.004750	2.12	6.17	10.21	3.27	9.13	49.0	±	27.5	0.0163	J1622 & HW Vir

[a] standard deviation of the normalised lightcurve in $R_{\rm B}$
[b] length of the observed lightcurve
[c] maximum inclination
[d] expected semi-amplitude of the RV curve
[e] maximal measured radial velocity shift
[f] time-span between the two radial velocity measurements
[g] type of system that can be excluded

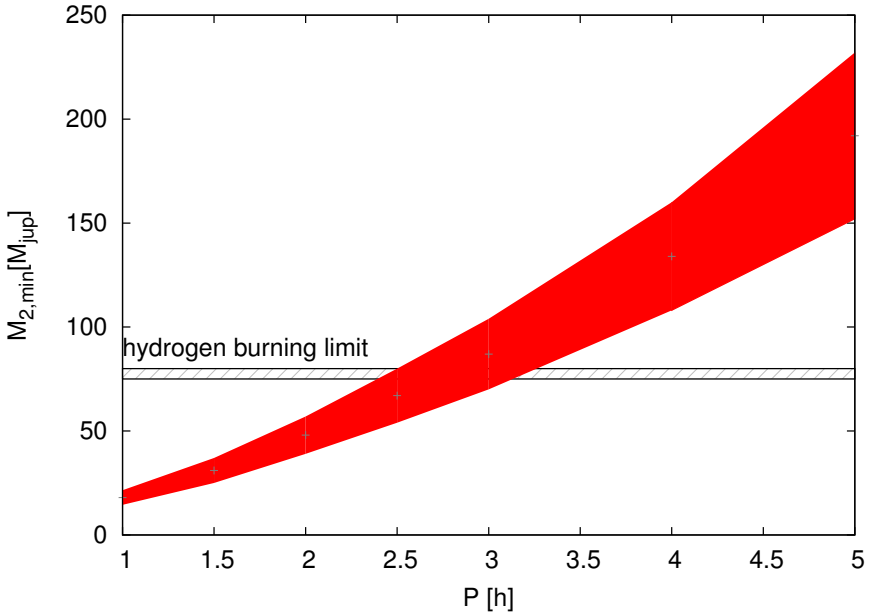

Figure 7.36.: Detectable minimum mass for the companion depending on the period of the system assuming an detectable minimum RV shift of 15-20 kms^{-1} in 30 min. As exact massed can only be determined in eclipsing binaries, we assume that only about 37% of the systems allow a definite determination of the nature of the companion. For the rest only minimum masses can be derived.

7.8.1. Selection effects

The substellar companions found until now are around $62 - 69 M_{\mathrm{jup}}$, very close to the hydrogen burning limit. To investigate the question which companions we can detect, we have to examine the selection effects of our follow-up. We assume an sdB mass of 0.47 $M_{\odot}$. For our follow-up we selected targets with significant RV variations until 17.5 mag to get sufficient S/N for the lightcurve within a sufficiently short exposure time, as we were looking for light variations with very short periods, our maximum exposure time was set to 3 min and each star was observed for about 1.5-2.5 h. The typical errors in RV are about 15 to 20 kms^{-1}, which we therefore assume as the minimum detectable RV shift. As the observing conditions vary much the photometric quality varied as well, with a typical scatter of between 0.5 to 1%. As shown in Schaffenroth et al. (2014a), it is not possible to derive the inclination in a non-eclipsing system. That is why only eclipsing systems allow a mass determination. For typical periods and radius ratios in a HW Virginis system, the minimum inclination to detect eclipses is around $66 - 68°$. The probability, that a binary has an inclination higher than a certain angle, can be calculated as described in Gray (2005), $P_{i>i_0} = 1 - (1 - \cos i_0)$, for an inclination of $> 68°$ the probability is 37%. The expected light variation of an reflection effect for an inclination $i > 68°$ and a period of 6 h is about $5 - 10$%. As the radius for companion masses between 0.02 and 0.15 $M_{\odot}$ is varying only slightly with a minimum radius around $0.065\,M_{\odot}$, the same applies also for very low-mass companions. Therefore, the photometric follow-up should not miss any systems with an inclination $i > 68°$ with periods smaller than 6 h, despite the fact that the stars were observed only for 1.5-2.5 h. As the time difference between the single SDSS spectra is typically 15 min, and we have at least three subsequent taken observations, we assume that the minimum RV shift we can detect is $\sim 15 - 20\,\mathrm{kms}^{-1}$ in 30 min, which is the usual error in RV. For stars with a second epoch the minimum RV shift would be even lower. Figure 7.36 shows the minimum mass that is detectable under these assumptions ($i = 68° - 90°$, $K_{1,\mathrm{min}} = 15 - 20\,\mathrm{kms}^{-1} \cdot P \cdot \mathrm{h}$). With our photometric follow-up, we are able to determine

the masses of about 37% of the systems with companions larger than the minimum mass. However, the reflection effect would be detectable for even lower inclinations. Until now all detected HW Vir systems with confirmed BD companions have periods shorter than 2.3 h. As most HW Vir systems are found in photometric surveys this is most likely not due to an selection effect. The HW Vir system with the smallest period is V2008 with a period of 1.56 h (Schaffenroth et al., in press, Sect. 7.6). With our selection criteria, it should be possible to detect substellar companions up to a period of about 2.5-3 h (see Fig. 7.36). With a period of 1.5 h also companions of 25 to 35 $M_{\rm jup}$ could be found. In our photometric follow-up, we found three eclipsing system. The analyses of these systems are are presented in the previous sections. Moreover, only one other system showing a reflection effect together with pulsations was found (Østensen et al. 2013). The minimum mass for the companion is 0.082 $M_{\odot}$, assuming an maximum inclination $i < 65^{\circ}$ because of the absence of eclipses. No other reflection effect binaries could be found. Therefore, we can exclude a reflection effect with an amplitude larger than about 2%.

7.8.2. Discussion

The usual way to find eclipsing sdB+dM systems was via photometric surveys like for example the OGLE survey (see Pietrukowicz et al. 2013), in which 10 new HW Virginis systems were found, with the help of the characteristic lightcurve. These systems have short periods, deep eclipses, and show a reflection effect. Such a lightcurve with these short periodicities is unique to these type of systems.
Our strategy is completely different. We selected our targets from radial velocity variations. Therefore, we can really determine the percentage of systems with reflection effect and/or eclipses. Nine of our observed systems were sdOs or He-sdOs, which are not understood very well until now. All of them show RV variations, but it was not possible to determine periodicitiesm. One of our sdO lightcurves also shows random light variations, which cannot be explained (Geier et al. 2015). Only one of the He-sdOs shows a lightcurve variation that could indicate an ellipsoidal deformation of the sdO. From 49 observed sdB, sdO, or sdOB binaries we found four showing a reflection effect. Three of them showed eclipses and two of them even brown dwarf companions the first two eclipsing sdB+BD systems found (Geier et al. 2011c; Schaffenroth et al. 2014a). Therefore, we conclude that more than 8% of the sdB binaries are showing a reflection effect and more than 4% of the companions to sdBs are substellar objects, which is much more frequent as found in other binaries, which raises the question, if substellar objects can influence stellar evolution.
For most of the observed sdB or sdOB systems, it is possible to exclude typical sdB+dM systems with parameters similar to HW Vir or sdB+BD systems with parameter similar to J1622 with the help of the photometric follow-up. For some targets the lightcurves are too noisy because of bad weather, and/or the measured RV shift is too small. The presence or absence of light variations can help to select very interesting targets for a spectroscopic follow-up. We found several eclipsing binaries, which are very important for the better understanding of the formation of hot subdwarfs and the role of substellar companions. Furthermore, they can help to improve the understanding of the common envelope phase. Systems without reflection effect and high RV shifts are good candidates for white dwarf or even more compact companions like neutron stars or black holes, which were the main goal of the MUCHFUSS project in the beginning.
Figure 7.37 shows the period distribution of the known HW Virginis systems. The fact that in photometric surveys, for which the main selection effect is due to the period and not the mass of the companion, no HW Vir systems with masses below 0.062 $M_{\odot}$ have been found, suggests that they are much less abundant. One explanation for that would be their destruction during the common-envelope phase. The lack of companion masses around 0.1 $M_{\odot}$ cannot be

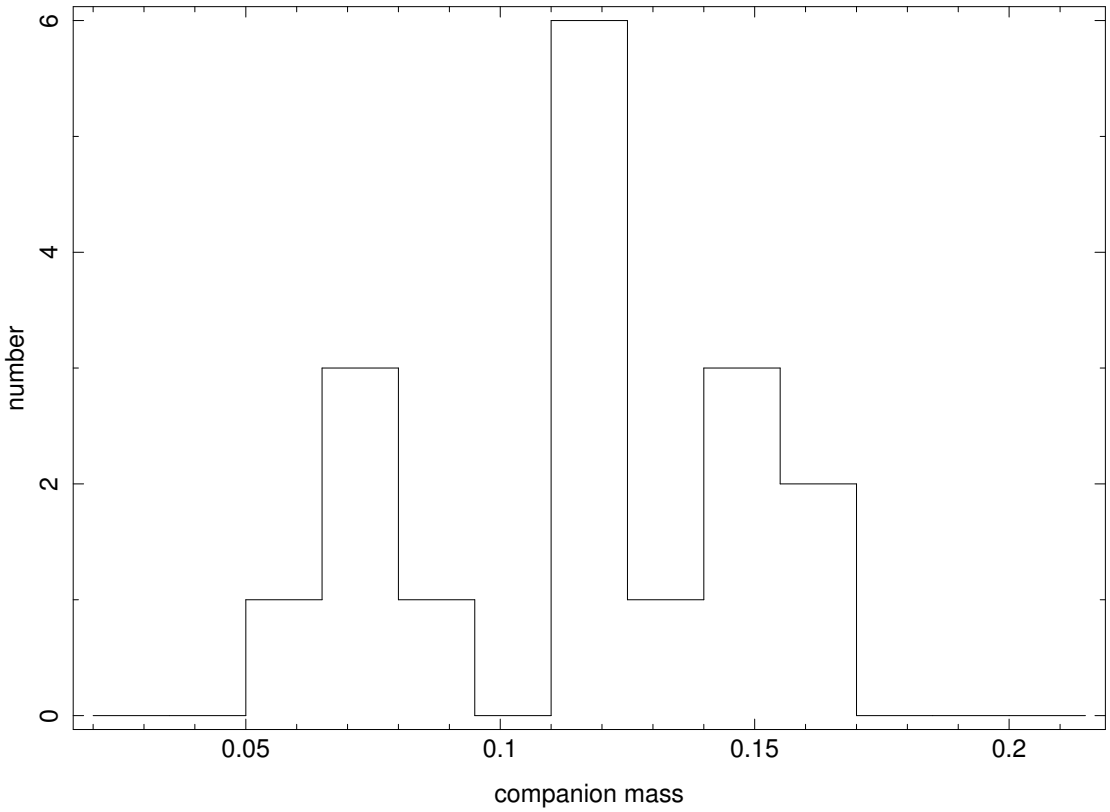

Figure 7.37.: Distribution of the companion masses of the known HW Vir systems.

explained.
Last year the new SDSS data release 10 was published were we discovered $\sim$ 860 new hot subdwarf stars. Therefore, there are many more interesting targets available to extend our photometric and spectroscopic campaigns. Moreover, ten more HW Vir systems were found in the OGLE survey with periods between 0.075 an 0.5 d, which almost doubles the number of known systems. There are also more photometric surveys available that are suitable to find these particular systems. This will allow us to study close binary evolution and especially the, until now, not really understood common envelope phase. With eclipsing post common-envelope systems it is possible to constrain the current prescription of CEE by reconstructing the evolution of post-common-envelope binaries with sdB and low-mass main-sequence companions. This was already done for PCEBs with white dwarf and main-sequence companions (Zorotovic & Schreiber 2013) and could be extended to the HW Virginis systems.

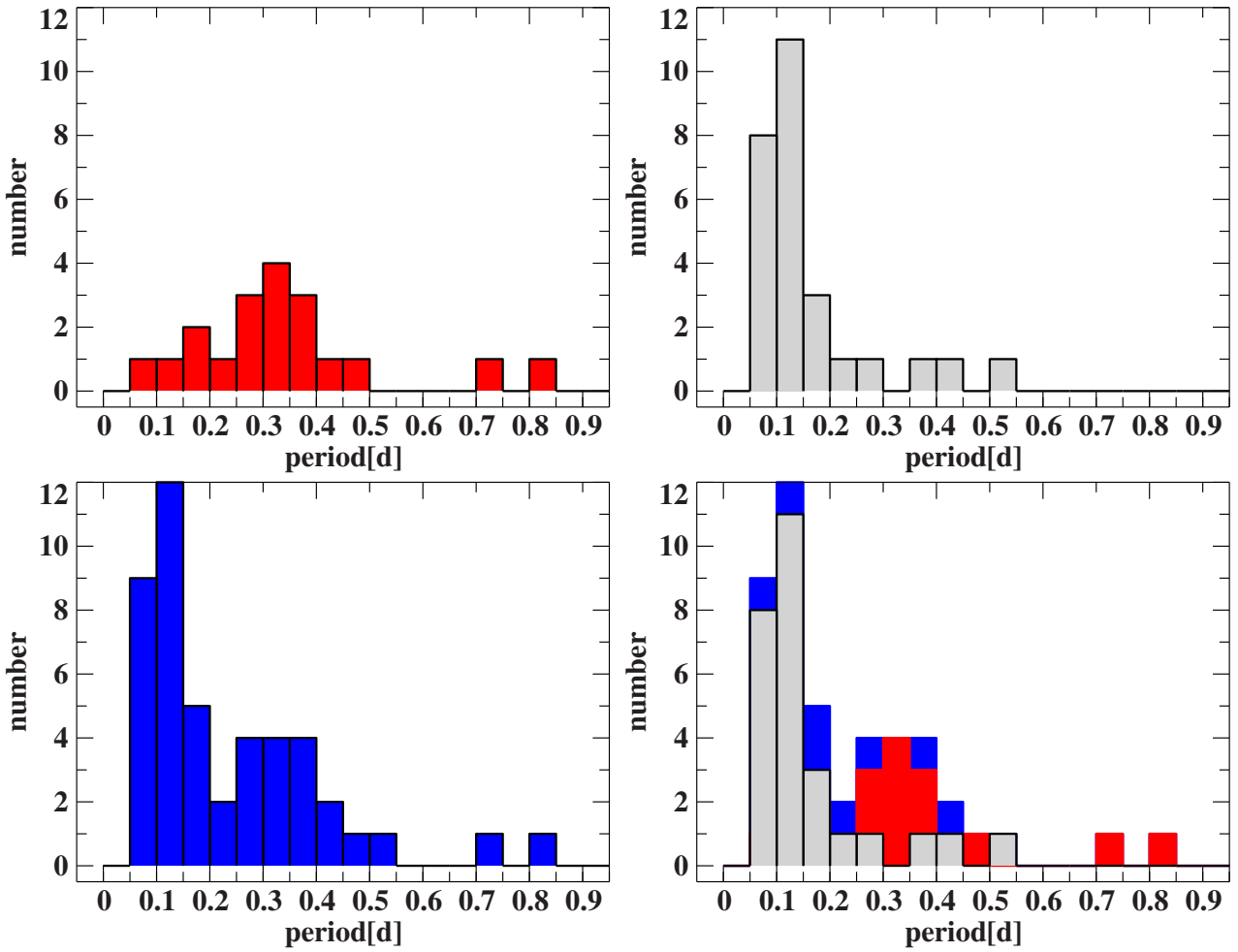

Figure 7.38.: Period distribution: reflection effect binaries (red), HW Vir systems (grey), sum of both (blue)

7.9. Statistics of hot subdwarfs with cool companions

As now already 28 HW Virginis systems, from which 17 have been analysed, are known, we have a large enough sample to investigate the distributions of the different system parameters. This can be compared to the distributions of reflection effect binaries and post common-envelope systems containing white dwarf and late-type main-sequence companions.

Figure 7.38 shows the period distribution of the known sdB+dM systems. The difference between reflection effect binaries and HW Virginis systems are only the eclipses which means the inclination. The probability of an eclipse depends on the radius ratio and the separation of the system. This means that the probability of eclipses decreases with the period.

The period distribution of the HW Virginis systems clearly shows a sharp maximum at around 0.1 d and then a tail until the longest period HW Vir system OGLE-GD-ECL-08577. The reflection effect binaries have larger periods as expected. They show a maximum around 0.35 d. The decrease is probably due to an selection effect, as the reflection effect gets weaker with increasing separation. That means only systems with high inclinations and/or large companions can be detected. Moreover, reflection effect binaries are harder to identify in photometric surveys. To distinguish them from ellipsoidal deformation multi-colour photometry is necessary, which is often not available. Most of the reflection effect binaries with very large periods are pulsators and have been identified due to the reason that long lightcurves have been taken to perform asteroseismology.

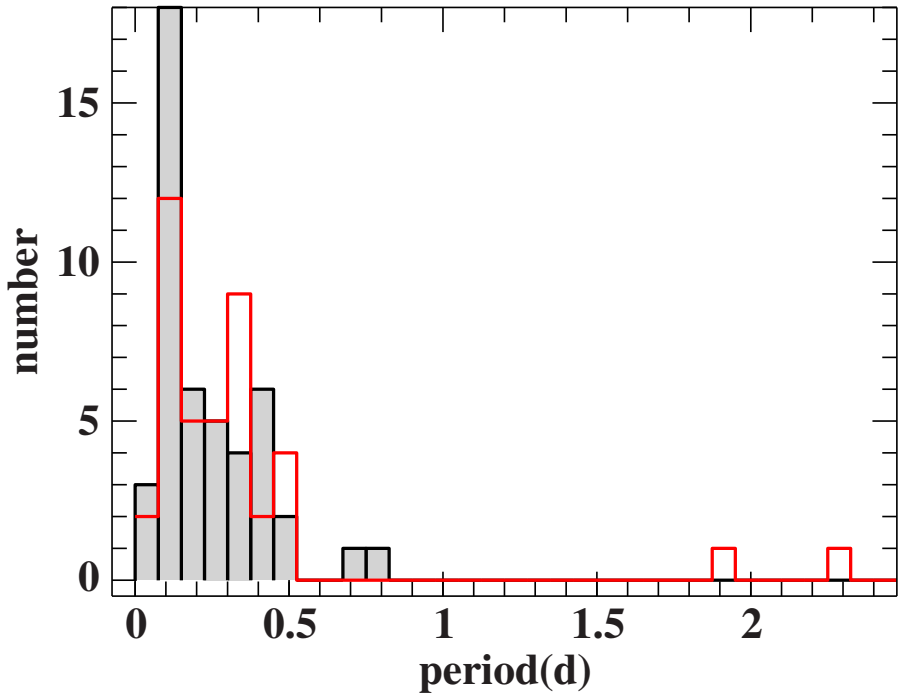

Figure 7.39.: Comparison of the period distribution of sdB+dM (grey) vs WD+dM binaries (red line)

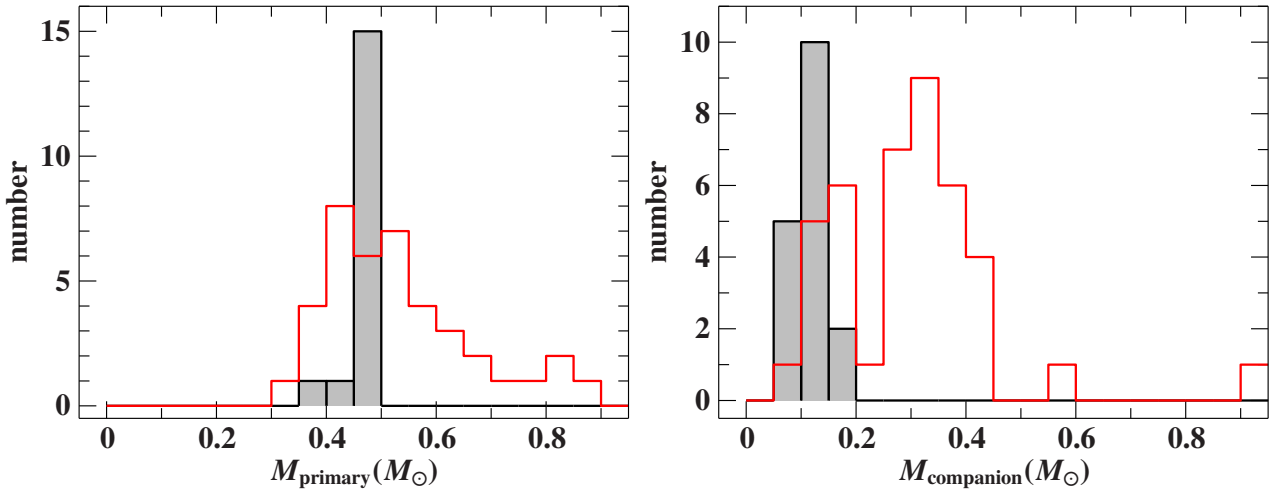

Figure 7.40.: Comparison of the mass distribution of the primary and the secondary companion of the HW Vir systems (grey) to the eclipsing WD+dM systems (red line)

The period distribution of all sdB+dM systems (HW Vir and reflection effect binaries together), however, also shows a bi-modality of the period distribution. Around a period of 0.2 d only few sdB+dM systems were found. This cannot be explained by an selection effect.
WD+dM systems on the other hand have a much higher probability to be eclipsing as sdB+dM systems because of the large radius difference, which is also very sensitive to the white dwarf mass. Therefore, they are found to be eclipsing to very large periods. That is way we compare the period distribution of the eclipsing WD+dM systems with all known sdB+dM systems. This is shown in Figure 7.39. It is visible that both period distributions look very similar. For the eclipsing systems it is furthermore possible to compare the mass distributions of both the primary and the secondary. This is displayed in Fig. 7.40. As expected by theory the mass distribution of the sdBs shows a sharp peak around 0.47 $M_\odot$. The WD mass distribution shows a broader peak with the maximum at a similar mass.

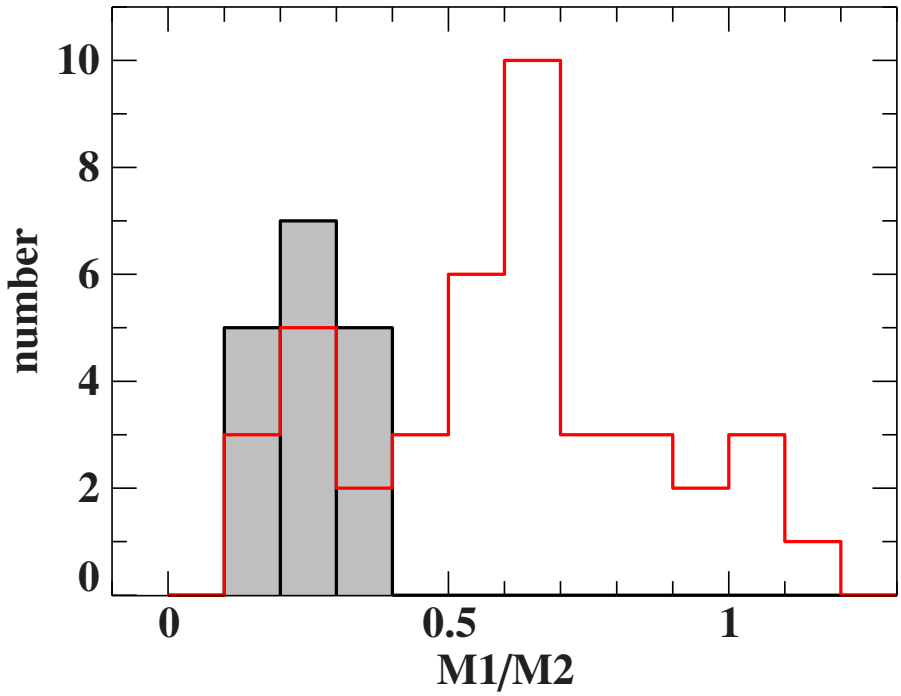

Figure 7.41.: Comparison of the mass ratio distribution of the HW Vir systems (grey) to the eclipsing WD+dM system (red line)

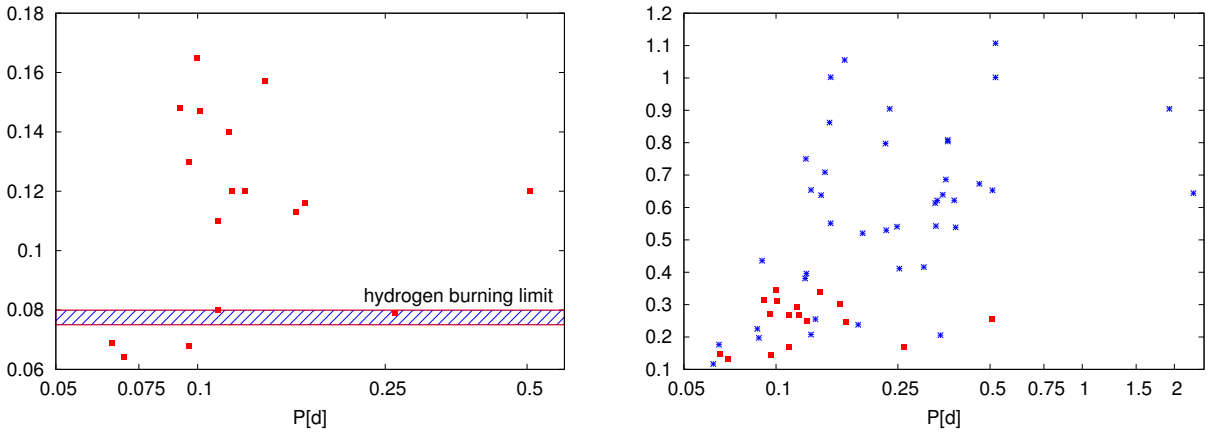

Figure 7.42.: Mass of the companion as function of the period for the HW Virginis systems (left panel) and mass ratio vs period for the HW Vir systems (green x) and WD+dM systems (red +) on the right panel.

Most of the WDs have masses between 0.3 to 0.7 $M_{\odot}$. This is quite different from the mass distribution of all white dwarfs, which shows a maximum around 0.6 $M_{\odot}$ with a much smaller hump at 0.4 $M_{\odot}$ (Kepler et al. 2007). The reason for the smaller mass is probably the additional mass loss during the common-envelope phase.

The distribution of the companions in HW Vir systems shows a peak between 0.06 to 0.2 $M_{\odot}$. As companions with larger masses should be easier to find the absence of companions with masses larger than 0.2 $M_{\odot}$ cannot be a selection effect unless the period for sdB+dM systems with larger masses is much longer. The mass distribution of M dwarf companion in eclipsing WD binaries shows a bi-modal mass distribution, which is even clearer in the mass ratio distribution (Fig. 7.41). One peak can be detected around a companion mass of 0.15 $M_{\odot}$ another peak around 0.35 $M_{\odot}$. The first peak coincides with the peak found in eclipsing sdB binaries but

seems shifted to a bit higher masses. To correct for the broader WD mass distribution the mass ratio distribution is shown. It is clearly visible that the mass ratio distribution shows a broad peak around a mass ratio of 0.32 as expected by the mass distribution. The mass ratio of the WD+dM systems shows the same peak together with a second peak around a mass ratio of 0.65. Four companions to WDs have even larger masses as the WDs. The question is whether this indicates a population similar to sdB+dM systems as well as another population. As all sdB+dM systems will evolve to WD+dM systems but they are not the only progenitors this statement is reasonable.

As already stated before the common-envelope phase is still poorly understood. In a rather simplistic picture the orbital energy of the binary, which scales with the mass of the companion, is deposited into the envelope. If a more massive companion ejects the common envelope earlier, and therefore at a wider orbit than a less massive companion, a correlation between orbital period and minimum companion mass would the expected. However, even if the core masses of the sdB progenitors were very similar, their total masses (core + envelope) might have been quite different, implying different energies to expel the envelope and different final orbital separations. This can partly explain that no correlation can be seen (see Fig. 7.42). Only the substellar companions show the periods shorter than the rest. For all M dwarf companions no correlation is apparent and even the companion to the HW Vir system with the by far largest period OGLE-GD-ECL-08577 has a companion with a quite small mass of only 0.12 $M_{\odot}$. There is also no correlation for the mass ratio with the period for sdB/WD+dM systems. It only looks like that there is a minimum mass ratio that is growing with the period, which could however be a selection effect, as low-mass companions are more difficult to detect as the period increases.

8. Spectrum Synthesis in the UV

The second part of this thesis deals with the analysis of B stars in the UV and the investigation of the unique runaway star HD 271791. In the optical spectra of B stars few metals show spectral lines only some lines (e.g., C, N, O, Si, S). The situation changes in te UV spectral region, where larger number of elements, in particular of the iron group, give rise to a line forest. This comprises also elements beyond the iron group, which are most interesting in connection with the investigation of nucleosynthesis in a core-collapse supernova. In order to facilitate quantitative analyses for the various chemical species, the spectrum synthesis in the UV had to be extended to account for these, which is described in the following.

8.1. Hybrid LTE/NLTE approach

The calculation of a model atmosphere and the resulting spectrum in full NLTE can be highly time consuming on the order of tens of hours on a modern CPU. Even then the complexity of model atoms has to be restricted e.g., by the use of superlevels, i.e. by binning a large number of energy levels into one. While this approach is sufficient for the computation of the model atmosphere, the calculation of realistic synthetic requires a more detailed treatment. Moreover, the determination of the stellar parameter and the abundances typically relies on a grid of synthetic spectra covering a multi-dimensional parameter space ($T_{\rm eff}$, $\log g$, ξ, $n(x)$, ...), which makes the calculation of a large number of synthetic spectra necessary. To limit the numerical effort and use as complex model atoms as possible we employ a hybrid LTE/NLTE approach, i.e. we calculate the atmospheric structure in LTE, and perform line formation calculations in NLTE. This approach is discussed in detail by Nieva & Przybilla (2007) and Przybilla et al. (2011), who also have shown that this is consistent with full NLTE calculations for B-type stars on the main sequence. It is based on the idea that NLTE effects affect the individual spectral lines through departure of the population numbers from LTE values via the line source function, but the overall effects on the atmospheric structure are small, at least in the line forming region. The differences between the atmospheric structure calculated in LTE (Atlas 9, Atlas 12) and NLTE (Tlusty, Fastwind) codes are shown in Fig. 8.3 and will be discussed in detail later. The calculation of a synthetic spectrum is performed in several steps, which use different codes:

- Atlas 12 (Kurucz 1996): computation the atmospheric structure in LTE
- Detail (Giddings 1981; Butler & Giddings 1985): based on the fixed stellar atmosphere calculated by Atlas 12, the coupled radiative transfer and statistical equilibrium equations are solved by Detail to obtain the population numbers and the radiation field in NLTE.
  An important simplification in the hybrid LTE/NLTE approach with respect to full NLTE calculations is that the population number densities of the individual elements are computed separately, i.e. they are treated as a trace species. The line opacity due to other metals is approximated via opacity sampling in LTE usually, as are the metal bound-free background opacities. Hydrogen and helium are always treated in NLTE.
- Surface (Giddings 1981; Butler & Giddings 1985): based on the population numbers determined by Detail, the final synthetic spectrum is calculated by Surface using a

fine frequency grid and detailed line profiles.

8.2. Calculation of oscillator strengths

For the linelists used in SURFACE to calculate the synthetic spectra the line wavelength and the oscillator strength, which is directly related to the line strength, are the most important parameter. Hence, I will give hear a short overview about the different methods used to the oscillator strengths used in this thesis. These oscillator strengths were adopted from different sources. Most of them are calculated, with several teams applying different ab-initio methods. Some were measured in the laboratory. In the following a short overview over the different oscillator strength determinations will be given. Critically evaluated oscillator strengths are provided by the NIST Atomic Spectra Database[1]. However, for heavier elements little data is available there. Therefore, the main source of oscillator strengths were the linelists by Kurucz[2], who collected atomic data from different sources or calculated them with the atomic structure codes by Cowan [3]. Moreover, several other sources were used as indicated in Tables A2 and A3.

8.2.1. Experimental measurement of oscillator strengths

Experiments in absorption and emission spectroscopy have been developed for the determination of oscillator strength values. The state-of-the-art is reviewed by Wahlgren (2010). In emission line spectroscopy an excited level is populated and the subsequent radiation emitted upon its decay is measured. In time-dependent experiments also the rate of decay of the upper-level population and the mean lifetime τ_j of the excited level can be measured. A conversion between emission and absorption oscillator strength is given by the relation

$$f_{ij} = -\frac{g_j}{g_i} f_{ji} \tag{8.1}$$

where g_j and g_i are the statistical weights of the upper and lower level of the transition. Highly important in this context is the so-called branching fraction BF, which is the ratio of the intensity of the line of interest relative to the combined intensity of all emission lines originating from the same upper level. Finally, the oscillator strength can be derived by:

$$f_{ji} = 1.499 \cdot 10^{-8} \lambda^2 \frac{g_j}{g_i} \frac{(BF)_{ji}}{\tau_j} \tag{8.2}$$

where the wavelength λ is given in Å and the life time τ_j in 10^{-8} s.
It is also possible to determine oscillator strength values directly from emission line intensity calibrated by already published values. For this also the temperature of the arc source and the electron density have to be known.

8.2.2. R-matrix method

For the calculation of transition data and electron excitation cross-sections the R-matrix method is one of the most accurate and is used for the atomic data in the NLTE model atoms and some of the oscillator strengths. It solves the many-body time-independent Schrödinger equation :

$$H_{N+1}\Psi = E\Psi = \sum_{i=1}^{N+1} \left\{ -\nabla_i^2 - \frac{2Z}{r_i} + \sum_{j>i}^{N+1} \frac{2}{r_{ij}} \right\} \Psi \tag{8.3}$$

The first term of the Hamiltonian describes the kinetic energy of the electrons, the second the potential energy of the electrons in the field of the nucleus and the third the Coulomb interactions of the electrons with each other.

[1] http://www.nist.gov/pml/data/asd.cfm
[2] http://kurucz.harvard.edu/linelists/
[3] https://www.tcd.ie/Physics/people/Cormac.McGuinness/Cowan/

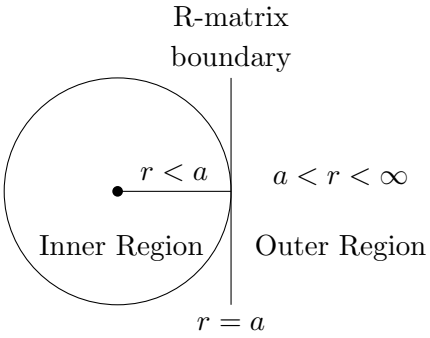

Figure 8.1.: Configuration space in the R-matrix method

The R-matrix method is explained in detail by Hummer et al. (1993) and Berrington et al. (1987), a short summary is also given in the textbook by Pradhan & Nahar (2011). In the $R-$matrix theory the problem is split into two parts. For a radial distance $r > a$ – in the so-called outer region – interactions between the scattered and the target electrons are negligible and the problem is solved using Coulomb functions and, possibly, perturbation theory. In the inner region, $r \leq a$, electron exchange and correlation between the scattered electron and the N-electron target are important, and a non-trivial eigenvalue problem has to be solved. The inner and outer region solutions have to match at $r = a$, as a boundary condition. This is sketched in Fig. 8.1.

To carry out the calculations the $N-$electron target eigenstates Φ_i (with total orbital angular momentum L_i and total spin angular momentum S_i) have to be determined by the diagonalization of the target Hamiltonian $\langle \Phi_i | H_N | \Phi_j \rangle = \epsilon_i \delta_{ij}$. With this help the wavefunction of the complete (N+1) electron system can be determined using the close-coupling (CC) approximation of electron-atom collision theory. In the CC approximation, the (e+ion) atomic system is described by a system of $(N + 1)$ electrons. The ion core, also called target, consists of $N-$ electron states; the $(N+1)$th electron is the "free" electron. The quantum numbers $SLM_SM_L\pi$ give the total angular momenta, spin and parity of the (e + ion) system; these are conserved during the collision process. Each possible transitions $S_iL_il_is_i \rightarrow SL\pi$ is called a channel. In this approximation we get a wavefunction:

$$\Psi = \mathcal{A} \sum_i \Phi_i(x_1, ..x_{N+1}) \frac{1}{r} F_i(r) + \sum_j \chi_j(x_1, ..x_{N+1}) c_j \tag{8.4}$$

Here the Φ_i are the N-electron target wavefunctions for electron coordinates x_i (position+spin), $F_i(r)$ is the radial wavefunction of the colliding electron, and $\mathcal{A} = (N + 1^{-1/2} \sum_{n=1}^{N+1} (-1)^n)$ is the antisymmetrization operator, which ensures that the Pauli exclusion principle is obeyed. The second term in is introduced for the N +1 electron system to allow for electron correlation effects and to ensure completeness of the total wavefunction.

A transition between energy levels is described with the help of a transition matrix $\langle R_{ik} = \Psi_k | \mathbf{P} | \Psi_i \rangle$, where Ψ_k and Ψ_i are the wave functions of the final and initial state, and R_{ik} the transition matrix element of the appropriate multipole operator $\mathbf{P}$. For a electric dipole transition this operator is given either by the dipole length operator $\mathbf{D_L} = e \sum_n \mathbf{r}_n$ or the dipole velocity operator $\mathbf{D_V} = -2e \sum_n \nabla_n$. This matrix can be used to determine the line strength $S = S(i,k) = S(k,i) = |R_{ik}|^2$. The accuracy achieved is given by difference between S_L and S_V. The oscillator strength can then be calculated from the line strength:

$$f_{ik} = \frac{8\pi^2 m \nu_{ik}}{he^2 g_i} S(k,i) \tag{8.5}$$

Table 8.1.: Selection rules for discrete transitions (Drake 2006)

		Electric dipole (E1) ("allowed")	Magnetic dipole (M1) ("forbidden")	Electric quadrupole (E2) ("forbidden")
Rigorous rules	1.	$\Delta J = 0, \pm 1$ (except $0 \nleftrightarrow 0$)	$\Delta J = 0, \pm 1$ (except $0 \nleftrightarrow 0$)	$\Delta J = 0, \pm 1, \pm 2$ (except $0 \nleftrightarrow 0, 1/2 \nleftrightarrow 1/2, 0 \nleftrightarrow 1$)
	2.	$\Delta M = 0, \pm 1$ (except $0 \nleftrightarrow 0$ when $\Delta J = 1$)	$\Delta M = 0, \pm 1$ (except $0 \nleftrightarrow 0$ when $\Delta J = 1$)	$\Delta M = 0, \pm 1 \pm 2$
	3.	Parity change	no parity change	no parity change
With negligible configuration interactions	4.	One electron jumping, with $\Delta l = \pm 1$, Δn arbitrary	No change in electron configuration; i.e., for all electrons, $\Delta l = 0, \Delta n = 0$	No change in electron configuration; or one electron jumping with $\Delta l = 0, \pm 2, \Delta n$ arbitrary
For LS coupling only	5.	$\Delta S = 0$	$\Delta S = 0$	$\Delta S = 0$
	6.	$\Delta L = 0, \pm 1$ (except $0 \nleftrightarrow 0$)	$\Delta L = 0$ $\Delta J = \pm 1$	$\Delta L = 0, \pm 1, \pm 2$ (except $0 \nleftrightarrow 0, 0 \nleftrightarrow 1$)

Depending on the mass of the atom also different approximations can be applied. For light atoms, where both Z and the residual charge $z = Z - N$ are small, the Schrödinger equation can be solved with the Hamiltonian given in eq. 8.3 in the Russell-Saunders (LS) coupling. In the case of heavier elements, like those of the iron group additional relativistic effects have to be considered, e.g. the spin-orbit interaction. This can be done by adopting the Hamiltonian in the low-Z Breit-Pauli approximation:

$$H_{N+1}^{\mathrm{BP}} = H_{N+1} + H_{n+1}^{\mathrm{mass}} + H_{n+1}^{\mathrm{Dar}} + H_{n+1}^{\mathrm{so}} = H_{N+1} - \frac{p^4}{8m^3c^2} - \frac{Ze^2\hbar^2}{8m^2c^2}\nabla^2\left(\frac{1}{r}\right) + \frac{Ze^2\hbar^2}{2m^2c^2r^3}\mathbf{l}\cdot\mathbf{s}, \quad (8.6)$$

where H_{N+1} is the non-relativistic Hamilton given in eq. 8.3, together with the one-body mass correction term, the Darwin term used to explain the fine-structure of hydrogen and the spin-orbit term resulting from the reduction of the Dirac equation to the Pauli form. For even heavier elements a more satisfactory approach is to use the Dirac Hamiltonian.

Radiative transitions are, moreover, restricted by selection rules, that are given in Table 8.1. Electric dipole transitions are called 'allowed' transitions as they have much higher transition probabilities than the 'forbidden' transitions, which can occur via magnetic or electric quadruple transitions. The forbidden transitions can typically be observed only in low density environments as for example planetary nebula because of their much lower transition probabilities.

8.2.3. Cowan code

A lot of the used oscillator strength values were calculated by the Cowan atomic structure code. This suite of four programs calculates atomic structures and spectra via the superposition-of-configuration method. In this method an approximate Hamiltonian is obtained by summing the one-electron operator for an N electron atom of nuclear charge Z:

$$H = H_{kin} + H_{e-nuc} + H_{e-e} + H_{s-o} = \sum_i \nabla_i^2 - \sum_i \frac{2Z}{r_i} + \sum_{i>j} \frac{2}{r_i j} + \sum_i \zeta_i(r_i)\mathbf{l}_i\mathbf{s}_i \quad (8.7)$$

with r_{ij} the distance of the ith electron from the nucleus and $\xi_i(R)$ is the spin-orbit interaction term. The multi-electron wavefunction is expanded in terms of one-electron Pauli spinors $\varphi(\mathbf{x})$ which are separated into radial, angular and spin parts.

$$\varphi(\mathbf{x}) = \frac{1}{r}P_{n_i l_i}(r)Y_{l_i m_i}(\theta,\phi)\chi_{m_{s_i}}(s_z) \quad (8.8)$$

with the principal quantum number of the ith electron n_i, the azimuthal quantum number l_i, the magnetic quantum number m_i, the spin quantum numberm_{s_i}, the radial wavefunction P_{nl}, the angular wave function Y_{lm} and the spin wave function χ_{m_s}. Then the basis of multi-electron,

antisymmetric wavefunctions are the determinants

$$\Phi = \begin{vmatrix} \varphi_1(\mathbf{x}_1) & . & \varphi_1(\mathbf{x}_N) \\ . & . & . \\ \varphi_N(\mathbf{x}_1) & . & \varphi_N(\mathbf{x}_N) \end{vmatrix} \tag{8.9}$$

The matrix elements of the Hamiltonian between determinant functions can be reduced to one and two electron terms

$$\langle \Phi | H | \Phi' \rangle = E_{av}\delta_{\Phi\Phi'} + \sum_{ijk}[f_k F_k(l_i l_j) + g_k G_k(l_i l_j)] + \sum_i d_i \zeta(l_i) \tag{8.10}$$

with the center-of-gravity energy (E_{av}), the radial coulomb integrals F_k and G_k, spin-orbit integrals ζ The calculations are carried out in intermediate coupling. The oscillator strengths are then calculated by a transition matrix, similar to the R-matrix method.

- the code RCN calculates one-electron radial wavefunctions (bound or free) for each of any number of specified electron configurations, using the Hartree-Fock or any of several more approximate methods. The principal output, for each configuration, consists of E_{av} of the configuration, and F_k, G_k and ζ required to calculate the energy levels for that configuration.

- the code RCN2 is an interface program that uses the output wave- functions from RCN to calculate the configuration-interaction Coulomb integrals (R_k) between each pair of interacting configurations, and the electric-dipole (E1) and/or electric quadrupole (E2) radial integrals between each pair of configurations.

- the code RCG sets up energy matrices for each possible value of the total angular momentum J, diagonalizes each matrix to get eigenvalues (energy levels) and eigenvectors (multi-configuration, intermediate- coupling wavefunctions in various possible angular-momentum-coupling representations), and then computes M1 (magnetic dipole), E2, and/or E1 radiation spectra, with wavelengths, oscillator strengths, radiative transition probabilities, and radiative lifetimes. Other options, when a continuum (free) electron is present, are photoionization cross- sections, autoionization transition probabilities, total lifetimes, branching ratios for autoionization, and plane-wave Born collision strengths.

- When higher accuracy results are desired, RCE can be used to vary the various radial energy parameters E_{av}, F_k, G_k, ζ, and R_k to make a least-squares fit of experimental energy levels by an iterative procedure. The resulting least-squares-fit parameters can then be used to repeat the RCG calculation with the improved energy levels and (presumeably) wavefunctions.

A detailed description is found in the textbook by Cowan (1981).

8.3. Atomic Data

We employed the available NLTE model atoms (see Table A1) as a starting point to assemble a database that facilitates UV spectrum synthesis to be performed. All additional elements are considered assuming LTE for the moment. Extended line lists comprising *all* the data that could be extracted from the literature had to be implemented for the formal solution with Surface. As the calculation of atomic data, in particular oscillator strengths is beyond the scope of this thesis, we collected for each transition the wavelength of the spectral line, the oscillator strengths, the energies of the levels of the transition, and the broadening parameters from different literature sources and formatted them according to the data requirements of Surface. Table A2 and A3 show the different sources used for the line-lists. Figure 8.2 shows a periodic table that indicates all elements available in our spectrum synthesis.

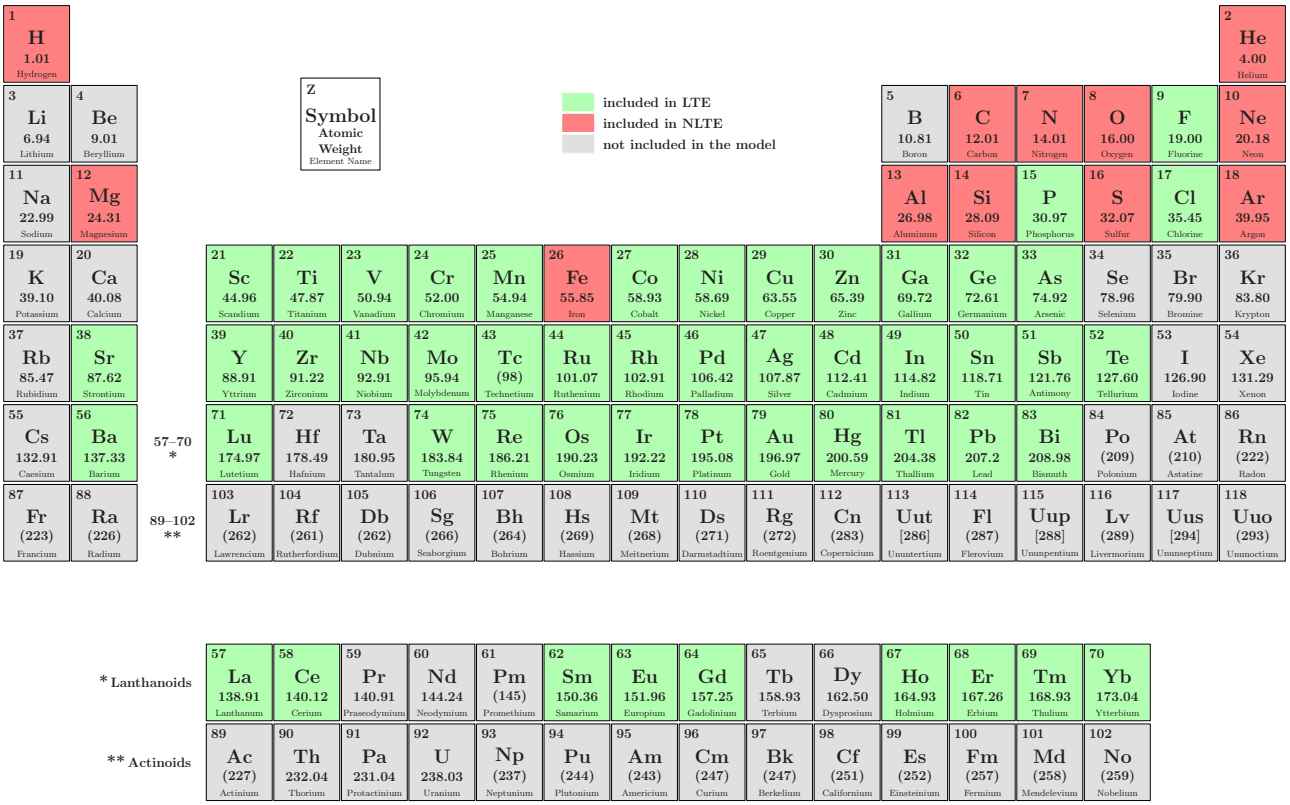

Figure 8.2.: Periodic table showing the elements included in our spectrum synthesis. Red marked elements were calculated in NLTE, green marked elements only in LTE.

8.4. Tests

In order to constrain the accuracy of our spectrum synthesis in the UV we performed several tests. Numerous very strong lines are found in the UV, which are formed throughout most parts of the atmosphere, from the deep continuum forming layers to the outermost layers in the near-black line cores. Thereby they trace the local conditions throughout the stellar atmosphere, facilitating the degree of realism of the model calculations to be tested. As we employ hydrostatic and plane-parallel atmosphere structures calculated in LTE by ATLAS, we first compared ATLAS models with the structure calculated by the NLTE codes TLUSTY (hydrostatic and plane-parallel) and FASTWIND (hydrostatic and spherical). This is displayed Fig. 8.3, which shows the temperature, pressure and density structure. One finds that all the different atmospheric structures agree well in all regions where the line formation takes place. The largest discrepancy show the structure calculated by the NLTE code FASTWIND, which also considers mass loss by stellar winds, calculated with a very low mass loss of $\dot{M} = 10^{-11}\,M_{\odot}\mathrm{yr}^{-1}$, which is expected for B-type stars. The comparison of the structure calculated by ATLAS with the NLTE TLUSTY atmospheric structure shows no difference in P and n_e and only small deviations of about 5-10% in T.

Moreover, we compared the spectral energy distribution of synthetic spectra calculated by different codes, see Fig. 8.4. Great agreement is found for all models in the optical. At wavelengths smaller than 2000 Å, on the other hand, the difference is increasing and is about 10% at 1200 Å. The deviation found between the synthetic spectrum calculated with ADS and the model calculated by FASTWIND might be because of the differences in the atmospheric structure. The discrepancy between ADS and TLUSTY SYNSPEC is probably due to different opacities used. The TLUSTY models consider only the light, some α-elements and iron. A final statement on which of the model approaches comes closest to reality cannot be given here, further

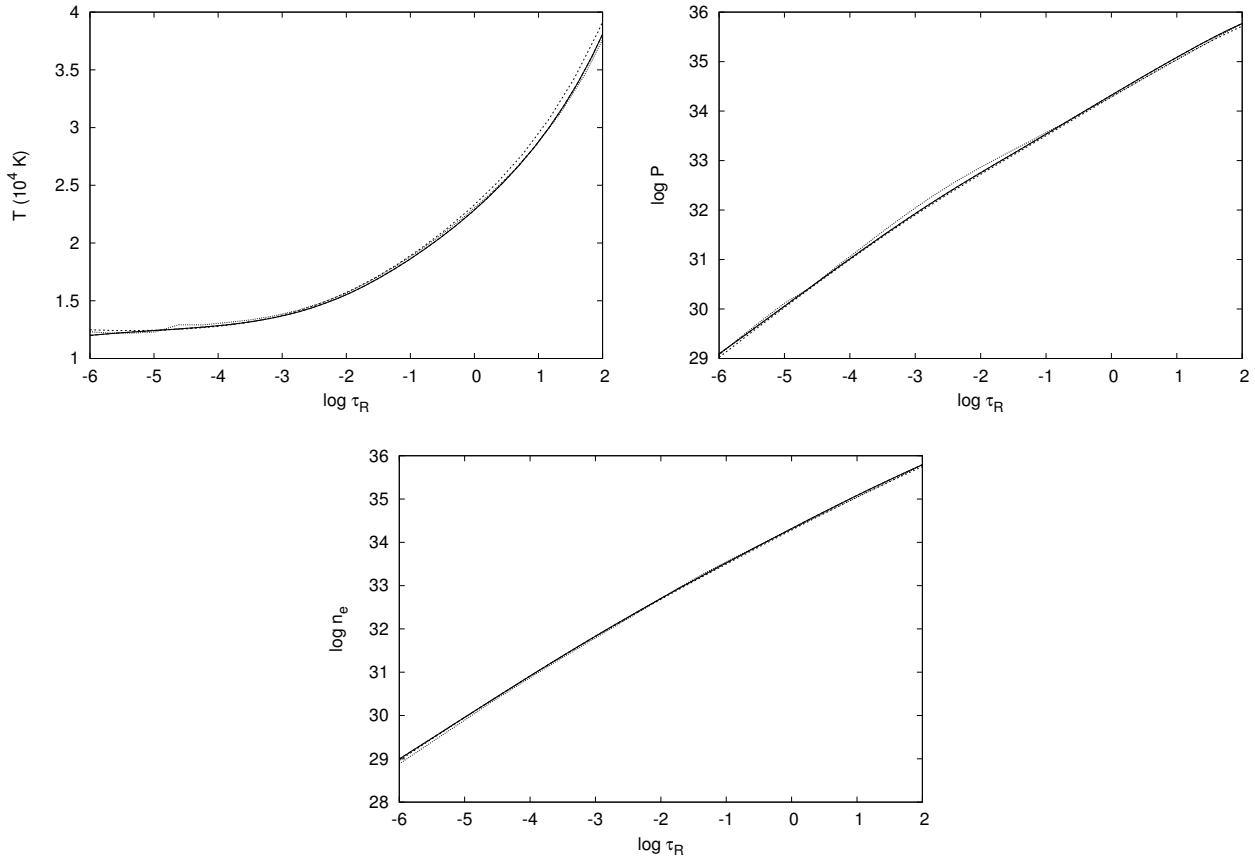

Figure 8.3.: Comparison of different present-day model atmospheres: temperature structure (top left), pressure structure (top right) and electron density (bottom)for a model with $T_{\rm eff} = 18000$ K and $\log g = 3.75$ as a function of the Rosseland optical depth. Full line: ATLAS 9, long-dashed line: ATLAS 12, short-dashed line: TLUSTY, dotted line: FASTWIND ($\dot{\rm M} = 10^{-11}\,M_{\odot}{\rm yr}^{-1}$)

investigations are required.

Another test compared the line profiles of the model calculated fully in NLTE by TLUSTY and SYNSPEC and our hybrid method. The comparison is displayed in Fig. 8.5 for two different wavelength ranges. The difference is shown in each case in the lower panel. Both models are very similar, however some small differences in the line depths are visible. Reasons for these may be differences in the atomic data employed, while the small differences in the temperature structure in the outer atmosphere do not seem to matter. Systematic effects are not found.

In order to check the reliability of the NLTE calculations in the case of iron, which gives rise to the majority of the lines the observed lines, we performed an abundance analysis for all singe, un-blended lines for a calculation of iron in NLTE and LTE in the star.

Figure 8.6 shows the difference between abundances determined in LTE and NLTE. As expected, the LTE abundances show a bigger scatter in the NUV. However, the NLTE abundances start to develop a scatter similar to that of the LTE abundances in the FUV. This may be better seen in Fig. 8.7, which shows only the NLTE abundances. For wavelengths longer than 2400 Å the scatter in the iron abundances is about 0.2 dex, which increases towards the blue the scatter to about 0.6 dex. A close inspection shows that the increase in scatter occurs mostly in Fe III, which could be interpreted in terms of deficits in the model atoms among the high-excitation levels of Fe III. This will require further investigations, which, however are beyond the scope of the present work.

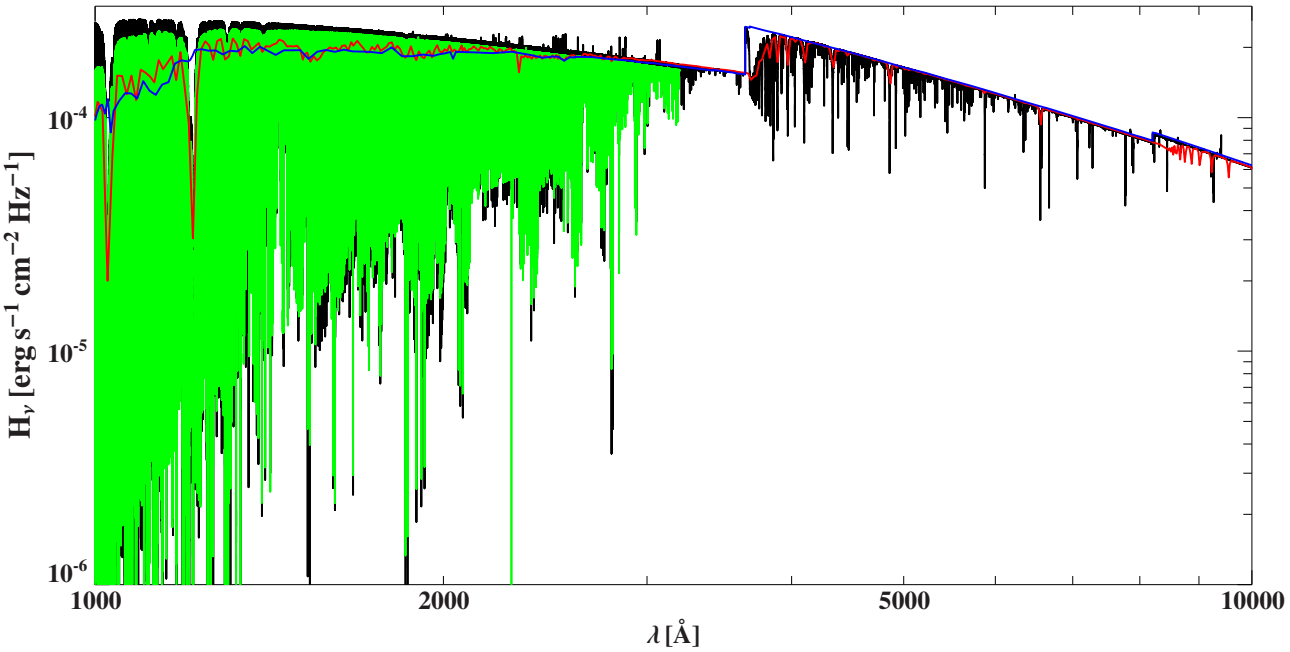

Figure 8.4.: Comparison of the spectral energy distribution of different models: ADS (black), TLUSTY Synspec (green), ATLAS (red), FASTWIND (blue)

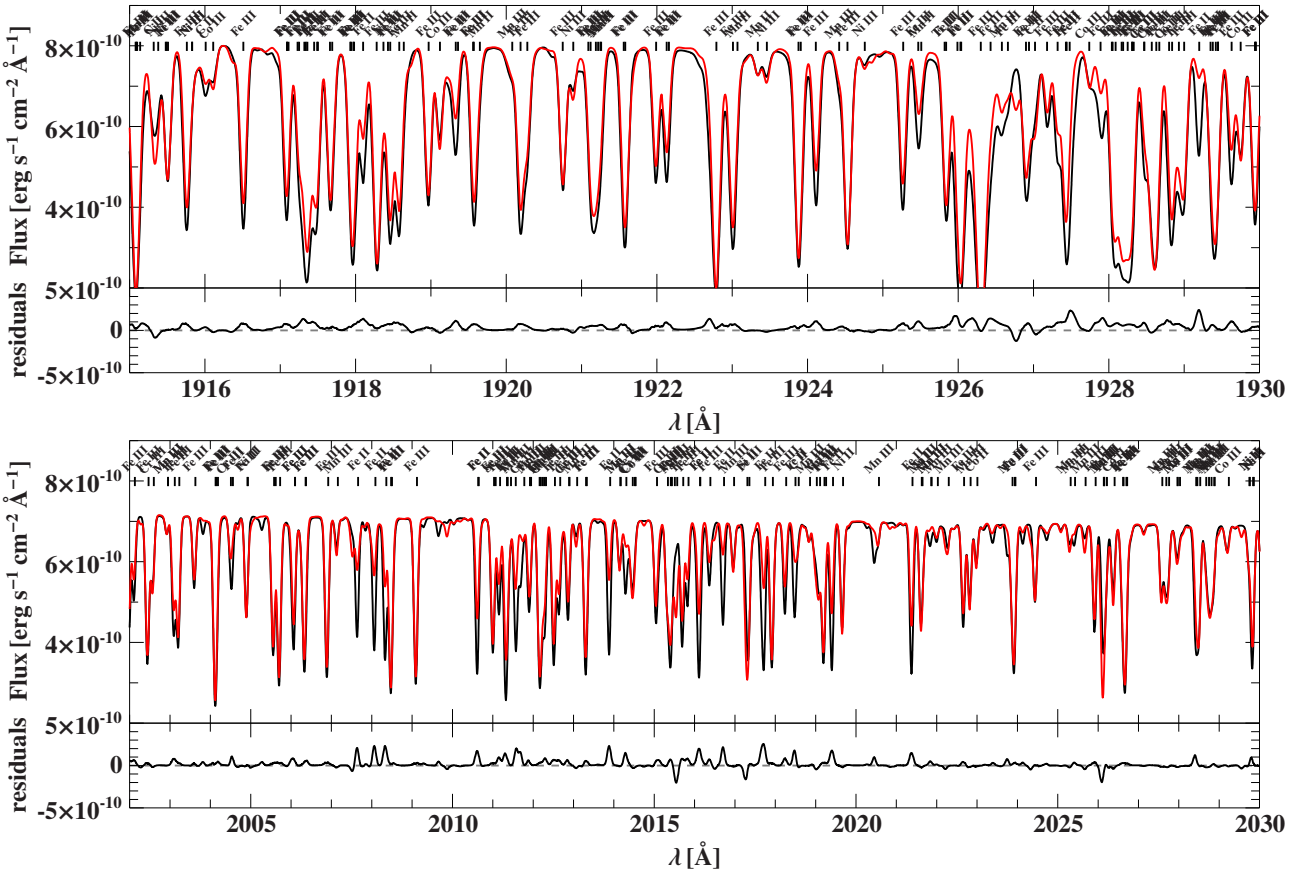

Figure 8.5.: Comparison of a synthetic spectrum with a temperature of $T_{\rm eff}$18000 K and a surface gravity $\log g = 3.75$ in different wavelength regions; the upper panel shows a model computed with TLUSTY/Synspec (red) and with ADS (black), the lower panel shows the differences between both models. The lower figures also shows the observation in blue.

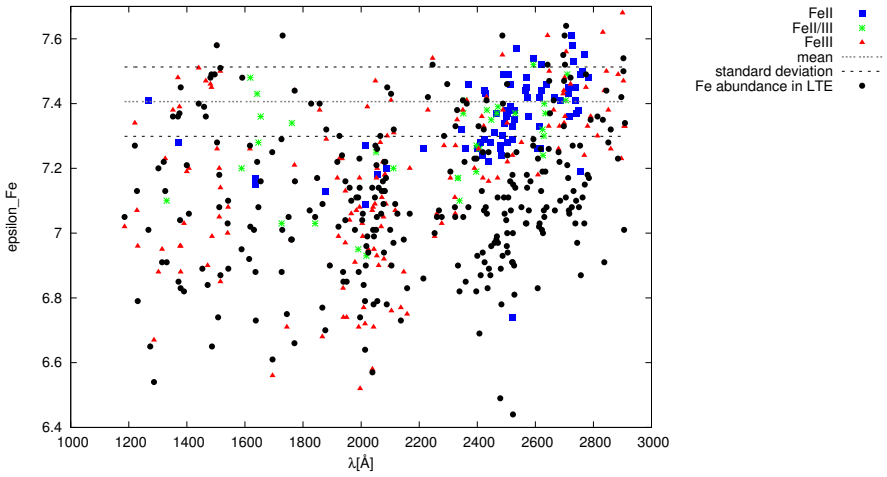

Figure 8.6.: Iron abundance for all single lines, which are not blended with lines from other elements for HR 1840 using a NLTE and a LTE model. Each point represents an abundance measurement at a certain wavelength. Points from abundance measurements in LTE and NLTE at the same wavelength belong to each other. The different symbols in the NLTE abundances illustrate the ionization stage of the measured line (Fe II or Fe III or blends between Fe II and III).

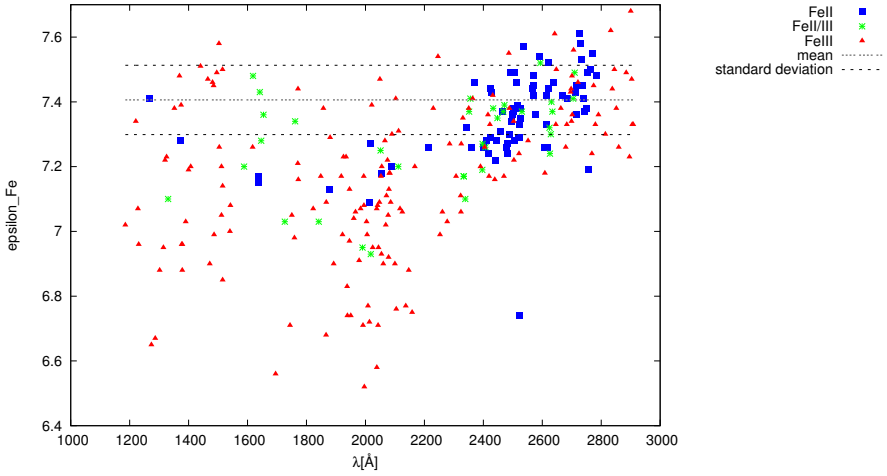

Figure 8.7.: Same as Fig. 8.6, with the LTE results removed. The wavelength range in the NUV with the much smaller scatter was used to determine the stellar iron abundance together with an error from the standard deviation.

Figure 8.8 shows LTE abundances for nickel. Similar to the case of iron we find a large scatter in the line-to-line abundance. In particular the systematically lower abundances for the lines of the minor ion Ni II by almost 0.6 dex lower than the abundances derived from Ni III indicate the presence of NLTE effects that are currently unaccounted for. As the atomic structure of nickel is similar to that of iron, the NLTE effects should be similar, i.e. driven by the overionization of Ni II with respect to Ni III. Consequently, low-lying Ni II are depopulated relative to LTE, which leads to weaker lines that are interpolated interpreted as indicative for low abundances in an LTE analysis.

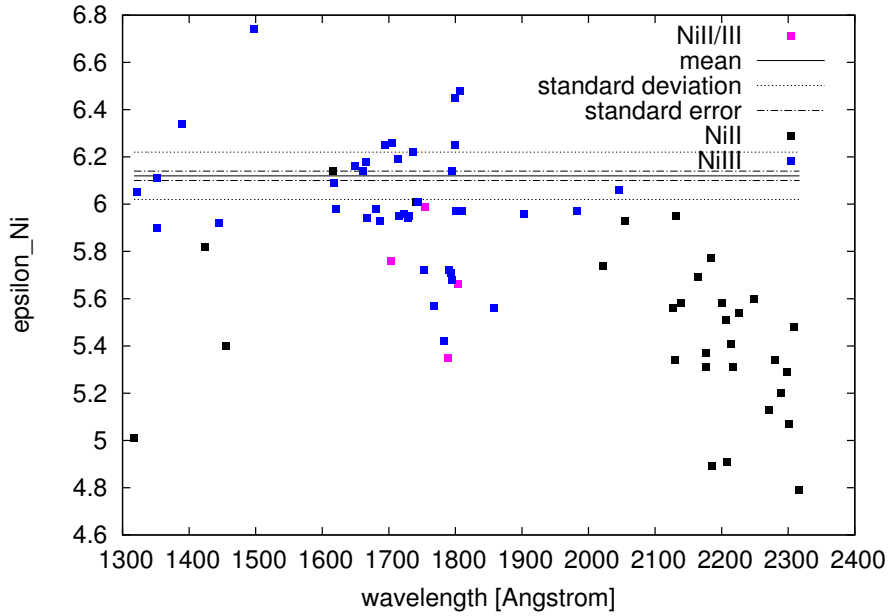

Figure 8.8.: LTE Nickel abundance for all single, unblended lines for HR 1840 from an LTE analysis. The large scatter and the systematically lower abundances for Ni II imply the presence of NLTE effects.

8.5. Spectral energy distribution

To test our model we also compared the spectral energy distribution to three flux standard stars from CALSPEC[4]. CALSPEC contains the composite stellar spectra that are flux standards on the HST system. It is based on three standard candles: the hot, pure hydrogen white dwarf stars G 191B2B, GD 153, and GD 71, which have TLUSTY NLTE flux calculations that require the atomic physics for only one atom. These model flux distributions are normalized to the absolute flux for Vega of $3.46 \cdot 10^{-9}$ erg cm^{-2} s^{-1}Å^{-1} at 5556 Å using precise Landolt V band photometry and the V bandpass function corrected for atmospheric transmission by M. Cohen. The three primary WD standards provide absolute flux calibrations for spectrophotometry from the instruments FOS, STIS, and NICMOS on the HST. 32 stellar spectral energy distributions (SEDs) with a complete wavelength coverage have been constructed with a primary pedigree from the STIS data, which extends from 1150 Å for the hot stars to a long wavelength limit of 1 μm. We adopted three different standard stars from this catalogue with different temperatures for our tests.

Alcaid

The second flux standard star we used for comparison is Alcaid (η Uma), which is a B3V star with a magnitude of $V = 1.86$. It has a similar temperature as the runaway star HD 271791 studied later in Chapt. 10. We calculated a model spectrum with $T_{\rm eff} = 17000$ K and $\log g = 4.3$ (adopted from Adelman et al. (2002) for this star. The comparison is shown in Fig. 8.9. The STIS spectrum from 1150 to 3070 Å, which is consistent with the wavelength coverage of the runaway star, is matched perfectly by our model.

[4] http://www.stsci.edu/hst/observatory/crds/calspec.html

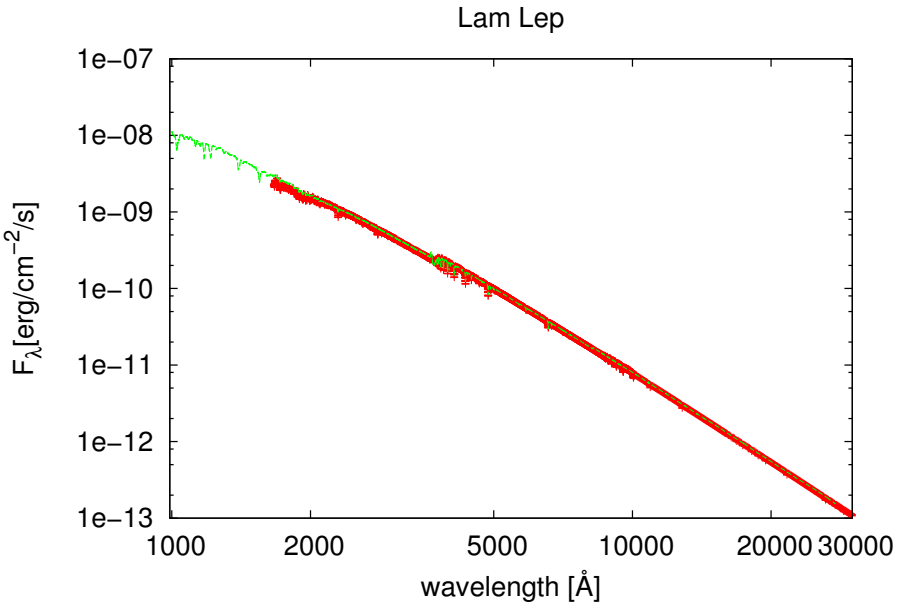

Figure 8.10.: Comparison of the STIS spectrum of λ Lep with an ADS model spectrum of $T_{\rm eff}$ = 30400 K and $\log g = 4.3$ (green line).

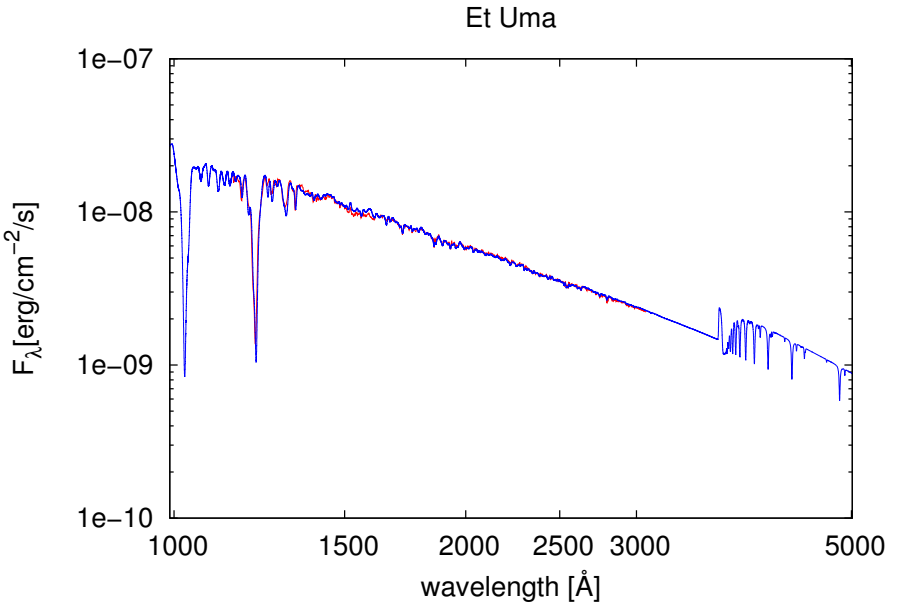

Figure 8.9.: Comparison of the STIS observation of Alcaid (red) with an ADS model spectrum with $T_{\rm eff}$ = 17000 K and $\log g = 4.3$.

λ Lep

To cover the early B stars, we also compared our model spectra to λ Lep, which is a B0.5V star with a magnitude of $V = 4.29$. We calculated a model with $T_{\rm eff}$ = 30400 K and $\log g = 4.3$ (adopted from Nieva & Przybilla (2012), which is compared to the STIS spectrum in Fig. 8.10. The available STIS spectrum covers only the wavelength larger than 1670 Å. A first comparison showed an two high flux of our model for wavelengths smaller than 2000 Å. This indicates we have to consider reddening. Figure 8.10 shows the comparison of our model with a reddening $E(B-V) = 0.02$.

9. Spectroscopic analysis of four bright B stars in the UV

The previous described line-formation calculations for the UV spectral region shall now be employed to derive abundances of the iron-group elements for four stars covering the temperature range of the early B-type stars. As the light at UV wavelengths is blocked by the Earth's atmosphere, only a space telescope is able to observe UV spectra.
The Hubble Space Telescope (HST) is a space telescope that was launched into low Earth orbit in 1990, and is still in operation. With a 2.4-meter (7.9 ft) mirror, Hubble's four main instruments can observe in the near ultraviolet, visible, and near infrared wavelength regions. The operation of the HST may continue until 2020. At the moment no successor is scheduled that is able to observe the UV.
For spectral observations with the HST two different spectrographs are available. The Space Telescope Imaging Spectrograph (STIS[1]) was installed onboard HST during Servicing Mission (SM) 2 in 1997 and operated until an electronic failure in 2004. After it was successfully repaired during SM4 in 2009 it was able to resume operations with all ultraviolet and optical channels. STIS is a versatile imaging spectrograph, providing spatially resolved spectroscopy in the UV and optical, high spatial resolution echelle spectroscopy in the UV, solar-blind imaging in the UV, and direct and coronagraphic imaging in the optical. More details of the design of STIS are described in Woodgate et al. (1998). In the UV, either low resolution long-slit spectra ($R \sim 1000 - 1500$) and medium resolution long-slit spectra ($R \sim 10\,000 - 17\,000$), or medium resolution echelle spectra with $R \sim 30\,000 - 45\,000$ with a broader wavelength coverage of about 550 Å, or with high resolution echelle spectra with $R = 114\,000$ with a small wavelength coverage of about 200 Å can be observed. STIS has three large-format (1024 x 1024 pixel) detectors, optimized for different wavelengths:

- CCD: Scientific Image Technologies (SITe) CCD with $\sim$ 0.05 arcsecond square pixels, covering a nominal 52 x 52 arcsecond square field of view (FOV), operating from $\sim$ 2000 to 10300 Å.
- NUV-MAMA: Cs2Te Multi-Anode Microchannel Array (MAMA) detector with $\sim$ 0.024 arcsecond square pixels, and a nominal 25 x 25 arcsecond square field of view (FOV), operating in the near ultraviolet from 1600 to 3100 Å.
- FUV-MAMA: Solar-blind CsI MAMA with $\sim$ 0.024 arcsec-pixels, and a nominal 25 x 25 arcsecond square FOV, operating in the far ultraviolet from 1150 to 1700 Å.

For the data reduction of STIS data a pipeline exists (calstis), which is part of the STSDAS[2]. (Space Telescope Science Data Analysis System) package running under IRAF:. Calstis is several pipelines in one, reflecting the complexity and diversity of STIS observing modes. More details can be found in the STIS data handbook[3]. The acquisition frames are not reduced by calstis. All other science data are processed through basic two-dimensional image reduction

[1] http://www.stsci.edu/hst/stis/
[2] http://www.stsci.edu/institute/software_hardware/stsdas
[3] http://www.stsci.edu/hst/stis/documents/handbooks/handbooks/currentDHB/

(available in IRAF as basic2d), which includes such things as bias subtraction, dark subtraction, flat fielding, and linearity correction. Spectral data that were taken using a sufficiently small aperture, and which were also taken together with a wavelength calibration spectrum, are then passed through spectroscopic reduction to produce flux and wavelength calibrated science data. For first order spectra modes, a two-dimensional rectified spectral image is produced, and for both echelle and first order modes, a one-dimensional, background subtracted spectrum is also produced. For first order spectral observations where the target was behind the fiducial bars of one of the long slits, only two-dimensional rectified spectra are produced. The resulting one-dimensional final science spectrum is saved in a FITS table. In the case of the echelle spectra all orders are stored in different table extensions and have to be co-added by hand.

During SM4 also another spectrograph, the Cosmic Origins Spectrograph[4] (COS), was installed on the HST. COS is designed to perform high-sensitivity, medium- and low-resolution spectroscopy of astronomical objects in the $1150-3200$ Å wavelength range. COS significantly enhances the spectroscopic capabilities of HST at ultraviolet wavelengths, providing observers with unparalleled opportunities for observing faint sources of ultraviolet light. COS has a simple optical design that minimizes the number of reflections required to disperse and detect ultraviolet light in its two channels. An optic selection mechanism configures either the low-dispersion grating ($R \sim 1500 - 4000$) or one of two medium-dispersion gratings ($R \sim 20\,000$) for the observation. The two COS detectors are photon-counting devices. The FUV detector is a windowless, crossed delay-line micro-channel plate (MCP) stack optimized for the 1150 to 1775 Å bandpass. To achieve the length required to capture the entire projected COS spectrum, two detector segments are placed end to end with a small gap between them. The two detector segments are independently operable. The NUV detector is a multi-anode microchannel array (MAMA) optimized for spectroscopic observations in the 1700-3200 Å bandpass, similar to the NUV MAMA used on STIS. The data reduction pipeline for COS (calcos) has been developed by the Space Telescope Science Institute (STScI) to support the calibration of HST/COS data. More details can be found in the COS data handbook[5]. Calcos is written in Python, which enables the pipeline and users to take advantage of an extremely productive, open-source, easy-to-read scripting language, with many libraries for data reduction and analysis. Calcos is part of the stsci_python package[6]. All science data, but the acquisition frames, are completely calibrated. This includes geometric and thermal correction for the FUV data, flat fielding, linearity corrections and pulse height filtering. The spectroscopic data are also flux calibrated and corrected for time dependence in the instrumental sensitivity. For spectral data, calcos extracts a spectrum from the flat-fielded image, computes associated wavelengths, and converts the count rates to flux densities, yielding a one-dimensional, background subtracted spectrum. For FUV data there are normally two spectra, one from segment A and one from segment B. For NUV data there will normally be three spectra, one for each spectral 'stripe'. When an observation consists of multiple exposures, these are combined into a single, summed spectrum.

The HST archive contains a large number of high-resolution data of bright B stars observed with the STIS spectrograph. The STIS data that can be downloaded from the HST archive, is already reduced with the HST pipeline. All high resolution data taken during the initial seven years of operations (1997-2004) of STIS are summarised in StarCAT[7] (HST STIS Echelle Spectral Catalog of Stars), which is based on 3184 echelle mode observations of 545 distinct targets. Not all of these spectra cover the whole UV wavelength range. Therefore, there now exists a HST Large Treasury Project, whose aim is to collect high-quality ultraviolet spectra of representative bright stars using STIS. This project is called ASTRAL[8] (HST STIS Advanced Spectral Library

[4] http://www.stsci.edu/hst/cos/
[5] http://www.stsci.edu/hst/cos/documents/handbooks/datahandbook
[6] http://www.stsci.edu/institute/software_hardware/pyraf/stsci_python/
[7] http://casa.colorado.edu/~ayres/StarCAT/
[8] http://casa.colorado.edu/~ayres/ASTRAL/

Project). In the case of hot stars 21 diverse objects were observed with an allocation of 230 orbits. The wavelength coverage over the whole UV (1150-3100 Å) was achieved by combing several spectra taken in multiple FUV (1150-1700 Å) and NUV (1600-3100 Å) prime grating settings of STIS in medium as well as high resolution.
Moreover, most bright B stars were observed with the International Ultraviolet Explorer (IUE), which performed spectrophotometry at high (0.1-0.3 Å) and low (6-7 Å) resolution between 1150 Å and 3200 Å. IUE was launched in January 1978. Over 104 000 ultraviolet spectra were obtained until the shut-down in 1996. The switch-off occurred for financial reasons, while the telescope was still functioning at near-original efficiency. However, the high quality of the STIS spectra was not reached by IUE, and the data will, therefore, not be used for abundance analyses.

9.1. SEDs

Our goal is to derive abundances from the UV. Therefore, we rely on the atmospheric parameter determined from the optical by Irrgang (2014). To verify the effective temperature we determine the spectral energy distribution for all our targets with the STIS and IUE spectra available. The SED is very sensitive to $T_{\rm eff}$.
After combining all available STIS spectra and downgrading them to lower resolution, we calculated a model spectrum with ADS to compare the spectral energy distribution. Moreover, we retrieved low resolution IUE data to check the flux calibration of STIS. For the optical we retrieved photometry from the VizieR Photometry viewer[9] in several photometric filters (SDSS ugriz, Johnson UBVJHK).

ι Her

ι Her is one of the targets of the ASTRAL project. It is a bright ($V = 3.8$), sharp-lined B3 IV star, which has a temperature very similar to our runaway HD 271791 and will therefore be used as a comparison star. This star is the primary in a binary, with a companion of unknown spectral type. The orbital period is 113.8 d. It is also a pulsator of the SPB (slowly pulsating B) type. Slowly pulsating B stars show both light and line profile variability. They are main sequence B2-B9 stars (3-9 $M_\odot$) that pulsate in high radial order, low degree g-modes. Periods may be multiple and range from 0.4 to 5 days and amplitudes are smaller than 0.1 magnitudes[10]. These has to be considered while analyzing these types of stars. We downloaded all 12 single spectra and combined them into one spectrum, which was downgraded to a lower resolution. We also took available photometry from the VizieR Photometry viewer. They were used to derive the spectral energy distribution of ι Her. We compare this to a model spectrum calculated with ADS for $T_{\rm eff} = 17500$ K and a $\log g = 3.85$. The model spectrum was convolved with a instrumental profile and reddened using the Fitzpatrick (1999) parametrization with $E(B-V) = 0.02$. This is shown in Fig. 9.1. A good match between observation and model is achieved.

HR 1840

HR 1840 is a sharp-lined B2 V star ($V = 6.315$), which was also observed within the ASTRAL project. Moreover, it was also observed in an HST project, which aimed at testing rotational mixing predictions with boron abundances in main-sequence B-type stars. All available 21 spectra were combined. The comparison of the STIS spectrum, together with an additional IUE spectrum and the photometry of HR 1840 with a model spectrum calculated with ADS

[9] http://vizier.u-strasbg.fr/vizier/sed/
[10] http://www.aavso.org/vsx/index.php?view=about.vartypes

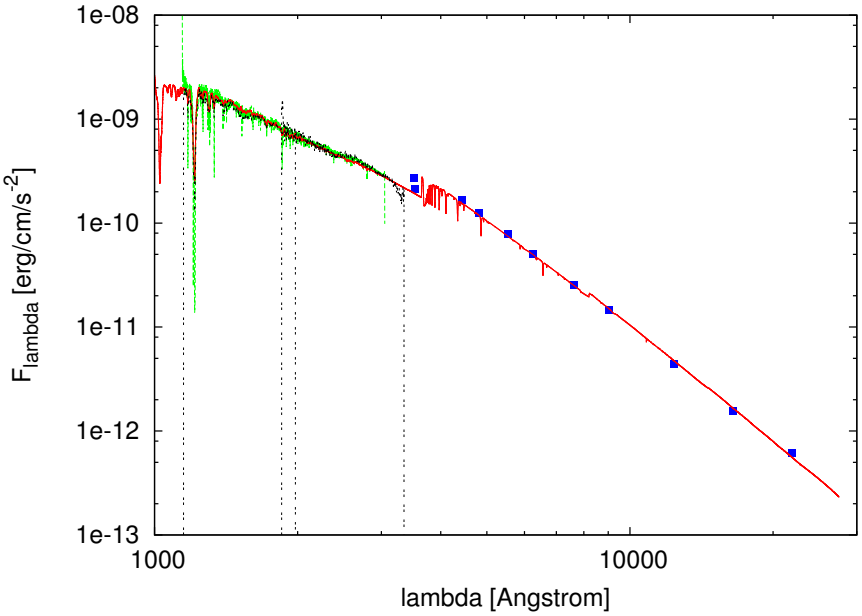

Figure 9.1.: SED of ι Her given by the STIS spectrum (green), IUE spectrum (dashed black) and the photometry (blue squares) compared to an ADS model with $T_{\rm eff}$ = 17500 K and a $\log g = 3.85$ (red).

($T_{\rm eff}$ = 22000 K and a $\log g = 4.20$), which was reddened by $E(B-V) = 0.033$, is shown in Fig. 9.2. Again excellent agreement ins found.

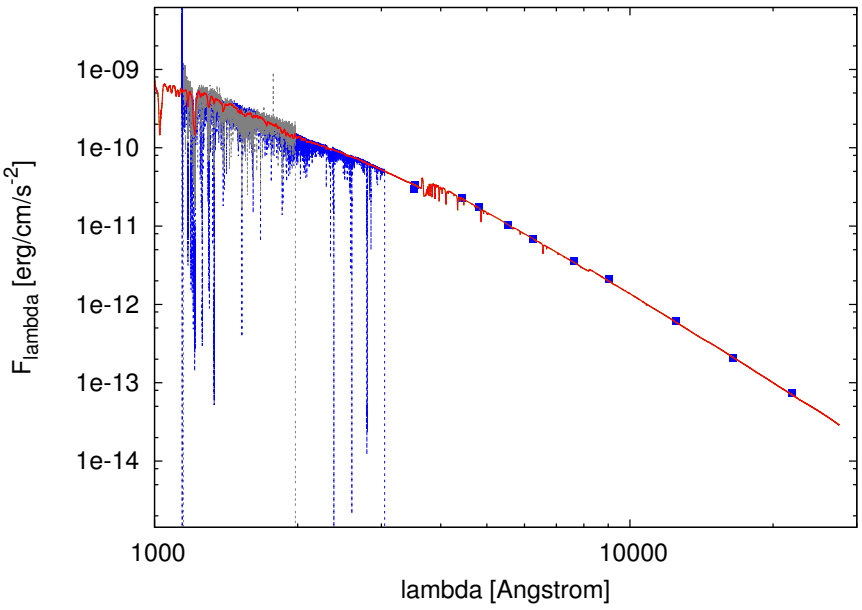

Figure 9.2.: SED of HR 1840 given by the STIS spectrum (blue), the IUE spectrum (grey) and the photometry (blue squares) compared to an ADS model with $T_{\rm eff}$ = 22000 K and a $\log g = 4.20$ (red).

HR 1861

HR 1861 is a sharp-lined B 1V star ($V = 5.34$). It was observed in a project, which wanted to derive boron abundances for a sample of main sequence and slightly evolved blue stars.

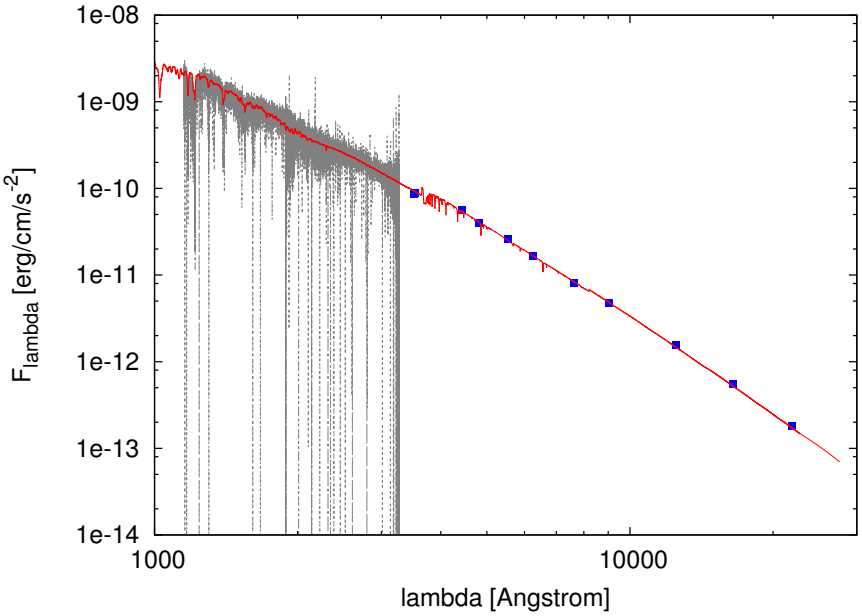

Figure 9.3.: SED of HR 1861 given by the IUE spectrum (grey) and the photometry (blue squares) compared to an ADS model with $T_{\rm eff} = 27000$ K and a $\log g = 4.18$ (red).

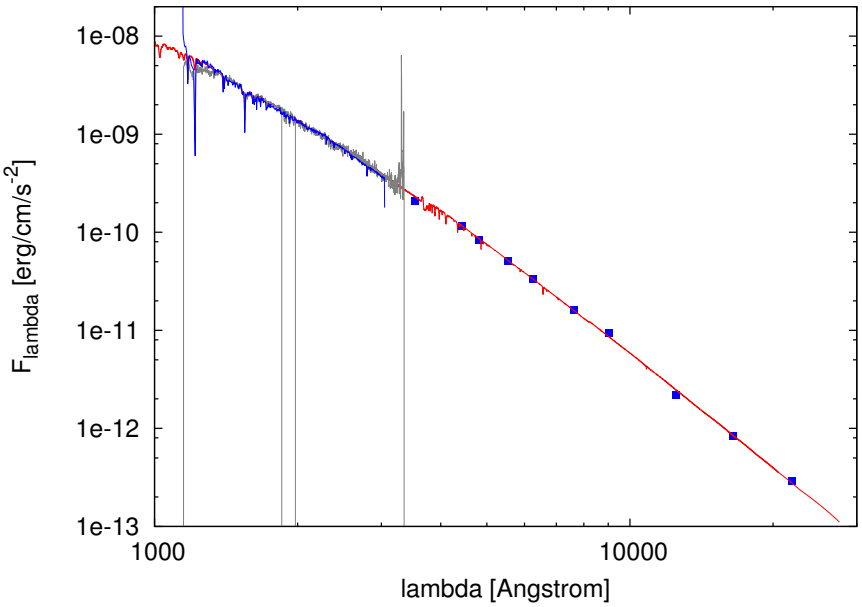

Figure 9.4.: SED of υ Ori given by the STIS spectrum (blue), the IUE spectrum (grey) and the photometry (blue squares) compared to an ADS model with $T_{\rm eff} = 33300$ K and $\log g = 4.25$ (red).

Hence, 7 spectra covering 1600-2670 Å are available from the HST archive, which we combined. However, there were some problems with the flux calibration. Therefore, we used the IUE spectra instead for the SED. We also calculated a model spectrum with ADS with $T_{\rm eff} = 27000$ K and $\log g = 4.18$. To be able to match the IUE spectrum together with the photometry of HR 1861, we had to redden the model spectrum with $E(B-V) = 0.055$ and $R_V = 4.8$, which differs from the usual value for the diffuse interstellar medium $R_V = 3.1$. The SED is shown in Fig. 9.3 and a good agreement is found.

Table 9.1.: Fundamental parameters of the four bright B stars (adopted from Irrgang (2014))

star	$T_{\rm eff}$ [K]	$\log g$ [cgs]	$v_{\rm rad}$ [km s^{-1}]	$v \sin(i)$ [km s^{-1}]	ζ [km s^{-1}]	ξ [km s^{-1}]
ι Her	17500 ± 400	3.74 ± 0.15	-31.5 ± 0.2	$0.0 + 2$	7.2 ± 1	1.66 ± 1
HR 1840	22000 ± 500	4.20 ± 0.15	22.5 ± 0.2	9.7 ± 1	8.2 ± 2	2.0 ± 1
HR 1861	27000 ± 600	4.11 ± 0.15	33.2 ± 0.2	$0.0 + 4$	13.2 ± 1	3.87 ± 0.8
υ Ori	33300 ± 700	4.24 ± 0.15	17.3 ± 0.3	9.5 ± 4	23.2 ± 1.5	7.74 ± 2

υ Ori

υ Ori (also named Thabit) is an O9.7 V star and is located in the Orion constellation ($V = 4.63$). It has been classified as a β Cepheid variable, which are non-supergiant pulsating O8-B6 stars with light and radial-velocity variations caused by low-order pressure and gravity mode pulsations. Periods are in the range of 0.1 - 0.6 days and light amplitudes range from 0.01 to 0.3 mag in V. The majority of these stars probably show radial pulsations, but some display nonradial pulsations; multi-periodicity is characteristic of many of these stars[11]. This causes changes in the line profiles and can lead to temperature changes of up to 2% (De Ridder et al. 2002), which can not be neglected in the analysis of spectra taken at different times. For the first analysis of this system, we however did not consider this effect. υ Ori is also a target of the ASTRAL project. All 12 spectra were downloaded and combined. For the energy distribution we also downloaded low resolution IUE spectra. The comparison of those spectra with an ADS model of $T_{\rm eff} = 33300$ K and $\log g = 4.25$ with a reddening of $E(B-V) = 0.05$ is shown in Fig. 9.4.

9.2. Abundances

For the determination of the elemental abundances from the UV, we combined all STIS data available in the HST archive per star. If spectra of different resolution were available, the spectra were binned to the lowest resolution, which was in all cases $R = 30\,000$. We did not derive the atmospheric parameters of the stars from the UV spectra, but instead we adopted them from the analysis in the optical performed in Irrgang (2014), as summarized in Table 9.1. For the abundance analysis we kept the parameters fixed, varying only the abundances in our calculation with Atlas9, Detail and Surface. The abundance for each element was derived from lines without blends from other elements. We derive the abundances from the near-UV ($\lambda > 2400$ Å), if possible because of the possibly lower reliability of our modeling in the far-UV (see Chapt. 8). We calculated only LTE models for the iron group elements other than iron. To minimize effects from neglected NLTE departures, we only considered lines of the main ionization stage, which depends on the temperature and therefore could differ from star to star. The resulting abundances for the four stars are summarized in Table 9.2 and 9.3. The uncertainties are 1-σ errors from the scatter in the abundances determined from the single lines. That implies that we did not consider the systematic errors due to uncertainties in the atmospheric parameter determination but only systematic errors caused by inaccurate atomic data. The uncertainties quoted for the abundances derived from the optical are only statistical errors caused mainly by the noise in the spectrum, also not considering the uncertainties in the atmospheric parameter determination. It is obvious that the uncertainties in the optical are much lower than the errors in the UV.

[11] http://www.sai.msu.su/gcvs/gcvs/iii/vartype.txt

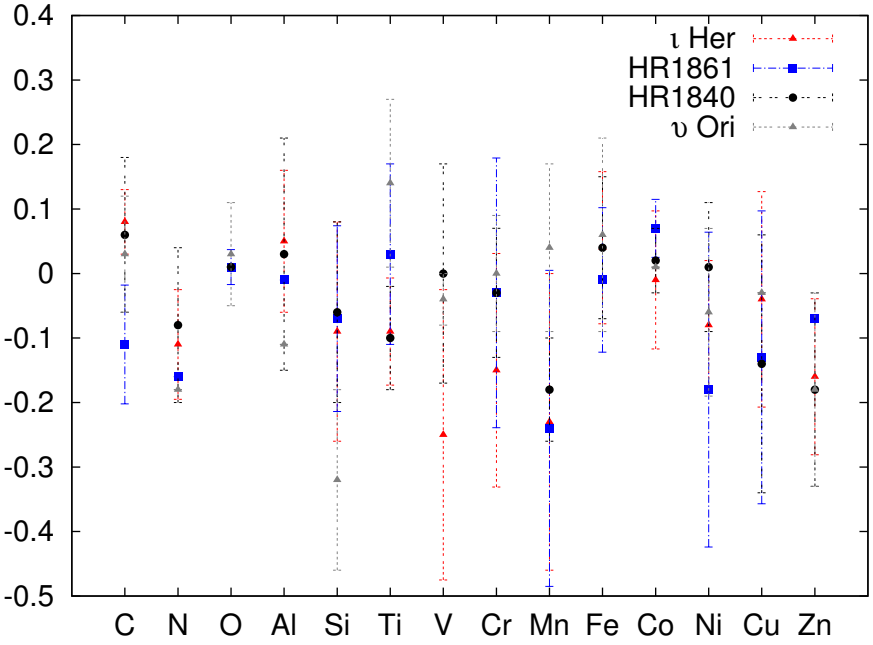

Figure 9.5.: Abundances for the four stars of different temperatures determined from the UV spectrum relative present-day cosmic abundances (CAS) from 63 mid B-type to late O-type stars (Irrgang 2014). The abundances from the iron group are compared to meteoric solar values. The errors are given by the standard deviation of the abundances determined from single lines.

Table 9.2.: NLTE abundances determined from the UV of four bright B stars

star		C	N	O	Al	Si	Fe
CAS[a]		8.35	7.77	8.70	6.26	7.46	7.37
ι Her	optical	8.44 ± 0.02	7.83 ± 0.02	8.81 ± 0.02	6.31 ± 0.02	7.56 ± 0.02	7.36 ± 0.02
	UV	8.43 ± 0.05	7.66 ± 0.08	–	6.19 ± 0.07	7.37 ± 0.17	7.41 ± 0.12
HR 1840	optical	8.30 ± 0.02	7.70 ± 0.02	8.75 ± 0.03	6.22 ± 0.02	7.38 ± 0.03	7.35 ± 0.02
	UV	8.41 ± 0.12	7.69 ± 0.12	8.71	6.29 ± 0.18	7.40 ± 0.14	7.41 ± 0.11
HR 1861	optical	8.24 ± 0.02	7.73 ± 0.01	8.65 ± 0.02	6.27 ± 0.03	7.31 ± 0.02	7.37 ± 0.02
	UV	8.24 ± 0.09	7.61	8.71 ± 0.03	6.25	7.39 ± 0.14	7.36 ± 0.11
υ Ori	optical	8.25 ± 0.02	7.59 ± 0.01	8.44 ± 0.02	6.23 ± 0.03	7.24 ± 0.02	7.24 ± 0.02
	UV	8.38 ± 0.09	7.59	8.73 ± 0.08	6.15	7.14 ± 0.14	7.43 ± 0.15

[a] Present-day cosmic abundances (CAS) from 63 mid B-type to late O-type stars (Irrgang in prep.).

Table 9.3.: LTE abundances determined from the UV of four bright B stars

star	Ti	V	Cr	Mn	Co	Ni	Cu	Zn
solar[a]	4.91	3.96	5.64	5.48	4.87	6.20	4.25	4.63
ι Her	4.82 ± 0.08	3.71 ± 0.22	5.49 ± 0.18	5.25 ± 0.23	4.86 ± 0.11	6.12 ± 0.10	4.21 ± 0.17	4.47 ± 0.12
HR 1840	4.81 ± 0.08	3.96 ± 0.17	5.60 ± 0.10	5.30 ± 0.08	4.89 ± 0.05	6.21 ± 0.10	4.11 ± 0.2	4.45 ± 0.15
HR 1861	4.94 ± 0.14	-	5.61 ± 0.21	5.24 ± 0.25	4.94 ± 0.05	6.02 ± 0.24	4.12 ± 0.23	4.56
υ Ori	5.05 ± 0.13	3.93 ± 0.04	5.64 ± 0.09	5.52 ± 0.13	4.88	6.14 ± 0.13	4.22	4.45 ± 0.15

[a] meteoritic solar values from Asplund et al. (2009)

This is mainly due to the thorough testing of the atomic data employed in the model atoms in the optical, which has so far not been undertaken for the UV spectral range (i.e. leaving room for improvements).

The observed spectrum of ι Her is compared to a model calculated, based on these abundances

and the atmospheric parameters from Table 9.1 in Appendix D, together with the residuals. The comparison looks overall good. Only few lines are absent in the model. The residuals reveal still deviations between model and observation in the line depths, which reflects the large scatter in the abundances in particular in the far-UV.
The abundances determined from the optical spectrum were compared to the present-day cosmic abundances (CAS) from 63 mid B-type to late O-type stars (Irrgang 2014). These abundances agree very good with the CAS determined by Nieva & Przybilla (2012) with only small deviations. The comparison is shown in Fig. 9.5. The abundances for the NLTE elements match the abundances determined from the optical spectrum very well. Within the errors they are all consistent. Therefore, we are confident that the determination of abundances based on our synthetic UV models is reliable. Hence, we are convinced that also the abundances for the iron group are reliable. This is also indicated by the good agreement with the solar abundances that are very similar the the present-day cosmic abundances derived from nearby B stars.

10. The extreme runaway HD 271791

HD 271791 is a bright (V=12.258), well known, apparently normal, B-type star at high Galactic latitude ($l = 276.65, b = -29.57$). Because of its large distance to the Galactic plane HD 271791 was regarded a runaway B star. HD 271791 attracted attention because of its very high radial velocity of 442 $\mathrm{km\,s^{-1}}$ (Kilkenny & Muller 1989). Due to the discovery of the hyper velocity stars (HVS), which are unbound to the Galaxy, a further investigation of this star became interesting. As it is much brighter than the other HVS it can be studied in great detail. Heber et al. (2008) re-investigated this star by using high-resolution, high-S/N spectra to constrain the nature of the star, its mass, distance, and evolutionary lifetime. Moreover, they investigated the space motion of HD 271791 to constrain its place of origin. They stated that HD 271791 is a massive B giant ($T_{\rm eff} = 17800 \pm 1000$ K, $\log g = 3.04 \pm 0.1$) with a mass of $M = 11 \pm M_{\odot}$ and an age of 25 ± 5 Myr. From the proper motions of the star they get a Galactic rest-frame velocity of $530 - 920\,\mathrm{km\,s^{-1}}$, which implies that this star is indeed unbound to the Galaxy. Moreover they calculated trajectories for HD 271791 back to the Galactic plane to identify its place of origin and found the birth-place to be on the outskirts of the Galactic disc with a Galactocentric distance of $\gtrsim 15$ kpc. They excluded the Galactic center as a possible origin, as the flight-time required to reach the current position exceeds the evolutionary life-time by a factor of three. As the Hills-mechanism can be excluded to be responsible for the acceleration of HD 271791, Przybilla et al. (2008) performed a quantitative analysis of the star to distinguish between the binary-supernova scenario and the dynamical ejection scenario. An accurate determination of the surface composition confirmed the low [Fe/H] expected for a star born in the outer Galactic rim. The detected $\alpha-$enhancement points towards an extreme case of the binary-supernova runaway scenario. The evolution of a binary with a very massive primary ($M \gtrsim 55\,M_{\odot}$) can lead to a suitable progenitor. After a common-envelope phase a Wolf-Rayet star (WR) with a close main sequence star of spectral type B is formed. An asymmetric supernova-explosion of the WR could explain both the $\alpha-$enhancement and the ejection at high velocity. As a high kick velocity is necessary to explain the very high Galactic rest-frame velocity of the star Gvaramadze (2009) doubted the responsibility of the BSS for the ejection of HD 271791. In order to shed further light on the topic we re-investigate here this highly interesting star by using higher S/N optical spectra taken with ESO-VLT/UVES, as well as UV spectra taken with HST/STIS and COS to investigate the abundances of the heavier elements. Moreover, we want to investigate the supernova scenario with simulations of the ejection of the companion in the supernova scenario calculated with the parameters of the progenitor system using the equations by Tauris & Takens (1998), analogue to Tauris (2015).

10.1. Analysis of the optical spectrum

To improve the abundance analysis in the optical high S/N spectra in several set-ups together covering the entire wavelength-range from 3050 to 10000 Å where taken with the ESO-VLT/UVES spectrograph at Cerro Paranal at 14 and 20 April 2009 with a resolution of about $R = 30000$. All spectra were reduced with the ESO-pipeline for UVES based on Reflex[1] (Freudling et al. 2013). It provides a graphical user interface to reduce the data fully

[1] `https://www.eso.org/sci/software/reflex`

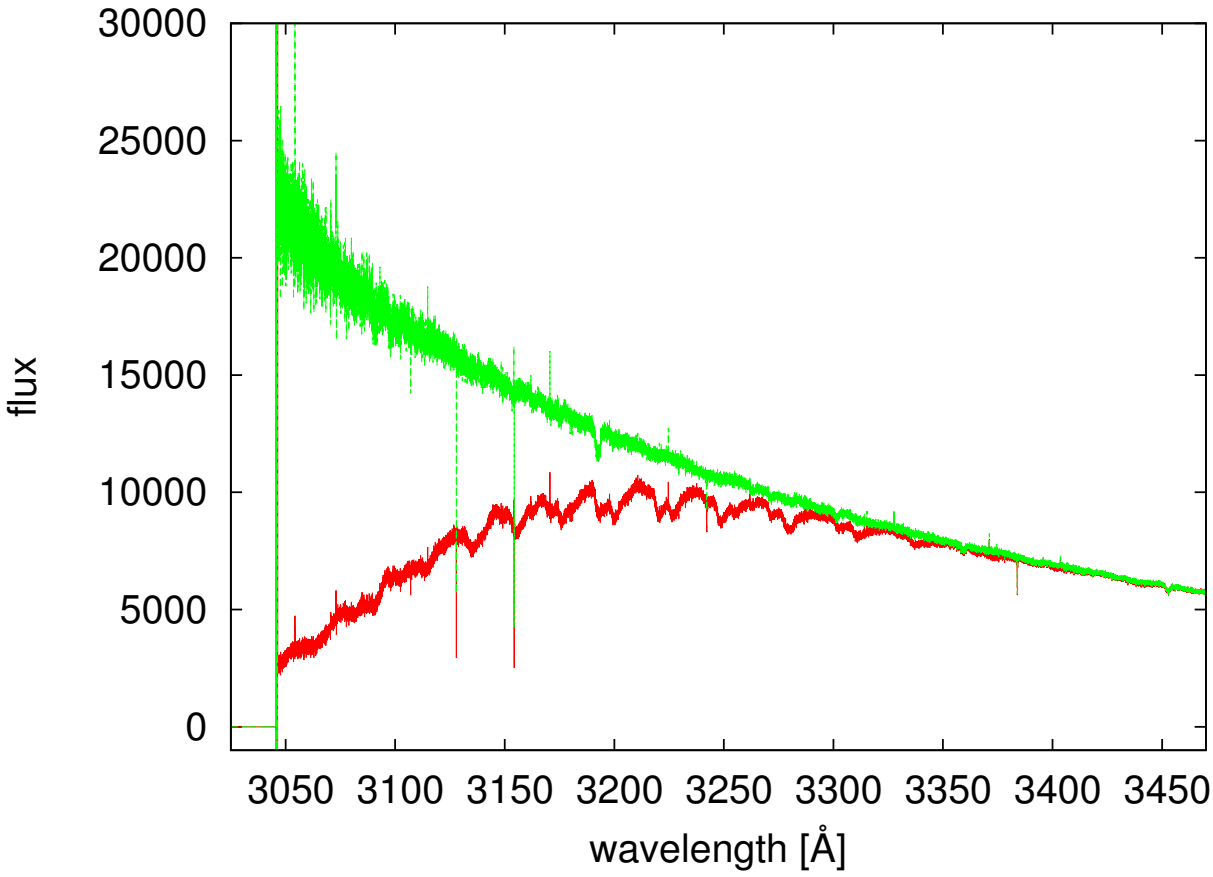

Figure 10.1.: UVES spectrum (red line) compared to the spectrum corrected by **molecfit**, with the best fitting ozone abundance.

automatically based on the ESO-pipelines for the VLT instruments. For the analysis all spectra were normalized and co-added. Moreover, we corrected the spectrum for telluric the features.

10.1.1. Correction of the O_3-Huggins Bands

Our UVES spectrum in the optical was taken with the ESO-VLT/UVES spectrograph on the ground. The absorption spectrum of the Earth's sky (shown in Fig. 10.2) is therefore imprinted on the absorption spectrum of the star. From $\lambda = 7000 - 10000$ Å the spectrum is dominated by molecule bands of H_2O an O_2 in the air. These are very sharp lines with little thermal broadening and can hence, easily be distinguished from the absorption lines of the star and be removed. However, from 3000 to 3500 Å we find the O_3 Huggins bands. These are broad bands caused by the blends of many lines with similar wavelengths. They have similar widths to one order in the echelle spectrum and are therefore more difficult to correct for. Hence, we use the program **molecfit** that was developed by the ESO-in kind group in Innsbruck for the telluric correction in this wavelength range. This program is fitting the abundances of the most relevant molecules in the atmosphere and calculates a transmission spectrum on a theoretical basis (Smette et al. 2015).

The wavelength range from 3000 to 3500 Å is covered by two different spectra observed within one hour. We fitted both spectra in regions without stellar lines to determine the abundances of ozone in the atmosphere. For the first spectrum we obtained a molecular gas column of $4.662 \cdot 10^{-1} \pm 2.056 \cdot 10^{-3}$ in ppmv (parts per million by volume), for the second spectrum we measured $4.755 \cdot 10^{-1} \pm 1.700 \cdot 10^{-3}$ ppmv. Both measurements are only sightly different.

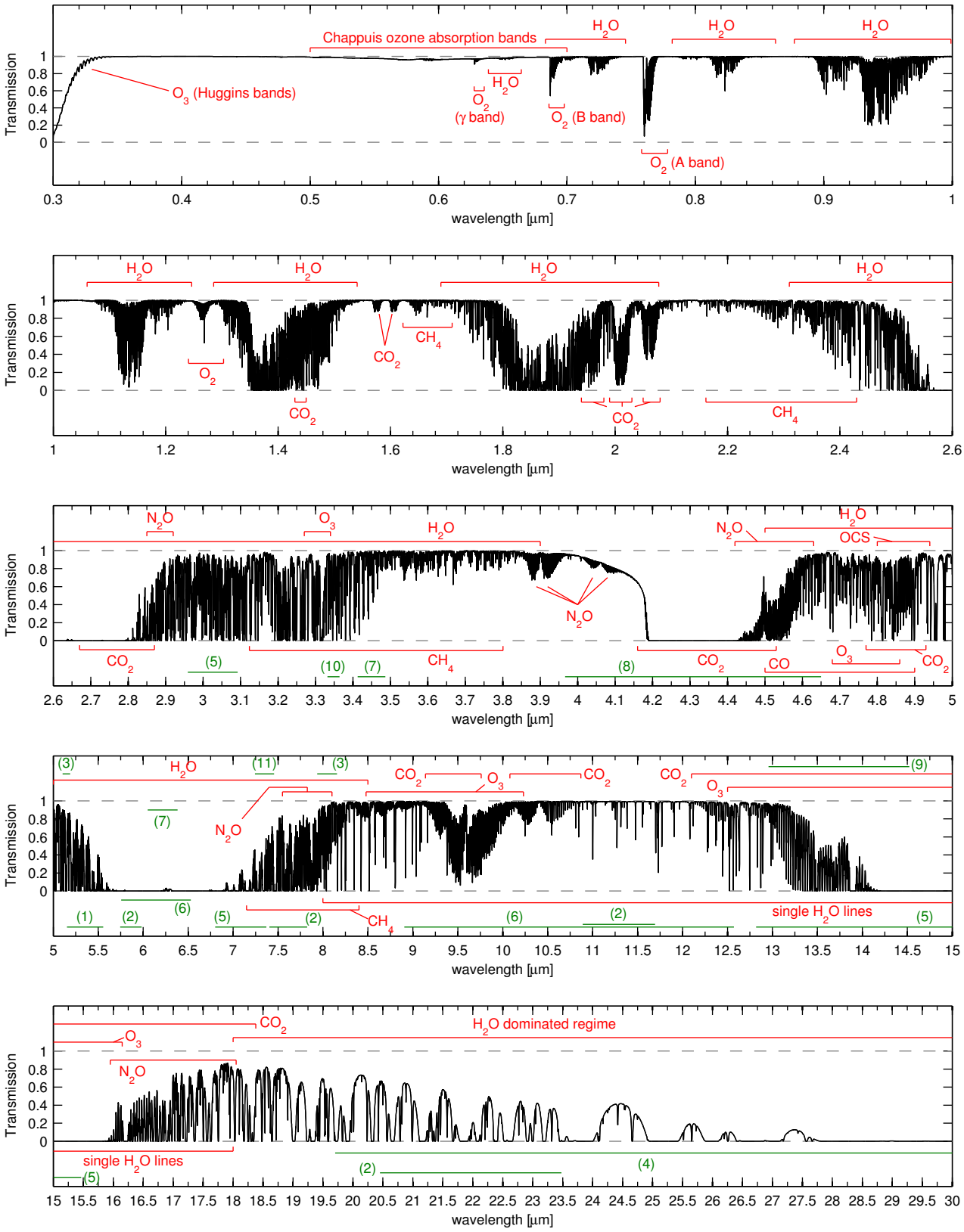

Figure 10.2.: Synthetic absorption spectrum as calculated by molecfit of the sky between 0.3 and 30 μm, adopted from Smette et al. (2015)

Figure 10.1 shows the original as well as the corrected spectrum. The ozone bands are corrected very well by **molecfit**, but the correction degrades the S/N in particular in the bluest part of the spectrum.

10.1.2. Fundamental parameters and abundances from the optical spectrum

For the analysis of the normalized and corrected spectrum we employed the method introduced by Irrgang et al. (2014), which fits the spectrum simultaneously using the same grid of synthetic spectra. To find the best solution a χ^2 minimization is performed using different minimization algorithms (e.g., simplex algorithm, gradient method). Because of the large number of indicators the statistical error is small. However, the systematic errors are from our experience about 2% in $T_{\rm eff}$ and 0.1 dex in $\log g$. Taking this errors into account we can determine systematic errors for the abundances. The position in the $T_{\rm eff} - \log g$-diagram was then compared to evolutionary

Table 10.1.: Parameters of HD 271791

$T_{\rm eff}$ [K]	$\log g$ [cgs]	ξ [km s^{-1}]	$v \sin(i)$ [km s^{-1}]	ζ [km s^{-1}]	$v_{\rm rad}$ [km s^{-1}]
$18700 \pm 370 \pm 40$	$3.16 \pm 0.1 \pm 0.02$	5.9 ± 1	128 ± 1	22 ± 4	443 ± 1
R [$R_\odot$]	M [$M_\odot$]	age [Myr]	$\log L$ [$L_\odot$]	d [pc]	
15.1 ± 1.5	11.7 ± 0.5	18 ± 2	4.44 ± 0.07	22.0 ± 2.55	

tracks, as described in Sect. 6.2.2 to derive the mass, radius, age, and luminosity of the star. A fit of the measured photometry to a synthetic spectrum calculated for the atmospheric parameters, furthermore, determined the spectroscopic distance. All parameters of the star are summarized in Table 10.1. The results of our new analysis of the higher S/N spectrum are consistent with the results that were obtained by Przybilla et al. (2008). The measured abundances are summarized in Table 10.2 with statistical and systematical errors. To study

Table 10.2.: Abundances of HD 271791

C	N	O	Ne	Mg
$8.03 \pm 0.02 \pm 0.07$	$7.39 \pm 0.02 \pm 0.07$	$8.39 \pm 0.015 \pm 0.07$	$7.91 \pm 0.022 \pm 0.07$	$7.15 \pm 0.025 \pm 0.1$
Al	Si	S	Fe	
$5.99 \pm 0.02 \pm 0.07$	$7.27 \pm 0.035 \pm 0.1$	$6.94 \pm 0.02 \pm 0.07$	$7.00 \pm 0.03 \pm 0.07$	

the supernova scenario we perform a differential abundance study by comparing the abundances of HD 271791 to those from a representative sample of 63 nearby B-stars by Irrgang et al. (in prep.), which allows us to constrain the abundances of the supernova ejecta accreted by the runaway star. This is shown in Fig. 10.3. As it is not expected that the core-collapse SN ejecta that polluted the atmosphere of the runaway contained much iron, we use iron as a baseline. The iron abundance in HD 271791 is ~ 0.3 dex lower than in the comparison sample. This is consistent wit the star originating from the metal-poor outskirts of the Galaxy. On the other hand, several of the $\alpha-$elements, e.g. Ne, Mg, Si and S, are enhanced compared to abundance values expected for the metallicity of HD 271791.

To compare the abundances to calculated supernova yields some assumptions about the binary evolution and the accretion of the supernova ejecta have to be made. We employed the same assumption as used by Przybilla et al. (2008). To explain the extreme kinematic properties (see the next section for details) the progenitor system had to have been in a very tight binary system. That can only be explained, if the system has undergone a common-envelope phase. This happens only for mass ratios $q = M_1/M_2 \leq 0.2$. Therefore the companion of the runaway star had to have an initial mass $\geq 60 M_\odot$. The energy deposited in the envelope due to the spiral-in of the companion because of friction in the envelope leads to the ejection of the primary's hydrogen envelope. Accordingly, a binary system consisting of a WR and an early-type main-sequence B star is the most probably progenitor system of the SN-event that kicked out HD 271791. The radius of a 12 $M_\odot$ star on the main-sequence is about 4-5 $R_\odot$. The radius

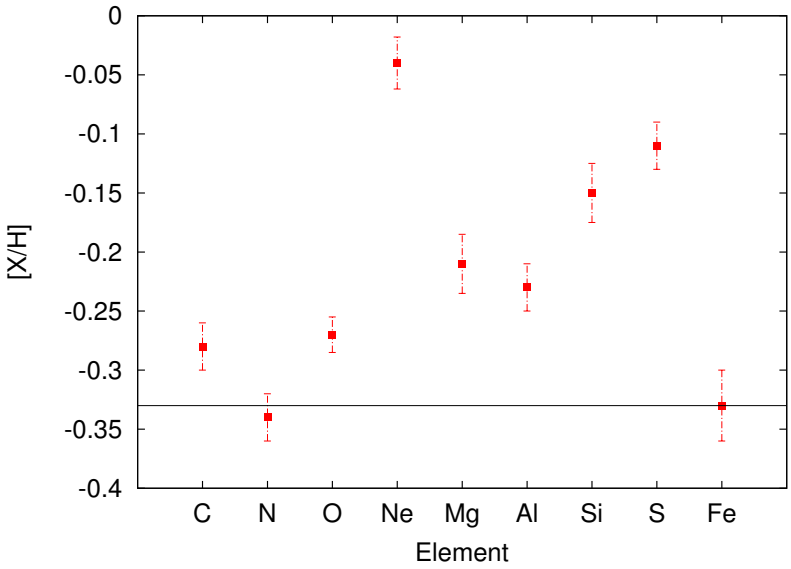

Figure 10.3.: Abundances of HD 271791 as determined from the optical spectrum relative to a representative B-star sample (Irrgang et al. in prep.). The baseline metallicity of HD 271791 relative to the B-star sample, [Fe/H], is marked by the solid line.

of a WR star $\leq 20\ M_\odot$ is about 1-2 $R_\odot$. Hence, the separation of the system can be as low as 10 $R_\odot$, so that the system is still detached, which means both stars are inside their Roche lobe. Due to the dense and strong wind of the WR star, at this point mass will probably transfered to the companion by wind accretion. We estimate that 0.04 $M_\odot$ of material rich in C, and less abundant in O and Ne could be deposited on the surface of the runaway progenitor. At the end of its lifetime the WR star will probably experience a core-collapse supernova of type Ic or a hypernova, if the initial mass was more than 100 $M_\odot$, onto a black hole with a mass around 5 $M_\odot$. Such an scenario is discussed by Fryer et al. (2002) in more detail. As the mass of the companion is changing abruptly and the (proto-) black hole experiences a kick the binary is disrupted and the runaway is released with about its orbital velocity.
Thereby the second, major accretion event onto HD 271791 happened. The interaction of the runaway with the expanding SN shell is a complex hydrodynamical process involving ablation of the outer layers of the runaway and accretion from the shell, which is not completely understood (Fryxell & Arnett 1981). Moreover, interaction with fall-back material from the explosion may be significant. Therefore, we made a conservative assumption that only 10 % of the ejecta that could be accreted ($M_{\rm acc} = M_{\rm ejecta} R_2^2/4a^2$) is actually deposited on the surface of the runaway. Hence, about 0.04 $M_\odot$ of heavy elements is accreted of the 10 $M_\odot$ heavy metals expelled in total. On the other hand $\sim$ 1% (0.1 $M_\odot$) of the secondary's mass is ablated from the surface layers including most of the material accreted from the WR wind (Fryxell & Arnett 1981).
We also have to account for mixing of the accreted material with unpolluted matter from deeper layers for the past $\sim$ 13 Myr since the SN. In radiative envelopes the mixing is very slow and can be approximated by diffusion (Maeder & Meynet 2000). We assume a mixing of 0.12%/0.08% of the HN/SN ejecta with 1 $M_\odot$ unpolluted envelope material.
Figure 10.4 shows a comparison of the measured the elemental abundances of the SN ejecta considering all before mentioned assumptions (normalized to iron) with hypernova/supernova yields of Nomoto et al. (2006). A qualitative agreement between theory and observation is reached for both the hypernova and the supernova yields. Only the oxygen abundance is smaller than would be expected by theory. However, that may be explained because of the use of integrated yields. Chemical homogeneity is not expected within SN ejecta. Therefore, detailed simulations of the SN explosion and of the accretion of the SN ejecta on the runaway are

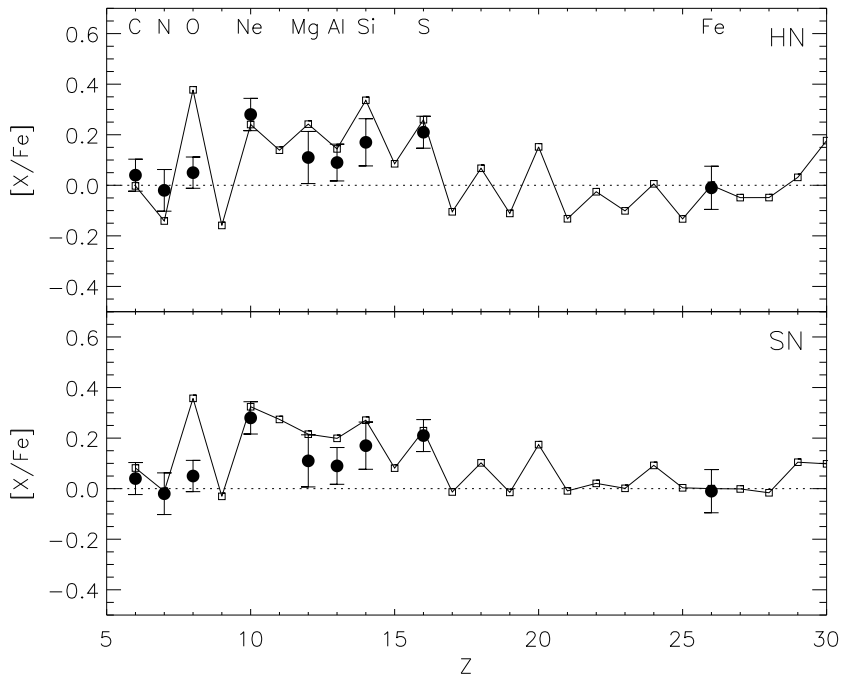

Figure 10.4.: Abundances of HD 271791 (normalised to iron) compared to hypernova/supernova (HN/SN) yields of Nomoto et al. (2006)

required to improve on the quantitative understanding. In any case, the observed enrichment in the α-elements indicates an ejection of HD 271791 by a SN explosion in a very tight system. Hence, the BSS is the most probable explanation for the ejection of HD 271791.

10.2. Kinematics

The Hipparcos satellite measured proper motions for HD 271791, which are listed in Table 10.3 together with photometric dots from Vizier[2]. Together with the radial velocity determined by the Doppler shift of the spectrum and the (spectroscopic) distance it is possible to derive the rest-frame velocity of the star.

Table 10.3.

Photometry											
proper motion		u'	H_P	B	g'	V	r'	i'	z'	J	H
$\mu_\alpha \cos(\delta)$	μ_δ	λ_0[Å]									
mas yr^{-1}		3520	4020	4440	4820	5540	6250	7630	9020	12500	16500
-1.08	6.75	12.53	12.277	12.12	12.08	12.272	12.44	12.68	12.88	12.596	12.581
±1.27	±1.45	±0.02	±0.01	±0.129	±0.02	±0.203	±0.02	±0.02	±0.02	±0.024	±0.021

We traced the orbit of the star back to the Galactic plane using different models for the Galactic potential taken from Irrgang et al. (2013). We performed 100000 Monte-Carlo runs by varying the kinematically relevant parameter within the given error margins. The results of the kinematic analysis are summarised with 1-σ errors in Table 10.4 . We derived coordinates (x,y,z) in a right handed Cartesian coordinate system (with the Galactic center at (0,0,0) and the Galactic disc in the x-y plane and with x pointing from the Sun to the Galactic center) the coordinates, the current velocity v_x, v_y, v_y, the Galactic rest-frame velocity $v_{\rm grf}$, the escape velocity $v_{\rm esc}$ with the probability of a bound orbit P_b, and the ejection velocity $v_{\rm ej}$, which

[2] `http://vizier.u-strasbg.fr/vizier/sed/`

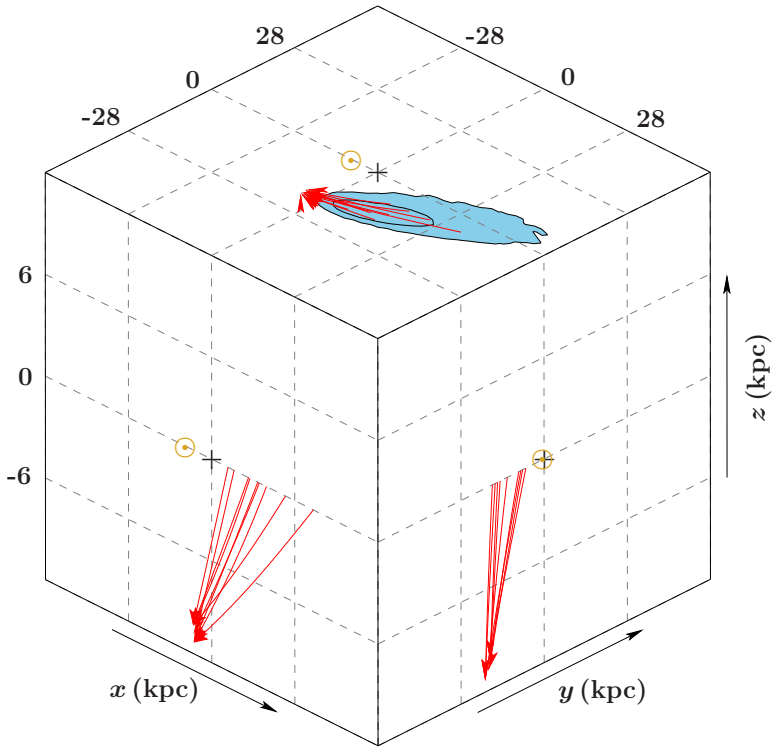

Figure 10.5.: Three-dimensional orbits of HD 271791. The nine trajectories (red lines; arrows indicate the star's current position) are traced back to the Galactic plane and sample the mean kinematic input data as well as variations in the distance, proper motions, and radial velocity. The black rimmed, blue shaded areas mark the 1-σ and 2-σ region for the intersection with the plane. The positions of the Sun and the Galactic center are marked by a yellow $\odot$ and a black $+$, respectively. Based on Milky Way mass Model I from Irrgang et al. (2013).

assumes an ejection with the Galactic rotation ($+230$ km s^{-1}), the flight-time $\tau_{\rm flight}$, and the birth-place of HD 271791 (x_d,y_d,z_d).

The current position of HD 271791 is about 10 kpc below the disc in the Halo. With a rest-frame velocity of 735 ± 145 km s^{-1} it is probably unbound to the Galaxy. Only $4-5\%$ of the orbits result in velocities smaller than the escape velocity, which are, hence, bound. Assuming an ejection of the runaway with the Galactic rotation we need only a ejection velocity from the binary system of 505 ± 145 km s^{-1} to account for the observed rest-frame velocity. The birth-place was traced back to the outskirts of the Galactic disc with a Galactocentric distance of 21 ± 7 kpc.

Figure 10.5 shows three-dimensional representations of the orbit of HD 271791. The birth-place is marked as a blue-shaded area, showing the 1-σ and 2-σ region for the intersection with the plane. The Galactic center is excluded completely within 3-σ as a possible birth-place not only because the flight-time to reach from the Galactic center to the current position would be about 3 times the evolutionary age. Our findings are overall consistent with the former kinematic analysis done by Heber et al. (2008).

The evolutionary age of HD 271791 determined from the $T_{\rm eff} - \log g$ diagram is with 18 ± 2 Myr slightly smaller than the age given by Heber et al. (2008) (25 ± 5 Myr). With a flight-time of 37 ± 18 Myr one may see a discrepancy between flight-time and age of HD 271791. For the comparison also the lifetime of the companion of about 5 Myr has to be considered. Therefore, within the 1-σ errors no overlap can be found. In Fig. 10.6 we show the possible ejection points in the x-y plane, which results in a flight-time below 20 (3.2%), 25 (17.8%), and 35 Myr (57.2 %). However, the determination of the age strongly depends on the stellar evolution models, which

Table 10.4.: Kinematics of HD 271791

model	x	y	z	v_x	v_y	v_z	$v_{\rm grf}$	$v_{\rm grf} - v_{\rm esc}$	$v_{\rm ej}$	P_b	x_d	y_d	r_d	$\tau_{\rm flight}$
	[kpc]			[km s^{-1}]						[%]	[kpc]			[Myr]
AS[1]	-6.2	-19.0	-10.9	-650	-155	-300	735	185	505	5.2	18.2	-10.4	21	37.4
	±0.10	±0.8	±0.5	±155	±70	±115	±145	±145	±145		±13	±8	±7.0	± 18
MN^2_{NFW}	-6.2	-19.0	-10.9	-625	-240	-340	750	200	520	3.8	18.2	-10.2	20.9	36.4
	±0.10	±0.8	±0.5	±155	±75	±100	±140	±140	±140		±12	±7.5	±6.6	± 18
MN^3_{TF}	-6.2	-19.0	-10.9	-635	-230	-335	750	200	520	4.3	18.9	-10.3	21.5	37.2
	±0.10	±0.8	±0.5	±155	±75	±100	±140	±140	±140		±8	±8	±7.8	± 19

[1] revised Galactic gravitational potential by Allen & Santillan, Model I in Irrgang et al. (2013)
[2] potential with a Miyamoto & Nagai bulge and disk component and a Navarro, Frenk, & White dark matter halo, Model III in Irrgang et al. (2013)
[3] potential with a Miyamoto & Nagai bulge and disk component and a truncated, flat rotation curve halo model

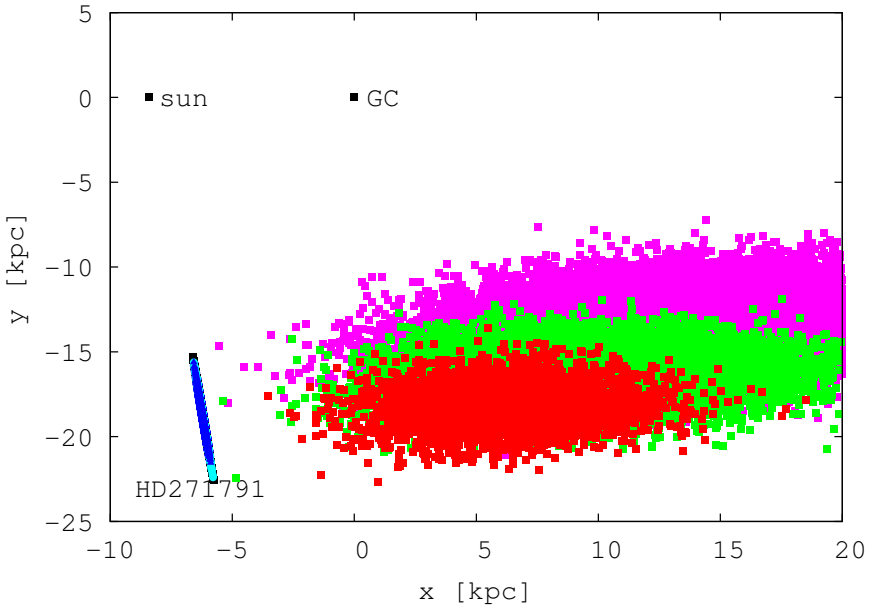

Figure 10.6.: Ejection and current position of HD 271791 in the x-y plane. The red squares mark the crossing of the Galactic disc for orbits with $\tau < 20$ Myr (3.2% of total orbits); green squares: $\tau < 25$ Myr (17.8% of total orbits); pink squares prob $\tau < 35$ Myr: 57.2%

are for single-stars. It has been found that mass transfer in a binary system can rejuvenate the companion. As the evolution in a close binary deviates significantly from single-star evolution this is only an estimate. Already 57.2% of the orbits have a flight-time smaller than 35 Myr. The mismatch between the evolutionary lifetime and the measured flight-time of HD 271791 has to be investigated further.

Gvaramadze (2009) doubted the binary-supernova scenario could be responsible to accelerate a B main-sequence star to velocities as observed for HD 271791. He suggested that HD 271791 was ejected by the dynamical ejection scenario while being a member of a massive post-supernova binary. They claim that the supernova could not disrupt the binary system, which means the 12 $M_\odot$ B MS-star together with a 5 $M_\odot$ black hole remained gravitationally bound. As most massive stars are formed in open clusters the probability of dynamical interactions in a young, dense cluster with other binaries or stars is very likely. Runaways produced by binary-binary encounters are frequently ejected at velocities compared to the orbital velocities of the binary components (Leonard 1991). Moreover, they proposed another possibility involving a close

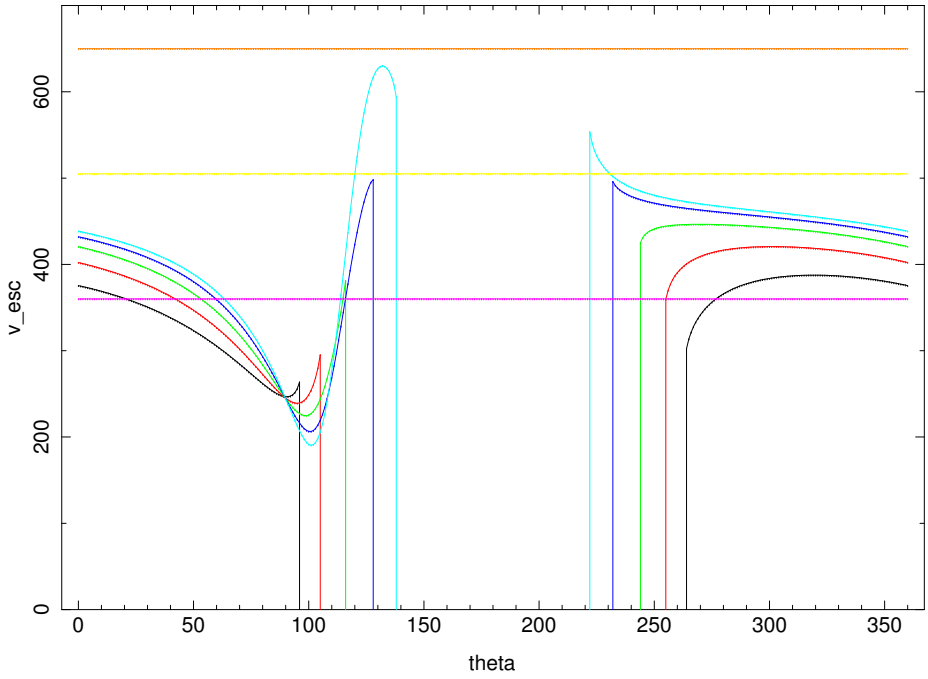

Figure 10.7.: Ejection velocity of HD 271791 depending on the angle θ between kick vector and the direction of motion of the exploding star and the kick velocity [300 $\mathrm{km\,s^{-1}}$ (black line), 500 $\mathrm{km\,s^{-1}}$ (red line), 750 $\mathrm{km\,s^{-1}}$ (green line), 1000 $\mathrm{km\,s^{-1}}$ (blue line), 1200 $\mathrm{km\,s^{-1}}$ cyan line]; the horizontal lines give the measured rest-frame velocity-230 $\mathrm{km\,s^{-1}}$ and the error margins

encounter between massive hard binaries and a very massive star. However, in both scenarios normally the least massive object is ejected (Heggie 1975), which is the black hole in our case. Moreover, their simulation did not consider Galactic rotation and assumed an unrealistically high mass of 10 $M_\odot$ for the black hole.

Hence, we repeated the simulation of the ejection velocities with the parameter determined in our new analysis. The simulation calculates the ejection velocity of the secondary based on the equations (44-47) and (54-56) given in Tauris & Takens (1998). Figure 10.7 shows a re-calculation of Fig. 1 from Gvaramadze (2009). This shows the ejection velocity of HD 271791 depending on the angle θ between kick vector and the direction of motion of the exploding star for different kick velocities. For θ between $100 - 250°$ the ejection velocity is not defined, which means the binary remains bound.

It is obvious that for all calculated kick velocities solutions can be found that explain the minimum ejection velocity. However, to explain the maximum possible velocity a large kick of 1200 $\mathrm{km\,s^{-1}}$ is required.

Furthermore, we also performed a Monte-Carlo simulations with 10^6 MC runs using an isotropic kick distribution to investigate the ejection velocities as done by Tauris (2015). This is shown in Fig. 10.8. For a kick velocity of 300 $\mathrm{km\,s^{-1}}$ the minimum rest-frame velocity of HD 271791 is reached by 10% of the Monte-Carlo runs. To get the maximum velocity of HD 271791 on the other hand a kick velocity of at least 1200 $\mathrm{km\,s^{-1}}$ is needed and only 1% of the runs reach that high velocity. But there is no evidence yet for such a large kick of an black hole (e.g., Gualandris et al. 2005). In summary we can say that an ejection velocity until the mean rest-frame velocity found in our kinematic analysis should be possible to be explained with the binary-supernova scenario. For higher velocities the scenario becomes unlikely. With the current available proper motions and the spectroscopic distance a more accurate and more precise kinematic analysis is not possible. However, the Gaia satellite is measuring parallaxes and proper motions with an accuracy $< 20\,\mu$as, which will result in an error in d of 0.5 pc and

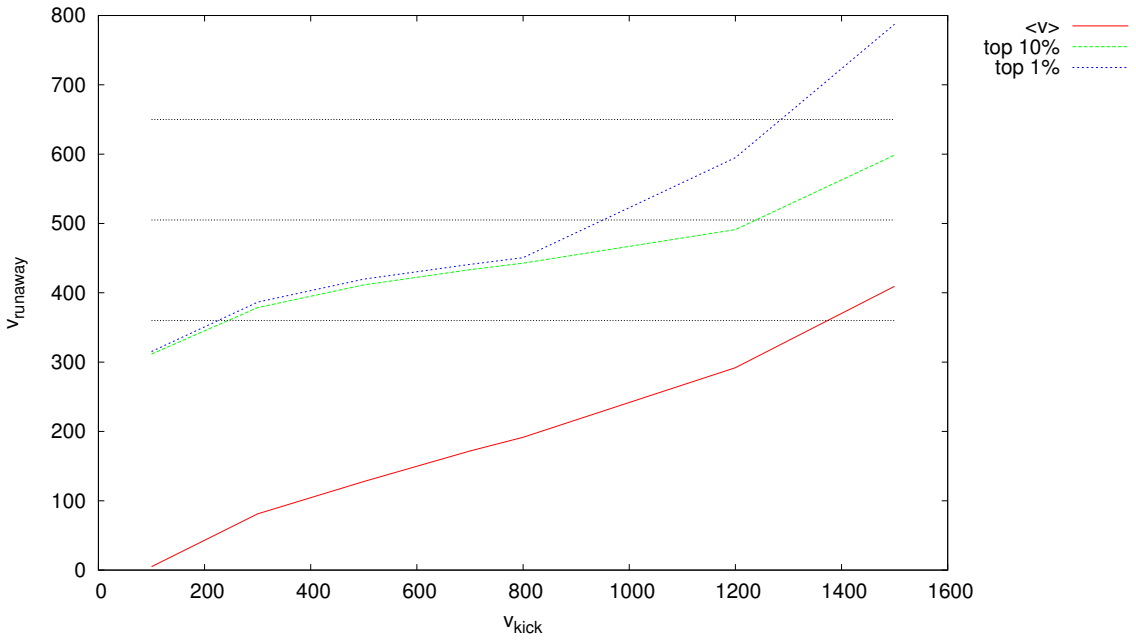

Figure 10.8.: Simulated ejection velocities of HD 271791 as a function of kick velocity using the equations from Tauris & Takens (1998); the dotted vertical lines give the measured rest-frame velocity$-230\,\mathrm{km\,s^{-1}}$ and the error margins.

an proper motion error of about $< 20\,\mu$as for HD 271791. The catalogue is expected in 2020, with first results becoming available already 2017. This will facilitate tighter constraints to be derived to distinguish between the possible scenarios.

10.3. Analysis in the UV

Two settings with HST/STIS and HST/COS were employed to measure spectra of HD 271791, covering the $1600-3120$ Å and $1130-1795$ Å, respectively. We also acquired a low-resolution long-slit spectrum to verify the flux calibration of the STIS and COS spectra. In order to construct a SED and check the flux calibration, we downgraded the resolution of the high-resolution STIS and COS spectra. We also compared the SED to an ADS spectrum calculated with $T_{\rm eff} = 18\,600$ K and $\log g = 3.15$, which was reddened with $E(B-V) = 0.05$ to test the effective temperature determined from the optical spectrum. Overall, good agreement is found, accept for some minor mismatches.

Table 10.5.: Abundances determined from the UV of HD 271791

star	C	N	Al	Si	Mg	Cr	Fe
CA[a]	8.35	7.77	6.26	7.46	7.40	5.64	7.37
HD 271791	8.0 ± 0.09	7.50	6.16 ± 0.04	7.21 ± 0.05	7.15 ± 0.09	5.43 ± 0.18	7.15 ± 0.11
star	V	Co	Ti	Mn	Ni	Cu	Zn
CA[a]	3.96	4.91	4.91	5.48	6.20	4.25	4.63
HD 271791	-	4.82 ± 0.08	4.74 ± 0.03	5.22 ± 0.12	6.03 ± 0.10	-	4.35 ± 0.15

[a] Present-day cosmic abundances (CA) from 63 mid B-type to late O-type stars (Irrgang in prep.). For the iron group solar abundances by Asplund et al. (2009) are taken.

To determine the abundances we took in a first step the few unblended lines to determine the abundances of C, Si, Mg and Fe. Based on these results we iteratively determined the

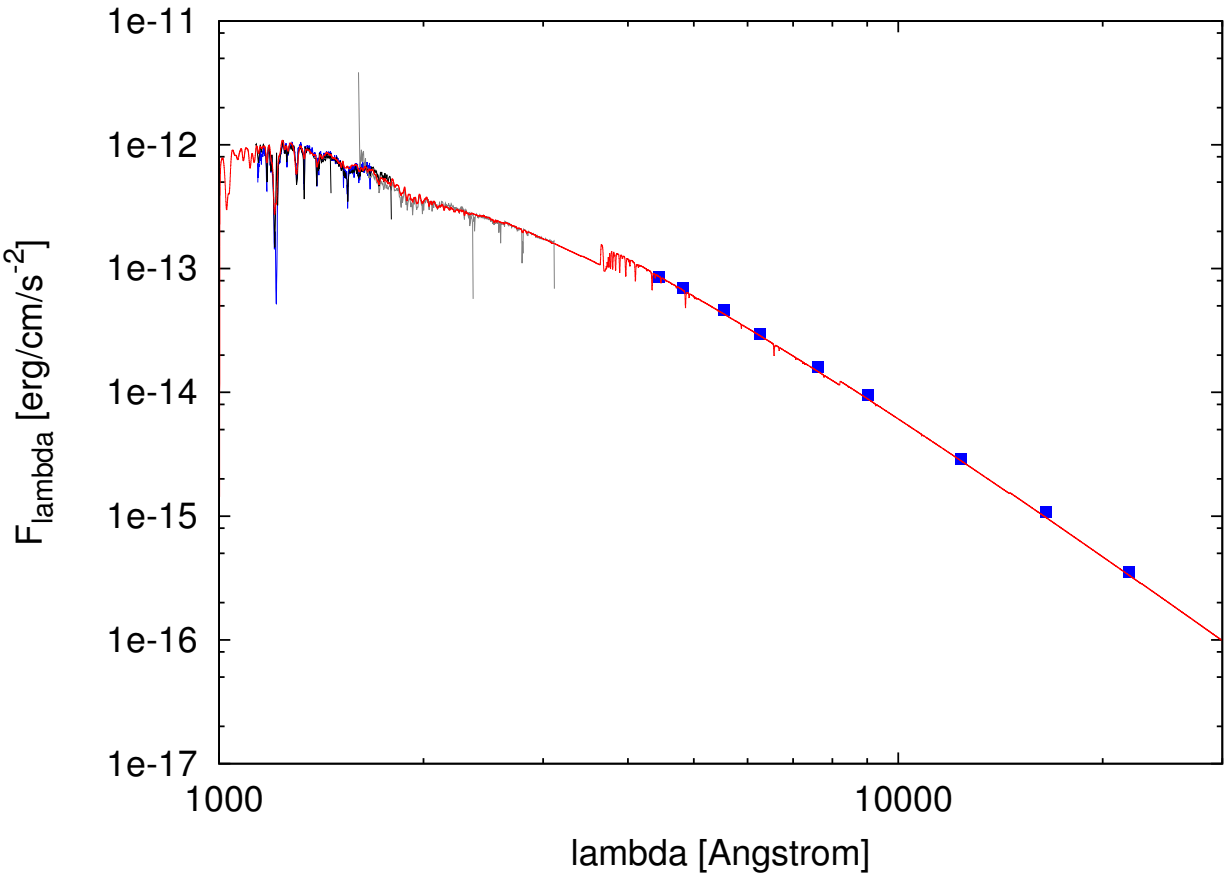

Figure 10.9.: SED of HD 271791 using COS spectra (black), high resolution STIS spectra (grey), low-resolution STIS (blue) and photometry of HD 271791 (blue squares).

abundances for the other elements from blended lines. The results can be found in Table 10.5. In Appendix E, we show the comparison of our model spectrum with the observations of HD 271791.

10.4. The supernova scenario: nucleosynthesis in a core-collapse supernova

New discoveries of massive, very close binaries and new stellar evolution calculations show that the possible separation of the progenitor system of the runaway HD 271791 can be smaller than expected before. This leads to a higher possible ejection velocity. Therefore, the supernova scenario can explain the rest-frame velocity of HD 271791, assuming an ejection in direction of the Galactic rotation. Gvaramadze (2009) appears to be suited ledd to explain all observational data. The analysis of a higher-quality spectrum confirms the $\alpha-$enhancement found before by Przybilla et al. (2008). However, to discriminate between different calculations for supernova yields, the systematic errors in the spectrum synthesis would need to be reduced significantly. The determination of the elements in the UV also confirms the findings of the abundance analysis in the optical. Due to the fact that almost all lines are blended in the UV, the abundance analysis is not so straightforward than in the sharp-lined stars. Large uncertainties are obtained in particular because several elements are analyzed in LTE, as more sophisticated NLTE model atoms are unavailable at the moment. Moreover, we could not derive abundances for all elements yet. This will, however, be done in the future by fitting several elements at once. The abundances in the iron-group are about 0.2 dex lower than found in the comparison stars. This coincides

with the iron abundance and was expected, as the runaway star has a lower metallicity due to its origin from the outskirts of the galaxy. As a next step, we will also determine the abundances of the trans-iron group elements, by comparing single lines of the runaway to the lines of our comparison star ι Her, but this is beyond the scope of this thesis.

11. Future work

11.1. Eclipsing hot subdwarf binaries – The EREBOS project

Currently we know 17 HW Vir systems. Three of them have substellar companions. The known HW Vir systems have been discovered using different methods and the sample is therefore very inhomogeneous. However, to study the properties of the population of hot subdwarf stars with low-mass stellar or substellar companions, a large and homogeneously selected sample of eclipsing binaries is essential. Most recently, thirty-six new HW Vir candidates have been discovered by the OGLE project (Pietrukowicz et al. 2013; Soszynski et al. 2015), tripling the number of such objects and providing the first large and homogeneously selected sample of eclipsing sdB stars. The stars have been identified by their blue colours and their characteristic light curve shapes in the I-band. These light curve shapes and the derived orbital periods leave no doubt that those are indeed HW Vir systems.

We already obtained time-resolved spectroscopy of two bright binaries from this sample with EFOSC2 and confirmed their HW Vir nature. Moreover, we got observing time with FORS2 on the VLT granted for two highly interesting short-period systems, which will be observed beginning of May 2015. To investigate this unique sample we start the EREBOS (Eclipsing Reflection Effect Binaries from the OGLE Survey) project that aims at measuring orbital and atmospheric parameters for all these systems. The most crucial part of the project is time-resolved spectroscopy of these rather faint and short-period binaries, because the individual exposure times must be short ($\sim$ 5% of the orbital period) to prevent orbital smearing. Therefore, a large amount of observing time is required for the spectroscopic and photometric follow-up. Hence, we already proposed for a large filler programme for VLT/FORS2 stretched over 4 periods to obtain phase resolved spectroscopy of the 23 newly discovered HW Vir systems with orbital periods $\lesssim$ 3 h and I-band magnitudes $\lesssim$ 19.5. Moreover, we proposed for spectroscopic and photometric follow-up with several additional telescopes within our collaboration.

This project will triple the number of well-studied HW Vir systems and due to the homogeneous selection it will allow us to study the population properties in a quantitative way for the first time. Due to the large fraction of substellar companions we found amongst the short period reflection effect binaries (see Sect 7.8), we expect up to 50% of all our systems to contain substellar companions. Five of the systems from the OGLE sample have orbital periods shorter than all the before known HW Vir systems. This means, we can systematically investigate the so far unstudied region at short periods shown in Fig. 7.20 where the least massive and closest companions might be located.

By analysing the time-resolved spectroscopy together with the lightcurves we will be able to determine the masses of both components and the separation of the system. This means we will increase the number of eclipsing post common-envelope binaries with sdB and low mass companions with known system parameters, which will help for a better understanding of the very important, but not well understood common-envelope phase. Moreover, the determination of accurate system parameters (orbit, mass, radius) of a large number of reflection effect binaries will help us to understand the reflection better, which can not be modelled physically until now, but is only parametrized by the albedo of the companion.

The discovery of the first HW Vir system with a BD companion containing a pulsating sdB

(Sect. 7.6) also opens new possibilities to study the role of substellar companions in the formation of sdB binaries. Asteroseismology allows an independent and accurate determination of the sdB mass. We already proposed for higher resolution spectroscopic and photometric follow-up time for this unique system with ESO-VLT/XSHOOTER and ESO-NTT/EFOSC2. This system could be a Rosetta stone for understanding sdB stars, their binary systems, their pulsations and the role of substellar companions.
The photometric surveys already found a large number of new eclipsing sdB binaries and will find more in the future. Therefore, they will become certainly a milestone for the understanding of low-mass companions on the stellar evolution and the common envelope phase.

11.2. Spectrum synthesis in the UV and runaway stars

The analysis of the four bright B stars of different temperatures and our tests showed that our spectrum synthesis in the UV works fine. We can now use it to determine the abundances of trans-iron elements in our runaway star, The finding of enhanced r-process abundances could prove core-collapse supernovae as sites of the r-process, which is debated upon (with merging binary neutron stars being an alternative site), but direct observational evidence is unavailable at the present.This will hopefully further confirm the origin of HD 271791 in a binary supernova scenario.
Moreover, we want to apply for observing time with HST and analyze more candidate runaway stars from the SN scenario, already found by Irrgang (2014), to study nucleosynthesis in a core-collapse SN further. These systems give us the unique opportunity to put observational constraints on the yields produced in a supernova. W Furthermore, we will seek collaborations with supernova modelers to simulate the process taking place in binary supernovae in order to to minimize the assumptions made in the calculation of the accretion and mixing of the supernova ejecta.
To minimize the error in the abundance analysis, we want to improve the synthetic model spectra by developing NLTE model atoms for iron-group elements, which give rise to most lines found in the UV.
Furthermore, I want to perform a comprehensive abundance study of bright B stars study using UV spectra from the HST archive to get present-day cosmic abundances for iron-group and higher mass elements in the solar neighborhood. Quantitative spectroscopy of B stars in the UV to that extent has not been performed before. A comprehensive study of the abundances of the iron group and trans-iron group elements of bright B stars is unavailable so far. All studies done so far concentrated on small wavelength ranges and single lines.

Appendix

A. Orbital parameters for known post common-envelope systems and their substellar companions

Table A1.: Orbital parameters for the known eclipsing PCEBs (sdB/WD+dM) and reflection effect binaries (sdB+dM) (after Zorotovic & Schreiber 2013; For et al. 2010; Jeffery & Ramsay 2014), including the systems analyzed in this thesis. Systems with suspected planets are marked in bold (see Table A2)

System	Alt. Name	$P_{\rm orb}$ [d]	M_1 [$M_\odot$]	M_2 [$M_\odot$]	References
Reflection effect/ eclipsing binaries					
HW Vir	**2M J1244-0840**	**0.11671955**	**0.485 ±0.013**	**0.142±0.004**	1,2
HS 0705+6700	**2M J0710+6655**	**0.095646625**	**0.483**	**0.134**	3, 4
HS 2231+2441	**2M J2234+2456**	**0.110588**	**0.47:**	**0.075:**	5
NSVS 14256825	**2M J2020+0437**	**0.1103741**	**∼0.46**	**∼0.21**	6
NY Vir	**PG 1336-018**	**0.101015967**	**0.459±0.005**	**0.122±0.001**	7, 8, 9
2M1938+4603	NSVS 05629361	0.1257653	0.48±0.03	0.12±0.01	10
NSVS 07826247	CSS06833	0.16177042	0.376±0.055	0.113±0.017	11
BUL-SC16 335	2M J1809-2641	0.12505028	0.5:	0.16:	12
SDSSJ0820+0008	GSC 0196.0617	0.097	∼0.25	0.045±0.03	15
			∼0.47	0.068±0.03	15
ASAS 10232	2M J1023-3736	0.13927	0.461±0.051	0.157±0.017	16
AA Dor	LB 3459	0.261539736	0.471±0.005	$0.0788^{+0.0075}_{-0.0063}$	17,18
EC 10246-2707		0.118507993	0.45±0.17	0.12±0.05	19
FBS 0747+725	VSX J075328.9+722424	0.2082535	–	–	37
SDSSJ1622+4730		0.0697885	0.48 ± 0.03	0.064 ± 0.004	41
SDSSJ1922+372220		0.168876	0.47	0.116 ± 0.007	33
V2008-1753		0.065817833	0.47 ± 0.03	0.069 ± 0.005	40
BUL-SC 16 335		0.125050278	0.47:	0.16 ± 0.05	70
PTF1 J07245+1253		0.09977	0.526 ± 0.05	0.174 ± 0.016	39
PTF1 J011302+2257		0.0917	–	–	42
OGLE GD ECL 10384		0.07753698	–	–	38
OGLE GD ECL 09869		0.09596148	–	–	38
OGLE GD ECL 07446		0.11659550	–	–	38
OGLE GD ECL 11471		0.1208333	–	–	38
OGLE GD ECL 09426		0.12980483	–	–	38
OGLE GD ECL 11388		0.14780615	–	–	38
OGLE GD ECL 00586		0.18660216	–	–	38
OGLE GD ECL 00998		0.39802830	–	–	38
OGLE GD ECL 03782		0.43537749	–	–	38
OGLE GD ECL 08577		0.50660638	0.47:	0.12:	38
reflection effect/non-eclipsing binaries					
PG 1017−086	XY Sex	0.073	–	–	20
HS 2333+3927		0.1718023	0.38	0.29	21
PG 1329+159	Feige 81, PB 3963	0.249699	–	0.35[a]	22

Table A1.: Orbital parameters for the known eclipsing PCEBs (sdB/WD+dM) and reflection effect binaries (sdB+dM) (after Zorotovic & Schreiber 2013; For et al. 2010; Jeffery & Ramsay 2014), including the systems analyzed in this thesis. Systems with suspected planets are marked in bold (see Table A2)

System	Alt. Name	$P_{\rm orb}$ [d]	M_1 [$M_\odot$]	M_2 [$M_\odot$]	References
		0.249702	–	–	23
2M 1926+3720	KBS 13	0.2923	–	–	24
PG 1438−029		0.33579	–	–	23
HE 0230−4323		0.4515	–	0.30[a]	25
JL 82		0.7371	–	0.21[a]	26
BPS CS 22169		0.1780	–	0.19[a]	27
FBS 0117+396		0.252	–	–	28
HS 2043+0615		0.3016	–	–	29
UVEX J0328+5035		0.11017	–	–	30
Feige 48		0.3438	–	–	31
KIC 11179657		0.3944	–	–	32
KIC 2991403		0.4431	–	–	32
V1405 Ori	KUV 04421+1416	0.398	–	–	34
B4 NGC6791		0.3985	–	–	35
EQ Psc		0.801	–	–	36
CPD−64°481		0.27736315	–	–	43
PHL 457		0.3131	–	–	43
Detached WD+MS PCEBs					
NN Ser	**2M J1552+1254**	**0.13008014**	**0.535±0.012**	**0.111±0.004**	44, 45
V471 Tau	**2M J0350+1714**	**0.52118343**	**0.84±0.05**	**0.93±0.07**	46, 47
QS Vir	**EC 13471-1258**	**0.1507575**	**0.78±0.040**	**0.430±0.040**	48
RR Cae	**2M J0421-4839**	**0.30370363**	**0.440±0.022**	**0.183±0.013**	49
DE Cvn	RX J1326.9+4532	0.364139315	$0.51^{+0.06}_{-0.02}$	0.41±0.06	50, 51
GK Vir	SDSSJ1415+0117	0.344330833	0.564±0.014	0.116±0.003	52
RX J2130.6+4710	2M J2130+4710	0.52103562	0.554±0.017	0.555±0.023	53
SDSSJ0110+1326	WD 0107+131	0.332687	0.47±0.02	0.255-0.380	54
SDSSJ0303+0054		0.1344377	0.878-0.946	0.224-0.282	54
SDSSJ0857+0342	CSS03170	0.06509654	0.51±0.05	0.09±0.01	55
SDSSJ1210+3347		0.12448976	0.415±0.010	0.158±0.006	56
SDSSJ1212-0123		0.3358711	0.439±0.002	0.273±0.002	51
SDSSJ1435+3733		0.125631	0.48-0.53	0.190-0.246	54
SDSSJ1548+4057		0.1855177	0.614-0.678	0.146-0.201	54
CSS06653	SDSSJ1329+1230	0.08096625	0.350±0.081	–	57, 58
CSS07125	SDSSJ1410-0202	0.363497	0.470±0.055	0.380±0.012	58, 59
CSS080408	SDSSJ1423+2409	0.3820040	0.410±0.024	0.255±0.040	58, 59
CSS080502	SDSSJ0908+0604	0.14943807	0.370±0.018	0.319±0.061	57, 58
CSS09704	SDSSJ2208-0115	0.1565057	0.37	–	59
CSS09797	SDSSJ1456+1611	0.229120	0.370±0.016	0.196±0.043	58, 59
CSS21357	SDSSJ1348+1834	0.2484	0.590±0.017	0.319±0.061	58, 59
CSS21616	SDSSJ1325+2338	0.1949589	–	–	57
CSS25601	SDSSJ1244+1017	0.227856	0.400±0.026	0,319±0.061	58, 59
CSS38094	SDSSJ0939+3258	0.3309896	0.520±0.026	0.319±0.061	57, 58
CSS40190	SDSSJ0838+1914	0.13011232	0.390±0.035	0.255±0.040	57, 58
CSS41631	SDSSJ0957+2342	0.15087074	0.430±0.025	0.431±0.108	57, 58
WD 1333+005	SDSSJ1336+0017	0.1219587	–	–	57
PTFEB11.441	PTF1 J004546.0+415030.0	0.3587	0.51±0.09	0.35±0.05	60
PTFEB28.235	PTF1 J015256.6+384413.4	0.3861	0.65±0.11	0.35±0.05	60
PTFEB28.852	PTF1 J015524.7+373153.8	0.4615	0.52±0.05	0.35±0.05	60
KIC-10544976	USNO-B1.0 1377-0415424	0.35046872	0.61±0.04	0.39±0.03	61

Table A1.: Orbital parameters for the known eclipsing PCEBs (sdB/WD+dM) and reflection effect binaries (sdB+dM) (after Zorotovic & Schreiber 2013; For et al. 2010; Jeffery & Ramsay 2014), including the systems analyzed in this thesis. Systems with suspected planets are marked in bold (see Table A2)

System	Alt. Name	$P_{\rm orb}$ [d]	M_1 [$M_\odot$]	M_2 [$M_\odot$]	References
SDSS J0821+4559		0.50909	0.66±0.05	0.431±0.108	58, 62
SDSS J0927+3329		2.30822	0.59±0.05	0.380±0.012	58, 62
SDSS J0946+2030		0.252861219	0.62±0.10	0.255±0.040	58, 62
SDSS J0957+3001		1.92612	0.42±0.05	0.380±0.012	58, 62
SDSS J1021+1744		0.14035907	0.50±0.05	0.319±0.061	58, 62
SDSS J1028+0931		0.23502576	0.42±0.04	0.380±0.012	58, 62
SDSS J1057+1307		0.1251621	0.34±0.07	0.255±0.040	58, 62
SDSS J1223-0056		0.09007	0.45±0.06	0.196±0.043	58, 62
SDSS J1307+2156		0.216322132	–	0.319±0.061	58, 62
SDSS J1408+2950		0.1917902	0.49±0.04	0.255±0.040	58, 62
SDSS J1411+1028		0.167509	0.36±0.04	0.380±0.012	58, 62
SDSS J2235+1428		0.14445648	0.45±0.06	0.319±0.061	58, 62
CVs					
UZ For	**2M J0335-2544**	**0.08786542**	**∼0.71**	**∼0.14**	63, 64
HU Aqr	**2M J2107-0517**	**0.08682041**	**0.80±0.04**	**0.18±0.06**	65, 66
DP Leo	**RX J2107.9-0518**	**0.06236286**	**1.2:**	**0.14:**	67, 68
			0.6:	**0.09:**	69

References. (1) Lee et al. (2009), (2) Beuermann et al. (2012b), (3) Drechsel et al. (2001), (4) Beuermann et al. (2012a), (5) Østensen et al. (2008), (6) Wils et al. (2007), (7) Vučković et al. (2007), (8) Charpinet et al. (2008), (9) Qian et al. (2012b), (10) Østensen et al. (2010), (11) For et al. (2010), (12) Polubek et al. (2007), (14) Geier et al. (2011c), (16) Schaffenroth et al. (2013), (17) Kilkenny (2011), (18) Klepp & Rauch (2011), (19) Barlow et al. (2013), (20) Maxted et al. (2002), (21) Heber et al. (2004), (22) Maxted et al. (2004b), (23) Green et al. (2004), (24) For et al. (2008), (25) Koen (2007), (26) Koen (2009), (27) Edelmann et al. (2005), (28) Østensen et al. (2013), (29) Geier et al. (2014), (30) Kupfer et al. (2014), (31) Latour et al. (2014), (32) Kawaler et al. (2010), (33) Schaffenroth et al. (2014b), Sect 7.8, (34) Koen et al. (1999), (35) Pablo et al. (2011), (36) Jeffery & Ramsay (2014), (37) Pribulla et al. (2013) (38) Pietrukowicz et al. (2013), (39) Schindewolf et al., submitted, (40) Schaffenroth et al. (2015), Sect. 7.6, (41) Schaffenroth et al. (2014c), Sect. 7.4, (42) Kupfer priv. comm, (43) Schaffenroth et al. (2014a), Sect. 7.5, (44) Parsons et al. (2010a), (45) Beuermann et al. (2010), (46) O'Brien et al. (2001), (47) Kundra & Hric (2011), (48) O'Donoghue et al. (2003), (49) Maxted et al. (2007), (50) van den Besselaar et al. (2007), (51) Parsons et al. (2010b), (52) Parsons et al. (2012), (53) Maxted et al. (2004a), (54) Pyrzas et al. (2009), (55) Parsons et al. (2011), (56) Pyrzas et al. (2012), (57) Backhaus et al. (2012), (58) Rebassa-Mansergas et al. (2012), (59) Drake et al. (2010), (60) Law et al. (2012), (61) Almenara et al. (2012), (62) Parsons et al. (2013), (63) Bailey & Cropper (1991), (64) Potter et al. (2011), (65) Schwarz et al. (2009), (66) Schwope et al. (2011), (67) Pandel et al. (2002), (68) Beuermann et al. (2011), (69) Schwope et al. (2002), (70) Polubek et al. (2007), ([a]) Geier et al. (2010) *Notes*: Very uncertain values are followed by ":". It generally means that the mass was assumed and not derived.

Table A2.: Best fits of the orbital parameters for the currently claimed planets around eclipsing PCEBs.

Name	Msin(i) [Mj]	P [yr]	asin(i) [AU]	e	Ref.	Notes
HW Vir c	14.3±1.0	12.7±0.2	4.69±0.06	0.40±0.10	1	
HW Vir d	30-120	55±15	12.8±0.2	0.05:	1	*
HS0705+6700 c	31.5±1.0	8.41±0.05	3.52	0.38±0.05	2	*
HS2231+2441 c	13.94±2.20	15.7	$\sim$ 5.16	–	3	
NSVS14256825 c	2.8±0.3	3.49±0.21	1.9±0.3	0.00±0.08	4	
NSVS14256825 d	8.0±0.8	6.86±0.25	2.9±0.6	0.52±0.06	4	
NY Vir c	2.78±0.19	8.18±0.18	3.39±0.19	–	5	
NY Vir d	4.49±0.72:	27±3.7	7.56±0.64	0.44±0.17	5	
NN Ser c	6.91±0.54	15.50±0.45	5.38±0.20	0.0	6	
NN Ser d	2.28±0.38	7.75±0.35	3.39±0.10	0.20±0.02	6	
V471 Tau c	46-111	33.2±0.2	$\sim 12.6 - 12.8$	0.26±0.02	7	*
QS Vir c	9.01	14.4	$\sim$ 6.32	0.62	8	
QS Vir d	56.59	16.99	$\sim$ 7.15	0.92	8	*
RR Cae c	4.2±0.4	11.9±0.1	5.3±0.6	0	9	
UZ For c	6.3±1.5	16+3	5.9±1.4	0.04±0.05	10	
UZ For d	7.7±1.2	5.25±0.25	2.8±0.5	0.05±0.05	10	
HU Aqr c	7.1	9.00±0.05	4.30	0.13±0.04	11	
DP Leo c	6.05±0.47	28.01±2.00	8.19±0.39	0.39±0.13	12	

References. (1) Beuermann et al. (2012b), (2) Beuermann et al. (2012a), (3) Qian et al. (2012b), (4) Almeida et al. (2013), (5) Lee et al. (2014), (6) Beuermann et al. (2010), (7) Kundra & Hric (2011), (8) Almeida & Jablonski (2011), (9) Qian et al. (2012a), (10) Potter et al. (2011), (11) Goździewski et al. (2012), (12) Beuermann et al. (2011) $*$ The claimed third body is more consistent with a BD than with a planet.
Notes: Very uncertain values are followed by ":".

B. Atomic Data

All atomic data used to derive the synthetic spectra. The model atoms in Table A1 are used in DETAIL to derive the population numbers. Table A2 and A3 summarize the data used in SURFACE to calculate the final synthetic spectrum.

Table A1.: Model atoms for NLTE calculations

Ion	Model atom
H	Przybilla & Butler (2004)
He I/II	Przybilla (2005)
C II-IV	Nieva & Przybilla (2006, 2008)
N II	Przybilla & Butler (2001)
O I/II	Przybilla et al. (2000); Becker & Butler (1988), updated
Ne I/II	Morel & Butler (2008), updated
Mg II	Przybilla et al. (2001)
Al II/III	Przybilla (in prep.)
Si II-IV	Przybilla & Butler (in prep.)
S II/III	Vrancken et al. (1996), updated
Ar I/II	Butler (in prep.)
Fe II/III	Becker (1998); Morel et al. (2006), corrected

Table A2.: Atomic Data for NLTE calculations

atomic number Z	element	ionization stage	linelist	energy levels	collisional broadening	natural broadening
6	C	I	1,2	1	2,a	b,2
		II	1,2	1	c,2,a	b,2
		III	1,2	1	2,a	b,2
		IV	1,2	1	2,a,d	b,2
7	N	I	1,2	1	a	b,2
		II	1,2	1	c,2,a	b,2
		III	1,2	1	a	b,2
8	O	I	1,2	1	2,a	b,2
		II	1,2	1	c,2,a	b,2
		III	1,2	1	a,d	b
12	Mg	II	1,2	1	a	b
13	Al	II	1,2	1	c,2,a	b,2
		III	1,2	1	a,d	b
14	Si	II	1,2	1	c,2,a	b,2
		III	1,2	1	2,a	b,2
		IV	1,2	1	d,2,a	b,2
16	S	II	1,2	1	a,c	b,2
		III	1,2	1	a	2
26	Fe	II	1,3	1	d,2,a	2
		III	1,3	1	2,a	2
		IV	1,3	1	2,a	2

(1) NIST: Ralchenko (2005), `http://www.nist.gov/pml/data/asd.cfm`
(2) Kurucz (2011), `http://kurucz.harvard.edu/linelists/`
(3) FERRUM project: Johansson et al. (2002)
(a) formula by Cowley (1971)
(b) Topbase: Cunto & Mendoza (1992), `http://cdsweb.u-strasbg.fr/topbase/topbase.html`
(c) Griem (1974)
(d) STARK-B: Sahal-Bréchot et al. (2014), `http://stark-b.obspm.fr/`

Table A3.: Atomic Data for LTE calculations

atomic number Z	element	ionization stage	linelist	energy levels	collisional broadening	natural broadening
9	F	I	2	1	a	b
		II	2	1	a	b
21	Sc	III	2	1	c,2	2
		IV	2	1	2	2
		V	2	1	2	2
		VI	2	1	2	2
22	Ti	III	2,3	1	2	2
		IV	2	1	c,2	2
		V	2	1	2	2
		VI	2,3	1	2	2
23	V	III	2	1	2	2
		IV	2	1	2	2
		V	2	1	2	2
		IV	2	1	2	2
24	Cr	III	2	1	a	2
		IV	2	1	2	2
		V	2	1	2	2
		VI	2	1	2	2
25	Mn	III	2,3	1	2	2
		IV	2	1	2	2
		V	2,3	1	2	2
		VI	2	1	2	2
26	Fe	V	2,3	1	2	2
		VI	2	1	2	2
27	Co	III	2	1	2	2
		IV	2,3	1	2	2
		V	2,3	1	2	2
		VI	2	1	2	2
28	Ni	III	2	1	2	2
		IV	2,3	1	2	2
		V	2,3	1	2	2
		VI	2	1	2	2
29	Cu	III	4	1	a	-
		IV	4	1	a	-
30	Zn	III	2	1	a	-
		IV	5	1	a	-
		V	5	1	a	-
31	Ga	II	6	1	a	-
	*	III	6	1	a	-
	*	IV	7	1	a	-
	*	V	7	1	a	-
	*	VI	7	1	a	-
32	Ge	II	2	1	a	-
		III	8	1	a	-
		IV	8	1	a	-
	*	V	9	1	a	-
	*	VI	9	1	a	-
33	As	II	8	1	a	-
		III	8	1	a	-
		IV	8	1	a	-
38	Sr	II	2	1	a	-

39	Y	II	2	1	a	-
		III	8	1	a	-
40	Zr	II	2	1	a	-
		III	8	1	a	-
41	Nb	II	2	1	a	-
42	Mo	II	2	1	a	-
	*	III	11	1	a	-
43	Tc	II	8	1	a	-
	*	IV	12	1	a	-
	*	V	12	1	a	-
	*	VI	12	1	a	-
44	Ru	II	2	1	a	-
		III	13	1	a	-
45	Rh	II	2	1	a	-
		III	14	1	a	-
46	Pd	II	2	1	a	-
		III	14	1	a	-
47	Ag	II	2	1	a	-
		III	14	1	a	-
48	Cd	II	2	1	a	-
49	In	II	2	1	a	-
		III	8	1	a	-
50	Sn	II	2	1	a	-
		III	8	1	a	-
		IV	8	1	a	-
51	Sb	II	8	1	a	-
		III	8	1	a	-
		IV	8	1	a	-
52	Te	II	8	1	a	-
		III	8	1	a	-
56	Ba	II	2	1	a	-
	*	V	15	1	a	-
	*	VI	15	1	a	-
	*	VII	15	1	a	-
57	La	II	2	1	a	-
		III	8	1	a	-
58	Ce	II	2	1	a	-
		III	8	1	a	-
		IV	8	1	a	-
62	Sm	II	2	1	a	-
	*	III	16	1	a	-
63	Eu	II	2	1	a	-
		III	8	1	a	-
64	Gd	II	2	1	a	-
		III	8	1	a	-
67	Ho	III	17,18	1	a	-
68	Er	III	19	1	a	-
69	Tm	III	20	1	a	-
70	Yb	II	2	1	a	-
		III	21	1	a	-
		IV	22	1	a	-

71	Lu	II	2	1	a	-
		III	8	1	a	-
72	Hf*	III	26	1	a	-
74	W	II	2	1	a	-
		III	21	1	a	-
	*	IV	25	1	a	-
75	Re	II	2	1	a	-
76	Os	II	2,23	1	a	-
77	Ir	II	2,24	1	a	-
78	Pt	II	8	1	a	-
79	Au	II	8	1	a	-
		III	8,27*	1	a	-
80	Hg	II	2	1	a	-
81	Tl	II	8	1	a	-
		III	8	1	a	-
82	Pb	II	2	1	a	-
		III	8	1	a	-
		IV	8	1	a	-
83	Bi	II	8	1	a	-
		III	8	1	a	-
		IV	8	1	a	-

(1) NIST: Ralchenko (2005), http://www.nist.gov/pml/data/asd.cfm
(2) Kurucz (2011), http://kurucz.harvard.edu/linelists/
(3) Iron project: Hummer et al. (1993), http://cdsweb.u-strasbg.fr/topbase/TheIP.html
(4) Hirata & Horaguchi (1994), http://cdsarc.u-strasbg.fr/viz-bin/Cat?VI/69
(5) Rauch et al. (2014a), http://cdsarc.u-strasbg.fr/viz-bin/Cat?J/A+A/564/A41
(6) Castelli & Parthasarathy (1995)
(7) Rauch et al. (2015)
(8) Morton (2000), http://iopscience.iop.org/0067-0049/130/2/403/fulltext/
(9) Rauch et al. (2012), http://cdsarc.u-strasbg.fr/viz-bin/Cat?J/A+A/546/A55
(10) Nilsson et al. (2010)
(11) Quinet (2015)
(12) Werner et al. (2015), http://cdsarc.u-strasbg.fr/viz-bin/Cat?J/A+A/574/A29
(13) Palmeri et al. (2009)
(14) Zhang et al. (2013)
(15) Rauch et al. (2014b), http://cdsarc.u-strasbg.fr/viz-bin/Cat?J/A+A/566/A10
(16) Biémont et al. (2003)
(17) Biémont et al. (2001c)
(18) Zhang et al. (2002)
(19) Biémont et al. (2001a)
(20) Li et al. (2001)
(21) Biémont et al. (2001b)
(22) Wyart et al. (2001)
(23) Quinet et al. (2006)
(24) Xu et al. (2007)
(25) Enzonga Yoca et al. (2012)
(26) Malcheva et al. (2009)
(27) Enzonga Yoca et al. (2008)
(a) formula by Cowley (1971)
(b) Topbase: Cunto & Mendoza (1992), http://cdsweb.u-strasbg.fr/topbase/topbase.html
(c) STARK-B: Sahal-Bréchot et al. (2014), http://stark-b.obspm.fr/

C. Line distribution of different elements at different effective temperatures

The following figures show the distributions from lines of different elements and ionization stages until the iron group over a wavelength from $1000 - 3000$ Å. Therefor we calculated synthetic spectra with our models. To illustrate the high dependence of the line distribution from the effective temperature of the star, the distribution was calculated for four different effective temperatures using the parameters of four different stars (see Table C1). The synthetic spectra were not broadened by macroscopic broadening mechanisms like rotation or macroturbulence, but only the natural broadening, pressure broadening and microturbulence.

Table C1.: Parameters used to calculate model spectra

star	effective temperature [K]	surface gravity [cgs]	microturbulence [$\mathrm{km\,s^{-1}}$]
ι Her	17500	3.85	2
γ Peg	21550	3.96	2
HR 1861	27000	4.18	4
τ Sco	31650	4.30	4

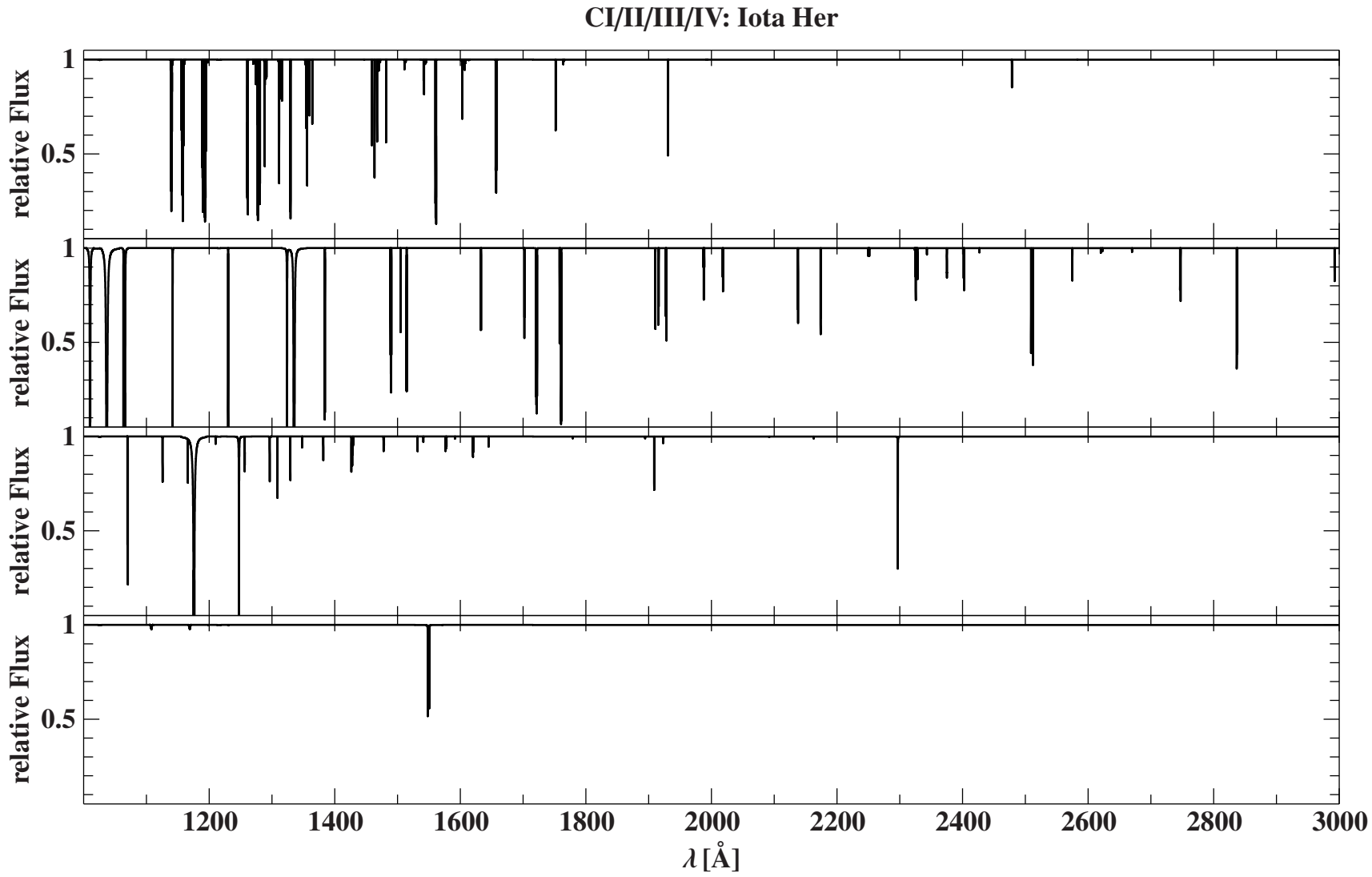
CI/II/III/IV: Iota Her
relative Flux
1
0.5
1200
1400
1600
1800
2000
2200
2400
2600
2800
3000
λ [Å]

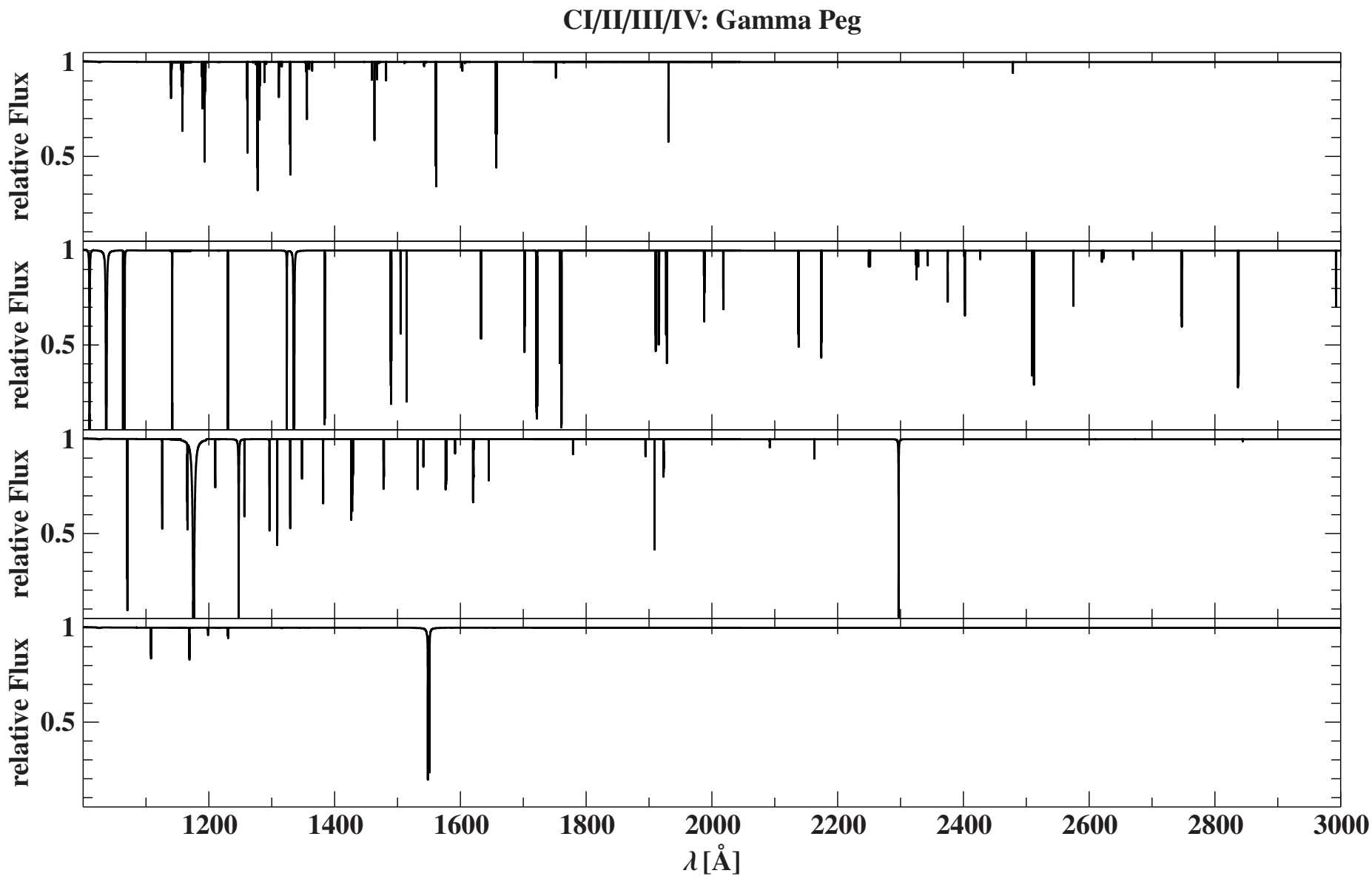
CI/II/III/IV: Gamma Peg
relative Flux
1
0.5
1200
1400
1600
1800
2000
2200
2400
2600
2800
3000
λ [Å]

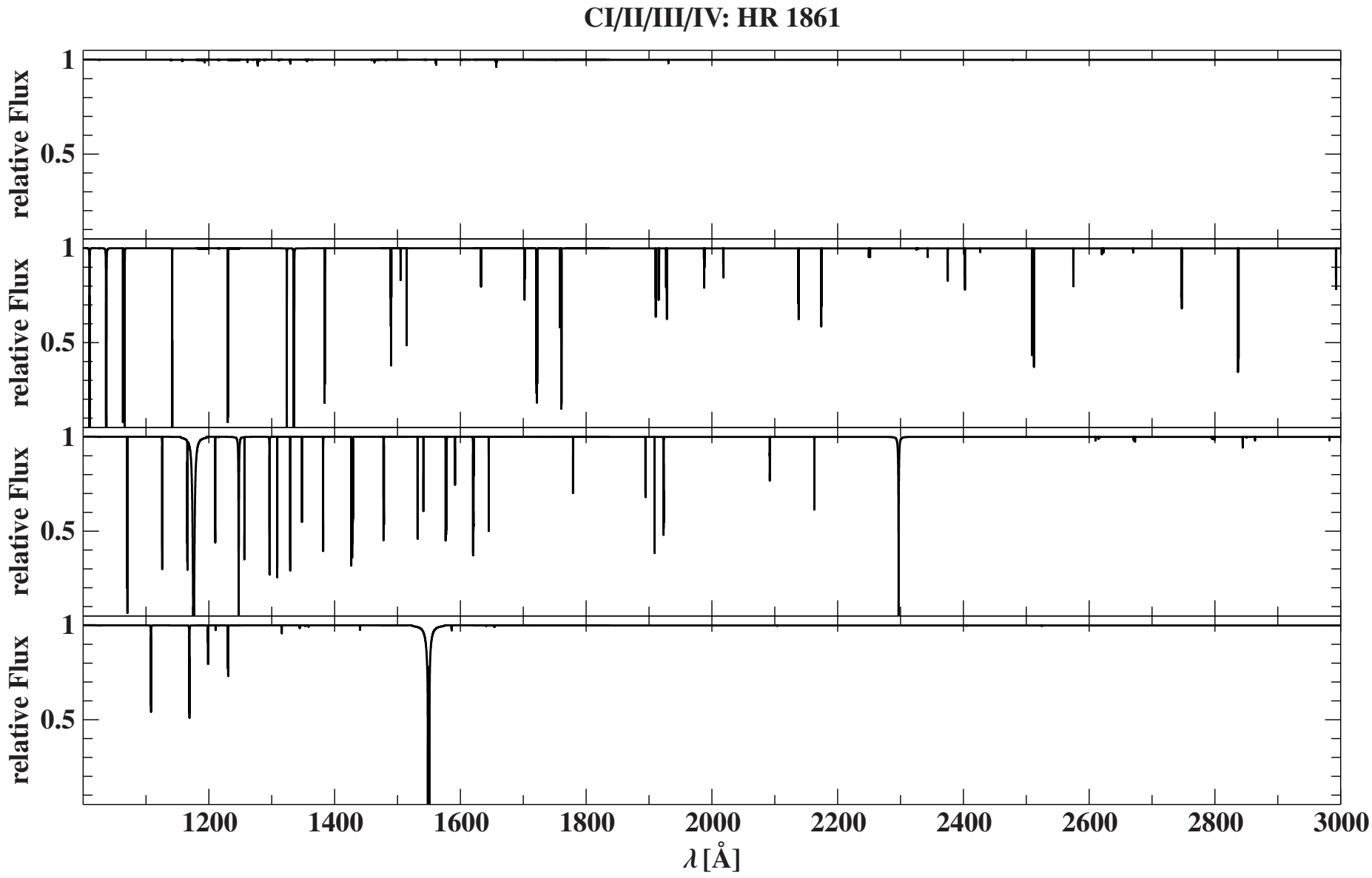
CI/II/III/IV: HR 1861
relative Flux
1
0.5
1200
1400
1600
1800
2000
2200
2400
2600
2800
3000
λ [Å]

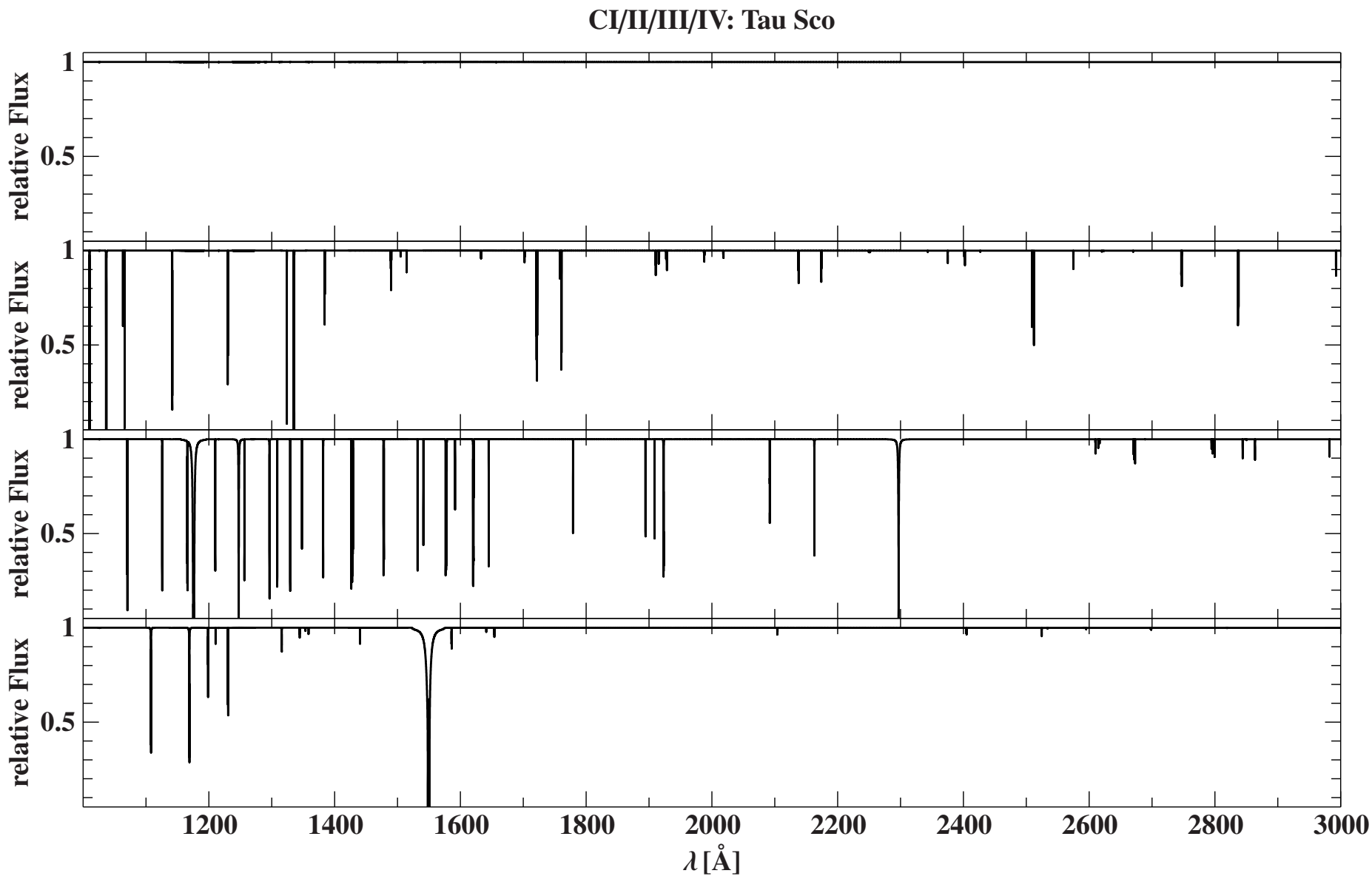
CI/II/III/IV: Tau Sco
relative Flux
1
0.5
1200
1400
1600
1800
2000
2200
2400
2600
2800
3000
λ [Å]

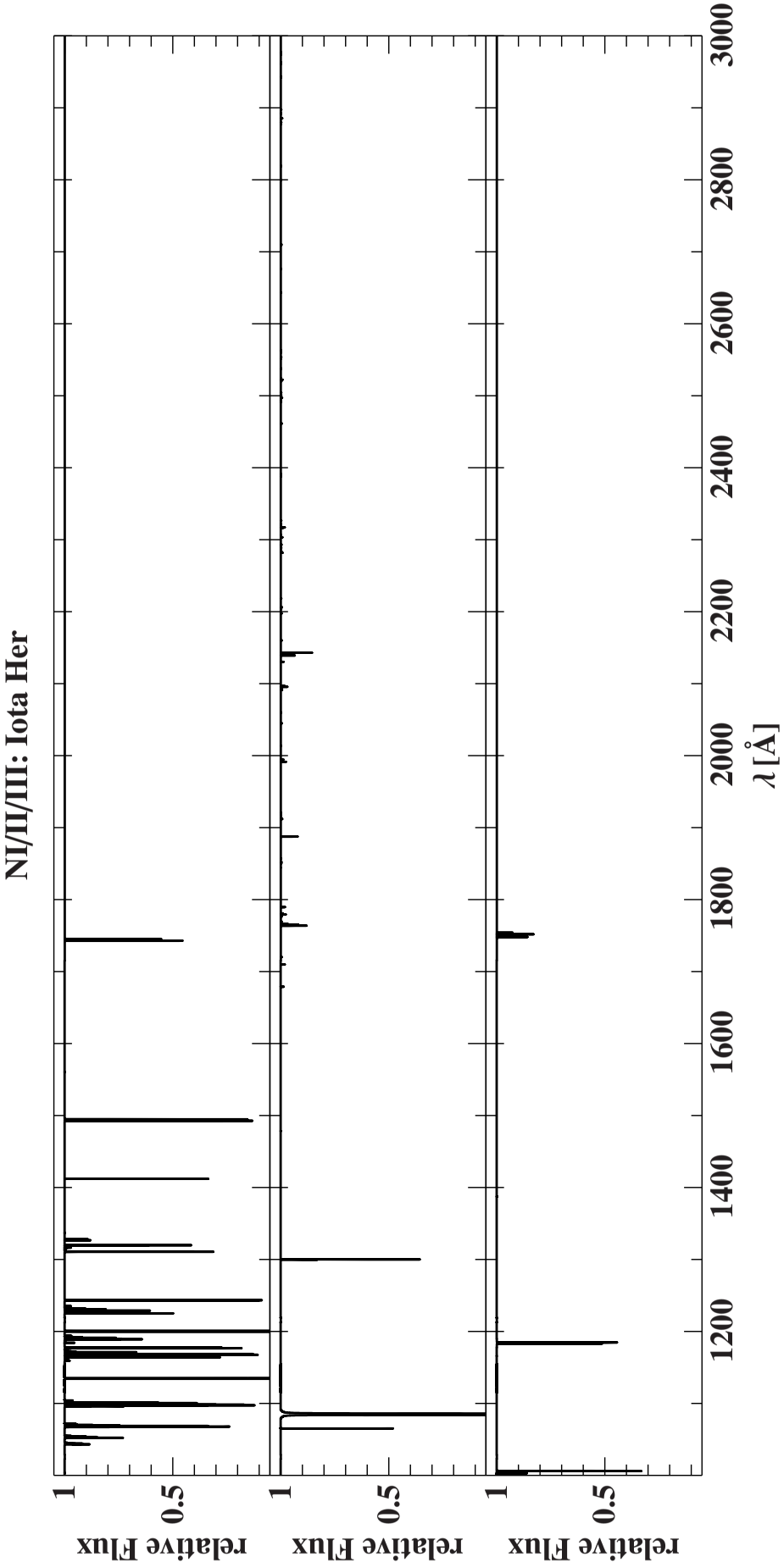
NI/II/III: Iota Her
relative Flux
relative Flux
relative Flux
1
0.5
1
0.5
1
0.5
1200
1400
1600
1800
2000
2200
2400
2600
2800
3000
λ [Å]

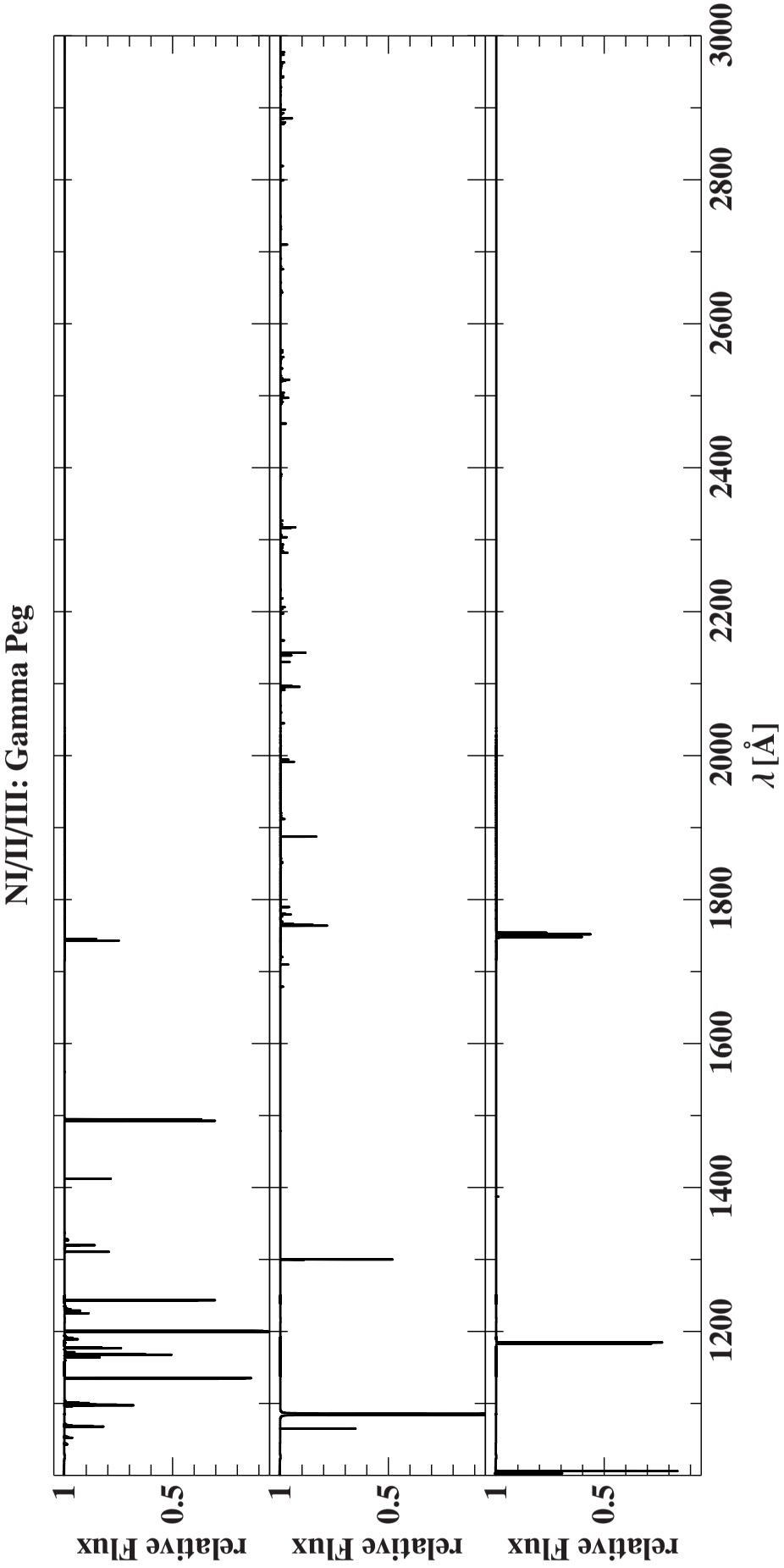
NI/II/III: Gamma Peg
relative Flux
relative Flux
relative Flux
1
0.5
1
0.5
1
0.5
1200
1400
1600
1800
2000
2200
2400
2600
2800
3000
λ [Å]

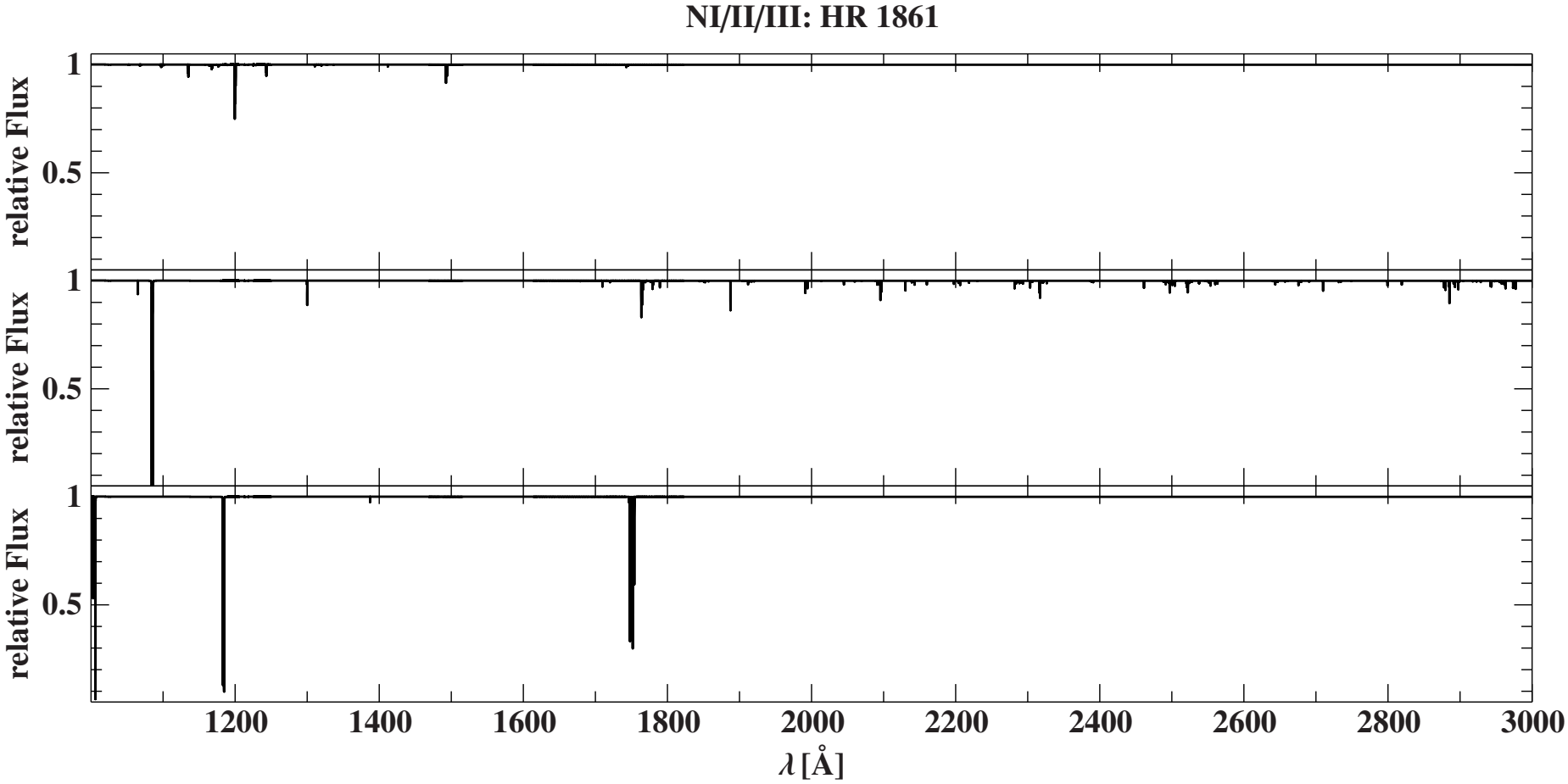
NI/II/III: HR 1861
relative Flux
1
0.5
1
relative Flux
0.5
1
relative Flux
0.5
1200
1400
1600
1800
2000
2200
2400
2600
2800
3000
λ [Å]

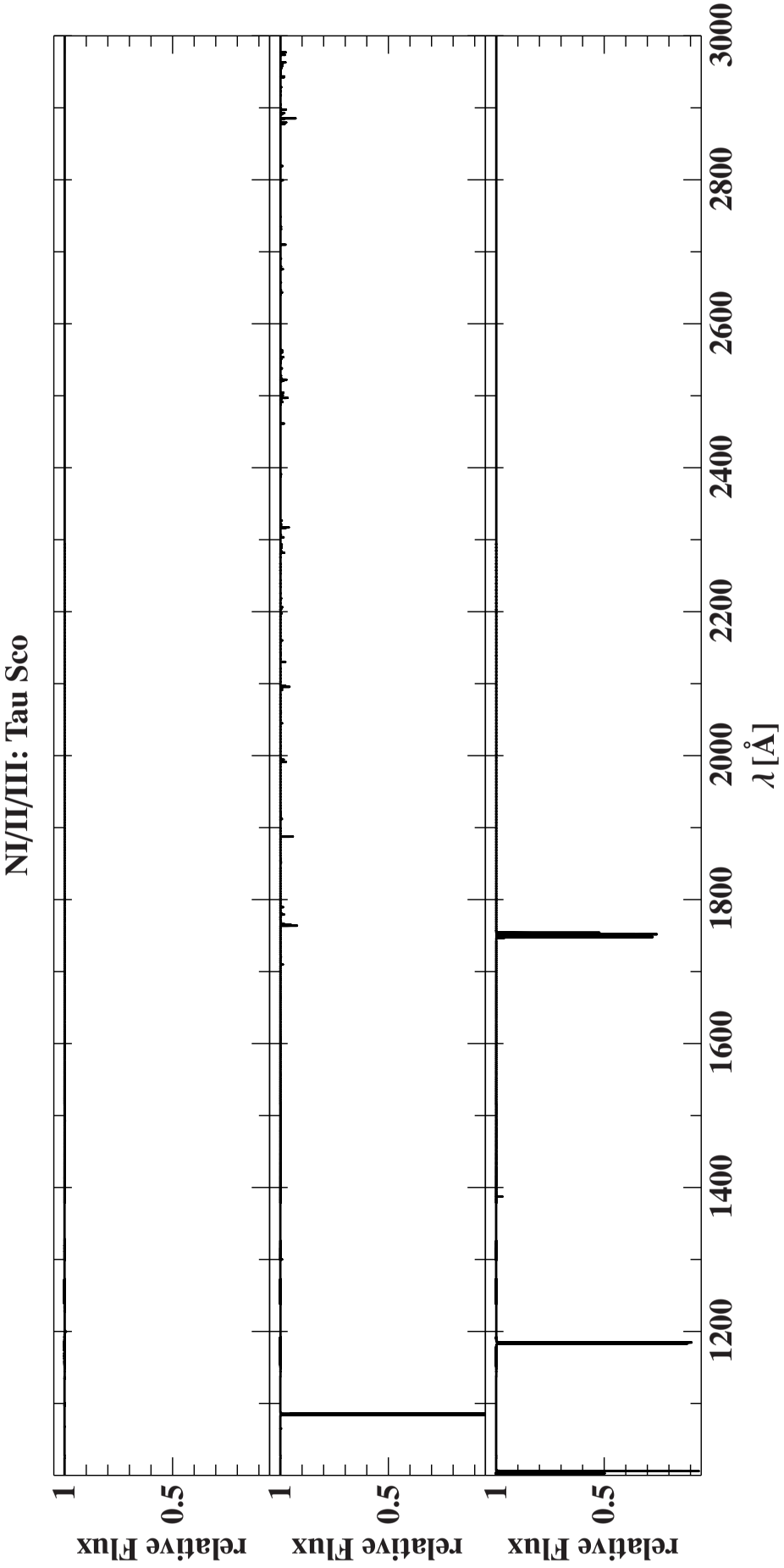
NI/II/III: Tau Sco
relative Flux
relative Flux
relative Flux
1
0.5
1
0.5
1
0.5
1200
1400
1600
1800
2000
2200
2400
2600
2800
3000
λ [Å]

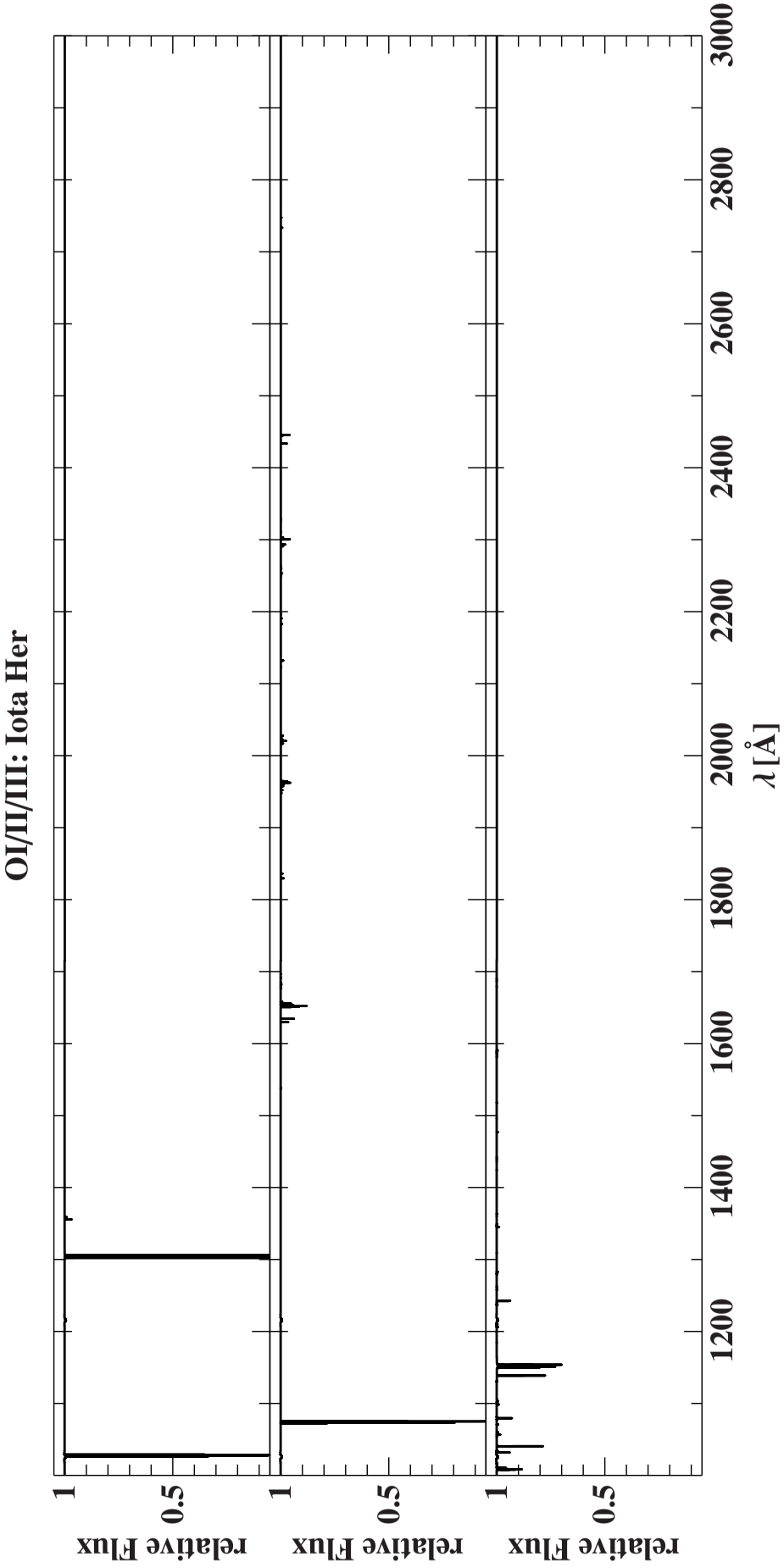
OI/II/III: Iota Her
relative Flux
relative Flux
relative Flux
1
0.5
1
0.5
1
0.5
1200
1400
1600
1800
2000
2200
2400
2600
2800
3000
λ [Å]

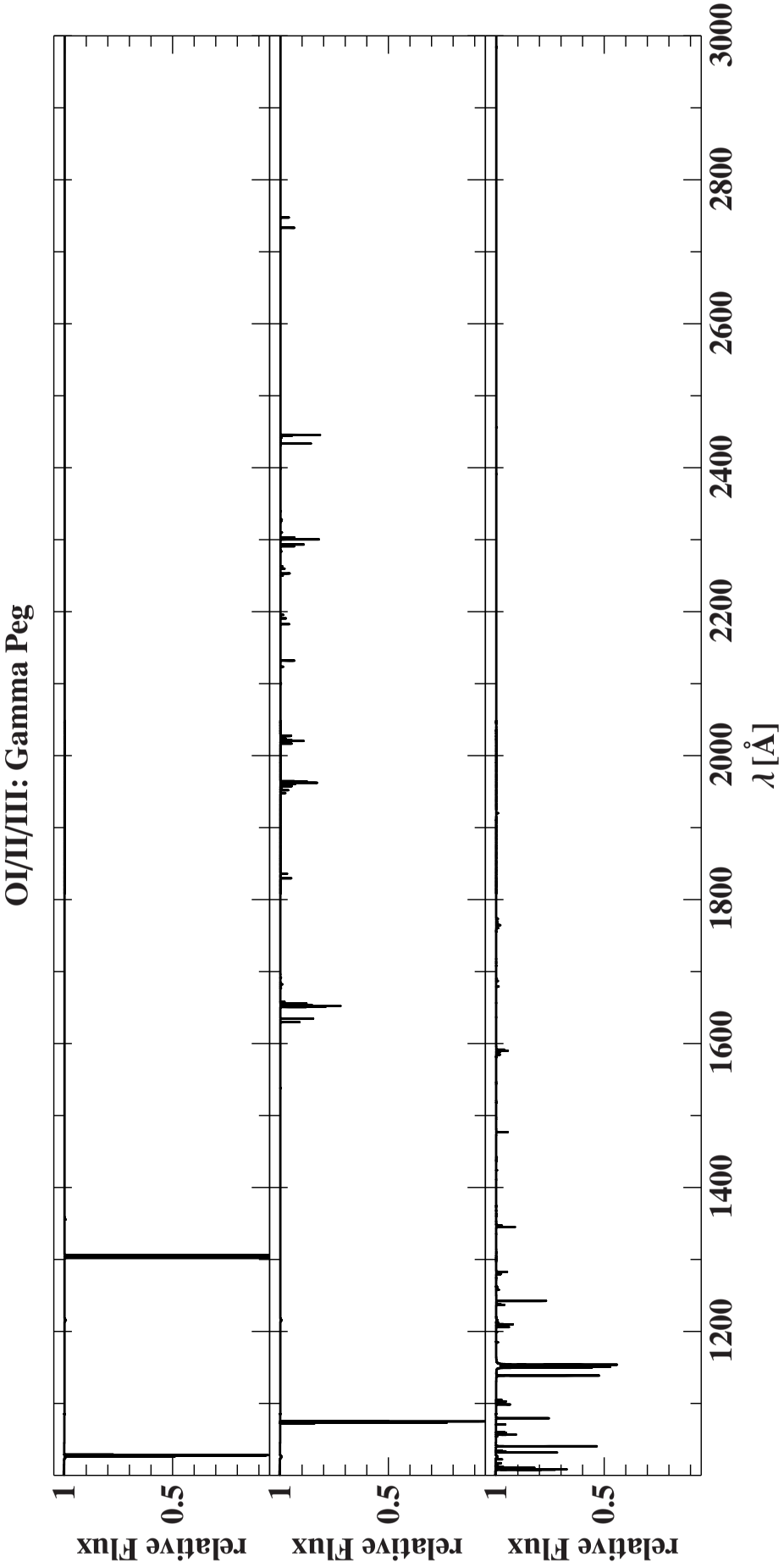
OI/II/III: Gamma Peg
relative Flux
relative Flux
relative Flux
1
0.5
1
0.5
1
0.5
1200
1400
1600
1800
2000
2200
2400
2600
2800
3000
λ [Å]

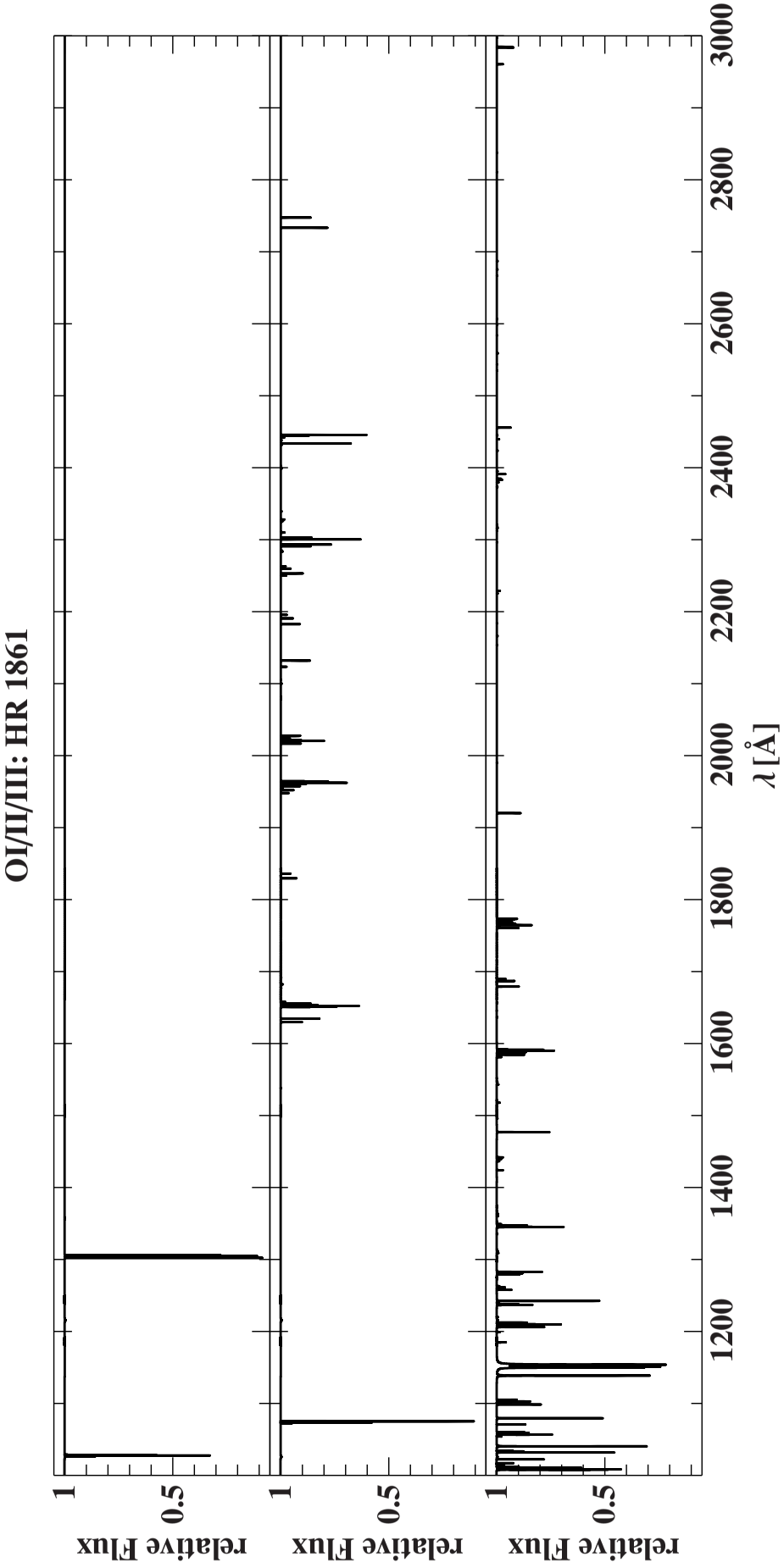
OI/II/III: HR 1861
relative Flux
relative Flux
relative Flux
1
0.5
1
0.5
1
0.5
1200
1400
1600
1800
2000
2200
2400
2600
2800
3000
λ [Å]

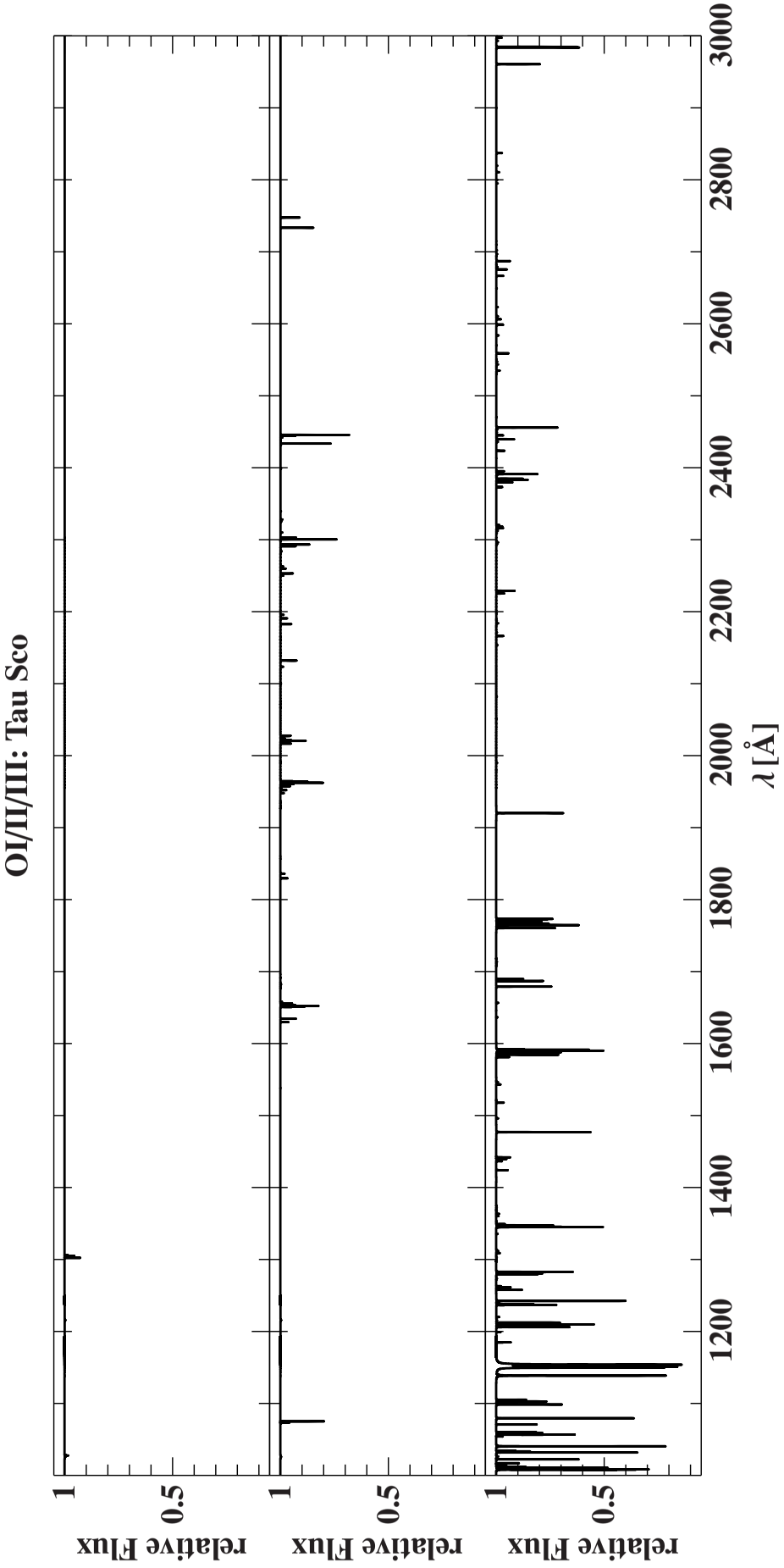
OI/II/III: Tau Sco
relative Flux
relative Flux
relative Flux
1
0.5
1
0.5
1
0.5
1200
1400
1600
1800
2000
2200
2400
2600
2800
3000
λ [Å]

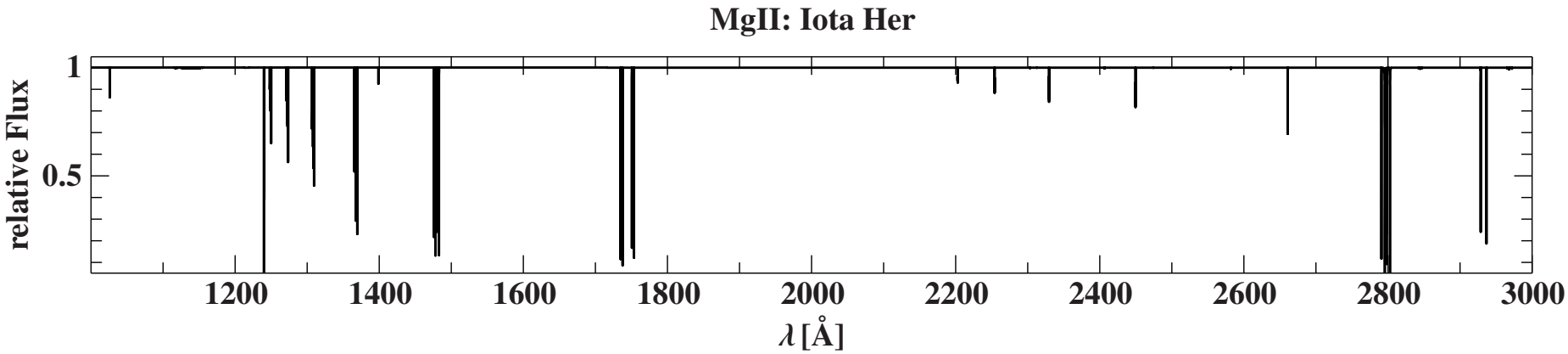
MgII: Iota Her
relative Flux
1
0.5
1200
1400
1600
1800
2000
2200
2400
2600
2800
3000
λ [Å]

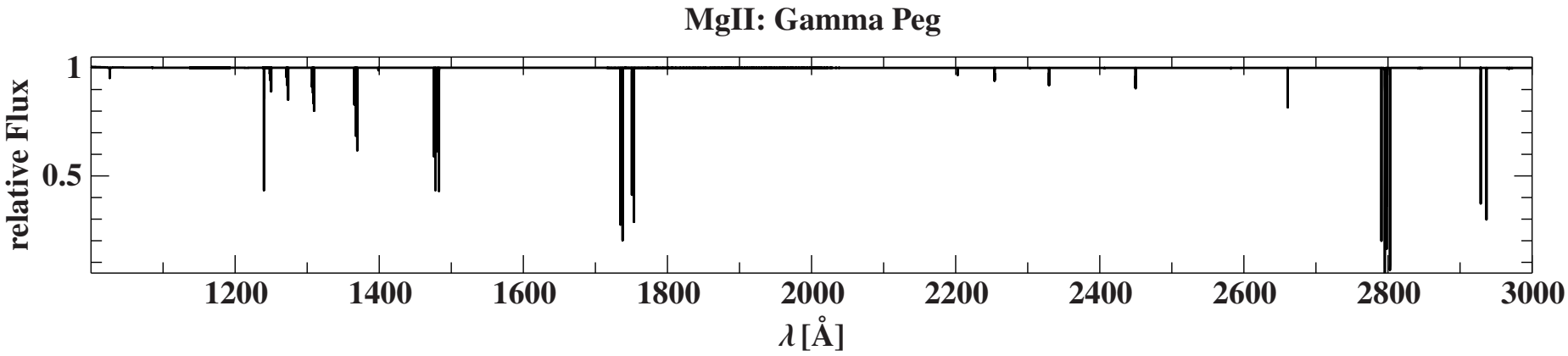
MgII: Gamma Peg
relative Flux
1
0.5
1200
1400
1600
1800
2000
2200
2400
2600
2800
3000
λ [Å]

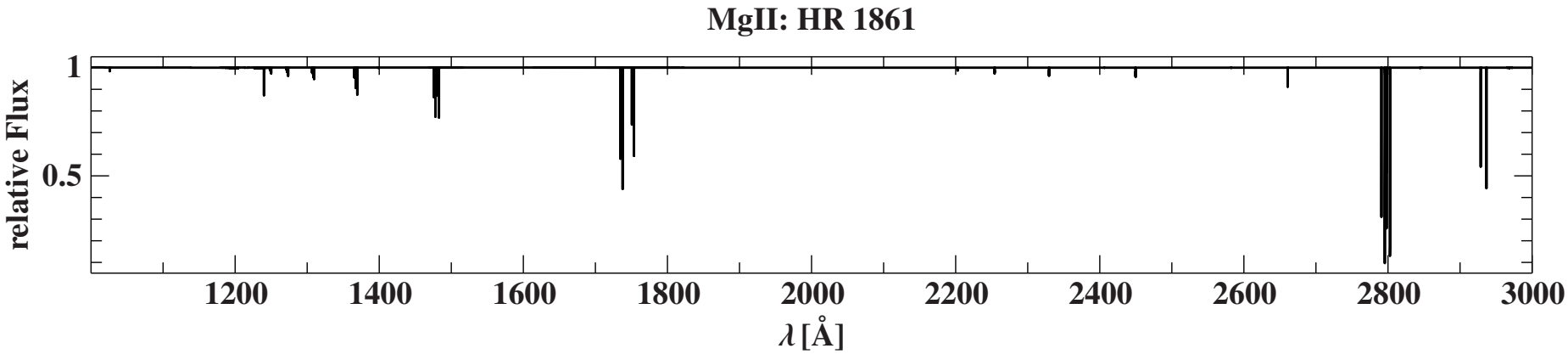
MgII: HR 1861
relative Flux
1
0.5
1200
1400
1600
1800
2000
2200
2400
2600
2800
3000
λ [Å]

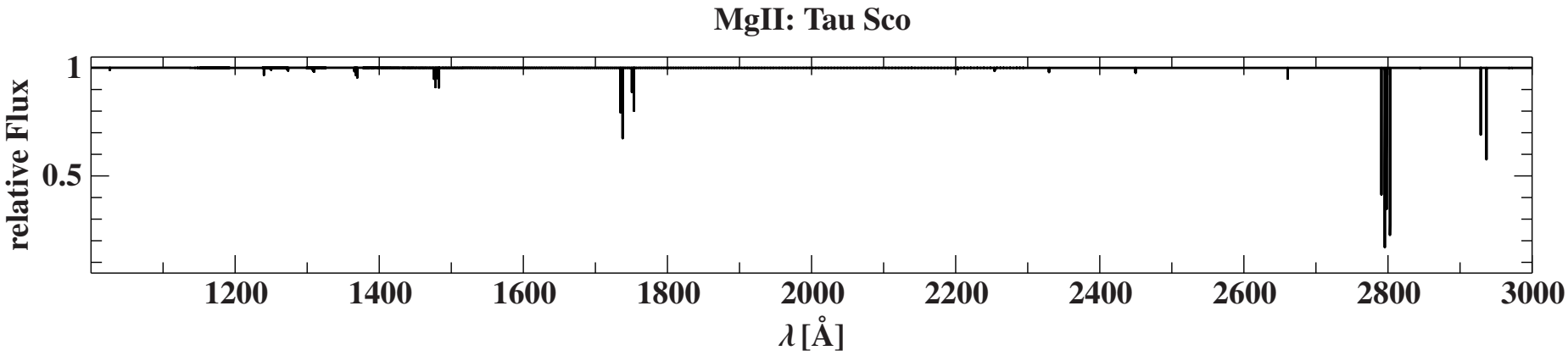
MgII: Tau Sco
relative Flux
1
0.5
1200
1400
1600
1800
2000
2200
2400
2600
2800
3000
λ [Å]

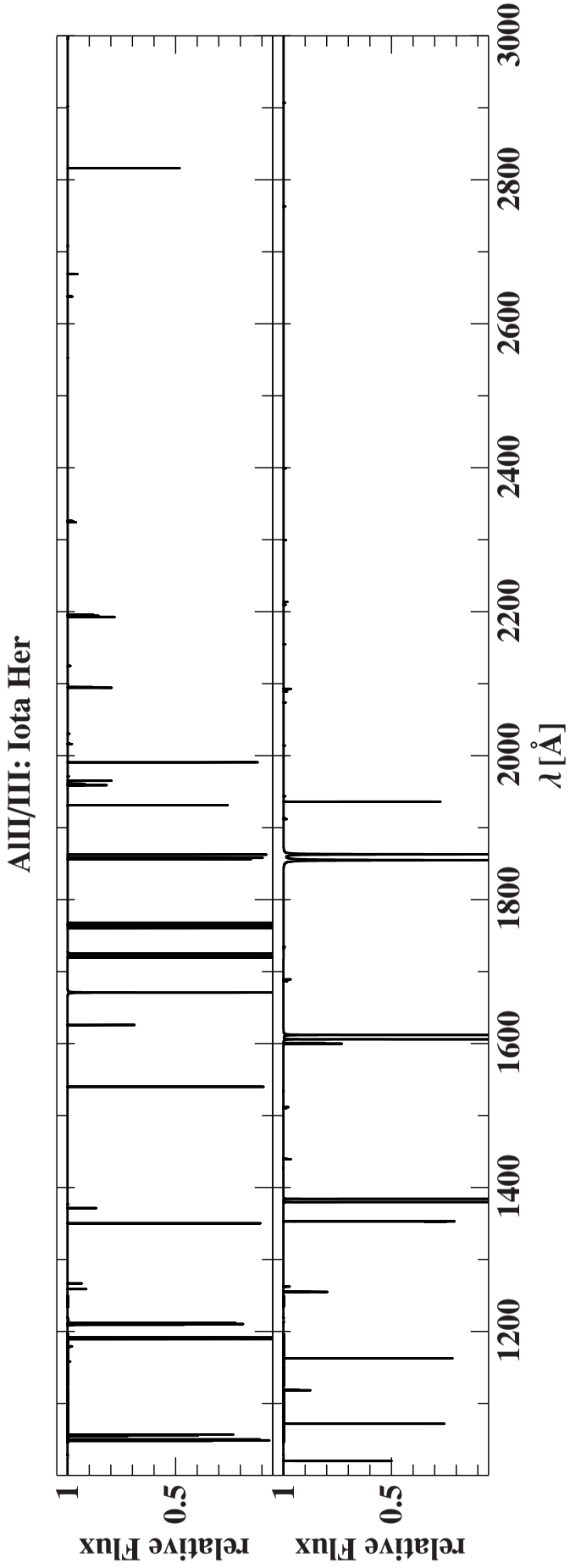
AIII/IIII: Iota Her
relative Flux
relative Flux
1
0.5
1
0.5
1200
1400
1600
1800
2000
2200
2400
2600
2800
3000
λ [Å]

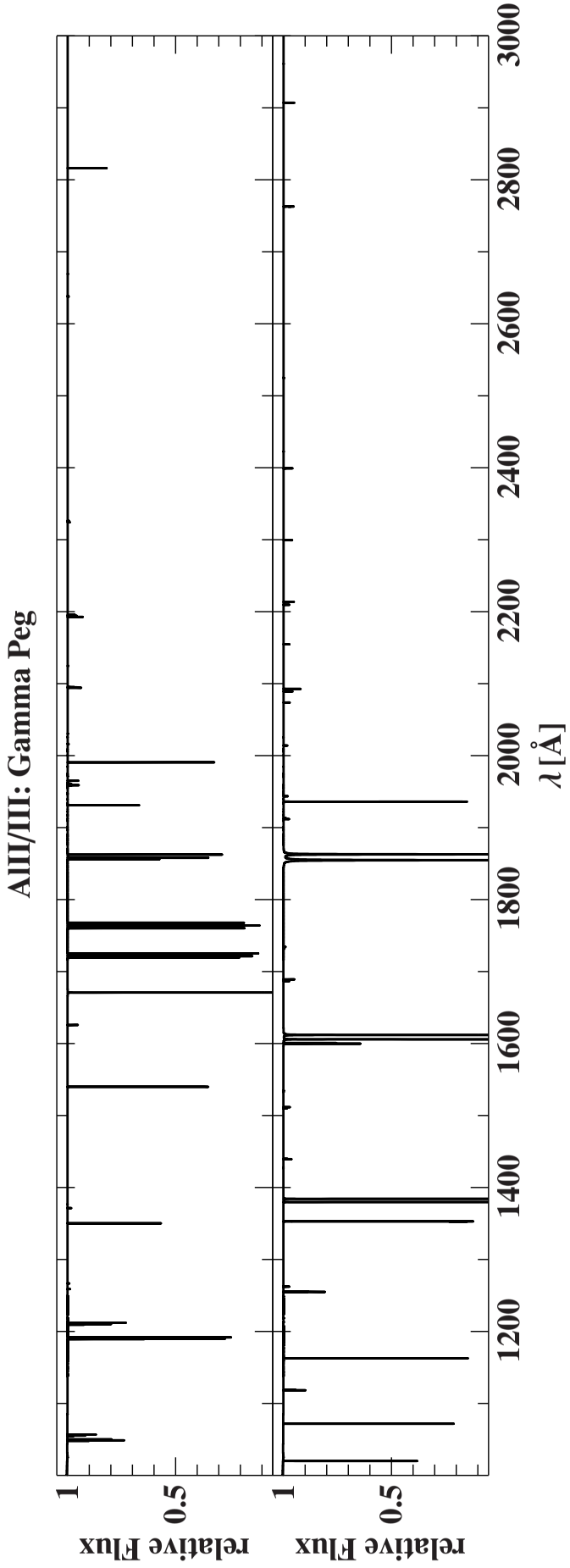
AlII/III: Gamma Peg
relative Flux
relative Flux
1
0.5
1
0.5
1200
1400
1600
1800
2000
2200
2400
2600
2800
3000
λ [Å]

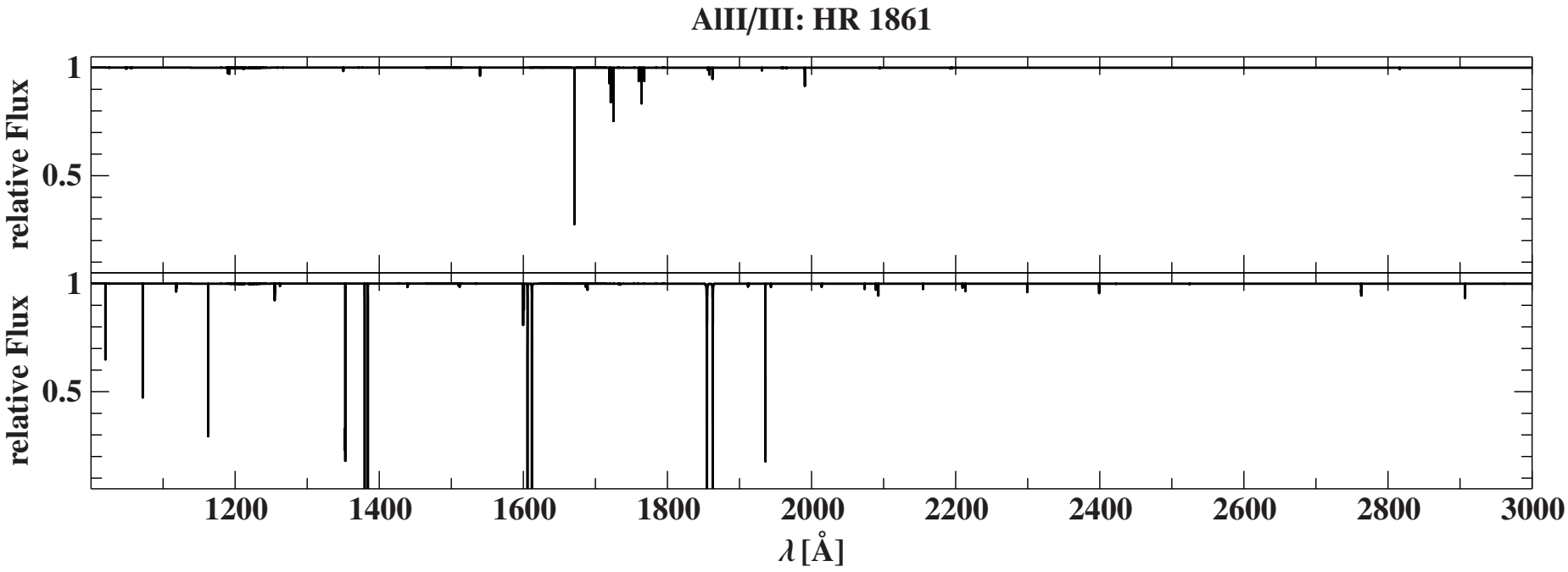
AlII/III: HR 1861
relative Flux
1
0.5
relative Flux
1
0.5
1200
1400
1600
1800
2000
2200
2400
2600
2800
3000
λ [Å]

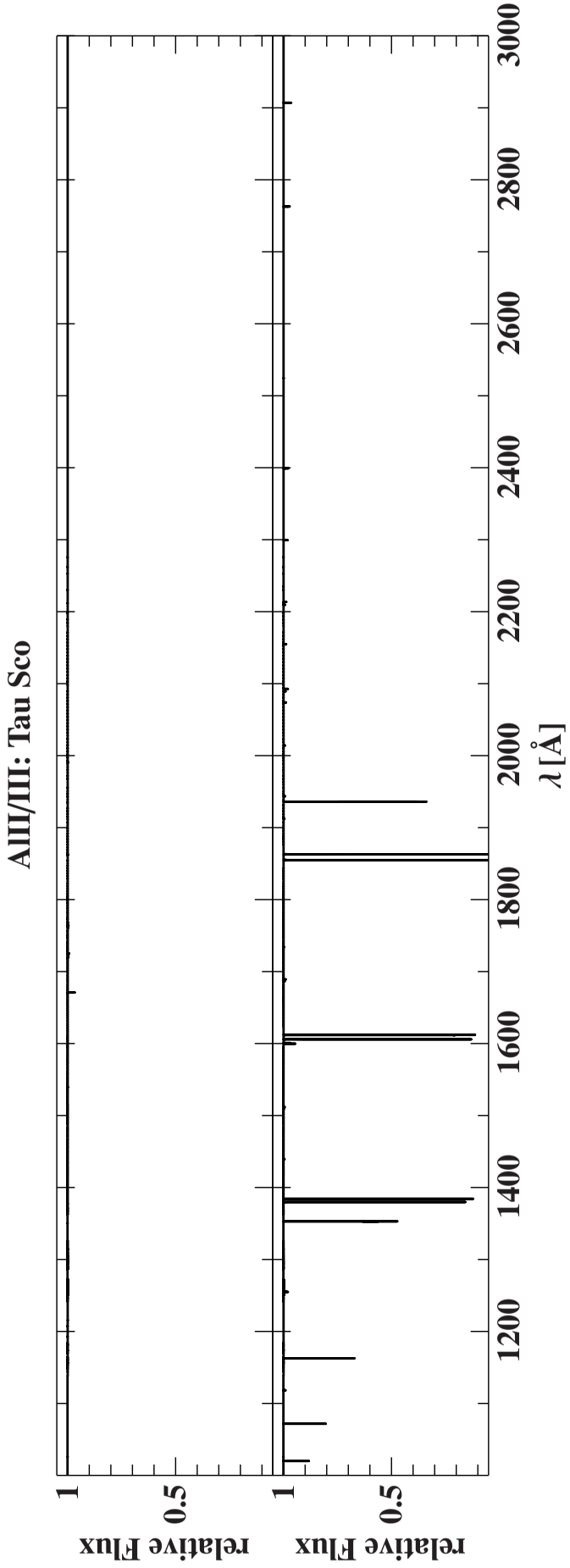
AlII/III: Tau Sco
relative Flux
relative Flux
1
0.5
1
0.5
1200
1400
1600
1800
2000
2200
2400
2600
2800
3000
λ [Å]

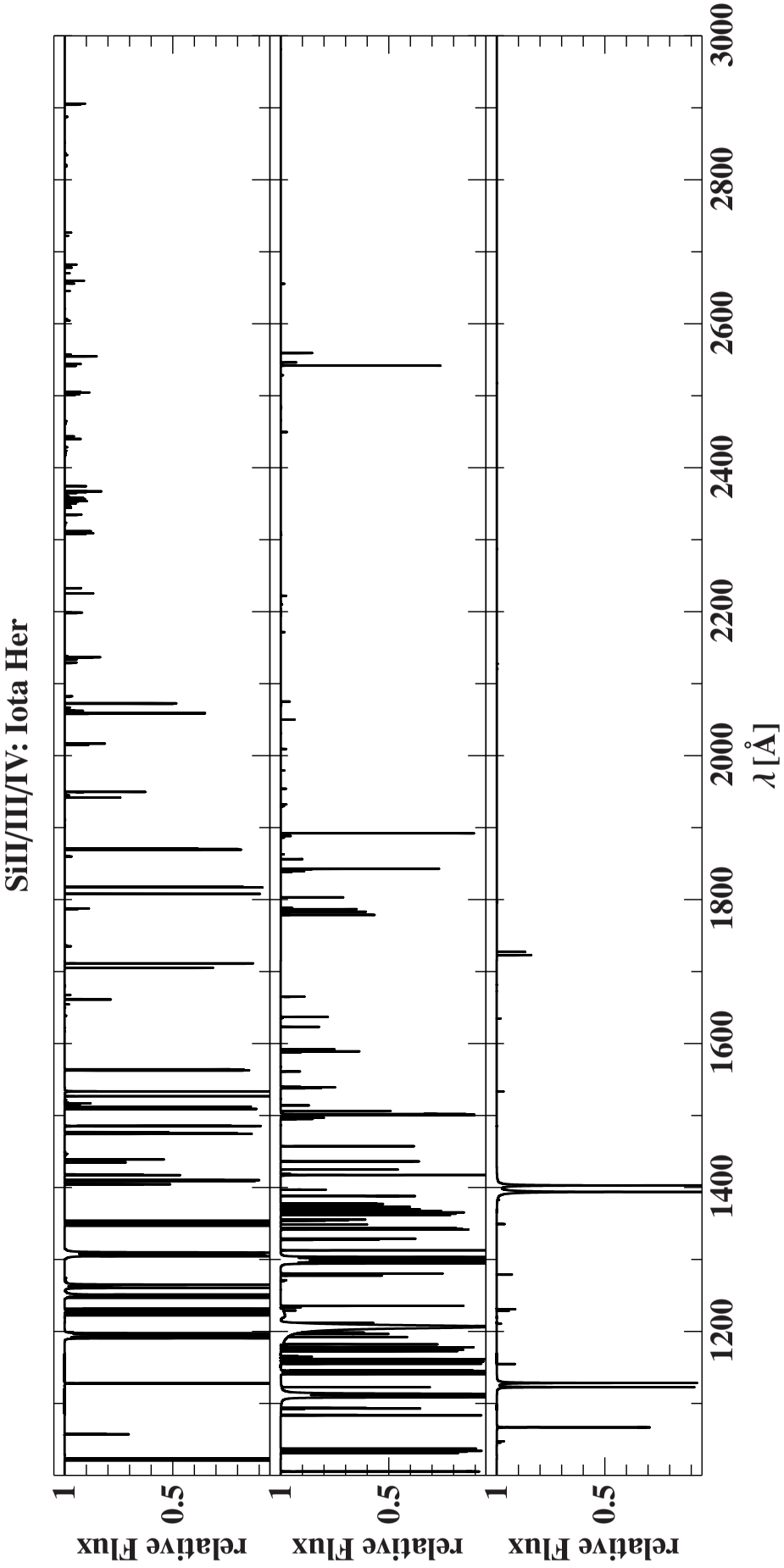
SiII/III/IV: Iota Her
relative Flux
relative Flux
relative Flux
1
0.5
1
0.5
1
0.5
1200
1400
1600
1800
2000
2200
2400
2600
2800
3000
λ [Å]

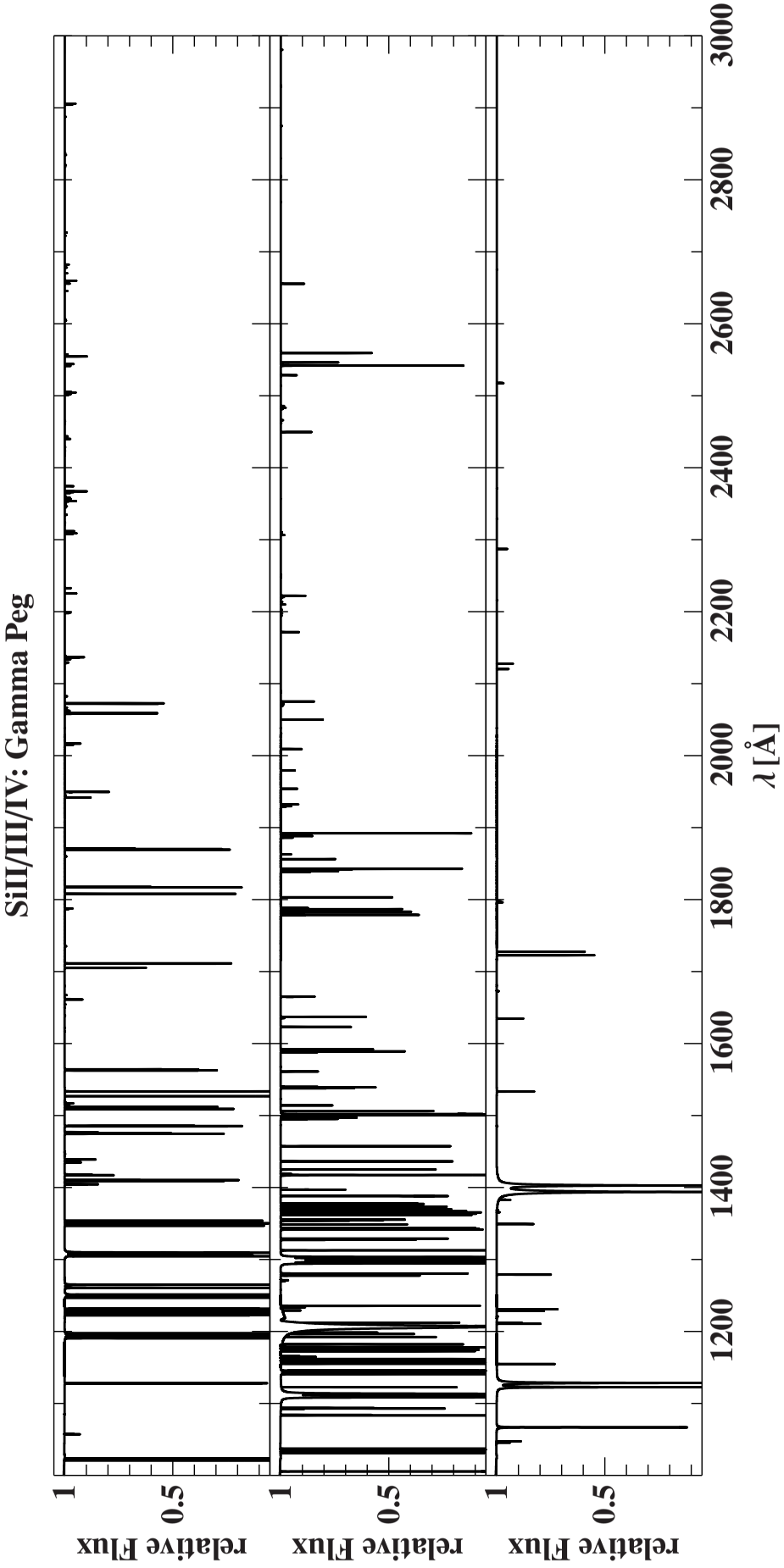
SiII/III/IV: Gamma Peg
relative Flux
relative Flux
relative Flux
1
0.5
1
0.5
1
0.5
1200
1400
1600
1800
2000
2200
2400
2600
2800
3000
λ [Å]

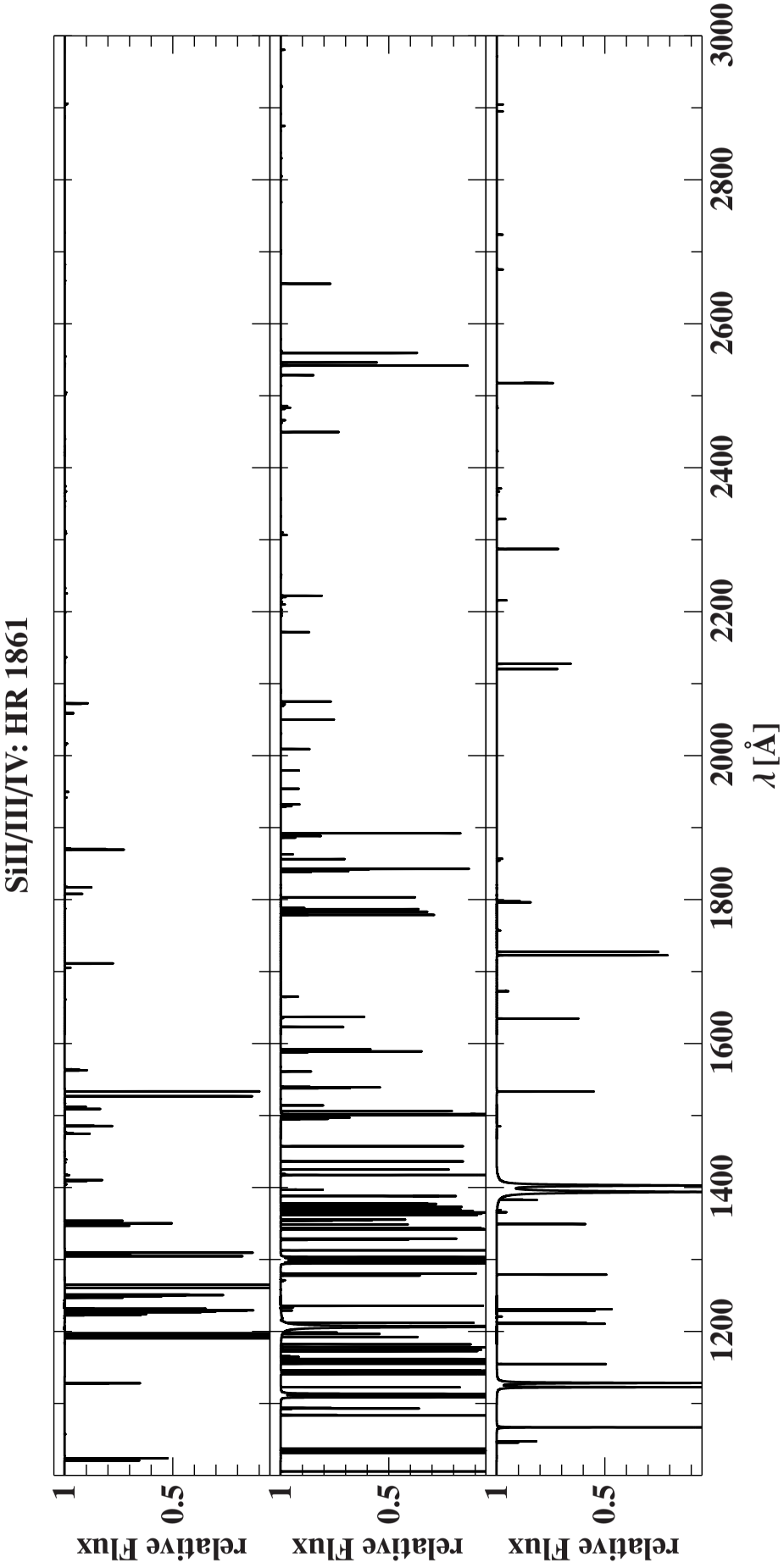
SiII/III/IV: HR 1861
relative Flux
relative Flux
relative Flux
1
0.5
1
0.5
1
0.5
1200
1400
1600
1800
2000
2200
2400
2600
2800
3000
λ [Å]

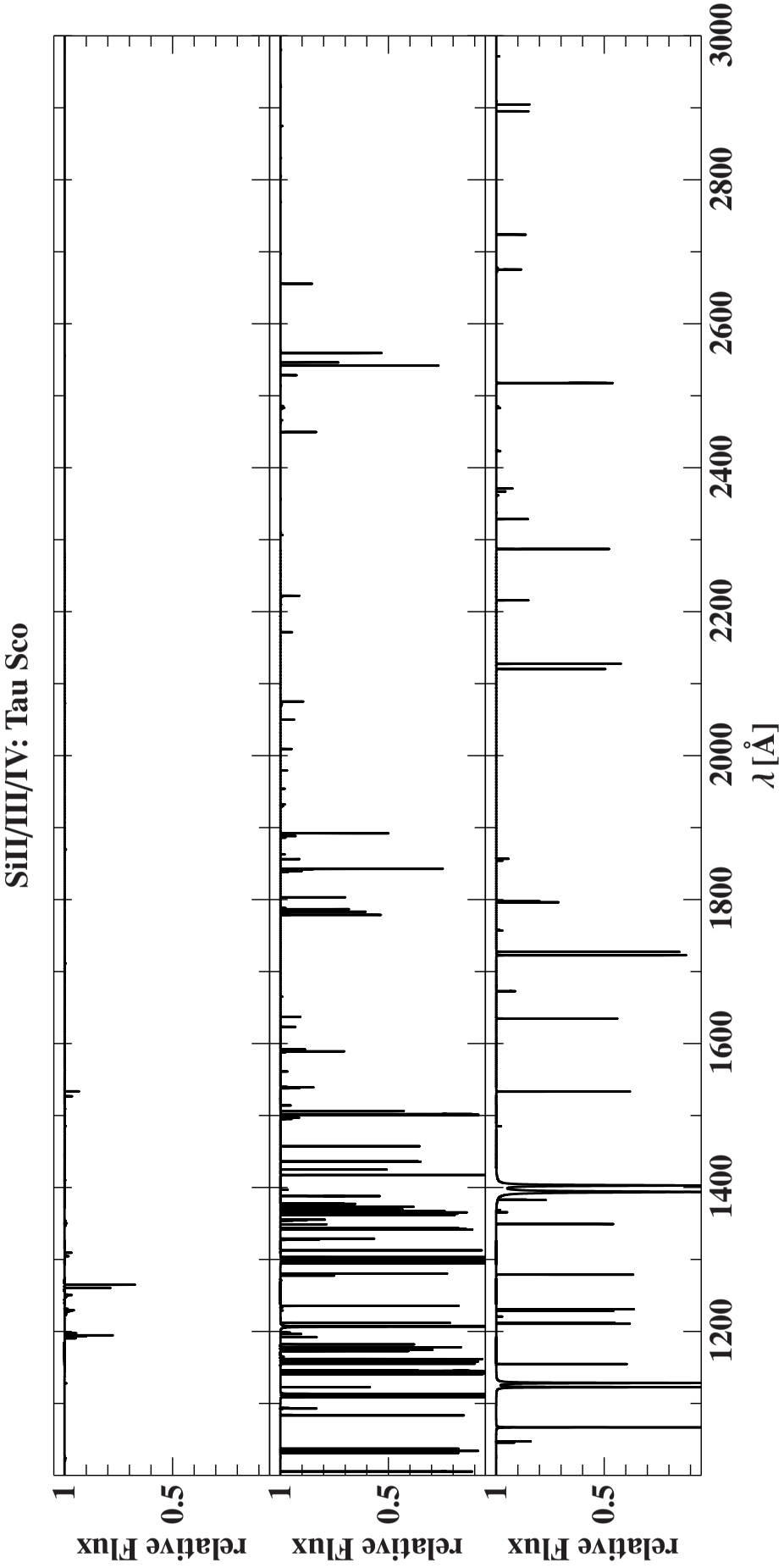
SiII/III/IV: Tau Sco
relative Flux
relative Flux
relative Flux
1
0.5
1
0.5
1
0.5
1200
1400
1600
1800
2000
2200
2400
2600
2800
3000
λ [Å]

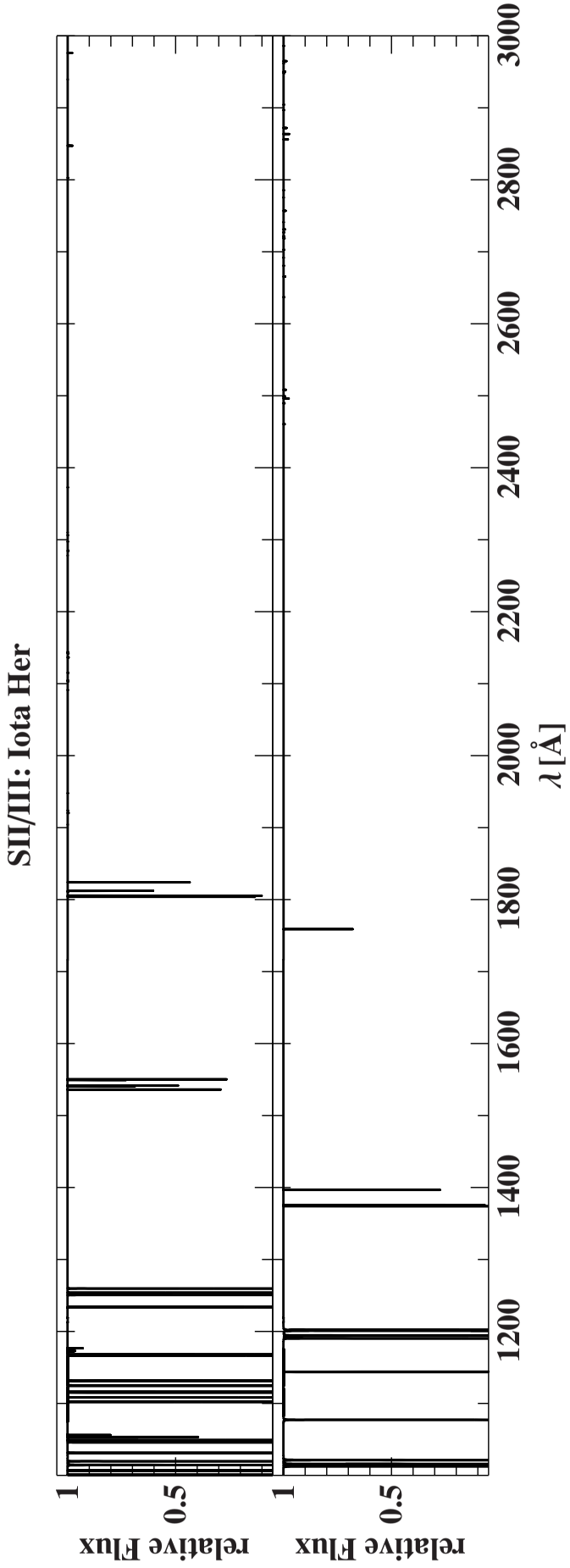
SII/III: Iota Her
relative Flux
relative Flux
1
0.5
1
0.5
1200
1400
1600
1800
2000
2200
2400
2600
2800
3000
λ [Å]

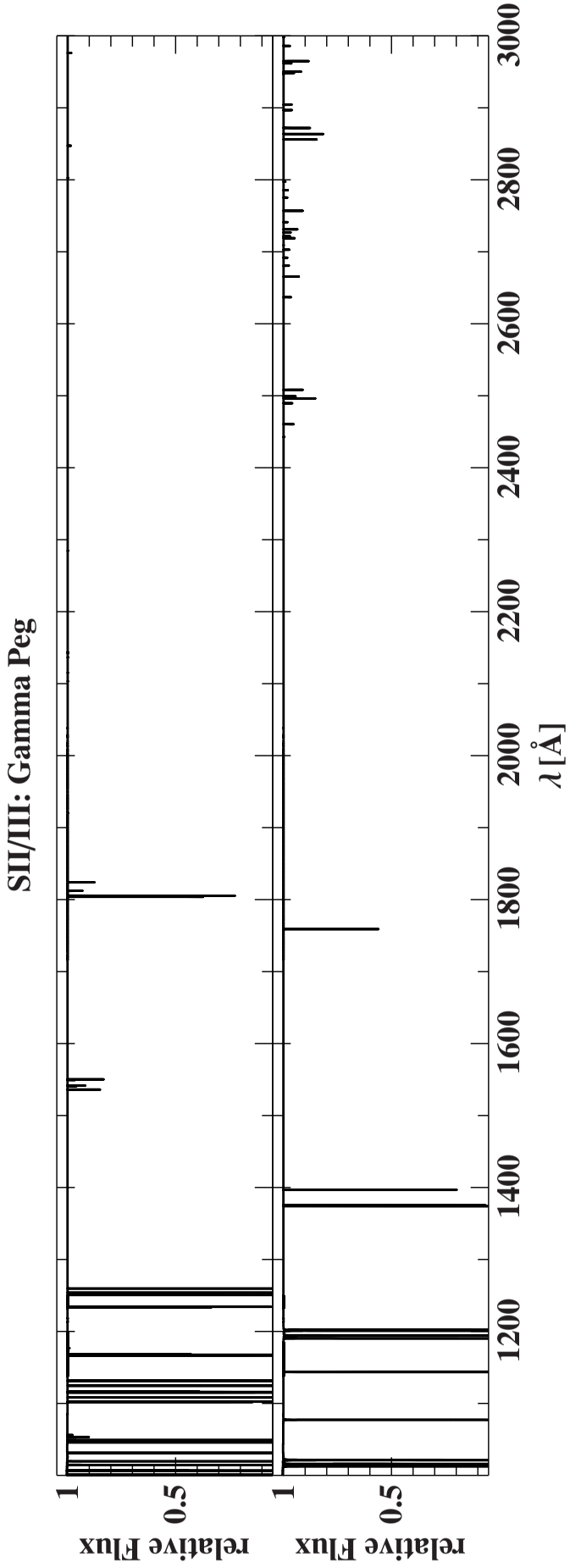
SII/III: Gamma Peg
relative Flux
relative Flux
1
0.5
1
0.5
1200
1400
1600
1800
2000
2200
2400
2600
2800
3000
λ [Å]

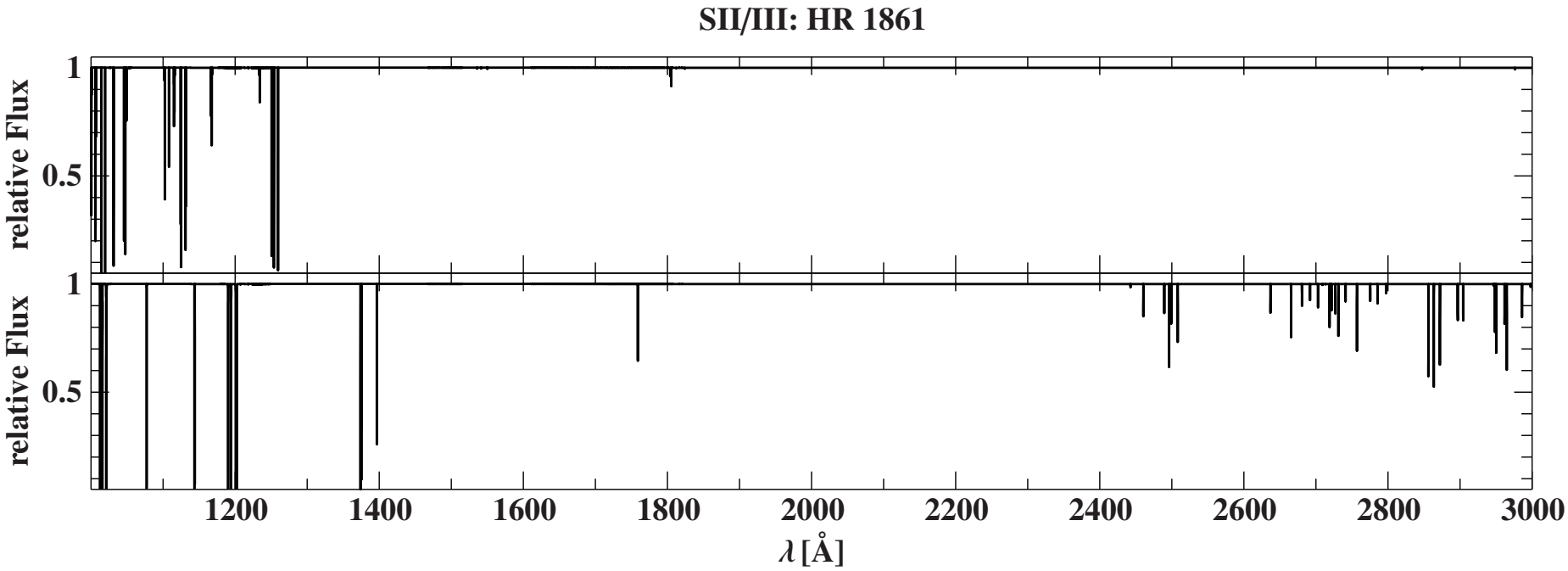
SII/III: HR 1861
relative Flux
1
0.5
relative Flux
1
0.5
1200
1400
1600
1800
2000
2200
2400
2600
2800
3000
λ [Å]

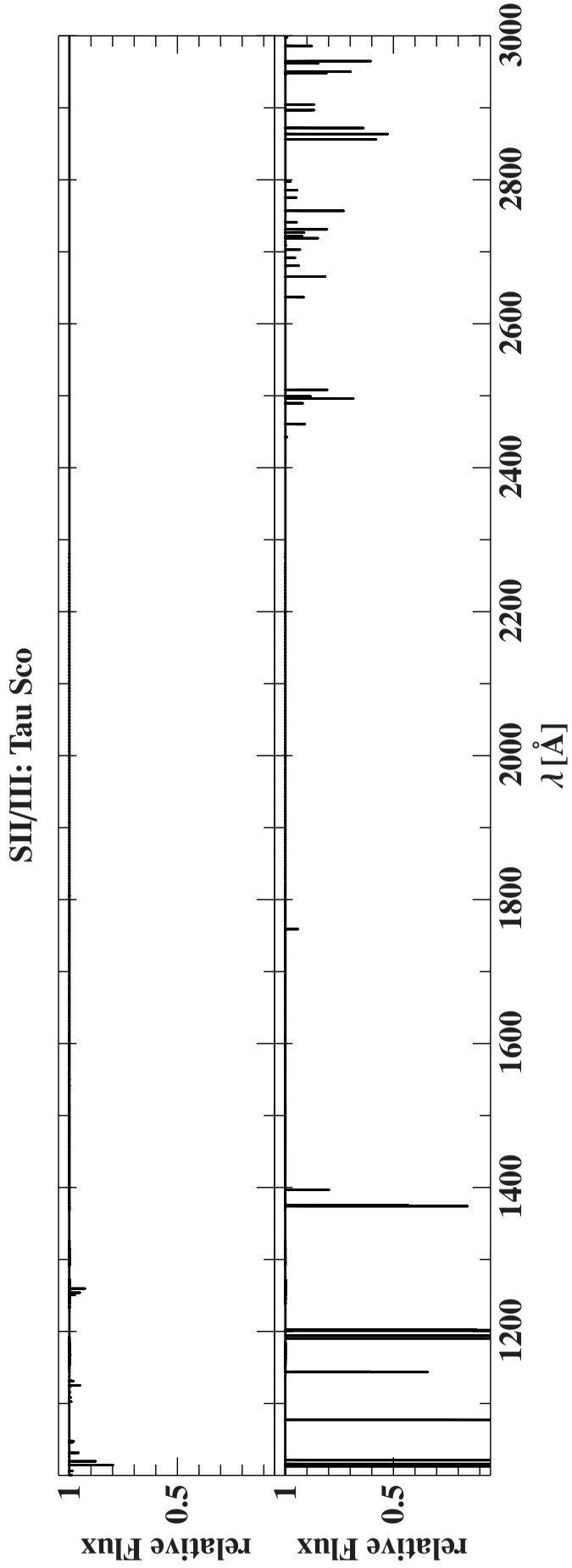
SII/III: Tau Sco
relative Flux
relative Flux
1
0.5
1
0.5
1200
1400
1600
1800
2000
2200
2400
2600
2800
3000
λ [Å]

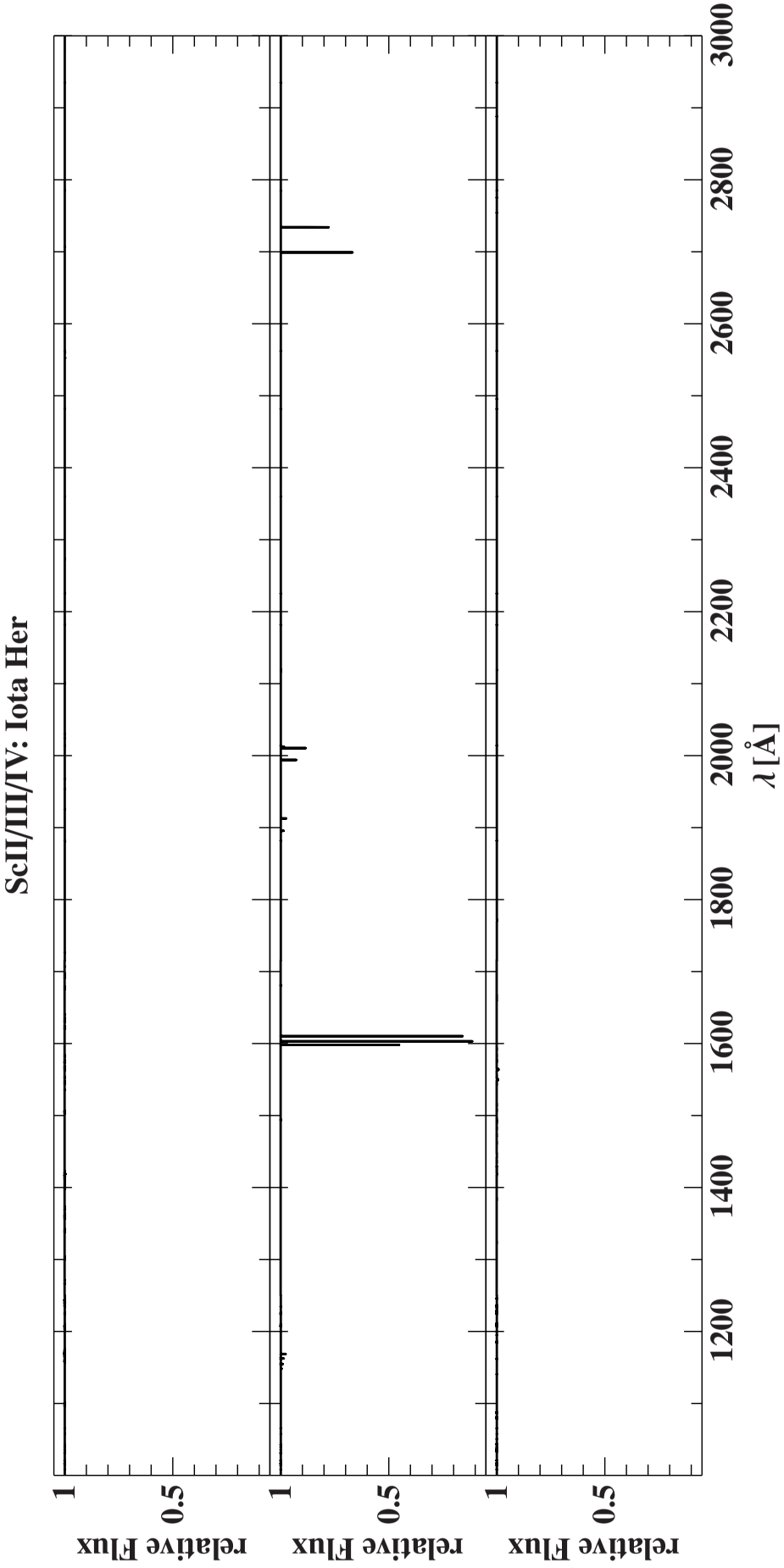
ScII/III/IV: Iota Her
relative Flux
relative Flux
relative Flux
1
0.5
1
0.5
1
0.5
1200
1400
1600
1800
2000
2200
2400
2600
2800
3000
λ [Å]

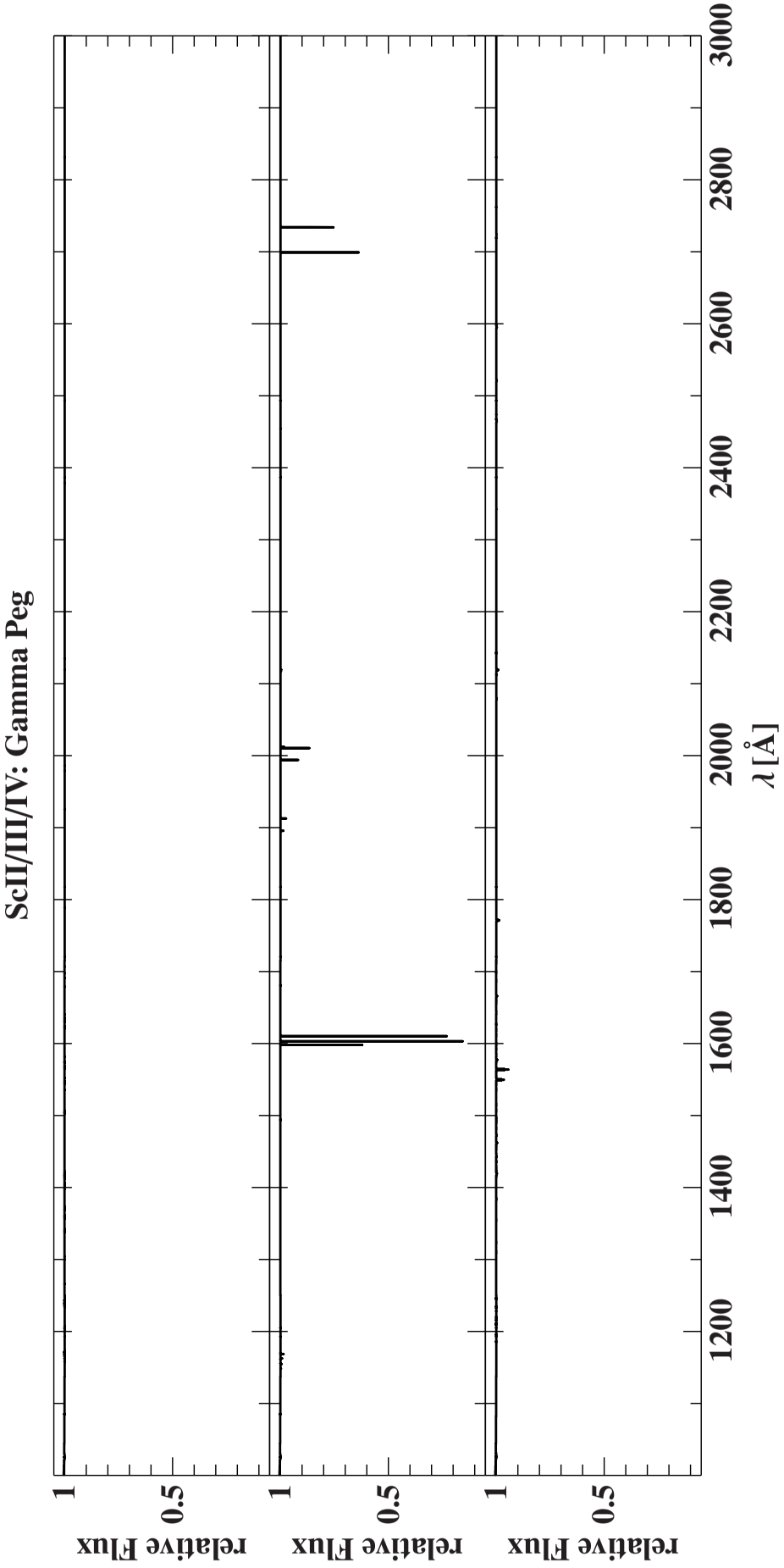
ScII/III/IV: Gamma Peg
relative Flux
relative Flux
relative Flux
1
0.5
1
0.5
1
0.5
1200
1400
1600
1800
2000
2200
2400
2600
2800
3000
λ [Å]

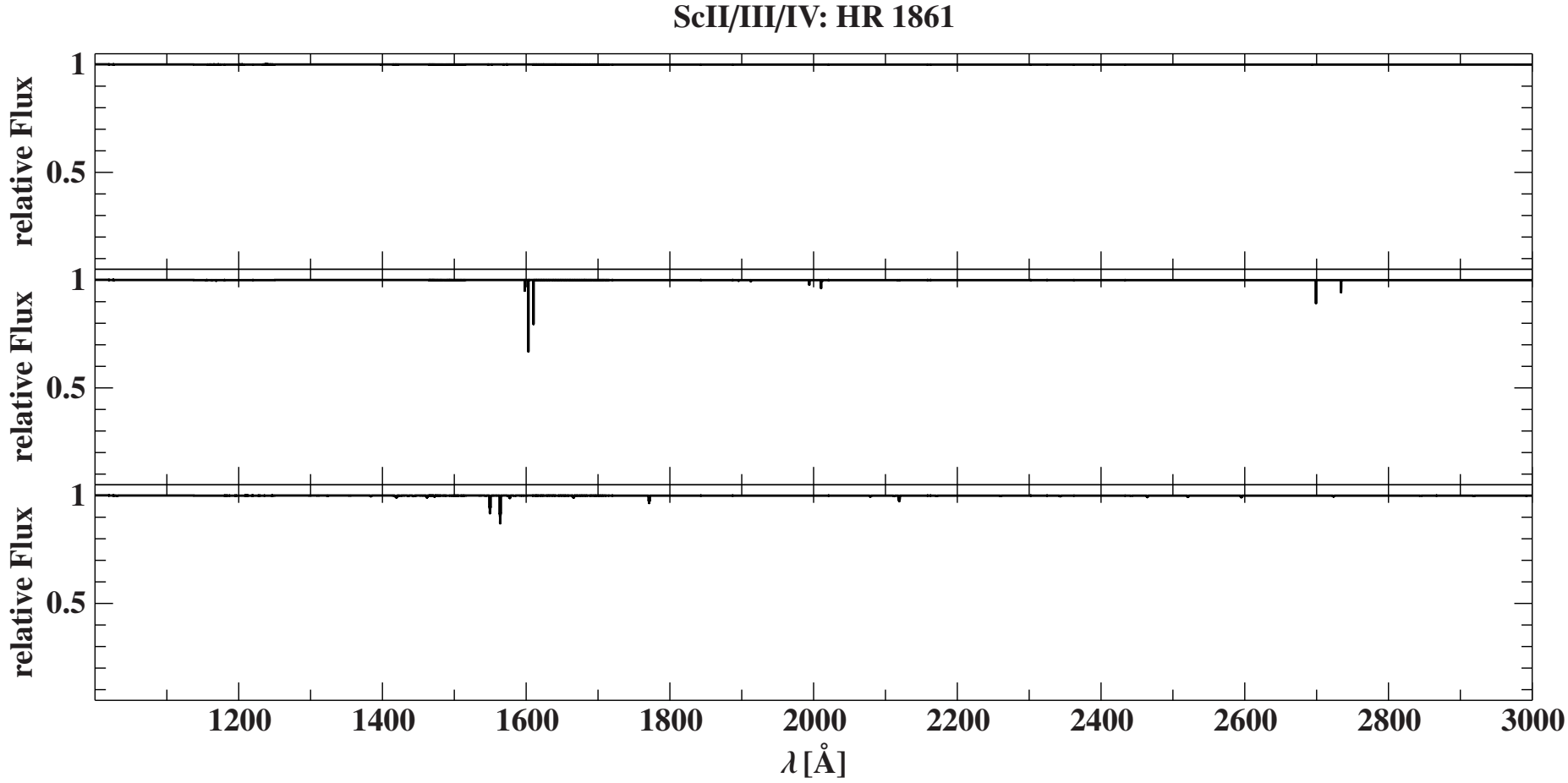
ScII/III/IV: HR 1861
relative Flux
relative Flux
relative Flux
1
0.5
1
0.5
1
0.5
1200
1400
1600
1800
2000
2200
2400
2600
2800
3000
λ [Å]

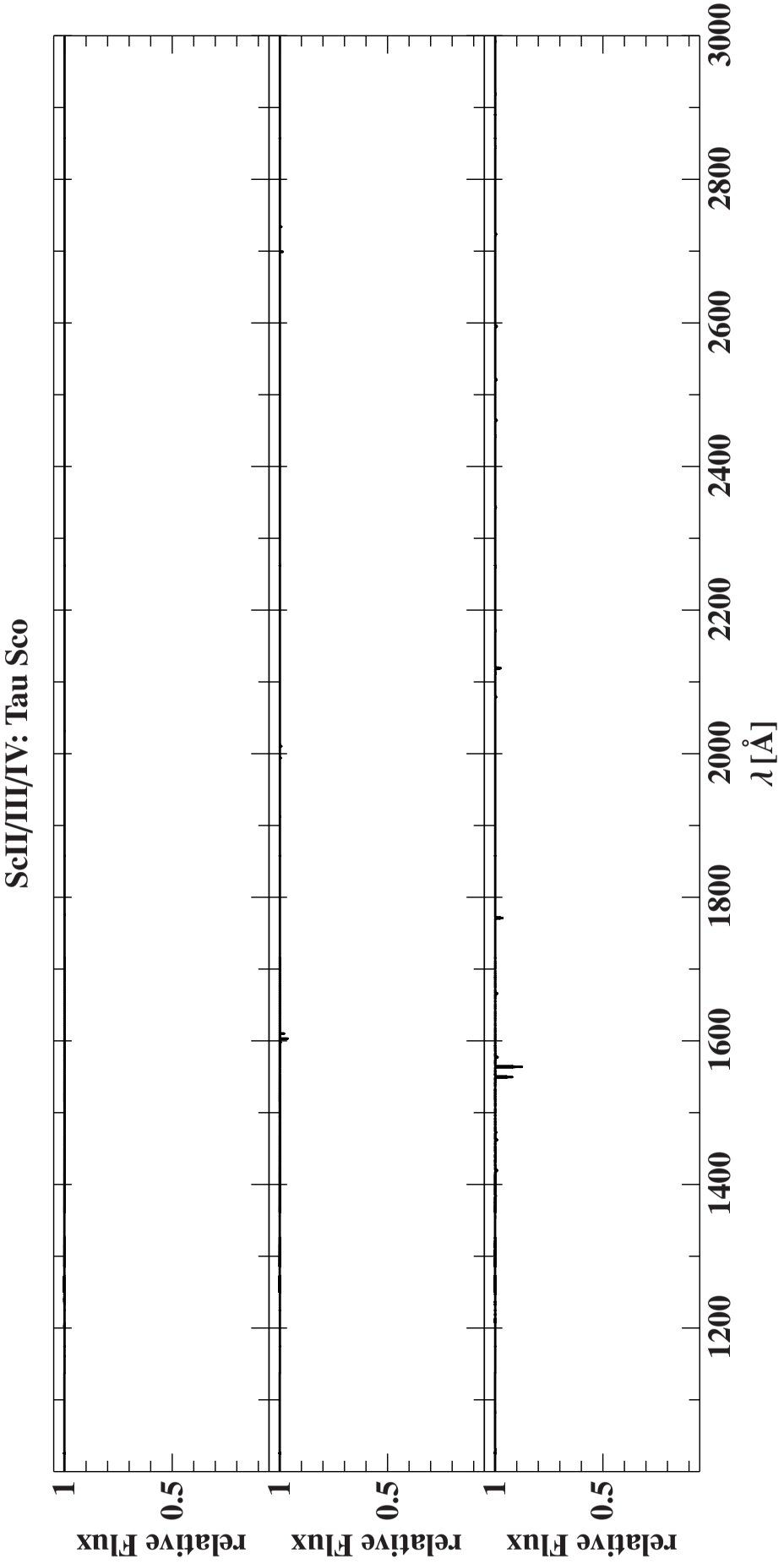
ScII/III/IV: Tau Sco
relative Flux
relative Flux
relative Flux
1
0.5
1
0.5
1
0.5
1200
1400
1600
1800
2000
2200
2400
2600
2800
3000
λ [Å]

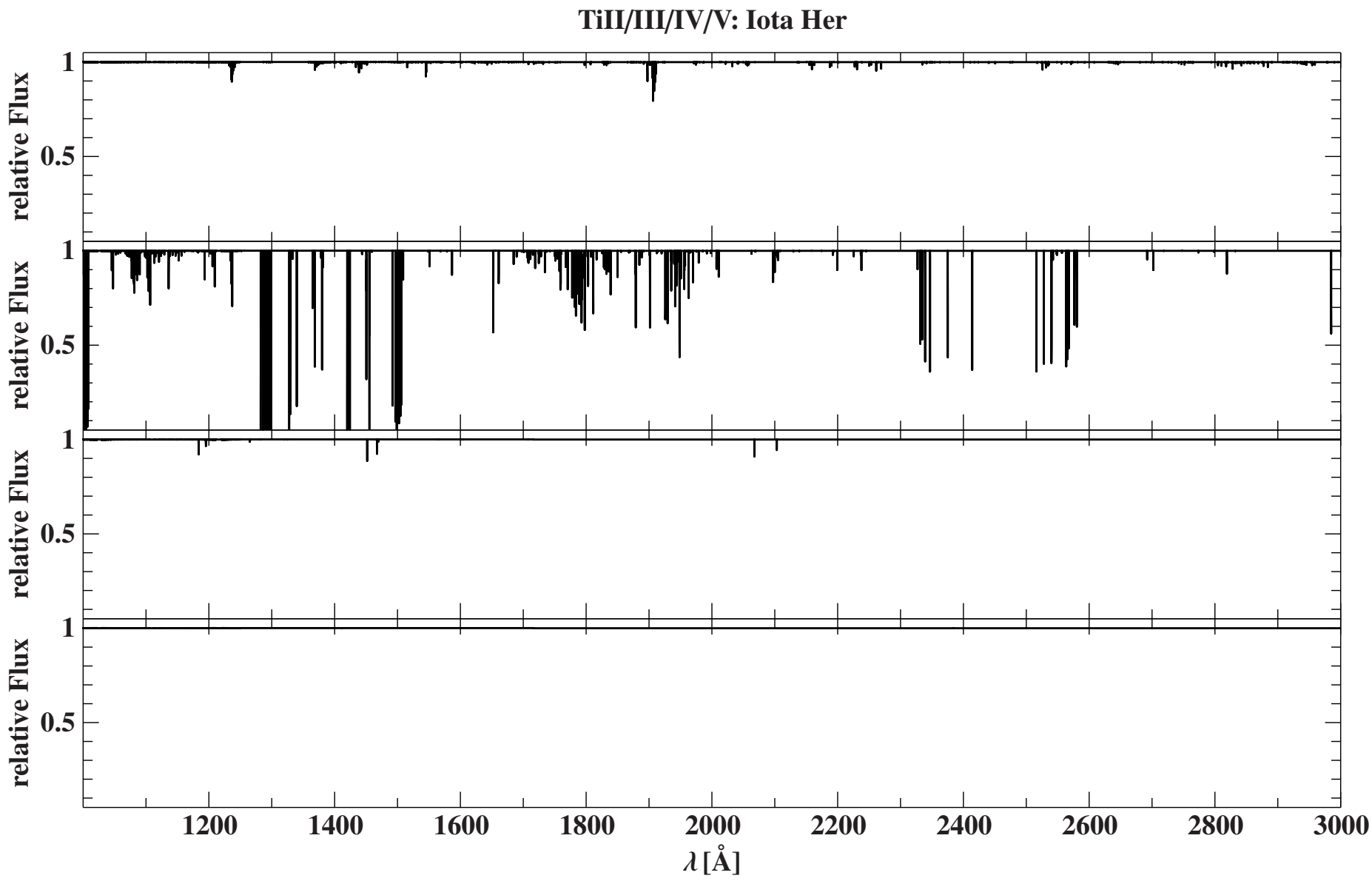
TiII/III/IV/V: Iota Her
relative Flux
1
0.5
1200
1400
1600
1800
2000
2200
2400
2600
2800
3000
λ [Å]

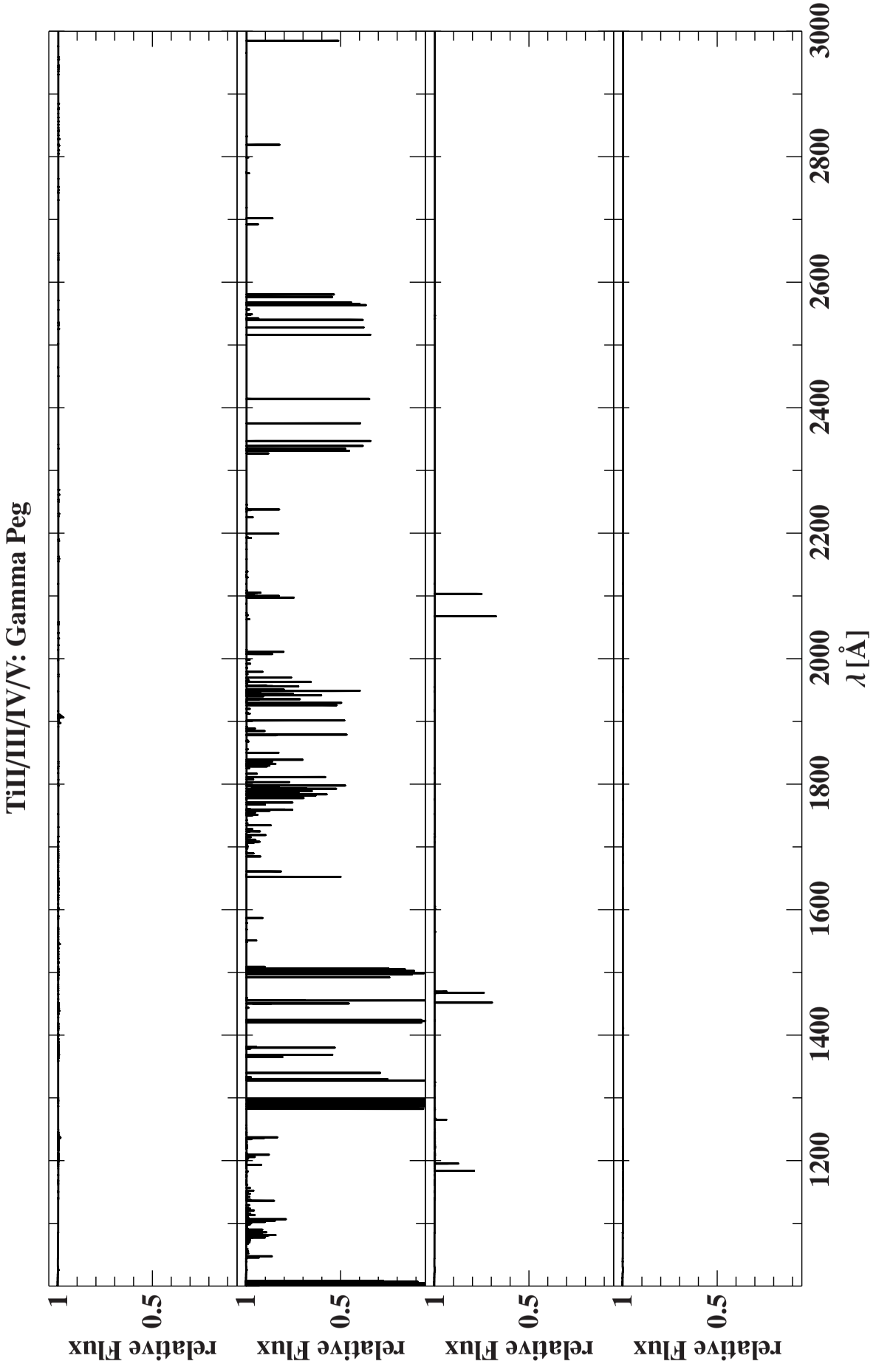
TiII/III/IV/V: Gamma Peg
relative Flux
relative Flux
relative Flux
relative Flux
1
0.5
1200
1400
1600
1800
2000
2200
2400
2600
2800
3000
λ [Å]

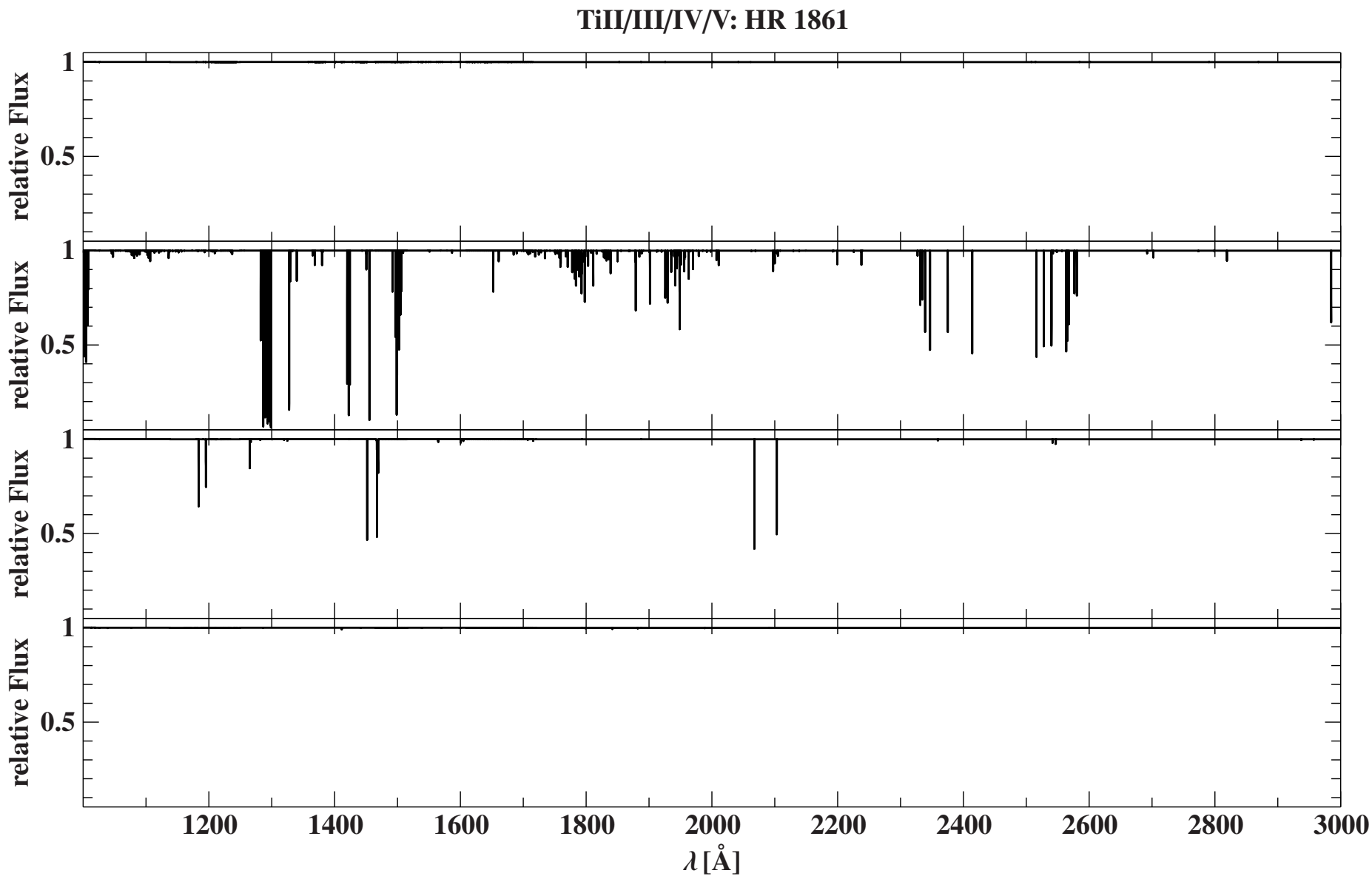
TiII/III/IV/V: HR 1861
relative Flux
1
0.5
1200
1400
1600
1800
2000
2200
2400
2600
2800
3000
λ [Å]

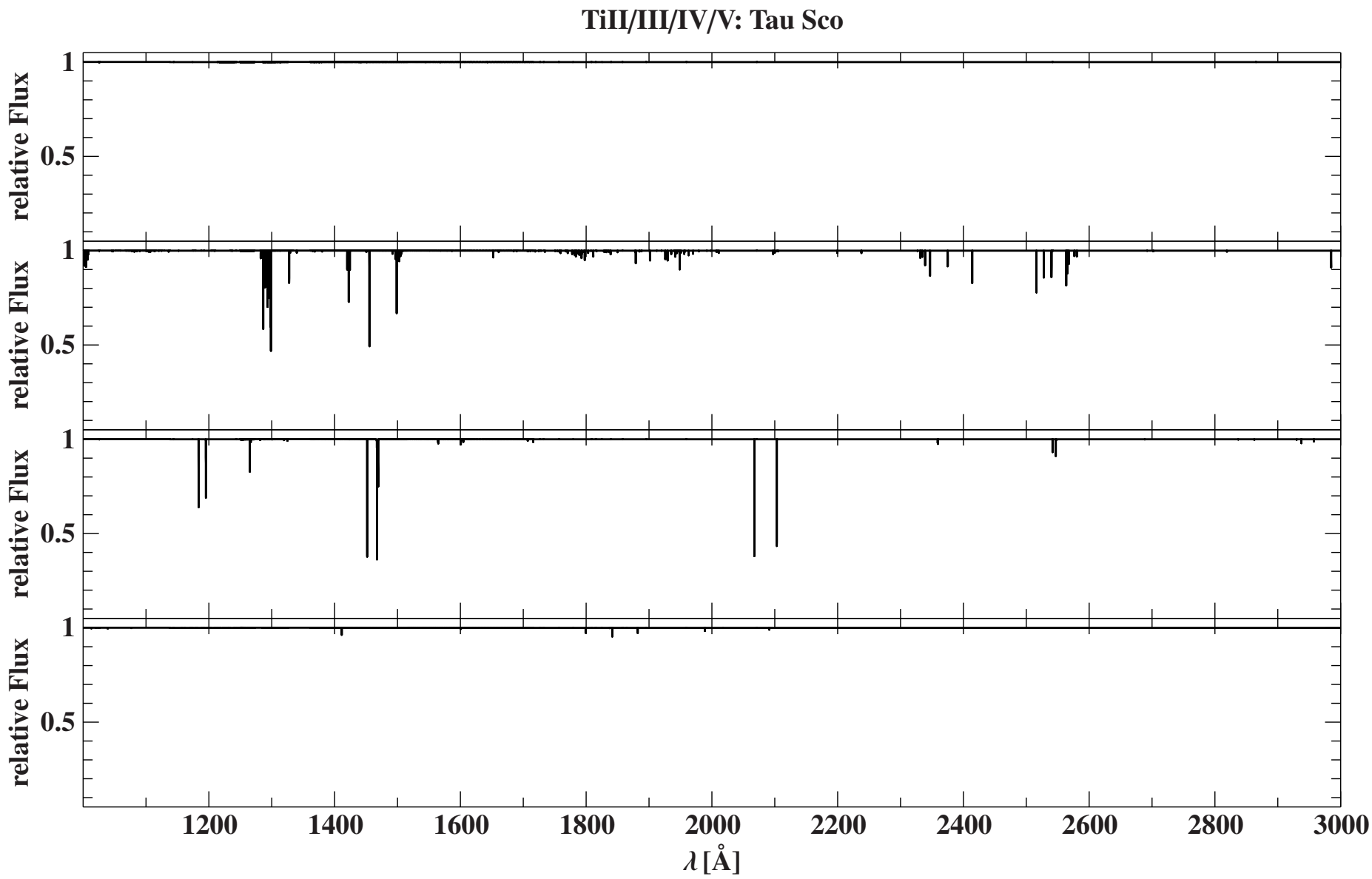
TiII/III/IV/V: Tau Sco
relative Flux
1
0.5
1200
1400
1600
1800
2000
2200
2400
2600
2800
3000
λ [Å]

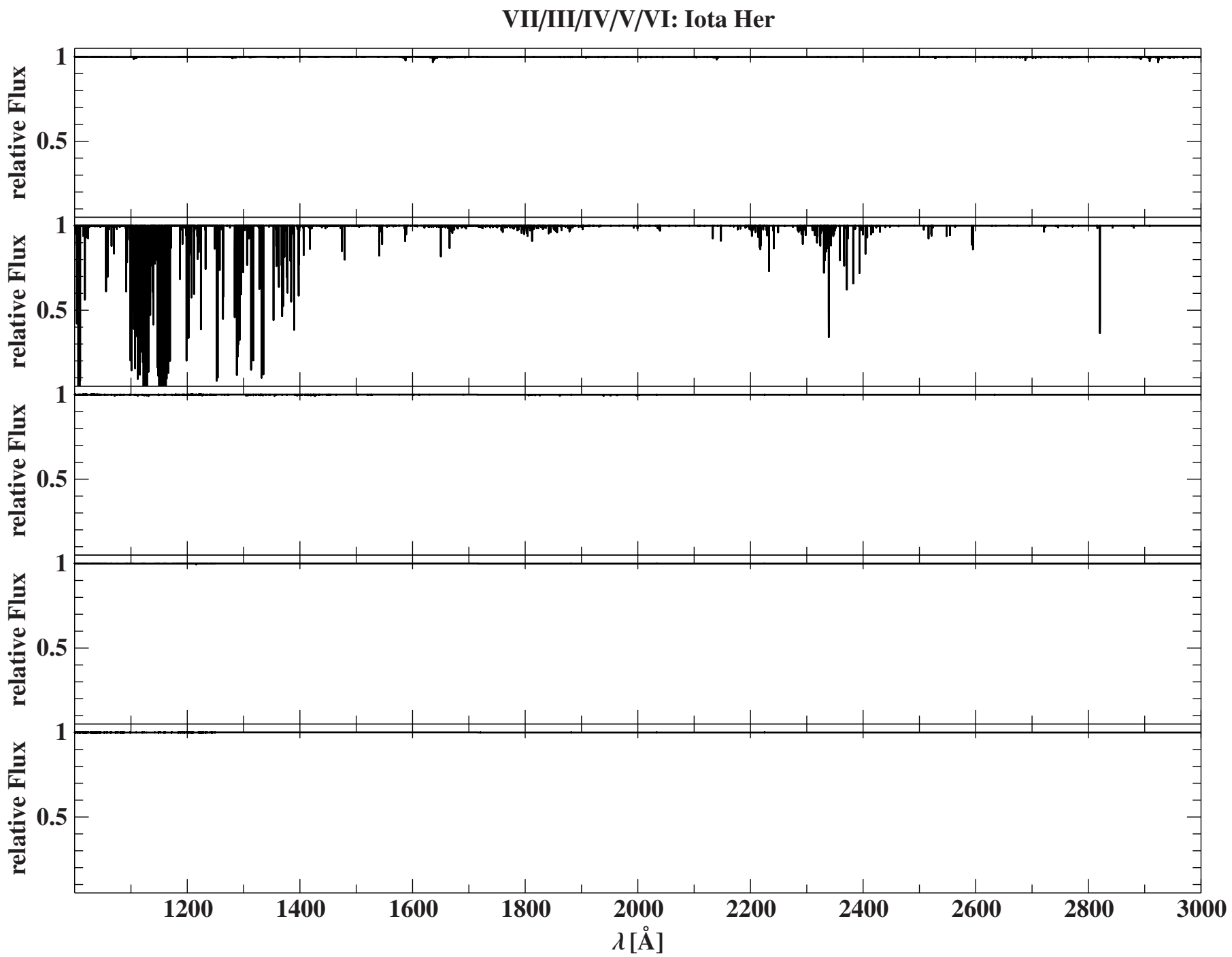
VII/III/IV/V/VI: Iota Her
relative Flux
1
0.5
1200
1400
1600
1800
2000
2200
2400
2600
2800
3000
λ [Å]

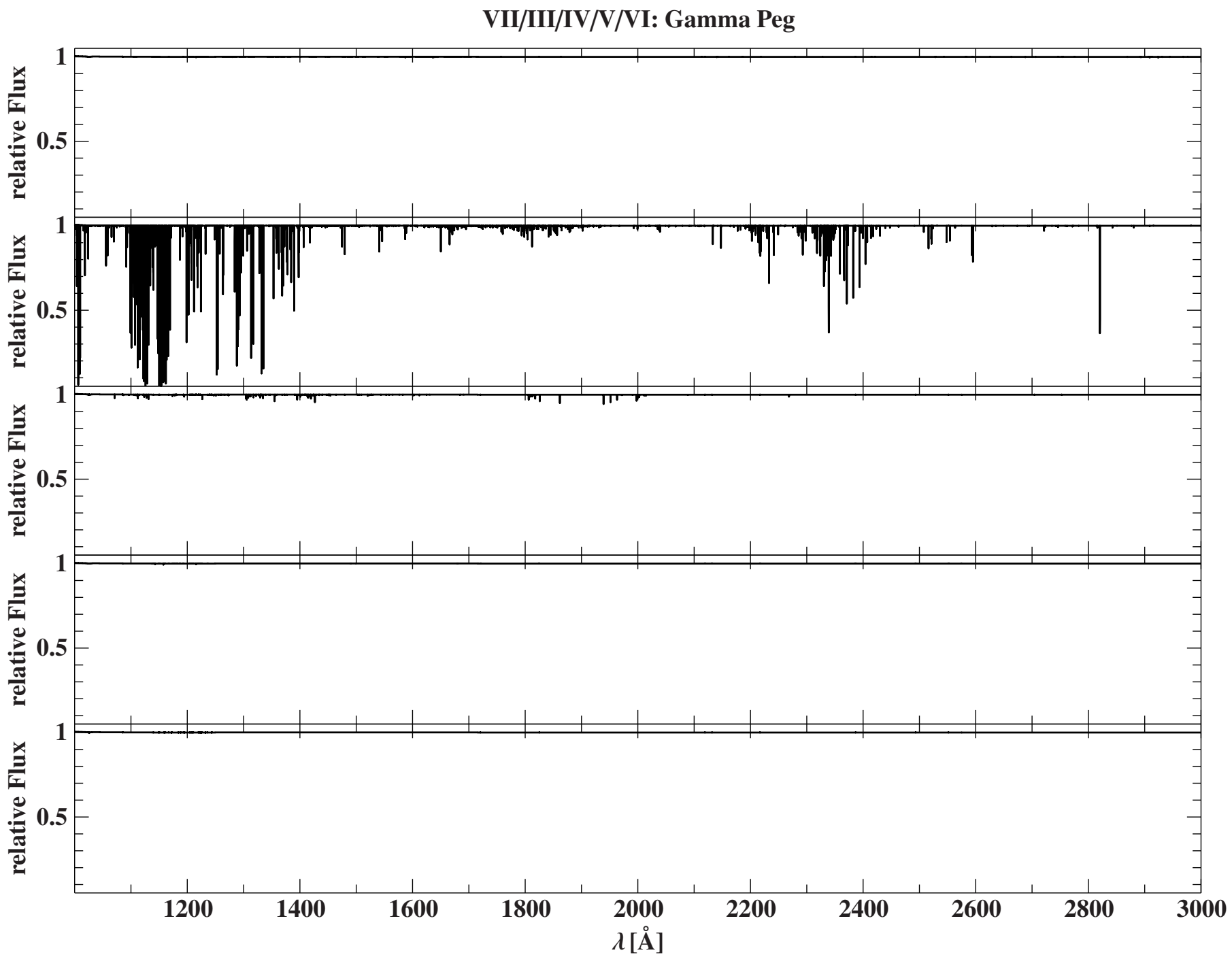
VII/III/IV/V/VI: Gamma Peg
relative Flux
1
0.5
1200
1400
1600
1800
2000
2200
2400
2600
2800
3000
λ [Å]

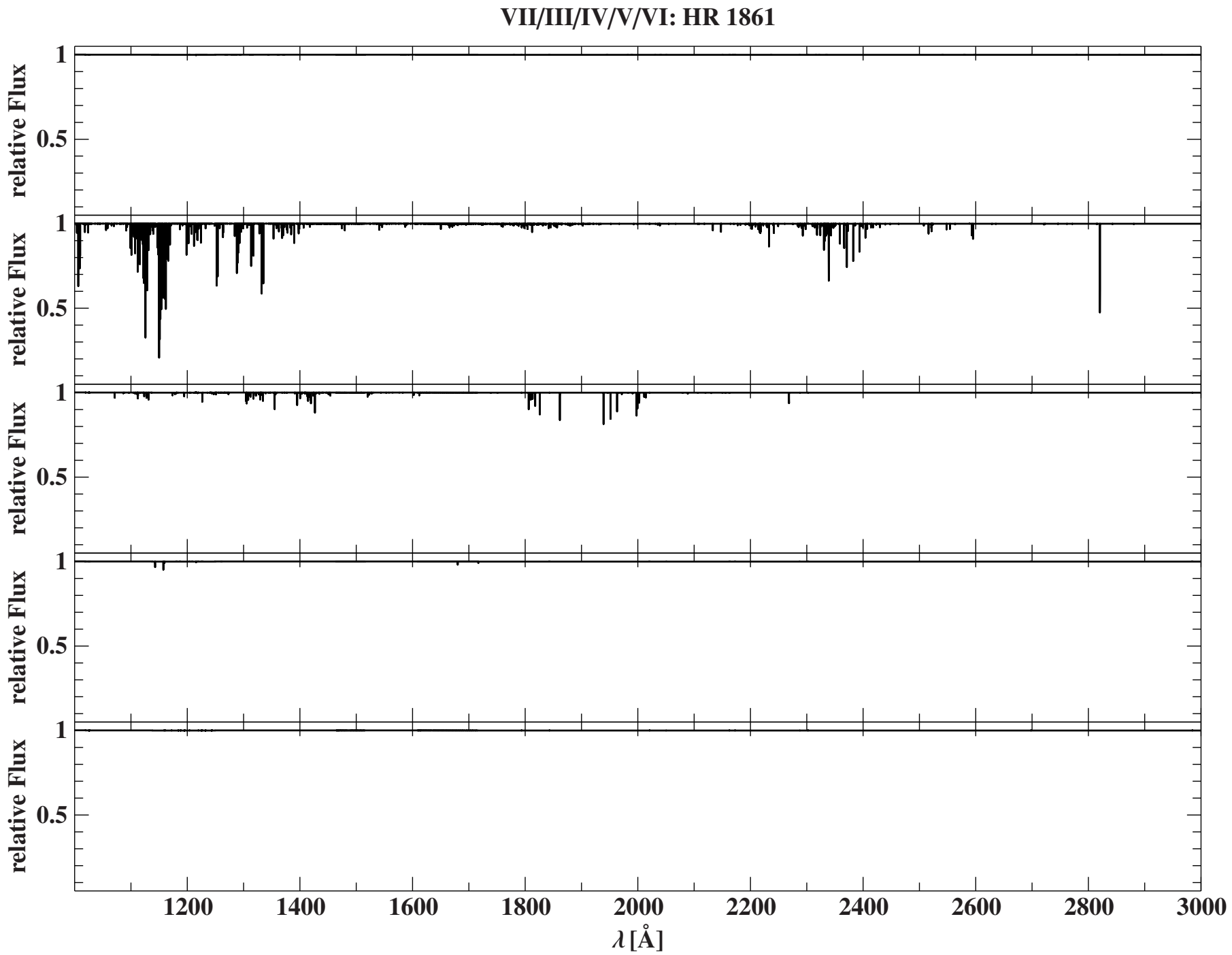
VII/III/IV/V/VI: HR 1861
relative Flux
1
0.5
1200
1400
1600
1800
2000
2200
2400
2600
2800
3000
λ [Å]

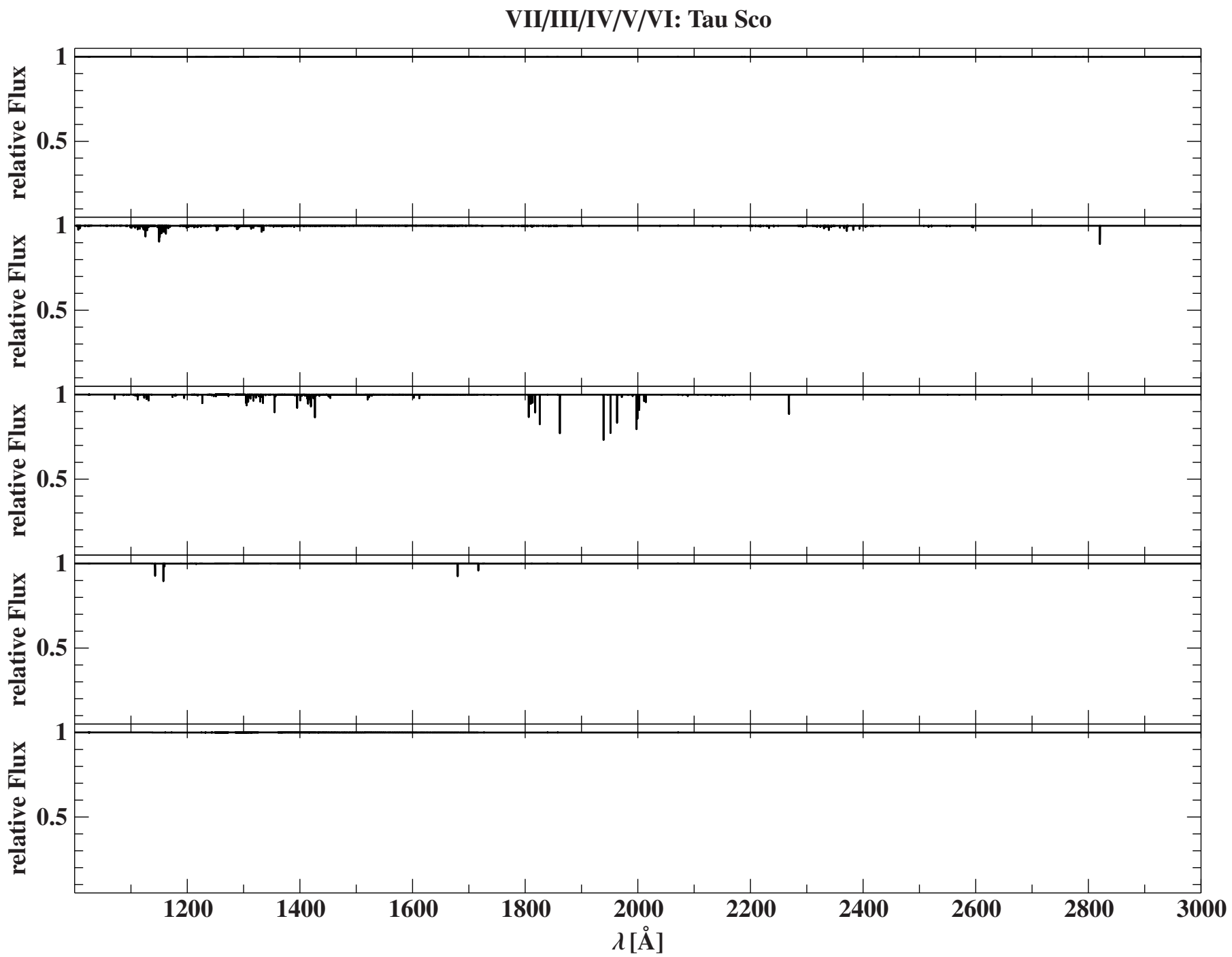
VII/III/IV/V/VI: Tau Sco
relative Flux
1
0.5
1200
1400
1600
1800
2000
2200
2400
2600
2800
3000
λ [Å]

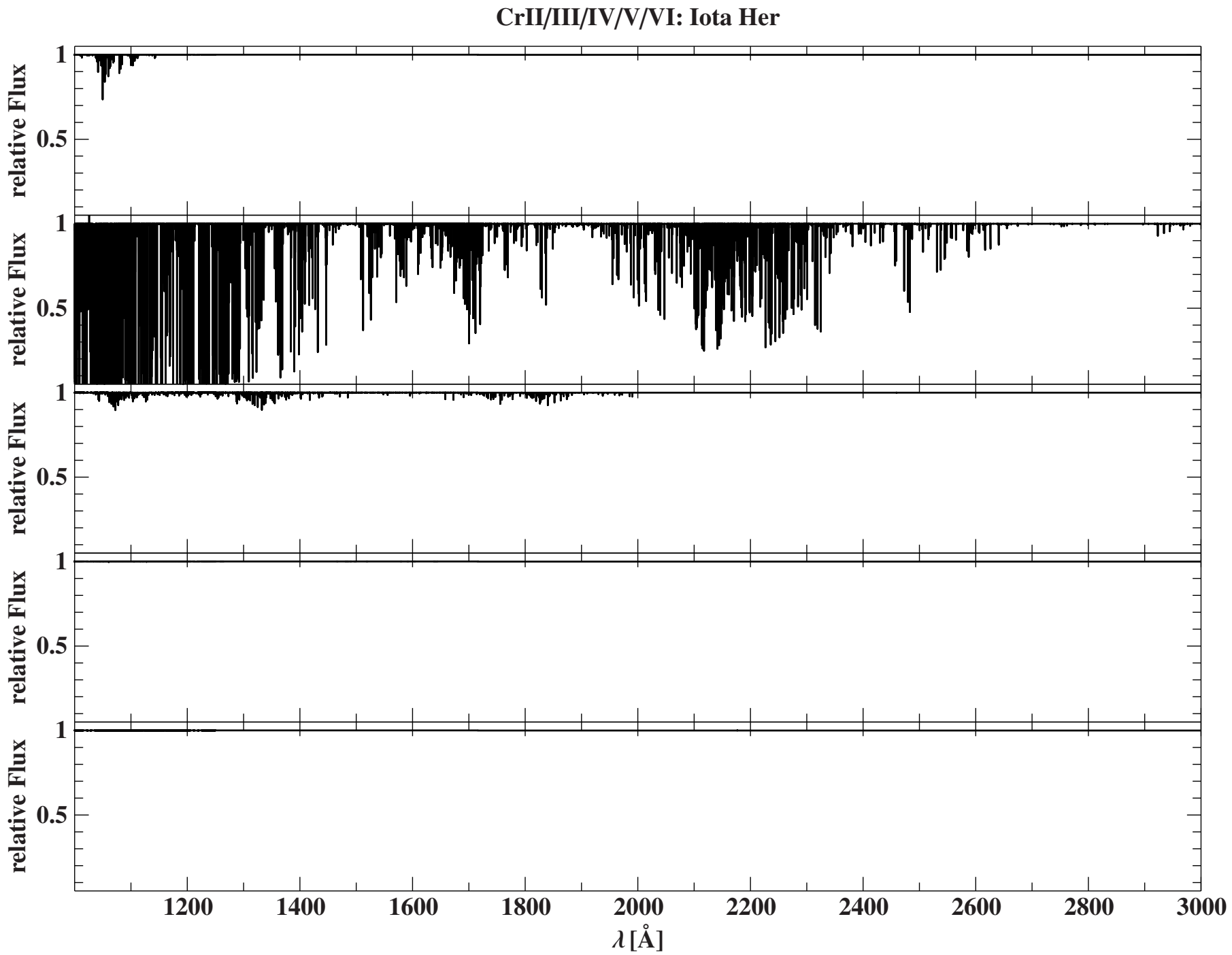
CrII/III/IV/V/VI: Iota Her
relative Flux
1
0.5
1200
1400
1600
1800
2000
2200
2400
2600
2800
3000
λ [Å]

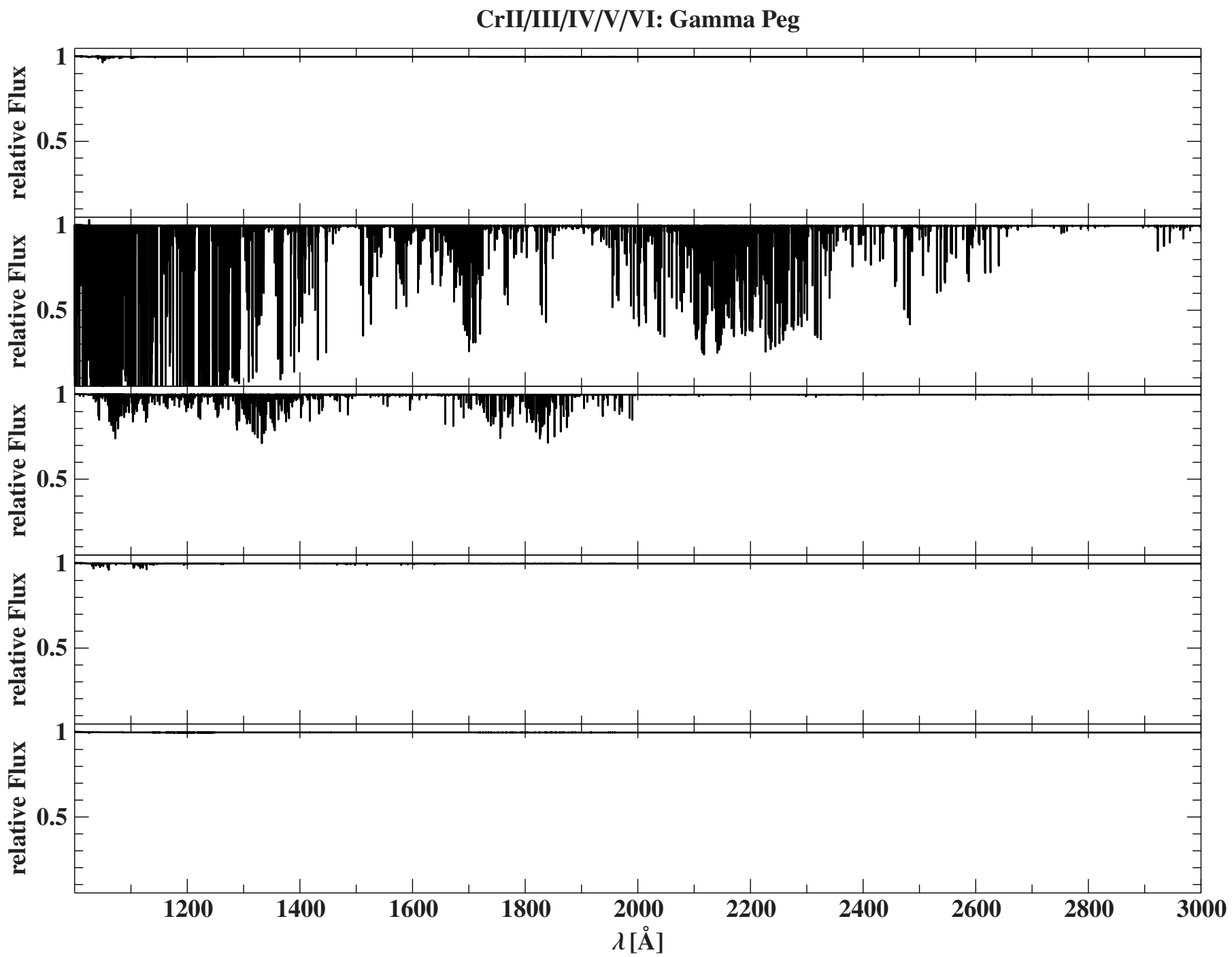
CrII/III/IV/V/VI: Gamma Peg
relative Flux
1
0.5
1200
1400
1600
1800
2000
2200
2400
2600
2800
3000
λ [Å]

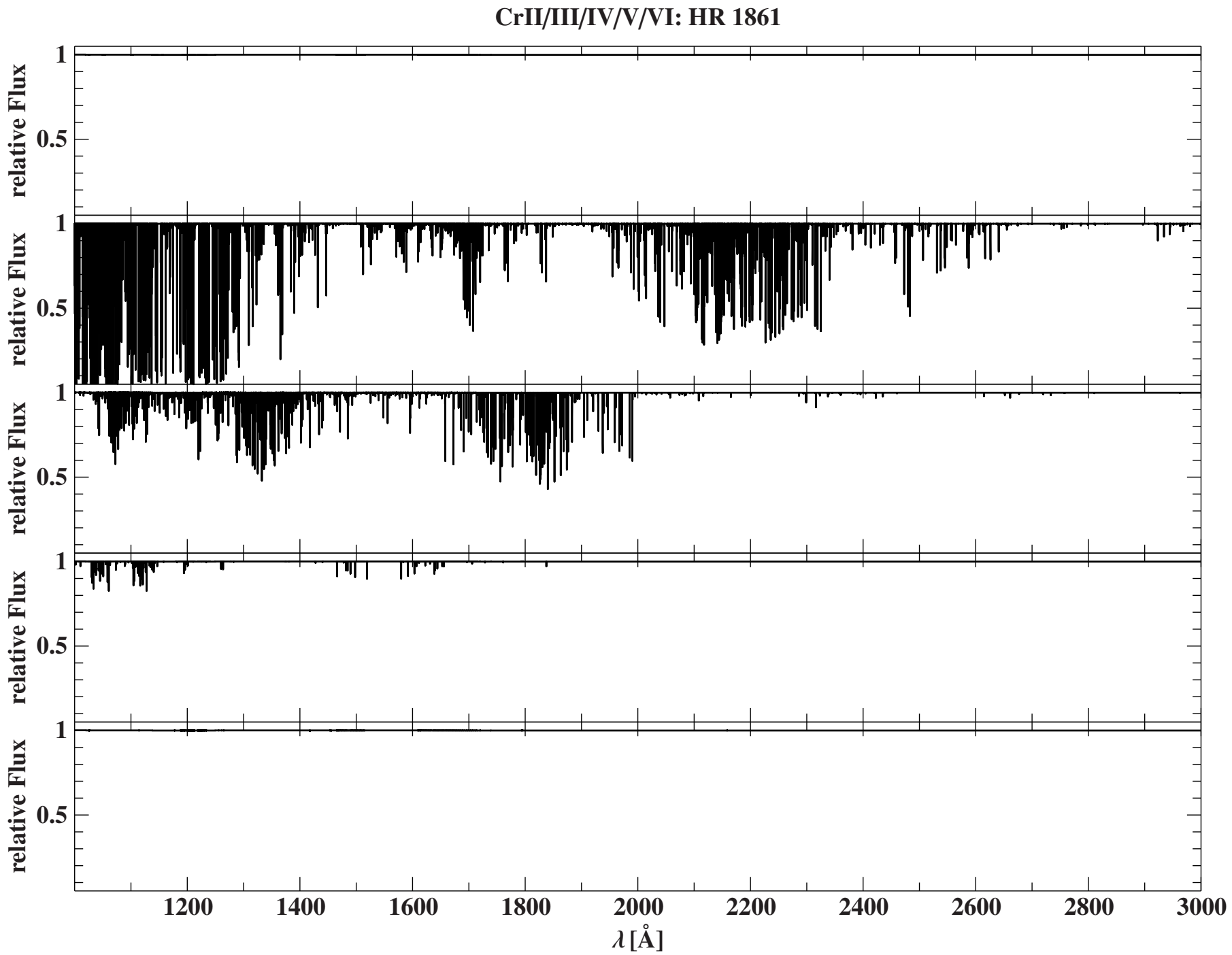
CrII/III/IV/V/VI: HR 1861
relative Flux
1
0.5
1200
1400
1600
1800
2000
2200
2400
2600
2800
3000
λ [Å]

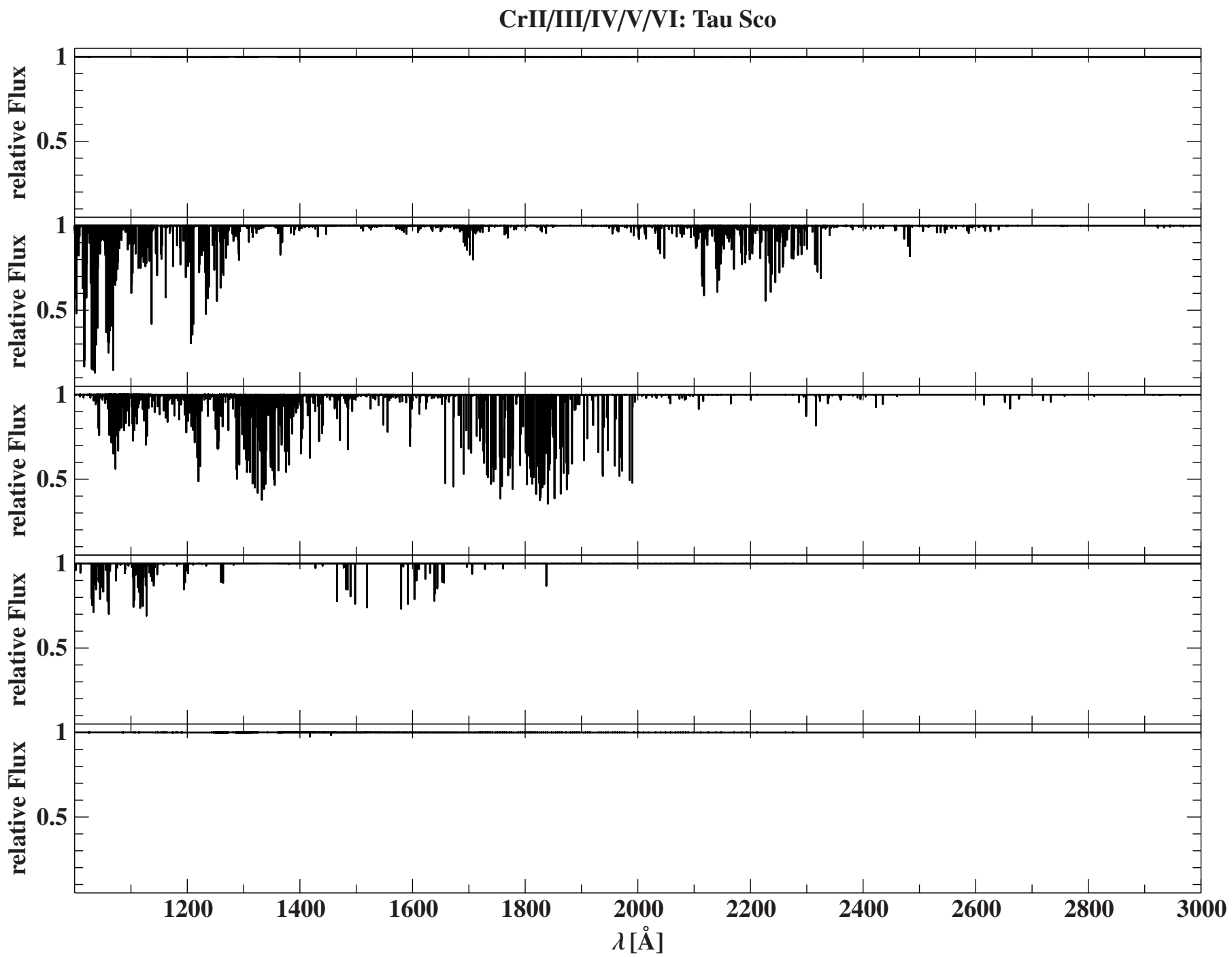
CrII/III/IV/V/VI: Tau Sco
relative Flux
1
0.5
1200
1400
1600
1800
2000
2200
2400
2600
2800
3000
λ [Å]

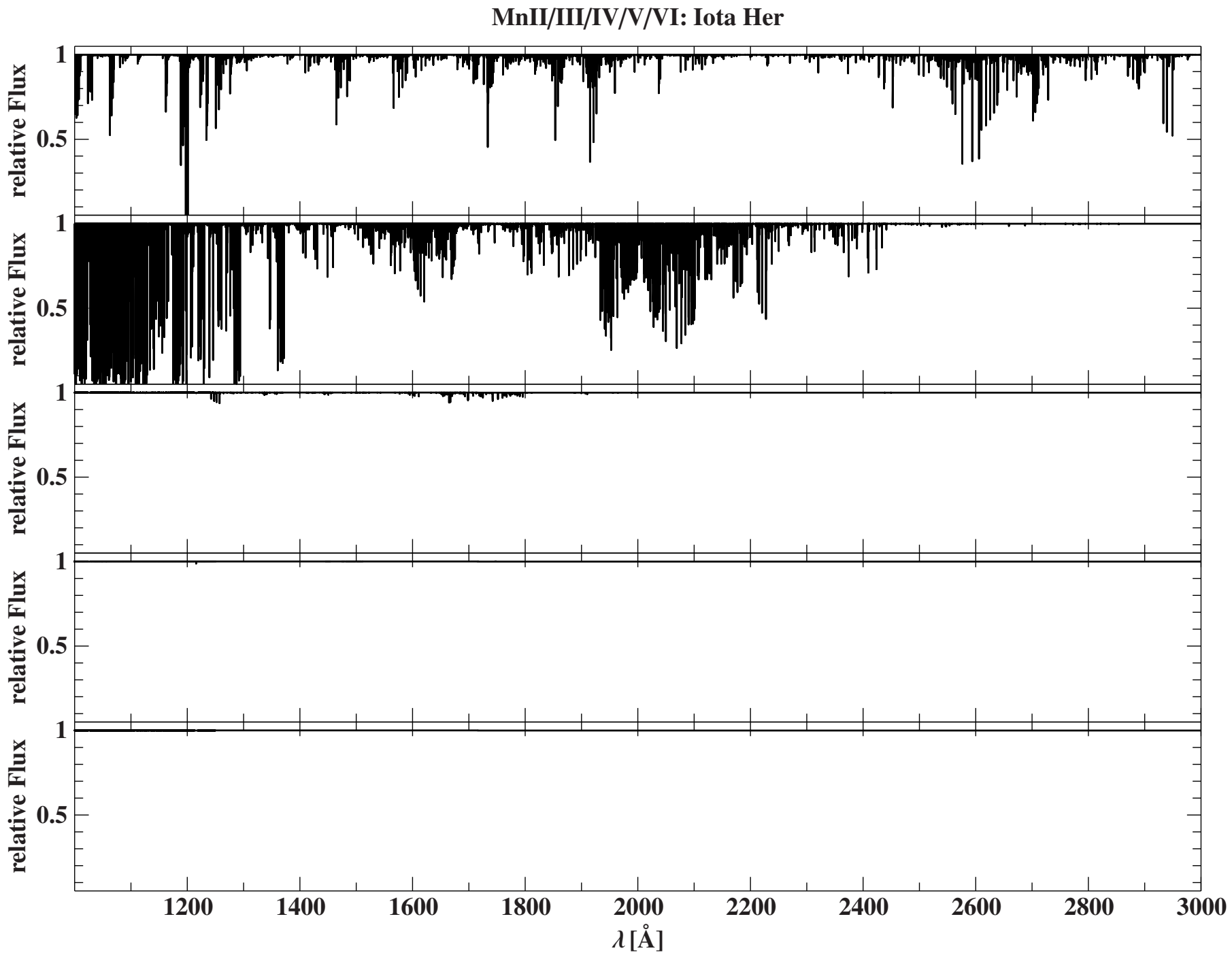
MnII/III/IV/V/VI: Iota Her
relative Flux
1
0.5
1200
1400
1600
1800
2000
2200
2400
2600
2800
3000
λ [Å]

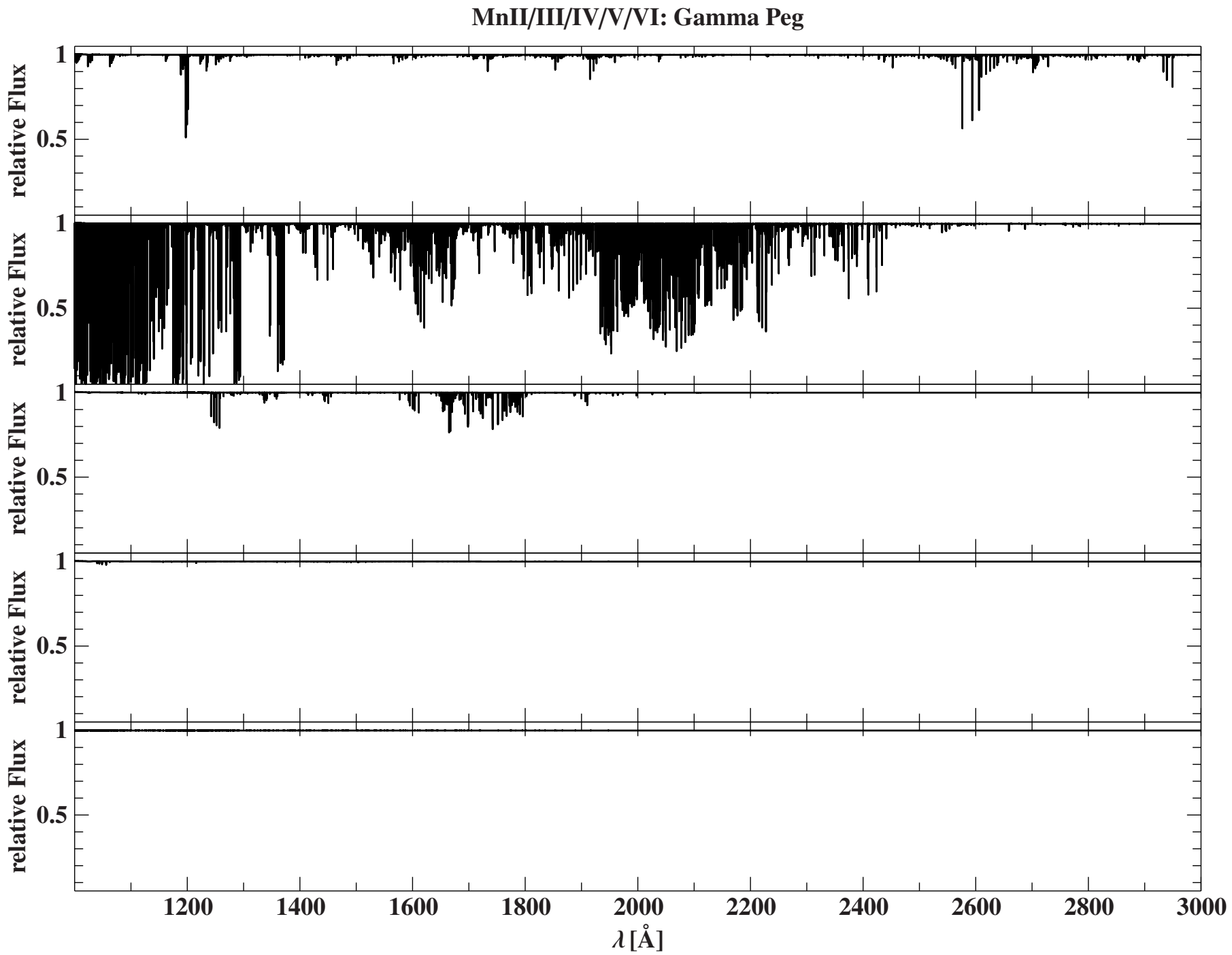
MnII/III/IV/V/VI: Gamma Peg
relative Flux
1
0.5
1200
1400
1600
1800
2000
2200
2400
2600
2800
3000
λ [Å]

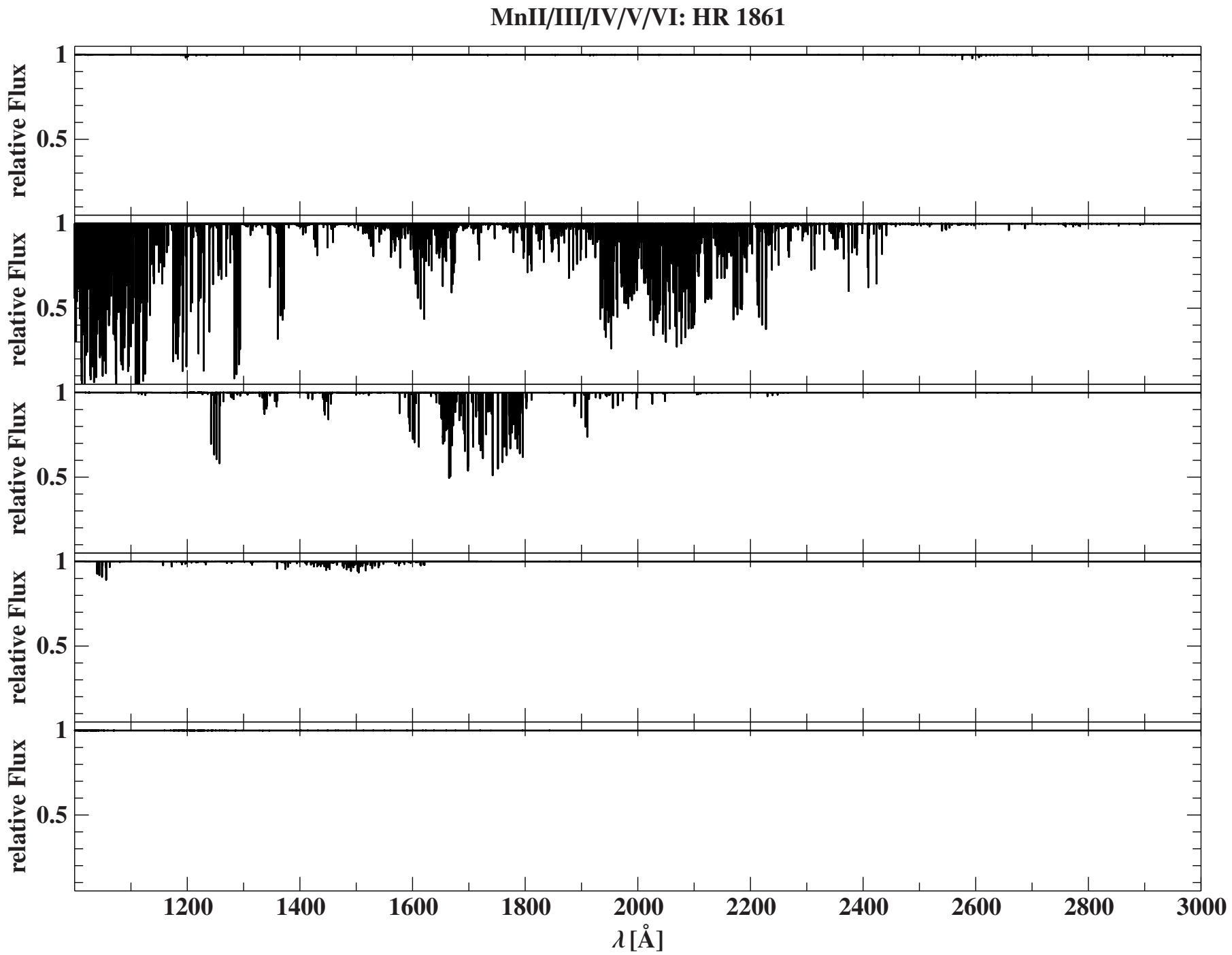
MnII/III/IV/V/VI: HR 1861
relative Flux
1
0.5
1200
1400
1600
1800
2000
2200
2400
2600
2800
3000
λ [Å]

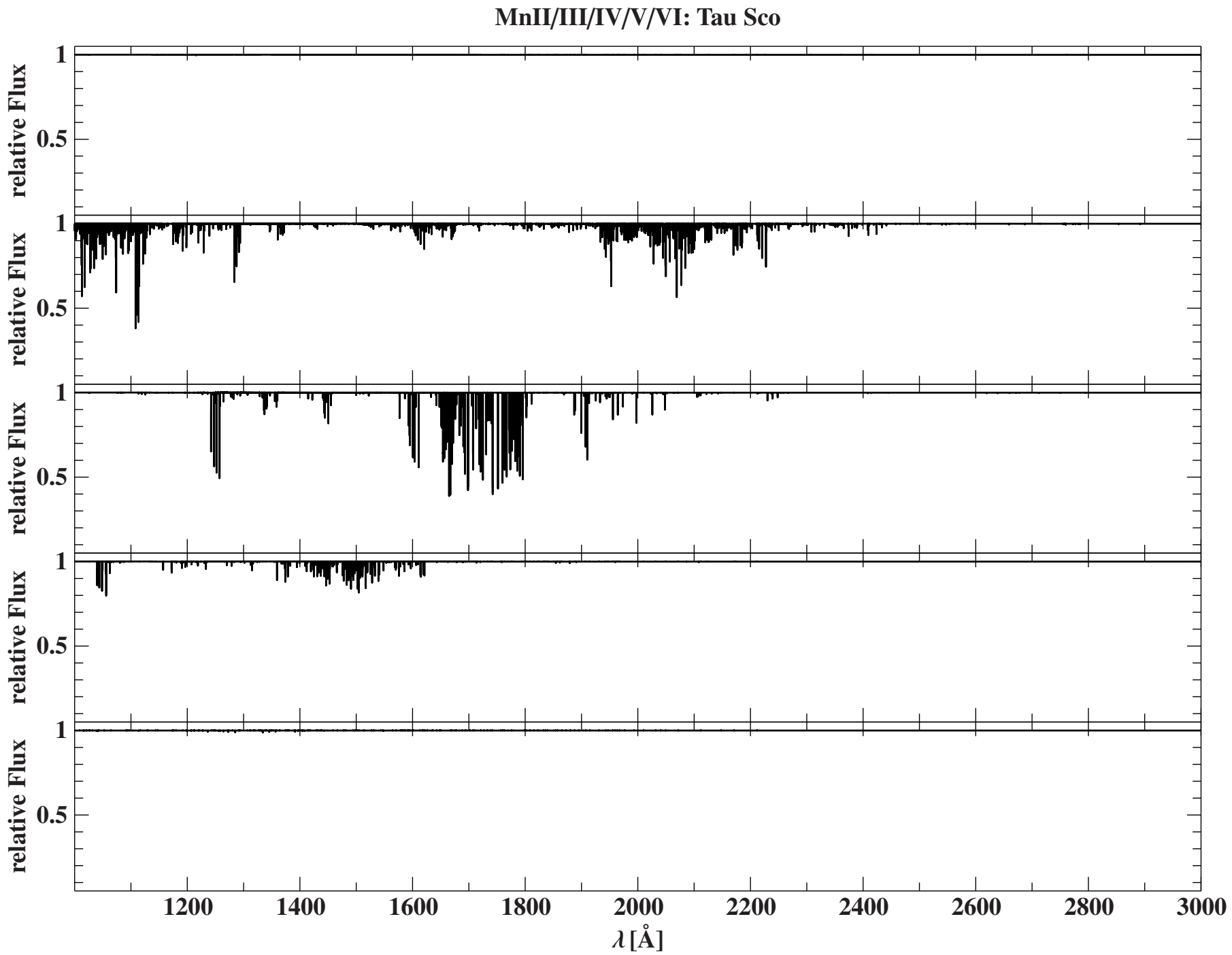
MnII/III/IV/V/VI: Tau Sco
relative Flux
1
0.5
1200
1400
1600
1800
2000
2200
2400
2600
2800
3000
λ [Å]

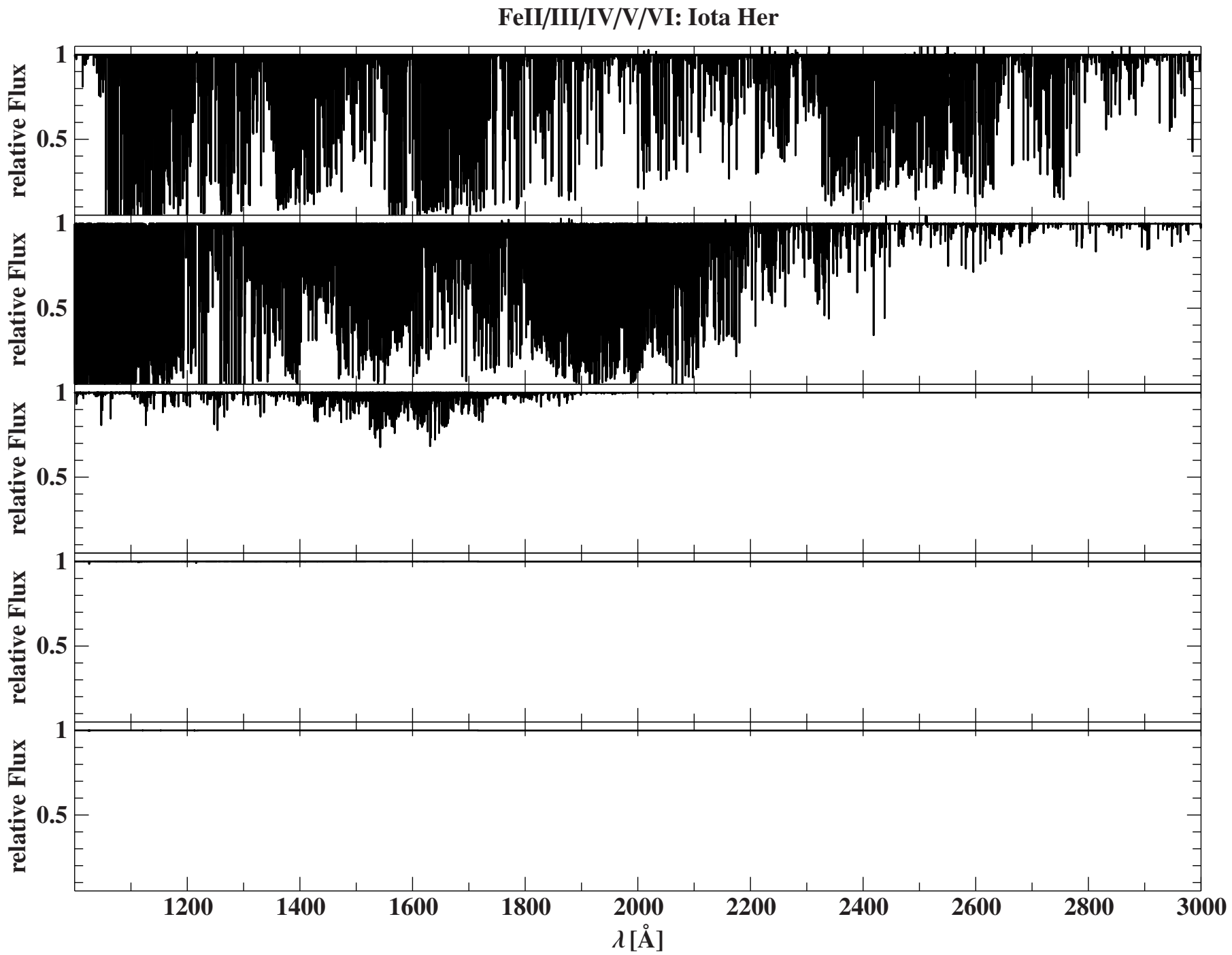
FeII/III/IV/V/VI: Iota Her
relative Flux
1
0.5
1200
1400
1600
1800
2000
2200
2400
2600
2800
3000
λ [Å]

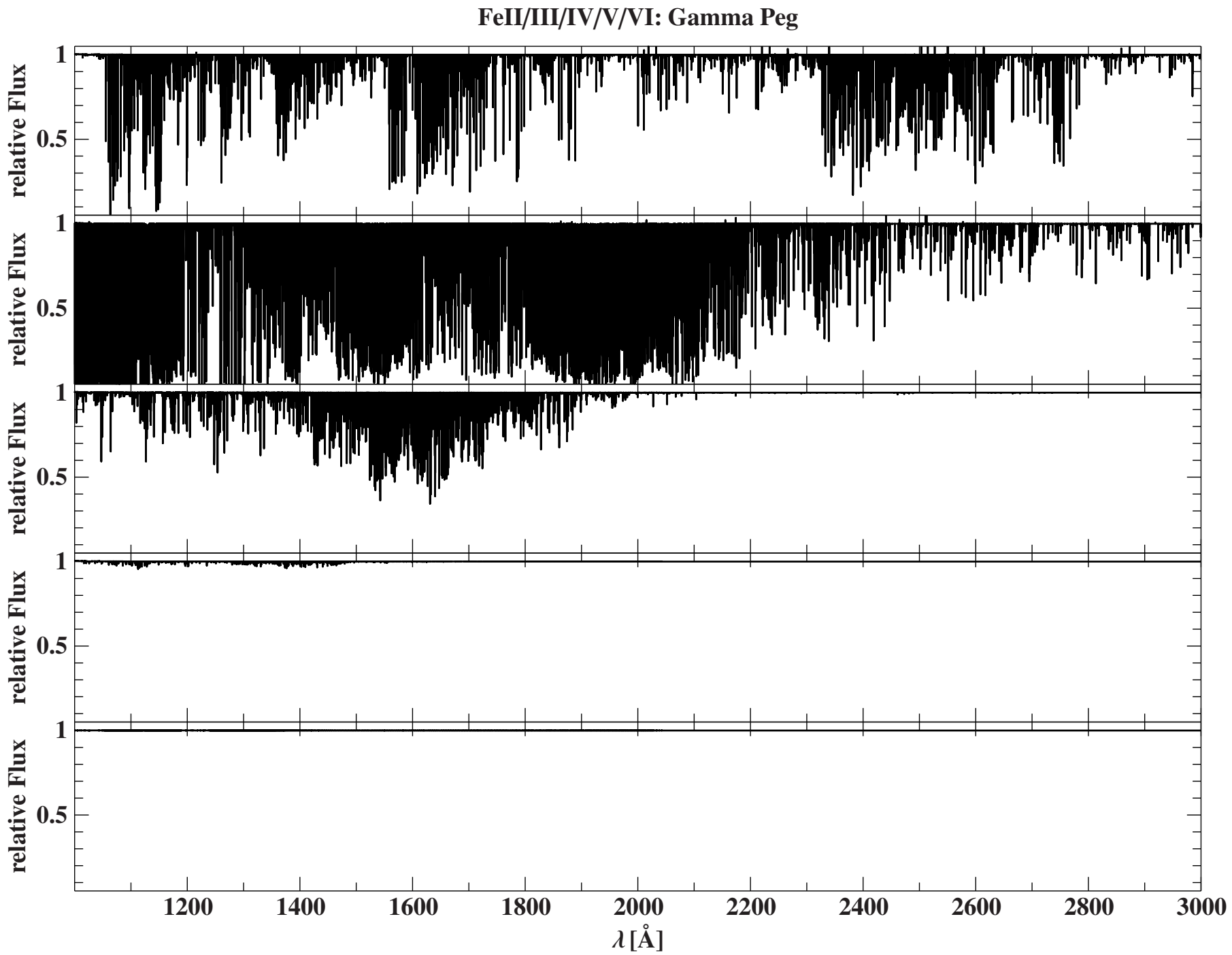
FeII/III/IV/V/VI: Gamma Peg
relative Flux
1
0.5
1200
1400
1600
1800
2000
2200
2400
2600
2800
3000
λ [Å]

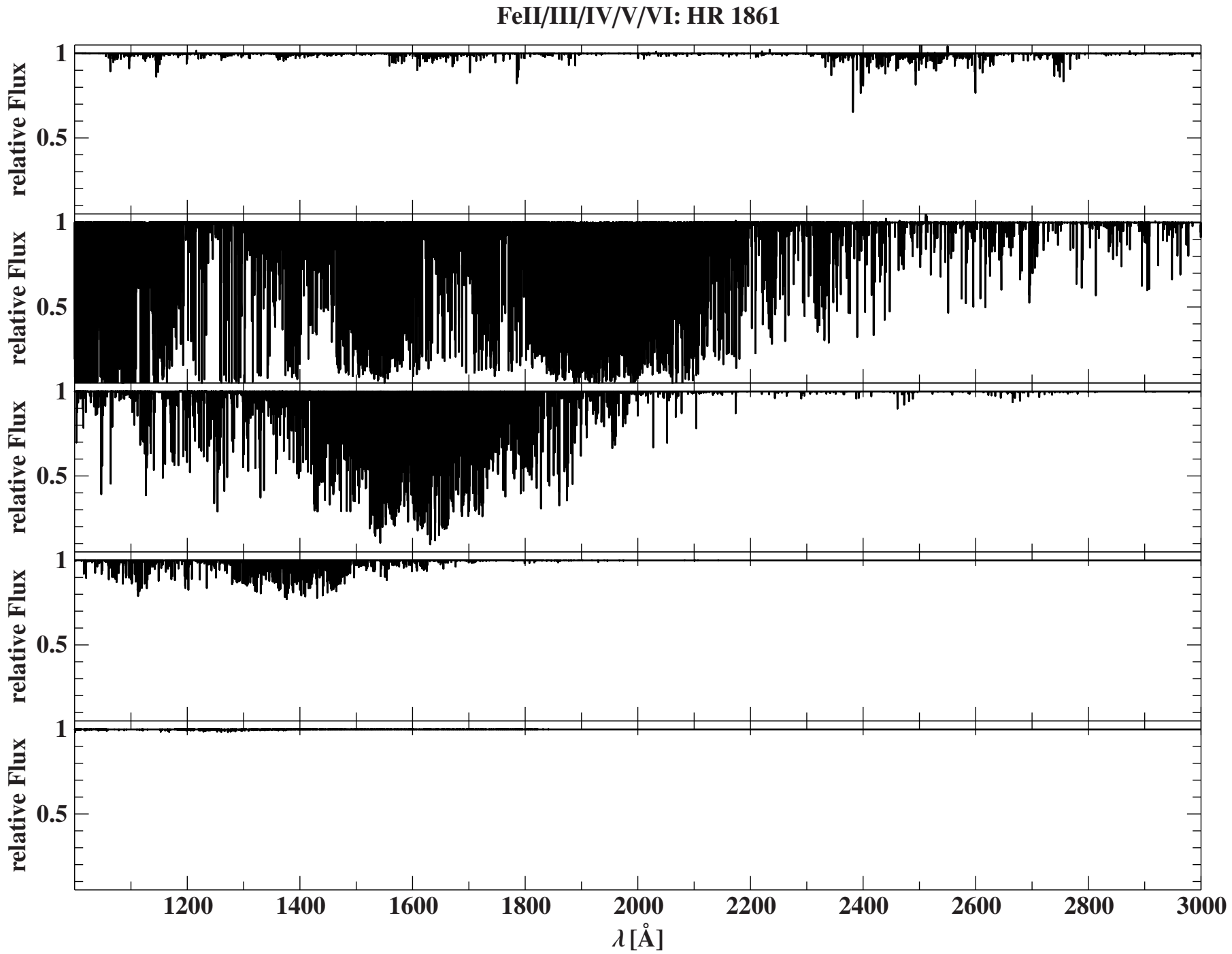
FeII/III/IV/V/VI: HR 1861
relative Flux
1
0.5
1200
1400
1600
1800
2000
2200
2400
2600
2800
3000
λ [Å]

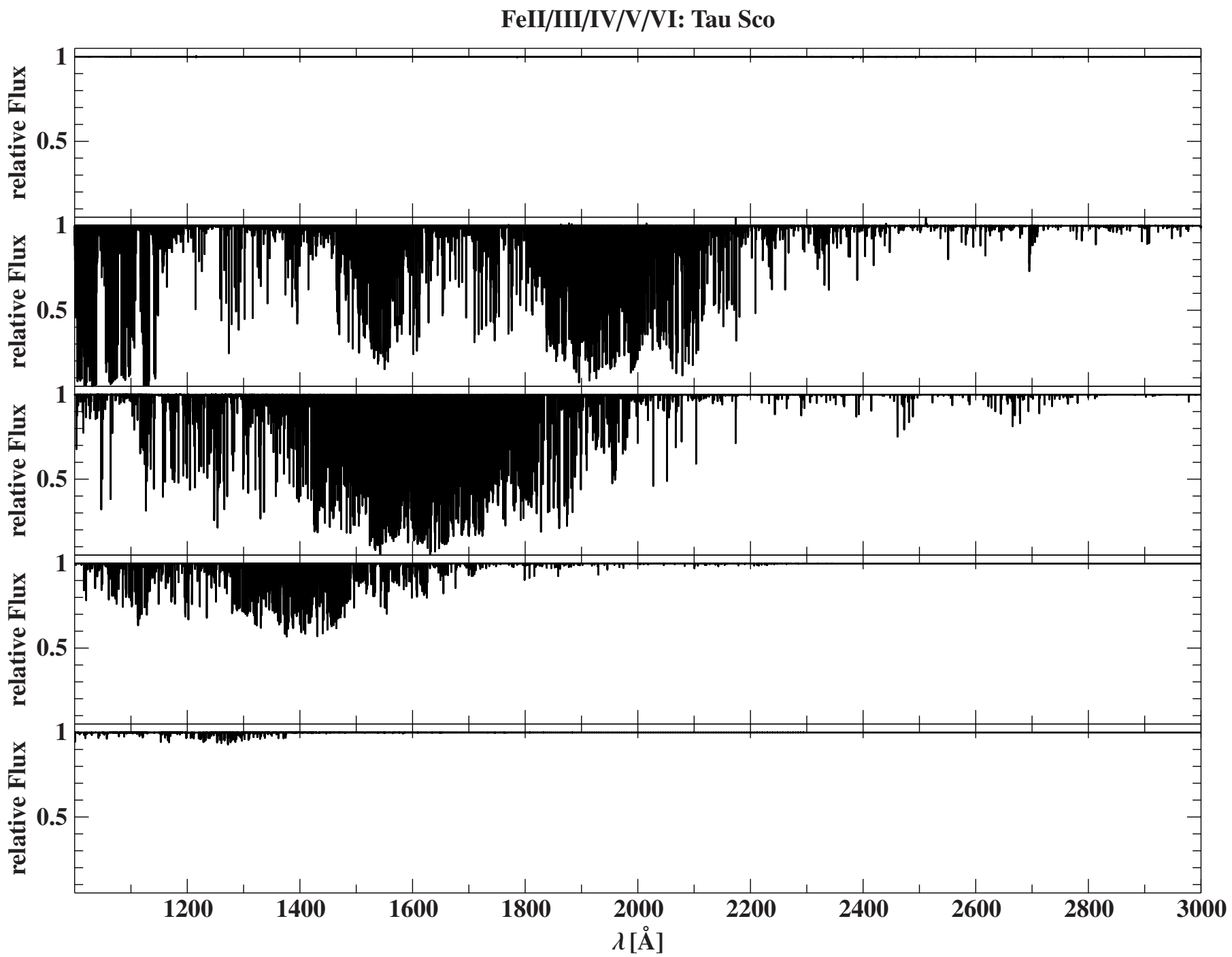
FeII/III/IV/V/VI: Tau Sco
relative Flux
1
0.5
1200
1400
1600
1800
2000
2200
2400
2600
2800
3000
λ [Å]

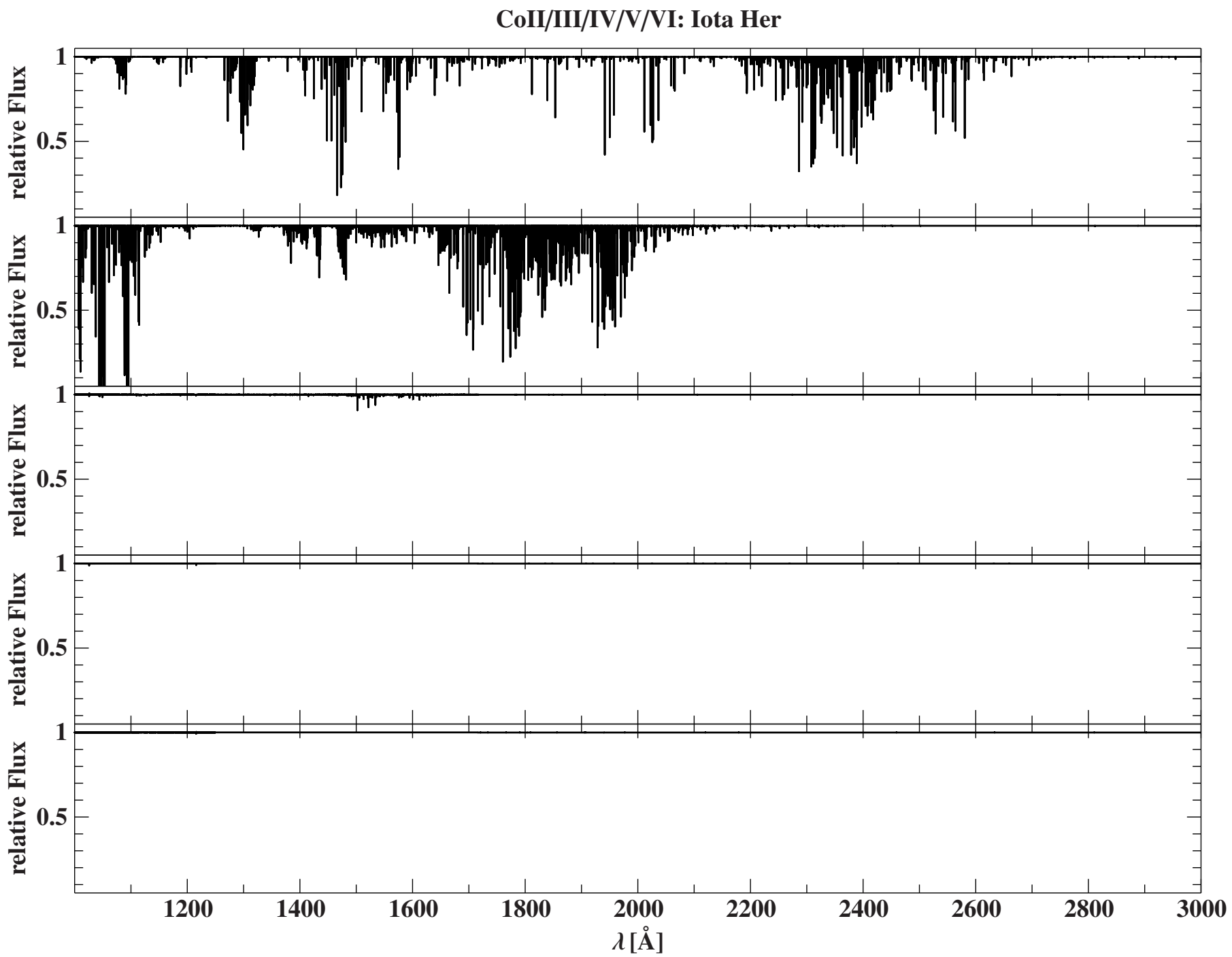
CoII/III/IV/V/VI: Iota Her
relative Flux
1
0.5
1200
1400
1600
1800
2000
2200
2400
2600
2800
3000
λ [Å]

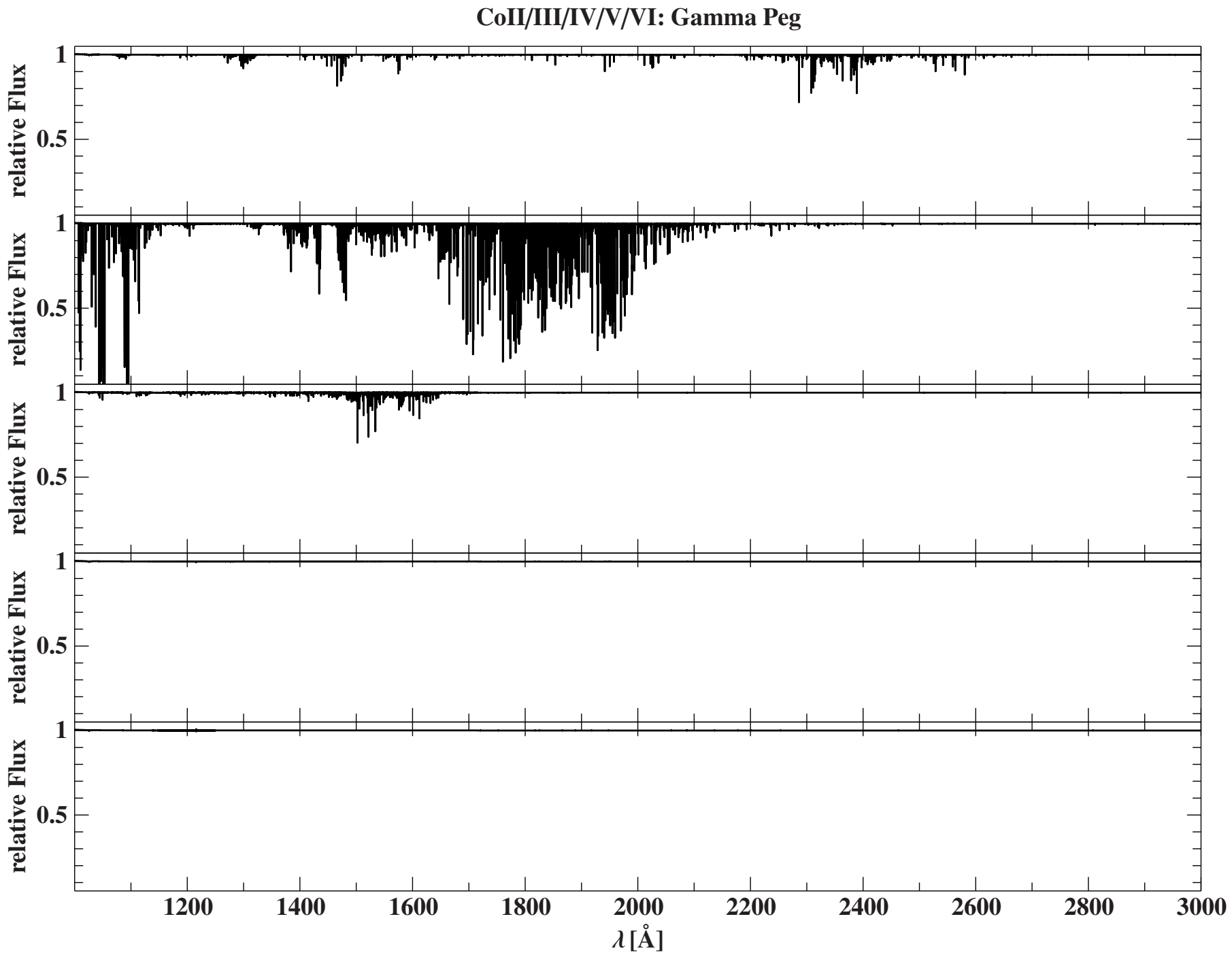
CoII/III/IV/V/VI: Gamma Peg
relative Flux
1
0.5
1200
1400
1600
1800
2000
2200
2400
2600
2800
3000
λ [Å]

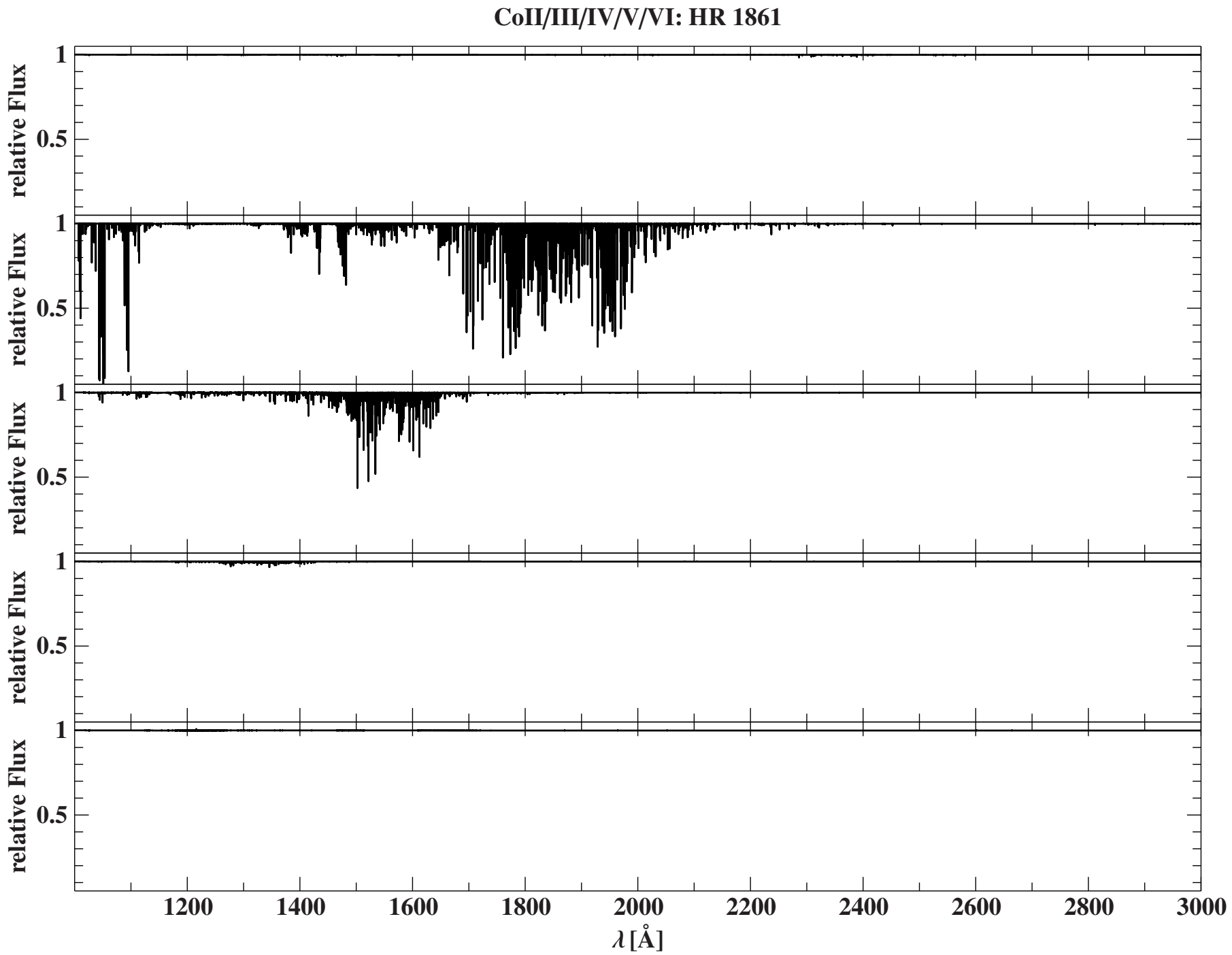
CoII/III/IV/V/VI: HR 1861
relative Flux
1
0.5
1200
1400
1600
1800
2000
2200
2400
2600
2800
3000
λ [Å]

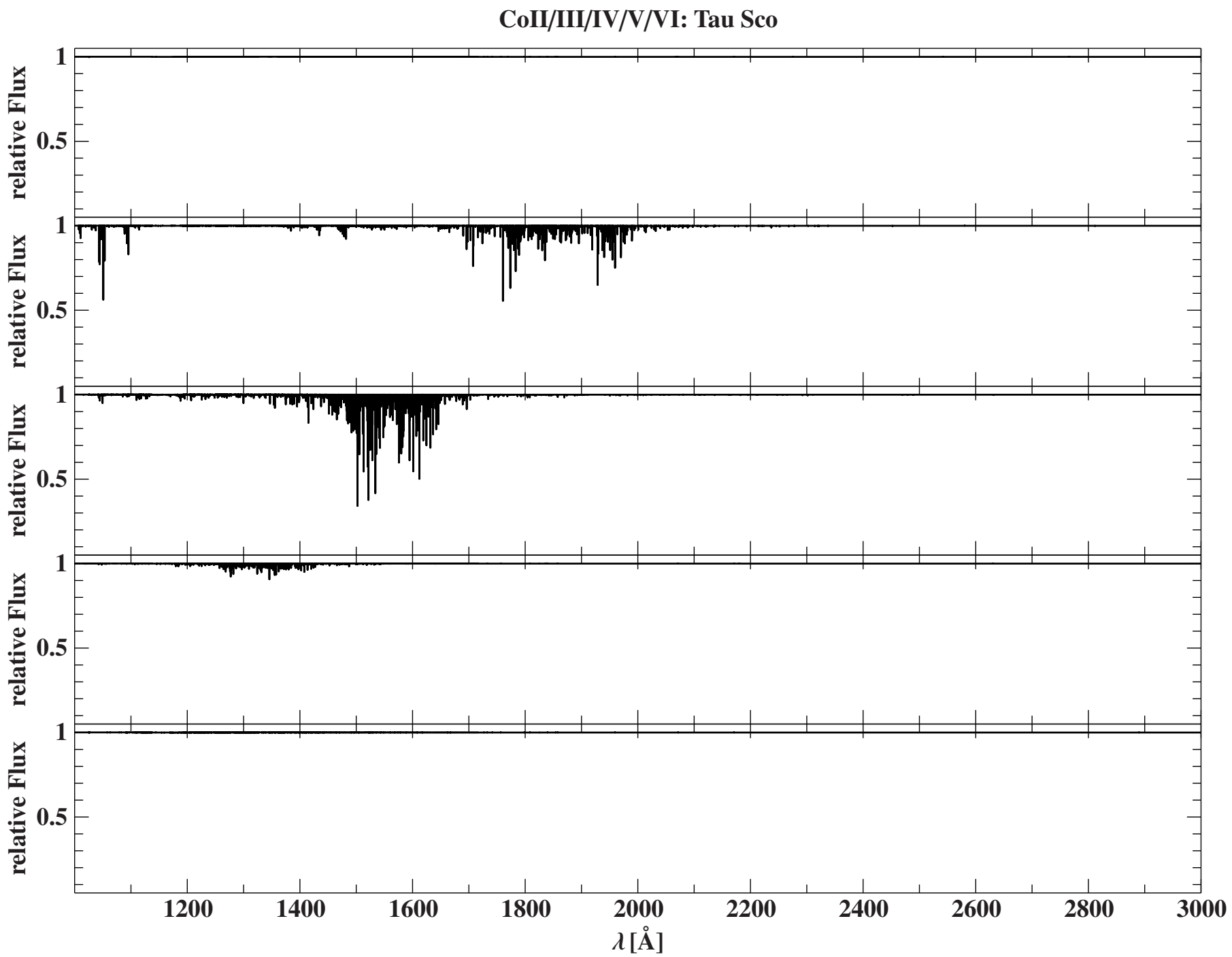
CoII/III/IV/V/VI: Tau Sco
relative Flux
1
0.5
1200
1400
1600
1800
2000
2200
2400
2600
2800
3000
λ [Å]

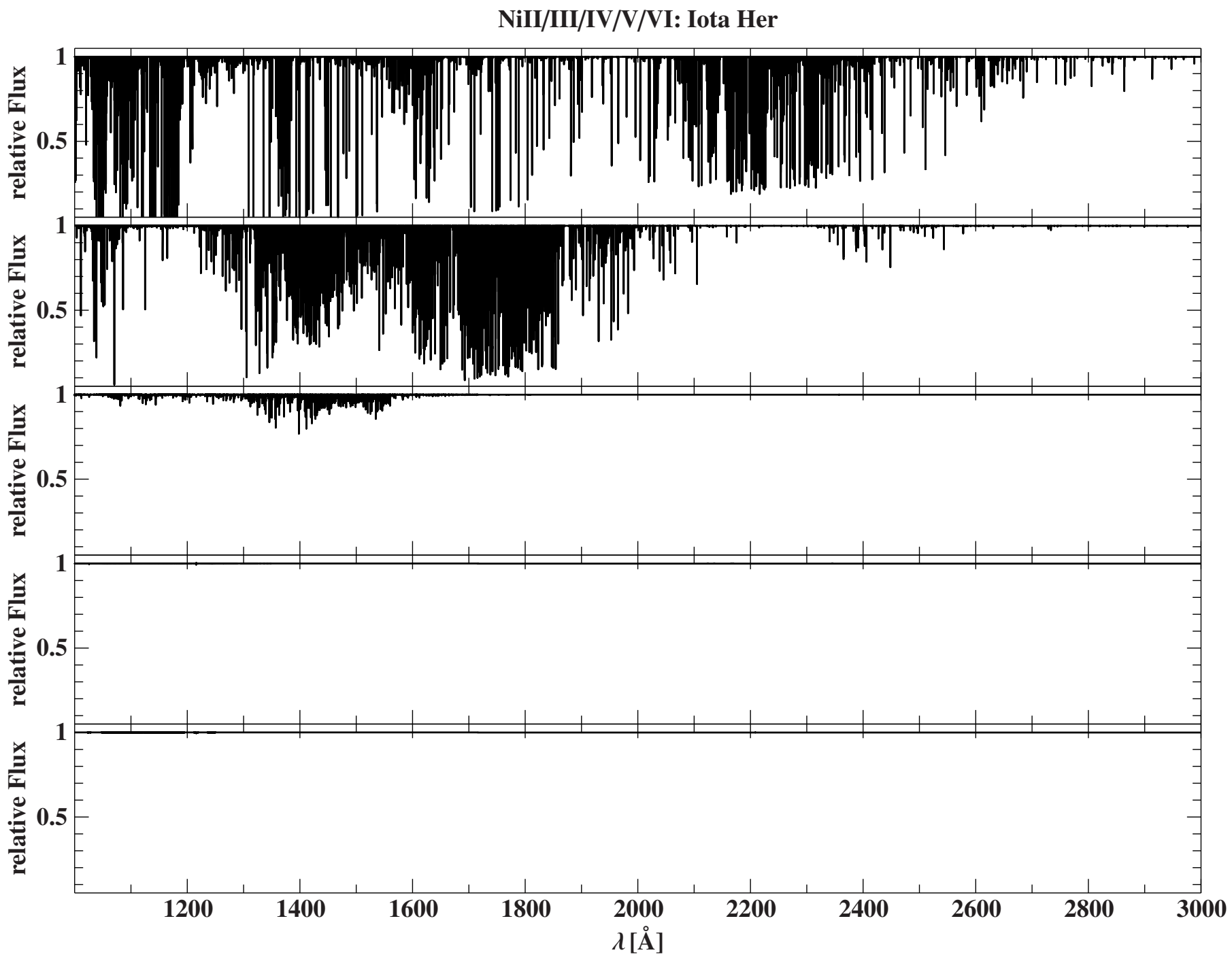
NiII/III/IV/V/VI: Iota Her
relative Flux
1
0.5
1200
1400
1600
1800
2000
2200
2400
2600
2800
3000
λ [Å]

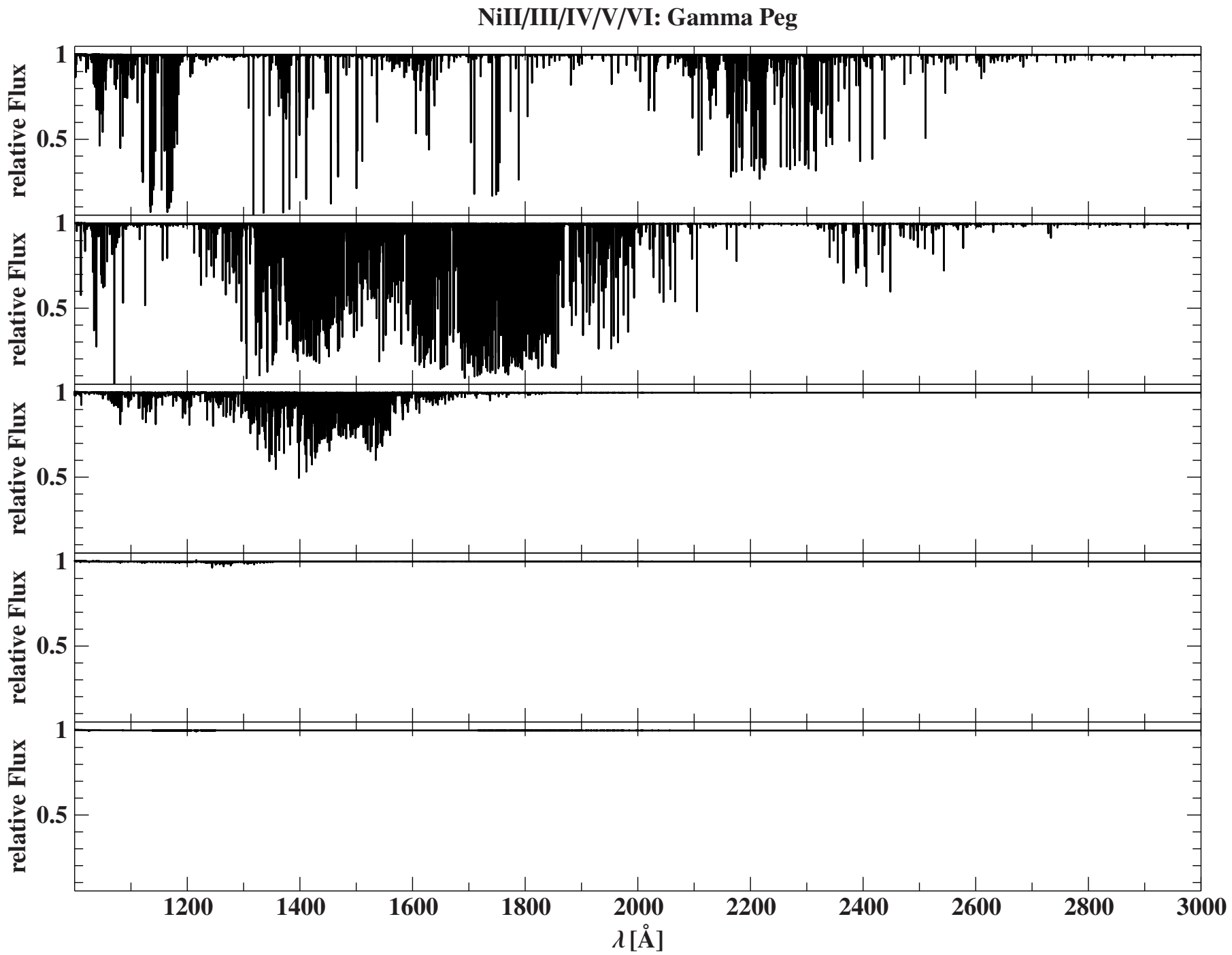
NiII/III/IV/V/VI: Gamma Peg
relative Flux
1
0.5
1200
1400
1600
1800
2000
2200
2400
2600
2800
3000
λ [Å]

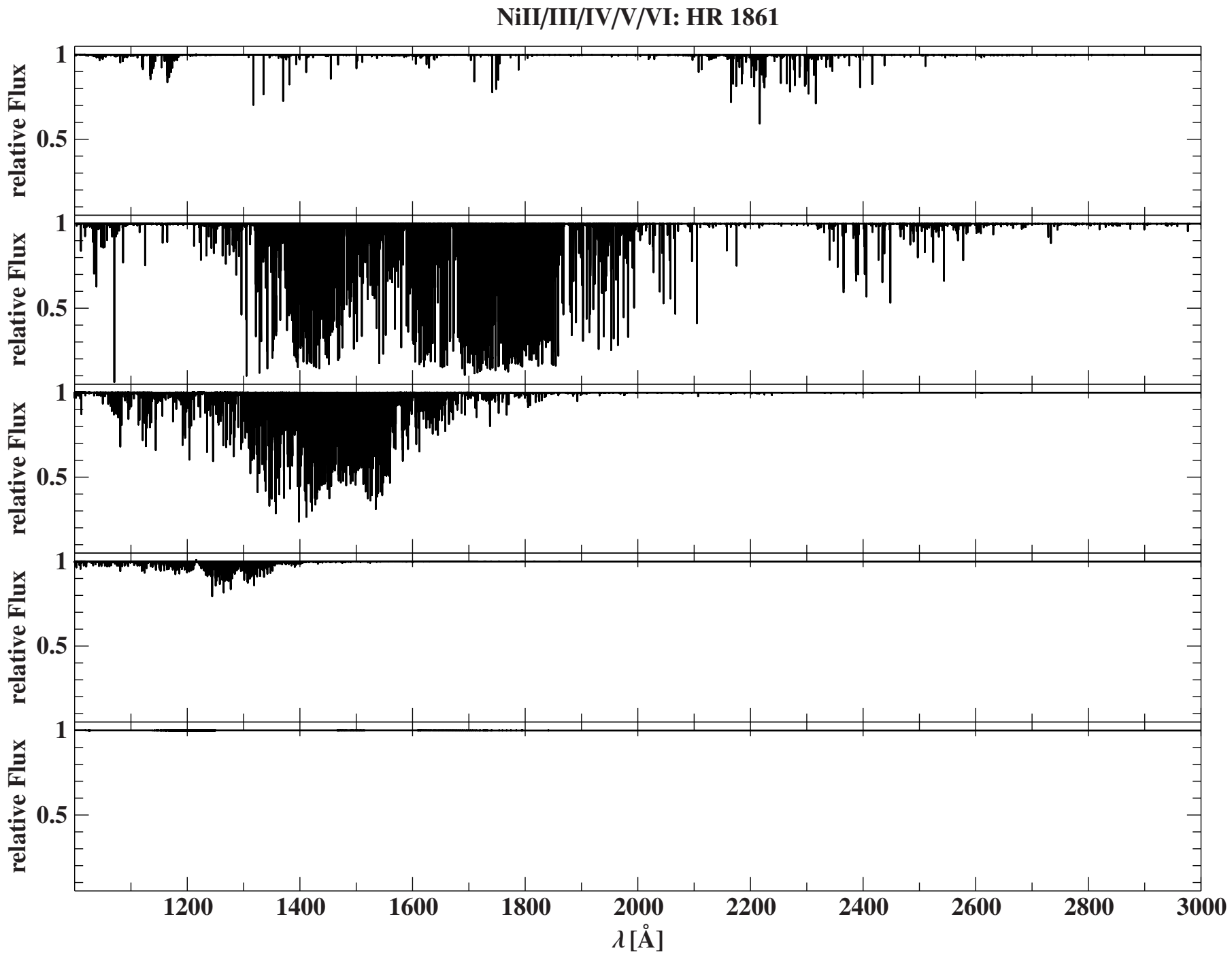
NiII/III/IV/V/VI: HR 1861
relative Flux
1
0.5
1200
1400
1600
1800
2000
2200
2400
2600
2800
3000
λ [Å]

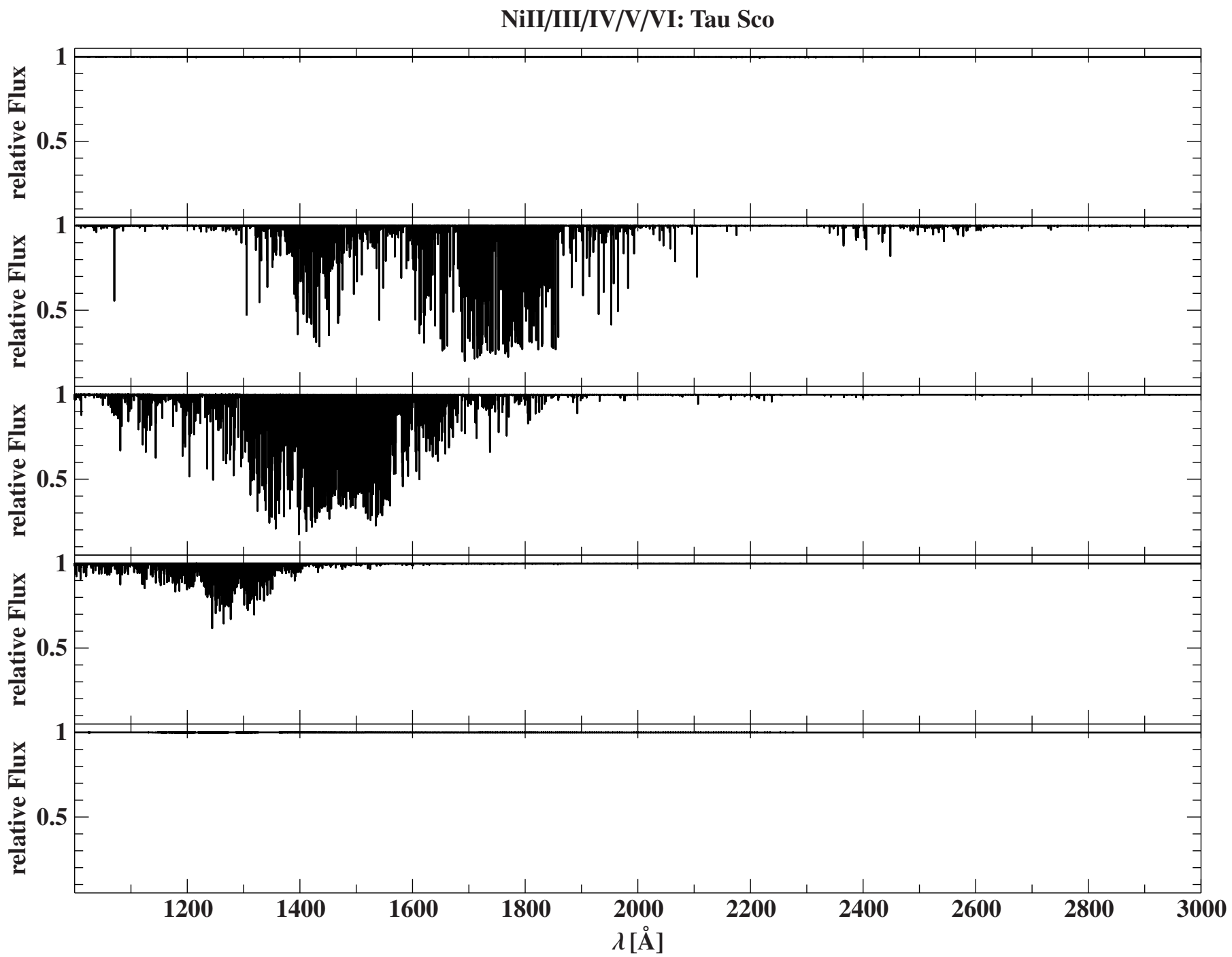
NiII/III/IV/V/VI: Tau Sco
relative Flux
1
0.5
1200
1400
1600
1800
2000
2200
2400
2600
2800
3000
λ [Å]

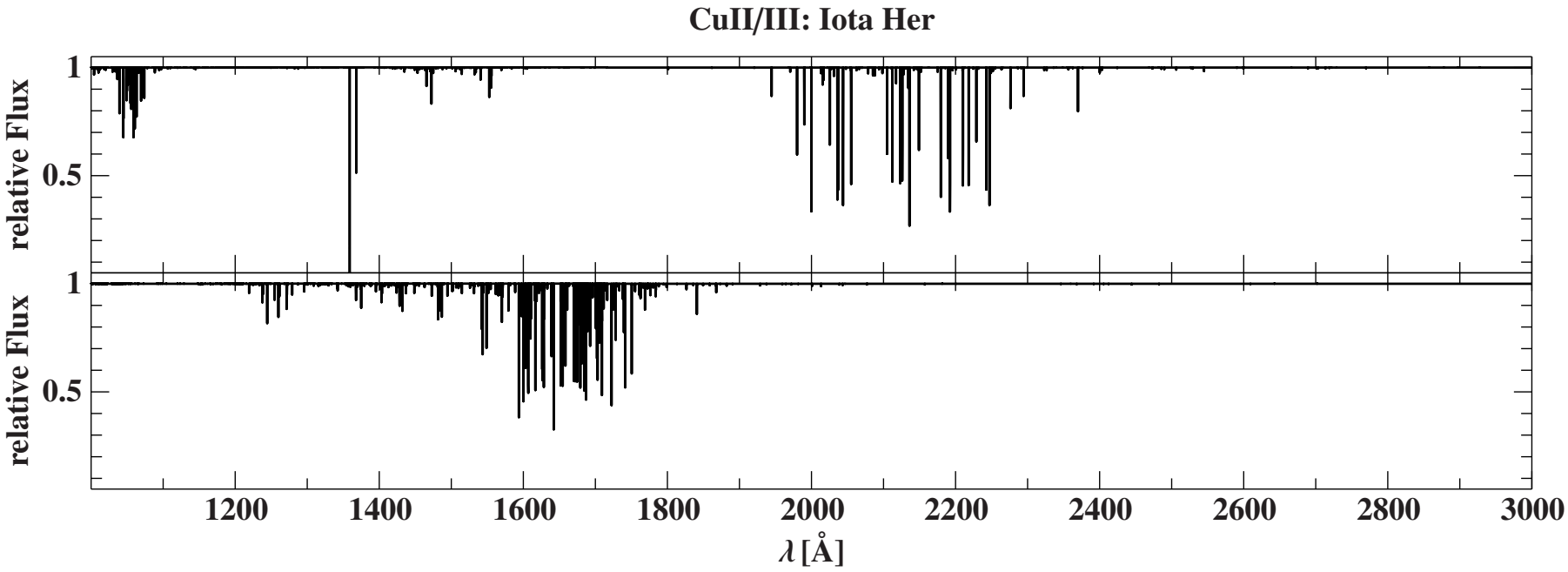
CuII/III: Iota Her
relative Flux
1
0.5
relative Flux
1
0.5
1200
1400
1600
1800
2000
2200
2400
2600
2800
3000
λ [Å]

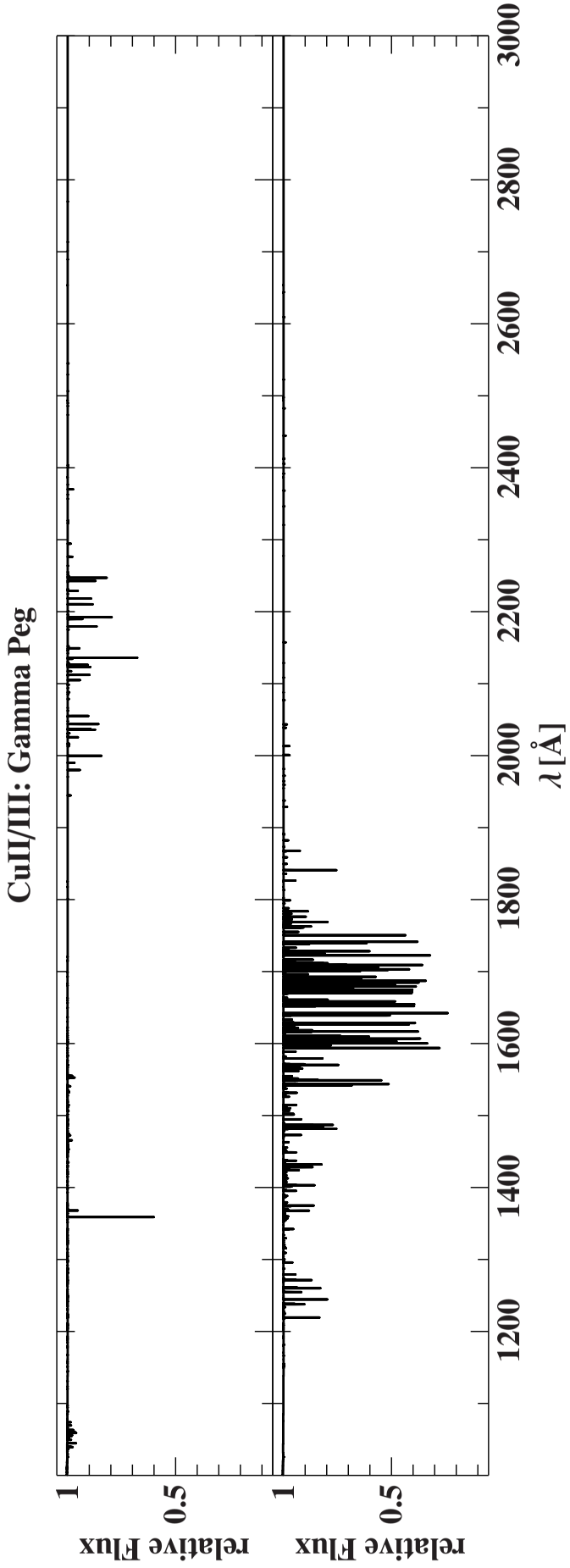
CuII/III: Gamma Peg
relative Flux
relative Flux
1
0.5
1
0.5
1200
1400
1600
1800
2000
2200
2400
2600
2800
3000
λ [Å]

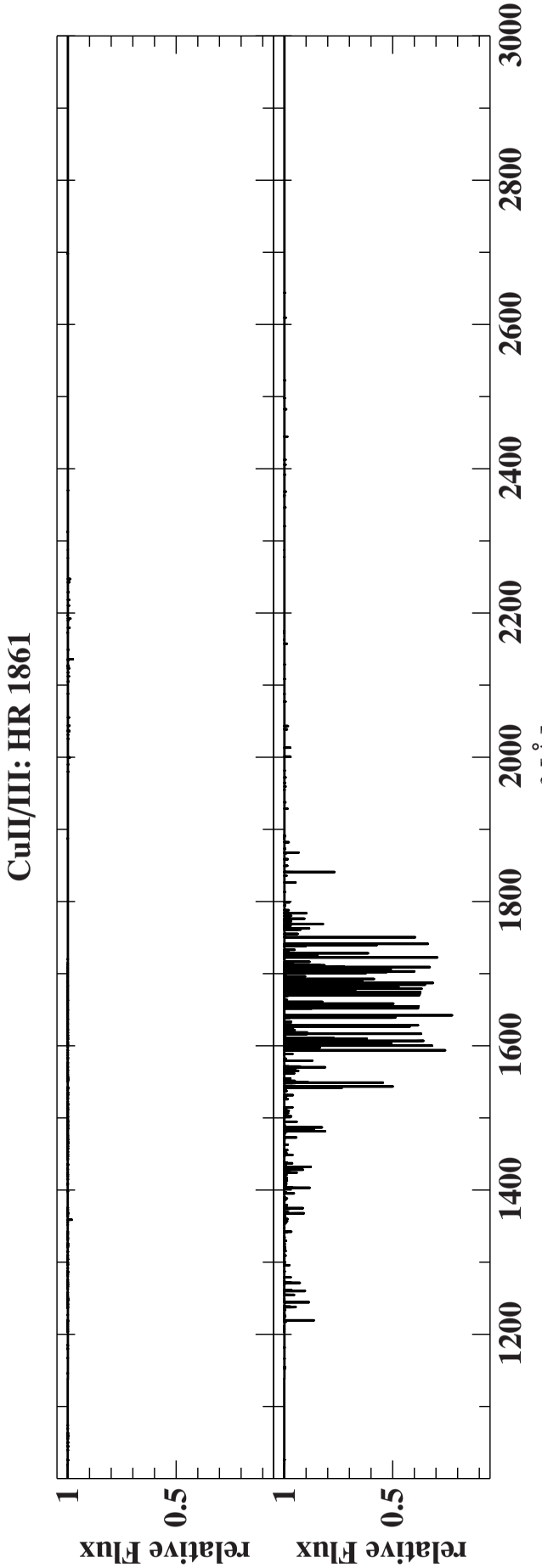
CuII/III: HR 1861
relative Flux
relative Flux
1
0.5
1
0.5
1200
1400
1600
1800
2000
2200
2400
2600
2800
3000
λ [Å]

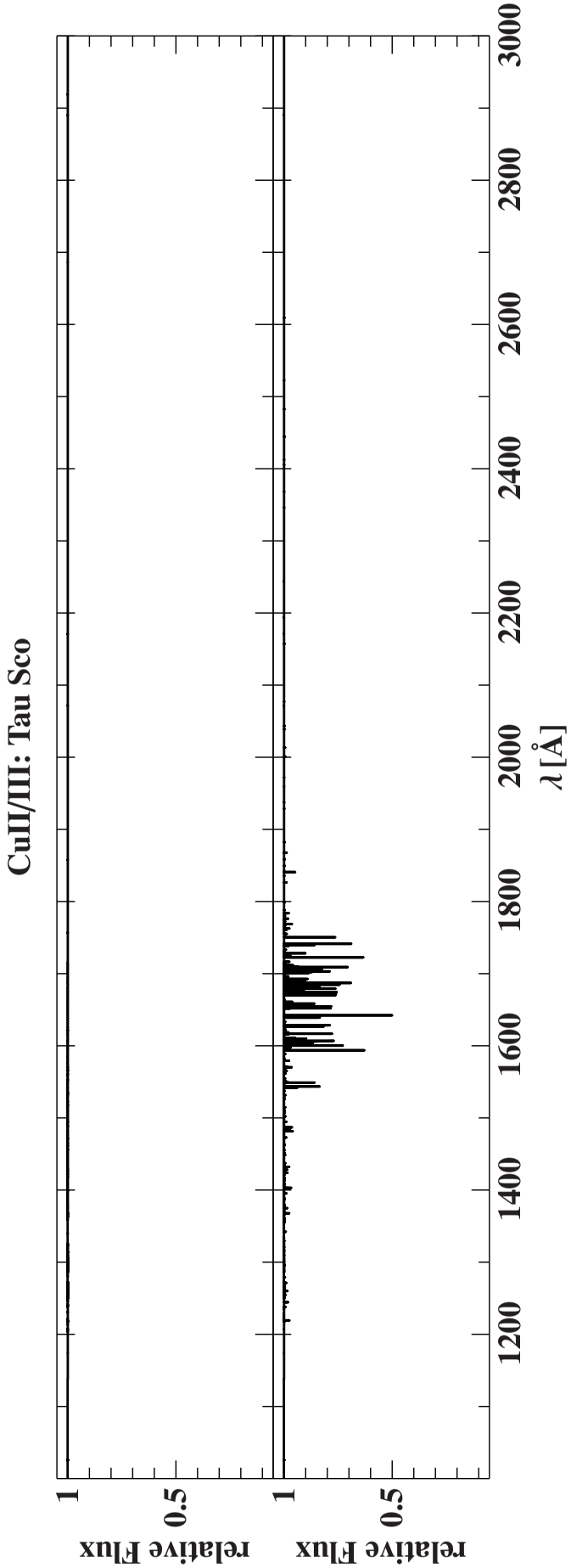
CuII/III: Tau Sco
relative Flux
1
0.5
1200
1400
1600
1800
2000
2200
2400
2600
2800
3000
λ [Å]

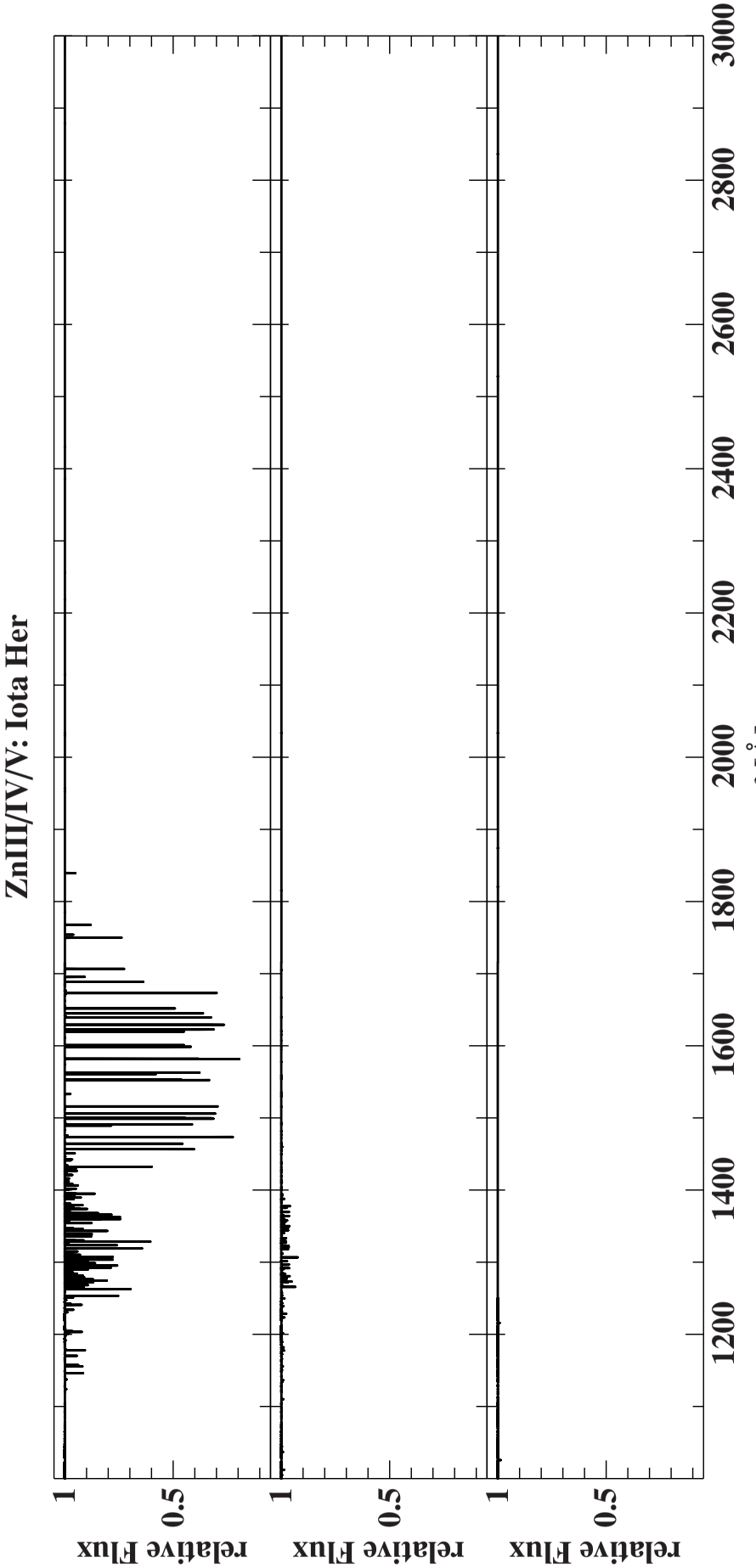
ZnIII/IV/V: Iota Her
relative Flux
relative Flux
relative Flux
1
0.5
1
0.5
1
0.5
1200
1400
1600
1800
2000
2200
2400
2600
2800
3000
λ [Å]

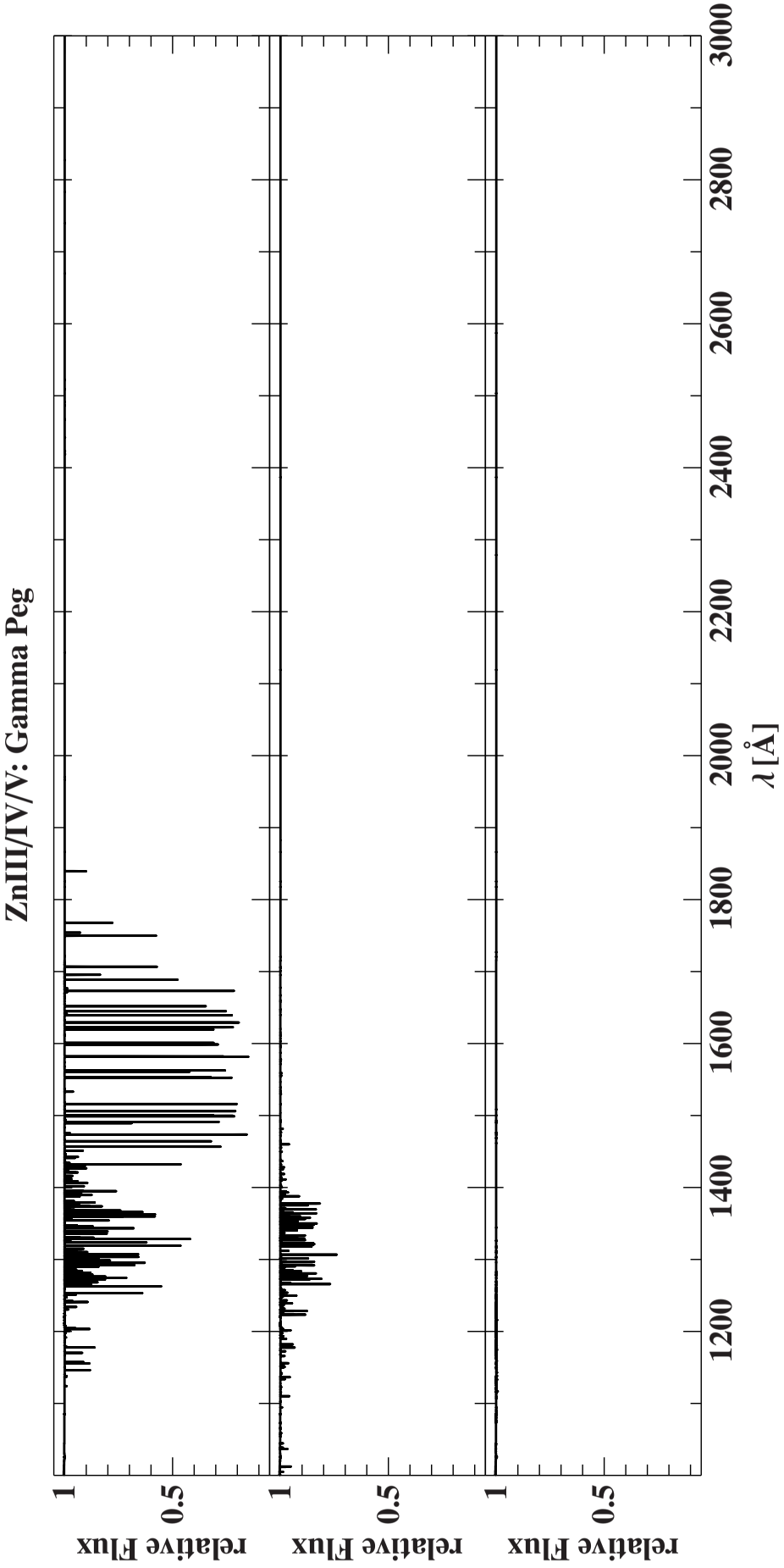
ZnIII/IV/V: Gamma Peg
relative Flux
relative Flux
relative Flux
1
0.5
1
0.5
1
0.5
1200
1400
1600
1800
2000
2200
2400
2600
2800
3000
λ [Å]

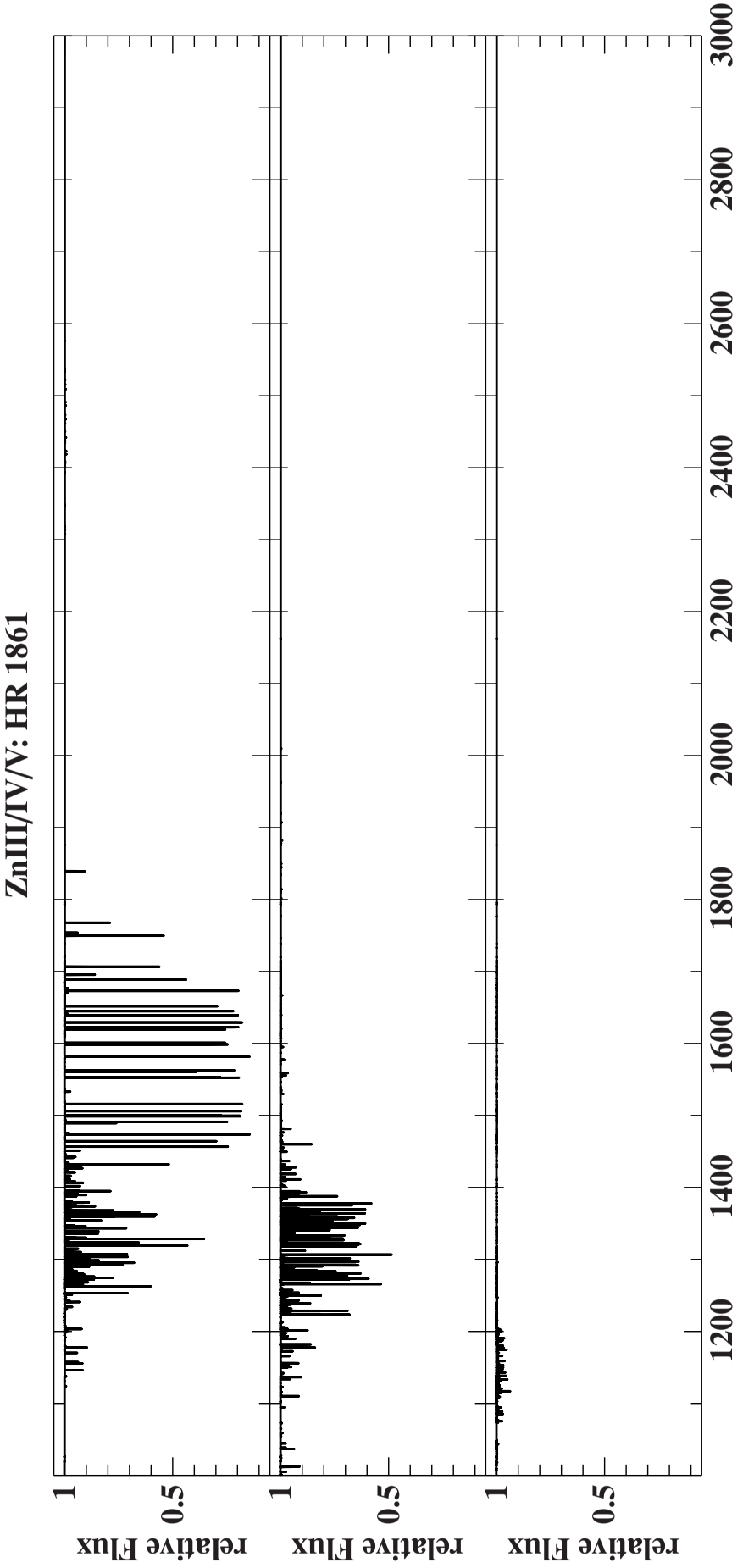
ZnIII/IV/V: HR 1861
relative Flux
relative Flux
relative Flux
1
0.5
1200
1400
1600
1800
2000
2200
2400
2600
2800
3000
λ [Å]

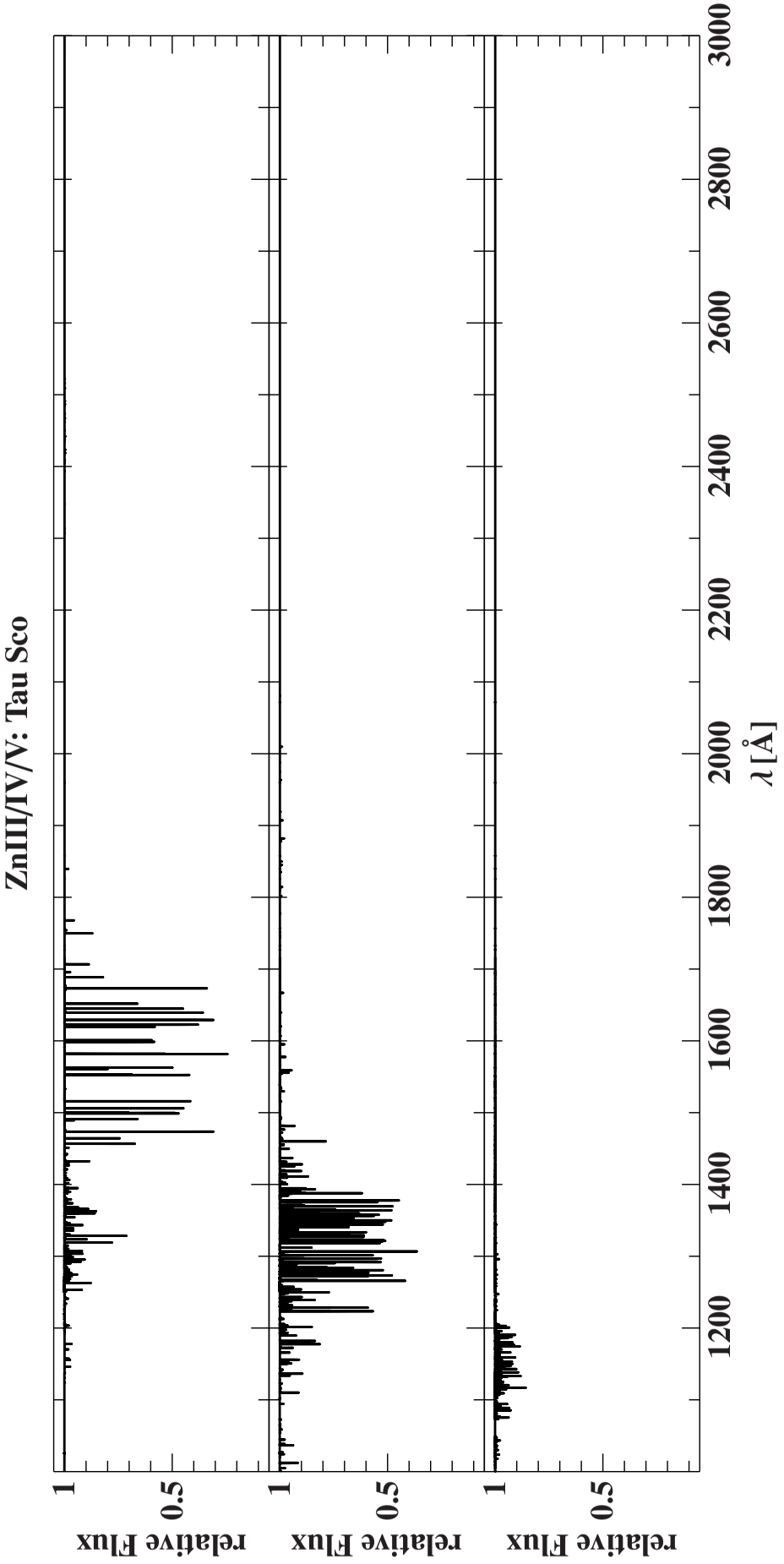
ZnIII/IV/V: Tau Sco
relative Flux
relative Flux
relative Flux
1
0.5
1
0.5
1
0.5
1200
1400
1600
1800
2000
2200
2400
2600
2800
3000
λ [Å]

D. UV spectrum of ι Her

Comparison of the HST/STIS observations of ι Her (black) with a synthetic model spectrum (red) calculated with ADS for the parameters of ι Her determined in Sect. 9.2 and summarized in Table 9.1 and 9.2.

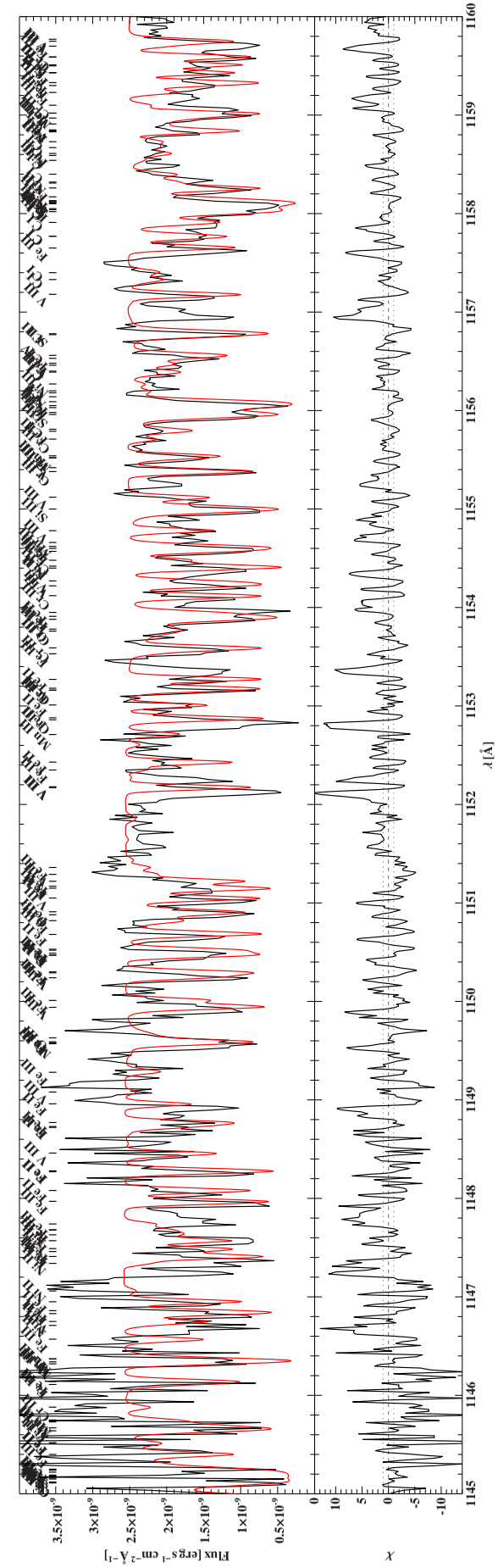
Flux [erg s^{-1} cm^{-2} Å^{-1}]
χ
λ [Å]

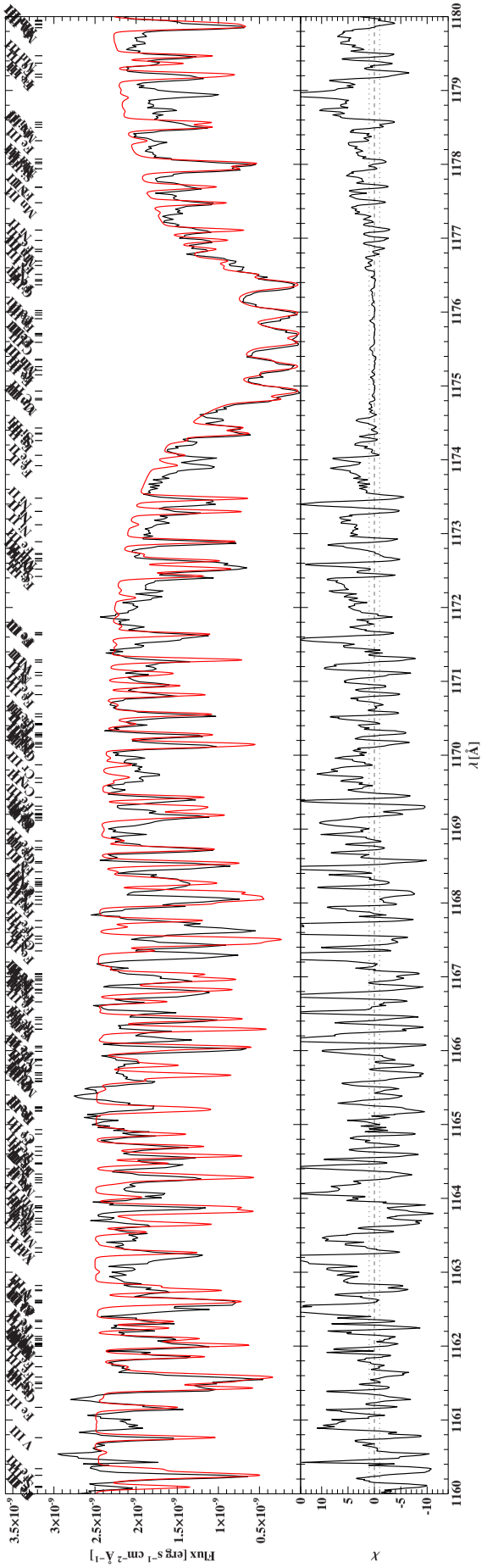
Flux [erg s^{-1} cm^{-2} Å^{-1}]
χ
λ [Å]

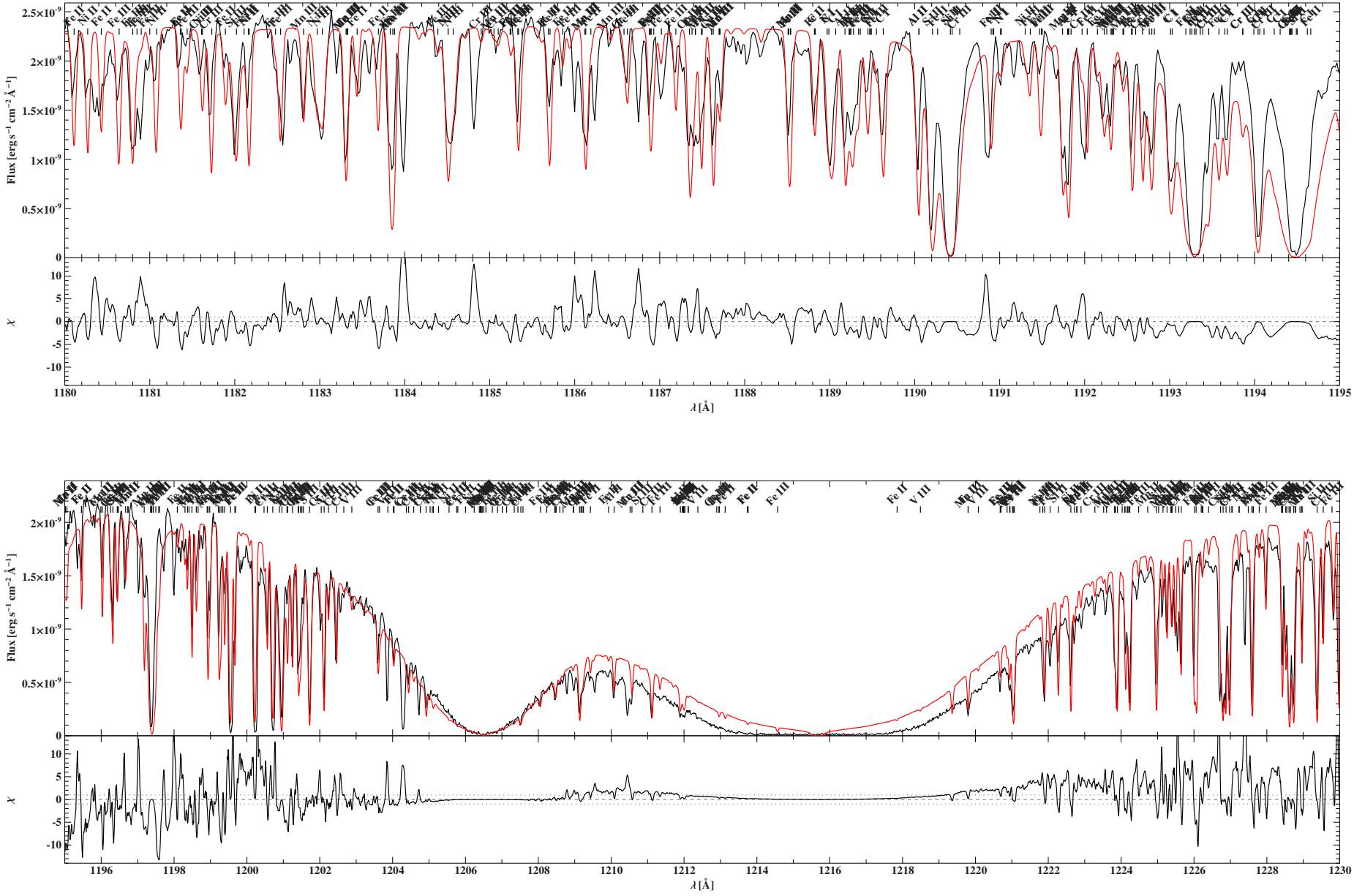
Flux [erg s^{-1} cm^{-2} Å^{-1}]
χ
λ [Å]

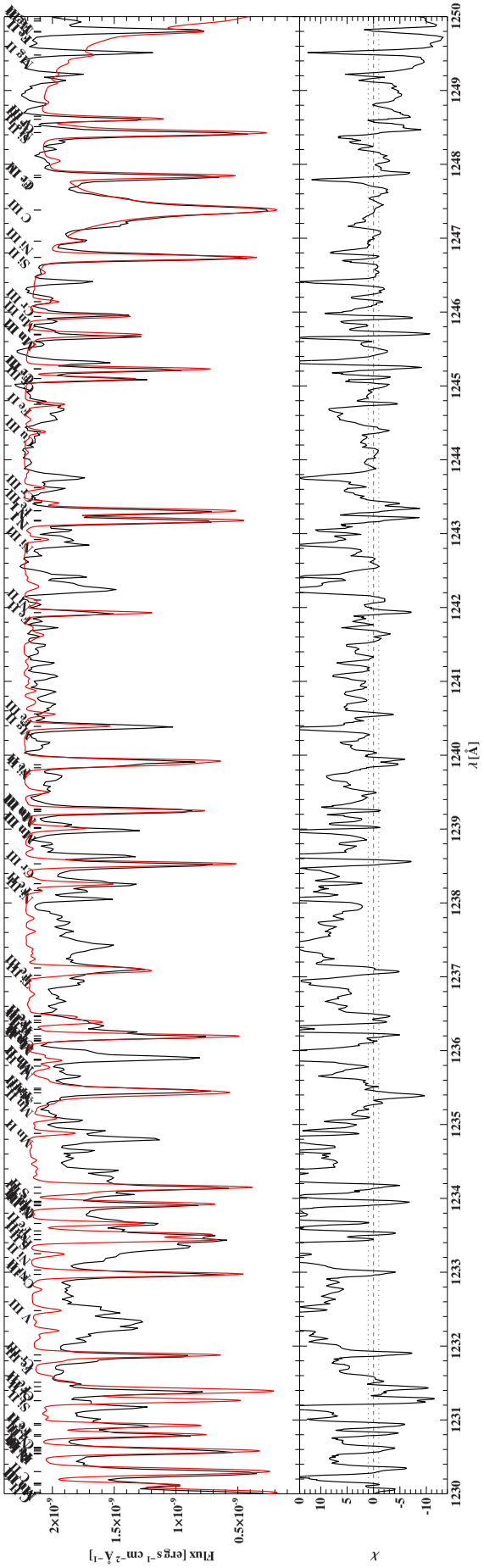
Flux [erg s^{-1} cm^{-2} Å^{-1}]
χ
λ [Å]

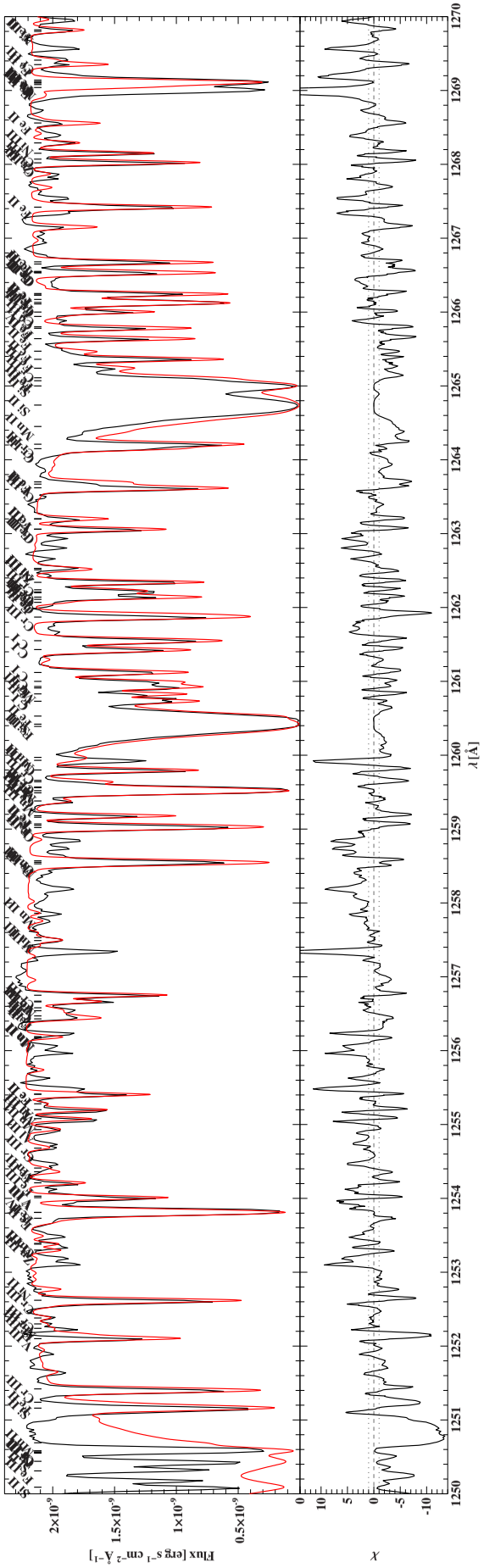
Flux [erg s^{-1} cm^{-2} Å^{-1}]
χ
λ [Å]

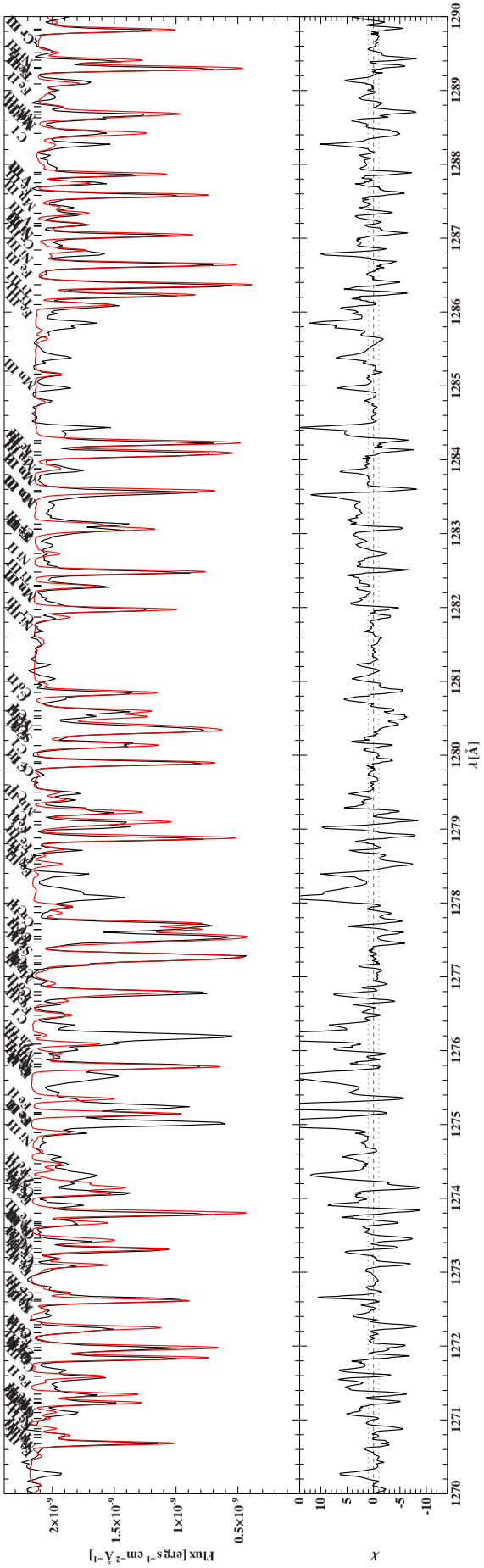
Flux [erg s^{-1} cm^{-2} Å^{-1}]
χ
λ [Å]

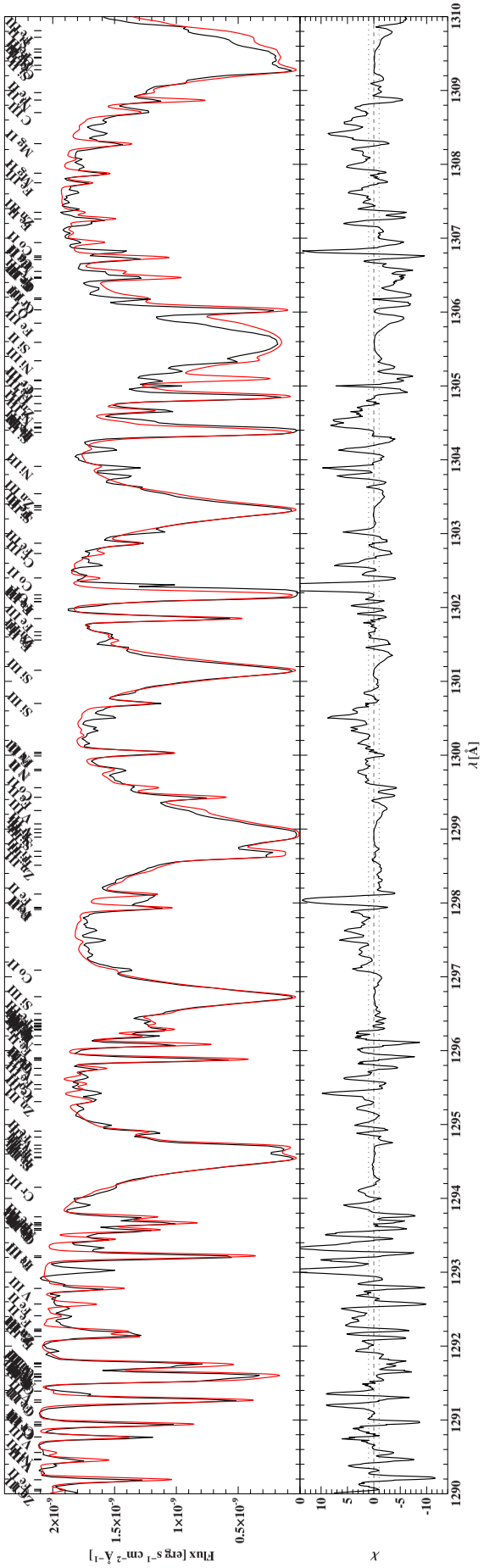
Flux [erg s^{-1} cm^{-2} Å^{-1}]
χ
λ [Å]

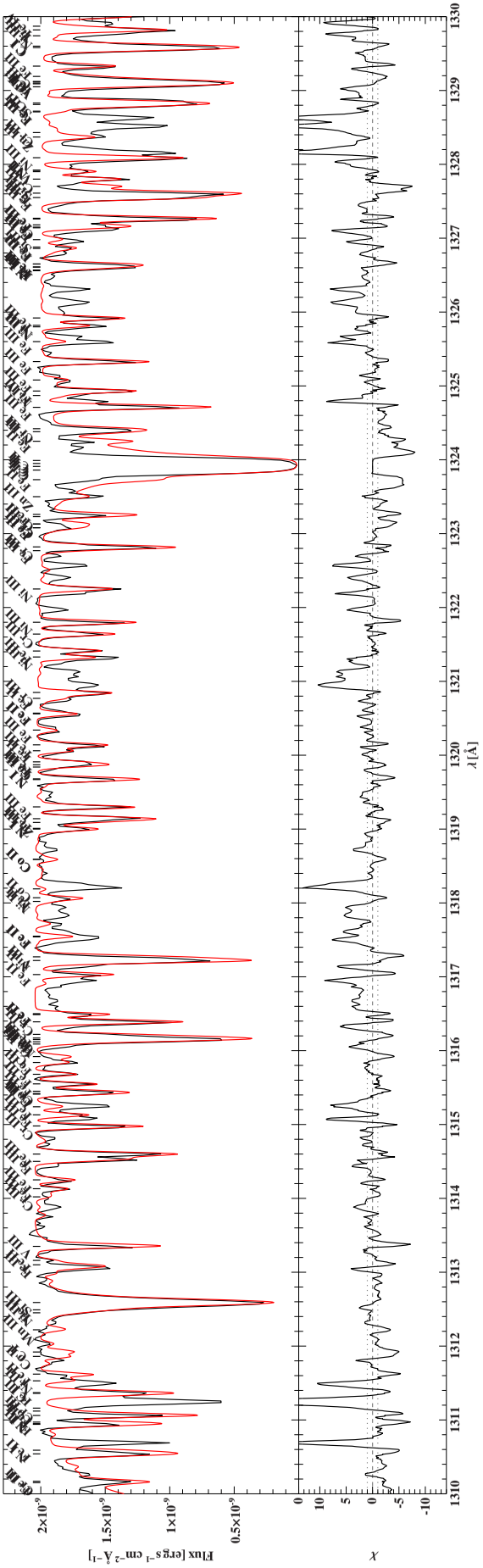
Flux [erg s^{-1} cm^{-2} Å^{-1}]
χ
λ [Å]

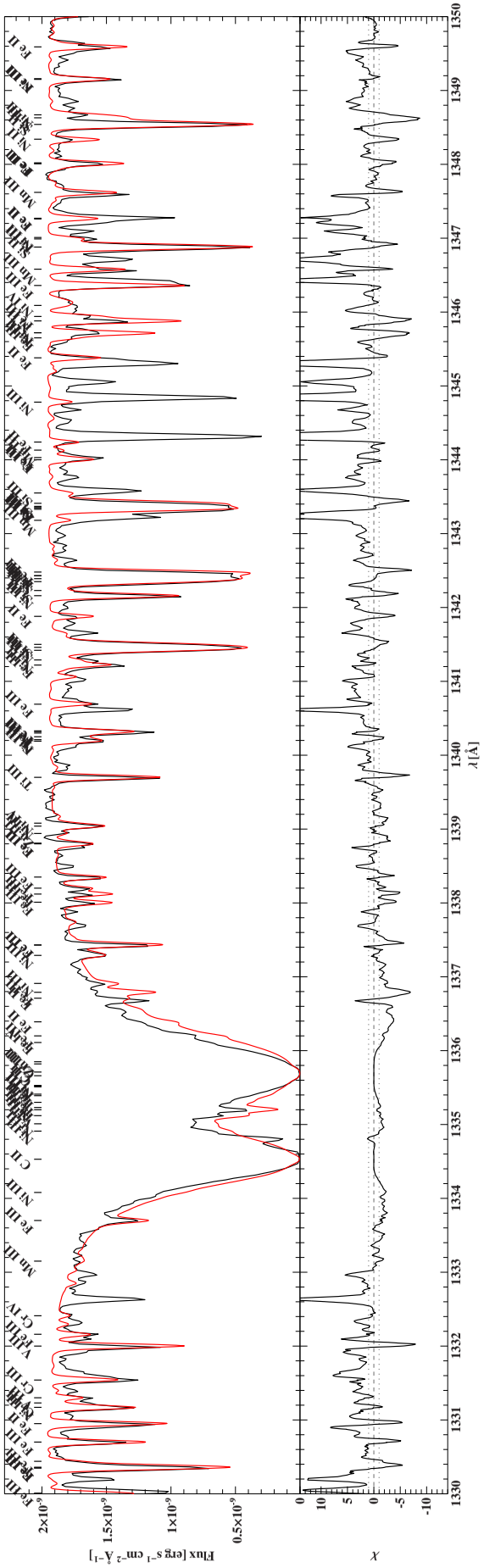
Flux [erg s^{-1} cm^{-2} Å^{-1}]
χ
λ [Å]

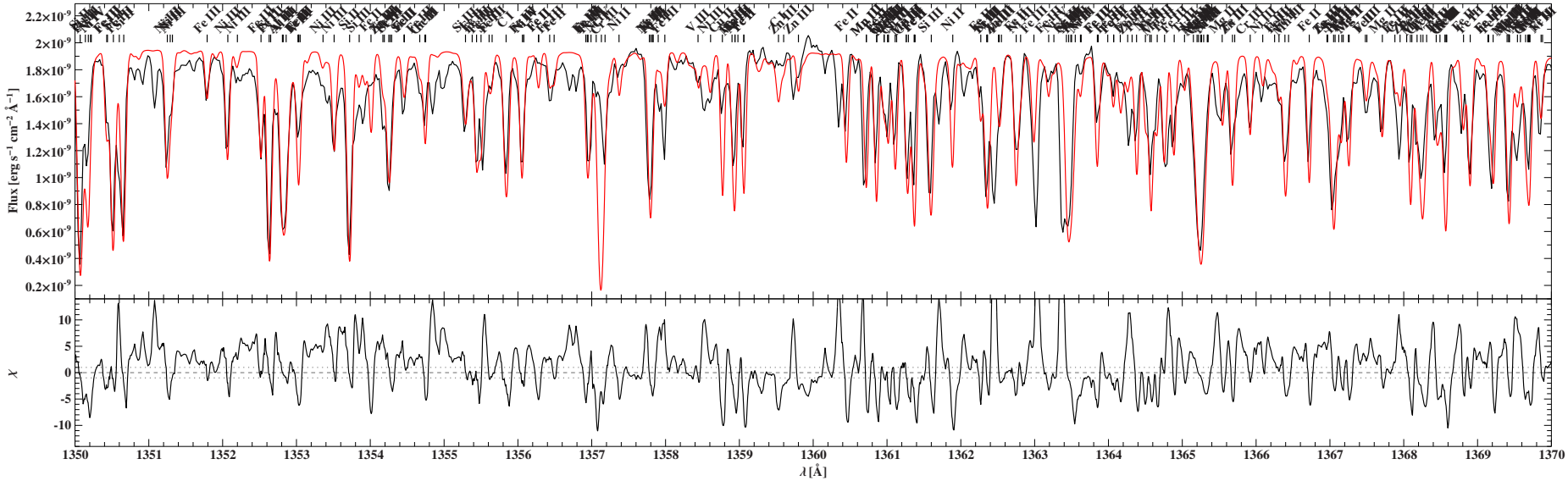
Flux [erg s^{-1} cm^{-2} Å^{-1}]
χ
λ [Å]

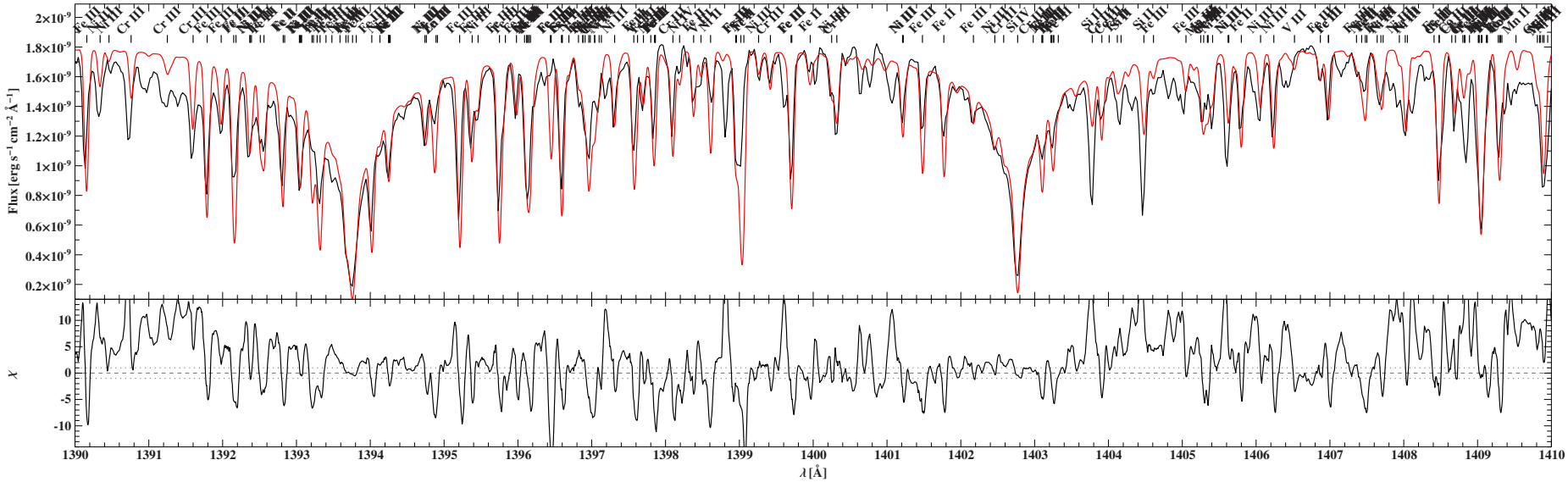
Flux [erg s^{-1} cm^{-2} Å^{-1}]
χ
λ [Å]

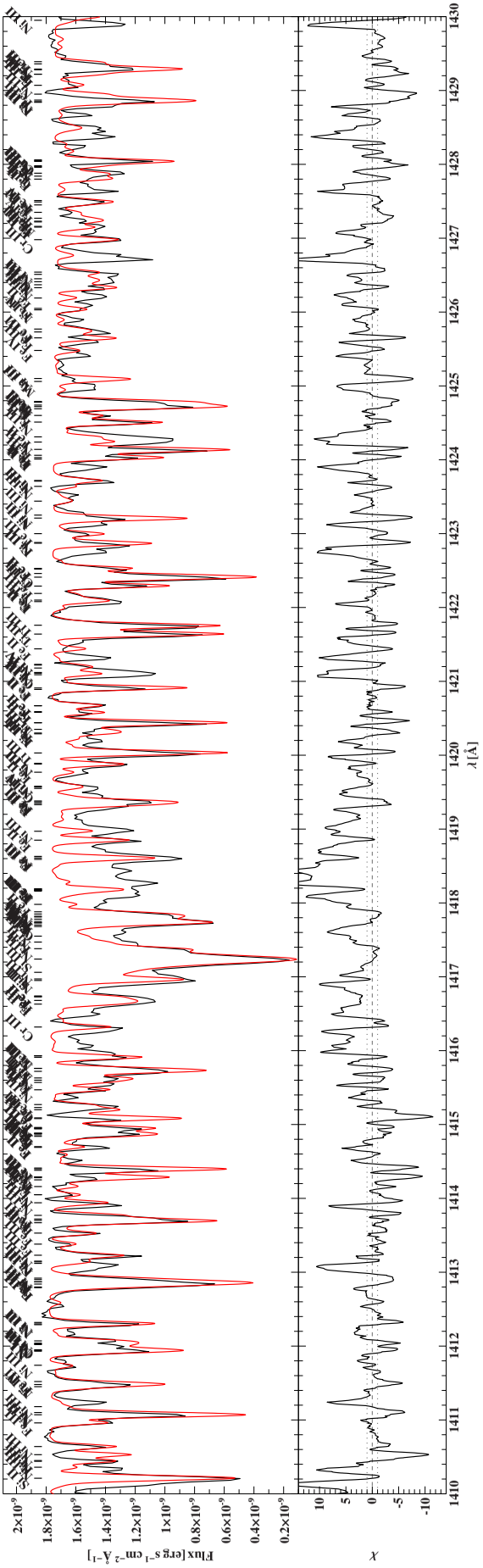
Flux [erg s^{-1} cm^{-2} Å^{-1}]
χ
λ [Å]

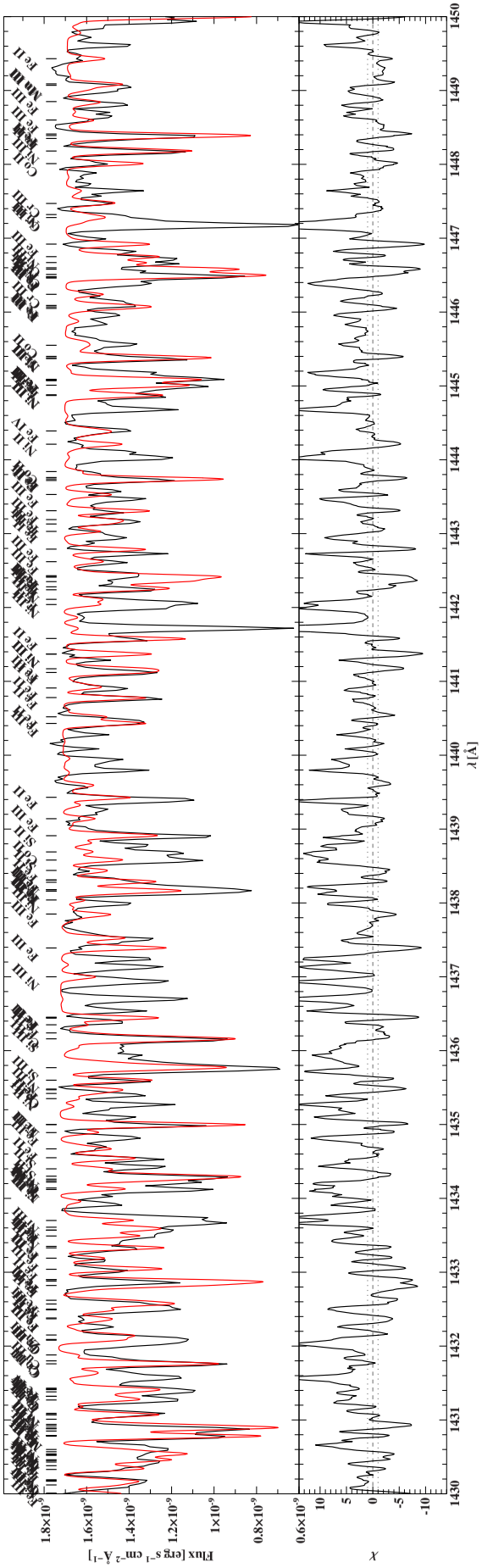
Flux [erg s^{-1} cm^{-2} Å^{-1}]
χ
λ [Å]

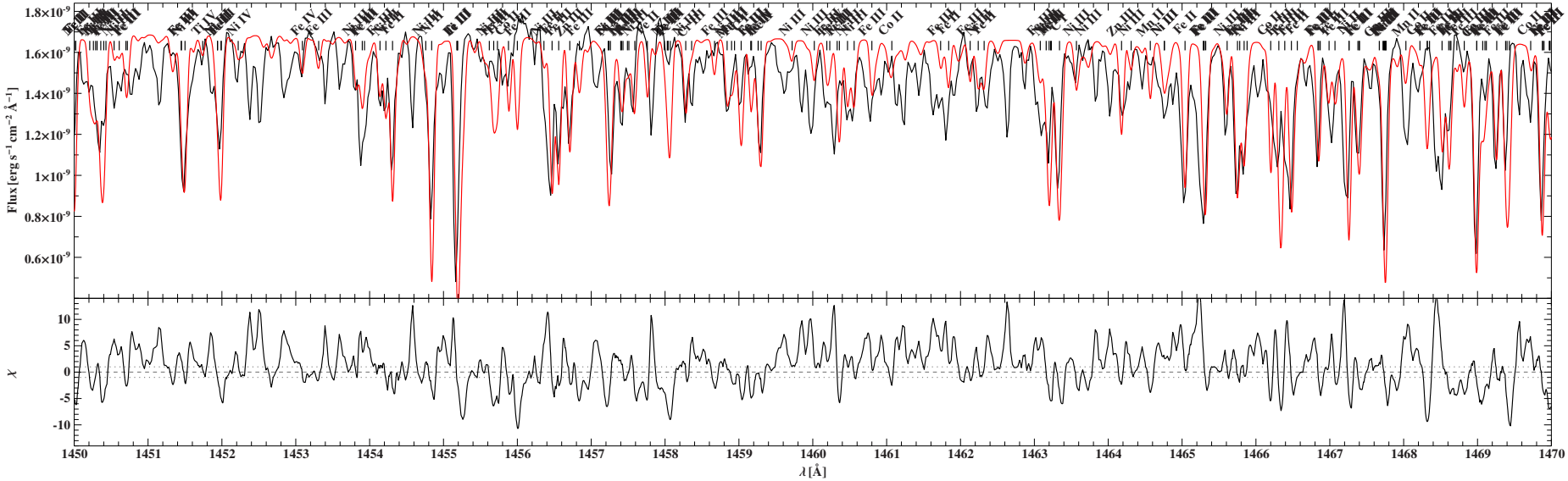
Flux [erg s^{-1} cm^{-2} Å^{-1}]
χ
λ [Å]

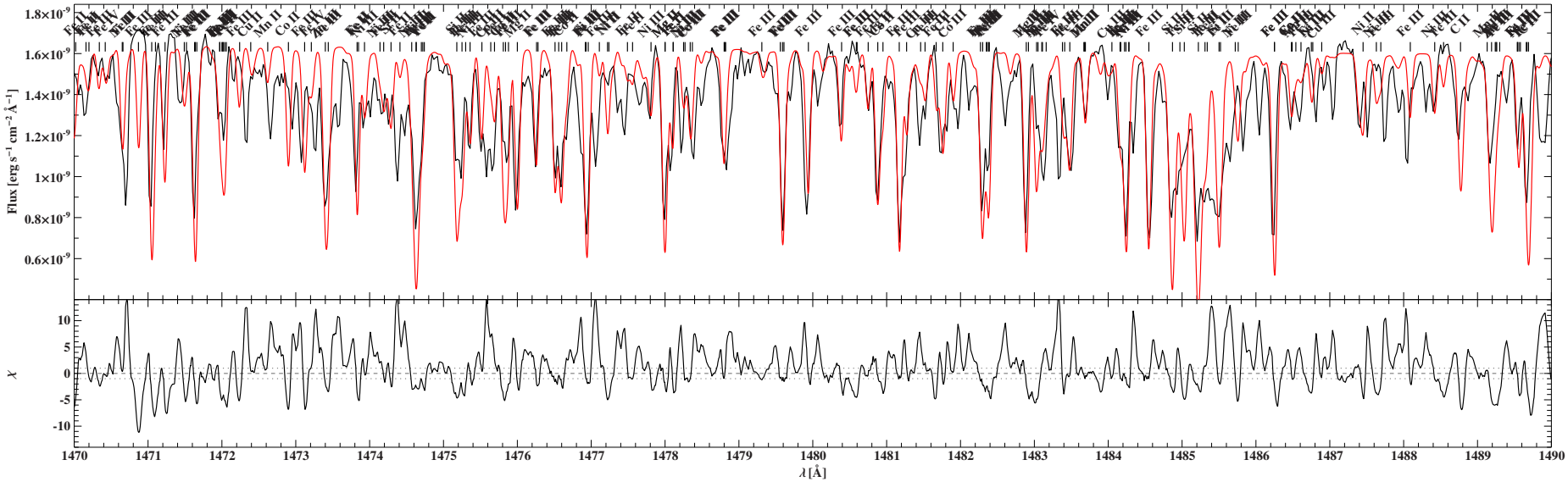
Flux [erg s^{-1} cm^{-2} Å^{-1}]
χ
λ [Å]

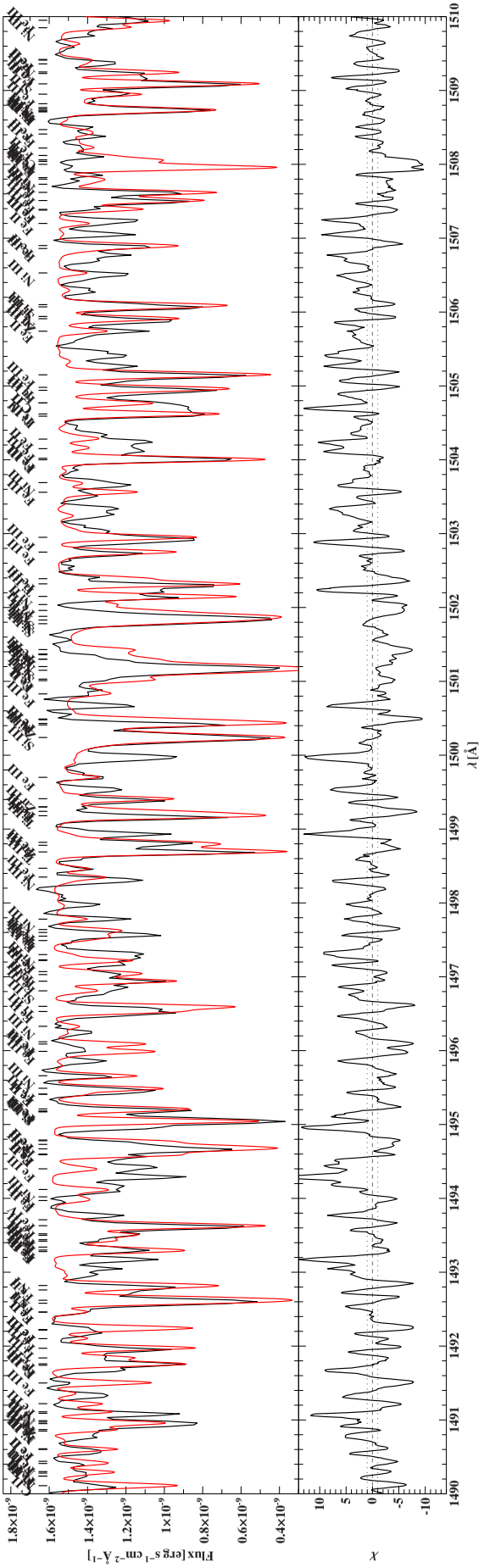
Flux [erg s⁻¹ cm⁻² Å⁻¹]
λ [Å]
χ

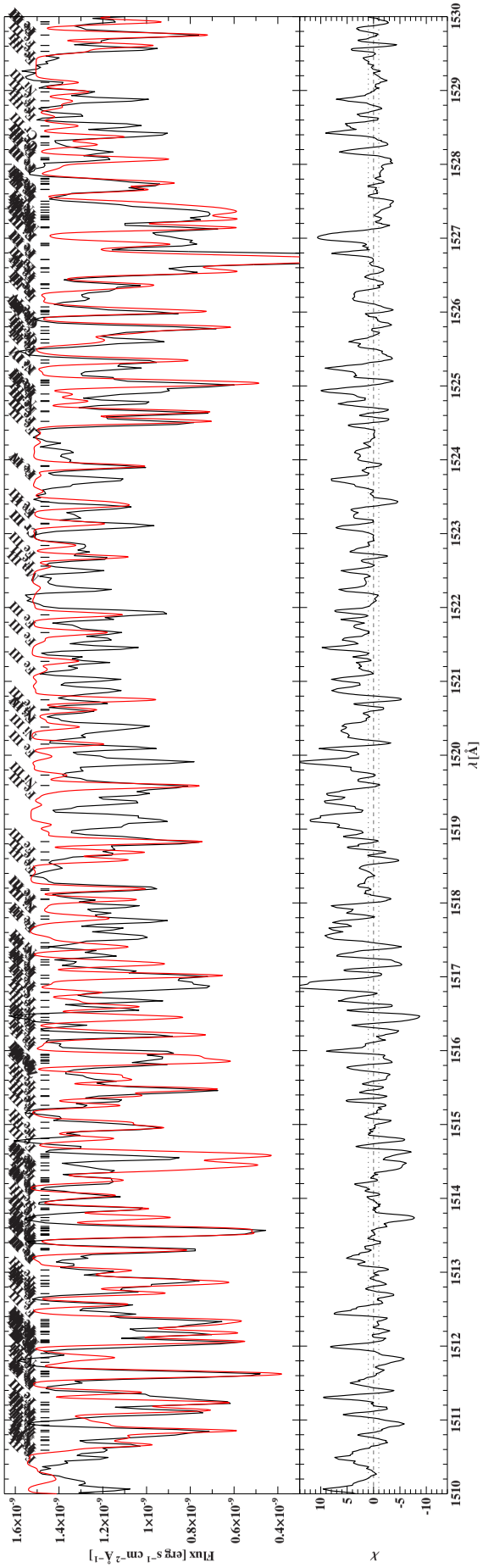
Flux [erg s⁻¹ cm⁻² Å⁻¹]
λ [Å]
χ

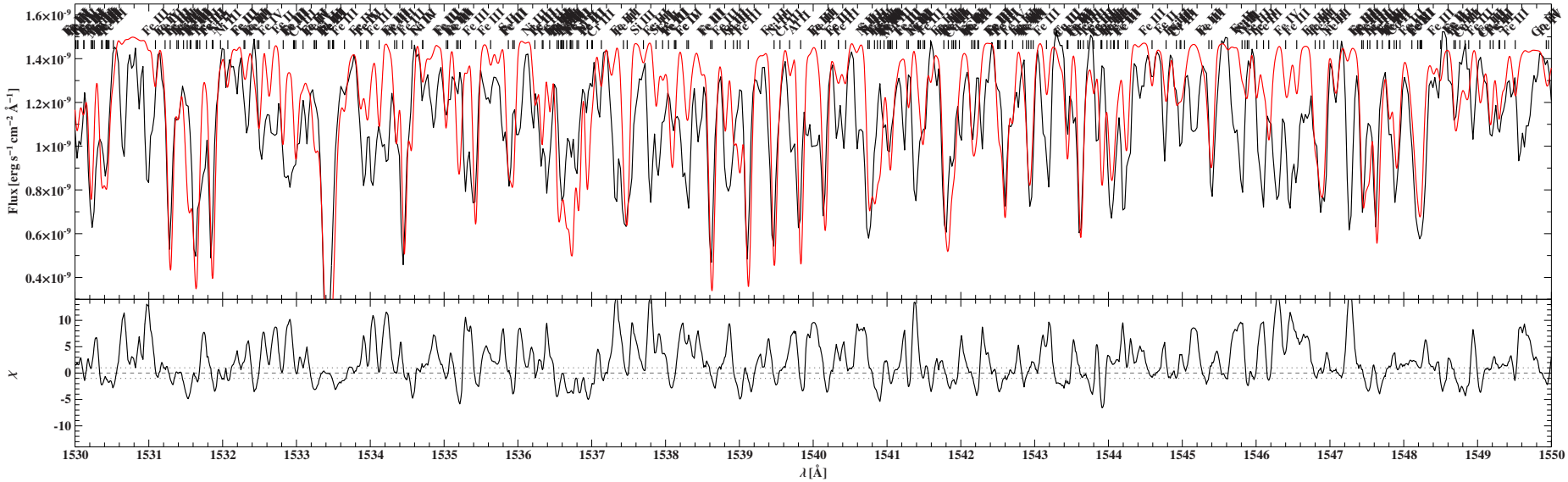
Flux [erg s^{-1} cm^{-2} Å^{-1}]
χ
λ [Å]

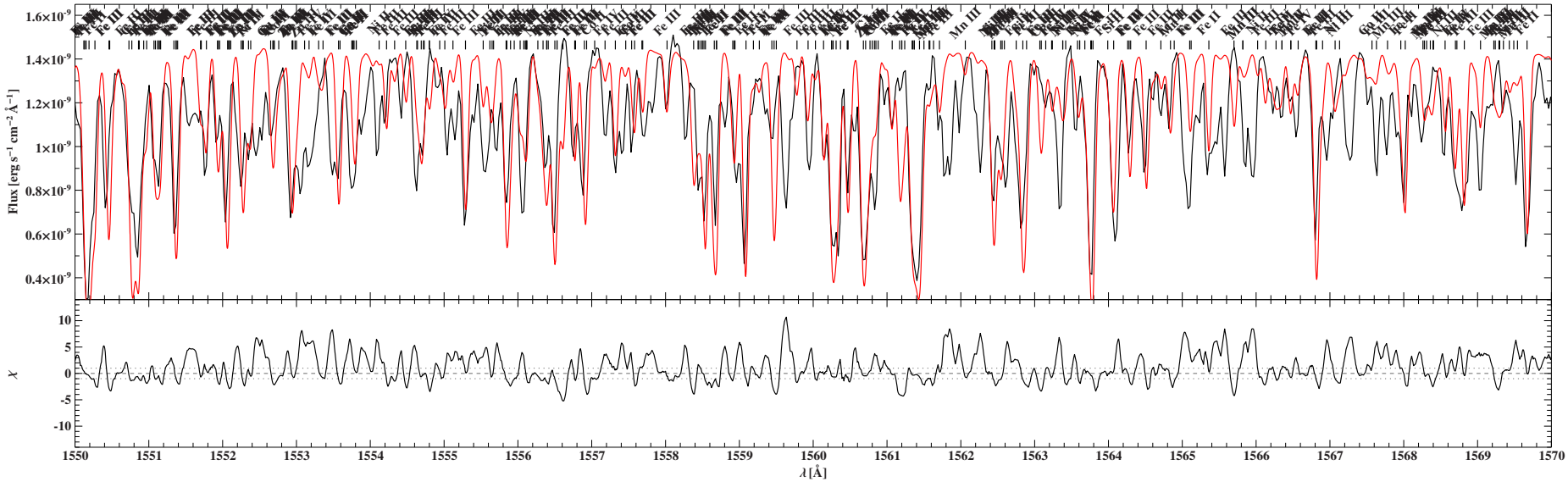
Flux [erg s^{-1} cm^{-2} Å^{-1}]
χ
λ [Å]

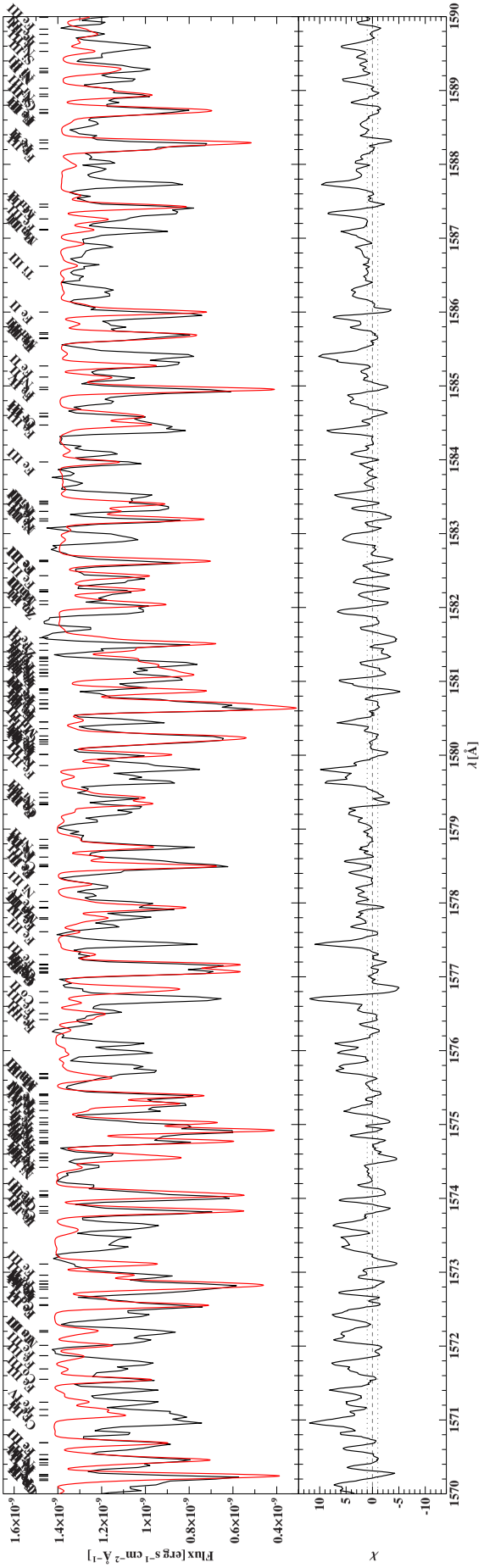
Flux [erg s^{-1} cm^{-2} Å^{-1}]
χ
λ [Å]

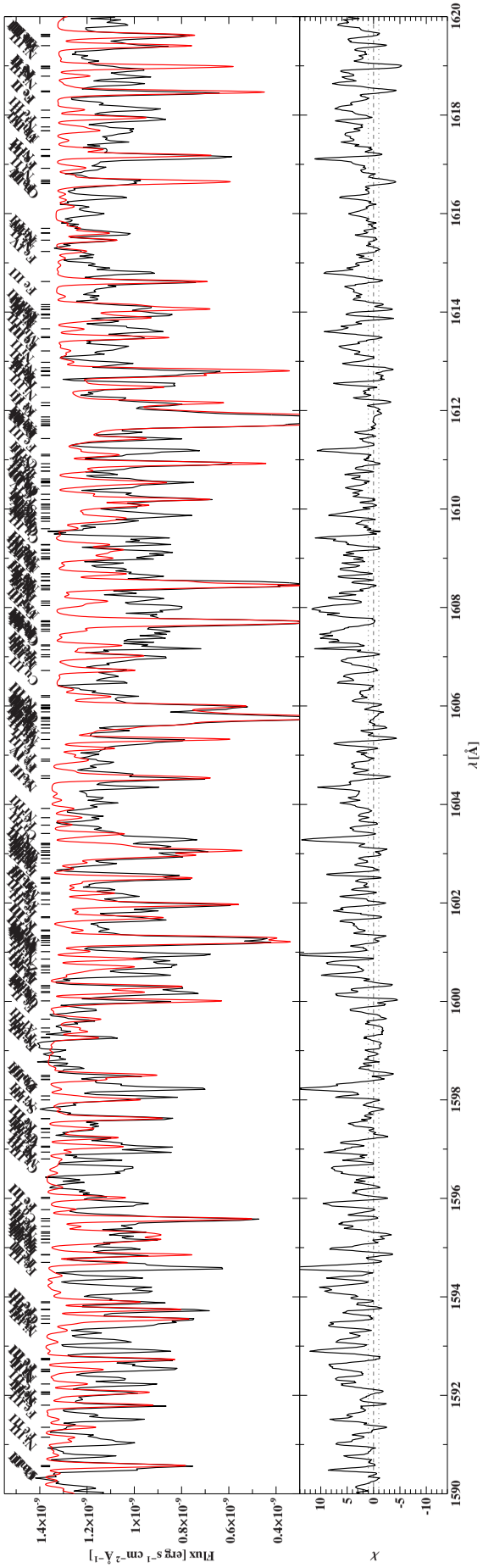
Flux [erg s^{-1} cm^{-2} Å^{-1}]
χ
λ [Å]

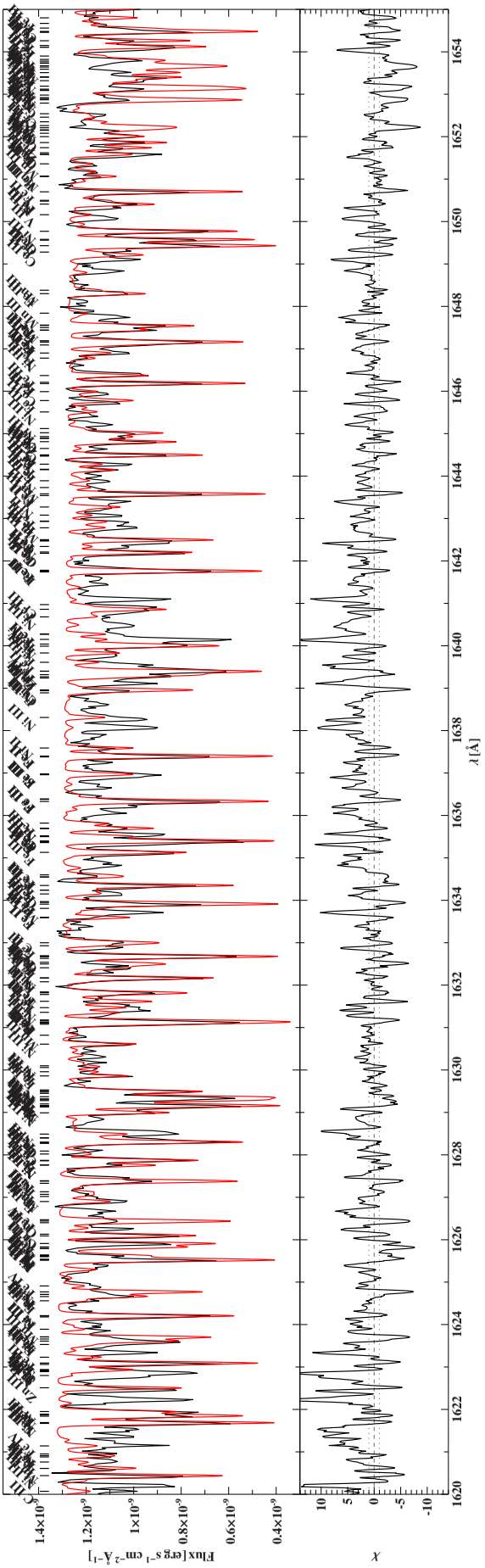
Flux [erg s^{-1} cm^{-2} Å^{-1}]
χ
λ [Å]

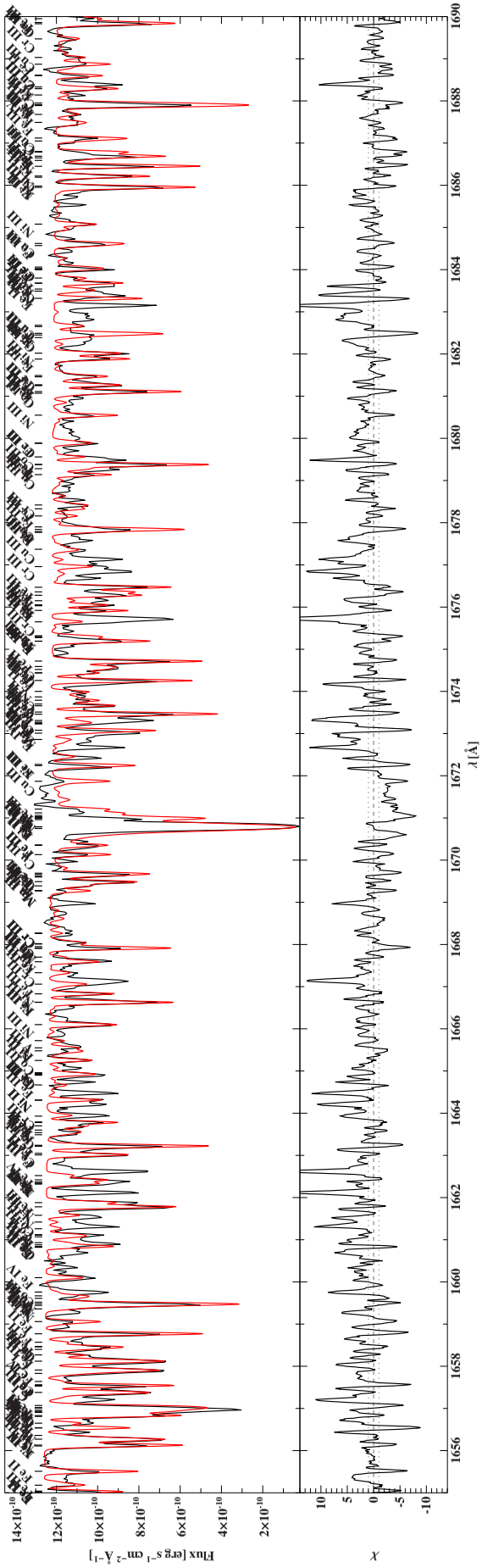
Flux [erg s^{-1} cm^{-2} Å^{-1}]
χ
λ [Å]

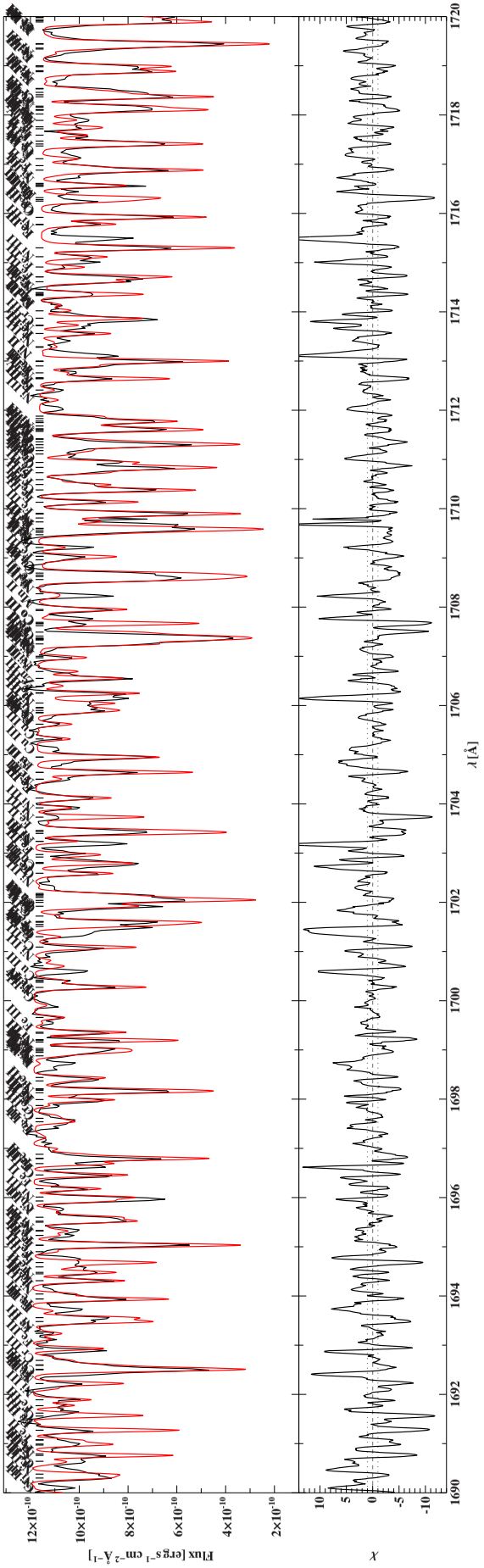
Flux [erg s^{-1} cm^{-2} Å^{-1}]
χ
λ [Å]

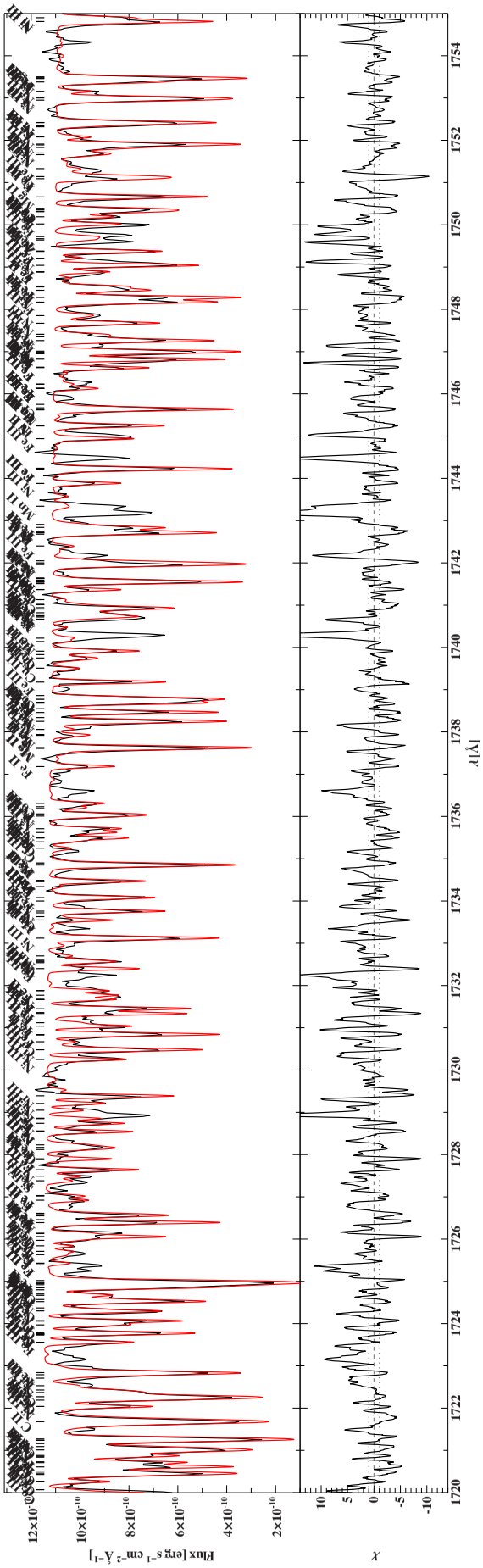
Flux [erg s^{-1} cm^{-2} Å^{-1}]
χ
λ [Å]

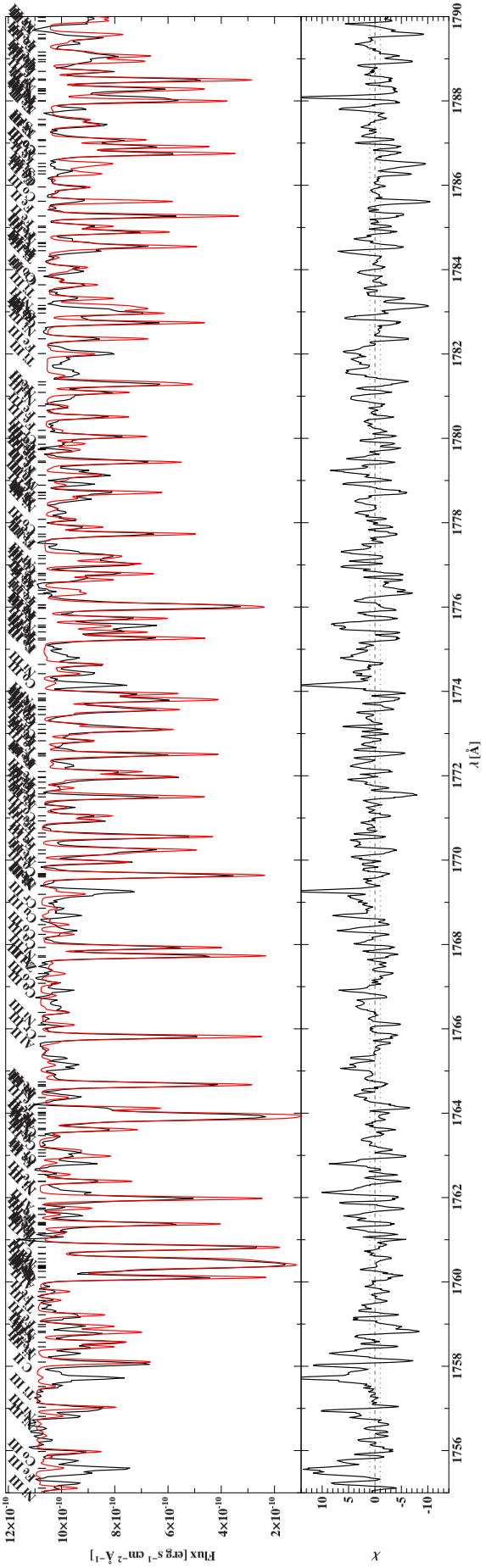
Flux [erg s^{-1} cm^{-2} Å^{-1}]
χ
λ [Å]

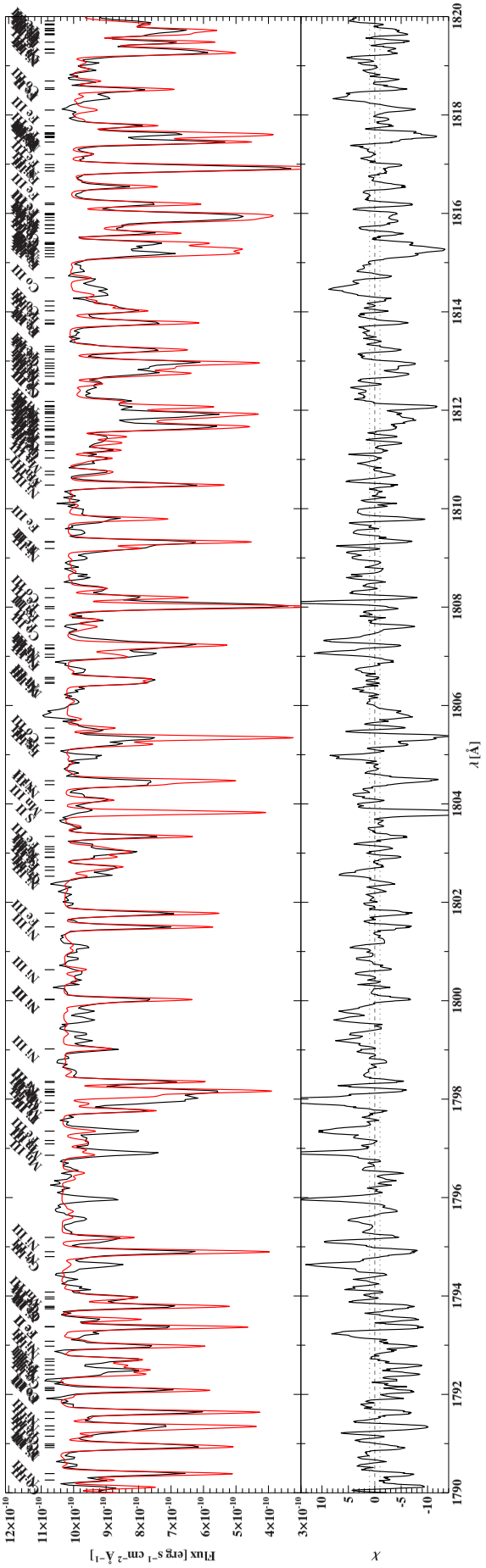
Flux [erg s^{-1} cm^{-2} Å^{-1}]
χ
λ [Å]

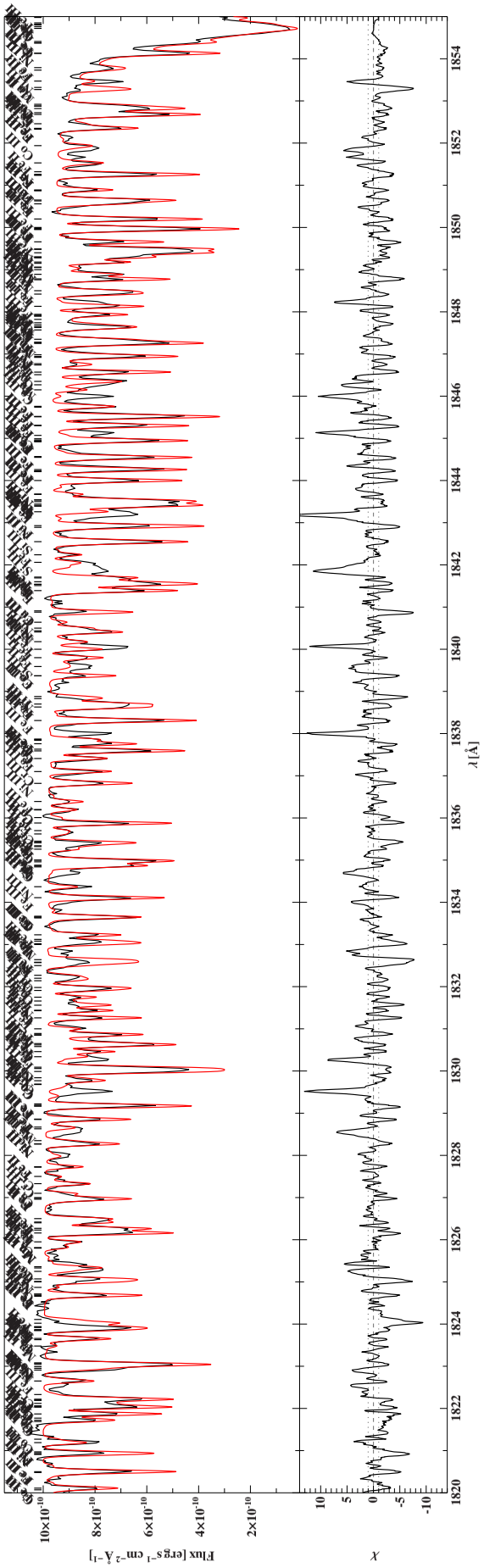
Flux [erg s^{-1} cm^{-2} Å^{-1}]
χ
λ [Å]

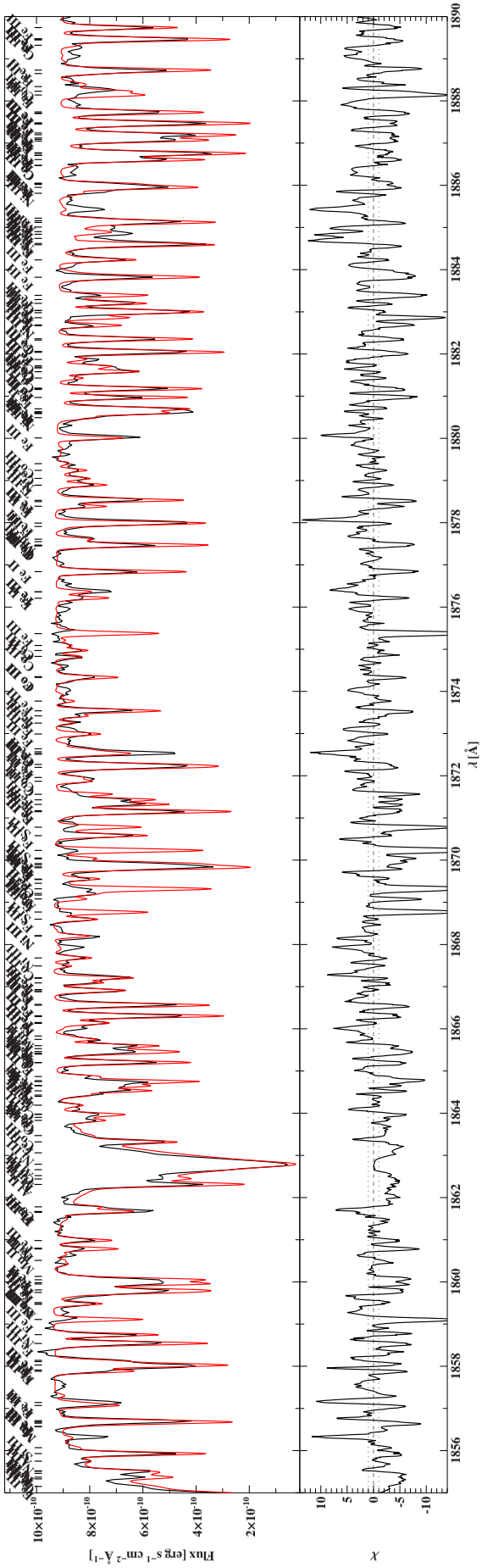
Flux [erg s^{-1} cm^{-2} Å^{-1}]
χ
λ [Å]

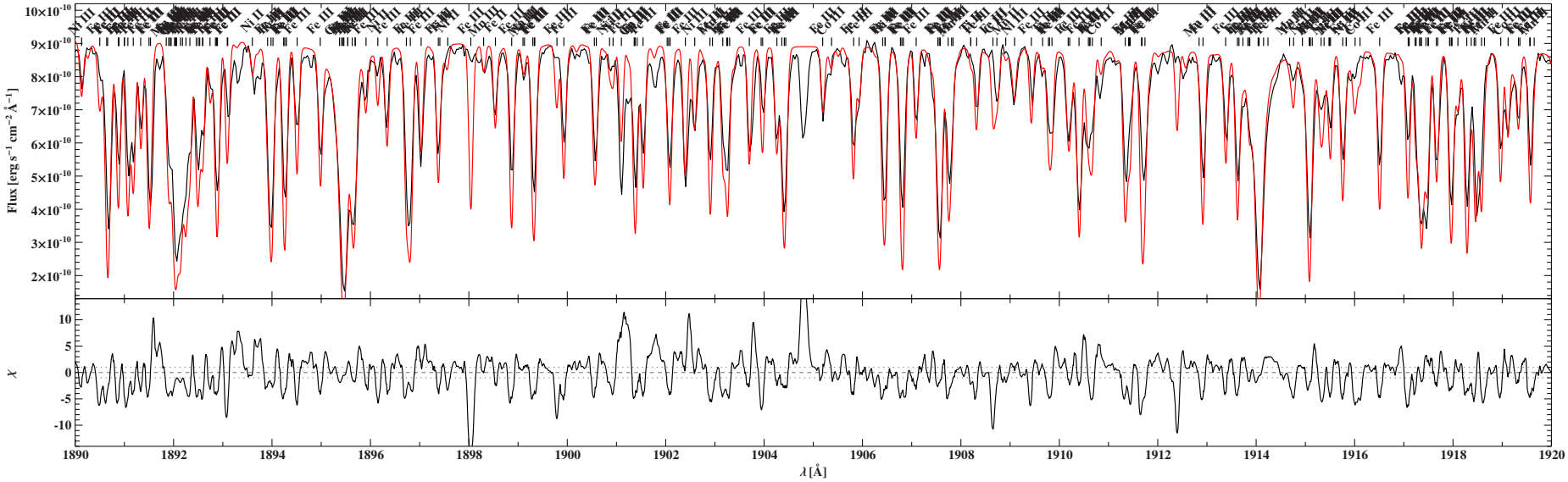
Flux [erg s^{-1} cm^{-2} Å^{-1}]
χ
λ [Å]

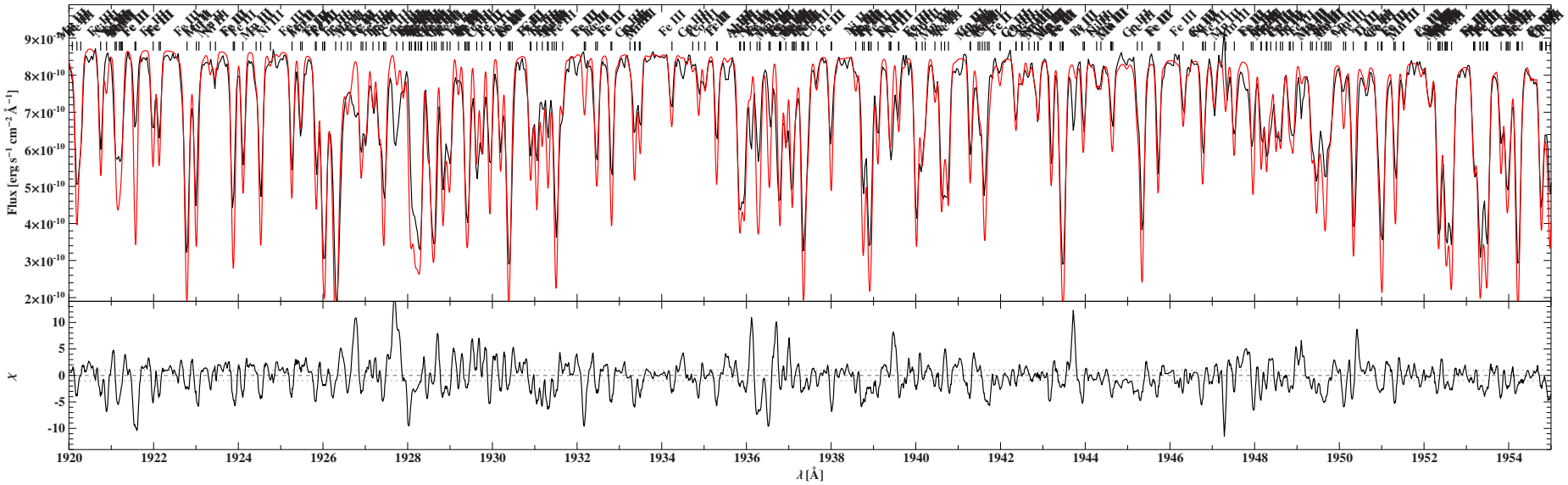
Flux [erg s^{-1} cm^{-2} Å^{-1}]
χ
λ [Å]

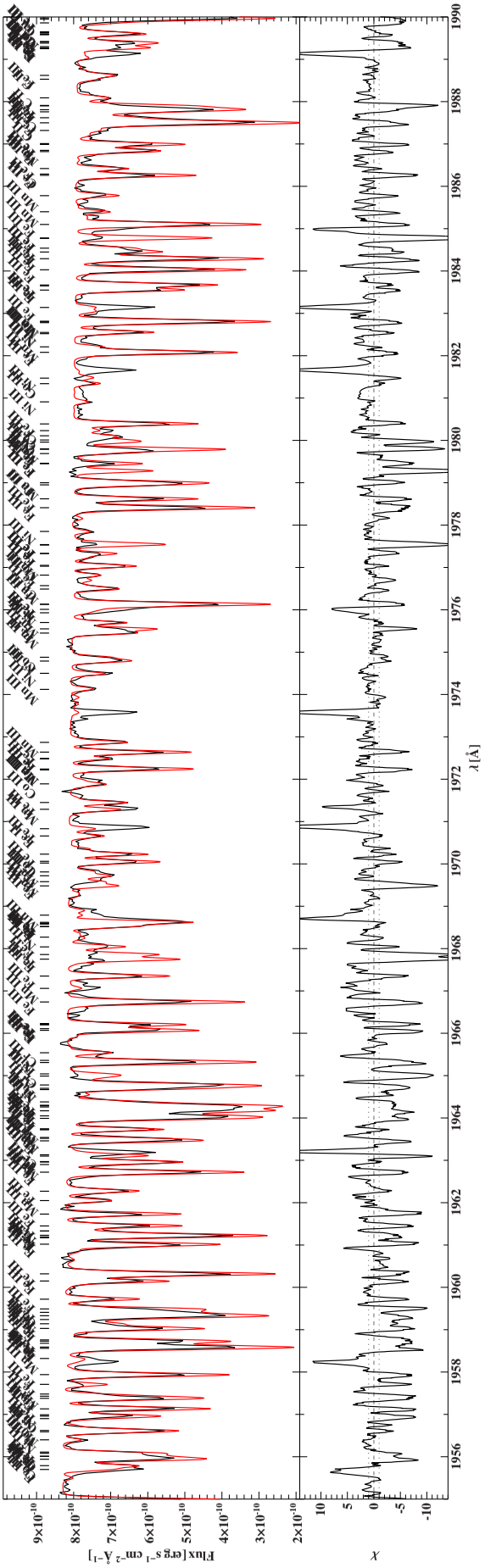
Flux [erg s^{-1} cm^{-2} Å^{-1}]
χ
λ [Å]

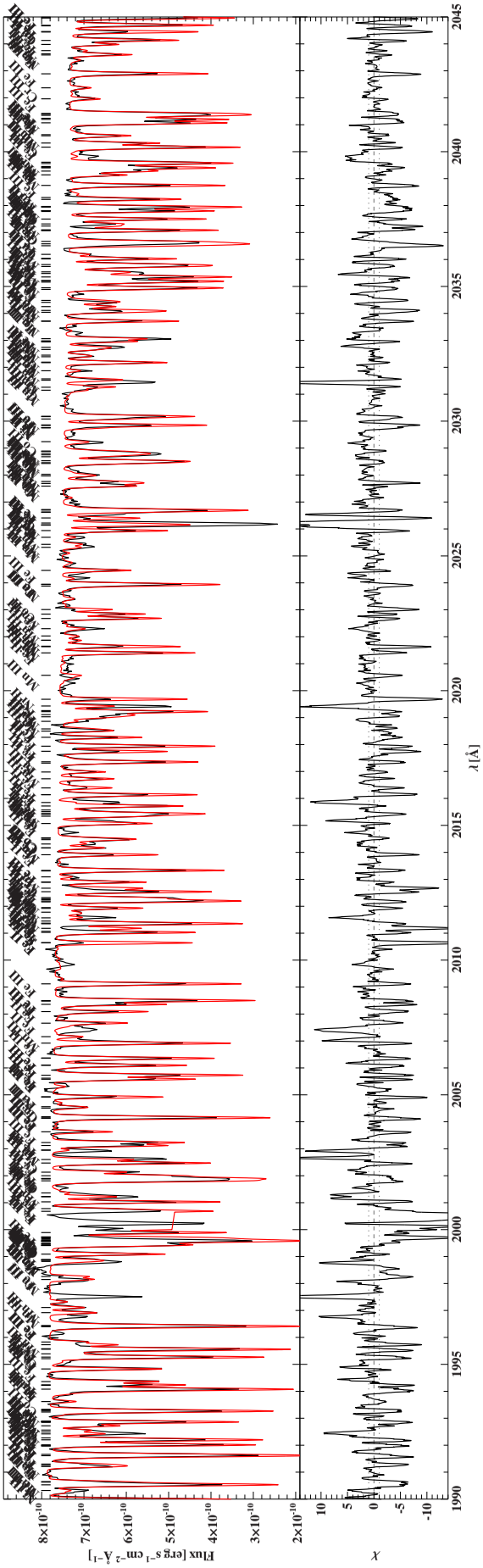
Flux [erg s^{-1} cm^{-2} Å^{-1}]
χ
λ [Å]

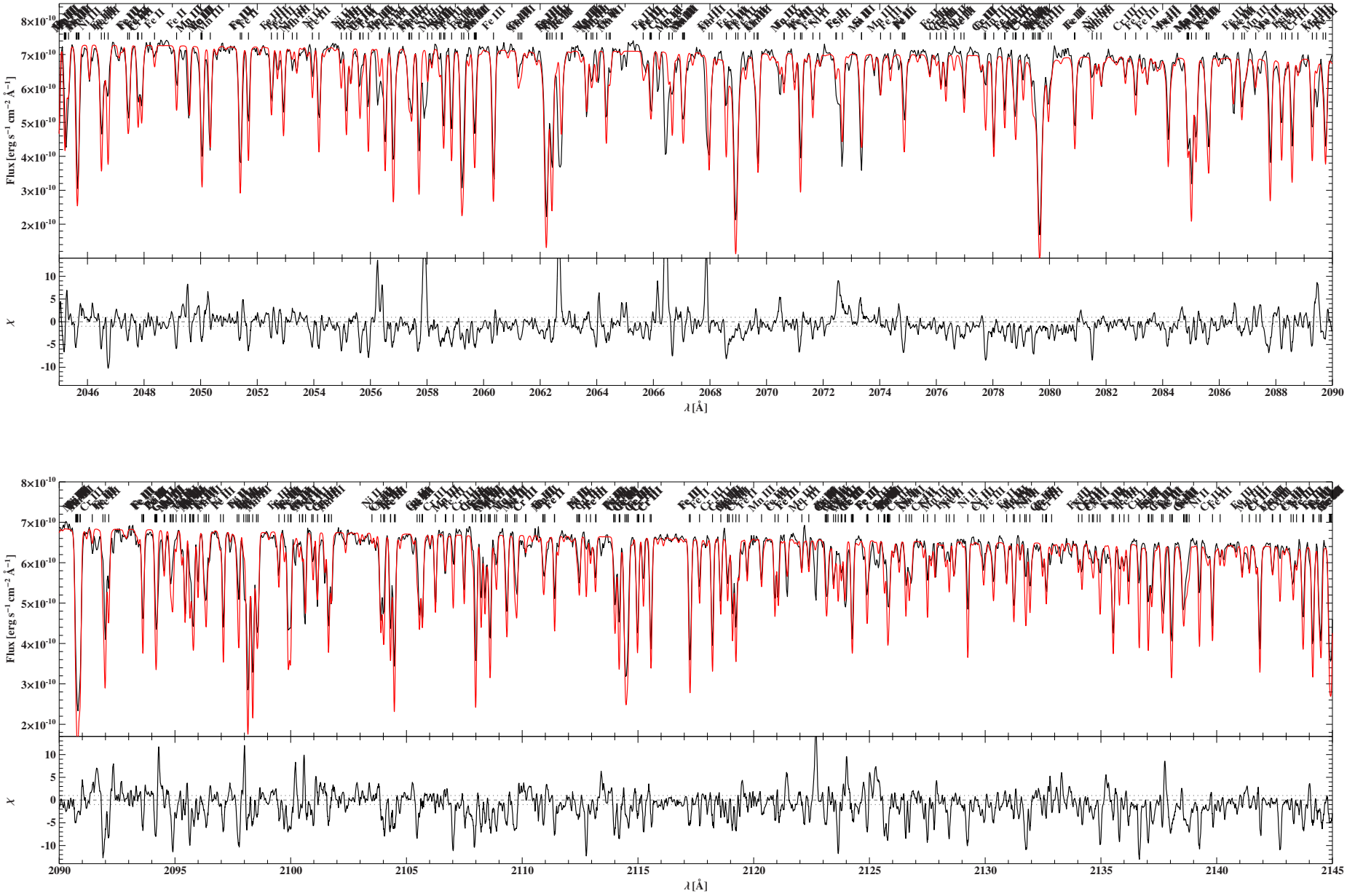
Flux [erg s^{-1} cm^{-2} Å^{-1}]
χ
λ [Å]

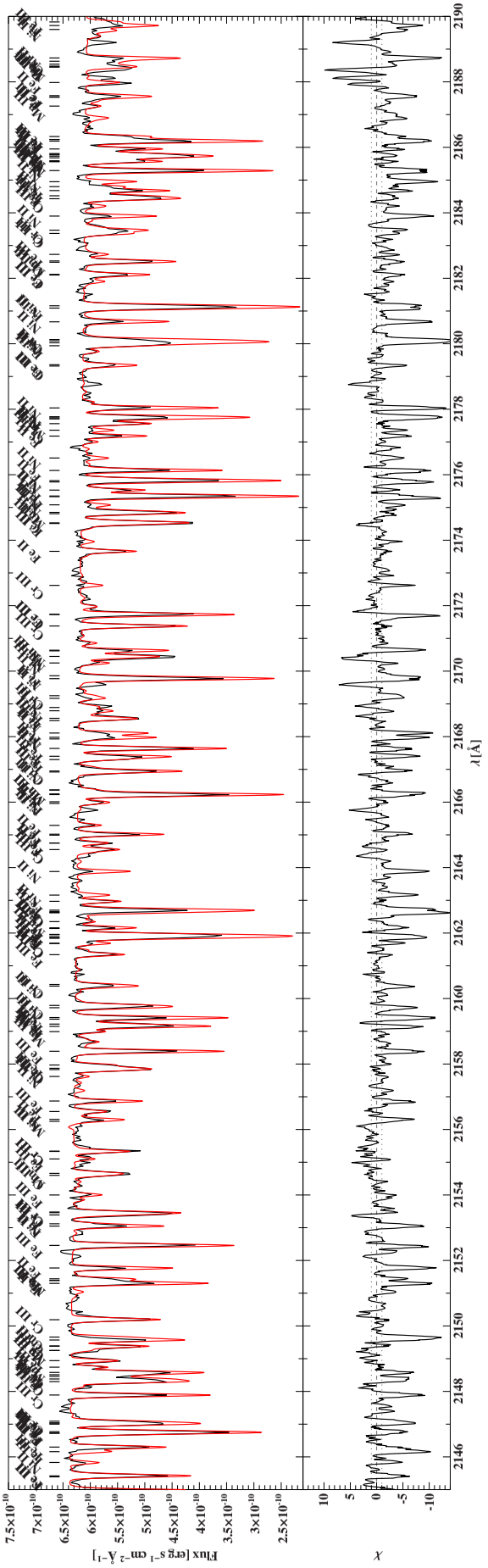
Flux [erg s⁻¹ cm⁻² Å⁻¹]
λ [Å]
χ

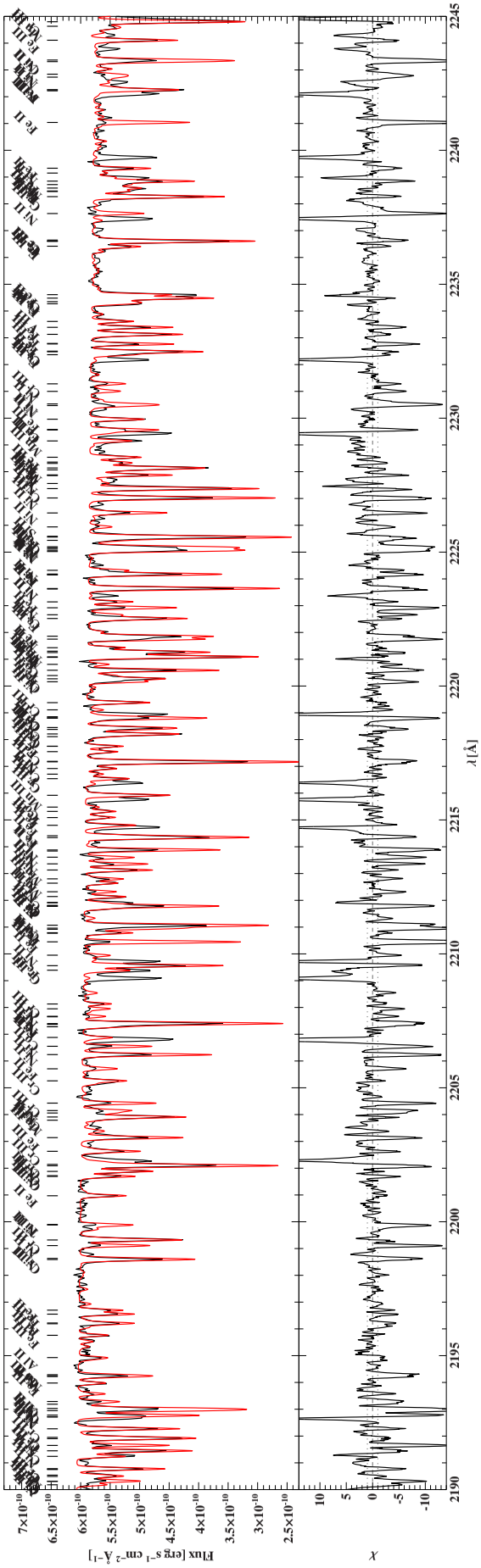
Flux [erg s⁻¹ cm⁻² Å⁻¹]
λ [Å]
χ

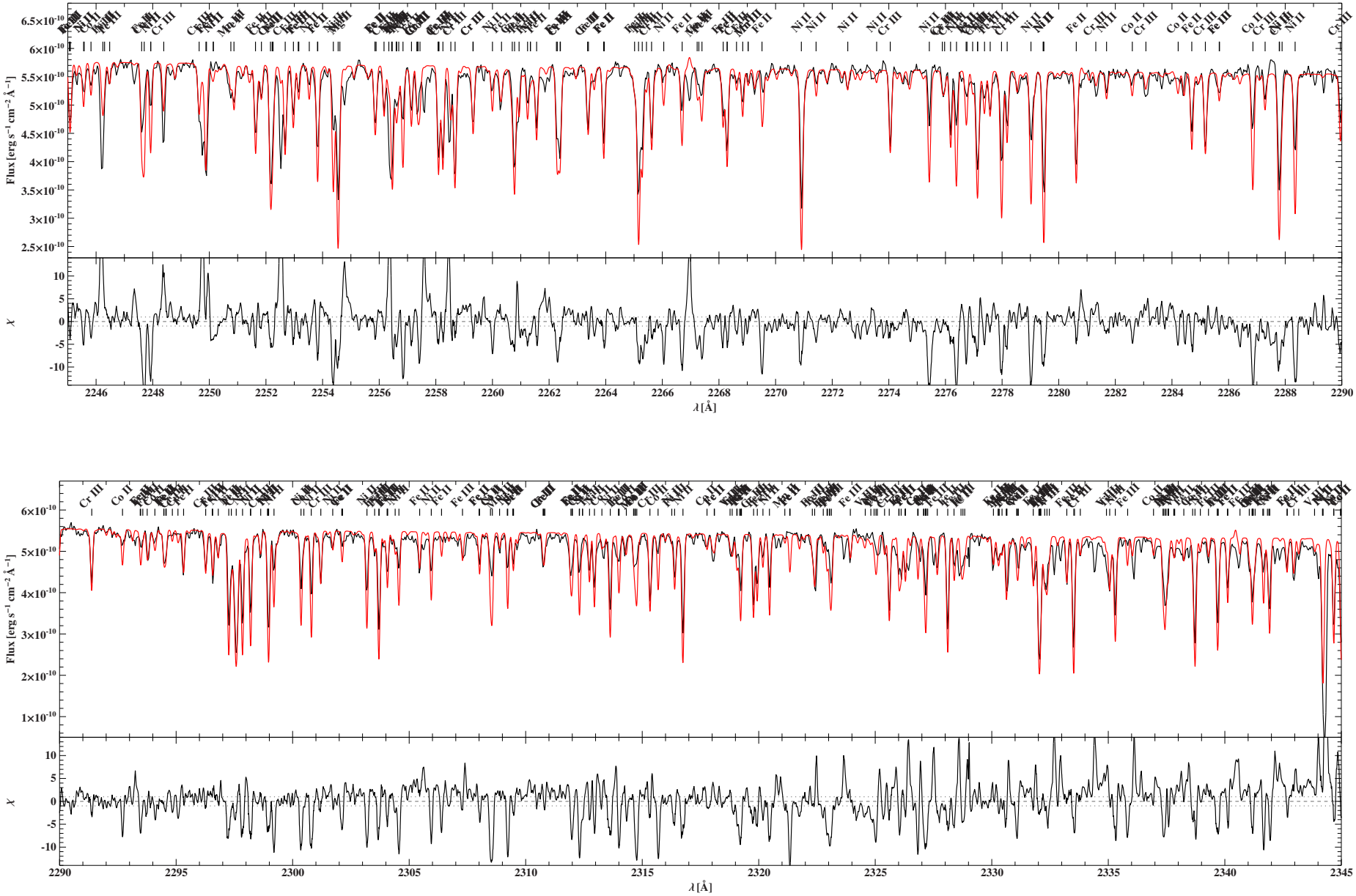
Flux [erg s^{-1} cm^{-2} Å^{-1}]
χ
λ [Å]
Cr III
Co II
Fe II
Ni II
Mn III
Co III
Fe III

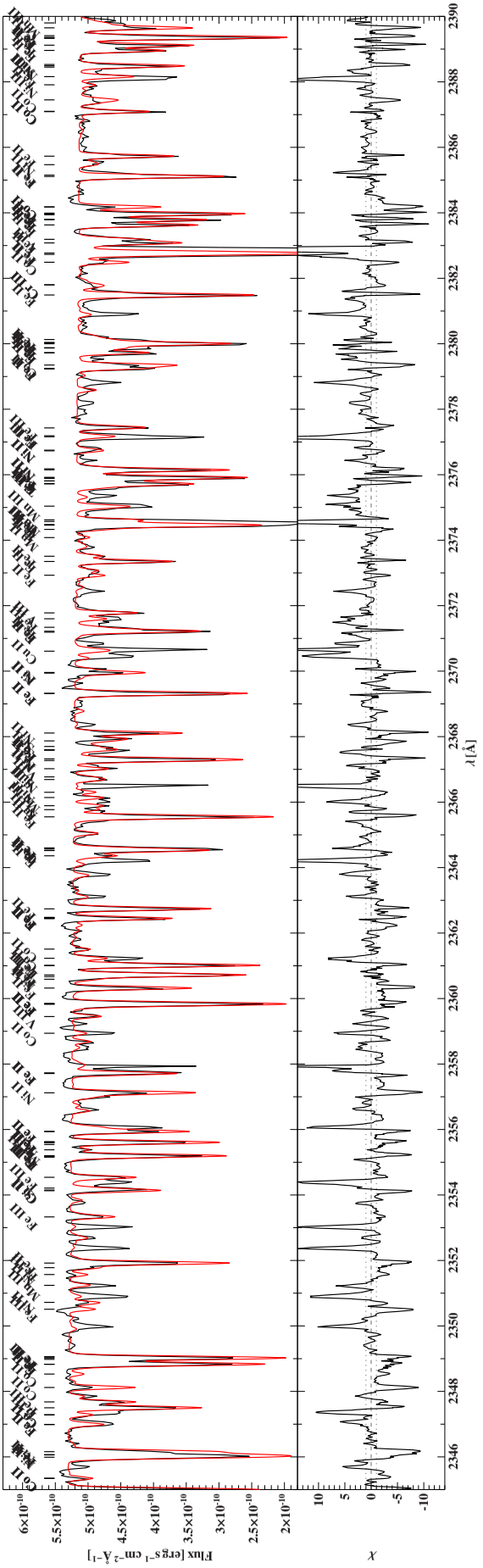
Flux [erg s⁻¹ cm⁻² Å⁻¹]
λ [Å]
χ

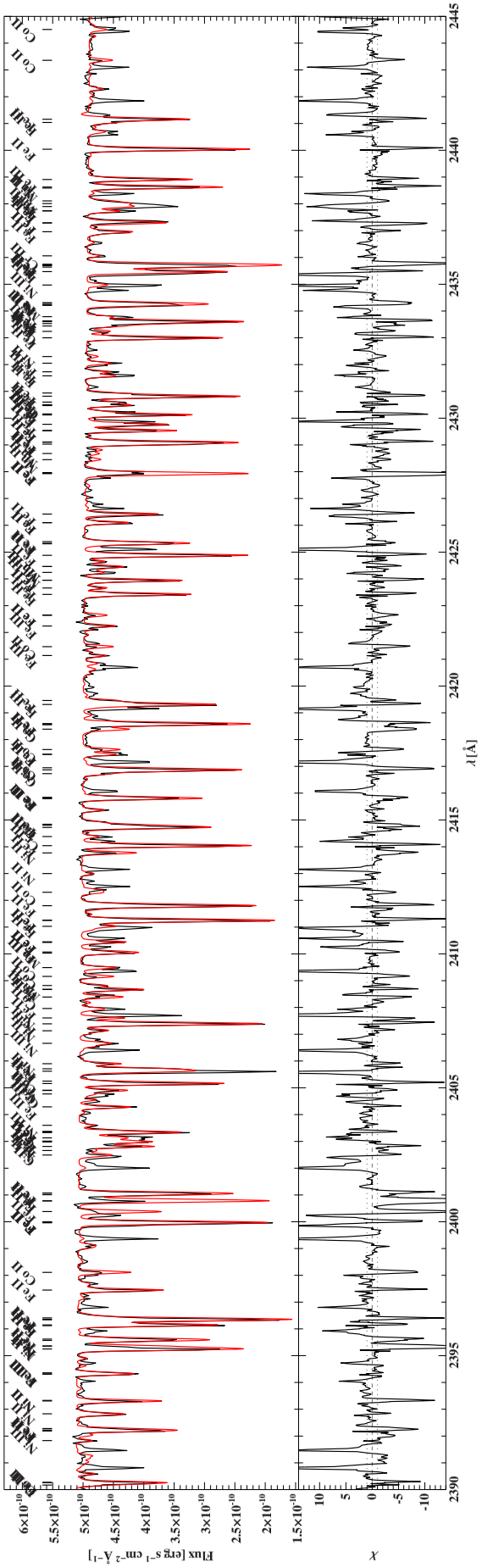
Flux [erg s⁻¹ cm⁻² Å⁻¹]
λ [Å]
χ

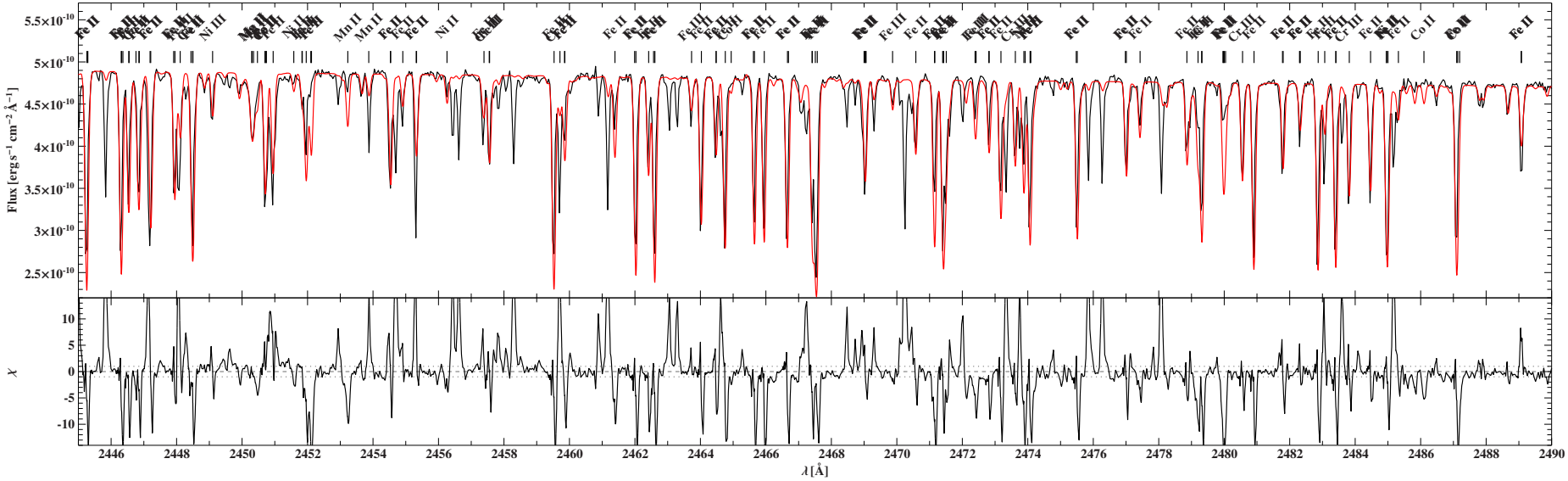
Flux [erg s^{-1} cm^{-2} Å^{-1}]
χ
λ [Å]

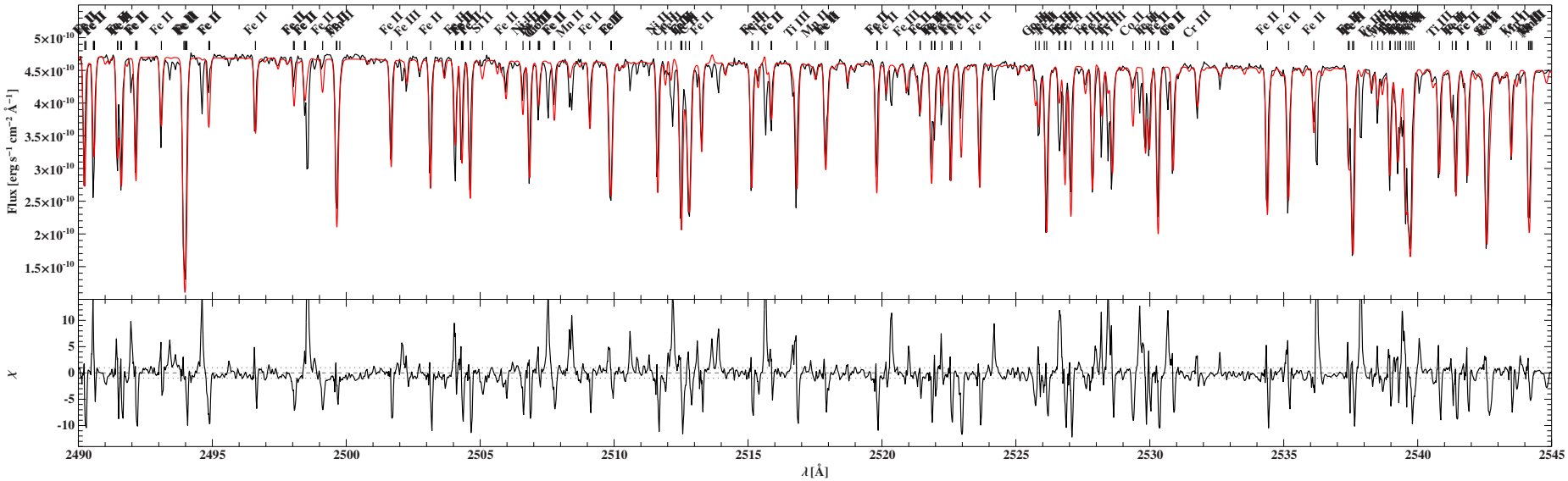
Flux [erg s^{-1} cm^{-2} Å^{-1}]
χ
λ [Å]

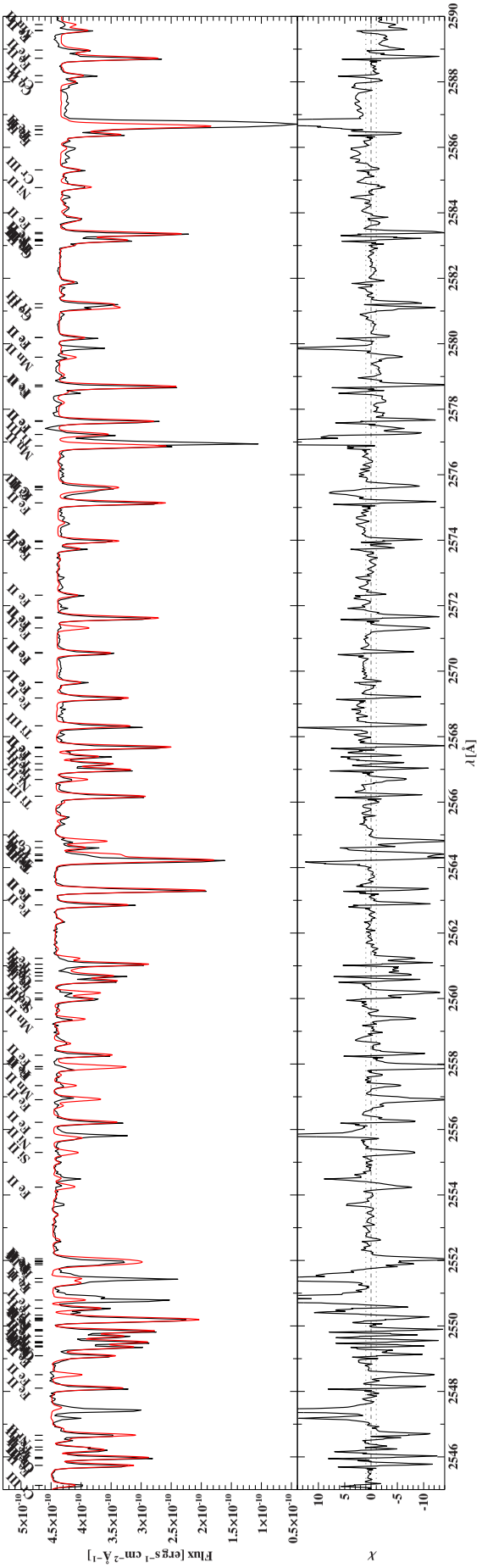
Flux [erg s⁻¹ cm⁻² Å⁻¹]
λ [Å]
χ

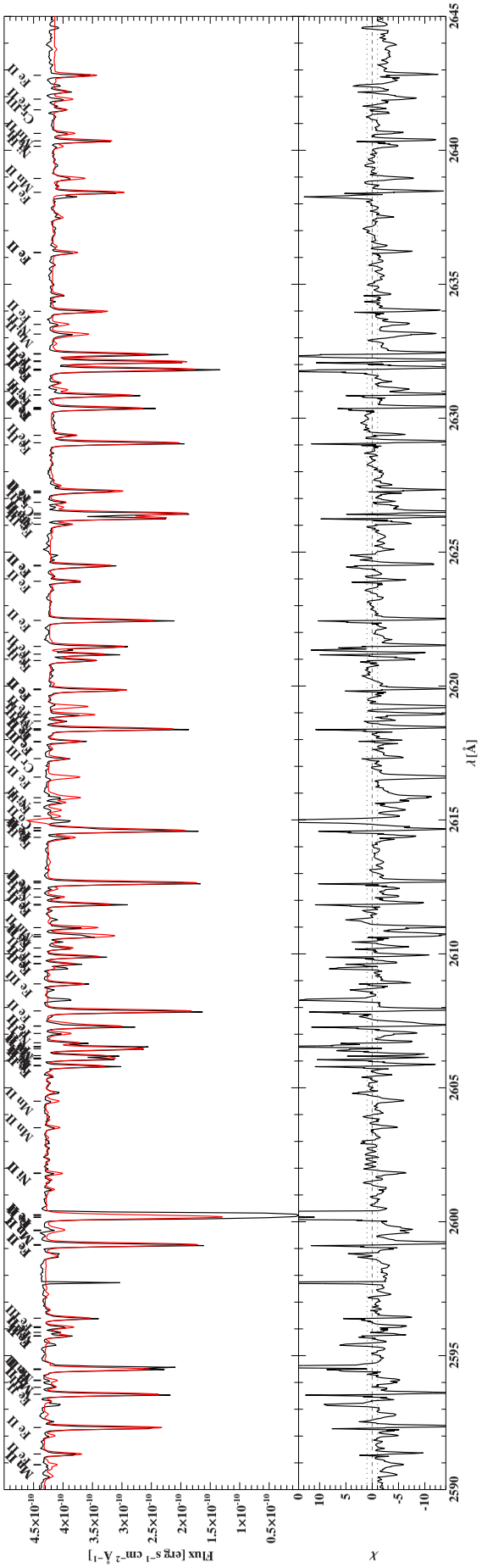
Flux [erg s⁻¹ cm⁻² Å⁻¹]
λ [Å]
χ

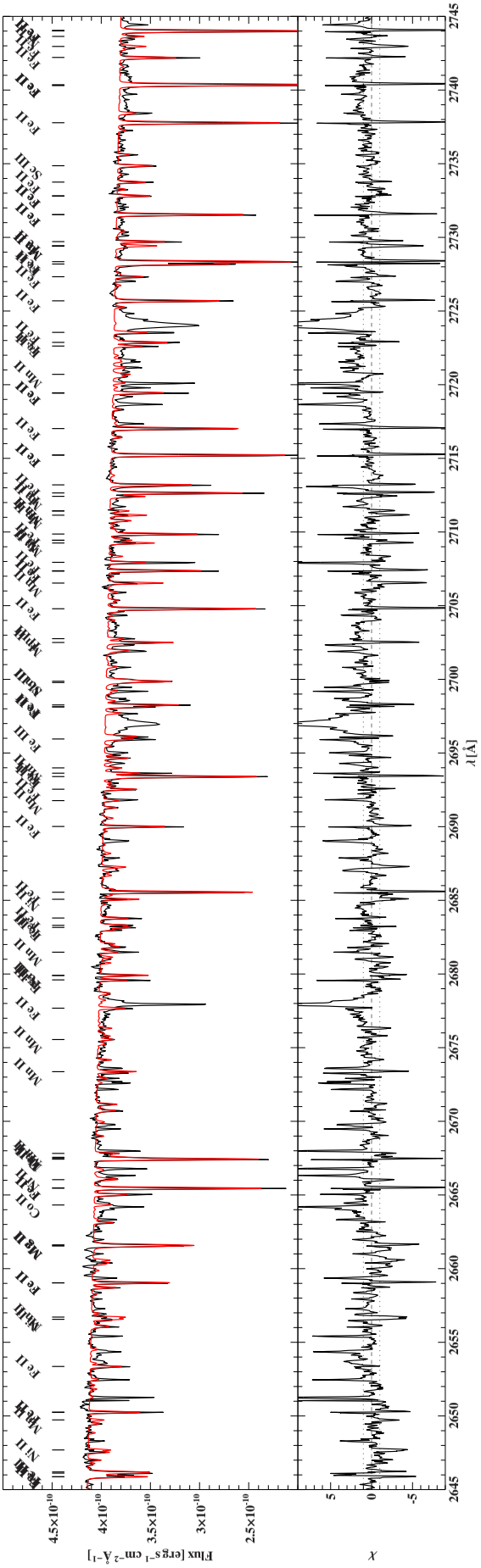
Flux [erg s^{-1} cm^{-2} Å^{-1}]
λ [Å]
χ

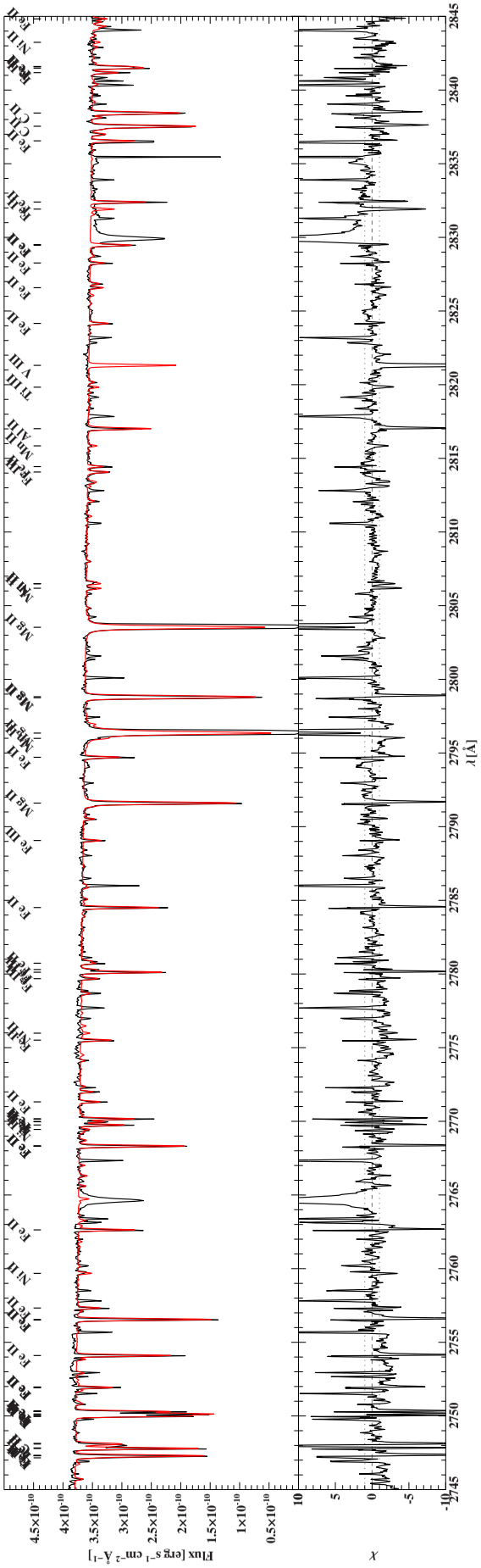
Flux [erg s^{-1} cm^{-2} Å^{-1}]
λ [Å]
χ

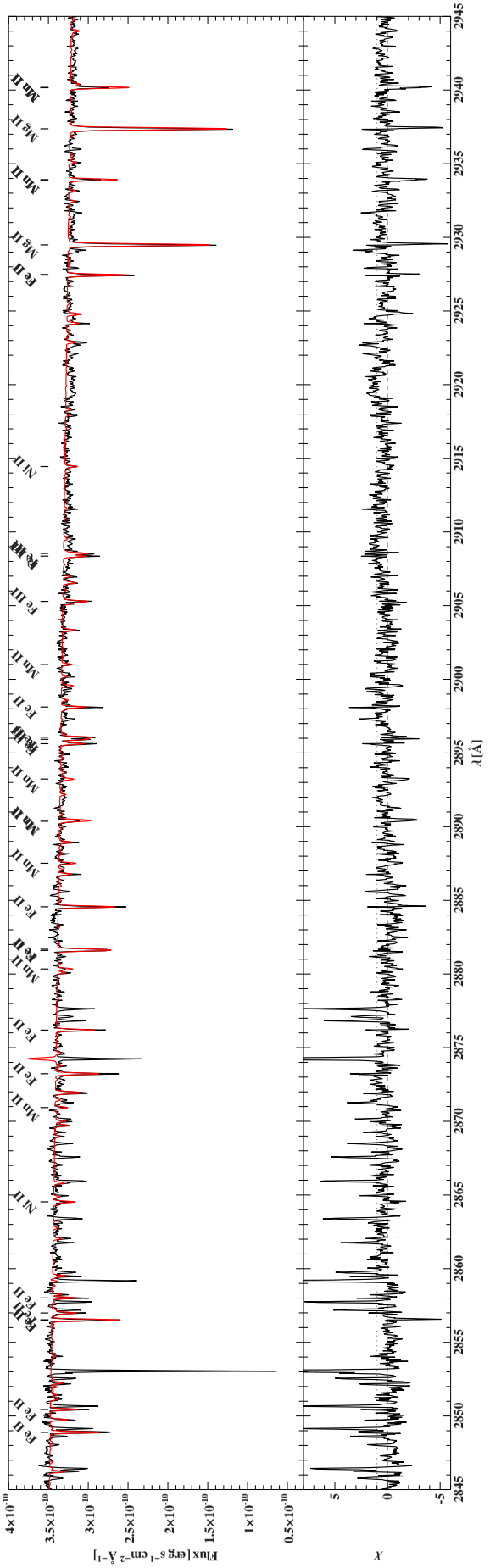
Fe II
Mn II
Ni II
Mg II
Fe III
Flux [erg s^{-1} cm^{-2} Å^{-1}]
χ
λ [Å]

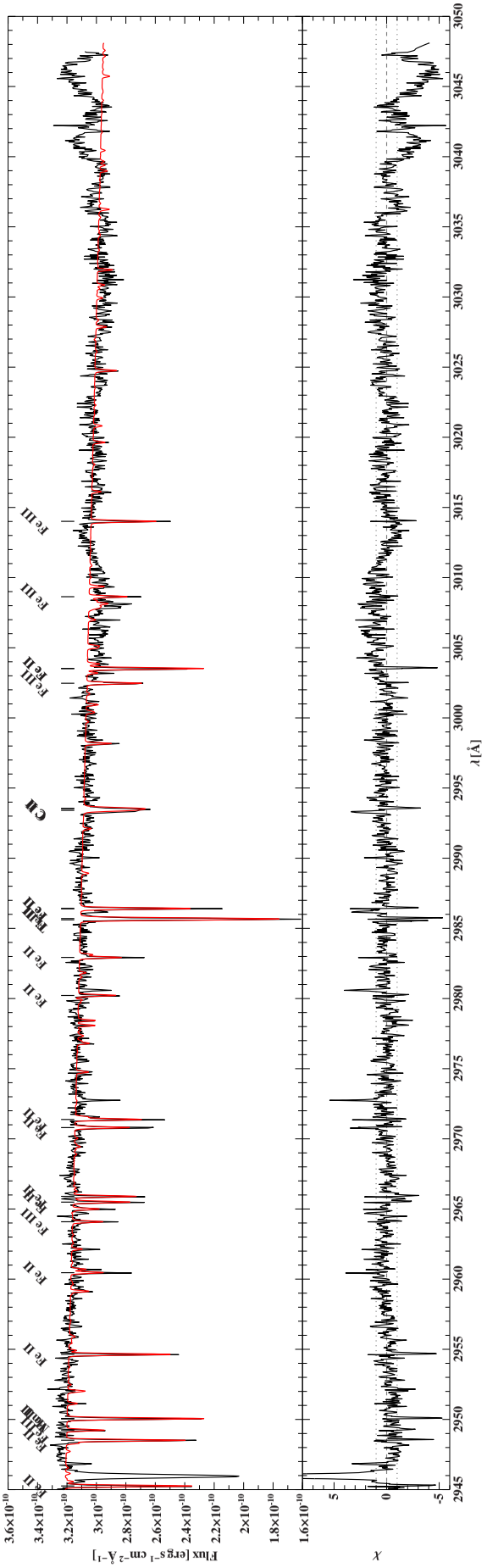
Fe II
Fe III
C II
Flux [erg s^{-1} cm^{-2} Å^{-1}]
χ
λ [Å]

E. UV spectrum of HD 271791

Comparison of the HST/STIS and HST/COS observations of HD 271791 (black) with a synthetic model spectrum (red) calculated with ADS for the parameters of HD 271791 determined in Chapter 10 and summarized in Table 10.2 and 10.3.

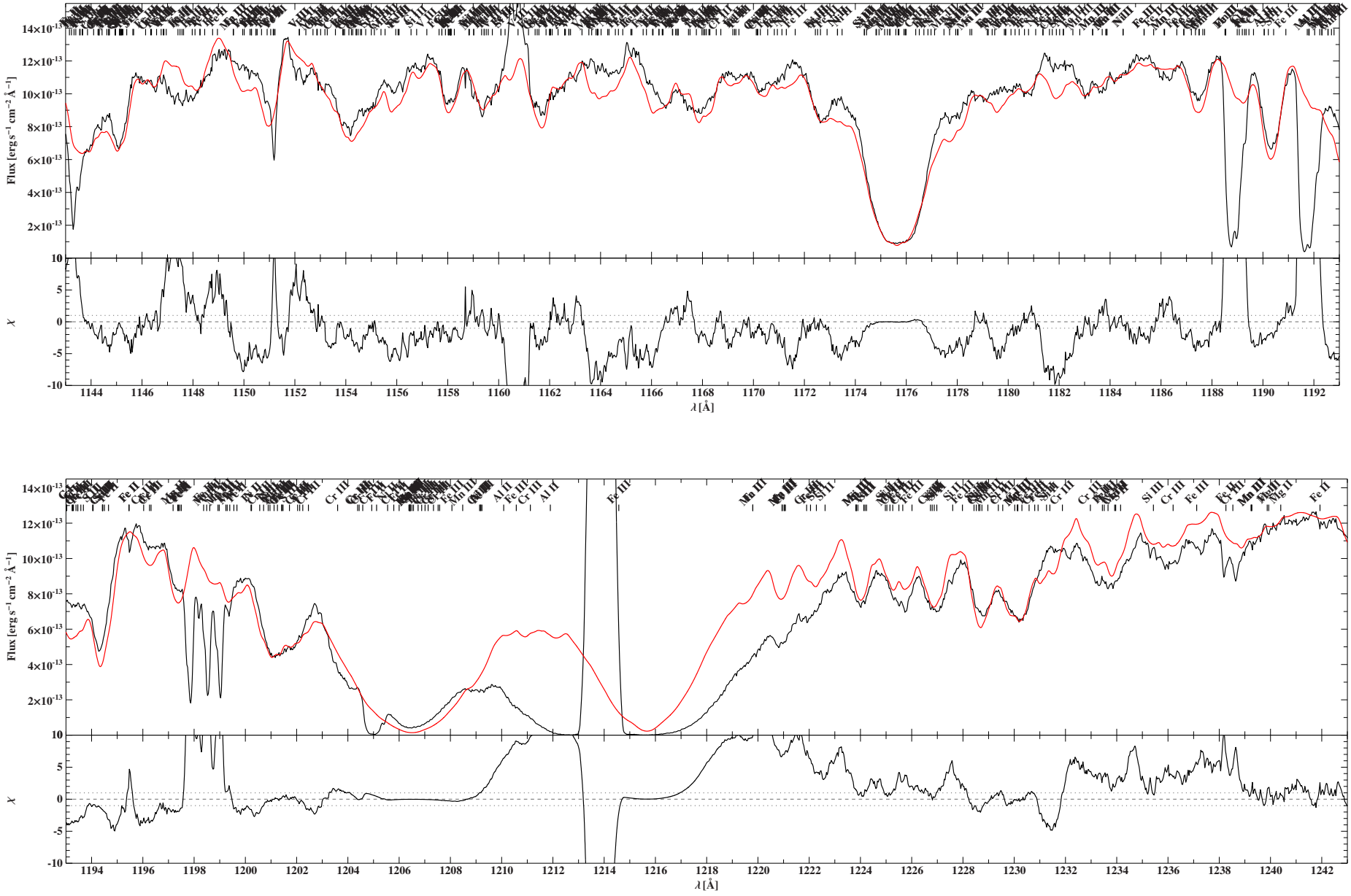
Flux [erg s^{-1} cm^{-2} Å^{-1}]
χ
λ[Å]

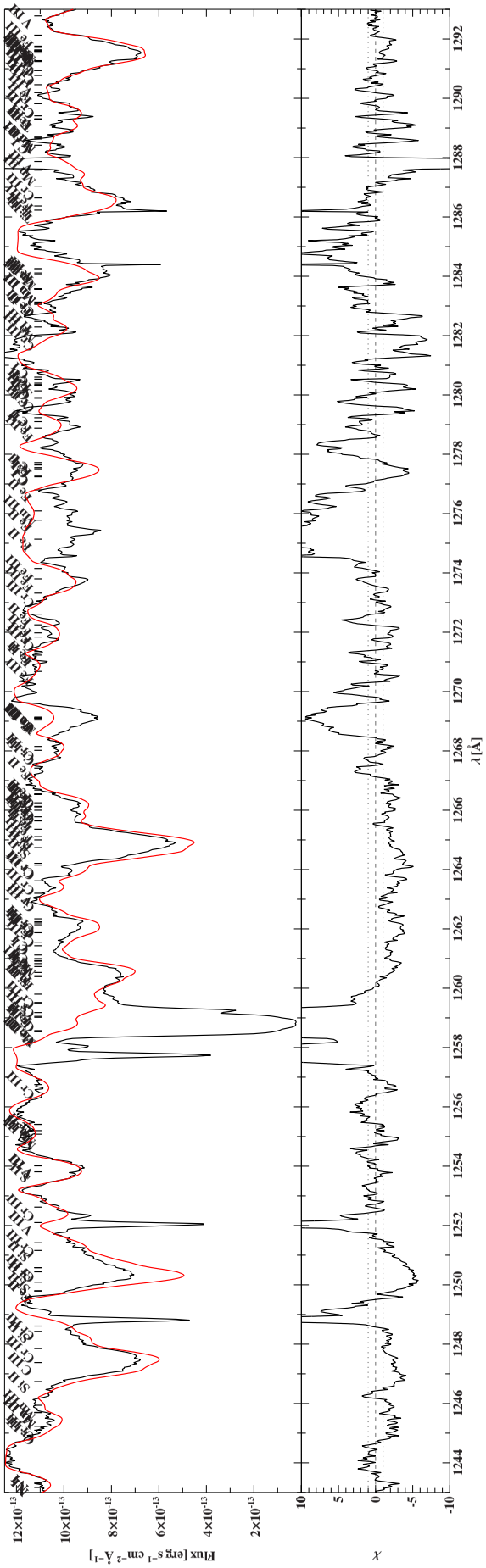
Flux [erg s^{-1} cm^{-2} Å^{-1}]
χ
λ [Å]

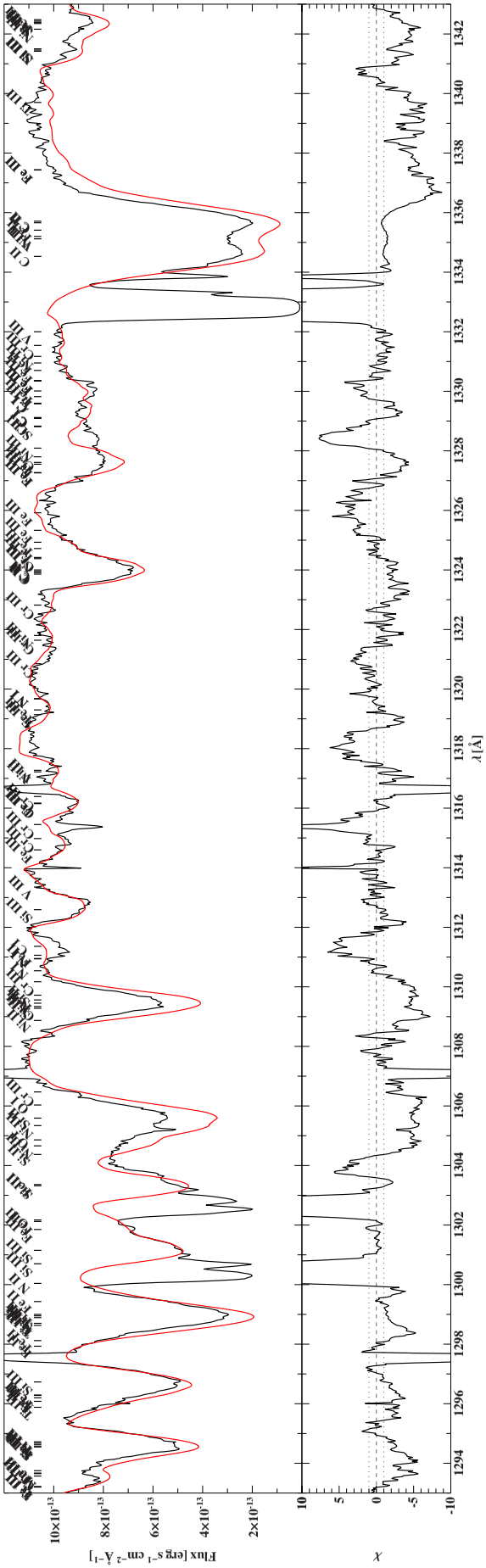
Flux [erg s^{-1} cm^{-2} Å^{-1}]
χ
λ [Å]

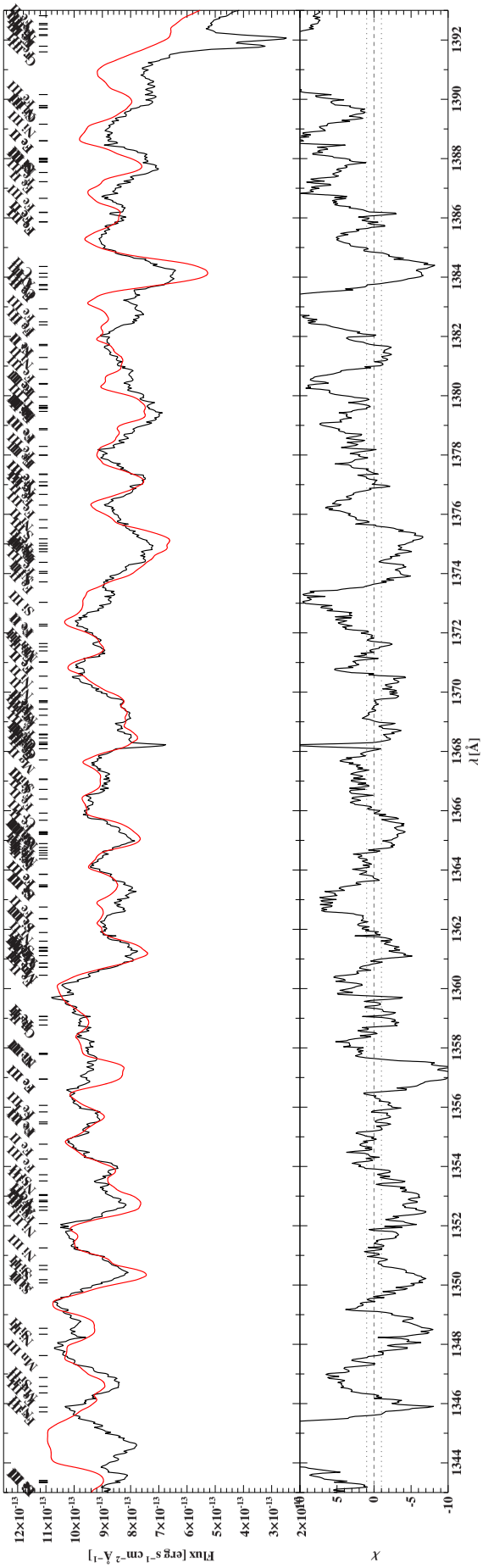
Flux [erg s⁻¹ cm⁻² Å⁻¹]
χ
λ [Å]

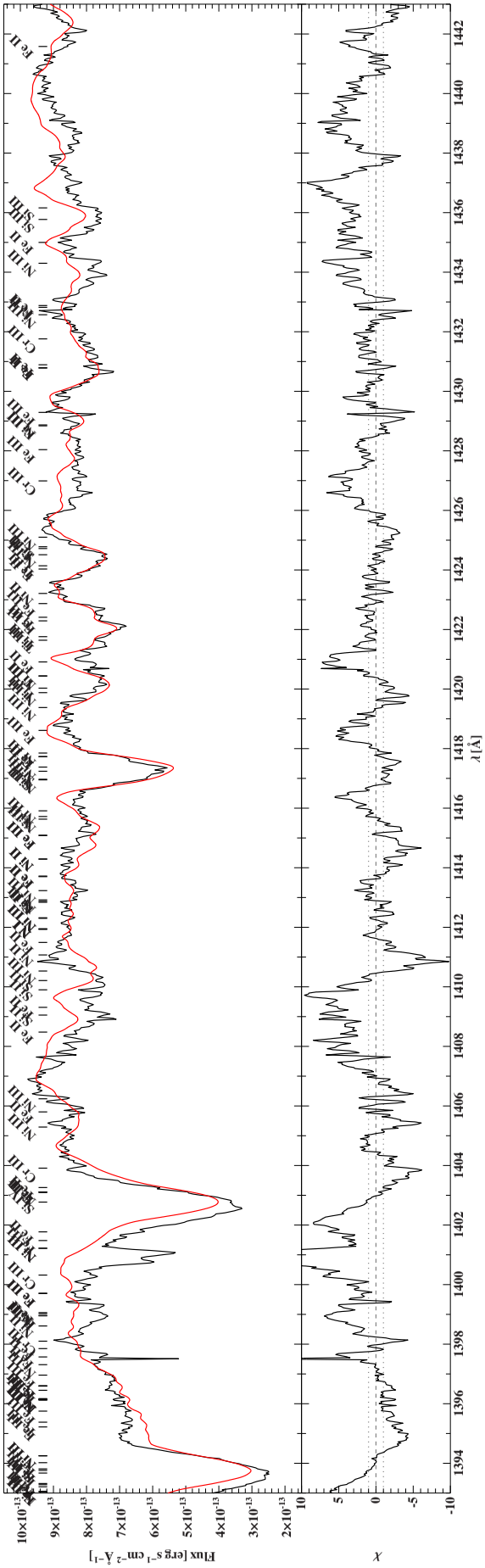
Flux [erg s⁻¹ cm⁻² Å⁻¹]
χ
λ [Å]

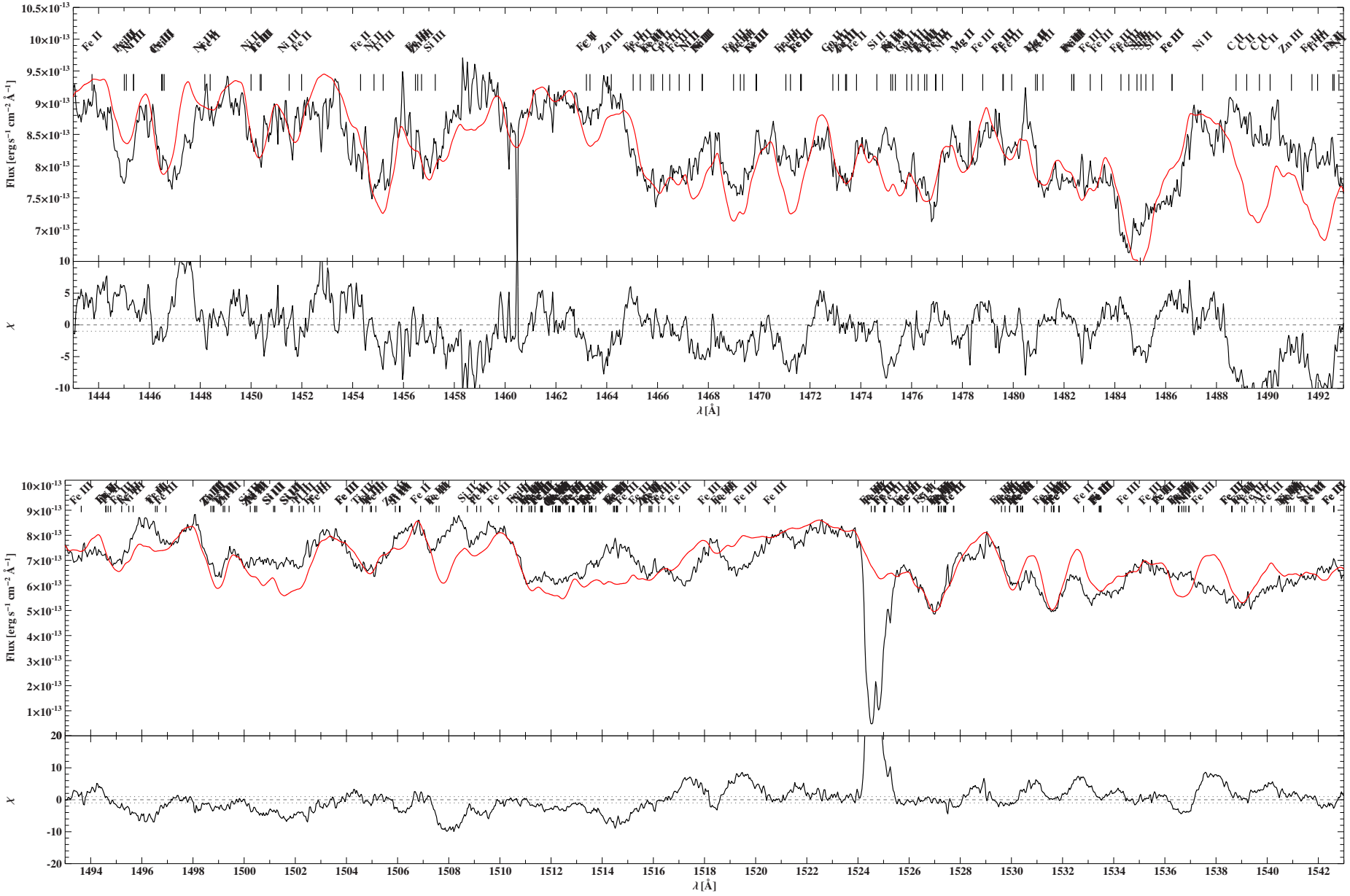
Flux [ergs^{-1} cm^{-2} Å^{-1}]
χ
λ [Å]
Flux [erg s^{-1} cm^{-2} Å^{-1}]
χ
λ [Å]

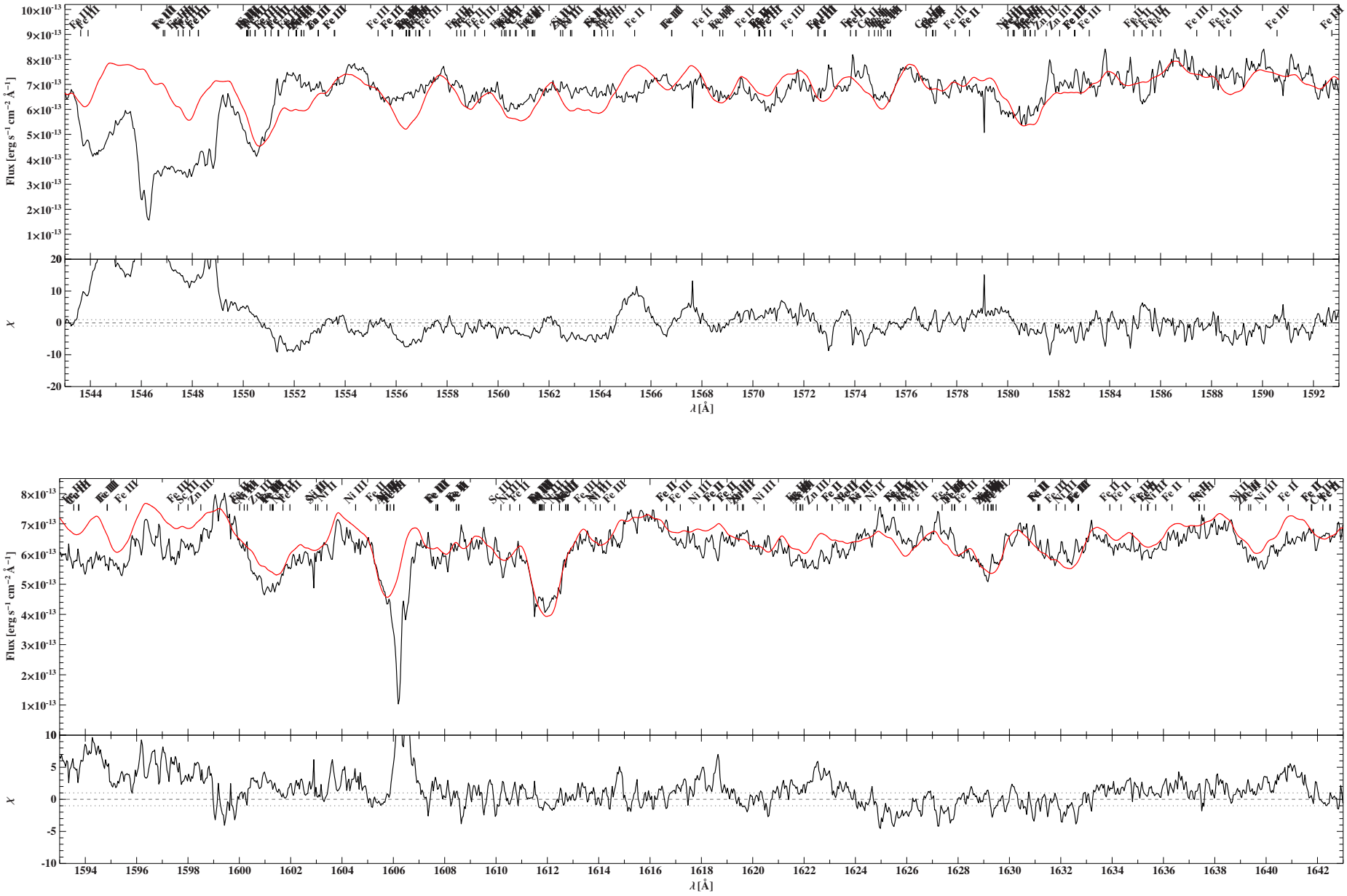
Flux [erg s^{-1} cm^{-2} Å^{-1}]
χ
λ [Å]

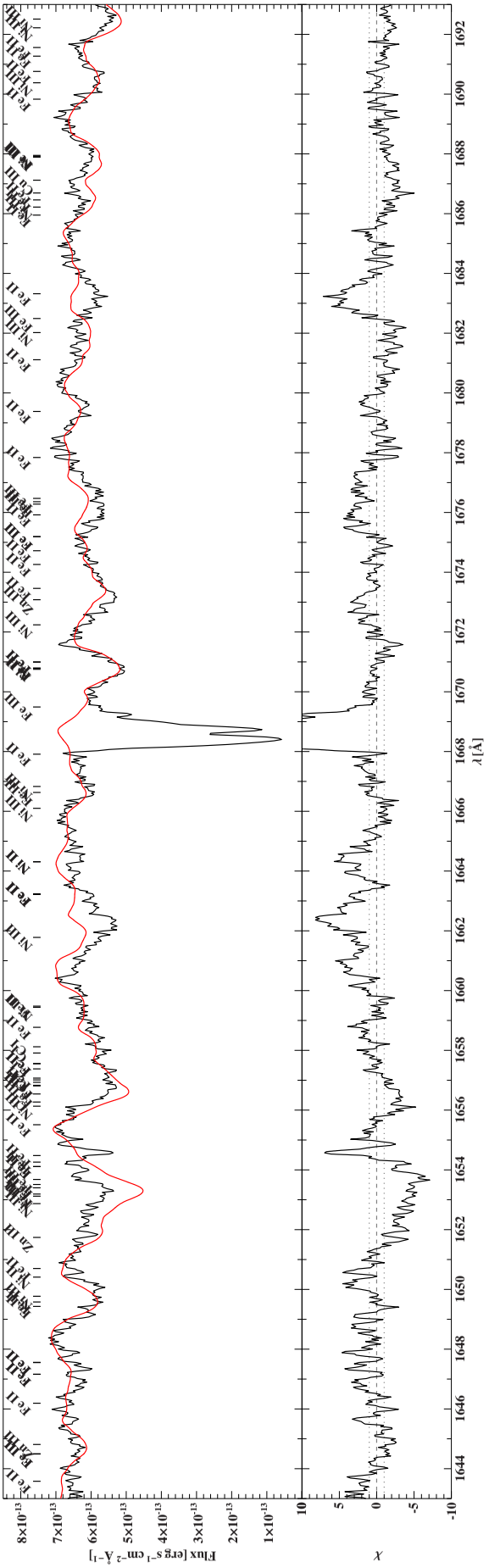
Flux [erg s⁻¹ cm⁻² Å⁻¹]
χ
λ [Å]

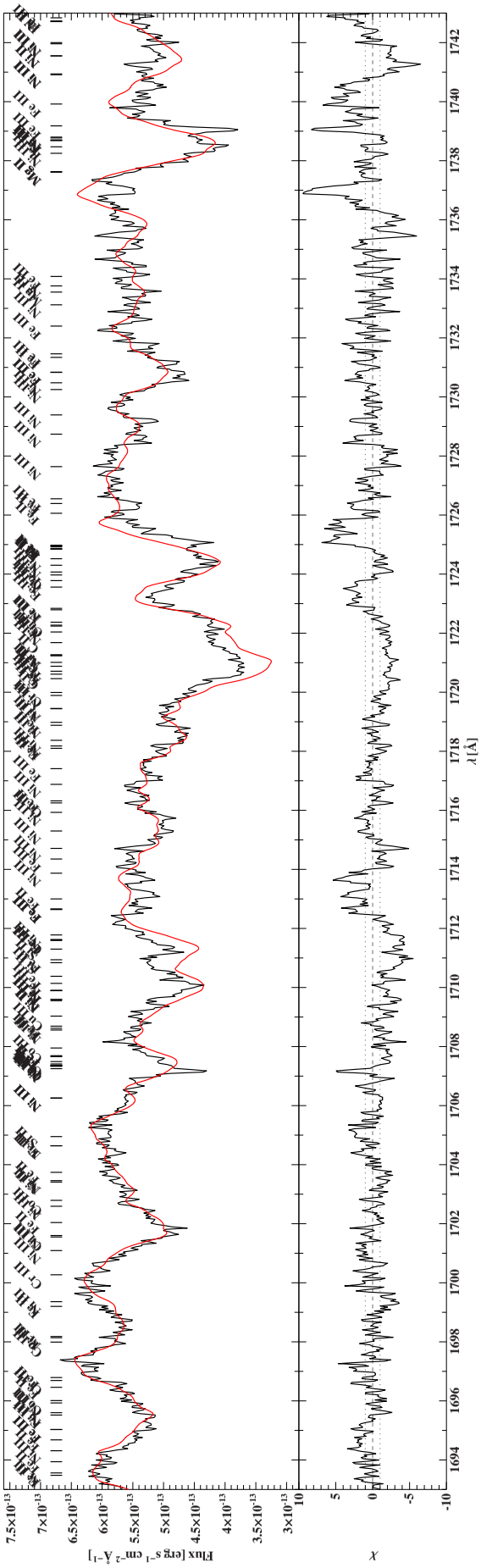
Flux [erg s⁻¹ cm⁻² Å⁻¹]
χ
λ [Å]

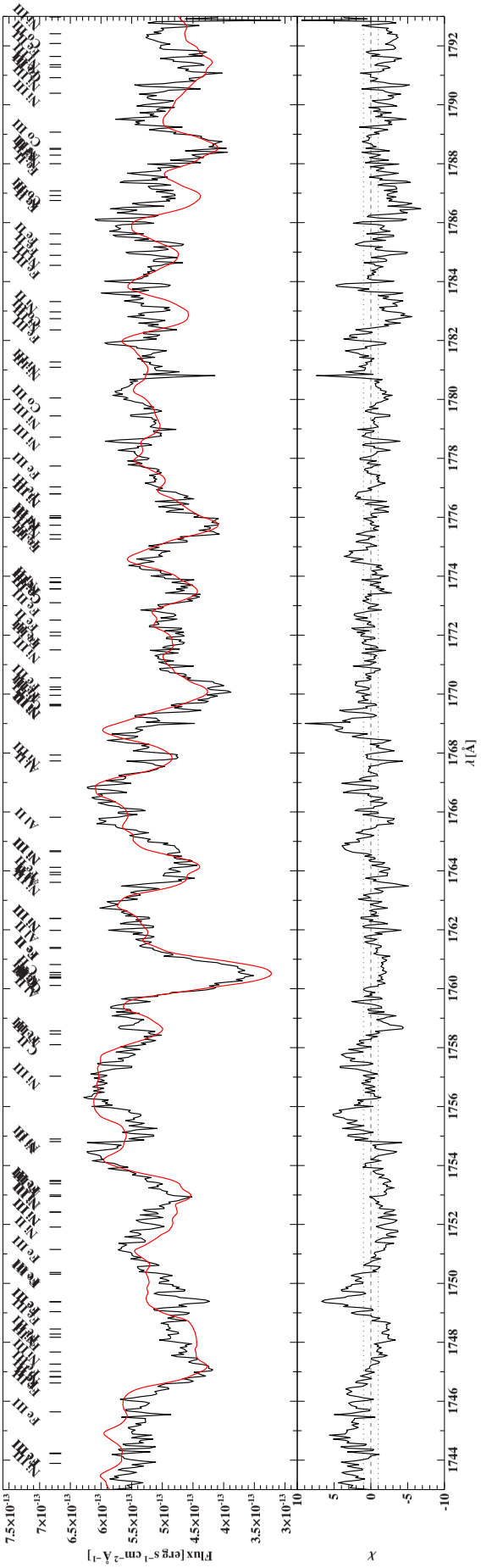
Flux [erg s⁻¹ cm⁻² Å⁻¹]
χ
λ [Å]

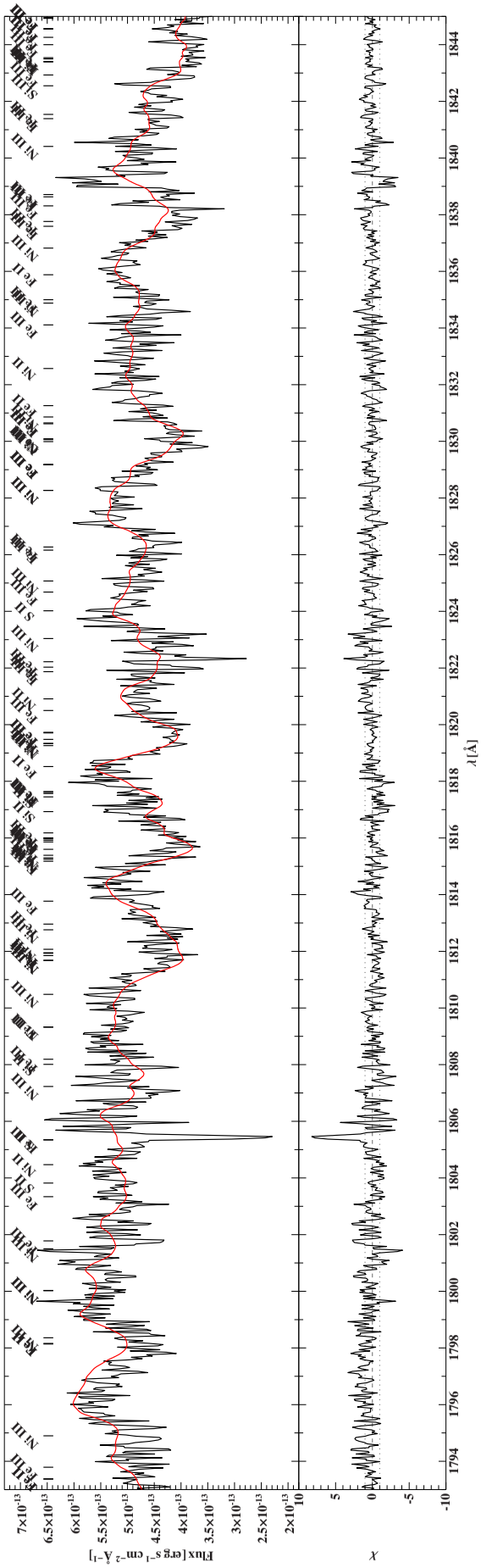
Flux [erg s⁻¹ cm⁻² Å⁻¹]
χ
λ [Å]

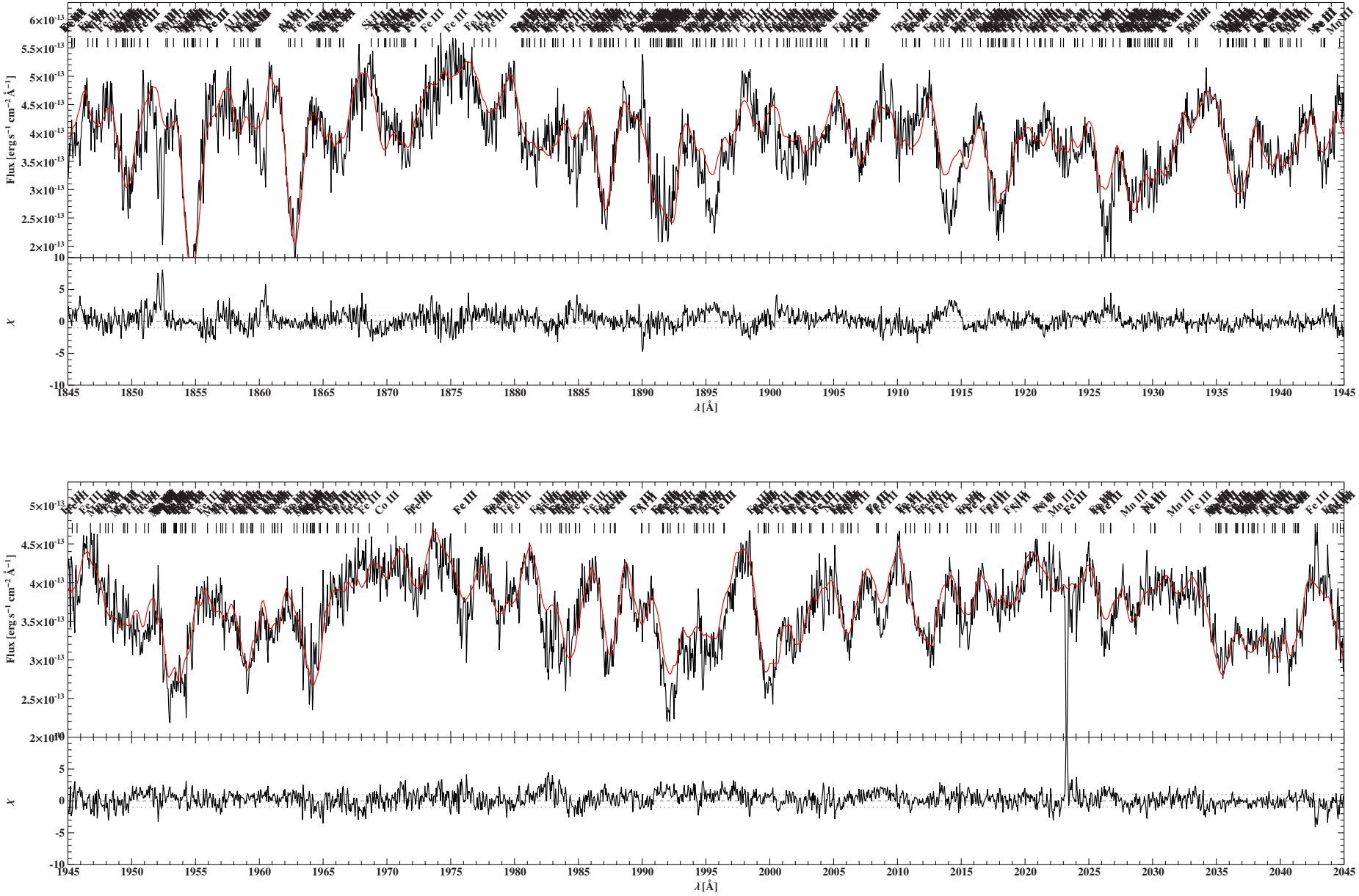
Flux [erg s^{-1} cm^{-2} Å^{-1}]
χ
λ [Å]

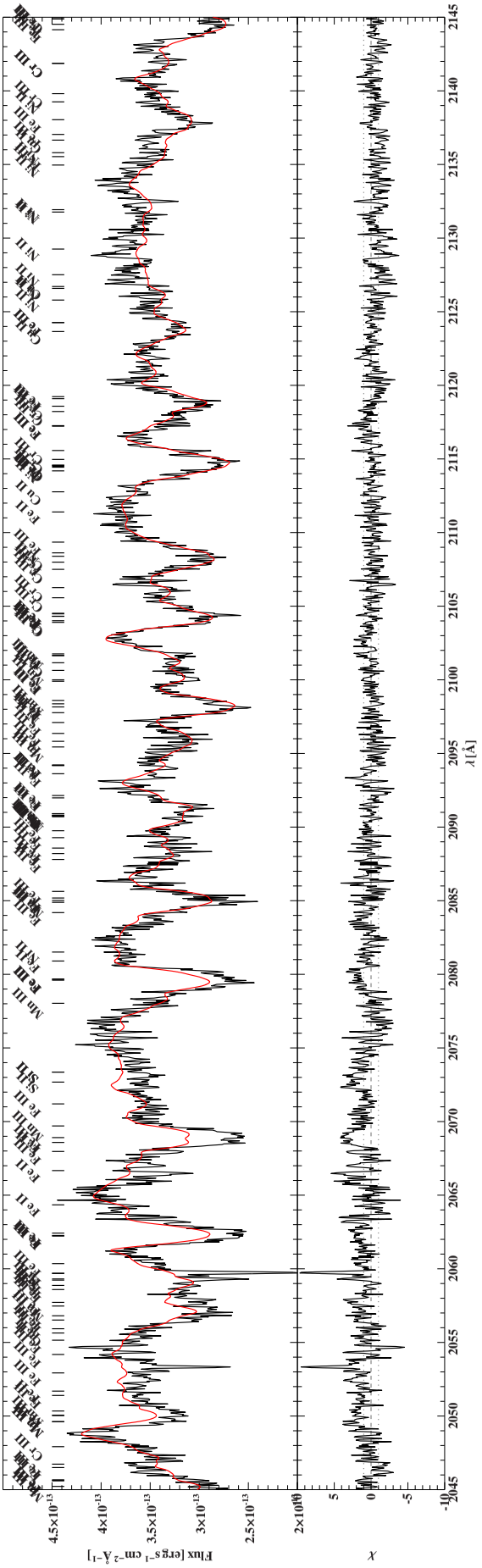
Flux [erg s⁻¹ cm⁻² Å⁻¹]
λ [Å]
χ

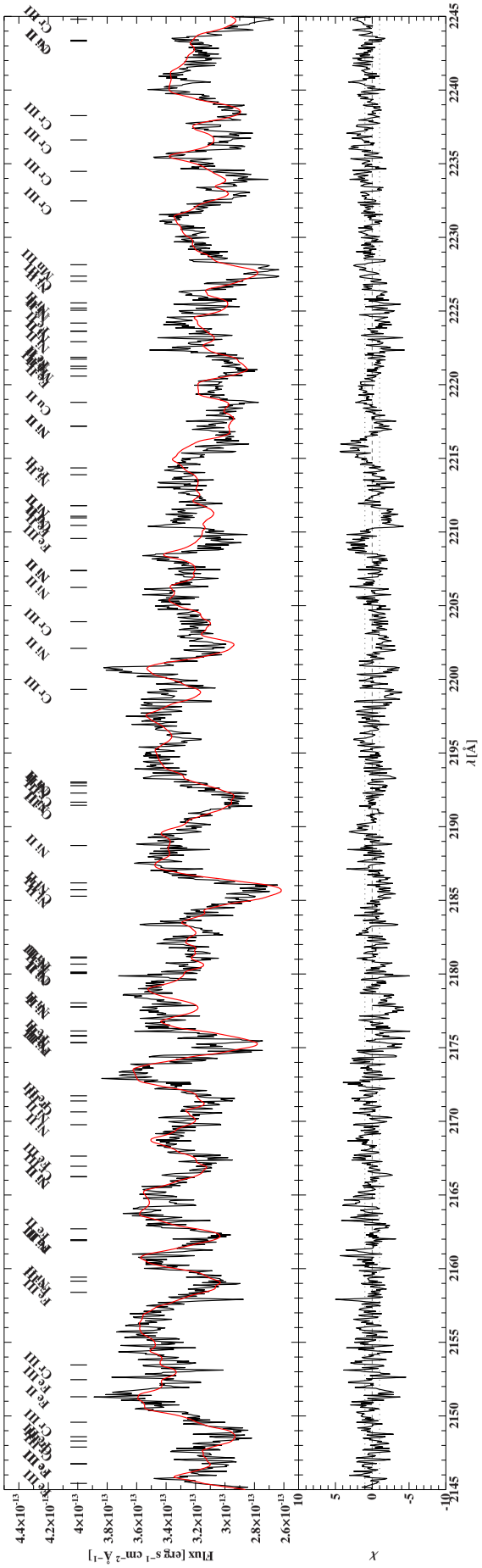
Flux [erg s⁻¹ cm⁻² Å⁻¹]
λ [Å]
χ

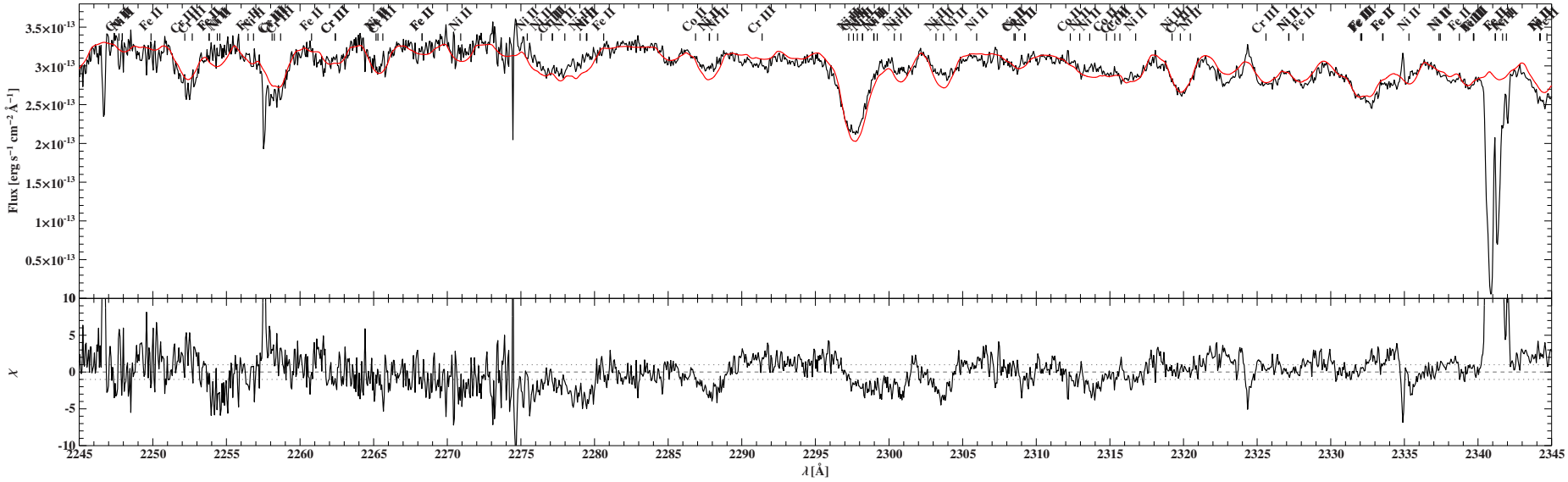
Flux [erg s^{-1} cm^{-2} Å^{-1}]
χ
λ[Å]

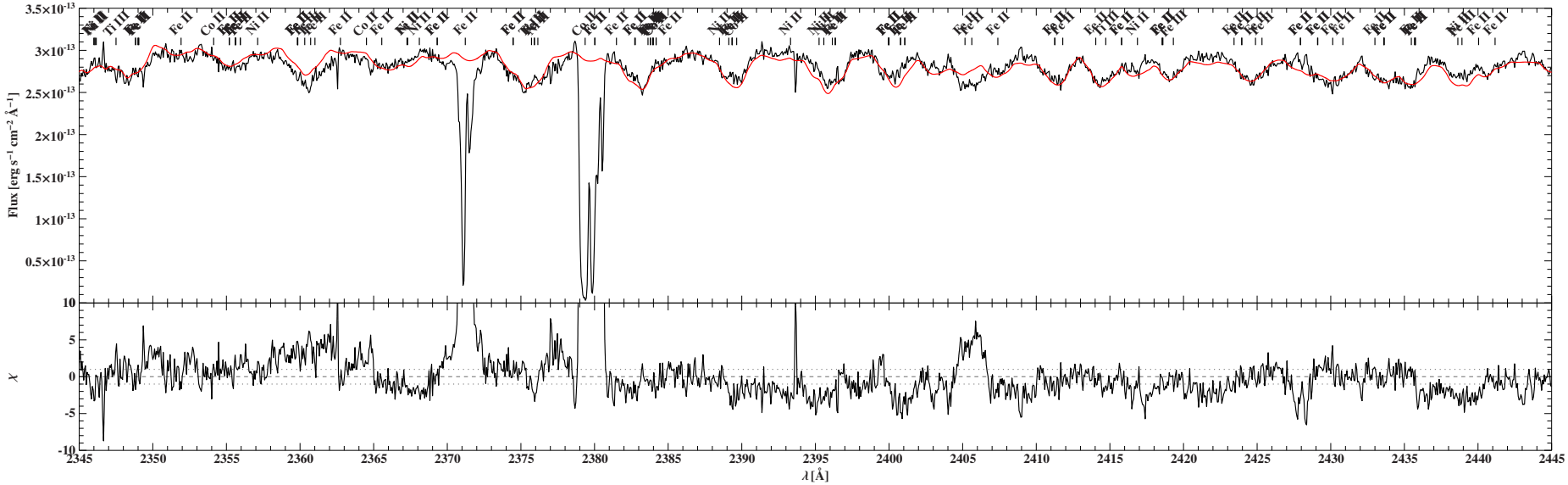
Flux [erg s^{-1} cm^{-2} Å^{-1}]
χ
λ[Å]

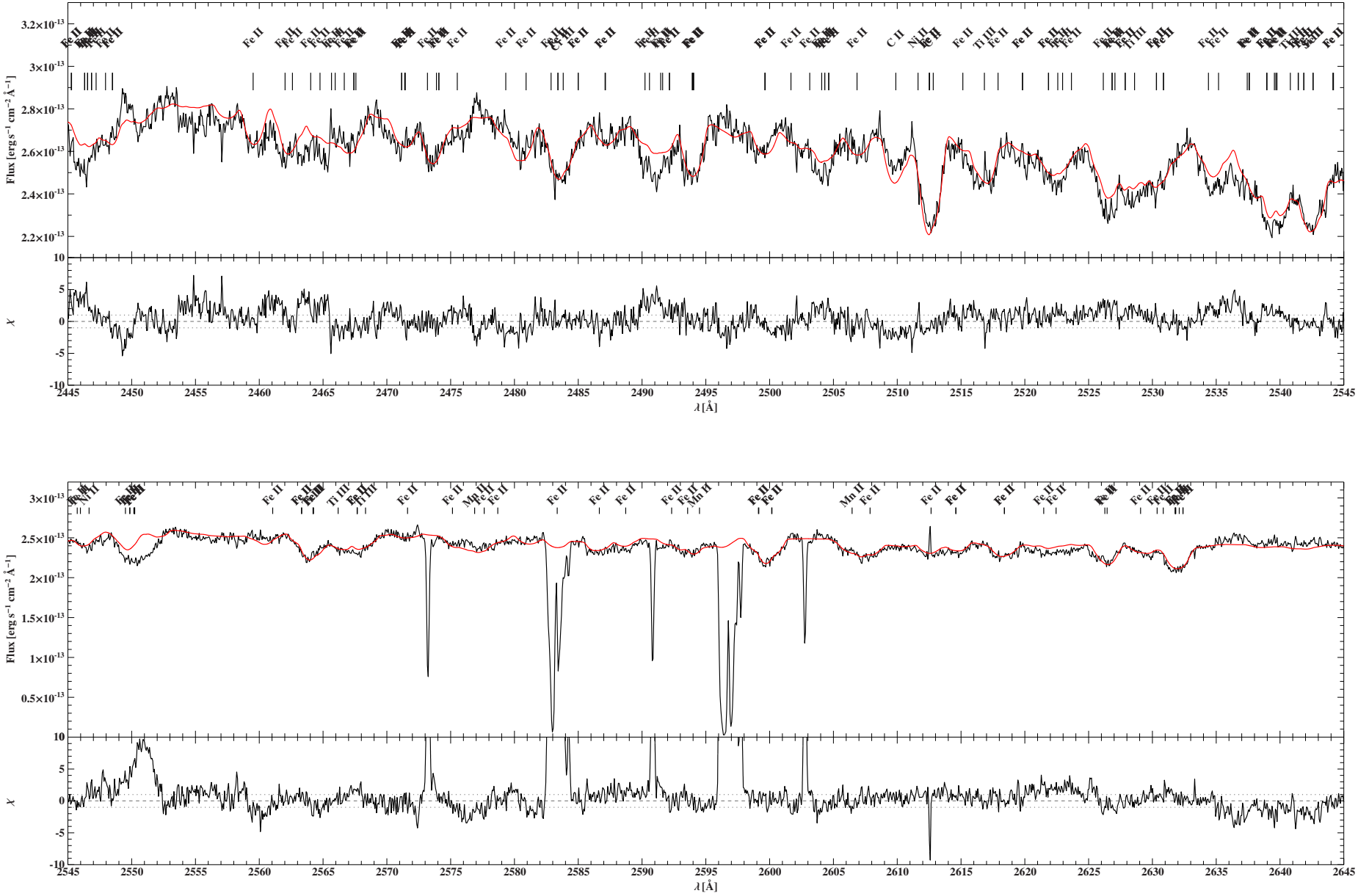
Flux [erg s^{-1} cm^{-2} Å^{-1}]
χ
λ [Å]
Fe II
C II
Ni II
Ti II
Ti III
Mn II

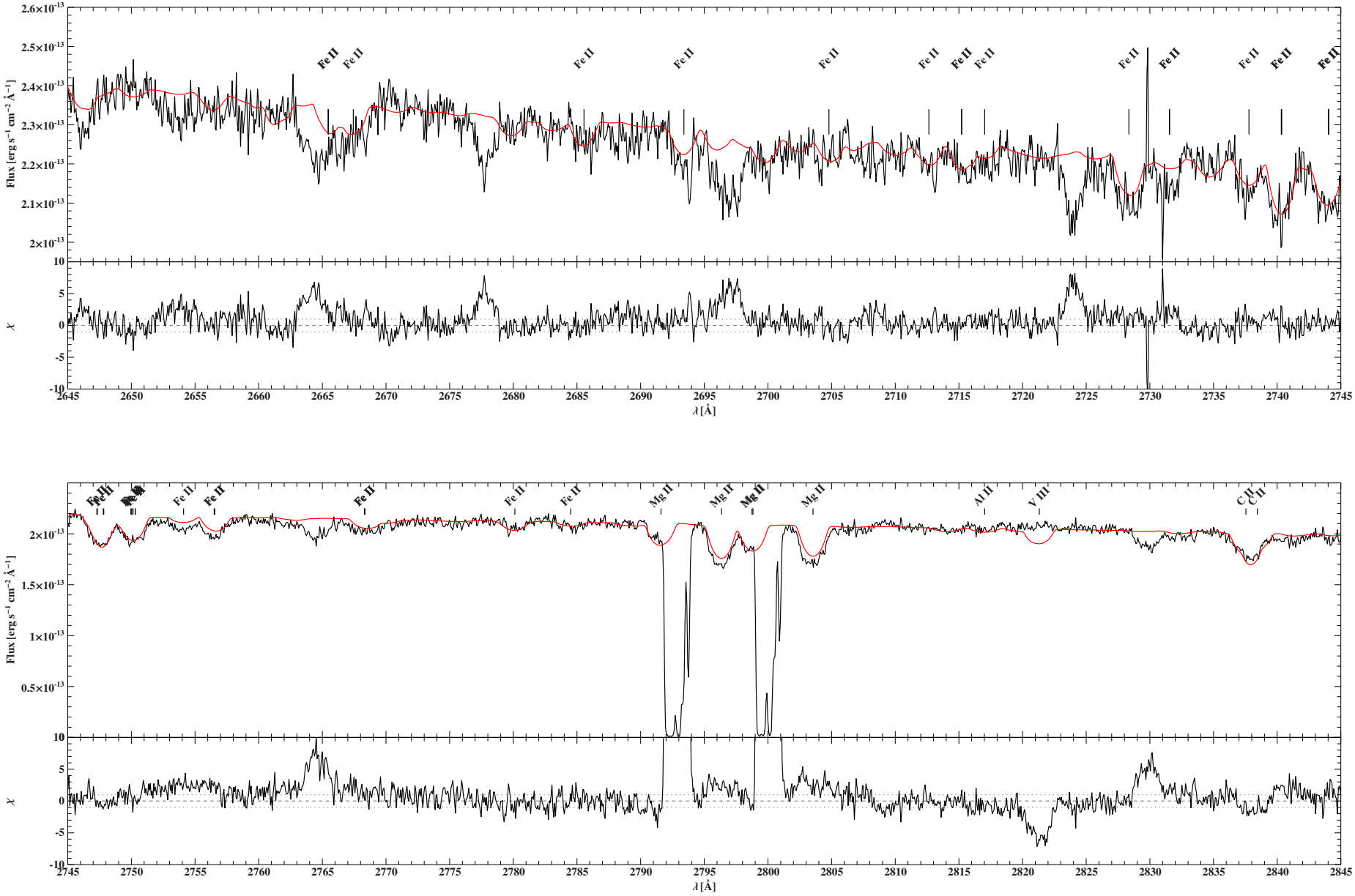
Flux [erg s^{-1} cm^{-2} Å^{-1}]
χ
λ[Å]
Fe II
Mg II
Al II
V III
C II

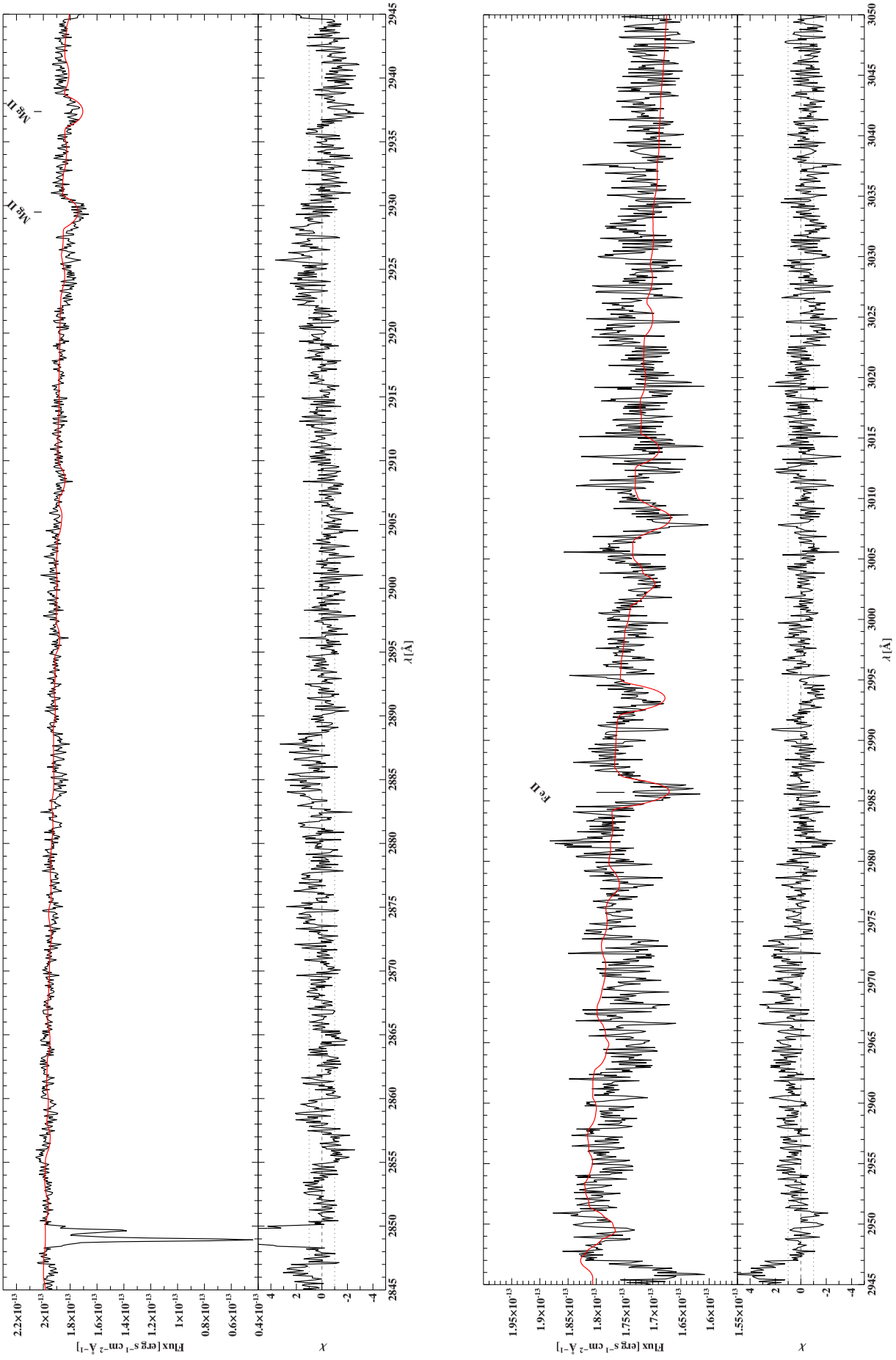
Mg II
Mg II
Fe II
Flux [erg s⁻¹ cm⁻² Å⁻¹]
χ
λ [Å]

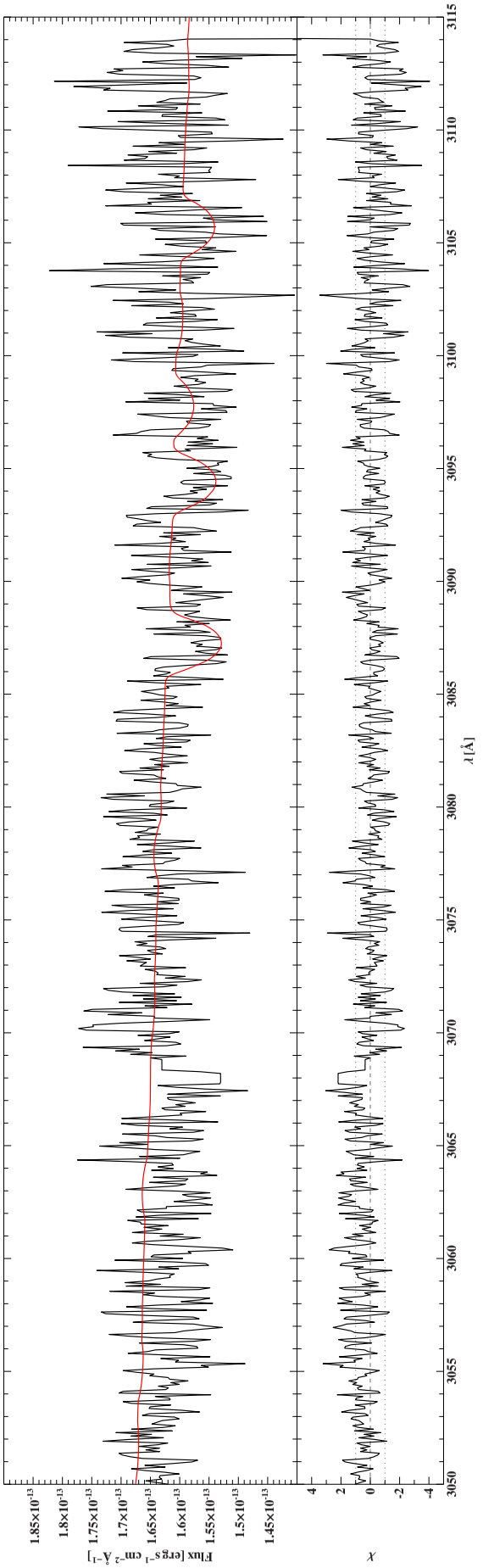
Flux [erg s⁻¹ cm⁻² Å⁻¹]
1.85×10⁻¹³
1.8×10⁻¹³
1.75×10⁻¹³
1.7×10⁻¹³
1.65×10⁻¹³
1.6×10⁻¹³
1.55×10⁻¹³
1.5×10⁻¹³
1.45×10⁻¹³
χ
4
2
0
-2
-4
3050
3055
3060
3065
3070
3075
3080
3085
3090
3095
3100
3105
3110
3115
λ [Å]

Bibliography

Abadi, M. G., Navarro, J. F., & Steinmetz, M. 2009, ApJ, 691, L63

Abazajian, K. N., Adelman-McCarthy, J. K., Agüeros, M. A., et al. 2009, ApJS, 182, 543

Adelman, S. J., Pintado, O. I., Nieva, M. F., Rayle, K. E., & Sanders, Jr., S. E. 2002, A&A, 392, 1031

Adelman-McCarthy, J. K., Agüeros, M. A., Allam, S. S., et al. 2008, ApJS, 175, 297

Aerts, C., Puls, J., Godart, M., & Dupret, M.-A. 2009, Communications in Asteroseismology, 158, 66

Almeida, L. A. & Jablonski, F. 2011, in IAU Symposium, Vol. 276, IAU Symposium, ed. A. Sozzetti, M. G. Lattanzi, & A. P. Boss, 495–496

Almeida, L. A., Jablonski, F., & Rodrigues, C. V. 2013, ApJ, 766, 11

Almeida, L. A., Jablonski, F., Tello, J., & Rodrigues, C. V. 2012, MNRAS, 423, 478

Almenara, J. M., Alonso, R., Rabus, M., et al. 2012, MNRAS, 420, 3017

Arcones, A. & Thielemann, F.-K. 2013, Journal of Physics G Nuclear Physics, 40, 013201

Asplund, M., Grevesse, N., Sauval, A. J., & Scott, P. 2009, ARA&A, 47, 481

Backhaus, U., Bauer, S., Beuermann, K., et al. 2012, A&A, 538, A84

Bailey, J. & Cropper, M. 1991, MNRAS, 253, 27

Baraffe, I., Chabrier, G., Barman, T. S., Allard, F., & Hauschildt, P. H. 2003, A&A, 402, 701

Barlow, B. N., Kilkenny, D., Drechsel, H., et al. 2013, MNRAS, 430, 22

Barlow, B. N., Wade, R. A., & Liss, S. E. 2012a, ApJ, 753, 101

Barlow, B. N., Wade, R. A., Liss, S. E., Østensen, R. H., & Van Winckel, H. 2012b, ApJ, 758, 58

Bear, E. & Soker, N. 2012, ApJ, 749, L14

Bear, E. & Soker, N. 2014, MNRAS, 444, 1698

Becker, S. R. 1998, in Astronomical Society of the Pacific Conference Series, Vol. 131, Properties of Hot Luminous Stars, ed. I. Howarth, 137

Becker, S. R. & Butler, K. 1988, A&A, 201, 232

Berrington, K. A., Burke, P. G., Butler, K., et al. 1987, Journal of Physics B Atomic Molecular Physics, 20, 6379

Beuermann, K., Breitenstein, P., Debski, B., et al. 2012a, A&A, 540, A8

Beuermann, K., Buhlmann, J., Diese, J., et al. 2011, A&A, 526, A53

Beuermann, K., Dreizler, S., Hessman, F. V., & Deller, J. 2012b, A&A, 543, A138

Beuermann, K., Hessman, F. V., Dreizler, S., et al. 2010, A&A, 521, L60

Biémont, E., Garnir, H. P., Bastin, T., et al. 2001a, MNRAS, 321, 481

Biémont, E., Garnir, H. P., Li, Z. S., et al. 2001b, Journal of Physics B Atomic Molecular Physics, 34, 1869

Biémont, E., Garnir, H. P., Litzén, U., et al. 2003, A&A, 399, 343

Biémont, E., Palmeri, P., Quinet, P., et al. 2001c, MNRAS, 328, 1085

Blaauw, A. 1961, Bull. Astron. Inst. Netherlands, 15, 265

Blaauw, A. 1993, in Astronomical Society of the Pacific Conference Series, Vol. 35, Massive Stars: Their Lives in the Interstellar Medium, ed. J. P. Cassinelli & E. B. Churchwell, 207

Blanchette, J.-P., Chayer, P., Wesemael, F., et al. 2008, ApJ, 678, 1329

Bouchy, F., Deleuil, M., Guillot, T., et al. 2011, A&A, 525, A68

Brandon, A. D., Humayun, M., Puchtel, I. S., Leya, I., & Zolensky, M. 2005, Science, 309, 1233

Brown, T. M., Bowers, C. W., Kimble, R. A., Sweigart, A. V., & Ferguson, H. C. 2000, APJ, 532, 308

Brown, T. M., Ferguson, H. C., Davidsen, A. F., & Dorman, B. 1997, APJ, 482, 685

Brown, W. R., Geller, M. J., & Kenyon, S. J. 2014, ApJ, 787, 89

Burrows, A., Hayes, J., & Fryxell, B. A. 1995, ApJ, 450, 830

Butler, K. & Giddings, J. R. 1985, in , Newsletter of Analysis of Astronomical Spectra, No. 9 (Univ. London)

Cannon, C. J. 1973, J. Quant. Spec. Radiat. Transf., 13, 627

Cantiello, M., Langer, N., Brott, I., et al. 2009, A&A, 499, 279

Carroll, B. W. & Ostlie, D. A. 2007, An introduction to Modern Astrophysics (Addison-Wesley)

Castelli, F. & Parthasarathy, M. 1995, in Astronomical Society of the Pacific Conference Series, Vol. 78, Astrophysical Applications of Powerful New Databases, ed. S. J. Adelman & W. L. Wiese, 151

Chabrier, G. & Baraffe, I. 1997, A&A, 327, 1039

Chabrier, G., Baraffe, I., Allard, F., & Hauschildt, P. 2000, ApJ, 542, L119

Charpinet, S., Fontaine, G., Brassard, P., & Dorman, B. 1996, ApJ, 471, L103

Charpinet, S., Fontaine, G., Brassard, P., & Dorman, B. 2000, ApJS, 131, 223

Charpinet, S., Fontaine, G., Brassard, P., et al. 2011, Nature, 480, 496

Charpinet, S., van Grootel, V., Reese, D., et al. 2008, A&A, 489, 377

Chevalier, C. & Ilovaisky, S. A. 1998, A&A, 330, 201

Claret, A. & Bloemen, S. 2011, A&A, 529, A75

Classen, L., Geier, S., Heber, U., & O'Toole, S. J. 2011, in American Institute of Physics Conference Series, Vol. 1331, American Institute of Physics Conference Series, ed. S. Schuh, H. Drechsel, & U. Heber, 297–303

Clayton, D. D. 1983, Principles of stellar evolution and nucleosynthesis

Copperwheat, C. M., Morales-Rueda, L., Marsh, T. R., Maxted, P. F. L., & Heber, U. 2011, MNRAS, 415, 1381

Cowan, R. D. 1981, The theory of atomic structure and spectra (University of California Press)

Cowley, C. R. 1971, The Observatory, 91, 139

Cunto, W. & Mendoza, C. 1992, Rev. Mexicana Astron. Astrofis., 23, 107

De Ridder, J., Dupret, M.-A., Neuforge, C., & Aerts, C. 2002, A&A, 385, 572

Dorman, B., Rood, R. T., & O'Connell, R. W. 1993, APJ, 419, 596

Drake, A. J., Beshore, E., Catelan, M., et al. 2010, ArXiv e-prints

Drake, G. W. F. 2006, Springer Handbook of Atomic, Molecular, and Optical Physics (Springer)

Drechsel, H., Haas, S., Lorenz, R., & Gayler, S. 1995, A&A, 294, 723

Drechsel, H., Heber, U., Napiwotzki, R., et al. 2001, A&A, 379, 893

Drilling, J. S., Jeffery, C. S., Heber, U., Moehler, S., & Napiwotzki, R. 2013, A&A, 551, A31

Duchêne, G. & Kraus, A. 2013, ARA&A, 51, 269

Eastman, J., Siverd, R., & Gaudi, B. S. 2010, PASP, 122, 935

Edelmann, H., Heber, U., Altmann, M., Karl, C., & Lisker, T. 2005, A&A, 442, 1023

Enzonga Yoca, S., Biémont, É., Delahaye, F., Quinet, P., & Zeippen, C. J. 2008, Phys. Scr, 78, 025303

Enzonga Yoca, S., Quinet, P., & Biémont, É. 2012, Journal of Physics B Atomic Molecular Physics, 45, 035001

Ferguson, D. H., Green, R. F., & Liebert, J. 1984, ApJ, 287, 320

Fitzpatrick, E. L. 1999, PASP, 111, 63

Fontaine, G., Brassard, P., Charpinet, S., et al. 2003, ApJ, 597, 518

Fontaine, G., Brassard, P., Charpinet, S., et al. 2012, A&A, 539, A12

For, B.-Q., Edelmann, H., Green, E. M., et al. 2008, in Astronomical Society of the Pacific Conference Series, Vol. 392, Hot Subdwarf Stars and Related Objects, ed. U. Heber, C. S. Jeffery, & R. Napiwotzki, 203

For, B.-Q., Green, E. M., Fontaine, G., et al. 2010, APJ, 708, 253

Freudling, W., Romaniello, M., Bramich, D. M., et al. 2013, A&A, 559, A96

Fryer, C. L., Heger, A., Langer, N., & Wellstein, S. 2002, ApJ, 578, 335

Fryxell, B. A. & Arnett, W. D. 1981, ApJ, 243, 994

Fujii, M. S. & Portegies Zwart, S. 2011, Science, 334, 1380

Geier, S. & Heber, U. 2012, A&A, 543, A149

Geier, S., Heber, U., Edelmann, H., et al. 2013a, A&A, 557, A122

Geier, S., Heber, U., Heuser, C., et al. 2013b, A&A, 551, L4

Geier, S., Heber, U., Podsiadlowski, P., et al. 2010, A&A, 519, A25

Geier, S., Hirsch, H., Tillich, A., et al. 2011a, A&A, 530, A28

Geier, S., Kupfer, T., Heber, U., et al. 2015, A&A, 577, A26

Geier, S., Maxted, P. F. L., Napiwotzki, R., et al. 2011b, A&A, 526, A39+

Geier, S., Østensen, R. H., Heber, U., et al. 2014, A&A, 562, A95

Geier, S., Schaffenroth, V., Drechsel, H., et al. 2011c, APJ, 731, L22+

Georgy, C., Ekström, S., Granada, A., et al. 2013, A&A, 553, A24

Giddings, J. R. 1981, Phd thesis, University of London

Gies, D. R. & Bolton, C. T. 1986, ApJS, 61, 419

Goździewski, K., Nasiroglu, I., Słowikowska, A., et al. 2012, MNRAS, 425, 930

Gray, D. F. 2005, The Observation and Analysis of Stellar Photospheres

Green, E., Johnson, C., Wallace, S., et al. 2014a, in Astronomical Society of the Pacific Conference Series, Vol. 481, 6th Meeting on Hot Subdwarf Stars and Related Objects, ed. V. van Grootel, E. Green, G. Fontaine, & S. Charpinet, 161

Green, E., Johnson, C., Wallace, S., et al. 2014b, in Astronomical Society of the Pacific Conference Series, Vol. 481, Astronomical Society of the Pacific Conference Series, ed. V. van Grootel, E. Green, G. Fontaine, & S. Charpinet, 161

Green, E. M., Fontaine, G., Hyde, E. A., For, B.-Q., & Chayer, P. 2008, in Astronomical Society of the Pacific Conference Series, Vol. 392, Hot Subdwarf Stars and Related Objects, ed. U. Heber, C. S. Jeffery, & R. Napiwotzki, 75

Green, E. M., Fontaine, G., Reed, M. D., et al. 2003, ApJ, 583, L31

Green, E. M., For, B., Hyde, E. A., et al. 2004, Ap&SS, 291, 267

Green, R. F., Schmidt, M., & Liebert, J. 1986, ApJS, 61, 305

Griem, H. R. 1974, Spectral line broadening by plasmas

Gualandris, A., Colpi, M., Portegies Zwart, S., & Possenti, A. 2005, ApJ, 618, 845

Gvaramadze, V. V. 2009, MNRAS, 395, L85

Haas, S. 1993, Diplomarbeit, Friedrich Alexander Universität Erlangen Nürnberg

Han, Z. 2008, A&A, 484, L31

Han, Z., Podsiadlowski, P., Maxted, P. F. L., & Marsh, T. R. 2003, MNRAS, 341, 669

Han, Z., Podsiadlowski, P., Maxted, P. F. L., Marsh, T. R., & Ivanova, N. 2002, MNRAS, 336, 449

Hardy, A., Schreiber, M. R., Parsons, S. G., et al. 2015, ApJ, 800, L24

Heber, U. 2009, ARA&A, 47, 211

Heber, U., Drechsel, H., Østensen, R., et al. 2004, A&A, 420, 251

Heber, U., Edelmann, H., Napiwotzki, R., Altmann, M., & Scholz, R.-D. 2008, A&A, 483, L21

Heber, U., Reid, I. N., & Werner, K. 2000, A&A, 363, 198

Heggie, D. C. 1975, MNRAS, 173, 729

Hills, J. G. 1988, Nature, 331, 687

Hirata, R. & Horaguchi, T. 1994, VizieR Online Data Catalog, 6069, 0

Hirsch, H. 2009, Phd thesis, Friedrich Alexander Universität Erlangen Nürnberg

Hirsch, H. A., Heber, U., & O'Toole, S. J. 2008, in Astronomical Society of the Pacific Conference Series, Vol. 392, Hot Subdwarf Stars and Related Objects, ed. U. Heber, C. S. Jeffery, & R. Napiwotzki, 131

Hoogerwerf, R., de Bruijne, J. H. J., & de Zeeuw, P. T. 2001, A&A, 365, 49

Hubeny, I. & Mihalas, D. 2015, Theory of Stellar Atmospheres (Princton University Press)

Humason, M. L. & Zwicky, F. 1947, ApJ, 105, 85

Hummer, D. G., Berrington, K. A., Eissner, W., et al. 1993, A&A, 279, 298

Iliadis, C. 2007, Nuclear Physics of Stars (Wiley-VCH Verlag)

Irrgang, A. 2014, Phd thesis, Friedrich Alexander Universität Erlangen Nürnberg

Irrgang, A., Przybilla, N., Heber, U., et al. 2014, A&A, 565, A63

Irrgang, A., Wilcox, B., Tucker, E., & Schiefelbein, L. 2013, A&A, 549, A137

Ivanova, N., Justham, S., Chen, X., et al. 2013, A&A Rev., 21, 59

Izzard, R. G. 2013, in EAS Publications Series, Vol. 64, EAS Publications Series, ed. K. Pavlovski, A. Tkachenko, & G. Torres, 13–20

Janka, H.-T., Hanke, F., Hüdepohl, L., et al. 2012, Progress of Theoretical and Experimental Physics, 2012, 010000

Jeffery, C. S. & Ramsay, G. 2014, MNRAS, 442, L61

Johansson, S., Derkatch, A., Donnelly, M. P., et al. 2002, Physica Scripta Volume T, 100, 71

Kallrath, J. & Linnell, A. P. 1987, APJ, 313, 346

Kawaler, S. D., Reed, M. D., Østensen, R. H., et al. 2010, MNRAS, 409, 1509

Kepler, S. O., Kleinman, S. J., Nitta, A., et al. 2007, MNRAS, 375, 1315

Kilkenny, D. 2011, MNRAS, 412, 487

Kilkenny, D., Koen, C., O'Donoghue, D., & Stobie, R. S. 1997, MNRAS, 285, 640

Kilkenny, D. & Muller, S. 1989, South African Astronomical Observatory Circular, 13, 69

Kilkenny, D., O'Donoghue, D., Koen, C., Lynas-Gray, A. E., & van Wyk, F. 1998, MNRAS, 296, 329

Kippenhahn, R. & Weigert, A. 1994, Stellar Structure and Evolution (Springer-Verlag)

Klepp, S. & Rauch, T. 2011, A&A, 531, L7+

Koen, C. 2007, MNRAS, 377, 1275

Koen, C. 2009, MNRAS, 395, 979

Koen, C., O'Donoghue, D., Kilkenny, D., Stobie, R. S., & Saffer, R. A. 1999, MNRAS, 306, 213

Kundra, E. & Hric, L. 2011, Ap&SS, 331, 121

Kupfer, T., Geier, S., Heber, U., et al. 2015, A&A, 576, A44

Kupfer, T., Geier, S., McLeod, A., et al. 2014, in Astronomical Society of the Pacific Conference Series, Vol. 481, 6th Meeting on Hot Subdwarf Stars and Related Objects, ed. V. van Grootel, E. Green, G. Fontaine, & S. Charpinet, 293

Kurucz, R. L. 1970, SAO Special Report, 309

Kurucz, R. L. 1996, in Astronomical Society of the Pacific Conference Series, Vol. 108, M.A.S.S., Model Atmospheres and Spectrum Synthesis, ed. S. J. Adelman, F. Kupka, & W. W. Weiss, 160

Kurucz, R. L. 2011, Canadian Journal of Physics, 89, 417

Langer, N. 2012, ARA&A, 50, 107

Latour, M., Fontaine, G., & Green, E. 2014, in Astronomical Society of the Pacific Conference Series, Vol. 481, 6th Meeting on Hot Subdwarf Stars and Related Objects, ed. V. van Grootel, E. Green, G. Fontaine, & S. Charpinet, 91

Law, N. M., Kraus, A. L., Street, R., et al. 2012, ApJ, 757, 133

Lee, J. W., Hinse, T. C., Youn, J.-H., & Han, W. 2014, MNRAS, 445, 2331

Lee, J. W., Kim, S.-L., Kim, C.-H., et al. 2009, AJ, 137, 3181

Leonard, P. J. T. 1991, AJ, 101, 562

Li, Z. S., Zhang, Z. G., Lokhnygin, V., et al. 2001, Journal of Physics B Atomic Molecular Physics, 34, 1349

Lisker, T., Heber, U., Napiwotzki, R., et al. 2005, A&A, 430, 223

Lorenz, R. 1988, Diplomarbeit, Friedrich Alexander Universität Erlangen Nürnberg

Lucy, L. B. 1967, Zeitschrift für Astrophysik, 65, 89

Lutz, R. 2011, Phd thesis, Georg-August-Universität Göttingen

Maeder, A. & Meynet, G. 2000, ARA&A, 38, 143

Malcheva, G., Yoca, S. E., Mayo, R., et al. 2009, MNRAS, 396, 2289

Markwardt, C. B. 2009, in Astronomical Society of the Pacific Conference Series, Vol. 411, Astronomical Data Analysis Software and Systems XVIII, ed. D. A. Bohlender, D. Durand, & P. Dowler, 251

Maxted, P. f. L., Heber, U., Marsh, T. R., & North, R. C. 2001, MNRAS, 326, 1391

Maxted, P. F. L., Marsh, T. R., Heber, U., et al. 2002, MNRAS, 333, 231

Maxted, P. F. L., Marsh, T. R., Morales-Rueda, L., et al. 2004a, MNRAS, 355, 1143

Maxted, P. F. L., Morales-Rueda, L., & Marsh, T. R. 2004b, Ap&SS, 291, 307

Maxted, P. F. L., O'Donoghue, D., Morales-Rueda, L., Napiwotzki, R., & Smalley, B. 2007, MNRAS, 376, 919

Menzies, J. W. & Marang, F. 1986, in IAU Symposium, Vol. 118, Instrumentation and Research Programmes for Small Telescopes, ed. J. B. Hearnshaw & P. L. Cottrell, 305

Meynet, G. & Maeder, A. 2003, A&A, 404, 975

Moehler, S., Richtler, T., de Boer, K. S., Dettmar, R. J., & Heber, U. 1990, A&AS, 86, 53

Morel, T. & Butler, K. 2008, A&A, 487, 307

Morel, T., Butler, K., Aerts, C., Neiner, C., & Briquet, M. 2006, A&A, 457, 651

Morton, D. C. 2000, ApJS, 130, 403

Napiwotzki, R., Karl, C. A., Lisker, T., et al. 2004a, Ap&SS, 291, 321

Napiwotzki, R., Yungelson, L., Nelemans, G., et al. 2004b, in Astronomical Society of the Pacific Conference Series, Vol. 318, Spectroscopically and Spatially Resolving the Components of the Close Binary Stars, ed. R. W. Hilditch, H. Hensberge, & K. Pavlovski, 402–410

Nelemans, G. & Tauris, T. M. 1998, A&A, 335, L85

Nieva, M. F. & Przybilla, N. 2006, ApJ, 639, L39

Nieva, M. F. & Przybilla, N. 2007, A&A, 467, 295

Nieva, M. F. & Przybilla, N. 2008, A&A, 481, 199

Nieva, M.-F. & Przybilla, N. 2010, in EAS Publications Series, Vol. 43, EAS Publications Series, ed. R. Monier, B. Smalley, G. Wahlgren, & P. Stee, 167–187

Nieva, M.-F. & Przybilla, N. 2012, A&A, 539, A143

Nieva, M.-F. & Przybilla, N. 2014, A&A, 566, A7

Nilsson, H., Hartman, H., Engström, L., et al. 2010, A&A, 511, A16

Nomoto, K., Tominaga, N., Umeda, H., Kobayashi, C., & Maeda, K. 2006, Nuclear Physics A, 777, 424

O'Brien, M. S., Bond, H. E., & Sion, E. M. 2001, ApJ, 563, 971

O'Donoghue, D., Koen, C., Kilkenny, D., et al. 2003, MNRAS, 345, 506

Østensen, R. H., Geier, S., Schaffenroth, V., et al. 2013, A&A, accepted

Østensen, R. H., Green, E. M., Bloemen, S., et al. 2010, MNRAS, 408, L51

Østensen, R. H., Oreiro, R., Hu, H., Drechsel, H., & Heber, U. 2008, in Astronomical Society of the Pacific Conference Series, Vol. 392, Hot Subdwarf Stars and Related Objects, ed. U. Heber, C. S. Jeffery, & R. Napiwotzki, 221–+

O'Toole, S. J. & Heber, U. 2006, A&A, 452, 579

Pablo, H., Kawaler, S. D., & Green, E. M. 2011, ApJ, 740, L47

Pablo, H., Kawaler, S. D., Reed, M. D., et al. 2012, MNRAS, 422, 1343

Pagel, B. E. J. 2009, Nucleosynthesis and Chemical Evolution of Galaxies

Palmeri, P., Quinet, P., Fivet, V., et al. 2009, Journal of Physics B Atomic Molecular Physics, 42, 165005

Pandel, D., Cordova, F. A., Shirey, R. E., et al. 2002, MNRAS, 332, 116

Parsons, S. G., Gänsicke, B. T., Marsh, T. R., et al. 2013, MNRAS, 429, 256

Parsons, S. G., Marsh, T. R., Copperwheat, C. M., et al. 2010a, MNRAS, 402, 2591

Parsons, S. G., Marsh, T. R., Copperwheat, C. M., et al. 2010b, MNRAS, 407, 2362

Parsons, S. G., Marsh, T. R., Gänsicke, B. T., et al. 2012, MNRAS, 420, 3281

Parsons, S. G., Marsh, T. R., Gänsicke, B. T., & Tappert, C. 2011, MNRAS, 412, 2563

Pietrukowicz, P., Mróz, P., Soszyński, I., et al. 2013, Acta Astron., 63, 115

Podsiadlowski, P. 2008, in Astronomical Society of the Pacific Conference Series, Vol. 391, Hydrogen-Deficient Stars, ed. A. Werner & T. Rauch, 323

Polubek, G., Pigulski, A., Baran, A., & Udalski, A. 2007, in Astronomical Society of the Pacific Conference Series, Vol. 372, 15th European Workshop on White Dwarfs, ed. R. Napiwotzki & M. R. Burleigh, 487

Portegies Zwart, S. F. 2000, ApJ, 544, 437

Potter, S. B., Romero-Colmenero, E., Ramsay, G., et al. 2011, MNRAS, 416, 2202

Poveda, A., Ruiz, J., & Allen, C. 1967, Boletin de los Observatorios Tonantzintla y Tacubaya, 4, 86

Pradhan, A. K. & Nahar, S. N. 2011, Atomic Astrophysics and Spectroscopy (Cambridge University Press)

Press, W. H. & Rybicki, G. B. 1989, ApJ, 338, 277

Pribulla, T., Dimitrov, D., Kjurkchieva, D., et al. 2013, Information Bulletin on Variable Stars, 6067, 1

Przybilla, N. 2005, A&A, 443, 293

Przybilla, N. & Butler, K. 2001, A&A, 379, 955

Przybilla, N. & Butler, K. 2004, ApJ, 609, 1181

Przybilla, N., Butler, K., Becker, S. R., & Kudritzki, R. P. 2001, A&A, 369, 1009

Przybilla, N., Butler, K., Becker, S. R., Kudritzki, R. P., & Venn, K. A. 2000, A&A, 359, 1085

Przybilla, N., Nieva, M.-F., & Butler, K. 2011, Journal of Physics Conference Series, 328, 012015

Przybilla, N., Nieva, M. F., Heber, U., & Butler, K. 2008, ApJ, 684, L103

Pyrzas, S., Gänsicke, B. T., Brady, S., et al. 2012, MNRAS, 419, 817

Pyrzas, S., Gänsicke, B. T., Marsh, T. R., et al. 2009, MNRAS, 394, 978

Qian, S.-B., Liu, L., Zhu, L.-Y., et al. 2012a, MNRAS, 422, L24

Qian, S.-B., Zhu, L.-Y., Dai, Z.-B., et al. 2012b, ApJ, 745, L23

Quinet, P. 2015, Phys. Scr, 90, 015404

Quinet, P., Palmeri, P., Biémont, É., et al. 2006, A&A, 448, 1207

Ralchenko, Y. 2005, Memorie della Societa Astronomica Italiana Supplementi, 8, 96

Rauch, T., Werner, K., Biémont, É., Quinet, P., & Kruk, J. W. 2012, A&A, 546, A55

Rauch, T., Werner, K., Quinet, P., & Kruk, J. W. 2014a, A&A, 564, A41

Rauch, T., Werner, K., Quinet, P., & Kruk, J. W. 2014b, A&A, 566, A10

Rauch, T., Werner, K., Quinet, P., & Kruk, J. W. 2015, ArXiv e-prints

Rebassa-Mansergas, A., Nebot Gómez-Morán, A., Schreiber, M. R., et al. 2012, MNRAS, 419, 806

Reed, M. D., Brondel, B. J., & Kawaler, S. D. 2005, ApJ, 634, 602

Reed, M. D. & Whole Earth Telescope Xcov 21 and 23 Collaborations. 2006, Mem. Soc. Astron. Italiana, 77, 417

Reif, K., Bagschik, K., de Boer, K. S., et al. 1999, in Society of Photo-Optical Instrumentation Engineers (SPIE) Conference Series, Vol. 3649, Society of Photo-Optical Instrumentation Engineers (SPIE) Conference Series, ed. M. M. Blouke & G. M. Williams, 109–120

Rybicki, G. B. & Hummer, D. G. 1991, A&A, 245, 171

Rybicki, G. B. & Hummer, D. G. 1992, A&A, 262, 209

Sahal-Brechot, S. 1969a, A&A, 1, 91

Sahal-Brechot, S. 1969b, A&A, 2, 322

Sahal-Brechot, S. 1974, A&A, 35, 319

Sahal-Bréchot, S., Dimitrijević, M. S., Moreau, N., & Ben Nessib, N. 2014, in SF2A-2014: Proceedings of the Annual meeting of the French Society of Astronomy and Astrophysics, ed. J. Ballet, F. Martins, F. Bournaud, R. Monier, & C. Reylé, 515–521

Sana, H., de Mink, S. E., de Koter, A., et al. 2012, Science, 337, 444

Sandage, A. & Wallerstein, G. 1960, ApJ, 131, 598

Sandage, A. & Wildey, R. 1967, ApJ, 150, 469

Schaffenroth, V. 2010, Diplomarbeit, Friedrich Alexander Universität Erlangen Nürnberg

Schaffenroth, V., Barlow, B. N., Drechsel, H., & Dunlap, B. H. 2015, ArXiv e-prints

Schaffenroth, V., Classen, L., Nagel, K., et al. 2014a, A&A, 570, A70

Schaffenroth, V., Geier, S., Barbu-Barna, I., et al. 2014b, in Astronomical Society of the Pacific Conference Series, Vol. 481, Astronomical Society of the Pacific Conference Series, ed. V. van Grootel, E. Green, G. Fontaine, & S. Charpinet, 253

Schaffenroth, V., Geier, S., Drechsel, H., et al. 2013, A&A, 553, A18

Schaffenroth, V., Geier, S., Heber, U., et al. 2014c, A&A, 564, A98

Schechter, P. L., Mateo, M., & Saha, A. 1993, PASP, 105, 1342

Schwarz, R., Schwope, A. D., Vogel, J., et al. 2009, A&A, 496, 833

Schwarzenberg-Czerny, A. 1996, ApJ, 460, L107

Schwope, A. D., Hambaryan, V., Schwarz, R., Kanbach, G., & Gänsicke, B. T. 2002, A&A, 392, 541

Schwope, A. D., Horne, K., Steeghs, D., & Still, M. 2011, A&A, 531, A34

Silvotti, R., Schuh, S., Janulis, R., et al. 2007, Nature, 449, 189

Smette, A., Sana, H., Noll, S., et al. 2015, ArXiv e-prints

Smith, E. W., Cooper, J., & Vidal, C. R. 1969, Physical Review, 185, 140

Sneden, C. & Cowan, J. J. 2003, Science, 299, 70

Soker, N. 1998, AJ, 116, 1308

Soszynski, I., Stepien, K., Pilecki, B., et al. 2015, ArXiv e-prints

Stetson, P. B. 1987, PASP, 99, 191

Stone, R. C. 1991, AJ, 102, 333

Tassoul, M. & Tassoul, J.-L. 1992, ApJ, 395, 604

Tauris, T. M. 2015, MNRAS, 448, L6

Tauris, T. M. & Takens, R. J. 1998, A&A, 330, 1047

Tetzlaff, N., Dinçel, B., Neuhäuser, R., & Kovtyukh, V. V. 2014, MNRAS, 438, 3587

Turatto, M. 2003, in Lecture Notes in Physics, Berlin Springer Verlag, Vol. 598, Supernovae and Gamma-Ray Bursters, ed. K. Weiler, 21–36

Udalski, A. 2003, Acta Astron., 53, 291

Udalski, A., Pont, F., Naef, D., et al. 2008, A&A, 482, 299

Udalski, A., Szymanski, M., Kaluzny, J., et al. 1993, Acta Astron., 43, 289

van den Besselaar, E. J. M., Greimel, R., Morales-Rueda, L., et al. 2007, A&A, 466, 1031

Van Grootel, V., Charpinet, S., Brassard, P., Fontaine, G., & Green, E. M. 2013, A&A, 553, A97

Van Noord, D. M., Molnar, L. A., & Steenwyk, S. D. 2013, ArXiv e-prints

Vanbeveren, D., De Loore, C., & Van Rensbergen, W. 1998, A&A Rev., 9, 63

von Zeipel, H. 1924, MNRAS, 84, 665

Vos, J., Østensen, R. H., Németh, P., et al. 2013, A&A, 559, A54

Vrancken, M., Butler, K., & Becker, S. R. 1996, A&A, 311, 661

Vučković, M., Aerts, C., Östensen, R., et al. 2007, A&A, 471, 605

Vučković, M., Bloemen, S., & Østensen, R. 2014, in Astronomical Society of the Pacific Conference Series, Vol. 481, Astronomical Society of the Pacific Conference Series, ed. V. van Grootel, E. Green, G. Fontaine, & S. Charpinet, 259

Vučković, M., Østensen, R., Bloemen, S., Decoster, I., & Aerts, C. 2008, in Astronomical Society of the Pacific Conference Series, Vol. 392, Hot Subdwarf Stars and Related Objects, ed. U. Heber, C. S. Jeffery, & R. Napiwotzki, 199

Wade, R. A. & Rucinski, S. M. 1985, A&AS, 60, 471

Wahlgren, G. M. 2010, in EAS Publications Series, Vol. 43, EAS Publications Series, ed. R. Monier, B. Smalley, G. Wahlgren, & P. Stee, 91–114

Wellstein, S., Langer, N., & Braun, H. 2001, A&A, 369, 939

Werner, K., Rauch, T., Kučas, S., & Kruk, J. W. 2015, A&A, 574, A29

Wils, P., di Scala, G., & Otero, S. A. 2007, Information Bulletin on Variable Stars, 5800, 1

Wilson, R. E. & Devinney, E. J. 1971, APJ, 166, 605

Wood, J. H. & Saffer, R. 1999, MNRAS, 305, 820

Woodgate, B. E., Kimble, R. A., Bowers, C. W., et al. 1998, PASP, 110, 1183

Wyart, J.-F., Tchang-Brillet, W.-Ü. L., Spector, N., et al. 2001, Phys. Scr, 63, 113

Xu, H. L., Svanberg, S., Quinet, P., Palmeri, P., & Biémont, É. 2007, J. Quant. Spec. Radiat. Transf., 104, 52

Yi, S. K. 2008, in Astronomical Society of the Pacific Conference Series, Vol. 392, Hot Subdwarf Stars and Related Objects, ed. U. Heber, C. S. Jeffery, & R. Napiwotzki, 3

Zahn, J.-P. 1977, A&A, 57, 383

Zhang, W., Palmeri, P., & Quinet, P. 2013, Phys. Scr, 88, 065302

Zhang, Z. G., Somesfalean, G., Svanberg, S., et al. 2002, A&A, 384, 364

Zima, W. 2008, Communications in Asteroseismology, 157, 387

Zorotovic, M. & Schreiber, M. R. 2013, A&A, 549, A95

Zorotovic, M., Schreiber, M. R., Gänsicke, B. T., & Nebot Gómez-Morán, A. 2010, A&A, 520, A86

Acknowledgements

I would like to thank my supervisors Uli Heber and Norbert Przybilla. I am very grateful for the opportunity to investigate this fascinating scientific topic. Moreover, I would like to thank for the chance to follow my own science and for not putting any pressure, but letting me influencing the direction of this thesis and pursuing my own research. Also I am very grateful for the always open door and the discussions. I would like to thank for giving me the opportunity to broaden my observing experience. Furthermore, I am thankful for the chance of participating in a large number of international conferences. Thereby I would like to thank Australian National University for support to participate in the Nuclei in the Cosmos summer school. I am also grateful for the opportunity to move to the beautiful Innsbruck during my thesis. I am thanking the University of Innsbruck for providing me with the facilities necessary to finish my thesis.
Furthermore, I would like to thank Stephan Geier for the long discussions and the great support and for the opportunity to be a part of the MUCHFUSS project. and for encouraging me to start my own project. I am also grateful for his invitation to stay at ESO for one week, which was a great experience.
I am thanking also Thomas Kupfer for his contribution by getting observing time essential for this thesis. Moreover, I am grateful to Oliver Cordes for sharing his observation time with us.
Many thanks also to our Bachelor students Ingrid Barbu-Barna and Kathrin Nagel for their contributions to this work.
I want to thank my colleges at the Remeis observatory and my colleges at the Institute for Astro-and Particle Physics for the great working environment, which not only consisted of work. Especially, I want to thank my office mate Andreas Irrgang for his help introducing me to the subject of abundance studies, his help with ISIS and the discussions. I am, moreover, grateful for the open door, support and many discussions with Horst Drechsel.
I also want to thank Joe Schafer for his helping hand on whatever computer problem and Silvia Öttl, Miguel Urbaneja, Felix Niederwanger and Fernanda Nieva for listening to my problems.
I also would like to thank the subdwarf community for the great time at several meetings and the many collaborations that resulted from them. Especially I want to thank Brad Barlow for giving me to take the lead on our project and also sharing with me the lead in our future big project. I also want to thank Dave Kilkenny, Pierre Maxted, Roy Østensen for the collaboration.
Moreover, I am grateful to ESO and Calar Alto for granting us observing time, for the staff in the great support during the observations and for ESO and DFG for the travel grants.
This work is supported by the Deutsches Zentrum für Luft- und Raumfahrt (grant 50 OR 1110) and by the Erika-Giehrl-Stiftung.
Furthermore, I would like to thank my parents and my husband for their support and understanding in this stressful time, especially at the end while finishing the thesis. And I am grateful to Guy Burns to agreeing to proofread this very long thesis.